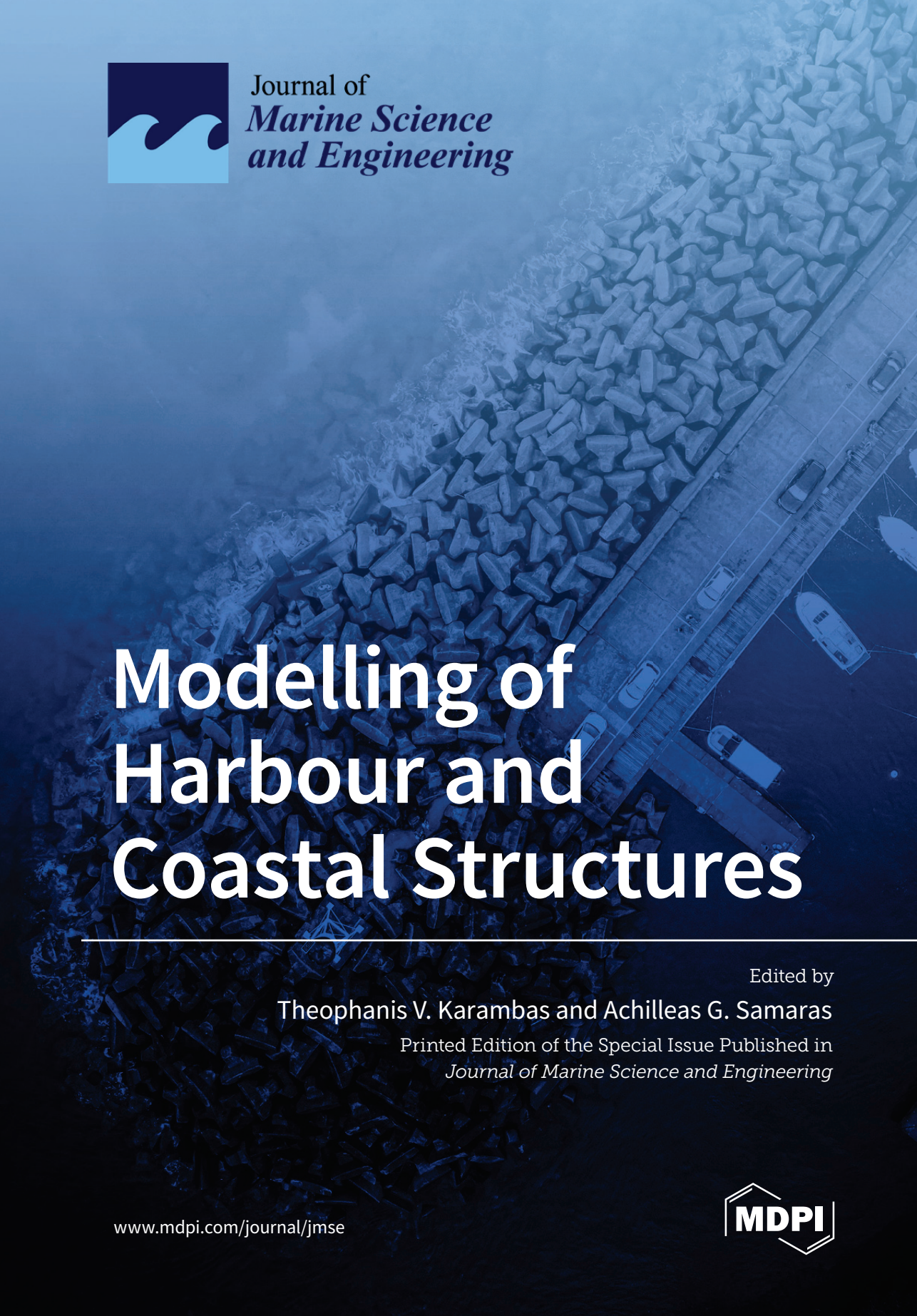

Journal of
Marine Science and Engineering

Modelling of Harbour and Coastal Structures

Edited by
Theophanis V. Karambas and Achilleas G. Samaras

Printed Edition of the Special Issue Published in
Journal of Marine Science and Engineering

www.mdpi.com/journal/jmse

MDPI

Modelling of Harbour and Coastal Structures

Modelling of Harbour and Coastal Structures

Editors

Theophanis V. Karambas
Achilleas G. Samaras

MDPI • Basel • Beijing • Wuhan • Barcelona • Belgrade • Manchester • Tokyo • Cluj • Tianjin

Editors
Theophanis V. Karambas
Aristotle University of Thessaloniki
Greece

Achilleas G. Samaras
Democritus University of Thrace
Greece

Editorial Office
MDPI
St. Alban-Anlage 66
4052 Basel, Switzerland

This is a reprint of articles from the Special Issue published online in the open access journal *Journal of Marine Science and Engineering* (ISSN 2077-1312) (available at: https://www.mdpi.com/journal/jmse/special_issues/model_harbour_coastal_struct).

For citation purposes, cite each article independently as indicated on the article page online and as indicated below:

LastName, A.A.; LastName, B.B.; LastName, C.C. Article Title. *Journal Name* **Year**, *Volume Number*, Page Range.

ISBN 978-3-0365-2464-1 (Hbk)
ISBN 978-3-0365-2465-8 (PDF)

Contents

About the Editors

Theophanis V. Karambas is Professor of Coastal Engineering at the School of Civil Engineering in Aristotle University of Thessaloniki (AUTh). He holds a Civil Engineering Diploma (AUTh, 1986), an M.Sc. degree in Maritime Civil Engineering (University of Liverpool, UK, 1988), and a Ph.D. in Civil Engineering (AUTh, 1991). He has more than 30 years of teaching, professional and research experience on the numerical modelling of coastal hydrodynamics and wave-induced processes (wave propagation and breaking, surf zone hydrodynamics, sediment and pollutants transport, storm surges), design of ports, coastal protection works and structures, environmentally friendly coastal protection, coastal zone management, and climate change effects on coastal zones. He has participated in more than 35 research projects as a scientific responsible, work package leader and partner financed by National (Greece) and EU funds. He has published more than 180 papers in scientific journals and conferences on related subjects and has supervised five Ph.D. students.

Achilleas G. Samaras is Assistant Professor of Maritime Hydraulics, Port and Harbour Engineering at the Department of Civil Engineering in Democritus University of Thrace. He holds a Civil Engineering Diploma (AUTh, 2005), an M.Sc. degree in Environmental Protection and Sustainable Development (AUTh, 2006) and a Ph.D. in Civil Engineering (AUTh, 2010). He has 15 years of experience in research and engineering practice in the fields of wave dynamics and hydrodynamics in marine and coastal areas, sediment transport and coastal morphodynamics, design of harbour and coastal structures, adaptation to climate change in coastal zones, oil spill dynamics, as well as on the dynamics of watershed-coast systems, focusing on the numerical modelling of the above. He has participated in more than 15 research projects and special consultancy projects financed by National (Greece, Italy) and EU funds. He has more than 50 papers in scientific journals and conferences on related subjects.

Journal of
Marine Science and Engineering

MDPI

Editorial

Modelling of Harbour and Coastal Structures

Theophanis V. Karambas [1] and Achilleas G. Samaras [2,*]

[1] Department of Civil Engineering, Aristotle University of Thessaloniki, 54124 Thessaloniki, Greece; karambas@civil.auth.gr
[2] Department of Civil Engineering, Democritus University of Thrace, 67100 Xanthi, Greece
* Correspondence: achsamar@civil.duth.gr or achilleas.samaras@gmail.com

The world's coasts are being continuously reshaped by the interplay between natural- and human-induced pressures. Projected climate change-driven variations in mean sea level, wave conditions and storm surges will add to the existing pressures, as already manifested by the effects of the presently observed climate variability on the frequency and intensity of extremes.

Being the most heavily populated areas in the world, coastal zones host the majority and some of the most important human settlements, infrastructure and economic activities. Harbour and coastal structures are essential to the above, facilitating the transport of people and goods through ports, and protecting low lying areas against flooding and erosion. While based on relatively rigid concepts about service life in the past, nowadays, the design of these structures—or the upgrading of existing structures—should effectively proof them against future pressures, enhancing their resilience and long-term sustainability (i.e., their compliance to performance and operability criteria).

In the above context, the scope of this Special Issue has been to investigate various aspects and methodological approaches on the modelling of harbour and coastal structures. The collection of articles published in the Special Issue is deemed to successfully serve this scope, as the body of work presented in the following covers a wide array of topics on the design of such structures through the study of their interactions with waves and coastal morphology, as well as on their role in coastal protection and harbour design.

Starting with studies that combine traditional and modern approaches for the evaluation of breakwater stability, ref. [1] presents two novel data-driven models based on the Extreme Machine Learning algorithm for the stability assessment of rubble-mound breakwaters, and compare their results to a well-established formula and two formulae derived from machine learning and genetic programming methods. On the same topic, ref. [2] investigates the conventional deterministic approach for the design of composite caisson breakwaters using reliability approaches (combining reliability methods and Monte Carlo simulations), and compares results for the evaluation of the three most significant failure modes of nine breakwaters in Korea. Shifting the focus to the use of advanced numerical models, ref. [3] presents a model based on the modified two-dimensional Navier–Stokes equations for two-phase flows in porous media and uses it to study the effect of various design parameters on the hydrodynamics and flow behavior in the vicinity of rubble-mound, permeable, zero-freeboard breakwaters. On the same topic, ref. [4] combines hydrodynamics and morphodynamics modelling in order to study the scour depth and patterns in front of vertical-wall breakwaters, presenting a coupled model that consists of a hydrodynamic model based on the Reynolds-Averaged Navier–Stokes equations (developed on the OpenFOAM toolbox) and a morphodynamics model based on a new formulation for the estimation of bed and suspended sediment load. On the general topic of damage evaluation in rubble-mound breakwaters, discussion, analysis and useful insights can be found in the companion review papers of [5,6], which cover aspects from the historical review of damage models to damage identification and assessment.

Citation: Karambas, T.V.; Samaras, A.G. Modelling of Harbour and Coastal Structures. *J. Mar. Sci. Eng.* **2021**, *9*, 1108. https://doi.org/10.3390/jmse9101108

Received: 9 October 2021
Accepted: 11 October 2021
Published: 12 October 2021

Moving to topics related to harbour structures and harbour layout design, ref. [7] investigates the siltation problems in the harbour basin and approach channel of the Nowshahr Port in the Caspian Sea through the evaluation of field measurements and numerical modelling, using for the latter the wave, hydrodynamics and morphodynamics models of the DHI MIKE software package in coupled runs. Incorporating an aspect most interesting for natural hazard mitigation to the same general topic, ref. [8] studies the impact of tsunamis on wave agitation and related damages in harbours through a combination of numerical modelling (DHI MIKE software package) and damage mechanisms/threshold analysis; the event studied is the 2003 Boumerdès Earthquake and the analysis regards three ports in the Western Mediterranean.

Regarding approaches related to the design of protection and adaptation measures for coastal areas, ref. [9] presents a methodology for the design of coastal protection projects combining morphological modelling using an in-house model and a new nourishment performance index, the authors' case study being a project (groin field + beach nourishment) in Abu Dhabi, UAE. Shifting the focus to improving the operational usefulness of coastal evolution models, ref. [10] present a wave input-reduction method based on the Shields criterion of incipient motion, applying the wave, hydrodynamics and morphodynamics models of the DHI MIKE software package in coupled runs, along with an in-house model, to a case study in Crete, Greece. Incorporating the impact of climate change on the same general topic, ref. [11] presents a set of interoperable in-house models (i.e., a large-scale wave propagation model, a storm-induced circulation model and an advanced nearshore wave propagation model based on the higher order Boussinesq-type equations) and applies them for projected scenarios of climate change-induced wave and storm surge events, simulating coastal flooding over the low-lying areas of a semi-enclosed bay and testing the effects of different structures on a typical sandy beach (both in northern Greece).

Concluding with studies that incorporate structural and geotechnical analysis aspects to the studied topics, ref. [12] investigates the hydrodynamic coefficients of column-stabilized structures in the coastal environment through combined physical and numerical modelling, the latter using the finite element software ANSYS. Following a combined physical and numerical modelling approach as well, ref. [13] investigates the interaction between wave loading and structural response for mortar-grouted riprap revetments, adopting the Plate on an Elastic Foundation model for the in-house algorithm developed for their numerical analyses. Focusing on an issue relevant to the stability of most structures built in the marine environment, ref. [14] investigates the uncertainty in settlement prediction of pile foundations, studying the performance of an embankment built by hydraulic filling with the use of an analytical model fitted to pile load test outputs, and afterwards tested by a probabilistic approach.

All in all, readers of this Special Issue will find in it a versatile collection of articles on the modelling of harbour and coastal structures, covering a variety of aspects, viewpoints and methodological approaches on the studied topics. The Editors hope that this Special Issue will contribute to research efforts in the field, as well as to the general discussion towards effectively designed coastal protection and adaptation measures in present and future climates.

Author Contributions: Writing, review, editing, T.V.K. and A.G.S. All authors have read and agreed to the published version of the manuscript.

Funding: This research received no external funding.

Institutional Review Board Statement: Not applicable.

Informed Consent Statement: Not applicable.

Data Availability Statement: Not applicable.

Acknowledgments: The Editors would like to thank all people who have contributed to the successful conclusion of the Special Issue (SI) "Modelling of Harbour and Coastal Structures": authors for supporting the SI with their valuable research, reviewers for dedicating their time and expertise

to manuscript evaluation, and, finally, Esme Wang, Managing Editor of JMSE, for the excellent collaboration and continuous support throughout the process.

Conflicts of Interest: The authors declare no conflict of interest.

References

1. Wei, X.; Liu, H.; She, X.; Lu, Y.; Liu, X.; Mo, S. Stability Assessment of Rubble Mound Breakwaters Using Extreme Learning Machine Models. *J. Mar. Sci. Eng.* **2019**, *7*, 312. [CrossRef]
2. Doan, N.S.; Huh, J.; Mac, V.H.; Kim, D.; Kwak, K. Probabilistic Risk Evaluation for Overall Stability of Composite Caisson Breakwaters in Korea. *J. Mar. Sci. Eng.* **2020**, *8*, 148. [CrossRef]
3. Koutrouveli, T.I.; Dimas, A.A. Wave and Hydrodynamic Processes in the Vicinity of a Rubble-Mound, Permeable, Zero-Freeboard Breakwater. *J. Mar. Sci. Eng.* **2020**, *8*, 206. [CrossRef]
4. Karagiannis, N.; Karambas, T.; Koutitas, C. Numerical Simulation of Scour Depth and Scour Patterns in Front of Vertical-Wall Breakwaters Using OpenFOAM. *J. Mar. Sci. Eng.* **2020**, *8*, 836. [CrossRef]
5. Campos, Á.; Castillo, C.; Molina-Sanchez, R. Damage in Rubble Mound Breakwaters. Part I: Historical Review of Damage Models. *J. Mar. Sci. Eng.* **2020**, *8*, 317. [CrossRef]
6. Campos, Á.; Molina-Sanchez, R.; Castillo, C. Damage in Rubble Mound Breakwaters. Part II: Review of the Definition, Parameterization, and Measurement of Damage. *J. Mar. Sci. Eng.* **2020**, *8*, 306. [CrossRef]
7. Mahmoodi, A.; Lashteh Neshaei, M.A.; Mansouri, A.; Shafai Bejestan, M. Study of Current- and Wave-Induced Sediment Transport in the Nowshahr Port Entrance Channel by Using Numerical Modeling and Field Measurements. *J. Mar. Sci. Eng.* **2020**, *8*, 284. [CrossRef]
8. Masina, M.; Archetti, R.; Lamberti, A. 21 May 2003 Boumerdès Earthquake: Numerical Investigations of the Rupture Mechanism Effects on the Induced Tsunami and Its Impact in Harbors. *J. Mar. Sci. Eng.* **2020**, *8*, 933. [CrossRef]
9. Hamza, W.; Tomasicchio, G.R.; Ligorio, F.; Lusito, L.; Francone, A. A Nourishment Performance Index for Beach Erosion/Accretion at Saadiyat Island in Abu Dhabi. *J. Mar. Sci. Eng.* **2019**, *7*, 173. [CrossRef]
10. Papadimitriou, A.; Panagopoulos, L.; Chondros, M.; Tsoukala, V. A Wave Input-Reduction Method Incorporating Initiation of Sediment Motion. *J. Mar. Sci. Eng.* **2020**, *8*, 597. [CrossRef]
11. Samaras, A.G.; Karambas, T.V. Modelling the Impact of Climate Change on Coastal Flooding: Implications for Coastal Structures Design. *J. Mar. Sci. Eng.* **2021**, *9*, 1008. [CrossRef]
12. Zhao, Y.-P.; Chen, Q.-P.; Bi, C.-W.; Cui, Y. Experimental Investigation on Hydrodynamic Coefficients of a Column-Stabilized Fish Cage in Waves. *J. Mar. Sci. Eng.* **2019**, *7*, 418. [CrossRef]
13. Kreyenschulte, M.; Schüttrumpf, H. Tensile Bending Stresses in Mortar-Grouted Riprap Revetments Due to Wave Loading. *J. Mar. Sci. Eng.* **2020**, *8*, 913. [CrossRef]
14. Bueno Aguado, M.; Escolano Sánchez, F.; Sanz Pérez, E. Model Uncertainty for Settlement Prediction on Axially Loaded Piles in Hydraulic Fill Built in Marine Environment. *J. Mar. Sci. Eng.* **2021**, *9*, 63. [CrossRef]

Journal of
Marine Science and Engineering

MDPI

Article

Stability Assessment of Rubble Mound Breakwaters Using Extreme Learning Machine Models

Xianglong Wei [1,2], Huaixiang Liu [2], Xiaojian She [2], Yongjun Lu [2,*], Xingnian Liu [1] and Siping Mo [2]

[1] State Key Laboratory of Hydraulics and Mountain River Engineering, College of Water Resource and Hydropower, Sichuan University, Chengdu 610065, China
[2] State Key Laboratory of Hydrology-Water Resources and Hydraulic Engineering, Nanjing Hydraulic Research Institute, Nanjing 210029, China
* Correspondence: yjlu@nhri.cn

Received: 7 August 2019; Accepted: 4 September 2019; Published: 7 September 2019

Abstract: The stability number of a breakwater can determine the armor unit's weight, which is an important parameter in the breakwater design process. In this paper, a novel and simple machine learning approach is proposed to evaluate the stability of rubble-mound breakwaters by using Extreme Learning Machine (ELM) models. The data-driven stability assessment models were built based on a small size of training samples with a simple establishment procedure. By comparing them with other approaches, the simulation results showed that the proposed models had good assessment performances. The least user intervention and the good generalization ability could be seen as the advantages of using the stability assessment models.

Keywords: breakwater; extreme learning machine; stability assessment; machine learning

1. Introduction

The determination of the armor unit's weight is an important component in the rubble mound breakwater design process, and the armor units play a key role in maintaining the stability of breakwaters under wave attacks. The armor unit's weight can be computed using the stability number of rubble mound breakwaters, N_s, which is commonly obtained from the Hudson formula [1] or the van der Meer formula [2]. Hudson's formula is widely used in breakwater design because of its convenient calculation of the unit mass and stability number. Some important physical factors are not involved in the formula, such as the wave period, wave length and the water depth in front of the breakwater, so other researchers did further research. van der Meer [2] proposed the following formula based on more than 300 runs of breakwater experiments under irregular wave attack. Compared to the Hudson formula, more parameters are included in the van der Meer formula (VM formula), such as the number of wave attacks and the breakwater permeability.

$$N_s = 6.2P^{0.18}\left(\frac{S_d}{\sqrt{N_w}}\right)^{0.2}\frac{1}{\sqrt{\xi_m}} \quad \xi_m < \xi_c \tag{1}$$

$$N_s = 1.0P^{-0.13}\left(\frac{S_d}{\sqrt{N_w}}\right)^{0.2}\cot\alpha\xi_m^p \quad \xi_m \geq \xi_c \tag{2}$$

where P is the permeability of the breakwater, S_d is the damage level, N_w is the number of wave attacks, ξ_m is the surf similarity parameter, ξ_c is the transition condition of the surf similarity, and α is the slope angle. N_s can be expressed as follows in the study of van der Meer [2]:

$$N_s = \frac{H_s}{\Delta D_n} \tag{3}$$

where H_s is the significant wave height, D_n is the nominal median diameter of the stones used in the breakwater, and Δ is the relative mass density, which can be expressed as follows:

$$\Delta = \frac{\rho_\gamma}{\rho} \tag{4}$$

where ρ_γ is the stone mass density and ρ is the water mass density.

Over the past decades, van der Meer's formula has proven to be the most widely used formula to guide rubble mound breakwater design, while at the same time a developed formula was proposed by van der Meer [3,4] to assess the stability of the toe structure of rubble mound breakwaters, based on a new series of experiments. In addition to the studies of Hudson and van der Meer, some other researchers have proposed some novel formulas to assess the stability by analyzing the experimental results, such as [5], Hanzawa, et al. [6], Vidal, et al. [7], Etemad-Shahidi and Bonakdar [8] and Van Gent and Der Werf [9]. Previous studies have shown that the definition equation of the stability number N_s is stable, and that it is a function of the wave height and the relative density and nominal diameter of the stone. Meanwhile, in different studies, the damage condition of the breakwater section used to compute the stability number has various definitions. In the studies of Thompson [10] and Hanzawa [6], a damage parameter was proposed to describe the damage condition of the breakwater section, which was a function of the stone density, stone size, wave height, wave number and erosion area in a cross section, while in the studies of van der Meer [2,3] and Kajima [5], a simple damage level was proposed. A summary of the definitions is listed in Table 1 [11].

Table 1. Various definitions for the damage parameter (damage level).

Definition	Formula	Researcher
Damage parameter	$N_\Delta = \frac{A\rho_r 9 D_{50}}{\rho_a D_{50}^3 \frac{\pi}{6}}$	Thompson and Shuttler (1975) [10]
Damage parameter	$N_0 = \left(\frac{H_{1/3}/\Delta Dn - 1.33}{2.32}\right)^2 N_w^{0.5}$	Hanzawa et al. (1996) [6]
Damage level	$S = \frac{A}{D_{50}^3}$	van der Meer (1988) [2]
Damage level	$N_{od} = \frac{M}{B/D_n}$	van der Meer (1998) [3]
Damage level	$S = 0.6D'$	Kajima (1994) [5]

Note: A is the erosion area in a cross section, ρ_r is the bulk density of the material as laid on the slope, ρ_a is the mass density of the stone, D_{50} is the median diameter of the stone, $H_{1/3}$ is the average wave height of the $N_w/3$ highest waves reaching a rubble mound breakwater of a sea state composed of Nw waves, M is the number of stones removed from the structure in a strip, B is the length of the test section, and D' is the ratio of the number of displaced units to the total number of units.

Besides the empirical formula, N_s can also be predicted by using the machine learning approaches. In the past two decades, a large and growing body of literature has investigated the machine learning approaches to assess the stability of rubble mound breakwaters, such as Artificial Neural Networks (ANN) [12–15], Fuzzy Neural Networks (FNN) [16,17], Model Tress (MT) [8,18], Support Vector Machine (SVM) [19–22], and Genetic Programing (GP) [23]. These studies have shown that the performance of machine learning approaches is better than that of the traditional formulas [23,24]. The study of Balas, Koç and Tür [13] provides new insights into improving the prediction accuracy of ANN models via the principal component analysis, which could reduce the needed amount of training data and transform the original data set into a set of uncorrelated variables that capture all of the variance of the original data set [25], but many methods still suffered from complex establishment procedures and large demands for the training sets' size. Thus, reducing the parameter counts and the training data size, and simplifying the training process, should be a concern for further research.

Besides the empirical formula, N_s can also be predicted by using the machine learning approaches. In the past two decades, a large and growing body of literature has investigated the machine learning approaches to assess the stability of rubble mound breakwaters, such as Artificial Neural Networks (ANN) [12–15], Fuzzy Neural Networks (FNN) [16,17], Model Tress (MT) [8,18], Support Vector

Machine (SVM) [19–22], and Genetic Programing (GP) [23]. These studies have shown that the performance of machine learning approaches is better than that of the traditional formulas [23,24]. The study of Balas, Koç and Tür [13] provides new insights into improving the prediction accuracy of ANN models via the principal component analysis, which could reduce the needed amount of training data and transform the original data set into a set of uncorrelated variables that capture all of the variance of the original data set [25], but many methods still suffered from complex establishment procedures and large demands for the training sets' size. Thus, reducing the parameter counts and the training data size, and simplifying the training process, should be a concern for further research.

The Extreme Learning Machine is a robust machine learning algorithm based on the Single-Hidden Layer Feedforward Network (SLFN) [26], which was very simple in t neural network architecture. Previous studies have shown that the ELM could be used in wide areas, such as classification [27–30] and regression [31–34], and that it showed a good generalization performance at fast learning speeds [35]. The main advantage of ELM is that the user-defined parameters for training an assessment ELM model only include the kind of activation function and the number of hidden neurons, which makes the model establishment very convenient; besides, the ELM model can obtain a high prediction accuracy based on a small size of training data sets. Based on this, the ELM method was proposed to develop a novel and simple stability assessment model of rubble mound breakwaters. This is the first study on the application of ELM in the stability assessment of rubble mound breakwaters. Therefore, the findings in this study make a contribution to the stability assessment and to the design of the rubble mound breakwaters.

This paper is organized as follows. The fundamentals of the ELM approach and the model establishment are introduced in Section 2. In Section 3, the application of the ELM approach for the stability assessment of rubble-mound breakwaters is discussed, and a comparison between the ELM approach and other approaches is given. The main findings of this paper are summarized in Section 4.

2. Extreme Learning Machine Models

The Extreme Learning Machine is widely used in regression and classification [36]. However, up to now, few studies involving applications of ELM in coastal engineering have been published. A search of the literature revealed that ELM was once used to predict the sea level, tide, and wave heights [37–40]. In the following subsection, a brief introduction about the fundamentals of Extreme Learning Machine models is given to clarify the process details of the ELM model establishment. More information about ELM models can be found in Huang, Zhu and Siew [26,35], Huang, Huang, Song and You [36].

2.1. Fundamental of Extreme Learning Machine Model

The goal of the learning process is to find the relation between input training data sets and output training labels. Considering an ELM neural network with n neurons in the input layer, l neurons in the hidden layer, and m neurons in the output layer, the general structure of ELM is shown in Figure 1:

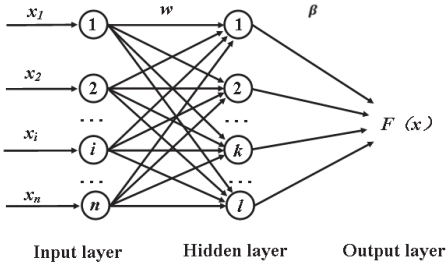

Figure 1. General structure of ELM.

The weight w between the neurons in the input layer and the neurons in the hidden layer can be expressed as:

$$w = \begin{bmatrix} \omega_{11} & \cdots & \omega_{1n} \\ \vdots & \vdots & \vdots \\ \omega_{l1} & \cdots & \omega_{ln} \end{bmatrix}_{l \times n} \tag{5}$$

where w_{ji} is the weight between the neuron i in the input layer and the neuron j in the hidden layer.

Meanwhile, the weight β between the neurons in the hidden layer and the neurons in the output layer can be expressed as:

$$\beta = \begin{bmatrix} \beta_{11} & \cdots & \beta_{1m} \\ \vdots & \vdots & \vdots \\ \beta_{l1} & \cdots & \beta_{lm} \end{bmatrix}_{l \times m} \tag{6}$$

where β_{jm} is the weight between the neuron j in the hidden layer and the neuron m in the output layer.

The bias b in the hidden layer is:

$$b = \begin{bmatrix} b_1 \\ b_2 \\ \vdots \\ b_l \end{bmatrix} \tag{7}$$

For the given training samples X and the output matrix Y:

$$X = \begin{bmatrix} x_{11} & \cdots & x_{1Q} \\ \vdots & \vdots & \vdots \\ x_{n1} & \cdots & x_{nQ} \end{bmatrix}_{n \times Q} \tag{8}$$

$$Y = \begin{bmatrix} y_{11} & \cdots & y_{1Q} \\ \vdots & \vdots & \vdots \\ y_{m1} & \cdots & y_{mQ} \end{bmatrix}_{m \times Q} \tag{9}$$

Assuming that the activation function in the hidden layer was $g(x)$, then the output T is:

$$T = \left[t_1, t_2, \ldots t_Q\right],\ t_j = \begin{bmatrix} t_{1j} \\ \vdots \\ t_{mj} \end{bmatrix} = \begin{bmatrix} \sum_{i=1}^{l} \beta_{j1} g\left(w_i x_j + b_i\right) \\ \vdots \\ \sum_{i=1}^{l} \beta_{im} g\left(w_i x_j + b_i\right) \end{bmatrix} (\mathrm{j} = 1, 2, 3, \ \ldots, \ \mathrm{Q}) \tag{10}$$

where $\omega_i = [\omega_{i1}, \omega_{i2}, \ldots \omega_{im}]$, and $x_j = \left[x_{1j}, x_{2j}, \ldots, x_{nj}\right]^T$.

Equation 11 can be rewritten in the following form:

$$H\beta = T' \tag{11}$$

where T' is the transposed matrix of T. H is the hidden layer output matrix of the neural network, which is as follows:

$$H\left(\omega_1, \omega_2, \ldots \omega_l,\ b_1, b_2, \ldots b_l, x_1, x_2, \ldots, x_Q\right) = \begin{bmatrix} g(w_1, b_1, x_1) & \cdots & g(w_l, b_l, x_1) \\ & \vdots & \\ g\left(w_1, b_1, x_Q\right) & \cdots & g\left(w_l, b_l, x_Q\right) \end{bmatrix}_{Q \times l} \tag{12}$$

The minimum norm least-squares solution of $\min_{\beta} H\beta - T'$ is unique:

$$\hat{\beta} = H^{+}T' \tag{13}$$

where H^{+} is the Moore-Penrose generalized inverse of the matrix of H.

More details about the ELM theory can be found in the studies of Huang, Zhu and Siew [35], Huang, Huang, Song and You [36].

The activation functions used in this paper are as follows:

Sigmoid function:

$$g(w_i x + b_i) = \frac{1}{1 + (\exp(-w_i x + b_i))} \tag{14}$$

Sin function:

$$g(w_i x + b_i) = \sin(w_i x + b_i) \tag{15}$$

Hardlim function:

$$g(w_i x + b_i) = \begin{cases} 1\ w_i x + b_i \geq 0 \\ 2\ w_i x + b_i < 0 \end{cases} \tag{16}$$

Trigonometric basis function:

$$g(w_i x + b_i) = \begin{cases} 1 - |w_i x + b_i| \ -1 \leq w_i x + b_i \leq 1 \\ 0 \text{ else} \end{cases} \tag{17}$$

Radial basis function:

$$g(w_i x + b_i) = \exp\left(-\frac{\|x - w_i\|^2}{b_i^2}\right) \tag{18}$$

2.2. Model Establishment

Based on the damage level of the breakwater sections, two ELM models were built to predict the stability number of breakwaters. The first model (M1) was aimed at predicting the stability number of the breakwater sections whose damage level was in the range of 2 to 8. The other model (M2) was aimed at predicting the stability number of the breakwater sections whose damage level was in the range of 8 to 32 (8 was not included). High damage levels (S > 8) are not common in design practice [18]. Basheer and Hajmeer [41] (cited in Balas, Koç and Tür [13]) pointed out that there are no mathematical rules to determine the required amounts of training data and testing data. The number of the training data sets ranges from 90 to 579 in the previous studies discussed earlier. In the current study, 100 data points for training and 100 data points for testing were randomly selected for each model (M1, M2) from the experimental data of van der Meer [2], according to the damage level of the data, which can be found in in the Supplementary Materials. Five parameters we selected as the input nodes: the permeability, damage level, wave attack number, slope angle, and surf similarity parameter. The range of parameters used in the M1 and M2 models were presented in Figure 2 and Table 2.

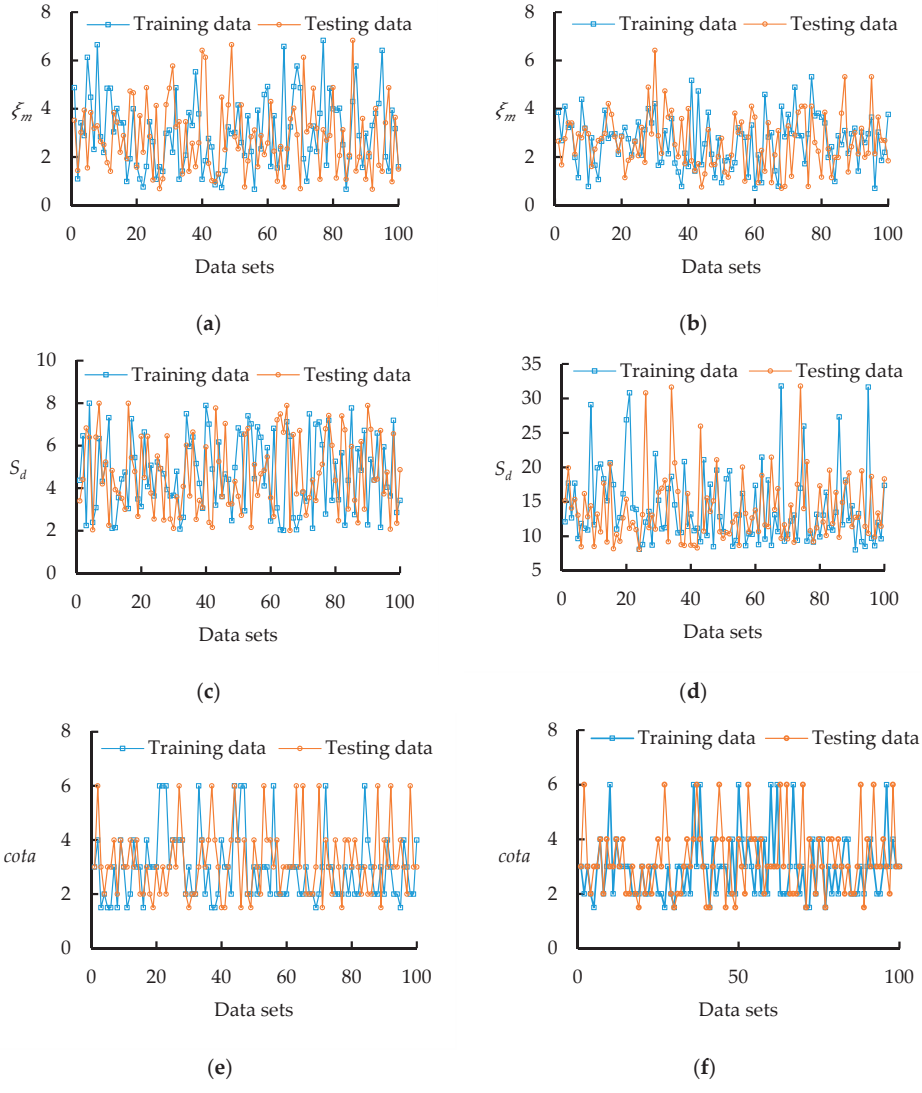

Figure 2. Parameters used in the M1 and M2 models: (**a**) the permeability of M1; (**b**) permeability of M2; (**c**) damage level of M1; (**d**) damage level of M2; (**e**) slope angle of M1; and (**f**) slope angle of M2.

Table 2. The range of parameters used in the M1 and M2 models.

Parameters	M1 Training Data	M1 Testing Data	M2 Training Data	M2 Testing Data
P	0.1, 0.5, 0.6	0.1, 0.5, 0.6	0.1, 0.5, 0.6	0.1, 0.5, 0.6
S_d	2–8	2–8	8–32	8–32
cot a	1.5–6	1.5–6	1.5–6	1.5–6
N_w	1000, 3000	1000, 3000	1000, 3000	1000, 3000
ξ_m	0.67–6.83	0.67–6.83	0.7–5.8	0.7–6.4
Ns	1.19–3.61	1.17–4.62	1.41–4.3	1.41–4.3

The flow chart of the ELM model establishment is shown in Figure 3. For each model, 5000 learning runs from the training data are necessary before the assessment model establishment. In order to evaluate the assessment performance of these ELM models, the bias (*BIAS*), correlation coefficient (*CC*), scatter index (*SI*) and index of agreement (I_a) are introduced as follows:

$$BIAS = \sum_{i=1}^{N} \frac{1}{N}(Y_i - X_i) \tag{19}$$

$$SI = \frac{\sqrt{\frac{1}{N}\sum_{i=1}^{N}(Y_i - X_i)^2}}{\overline{X_i}} \tag{20}$$

$$CC = \frac{\sum_{i=1}^{N}\left(X_i - \overline{X}\right)\left(Y_i - \overline{Y}\right)}{\sqrt{\sum_{i=1}^{N}\left(X_i - \overline{X}\right)^2 \sum_{i=1}^{N}\left(Y_i - \overline{Y}\right)^2}} \tag{21}$$

$$I_a = 1 - \frac{\sum_{i=1}^{N}(Y_i - X_i)^2}{\sum_{i=1}^{N}\left(\left|\left(Y_i - \overline{X}\right)\right| + \left|\left(X_i - \overline{X}\right)\right|\right)^2} \tag{22}$$

where X_i are the measured values, and their average is $\overline{X}$; Y_i are the predicted values, and their average is $\overline{Y}$; and N is the number of observations.

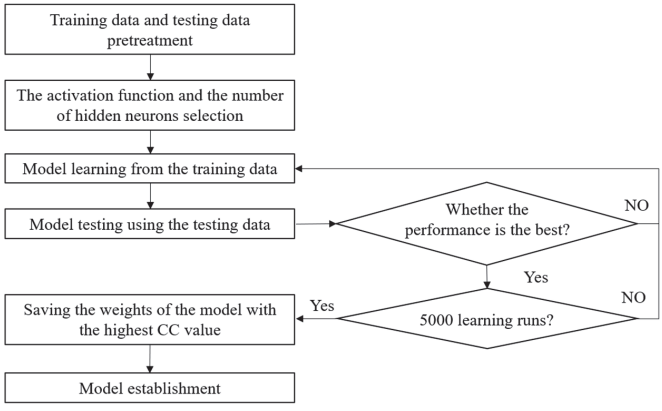

Figure 3. Flow chart of the ELM model establishment.

A search of the literatures shows that the *CC* parameter was the most widely used index to evaluate the model performances, meanwhile, when the *CC* value of the model reaches the highest value, the *Ia* value may not, so in the training process, the value of *CC* was selected as the only evaluation index of the models. After the training process, the weights of the model with the highest *CC* value are recorded, which can be used for the stability assessment. The data used for establishing the models is provided in the Supplementary Materials. The weights used in the M1 model and the M2 model are listed in Appendix A. The code used in this paper is provided in Appendix B.

3. Results and Discussion

3.1. The Influence of Hidden Neurons on the Assessment Performance of ELM Models with Different Activation Functions

The assessment performances of the ELM models are mainly determined by the number of the hidden neurons and the activation functions. Low damage levels (S < 8) are more common in the design practice for rubble mound breakwaters, as previously mentioned [18], and the selection of training data has little influence on this issue, so the M1 models (S < 8) were built to research the influence of the hidden neurons and the activation functions on the model performance.

Figure 4 shows the assessment performance of ELM models with different activation functions and different numbers of hidden neurons. The number of hidden neurons of these models were set from 5 to 90 with an interval of 5. It can be seen from the figures that the evaluation criteria *CC* and I_a are increasing following the addition of hidden neurons when the number of the hidden neurons is within the range of 5 to 20; then, the values of *CC* and I_a stay relatively constant when the number of the hidden neurons is above 20. The assessment performance criteria have a rapidly decreasing trend as the hidden neurons number increases in the range of 50 to 90, which indicates that too many hidden neurons lead to over-fitting. The models with the best assessment performance were the models built with 40–50 hidden neurons in the hidden layer, no matter what activation function was used in the models. What stands out in Figure 4 is that, for an ELM model with a randomly selected number of hidden neurons from 20 to 50, I_a is no less than 0.9 and CC is no less than 0.85. The selection of the activation function has little influence on the best performance of each model, which is mainly because the training data has few noisy data sets and is pure enough. The simulation results show that the ELM algorithm has a good generalization performance for the stability assessment.

A comparison of these results reveals that the ELM model with the maximum CC and I_a was the model built with 45 hidden neurons and the Sin function. The parameters for the model training and application were determined for these conditions.

3.2. Predicted Performance Comparison of Different Methods

Based on the previous results, the M1 assessment model and the M2 assessment model were built using the ELM algorithm with 45 hidden neurons in the hidden layer and the Sin function as the activation function. The M1 model was used to assess the stability numbers of the breakwater sections at a low damage level ($2 \le S \le 8$), and the M2 model was used to assess the stability numbers of the breakwater sections at a high damage level ($8 < S < 32$). In order to clarify the advantages of the M1 and M2 models, the VM formula [2], the EB formula [8], which was built using the model trees models with a high prediction accuracy, and the GPM1 formula [23], were selected to assess the stability using the same testing data. In the literatures, the EB formula and the GP method have the highest I_a values among those machine learning approaches, which indicates the best prediction performance. The GPM3 formula was not obtained in [23], and the GPM1 model has a similar performance to the GPM3 model presented in [23], so the GPM1 model was selected. These assessment results, predicted by different methods, were prepared and are shown in Figures 5 and 6, respectively.

Figure 5 provides the assessment performance for the breakwater sections that were at a low damage level using the VM formula, EB formula, GPM1 formula and M1 model. As shown in Figure 5, more than half of the predicted stability numbers of the breakwater sections were smaller than the measured values using the VM formula, the EB formula and the GPM1 formula. The assessment performance of the M1 model was more balanced: about half of the predicted stability numbers were smaller than the measured values, while the other half were larger than the measured values.

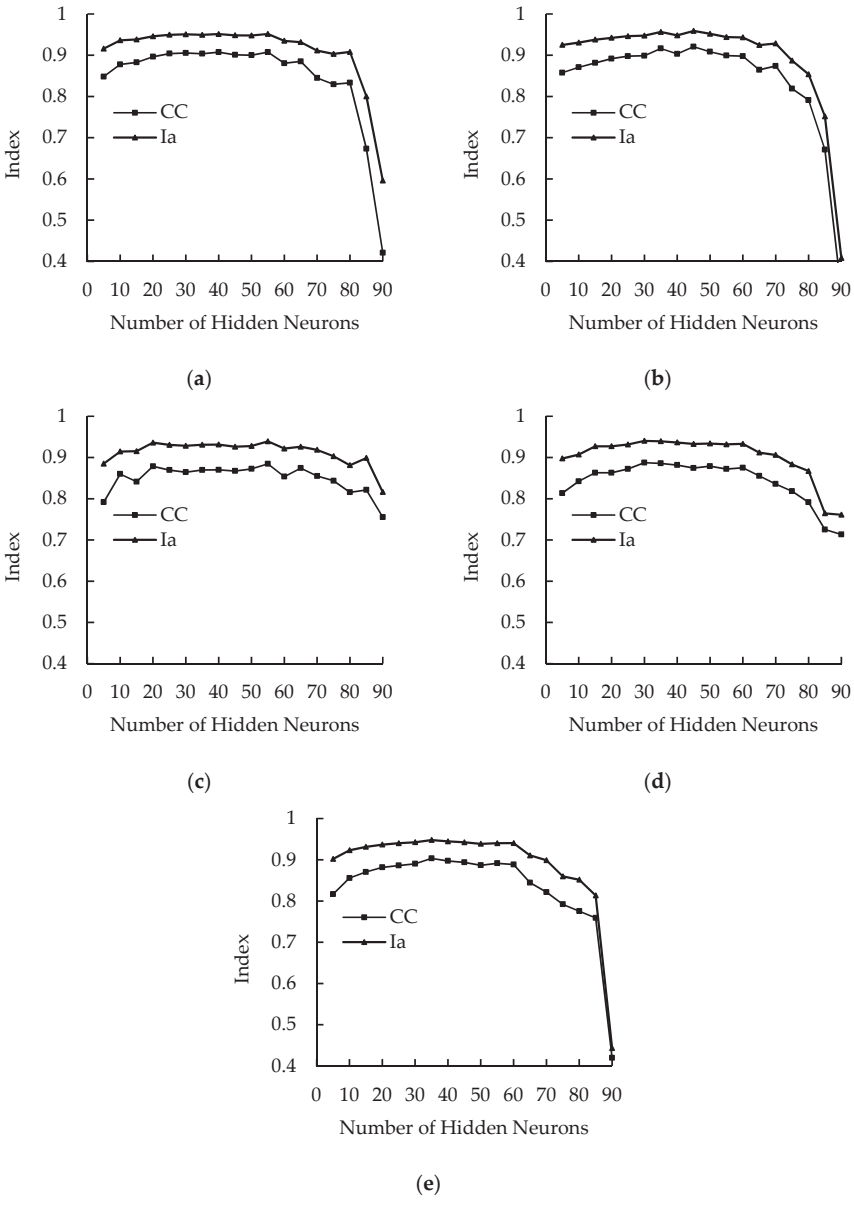

Figure 4. Performances of the ELM models with different hidden nodes: (**a**) Sigmoid function; (**b**) Sin function; (**c**) Hardlim function; (**d**) Tribas function; and (**e**) Radbas function.

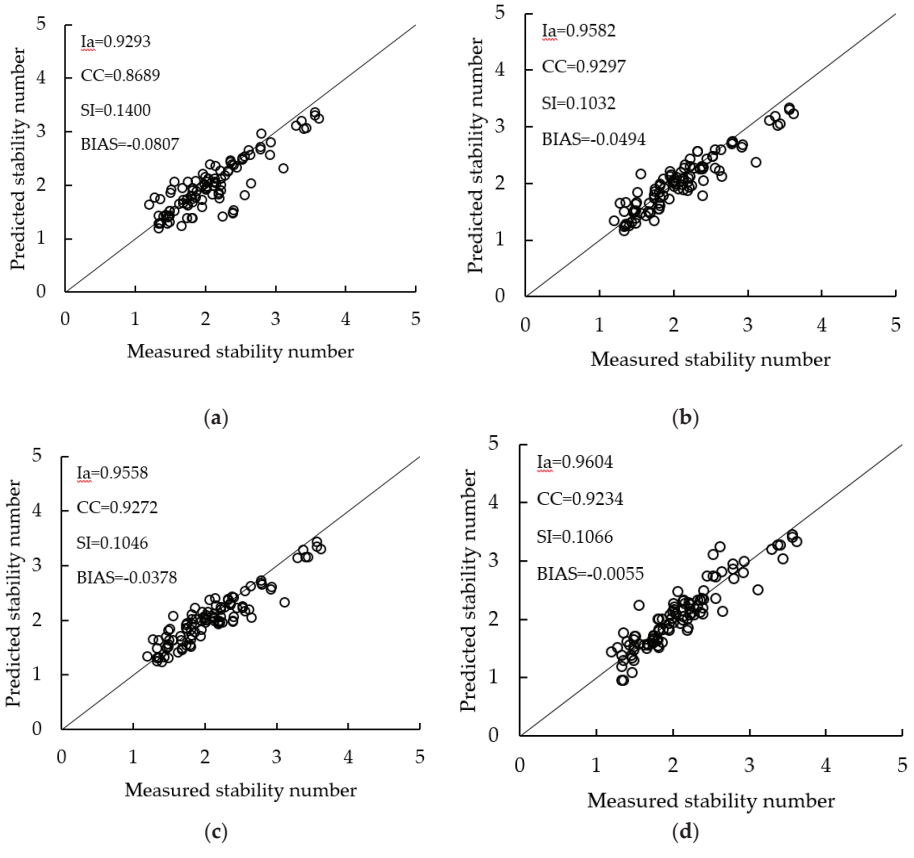

Figure 5. A performance comparison of different methods: (**a**) the van der Meer formula; (**b**) Etemad-Bonakdar formula; (**c**) GPM1 formula; and (**d**) M1 model.

Several statistical indices were introduced to assess the prediction performance of these approaches, such as the *BIAS*, *CC*, *SI*, and I_a. Lower values of *BIAS* and *SI* represent a better assessment performance, and higher values of *CC* and I_a indicate a better prediction agreement. When the values of *CC* and I_a are close to 1, this indicates a perfect agreement between the predicted and measured stability numbers. Table 3 lists the statistical index values of the three approaches. As shown in the table, the *CC* and I_a values of the VM formula are the smallest among these three assessment approaches, while the *BIAS* and the *SI* values are the largest, which indicates that the performance of the VM formula has the lowest quality agreement. The *CC* and I_a values of the EB formula, the GPM1 formula and the M1 model are nearly the same, while on the other hand the *SI* values of the two methods are also nearly the same. The evaluation indices show that the EB formula, the GPM1 formula and the M1 model have similar abilities for predicting the stability number of breakwaters with a low damage level, but that the M1 model was built based on a smaller size of training data, which indicates that the M1 model has a good generalization ability.

The performance of different approaches was also evaluated for a wider range of damage levels, i.e., $8 < S < 32$. The performances of the VM formula, EB formula, GPM1 formula and M2 model are discussed in the following paragraphs. All the predicted results are shown in Figure 6.

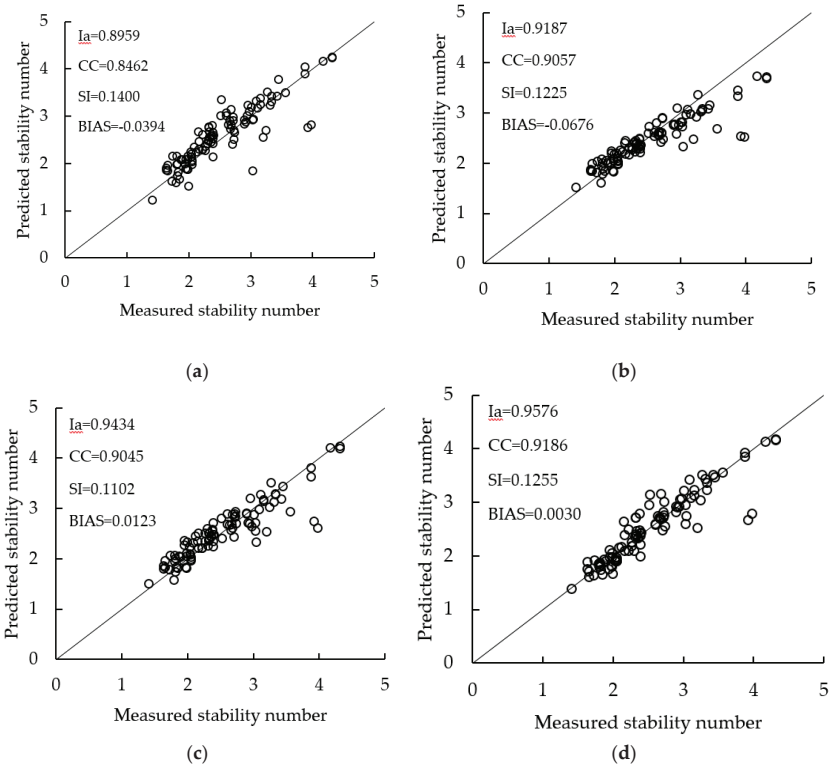

Figure 6. A performance comparison of different methods: (**a**) the van der Meer formula; (**b**) Etemad-Bonakdar formula; (**c**) GPM1 formula; and (**d**) M2 model.

Table 3. The evaluation indices of the performance of different models ($2 \leq S \leq 8$).

Methods	*BIAS*	*SI*	*CC*	I_a
VM	−0.0807	0.1400	0.8689	0.9293
EB	−0.0494	0.1032	0.9297	0.9582
GPM1	−0.0378	0.1046	0.9272	0.9558
ELM(M1)	−0.0055	0.1066	0.9234	0.9604

As shown in Figure 6, the VM formula overestimates most of the stability numbers; the same finding could also be found in the study of Etemad-Shahidi and Bali [18]. Meanwhile, on the opposite side, many stability numbers are underestimated by the EB formula. The number of overestimated and underestimated stability numbers is nearly the same for the predictions using the GPM1 model and the M2 model. In addition, the stability numbers predicted by the M2 model are more concentrated on the line of complete agreement than those of the other two approaches. The evaluation indices of these approaches are listed in Table 4. As seen in Table 4, the *CC* and I_a of the M2 model are the highest, while the *BIAS* and *SI* of the M2 model are the lowest, which indicates that the M2 model has the best performance for the stability number prediction of the breakwater sections with a wider damage level range.

Further research was done on the comparison of the assessment performance of different artificial neural network approaches from previous studies. The training parameters and the evaluation indices for these models are listed in Table 5. As can be seen, many kinds of machine learning approaches have been applied in predicting the stability numbers for breakwaters. The number of input parameters

of the training models have ranged from 4 to 8, and the number of the training data sets has ranged from 100 to 554. In the current paper, 5 input parameters and 100 sets of training data were used in the training processes of the M1 and M2 models, and the I_a values of the M1 and M2 models are higher than those in many of the previous studies, whose models were built using a larger size of training data and more input parameters. It should also be noted that the I_a or *CC* values should not be the only evaluation criteria in comparing different methods, since the testing data for each model was not the same. A comparison between the MT2 model (EB formula), GPM1 formula and the ELM method was made in the previous section by using the same testing data, which presented the advantages of the ELM method. The testing data for the MT2 model and the GPM1 formula in [8,23] is not the same testing data used in this paper, which leads to the different I_a and *CC* values presented in Tables 3–5. The *CC* values of HNN models in the study of Balas, Koç and Tür [13] are slightly higher than the *CC* values of the M1 and M2 models in the current paper, while the training data is pre-processed by using the principal component analysis (PCA), and the original data sets are 554 sets of experimental data. The PCA could remove the noisy data from the training data and extract the required information [13], so the use of PCA enhances the prediction ability of the machine learning models. It could also be expected that a PCA-ELM model will get a better prediction performance.

Table 4. The evaluation indices of the performance of different models (8 < S < 32).

Methods	*BIAS*	*SI*	*CC*	I_a
VM	−0.0394	0.1400	0.8462	0.8959
EB	−0.0676	0.1225	0.9057	0.9189
GPM1	0.0123	0.1102	0.9045	0.9434
ELM(M2)	0.0030	0.1022	0.9186	0.9576

Table 5. Calculation details of different machine learning approaches.

Researchers		*CC*	I_a	Training Data	Input Parameters	Testing Data
Mase, Sakamoto and Sakai [24]		0.91		100	6	No
Dong and Park [12]	I		0.914	100	6	641
	II		0.906	100	5	641
	III		0.902	100	6	641
	IV		0.915	100	7	641
	V		0.952	100	8	641
Kim, Dong and Chang [15]	I	0.905	0.948	207	5	119
	II	0.913	0.954	201	5	114
Erdik [16]	FL		0.945	579	6	579
Balas, Koç and Tür [13]	HNN-1	0.936		180 (PCA)	5	76
	HNN-2	0.927		180 (PCA)	4	76
Koç and Balas [17]	GA-FNN		0.932	166 (PCA)	5	42
	HGA-FNN		0.947	166 (PCA)	5	42
Etemad-Shahidi and Bonakdar [8]	MT1	0.931	0.97	386	5	193
	MT2	0.968	0.976	386	6	193
Koc, Balas and Koc [23]	GPM1		0.98	207	7	372
	GPM2		0.95	40	7	22
	GPM3		0.989	207	7	372
	GPM4		0.991	40	7	22
	VM		0.969			372
	VM		0.65			22
Current Study	ELM-M1	0.923	0.960	100	5	100
	ELM-M2	0.919	0.958	100	5	100

4. Conclusions

The aim of the present research was to develop novel and simple Extreme Learning Machine models to predict the stability number for rubble mound breakwater sections. Two ELM models were established to predict the stability number for breakwater sections: the M1 model for low damage levels ($2 \leq S \leq 8$) and the M2 model for high damage levels ($8 < S < 32$). It was shown that the prediction performances of ELM models were determined by the hidden neurons number, the size of the training data sets and the leaning times; furthermore, the selection of the activation function had little influence on the performance of these models. A comparison of the ELM models and other approaches suggested that the ELM models achieve a good performance with small user-defined parameters and a small training data set size. The key strength of this ELM approach is its good generalization ability and the simple process in establishing the models, which suggested that the ELM models could be an effective and simple tool for breakwater design and stability assessment. In the future, it would be interesting to study the hybrid ELM model, such as the PCA-ELM model, to assess the stability number for rubble mound breakwaters.

Supplementary Materials: The following are available online at http://www.mdpi.com/2077-1312/7/9/312/s1, training data of M1; testing data of M1; training data of M2; testing data of M2.

Author Contributions: Conceptualization, X.W. and Y.L.; methodology and software, X.W.; writing—original draft preparation, X.W., H.L.; writing—review and editing, Y.L., H.L., X.S., S.M. and X.L.; supervision, Y.L.

Funding: This research was funded by the National Natural Science Foundation of China (Grant No. 51520105014), the Postgraduate Research & Practice Innovation Program of Jiangsu Province (Grant No. KYCX19_2328), and the National Key R&D Program of China (Grant No. 2016YFC0402108 & Grant No. 2017YFC0405900).

Acknowledgments: The authors wish to sincerely thank van der Meer for his free database on the stability of rubble mound breakwaters. We also appreciate the reviewers for their valuable suggestions and questions.

Conflicts of Interest: The authors declare no conflict of interest.

Appendix A

Table A1. Weights of M1.

0.5241	26.4975	0.8109	−0.4255	0.6935	−0.2008
0.5979	−3.6891	0.8853	0.6774	0.6278	−0.9448
0.6609	4.1169	0.1518	0.2682	0.2991	0.0216
0.9402	1.1036	−0.5524	0.7574	0.7449	−0.6862
0.1974	−32.1789	−0.3415	0.2084	−0.7634	−0.1137
0.8710	−3.2400	−0.6313	0.8539	−0.3247	0.9143
0.7430	−29.8057	0.3799	−0.2154	−0.7326	−0.9678
0.2418	5.5068	−0.8844	0.7903	0.7482	−0.7737
0.5977	−22.8297	0.1486	−0.9762	0.4362	0.0493
0.7125	1.7637	0.1595	0.5090	−0.9902	0.1901
0.1448	21.5258	−0.5829	0.0194	−0.7497	−0.6622
0.4441	−4.4733	−0.8343	0.7352	0.8387	−0.2093
0.1918	6.0145	−0.7073	0.0374	0.8523	0.7221
0.7374	52.4679	−0.4033	−0.0100	0.8501	−0.7359
0.1496	−9.1100	0.6958	−0.2846	0.9258	−0.7403
0.1726	−3.6265	0.4105	−0.9711	0.5676	−0.2996
0.8718	−8.6176	−0.9463	−0.0608	−0.5387	−0.6198
0.8638	32.5670	0.7170	0.0887	−0.4715	−0.5685
0.2632	13.7757	0.1976	−0.0730	−0.7203	−0.0630
0.1091	−9.6165	0.0072	−0.6522	0.2843	0.5996
0.3324	3.5370	0.3308	0.2424	−0.6404	0.6969

Table A1. *Cont.*

BHN_1=	0.1969	InW_1=	−30.1128	InW_2=	−0.7382	−0.5162	−0.7029	0.4078
	0.5033		40.9492		−0.1724	−0.1571	0.2812	−0.6081
	0.7217		−2.1417		0.0027	−0.1367	0.9792	−0.1936
	0.0935		−4.5602		0.7380	−0.4168	0.7734	−0.7967
	0.8949		−7.4840		−0.8876	−0.7521	0.7573	0.1826
	0.9296		−51.8195		−0.3970	0.0788	0.6631	−0.9412
	0.3114		−32.1941		0.5991	0.3968	−0.0596	0.2747
	0.8365		0.7267		0.9239	0.6791	0.7207	−0.1689
	0.6055		35.3792		−0.4155	−0.4794	−0.8263	−0.0045
	0.1465		5.8143		−0.9828	−0.4143	0.2699	0.9241
	0.9326		−14.1016		0.5911	0.8271	0.5772	0.0635
	0.1928		9.7569		−0.4223	−0.3700	0.2338	0.7443
	0.4138		2.4507		−0.1683	−0.2665	−0.5608	0.6952
	0.0855		−7.5543		−0.9139	−0.9217	−0.7361	−0.3699
	0.7125		8.2359		−0.7147	0.3655	−0.7379	−0.7774
	0.5891		3.9906		0.4442	0.7030	0.2163	0.0113
	0.8273		1.0311		0.9852	0.9763	−0.4108	−0.4178
	0.4677		11.6137		−0.2928	−0.8980	−0.1545	0.3437
	0.6765		6.5585		0.2751	0.9346	0.7867	0.6949
	0.3229		−7.2543		−0.1302	0.1766	0.9851	−0.9479
	0.7244		−8.8476		−0.4926	0.8206	0.0350	−0.9965
	0.1206		−10.8684		0.0382	−0.5207	0.0727	0.9225
	0.5268		−5.1499		−0.1425	−0.2191	0.4494	−0.9388
	0.2891		8.4672		0.6724	0.1706	−0.4620	0.9983

Table A2. Weights of M2.

0.4319	−42.0761	−0.9071	−0.2011	0.4272	0.8116
0.0320	−20.9949	−0.3291	−0.0591	−0.4020	0.8705
0.5944	−32.7021	−0.8404	−0.6064	0.8841	0.6630
0.6627	43.8901	−0.7591	−0.2472	0.8186	0.9823
0.9264	13.2387	0.8394	−0.8762	−0.1618	−0.3568
0.5949	−20.2892	0.5871	0.8688	−0.0913	0.7016
0.8525	−63.1985	0.3422	−0.7897	−0.4640	−0.2132
0.8806	−116.6938	0.2035	−0.5851	−0.2849	−0.8588
0.6270	−13.5202	0.7838	0.9148	−0.8121	0.6147
0.2328	35.2013	−0.1258	−0.3481	−0.7869	−0.1297
0.2941	3.1475	−0.8012	0.0277	−0.4674	−0.6218
0.2577	12.4026	−0.8559	−0.6591	−0.9608	0.2650
0.6162	0.2601	−0.4507	−0.2077	−0.4970	0.7523
0.1584	−3.0225	0.9716	0.8243	−0.4446	0.6805
0.5654	−7.7516	−0.6291	−0.5789	−0.5272	0.3921
0.5730	5.6515	−0.2855	−0.5305	0.4384	0.8396
0.6728	27.5190	0.0217	0.4931	−0.1090	−0.5729
0.7424	0.7453	−0.4198	0.1380	0.4327	−0.9063
0.7593	36.1610	0.4848	0.2726	0.6648	0.6994
0.7122	44.1426	−0.6639	−0.4197	0.5753	0.2885
0.6100	−16.2722	−0.0565	−0.0394	0.8366	−0.8595

Table A2. *Cont.*

BHN_2=	0.0537	InW_2=	−1.1557	InW_2=	−0.7270	−0.1948	−0.1188	−0.1234
	0.4458		22.3288		0.5387	0.8696	−0.4597	0.9628
	0.8475		−1.6268		0.7513	−0.9025	−0.6607	0.6460
	0.9733		−83.7627		0.3622	−0.6518	−0.4596	−0.5125
	0.8544		22.4302		0.8799	−0.2234	−0.4083	−0.7212
	0.3858		−21.6072		−0.5399	0.1999	0.1068	−0.4392
	0.9096		−2.8837		−0.4029	−0.6285	0.8447	−0.2820
	0.1069		−28.1949		−0.7637	0.7851	−0.3326	−0.1881
	0.2582		−18.8255		−0.0014	−0.1194	0.5881	0.2810
	0.5765		47.8772		0.5480	−0.4075	−0.7139	−0.6196
	0.3990		−5.0568		0.8476	0.1595	−0.4691	0.1434
	0.3779		9.6864		0.7929	−0.4492	−0.8683	−0.4401
	0.3411		10.6359		−0.4233	0.5854	−0.9226	0.3489
	0.2897		3.4956		0.8980	−0.7244	0.0454	0.2533
	0.7287		45.6903		−0.4528	0.5858	0.1254	−0.0241
	0.7738		−45.6212		0.8116	−0.2095	−0.0985	−0.6733
	0.5252		25.9720		0.2493	−0.7998	−0.2112	−0.3585
	0.8545		−50.5003		−0.0441	0.5296	−0.0523	0.2865
	0.0416		3.4476		−0.8948	0.9645	−0.8378	0.9041
	0.6695		8.8539		−0.6859	−0.9783	−0.8757	−0.9541
	0.8819		20.7560		0.0010	0.8347	−0.0483	−0.2737
	0.9352		133.8480		0.2844	−0.8046	−0.2266	−0.8481
	0.1300		5.0666		0.6626	−0.6074	0.4537	−0.5816
	0.9134		14.3699		−0.5942	0.5127	−0.0012	−0.3285

Appendix B

The code for the Extreme Learning Machine can be downloaded on the following website: http://www.ntu.edu.sg/home/egbhuang/.

References

1. Hudson, Y. Laboratory investigation of rubble-mound breakwater. *Proc. ASCE* **1959**, *85*, 93–122.
2. Van der Meer, J.W. *Rock Slopes and Gravel Beaches under Wave Attack*; Delft University of Technology: Delft, The Netherlands, 1988.
3. Pilarczyk, K. *Dikes and Revetments Design, Maintenance and Safety Assessment*; Routledge: London, UK, 1998.
4. Meulen, T.v.d.; Schiereck, G.J.; d'Angremond, K. Rock toe stability of rubble mound breakwaters. *Coast. Eng.* **1996**, *83*, 1971–1984.
5. Kajima, R. A new method of structurally resistive design of very important seawalls against wave action. In Proceedings of the Wave Barriers in Deepwaters, Yokosuka, Japan, 10–14 January 1994; pp. 518–536.
6. Hanzawa, M.; Sato, H.; Takahashi, S.; Shimosako, K.; Takayama, T.; Tanimoto, K. Chapter 130 New Stability Formula for Wave-Dissipating Concrete Blocks Covering Horizontally Composite Breakwaters. In Proceedings of the Coastal Engineering 1996, Orlando, FL, USA, 2–6 September 1996.
7. Vidal, C.; Medina, R.; Lomónaco, P. Wave height parameter for damage description of rubble-mound breakwaters. *Coast. Eng.* **2006**, *53*, 711–722. [CrossRef]
8. Etemad-Shahidi, A.; Bonakdar, L. Design of rubble-mound breakwaters using M5′ machine learning method. *Appl. Ocean Res.* **2009**, *31*, 197–201. [CrossRef]
9. Van Gent, M.R.A.; Der Werf, I.V. Rock toe stability of rubble mound breakwaters. *Coast. Eng.* **2014**, *83*, 166–176. [CrossRef]
10. Thompson, D.M.; Shuttler, R.M. *Riprap Design for Wind-Wave Attack, a Laboratory Study in Random Waves*; HR Wallingford: Wallingford, UK, 1975.
11. Wei, X.; Lu, Y.; Wang, Z.; Liu, X.; Mo, S. A Machine Learning Approach to Evaluating the Damage Level of Tooth-Shape Spur Dikes. *Water* **2018**, *10*, 1680. [CrossRef]
12. Dong, H.K.; Park, W.S. Neural network for design and reliability analysis of rubble mound breakwaters. *Ocean Eng.* **2005**, *32*, 1332–1349.

13. Balas, C.E.; Koç, M.L.; Tür, R. Artificial neural networks based on principal component analysis, fuzzy systems and fuzzy neural networks for preliminary design of rubble mound breakwaters. *Appl. Ocean Res.* **2010**, *32*, 425–433. [CrossRef]
14. Dong, H.K.; Kim, Y.J.; Dong, S.H. Artificial neural network based breakwater damage estimation considering tidal level variation. *Ocean Eng.* **2014**, *87*, 185–190.
15. Kim, D.; Dong, H.K.; Chang, S. Application of probabilistic neural network to design breakwater armor blocks. *Ocean Eng.* **2008**, *35*, 294–300. [CrossRef]
16. Erdik, T. Fuzzy logic approach to conventional rubble mound structures design. *Expert Syst. Appl.* **2009**, *36*, 4162–4170. [CrossRef]
17. Koç, M.L.; Balas, C.E. Genetic algorithms based logic-driven fuzzy neural networks for stability assessment of rubble-mound breakwaters. *Appl. Ocean Res.* **2012**, *37*, 211–219. [CrossRef]
18. Etemad-Shahidi, A.; Bali, M. Stability of rubble-mound breakwater using H 50 wave height parameter. *Coast. Eng.* **2012**, *59*, 38–45. [CrossRef]
19. Kim, D.; Dong, H.K.; Chang, S.; Lee, J.J.; Lee, D.H. Stability number prediction for breakwater armor blocks using Support Vector Regression. *KSCE J. Civ. Eng.* **2011**, *15*, 225–230. [CrossRef]
20. Narayana, H.; Lokesha; Mandal, S.; Rao, S.; Patil, S.G. Damage level prediction of non-reshaped berm breakwater using genetic algorithm tuned support vector machine. In Proceedings of the Fifth Indian National Conference on Harbour and Ocean Engineering (INCHOE2014), Goa, India, 5–7 February 2014.
21. Harish, N.; Mandal, S.; Rao, S.; Patil, S.G. Particle Swarm Optimization based support vector machine for damage level prediction of non-reshaped berm breakwater. *Appl. Soft Comput. J.* **2015**, *27*, 313–321. [CrossRef]
22. Gedik, N. Least Squares Support Vector Mechanics to Predict the Stability Number of Rubble-Mound Breakwaters. *Water* **2018**, *10*, 12. [CrossRef]
23. Koc, M.L.; Balas, C.E.; Koc, D.I. Stability assessment of rubble-mound breakwaters using genetic programming. *Ocean Eng.* **2016**, *111*, 8–12. [CrossRef]
24. Mase, H.; Sakamoto, M.; Sakai, T. Neural Network for Stability Analysis of Rubble-Mound Breakwaters. *J. Waterw. Port Coast. Ocean Eng. ASCE* **1995**, *121*, 294–299. [CrossRef]
25. Wold, S.; Esbensen, K.; Geladi, P. Principal component analysis. *Chemom. Intell. Lab. Syst.* **1987**, *2*, 37–52. [CrossRef]
26. Huang, G.B.; Zhu, Q.Y.; Siew, C.K. Extreme learning machine: A new learning scheme of feedforward neural networks. In Proceedings of the IEEE International Joint Conference on Neural Networks, Budapest, Hungary, 25–29 July 2004; Volume 982, pp. 985–990.
27. Rong, H.J.; Ong, Y.S.; Tan, A.H.; Zhu, Z.; Neucom, J. A fast pruned-extreme learning machine for classification problem. *Neurocomputing* **2008**, *72*, 359–366. [CrossRef]
28. Huang, G.B.; Ding, X.; Zhou, H. Optimization method based extreme learning machine for classification. *Neurocomputing* **2010**, *74*, 155–163. [CrossRef]
29. Pal, M.; Maxwell, A.E.; Warner, T.A. Kernel-based extreme learning machine for remote-sensing image classification. *Remote Sens. Lett.* **2013**, *4*, 853–862. [CrossRef]
30. Wei, L.; Chen, C.; Su, H.; Qian, D. Local Binary Patterns and Extreme Learning Machine for Hyperspectral Imagery Classification. *IEEE Trans. Geosci. Remote Sens.* **2015**, *53*, 3681–3693.
31. Cheng, L.; Zeng, Z.; Wei, Y.; Tang, H. Ensemble of extreme learning machine for landslide displacement prediction based on time series analysis. *Neural Comput. Appl.* **2014**, *24*, 99–107.
32. Abdullah, S.S.; Malek, M.A.; Abdullah, N.S.; Kisi, O.; Yap, K.S. Extreme Learning Machines: A new approach for prediction of reference evapotranspiration. *J. Hydrol.* **2015**, *527*, 184–195. [CrossRef]
33. Deo, R.C.; Şahin, M. Application of the extreme learning machine algorithm for the prediction of monthly Effective Drought Index in eastern Australia. *Atmos. Res.* **2015**, *153*, 512–525. [CrossRef]
34. Ćojbašić, Ž.; Petković, D.; Shamshirband, S.; Tong, C.W.; Ch, S.; Janković, P.; Dučić, N.; Baralić, J. Surface roughness prediction by extreme learning machine constructed with abrasive water jet. *Precis. Eng.* **2016**, *43*, 86–92. [CrossRef]
35. Huang, G.B.; Zhu, Q.Y.; Siew, C.K. Extreme learning machine: Theory and applications. *Neurocomputing* **2006**, *70*, 489–501. [CrossRef]
36. Huang, G.; Huang, G.B.; Song, S.; You, K. Trends in extreme learning machines: A review. *Neural Netw.* **2015**, *61*, 32–48. [CrossRef]

37. Alexandre, E.; Cuadra, L.; Nietoborge, J.C.; Candilgarcía, G.; Del Pino, M.; Salcedosanz, S. A hybrid genetic algorithm-extreme learning machine approach for accurate significant wave height reconstruction. *Ocean Model.* **2015**, *92*, 115–123. [CrossRef]
38. Yin, J.; Wang, N. An online sequential extreme learning machine for tidal prediction based on improved Gath-Geva fuzzy segmentation. *Neurocomputing* **2015**, *174*, 243–252.
39. Mulia, I.E.; Asano, T.; Nagayama, A. Real-time forecasting of near-field tsunami waveforms at coastal areas using a regularized extreme learning machine. *Coast. Eng.* **2016**, *109*, 1–8. [CrossRef]
40. Imani, M.; Kao, H.C.; Lan, W.H.; Kuo, C.Y. Daily sea level prediction at Chiayi coast, Taiwan using extreme learning machine and relevance vector machine. *Glob. Planet. Chang.* **2017**, *161*, S0921818117303715. [CrossRef]
41. Basheer, I.A.; Hajmeer, M. Artifical neural networks: Fundamentals, computing, design, and application. *J. Microbiol. Methods* **2000**, *43*, 3–31. [CrossRef]

Journal of
Marine Science and Engineering

MDPI

Article

Probabilistic Risk Evaluation for Overall Stability of Composite Caisson Breakwaters in Korea

Nhu Son Doan [1], Jungwon Huh [1,*], Van Ha Mac [1], Dongwook Kim [2] and Kiseok Kwak [3]

[1] Department of Architecture and Civil Engineering, Chonnam National University, Gwangju 61186, Korea; 188444@jnu.ac.kr (N.S.D.); 188456@jnu.ac.kr (V.H.M.)
[2] Department of Civil and Environmental Engineering, Incheon National University, Incheon 22012, Korea; wookdong2@gmail.com
[3] Underground Space Safety Research Center, Korea Institute of Civil Engineering and Building Technology, Goyang 10223, Korea; kskwak@kict.re.kr
* Correspondence: jwonhuh@chonnam.ac.kr; Tel.: +82-61-659-7247

Received: 1 February 2020; Accepted: 21 February 2020; Published: 25 February 2020

Abstract: In the present study, the overall stability of typical Korean composite caisson breakwaters that were initially designed following the conventional deterministic approach is investigated using reliability approaches. Therefore, the sensitivity of critical uncertainties regarding breakwater safety is analyzed. Uncertainty sources related to the structure, ocean conditions, and properties of the subsoil and rubble mound are considered in the reliability analysis. Sliding and overturning failures are presented as explicit equations, and three reliability methods, i.e., the mean value first-order second-moment, first-order reliability method, and Monte Carlo simulation, are applied in the evaluation process. Furthermore, the bearing capacity of the rubble mound and subsoil are analyzed using the discrete slice method conjugated with the Monte Carlo simulation. The results of this study establish that the sliding failure generally is the most frequent failure occurring among the above-mentioned overall stability failures (around 15 times more common than failures observed in the foundation). Additionally, it is found that the horizontal wave force primarily contributes to the sliding of the caisson body, whereas the friction coefficient is the main factor producing the resistance force. Furthermore, a much small probability of overturning failure implies that the overturning of a caisson around its heels uncommonly occurs during their lifetime, unlike other overall failure modes. Moreover, the failure in foundations may commonly encounter in the breakwater that has a high rubble mound structure compared with sliding mode. Particularly, the performance function of the all foundation bearing capacities presents a nonlinear behavior and positively skewed distribution when using the Monte Carlo simulation method. This phenomenon proves that simulation methods might be an appropriate approach to evaluate the bearing capacity of a breakwater foundation that can overcome several drawbacks of the conventional design approach.

Keywords: breakwater; vertical breakwater; reliability analysis; overall stability; sliding failure; overturning failure; bearing capacity analysis; breakwater's foundation failure

1. Introduction

A breakwater (BRW) is a vital structure that is used to mitigate effects of ocean random seas such as storm surges with extreme wave and tide variations, to provide a calm basin for protecting port facilities and mooring ships. BRWs play a critical role in the port operation, especially for ports located in the rough seas [1]. A composite BRW type generally consists of a precast concrete caisson filled with material and a rubble mound arranged above the seabed. The armor units can be made by the precast concrete block, such as Dolos or Tetrapod, that is placed beside the caisson structure to absorb most of

the incident wave energy. Vertical composite BRWs are widely used in deep-water sites because they are more cost-efficient compared with rubble mound types [2,3].

Vertical composite BRWs, which have a lot of advantages, were firstly applied in 1910 at Kobe Port. Thereafter, several catastrophic failures occurred, such as Bizerta (Tunisia) in 1915, Niigata West Port (Japan) in 1930, and Mustapha (Algiers) in 1934 [2,4]. Consequently, the vertical BRW was mostly abandoned in favor of the rubble mound type. However, at the end of the 1970s and in the early 1980s, the rubble mound BRW also experienced a series of failures. The severe damages was a catalyst for a different approach in the design of BRWs, namely the probabilistic method [3,5].

In the conventional design approach (CDA), the structures are classified as acceptable or unacceptable by comparing the nominal safety factors with those specified in the design standard. For instance, the safety factors against the sliding and overturning should not be lower than 1.2, as required in [6,7]. In general, the more important the structures, the higher the safety factors (FS) that should be selected. Thereby, the safety level of the structures can be increased. However, an increase in the specified FS without considering the inherent uncertainty of variables might not accurately reflect the overall contribution of the different input variables. In other words, the effects of all input variables may not contribute equally to the FS estimation. This assumption may cause a significant increase in the construction cost, whereas a sufficient safety level might not be obtained as expected.

In addition, the CDA might not account for most of the failure modes of BRWs, as stated by Oumeraci [5] in 1993. The author concluded that the dynamics analysis and probabilistic design approaches seem to be the only feasible solutions to solve the integrated stability problem of vertical BRWs. Moreover, additional statistical information needs to be provided before applying a reliability analysis, which is not necessary for the CDA. However, the valuable information from the reliability results makes it possible to provide more reasonable decisions in the design process compared with those obtained from the CDA [8]. The stability of armor layers was first studied by applying probabilistic approach in the work of Van der Meer [9]. Based on the probabilistic studies, systems of partial safety factor were developed for rubble mound BRWs by the Permanent International Association of Navigation Congresses (PIANC) Permanent Technical Committee II (PTC II) Working Group 12 [10,11] and for vertical BRW types by the PIANC PTC II Working Group 28 [12,13].

In Korea, BRW structures are primarily designed using the traditional deterministic method [6,14]. Recently, some failure modes based on reliability have been studied. Most of these studies deal with the stability of the armor layer or rubble mound BRWs [14,15]. Although the stability of vertical BRWs has also been studied, not as much attention has been paid to the overall failure modes compared with that for the sliding mode of the caisson on a rubble mound, as presented in previous researches [14,16,17]. However, BRWs are commonly located in enormous energy potential zones of ocean waves, so they intrinsically face various probable failure aspects. Possible ruptures, including overall and local failure modes, have been presented in previous studies [5,10,11,18,19]. Theoretically, all possible failure aspects need to be investigated before making any final design decisions. Furthermore, in Japan, the overall failure modes of BRWs, i.e., the caisson sliding [16,18,19] and foundation failure [4,10,13,20] have been reported as the most common failures observed. Therefore, the three most frequent overall failure modes, the caisson sliding on the rubble mound surface, insufficient foundation bearing capacity, and the overturning of a caisson around its heel, are examined in this study, as shown in Figure 1a–c. The parts labeled 1 and 2 are the caisson and rubble mound structures, respectively.

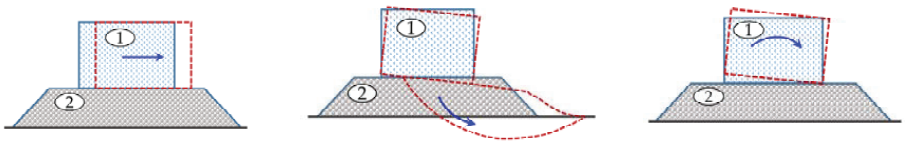

Figure 1. Overall failure mode of breakwaters (BRWs) studied: (**a**) Sliding, (**b**) Insufficient foundation bearing capacity, (**c**) Overturning.

In Europe, Level 1 and Level 2 probabilistic analyses have been developed, while Level 3 has been successfully carried out in Japan [19]. Notably, the Level 1 and Level 2 reliability design methods are based on the mean value first-order second-moment (MVFOSM), and first-order reliability method (FORM), respectively [11,12], whereas the Level 3 reliability design method is related to the estimation of the caisson sliding distance [18,19,21,22] or the expectation of damages occurring in the armor blocks of horizontal composite BRWs [23]. In this study, the safety of nine typical Korean vertical BRWs is estimated using different reliability analysis methods, MVFOSM, FORM, and the Monte Carlo Simulation (MCS). Hence, this study would provide a reliability-based comprehensive assessment of the overall stability of BRWs that were initially designed using the CDA.

Furthermore, three primary uncertainty sources [i.e., properties inherent to the structure itself (uncertainties in the density of materials), the hydraulic climate (randomness of tide level and wave force), and soil properties of the foundation] are also explored in this study. Thereafter, a sensitivity analysis is performed to find the most critical uncertainties that predominantly contribute to structural damage.

In order to obtain the above-mentioned purposes, several functions are developed in MATLAB to carry out the reliability-based analysis. By doing so, valuable insight into the overall BRW stability is provided. The rest of the study is presented as follows: Section 2 summarizes the reliability approaches used in the study. Section 3 focuses on the sliding and overturning failure modes of the caisson structure. Section 4 investigates the bearing capacity of the foundation by circular slip failure analysis using Bishop's simplified method (BSM) conjugated with MCS. Finally, Section 5 concludes the study.

2. Selection of Reliability Approaches

A reliability index (RI) called the Cornell reliability (CR) index was first estimated in 1969 by Cornell. The CR index is determined as the ratio of the first and second moments of the performance function (PF) at the mean value of all input variables [24]. However, accurate results can be obtained using this method only when the PF is linear and the variances of input variables are not too large [25]. In 1974, Hasofer and Lind [26] proposed another index called the Hasofer—Lind (HL) index, which overcomes the drawbacks of the CR index owing to the assumption on the distributions of the involved variables in the analysis [27]. The HL index is defined as the shortest distance from the origin to the PF surface plotted in the standard normalized space. Therefore, the estimation of the HL index becomes an optimization problem in the standard normalized space. In this problem, if the input variables have non-normal distributions, Rosenblatt's transformation is commonly applied to convert the variables from their space to the standard normalized space [25,27]. The most probable point (MPP) or the design point is the point that satisfies both constraint conditions, i.e., (1) belongs to the performance surface and (2) causes the shortest distance to the origin. The PF is estimated at the MPP as an equivalent linear function and nonlinear function corresponding to the FORM and the second-order equation (SORM) using Taylor's expansion.

The purpose of the Monte Carlo Simulation (MCS) is to simulate the PF on the space of the initial input variables, generally consisting of two steps. Firstly, all involved variables associated with their cumulative distribution are randomly generated. Secondly, the occurrence of failure states is evaluated by comparing the estimated PF value in each sampling with a certain boundary condition.

The probability of failure is then determined as the proportion of the total number of failures in the simulation [25,27].

Among the above-mentioned reliability methods, the best accuracy results can be achieved most frequently with the MCS, but it requires the most time for analysis. The MCS is the reasonable choice for large-dimension problems or when the PFs are nonlinear or implicitly defined, e.g., estimation of the bearing capacity of foundations by BSM. However, problems with low failure probabilities would require an extremely large simulation to recognize a sufficient number of failures. In these cases, the crude MCS process is too time-consuming. Hence, some variance reduction techniques should be applied as better options in the simulation [25,27].

The estimation of the CR index is the simplest method, in which the worst-case outcome is the result of the most severe combination of all involved variables (the mean values). Based on Taylor's expansion, the PF is approximated at the worst point of all the variables. However, Cornell's estimation is a conservative method in most cases because the simultaneous occurrences of all input variables while also contributing to the outcome are only an idealization. Moreover, the information on the distribution type of random variables is ignored, and the CR index might not capable when the random variables have a considerable variation.

The FORM is widely used in practice [28,29]. However, it is difficult to evaluate the PF accurately in both FORM and SORM in highly nonlinear problems, especially problems with high dimensions. In general, more accurate results can be achieved by applying a combination of the MCS and FORM, thereby overcoming the disadvantage of individual methods. In this study, three methods, MVFOSM, FORM, and MCS are applied to assess sliding and overturning conditions of caissons since the PFs are explicitly defined, while the MCS is merely applied to evaluate the foundation bearing capacity, which is defined as a sophisticated and implicit PF.

3. Sliding and Overturning Failure Modes

3.1. Breakwater Structures and Wave Force Model

The present study analyzes the vertical BRWs and nine BRWs are intuitively chosen along the Korean shoreline, as shown in Figure 2. The typical section of caissons is shown in Figure 3, while their overall design conditions are listed in Table 1. In Table 1 and Figure 3, B_c and H_c represent the width and the heights of the caisson, respectively. h_r indicates the height of the rubble mound. The ocean conditions are represented by the water depth at the site h, the water depth from the base of the caisson h', the water depth over the berm d, and the variation in the tide level WL. Finally, the wave conditions are represented by the design wave height H_D.

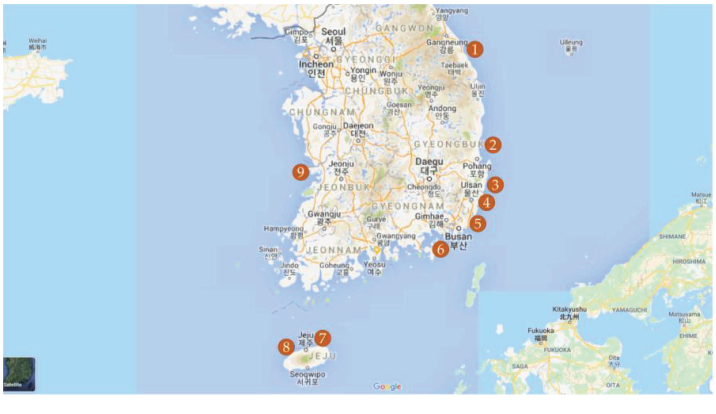

Figure 2. Locations of breakwaters considered in this study.

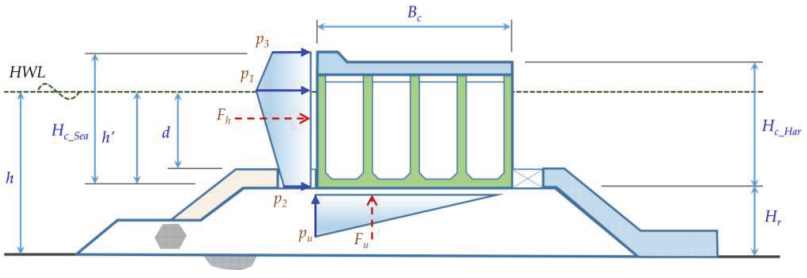

Figure 3. Typical cross-section of a BRW and wave force model.

Table 1. Dimensions and Environmental Characteristics of the breakwaters.

No.	Breakwater	Geometry Parameter				Ocean Condition				
		B_c	H_{c_Sea}	H_{c_Har}	h_r	h	h'	d	H_D	WL
1	Donghae	20.0	16.0	16.0	6.1	16.99	10.89	8.29	10.8	0.20
2	Pohang	14.0	12.0	12.0	3.5	11.75	8.25	7.25	8.58	0.12
3	Ulsan	19.0	21.5	17.5	3.0	18.66	15.66	14.16	9.9	0.30
4	Onsan	14.0	18.5	16.0	9.0	19.84	14.11	13.11	5.76	0.30
5	Busan	24.0	21.5	20.7	8.5	25.44	16.94	15.39	10.8	0.72
6	Gamcheon	20.0	18.0	17.5	3.0	17.28	14.28	12.08	10.8	0.64
7	Jeju Outer	24.0	25.8	22.8	1.3	24.83	17.83	16.03	11.7	1.42
8	Jeju Aewol	27.4	23.5	20.5	1.5	13.86	13.36	12.36	14.04	1.43
9	Gunsan	18.0	19.0	18.0	2.0	15.75	13.75	13.15	10.08	3.62

Notes: dimensions in meters.

The wave forces (F_h and F_u) acting on the upright section are calculated using Goda's formulae [30]. In Goda's model, wave forces are determined from the pressures distributed over the height and width of the upright section, which are estimated based on the design wave height, determined by the mean of the 0.4% largest wave heights in the recorded wave data. The pressure is distributed triangularly on the bottom of the caisson (maximum pressure p_u) and has a trapezoidal shape on the front face of the upright section (represented by pressure p_1, p_2, and p_3). Figure 3 illustrates the wave pressures following Goda's model on the caisson section.

3.2. Performance Functions and Considered Random Variables

In order to perform the reliability analysis, the PFs or limit state functions that consist of input variables need to be introduced. In the sliding case, the PF includes the driving force caused by the horizontal wave force and the resisting force related to the friction force between the bottom face of the caisson and the rubble mound surface. The friction force is a product of the effective normal force on the rubble mound and the friction coefficient. The PF for overturning conditions is similar to sliding but reflects the moments around the heels of the caisson. Namely, the mobilizing moment is generated by the wave forces and buoyancy force while the resisting moment is produced by the weight of the structure. Generally, sliding and overturning damages due to positive wave forces, i.e., from the seaside toward the harbor, are more critical than those from negative wave forces [19], which are also of interest in this study. The explicit performance equations, $g(X)$ are shown in Equations (1) and (2) corresponding to sliding and overturning states.

$$g(X) = f_c\left(D_c + D_{rc} + D_f - B - F_u\right) - F_h, \tag{1}$$

$$g(X) = D_c L_c + D_{rc} L_{rc} + D_f L_f - B L_b - F_h L_h - F_u L_u, \tag{2}$$

where L_c, L_{rc}, and L_f are the lever arms of the moments caused by the weights of the plain concrete structure (D_c), the reinforced concrete structure (D_{rc}), and the filling material (D_f), respectively. The

total weight of the materials comprising the caisson is represented as a summarized random input variable with a mean density of 2100 kg/m^3 in [19]. In this work, these dead loads are considered as uncertainties with different variations, which are dependent on not only the construction stage but also the construction method. For instance, the caisson body is a precast reinforced concrete structure, so it would have better quality control compared with the concrete cover slab or filling material built on sites. The friction coefficient between the concrete caisson and the rubble surface, f_c has been well studied and empirically obtained through various studies [13,18]. Here, its bias is presumed as a normal distribution with the mean value of 1.06 and coefficient of variation (COV) of 0.15. B stands for buoyancy force that is highly dependent on the submerged volume of the structure below the water level. Additionally, because tidal variations influence not only the buoyancy force but also wave pressures, the water level is studied as an uncertainty based on the tide fluctuations in this study. Tide levels rely on astronomical and meteorological tides and the increased water level caused by nearshore waves [28,29]. In the present study, different BRWs on the eastern, northern, or western coasts, as shown in Figure 2, are dissimilarly explored to consider the different variations in the tide levels.

Failures would occur whenever the mobilizing resultants exceed the resisting resultants. In principle, all parameters have themselves variation; however, some parameters with slight variations can be approximated as a deterministic approach with almost no effects on the final result [13]. Notably, because of the good quality managements, the dimensions of the caisson are assumed to be the same as the design, which means all lever arms in the overturning situation are treated in a deterministic manner in this study. The statistical information of the involved variables is summarized in the Table 2.

Table 2. Statistical properties of the uncertainties applied in the overall stability analysis.

No.	Notation	Mean of Bias	COV of Bias	Distribution	Random Variable
1	f_c	1.06	0.15	Normal	Friction coefficient
2	W_c	1.02	0.02	Normal	Weight of concrete
3	W_{rc}	0.98	0.02	Normal	Weight of reinforced concrete
4	W_f	1.02	0.04	Normal	Filling material
5	F_u	0.77	0.260	Normal	Vertical wave force
6	F_h	0.90	0.222	Normal	Horizontal wave force
7	W	1.00	COV [1]	Normal	Tidal level

[1] COV: 0.05/0.12/0.20 correspond to the West/South/East locations.

The vertical wave force, F_u, and horizontal wave force, F_h, estimated using Goda's expression, are the random input variables in the study. It is proved that the wave forces obtained following the Goda's formulae are conservative in the studies of Van der Meer et al. [13,31]. In other words, when Goda's model is applied, the bias factor, λ, must be taken into account, which is generally less than unity [13], as shown in Equation (3).

$$F_{h,v} = \lambda_{h,v} * F_{h,v}^{Goda}, \tag{3}$$

Van der Meer et al. [31] compared Goda's results with the model tests and proposed an overestimation of the Goda formulae. Vrijling [32] demonstrated through experiments that the derived standard deviation also included statistical uncertainty in the maximum wave height and the author suggested that the statistical information has a the lognormal distribution. Furthermore, Coastal Engineering Manual (CEM 2011) [28] in the United States proposed a somewhat different standard deviation relying on whether or not the model tests are performed. The statistical parameters related to wave forces are summarized in Table 3. In this study, the statistical parameters of Goda's formulae are applied referencing Van der Meer et al. [31] and Vrijling [32] to consider the different coefficients of horizontal and vertical wave forces.

Table 3. Statistical properties of reduced factor applying to Goda's formulae.

Parameter	Van der Meer et al. [31]	Vrijling [32]	CEM 2011 [28]	
			No Model Tests	Model Test Performed
Horizontal force, F_h	N(0.90, 0.20)	LN(0.90, 0.20)	N(0.90, 0.25)	N(0.90, 0.05)
Horizontal moment, M_h	N(0.81, 0.37)	LN(0.72, 0.37)	N(0.81, 0.40)	N(0.81, 0.10)
Vertical force, F_u	N(0.77, 0.20)	LN(0.77, 0.20)	N(0.77, 0.25)	N(0.77, 0.05)
Vertical moment, M_u	N(0.72, 0.34)	LN(0.72, 0.34)	N(0.72, 0.37)	N(0.72, 0.10)

Notes: N and LN are normal and lognormal distributions, respectively.

3.3. Reliability Analysis Using MVFOSM and FORM

Initially, the characteristic values of all involved variables in the PFs are determined as with the conventional design approach. The means of the variables are then estimated using the statistical characteristics listed in Table 2. Thereafter, results of the RIs are implemented with the mean of variables using MVFOSM and FORM. The failure probability, P_f, is converted from the result of the reliability index, β, using an approximation of the cumulative probability density of the standard normal distribution, Φ, as shown in Equations (4) and (5) [25,27].

$$P_f = \Phi(-\beta), \tag{4}$$

$$\beta = -\Phi^{-1}\left(P_f\right) = \Phi^{-1}\left(1 - P_f\right), \tag{5}$$

MVFOSM approximates the PF linearized at the mean values of the random variables based on the first-order Taylor's series. The RI is evaluated as the ratio of the mean, μ_g, and the standard deviation, σ_g, of the PF, g, as shown in Equation (6). Thereafter, the reliability index, β, is estimated at the mean values of all random variables, μ_X, as shown in Equations (7) and (8) [27].

$$\beta = \frac{\mu_g}{\sigma_g}, \tag{6}$$

where

$$\mu_g = g(\mu_X), \tag{7}$$

and

$$\sigma_g = \sqrt{\sum_1^n \sigma_i^2}, \tag{8}$$

In the FORM, the initial variables X can be converted to the standard normalized space U through the transformation $X = T(U)$. The transformation can be expressed as Equation (9) in the case of normal distribution $X \sim N(\mu_X, \sigma_X)$:

$$X = \mu_X + \sigma_X U, \tag{9}$$

In the first step, the design point can be assumed as the mean values of the involved variables. As noted previously, the HL index is the distance from the origin to the design point in the normalized space, which indicates that the RI can be addressed in Equation (10).

$$\beta = \sqrt{\sum_1^n U_i^2}, \tag{10}$$

Using the relationships in Equations (9) and (10) for the initial estimation, the first trial RI is determined for the assumed design point.

In the FORM analysis, the sensitivity of each variable, α_i, that affects the results of the FS is estimated as cosine direction at the most probable failure point as shown in Equation (11).

$$\alpha_i = \frac{\frac{\partial g}{\partial U_i}\Big|_{X^*}}{\sqrt{\sum_1^n \left(\frac{\partial g}{\partial U_i}\Big|_{X^*}\right)^2}}, \tag{11}$$

where X_i represents the input random variable i in the initial variable coordinates, and U_i stands for the variable in the normalized/reduced space. The subscript * shows the value of variables at the design point. The sensitivity factor is the cosine direction of the PF at the design point with for each variable.

A positive α_i shows the positive effect of the variable X_i on the PF and vice versa. Furthermore, more substantial sensitive factors show more significant effects on the PF. The design point in the normalized space U^* can be expressed as the product of the sensitivity factor and RI by using Equation (12).

$$U_i^* = -\beta\alpha_i, \tag{12}$$

The new value of the intermediate design point U^* is then determined. Thereafter, if it is similar to the assumed value, the estimated reliability is the acceptable outcome. If the values are not similar, the new intermediate design point is next used as the new trial point. This procedure is repeated until the difference in RI is not larger than 0.5%.

After associating the design point in the normalized space with the reliability index, the MPP of the variables in the initial space X^* is determined using Equation (13).

$$X_i^* = \mu_X + \alpha_i\sigma_i\beta, \tag{13}$$

By applying the FORM, the two following results, the reliability index and the sensitivity factors of the studied variables, are derived. These results for the nine BRWs are summarized in Table 4.

Table 4. Results of mean value first-order second-moment (MVFOSM) and first-order reliability method (FORM) for sliding failure mode.

No.	Port	Sensitivity						β		
		f_c	W_c	W_{rc}	W_f	F_u	F_h	WL	FORM	MVFOSM
1	Donghae	0.700	0.042	0.025	0.132	−0.158	−0.682	−0.016	1.671	1.692
2	Pohang	0.693	0.039	0.026	0.141	−0.164	−0.686	−0.013	1.608	1.624
3	Ulsan	0.714	0.032	0.026	0.172	−0.121	−0.667	−0.021	1.843	1.873
4	Onsan	0.837	0.015	0.032	0.151	−0.060	−0.521	−0.022	3.325	3.295
5	Busan	0.670	0.042	0.026	0.181	−0.183	−0.694	−0.033	1.441	1.557
6	Gamcheon	0.681	0.038	0.033	0.153	−0.169	−0.692	−0.050	1.510	1.616
7	Jeju Outer	0.738	0.032	0.029	0.160	−0.117	−0.642	−0.052	2.125	2.302
8	Jeju Aewol	0.702	0.029	0.022	0.162	−0.160	−0.672	−0.051	1.755	1.936
9	Gunsan	0.697	0.025	0.029	0.176	−0.147	−0.675	−0.068	1.705	1.799

The FSs based on the CDA and the corresponding RIs from FORM for the sliding state are plotted in Figure 4. A linear relationship is fitted where a high coefficient of determination (R^2 = 0.9933) indicates a good approximation of the fitting function. The intercept of the fitting function is then set to zero, and the new equation $\beta = 1.304FS$ can be obtained.

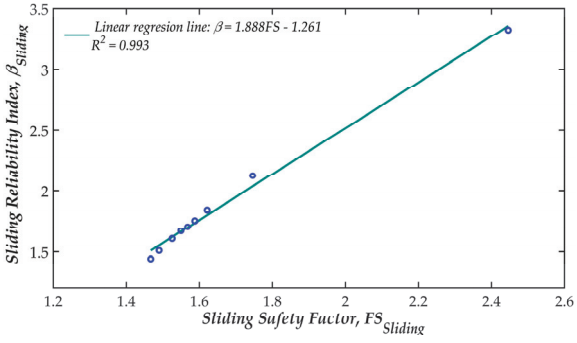

Figure 4. Relationship between the reliability index and safety factor for sliding failure mode.

3.4. Reliability Analysis Using MCS

In the MCS, the input variables are generated following their statistical information, and the PF is then evaluated to classify events as failure or success after each sampling. The number of failures is counted and the failure probability in the simulation, P_f, is determined using Equation (14).

$$P_f = \frac{1}{N_{MCS}} \sum_{i=1}^{N_{MCS}} I(g(X_i) < 0) = \frac{N_{fail}}{N_{MCS}}, \tag{14}$$

in which N_{MCS} and N_{fail} are the simulation size and the number of failures occurring in the simulation, respectively. $I(g(X) < 0)$ is an indicator function that reaches the value of unity if $g(X)$ is less than zero and reaches the value of zero in other cases.

Additionally, the probability of failure in the MCS is significantly affected by the number of simulation. The COV of the failure probability based on the MCS, COV_{Pf}, is approximated from the number of simulation, N_{MCS}, and the failure probability, P_f, as shown in Equation (15). Generally, the number of simulations, N_{MCS}, should be greater than ten times the reciprocal of P_f ($N_{MCS} > 10/P_f$) so that the COV of P_f estimated from the different MCS runs is less than 0.3 [33]. The relative error with a 95% confidence interval of binomial distribution of each simulation cycle is estimated with Equation (16) [27].

$$COV_{P_f} = \sqrt{\frac{1 - P_f}{NP_f}} \approx \frac{1}{\sqrt{NP_f}}, \tag{15}$$

$$\varepsilon\% = (200\%) \sqrt{\frac{1 - P_f}{NP_f}}, \tag{16}$$

In Figure 5, the sensitivity of the realization number on the failure probability is analyzed for Onsan BRW. More than 40,000 simulations are necessary to reach a variation less than 0.3. In this study, the size of MCS is taken as 10^5 for the sliding reliability analysis. This size of simulation is also applied to other BRWs because the RI based on the FORM of the Onsan BRW is the largest among the nine BRWs. Meanwhile, based on the FORM results, the RIs for the overturning conditions are much higher than those of sliding, which is discussed in detail in Section 3.5. Consequently, the failure probability against overturning might be minor. By assuming the normal distribution, Figure 6 depicts the correlation between the smallest number of realizations to encounter at least 10 overturning failure events in the simulation and the expected RI. Particularly, if it is needed to reach a failure probability less than 10^{-6} ($\beta > 4.75$), 10^7 should be the smallest number of realizations applied. This example demonstrates one of the disadvantages of MCS in comparison with other methods like FORM and MVFOSM. Moreover, the results for overturning are not critical. Therefore, the RIs for overturning are assumed as the same as the results from FORM and MVFOSM in this work.

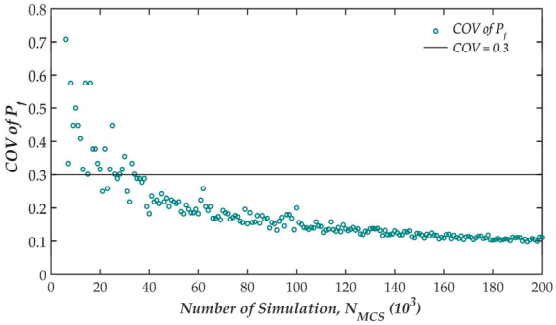

Figure 5. Convergence of the Monte Carlo simulation (MCS) for sliding failure mode, (Onsan BRW).

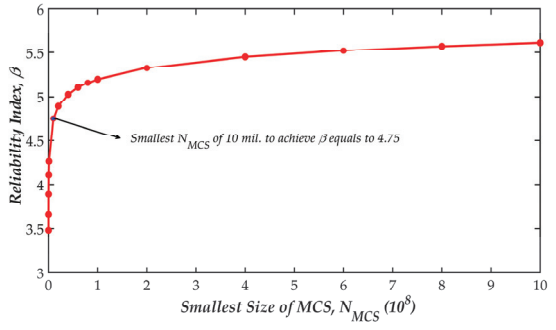

Figure 6. Relationship between the smallest number of simulations and the expected reliability index in MCS.

Figure 7 illustrates the histogram of the sliding FS ($FS_{Sliding}$) of the Onsan BRW compared with unity. The histogram shows a long tail on the right that declares that the distribution of the results is not symmetric even though the involved variables are considered as symmetric distributions. In these cases, the procedure proposed by Allen et al. [34], in which the sliding PF is plotted with the standard normal variable, can be applied to estimate the RI from the PF based on the MCS, as shown in Figure 8. The point at which the PF takes the zero value shows the negative RI. On the other hands, the point where performance line intersects with the horizontal axis illustrates the mean value of the PF. With the normal distributions, the slopes of the lines indicate the standard deviation of the PF. Finally, the RIs based on the three methods are plotted in Figure 9 for the sliding and overturning conditions. The results are discussed in detail in Section 3.5.

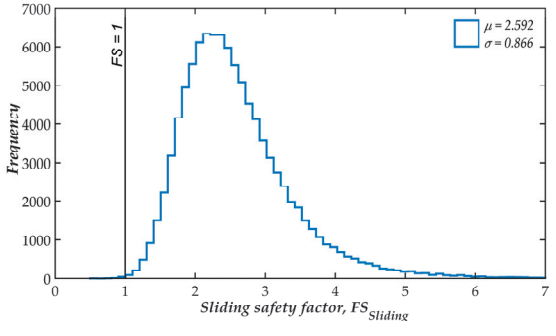

Figure 7. Histogram of the sliding safety factor in the case of Onsan breakwater.

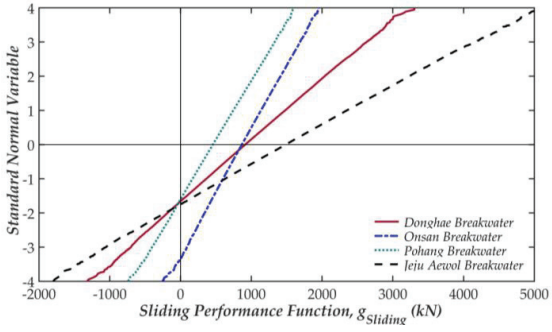

Figure 8. Cumulative density of the sliding performance function (PF) in the standard normal space.

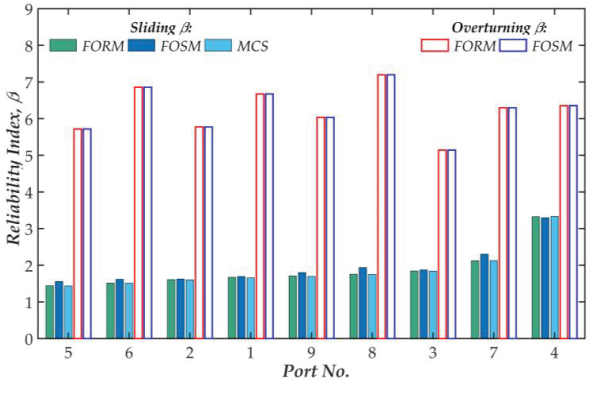

Figure 9. Reliability indices for sliding and overturning failure modes (sorted by $\beta_{Sliding}$).

3.5. Discussion on Sliding and Overturning Modes

A good agreement between the RIs for sliding and overturning failure modes by applying MVFOSM, FORM and MCS is achieved as shown in Figure 9. The MVFOSM corresponds better compared with FORM for the overturning conditions, implying that MVFOSM, the simplest method, should be applied for the linear PF. The average probability of overturning failure calculated using Equation (4) with the average of RIs is approximately 25×10^{-8}. The probability of the overturning of a caisson around its heel is considerably small, as expected, implying that the failures would occur in the subsoil before the caisson itself would overturn [19]. The bearing capacity of the foundation is, therefore, examined in the next section.

Figure 9 distinctly indicates that the RIs of the sliding modes are considerably lower than those of the overturning mode. These results signify that a sliding event could more commonly occur during the lifetime of the structure. The sensitivity coefficients listed in Table 4 illustrates that the friction coefficient is the most critical factor in the resisting resultant in most of the BRWs. In contrast, the horizontal wave force controls the driving resultant. Based on this expression, the designer should find ways to reduce the horizontal wave force, such as applying a perforated or sloping top caisson, to mitigate the action of the ocean wave. On the other hand, the interaction conditions between the bottom of the caisson and the top of the rubble mound govern the friction coefficient; hence, this should be comprehensively inspected during the construction stage. Furthermore, friction enhancement materials should be utilized to reduce the width of the caisson, such as a rubber or bituminous material.

Additionally, although the plain concrete structure and filling material are considered to have the same bias factor, their effects on all the RIs vary widely due to the difference in the variable's COV. It

can be found that the variables contribute unequally to the FSs in reliability analysis, unlike the CDA. Moreover, some unsuitable points of the CDA can be observed in Figure 8. First, although the means of the sliding PFs are quite similar for the Onsan and Donghae BRWs, the estimated RIs show nearly twice the difference between the two. Second, the same RIs for the Donghae, Pohang, and Jeju Aewol BRWs emerged from different values of PFs, illustrating the inconsistency of the deterministic method.

The most likely linear relationship between the FS following the conventional design method and the resulting RIs is shown in Figure 4. This approximation could provide an initial estimation of the RI in feasibility studies where the FS is the final target.

4. Bearing Capacity of Foundation by Circular Slip Failure Analysis

4.1. Selection of Bishop's Simplified Method

Failures in the foundations may be the results of insufficient soil bearing capacity with the wave action on the caisson structure and foundation. The damage related to the lack of bearing capacity might lead to the collapse of structures soon after substantial foundation failures. Circular slip failure is one of the prevailing damages that needs to be investigated to ensure the stability of structures [5,20].

In general, the safety of the BRW in preventing circular slip failure can be estimated based on the finite element analysis (FEA) or the limit equilibrium approach (LEA). In this study, the more classical method, the LEA, is applied because it is combined more readily with the probabilistic approach. In LEA, the failure mass corresponding to the range of candidate failure surfaces is divided into slices, and the FSs are estimated among the failure surfaces. The FS associated with each candidate failure surface is calculated by the ratio of the resisting force or moment to the mobilizing force or moment. As a result, the final FS of the slope stability is the smallest among those calculated. There are some LEAs in which the FSs are calculated with or without considering the inter-slice forces. Additionally, several methods evaluate the limit equilibrium against moments (Bishop's simplified method) or forces (Janbu's simplified method) or both moments and forces (Spencer, Morgenstern-Price's approaches) [35].

In the Probabilistic Design Tools for Vertical Breakwaters (PROVERB), the bearing capacities are calculated using the upper bound (UB) theory [13]. The FS derived from the UB theory would locate on the unsafe side of the correct solution compared to both FEA and LEA. However, the FS values are slightly different between those methods. Several limit equations corresponding to the failure modes related to predefined surfaces or a set of surfaces based on the UB theory have been derived [36]. These equations with simplifying hypotheses are expressed in explicit functions, resulting in them being more easily solved in the reliability approach, i.e., easy to estimate the derivatives compared with those based on FAE and LEA. However, PROVERB also recommends that more sophisticated methods should be performed, such as slip circle analysis, according to Bishop or FEA during the detailed design process.

Kobayashi et al. [20] performed several extensive bearing capacity tests of rubble mounds, using such equipment as the tri-axial apparatus, in both a large-scale and a centrifuge model test in the laboratory and field tests and investigations of the behavior of actual gravity structure. The authors suggested that the bearing capacity of a rubble mound, including the sub-soil under eccentric and inclined loads, should be calculated using the BSM [20]. Additionally, the BSM is recommended as the suitable method used in verifying the bearing capacity of a foundation, as required in the standard of Ministry of Land, Infrastructure, Transport and Tourism (MLIT) [29] in Japan (2009) and Coastal Engineering Manual (CEM 2011) [28] in the United States. Therefore, the BSM is combined with the MCS in this study to discover the bearing capacity of the rubble mound and sub-soil under induced eccentric and inclined loading conditions.

4.2. Performance Function and Involved Random Variables

The probabilistic approaches for analyzing the stability of the slopes have been studied for decades. Based on the MVFOSM and FORM, several researchers have proposed models to determine the critical

failure surface corresponding to the minimum RI, similar to the system reliability of the slope [37,38]. Conversely, others have proposed models to investigate the stability of the slope using the Gaussian random field process combined with the MCS [33,39,40]. However, the aforementioned studies do not mention about the slopes induced eccentric and inclined loads like a rubble mound structures.

Rubble mound structures are impacted by not only the dead load of the caisson structures but also the wave force action on the caisson. In this study, the bearing capacity of the caisson foundation, assuming circular slip conditions, is investigated concerning uncertainties in both the soil strength and acting forces. A combination of horizontal and vertical wave forces leads to eccentric and inclined loads on the caisson section, and the rupture slip surface might not separately divide the solid concrete caisson in parts. Therefore, the equilibrium of the caisson structure and the candidate failure soil mass, including a part of the rubble mound and a part of the subsoil, are individually considered [13]. Initially, the forces acting on the caisson structure are combined as "equivalent resultants" that can be expressed by the three parameters depicted in Figure 10: a horizontal force, F_h, at the top surface of the rubble mound; vertical force, F_u; and the distance of the vertical force to the harbor side heel, B_z. The equivalent resultants are then transmitted as reaction forces to the slope including the rubble mound and subsoil to determine the critical failure surface.

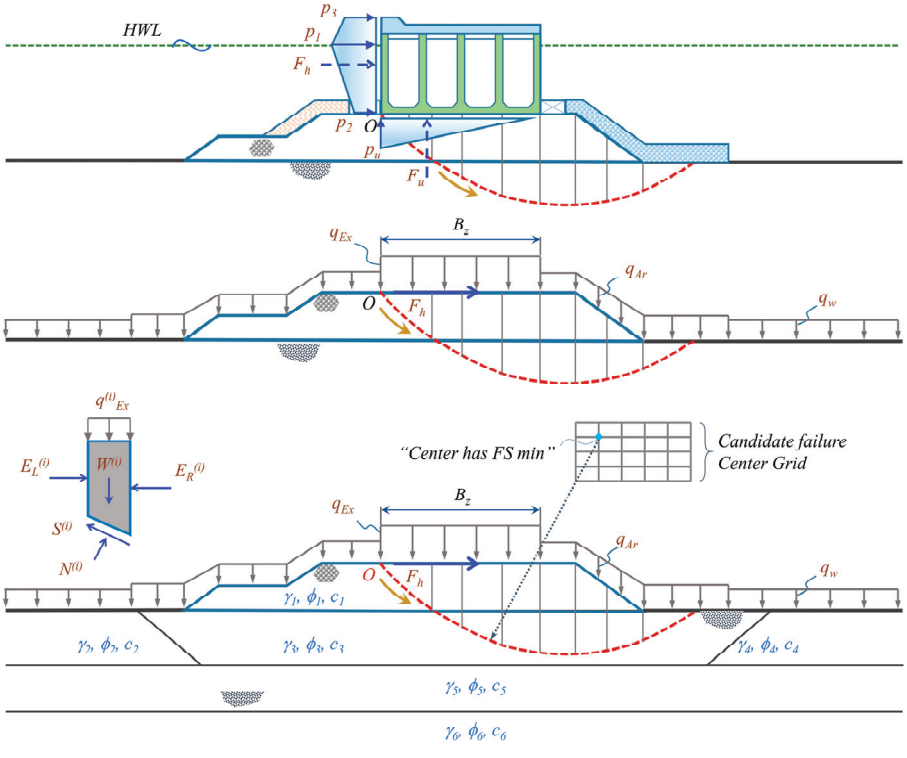

Figure 10. Mechanism applied to estimate the PF against bearing capacity using a combination of Bishop's simplified method and MCS.

Out of many slice methods, the BSM is a well-known selection in the stability analysis of slopes. In this approach, it is assumed that the resultants of the inter-slice forces are horizontal, i.e., the inter-slice shear forces are ignored. In that case, the FS is evaluated as the moment equilibrium around the center of the circular failure surface [41]. The FS can be determined using Equation (17), consequently, the PF

in the reliability analysis based on the BSM is addressed in Equation (18). Therefore, the failure would occur when the PF is less than zero (or $FS < 1$) and vice versa.

$$FS = \frac{\sum\left[\frac{\{cs+(w'+q_{Ex}s)\tan\phi\}\sec\theta}{1+\tan\theta\tan\phi/FS}\right]}{\sum\{(w+q_{\mathrm{Ex}}s)\sin\theta\}+aF_h/R}, \quad (17)$$

$$g(X) = FS - 1, \quad (18)$$

In Equation (17), w' and w are the effective weight and total weight of the comprising slice segment, respectively. q_{Ex} is the surcharge load distributing on the slice in the vertical direction. F_h and a correspond to the horizontal wave force and its lever arm about the failure center. c is the apparent cohesion of soil (or undrained shear strength in case of cohesive soil) while ϕ is the friction angle of soil along the base surface of each slice. s is the width of each slice. Finally, θ is the inclination angle, horizontal to the base surface. The studied variables, X, is shown as a vector of the involved variables in Equation (18). In the BSM, the FS is defined by a nonlinear and implicit equation; therefore, the FS is approximated with several iterative steps to reach the acceptable tolerance.

For each sampling of the MCS process, the FS of each trial failure surface is evaluated, and the smallest FS among the numerous candidate failure surfaces is considered as the final FS of the sampling. The effective dead load, wave forces acting on the caisson within each sampling are converted to the corresponding equivalent resultants, as in the previous discussion. In turn, the resultant is transposed to the rubble mound to estimate the FS using BSM. For each sampling, the FS is compared to unity as the margin between safety ($FS \geq 1$) and failure ($FS < 1$) state. The number of failures occurring throughout the simulation is then utilized to estimate the failure probability.

In the present study, not only uncertainties explored in the sliding and overturning conditions but also the strength parameters of each soil layer are considered as random variables. The nominal soil properties of each layer are determined from the field investigation. Afterward, the mean of soil properties can be approximated based on the bias factor λ of each uncertainty, as shown in Table 5.

Table 5. Statistical properties of foundation materials applied in bearing capacity analysis.

Notation	Mean of Bias	COV of Bias	Distribution	Random Variable
tanφ	1.00	0.10	Normal	Internal friction angle
c	1.00	0.10	Normal	Cohesion force
γ	1.00	0.10	Normal	Saturated soil density of Armor
		0.03		Saturated soil density of Sand
		0.02		Saturated soil density of Clay
		0.02		Saturated soil density of Rock

In most cases of geotechnical engineering, the parameters used in design may not be similar to their mean value. Therefore, the bias factors should be used to compensate for this difference. This gap can be caused by several reasons. First, some equations used in the design formulae do not always reflect exactly situation, i.e., biased phenomenon. Second, the result of the FS might have different shapes compared with those of the input variables, i.e., the dissimilar shapes of the density functions leading to a shift in the mean values.

Rubble mound structures generally consist of a homogeneous wide-graded mass of stone used to support a gravity structure. Previously, the strength properties of rubble mound material were well-defined based on various stability experiments, such as large-scale model, centrifuge and field loading tests [20]. By following that research, MLIT (2009) specified the shear strength parameters as 20 kN/m^2 for the apparent cohesion and 35° for the internal friction angle for typical rubble materials supporting the eccentric and inclined loads as standard values. Various geotechnical parameters of rubble mounds and the subsoil were investigated in PROVERB (2001), where the soil strength properties were assumed as either the normal or lognormal distribution. However, the unit weights of

the rubble mound and the subsoil were treated as deterministic variables [13]. In this work, when analyzing the bearing capacity of the foundation, both the unit weight of the rubble mound and subsoils are considered as random variables, similar to the sliding and overturning states.

In this study, the friction angle, undrained shear strength, and the unit weight of the rubble mound and subsoils are assumed to be unbiased (the mean of bias factors is unity) and exhibiting normal distribution for simplicity. The variation in the friction angle and the undrained shear strength is considered to have a value of 0.1 to account for the uncertainty in the estimated characteristic values. Notably, the variation in the subsoil density is less than the rubble mound density. Therefore, a slightly lower COV for the rubble mound is selected compared with that of the subsoil density. The stochastic information is summarized above in Table 5.

4.3. Result and Discussion of Bearing Capacity Analysis

Figure 11 presents an example of a failure event (FS less than unity) of the Gamcheon breakwater in a sampling. The safety factors are evaluated within the trial center grid consisting of 625 (25 × 25) points. The contour located in the upper part of the figure shows the convergence of the FSs in the estimation process. The blue line illustrates the most critical failure surface with a safety factor of 0.95, in which the failure mass consists of both rubble mound and subsoil portions.

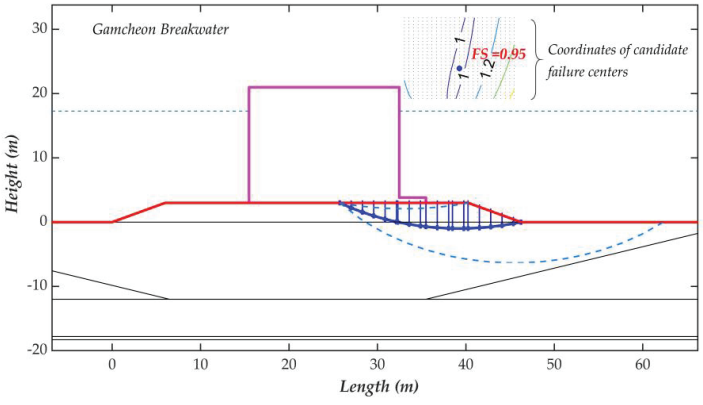

Figure 11. Bearing capacity analysis applying Bishop's simplified method (BSM) conjugated with MCS.

The nonlinear relationship between PF (through FS) and the standard normal variable is plotted in Figure 12 for the bearing capacity of foundations. The RI, in this case, should be determined from the points at which PF equals to zero ($FS = 1$) rather than inversion of the cumulative density function of the normal distribution. The results have illustrated that the MCS should be the most relevant approach when reliability analysis is applied to assess the bearing capacity of the foundation. Moreover, the point where the performance line is zero ($FS = 1$) provides a negative RI. Meanwhile, the mean value of PF is indicated when the standard normal variable equals zero.

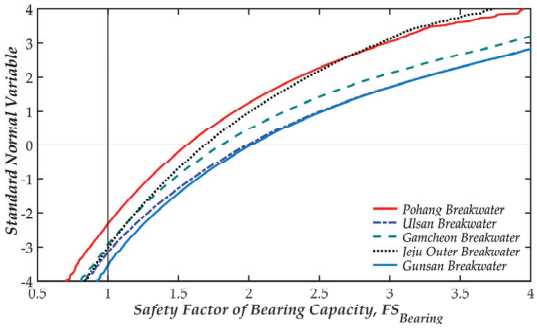

Figure 12. Cumulative density of the bearing capacity safety factor of foundation in the standard normal space.

Furthermore, Figure 12 demonstrates that the CDA may be unsuitable when compared with the reliability methods in the stability assessment of BRWs. First, although the mean values (intersect points of the performance function with the horizontal axis) of the safety factor are different, some estimated RIs are quite similar. For example, for the Jeju Outer, Gamcheon and Ulsan BRWs, the means of the safety factors are obtained corresponding to 1.622, 1.727 and 1.897, but the estimated RIs are all approximately 3.3. Second, the results of RIs that vary from 2.658 (Pohang case) to 3.769 (Gunsan BRW) corresponding to the failure probability of 0.01 and 0.0002 show a large difference. The huge variation of failure probabilities (50 times of difference) illustrates the inconsistent safety level of the BRWs achieved using CDA.

Additionally, the meaningful results of the nine BRWs and the corresponding errors of the MCS estimated using Equation (16) with the generation size of one hundred and fifty thousand are presented in Table 6. The maximum error of 0.37% ($COV_{Pf} \approx 0.18$) in the Gunsan case proves that the chosen size of simulation is suitable. Although all studied variables are assumed as normal distributions, the outcome of the FSs reveals a skewed distribution, as in the example shown in Figure 13 for the Gamcheon BRW. The skewness implies the asymmetry of the probability density function of the PFs, while a normal distribution (totally symmetric) would show a skewness value. The positive skew coefficients in all the studied cases imply that the PF's distribution have a longer tail on the right compared with that on the left. This phenomenon reflects the nonlinear relationship of the safety factor with all the involved variables in the BSM. Additionally, the positive skewness instances are more densely located on the left side of the mean value. This result demonstrates that the safety factors of the reliability analysis are predominantly distributed below the mean value.

Table 6. Results of the bearing capacity safety factor using Monte Carlo simulation.

No.	Port	P_f ($\times 10^{-3}$)	β	μ_{FS}	σ_{FS}	COV_{FS}	*Skewness*	*Error of* P_f (%)
1	Donghae	6.53	2.805	1.506	0.299	0.187	0.688	0.06
2	Pohang	10.19	2.658	1.495	0.321	0.201	0.788	0.05
3	Ulsan	0.81	3.419	1.897	0.484	0.236	0.885	0.18
4	Onsan	2.51	3.101	1.553	0.293	0.178	0.619	0.10
5	Busan	1.09	3.339	1.704	0.341	0.188	0.662	0.16
6	Gamcheon	1.70	3.214	1.727	0.425	0.228	1.001	0.13
7	Jeju Outer	1.28	3.294	1.622	0.304	0.177	0.628	0.14
8	Jeju Aewol	0.54	3.527	1.894	0.519	0.252	1.046	0.22
9	Gunsan	0.20	3.769	1.928	0.472	0.227	0.920	0.37

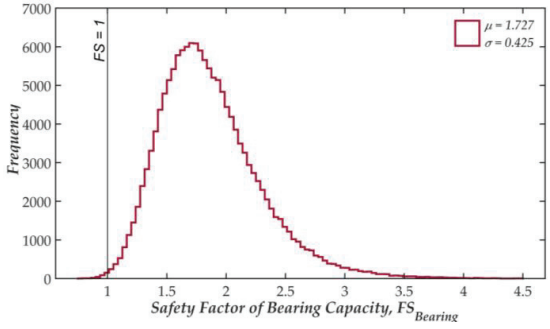

Figure 13. Histogram of the bearing capacity safety factor of foundation (Gamcheon BRW).

Figure 14 presents the reliability index of the nine BRWs with respect to the three overall failure modes, including sliding, overturning, and foundation. Except Onsan case, which has lowest reliability index for foundation bearing capacity, the eight breakwaters have the smallest RIs for the sliding mode. Meanwhile the largest value of RIs are always for overturning mode. Notably, the Onsan BRW shows the remarkably low design wave height compared with the others, while the height of rubble mound is about a half of the water depth. These special features may reduce the wave forces on the caisson, meanwhile the high rubble mound may face a frequent failure. The average RI values of the nine BRWs are approximately 1.89 ($P_f \approx 0.0417$) and 3.24 ($P_f \approx 0.0028$), corresponding to the sliding state and failure occurrence in the foundation. Thereby, under similar service conditions, sliding failures might be observed much more frequently (about 15 times) than foundation failures. However, lower failure probability for sliding state in comparison with failures in foundation does not suggest that sliding damages will always take place before failures occurring in the rubble mound or subsoil—sliding failures are merely more common among the three overall stability conditions.

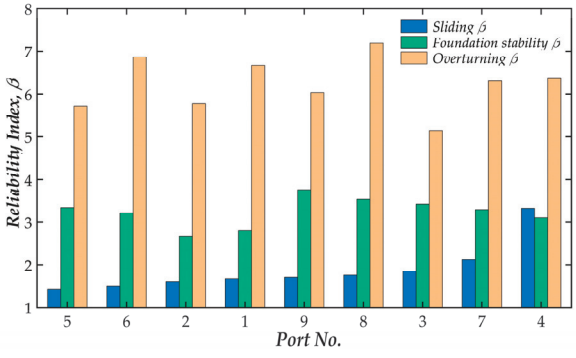

Figure 14. Reliability index in different overall failure modes of BRWs (sorted by $\beta_{Sliding}$).

5. Conclusions

The present study focuses on the evaluation of the three most significant failures related to the overall stability of typical Korean vertical composite breakwaters using reliability approaches. Three primary sources of uncertainties are considered to clarify the variables' sensitivity to the safety of breakwaters. The results presented in this work have provided the following conclusions.

First, among the three overall breakwater failure modes, the sliding mode is the most frequent failure state, so any such damage is a priority that needs to be surveyed to determine an appropriate width of caisson sections. Additionally, overturning may be rare in a breakwater failure because a remarkably low failure probability is obtained (25×10^{-8}).

Second, in the most critical failure mode, the sliding state, the friction coefficient, and horizontal wave force contribute much more significantly to the safety of a breakwater in comparison with other concerned uncertainties.

Third, the results of the three methods, MVFOSM, FORM and MCS, applied to explicit performance functions, agree well, validating that these methods could be performed to conduct a reliability-based analysis for sliding and overturning. However, the simpler methods, i.e., MVFOSM or FORM, should be applied for the explicit definition of performance functions. Furthermore, implicit or nonlinear problems like the evaluation of breakwater's foundation failure can be solved by applying reliability methods such as MCS.

Finally, a reliability analysis can overcome the drawbacks of the conventional deterministic design approach to provide a more consistent safety level of breakwaters. Additionally, it is expected that the reliability index of a breakwater against sliding state can be estimated from the results of the conventional deterministic design, i.e., the safety factor using the proposed linear regression line.

Author Contributions: Conceptualization, J.H., D.K. and N.S.D.; Methodology, N.S.D., J.H. and D.K.; Software, N.S.D and V.H.M.; Validation, J.H., N.S.D., K.K. and V.H.M.; Formal analysis, J.H., N.S.D, and V.H.M.; Resources, J.H. and K.K.; Writing-Original Draft Preparation, N.S.D, V.H.M. and J.H.; Writing—Review and Editing, J.H., N.S.D., and V.H.M.; Supervision, J.H. All authors have read and agreed to the published version of the manuscript.

Funding: This research was funded by the Ministry of Oceans and Fisheries, Korea, grant number 20180323.

Acknowledgments: This research was a part of the project entitled 'Development of Design Technology for Safe Harbor from Disasters' funded by the Ministry of Oceans and Fisheries, Korea.

Conflicts of Interest: The authors declare no conflict of interest.

References

1. Goda, Y. *Random Seas and Design of Maritime Structures*; University of Tokyo Press: Tokyo, Japan, 2000.
2. Bruining, J.W. Wave Forces on Vertical Breakwaters. Reliability of Design Formula. Master's Thesis, Degree-Granting University, Delft, The Netherlands, 1994.
3. Takahashi, S.; Shimosako, K.-I.; Kimura, K.; Suzuki, K. Typical failures of composite breakwaters in Japan. In Proceedings of the 27th International Conference on Coastal Engineering (ICCE), Sydney, Australia, 16–21 July 2000; pp. 1899–1910.
4. Takagi, H.; Esteban, M.; Shibayama, T. *Stochastic Design of Caisson Breakwaters: Lessons from Past Failures and Coping with Climate Change*; Elsevier Inc.: Amsterdam, The Netherlands, 2015; pp. 635–673. [CrossRef]
5. Oumeraci, H. Review and analysis of vertical breakwater failures—Lessons learned. *Coast. Eng. Spec. Issue Vert. Breakwaters* **1994**, *22*, 3–29. [CrossRef]
6. Kim, T.-M.; Takayama, T. Improved evaluation of the expected sliding distance of a caisson and practical parameters of uncertain factors. In Proceedings of the 2nd International Conference (Asian and Pacific Coasts, 2003), Makuhari, Japan, 29 February–4 March 2004; pp. 1–16. [CrossRef]
7. Ministry of Oceans and Fisheries. *Harbor and Fishing Port Design Standards*; Ministry of Oceans and Fisheries: Seoul, Korea, 2014.
8. Low, B.K.; Phoon, K.K. Reliability-based design and its complementary role to Eurocode 7 design approach. *Comput. Geotech.* **2014**, *65*, 30–44. [CrossRef]
9. Van der Meer, J.W. Rock slopes and gravel beaches under wave attack. Ph.D. Thesis, Degree-Granting University, Delft, The Netherlands, 1988.
10. Christiani, E. Application of Reliability in Breakwater Design. Ph.D. Thesis, Hydraulics & Coastal Engineering Laboratory, Department of Civil Engineering, Aalborg University University, Aalborg, Denmark, 1997.
11. Burcharth, H.F. Introduction of partial coefficients in the design of rubble mound breakwaters. In Proceedings of the Conference on Coastal Structures and Breakwaters, ICE, London, UK, 1 January 1992; pp. 543–565.
12. Burcharth, H.F.; Sorensen, J.D. Design of vertical wall caisson breakwaters using partial safety factors. In Proceedings of the 26th Conference on Coastal Engineering, Copenhagen, Denmark, 22–26 June 1998; pp. 2138–2151.
13. Oumeraci, H.; Kortenhaus, A.; Allsop, W.; de Groot, M.; Crough, R.; Vrijling, H.; Voortman, H. *Probabilistic Design Tools for Vertical Breakwaters*; Swets & Zeitlinger, B.V.: Lisse, The Netherlands, 2001.

14. Kim, S.W.; Suh, K.D. Application of reliability design methods to Donghae Harbor breakwater. *Coast. Eng. J.* **2006**, *48*, 31–57. [CrossRef]
15. Kim, S.W.; Suh, K.D. Reliability analysis of breakwater armor blocks: Case study in KOREA. *Coast. Eng. J.* **2010**, *52*, 331–350. [CrossRef]
16. Hong, S.Y.; Suh, K.D.; Kweon, H.M. Calculation of expected sliding distance of breakwater caisson considering variability in wave direction. *Coast. Eng. J.* **2004**, *46*, 119–140. [CrossRef]
17. Kim, S.W.; Suh, K.D. Evaluation of target reliability indices and partial safety factors for sliding of caisson breakwaters. *J. Coast. Res.* **2011**, *64*, 622–626.
18. Takayama, T.; Ikeda, N. *Estimation of Sliding Failure Probability of Present Breakwaters for Probabilistic Design*; Ministry of Transport: Yokosuka, Japan, 1992.
19. Goda, Y.; Takagi, H. A Reliability design method of caisson breakwaters with optimal wave heights. *Coast. Eng. J.* **2000**, *42*, 357–387. [CrossRef]
20. Kobayashi, M.; Terashi, M.; Takahashi, K. *Bearing Capacity of a Rubble Mound Supporting a Gravity Structure*; Ministry of Transport: Yokosuka, Japan, 1987.
21. Takagi, H.; Esteban, M. Practical methods of estimating tilting failure of caisson breakwaters using a Monte-Carlo simulation. *Coast. Eng. J.* **2013**, *55*. [CrossRef]
22. Shimosako, K.A.T.S. *Reliability Design Method of Composite Breakwater Using Expected slIding Distance*; Ministry of Transport: Yokosuka, Japan, 1998; pp. 4–30.
23. Hanzawa, M.; Sato, H.; Takahashi, S.; Shimosako, K.; Takayama, T.; Tanimoto, K. New stability formula for wave-dissipating concrete blocks covering horizontally composite breakwaters. In Proceedings of the Coastal Engineering Conference, Orlando, FL, USA, 2–6 September 1996; pp. 1665–1678.
24. Cornell, C.A. A probability-based structural code. *ACI J.* **1969**, *66*, 974–985. [CrossRef]
25. Ang, A.H.; Tang, W.H. *Probability Concepts in Engineering Planning and Design, Volume 2: Decision, Risk, and Reliability*; John Wiley & Sons: New York, NY, USA, 1984.
26. Hasofer, A.M.; Lind, N.C. Exact and Invariant Second-Moment Code Format. *ASCE J. Eng. Mech. Div.* **1974**, *100*, 111–121.
27. Haldar, A.; Mahadevan, S. *Probability, Reliability and Statistical Methods in Engineering Design*; John Wiley: Hoboken, NJ, USA, 2000.
28. United States Army Corps of Engineers. *Coastal Engineering Manual Part VI: Design of Coastal Project Elements (EM 1110-2-1100)*; Books Express Publishing: Washington, DC, USA, 2011; Volume 1100-2-110.
29. MLIT. *Technical Standard and Commentaries for Port and Harbor Facilities in Japan*; Ministry of Land, Infrastructure, Transport and Tourism (MLIT); Ports and Harbors Bureau: Tokyo, Japan, 2009.
30. Goda, Y. New wave pressure formulae for composite breakwaters. In Proceedings of the Proceedings International Conference Coastal Engineering (ICCE), Copenhagen, Denmark, 24–28 June 1974; pp. 1702–1720.
31. Van der Meer, J.W.; D'Angremond, K.; Juhl, J. Probabilistic calculations of wave forces on vertical structures. In Proceedings of the International Conference Coastal Engineering (ICCE), Kobe, Japan, 23–28 October 1994; American Society of Civil Engineers: Reston, VA, USA, 1994; pp. 1754–1767.
32. Vrijling, J.K. Evaluation of uncertainties and statistical descriptions. In Proceedings of the Task 4 Workshop Hannover, MAST III, PROVERBS-Project: Probabilistic Design Tools for Vertical Breakwaters, Hannover, Germany, September 1996.
33. Ching, J.; Phoon, K.K.; Hu, Y.G. Efficient evaluation of reliability for slopes with circular slip surfaces using importance sampling. *J. Geotech. Geoenviron. Eng.* **2009**, *135*, 768–777. [CrossRef]
34. Allen, T.M.; Nowak, A.S.; Bathurst, R.J. Calibration to Determine Load and Resistance Factors for Geotechnical and Structural Design. *Transp. Res. Circ.* **2005**. [CrossRef]
35. Duncan, J.M.; Wright, S.G. The accuracy of equilibrium methods of slope stability analysis. *Eng. Geol.* **1980**, *16*, 5–7. [CrossRef]
36. Vrijling, J.K. *Probabilistic Design Tools for Vertical Breakwaters. Final Report. Volume IId. Probabilistic Aspects*; Swets & Zeitlinger, B.V.: Lisse, The Netherlands, 1999.
37. Bhattacharya, G.; Jana, D.; Ojha, S.; Chakraborty, S. Direct search for minimum reliability index of earth slopes. *Comput. Geotech.* **2003**, *30*, 455–462. [CrossRef]
38. Chowdhury, R.N.; Xu, D.W. Geotechnical system reliability of slopes. *Reliab. Eng. Syst. Saf.* **1995**, *47*, 141–151. [CrossRef]

39. Cho, S.E. Effects of spatial variability of soil properties on slope stability. *Eng. Geol.* **2007**, *92*, 97–109. [CrossRef]
40. Griffiths, D.V.; Fenton, G.A.; Denavit, M.D. Traditional and advanced probabilistic slope stability analysis. In Proceedings of the Geotechnical Special Publication, Denver, CO, USA, 18–21 February 2007; p. 19.
41. Bishop, A.W. The use of the slip circle in the stability analysis of slopes. *Geotechnique* **1955**, *5*, 7–17. [CrossRef]

Journal of
Marine Science and Engineering

MDPI

Article

Wave and Hydrodynamic Processes in the Vicinity of a Rubble-Mound, Permeable, Zero-Freeboard Breakwater

Theofano I. Koutrouveli and Athanassios A. Dimas *

Department of Civil Engineering, University of Patras, 26500 Patras, Greece; thkoutrouv@upatras.gr
* Correspondence: adimas@upatras.gr

Received: 23 January 2020; Accepted: 13 March 2020; Published: 17 March 2020

Abstract: A numerical study for the effect of crest width, breaking parameter, and trunk permeability on hydrodynamics and flow behavior in the vicinity of rubble-mound, permeable, zero-freeboard breakwaters (ZFBs) is presented. The modified two-dimensional Navier-Stokes equations for two-phase flows in porous media with a Smagorinsky model for the subgrid scale stresses were solved numerically. An immersed-boundary/level-set method was used. The numerical model was validated for the cases of wave propagation over a submerged impermeable trapezoidal bar and a low-crested permeable breakwater. Five cases of breakwaters were examined, and the main results are: (a) The size of the crest width, B, does not notably affect the wave reflection, vorticity, and currents in the seaward region of ZFBs, while wave transmission, currents in the leeward side, and mean overtopping discharge all decrease with increasing B. A non-monotonic behavior of the wave setup is also observed. (b) As the breaking parameter decreases, wave reflection, transmission, currents, mean overtopping discharge, and wave setup decrease. This observation is also verified by relevant empirical formulas. (c) As the ZFB trunk permeability decreases, an increase of the wave reflection, currents, wave setup, and a decrease of wave transmission and mean overtopping discharge is observed.

Keywords: rubble-mound; zero-freeboard; porous-media; immersed-boundary; level-set; Smagorinsky subgrid scale model; wave reflection; wave transmission; wave overtopping; wave setup

1. Introduction

The role of rubble-mound low-crested breakwaters (LCBs) in coastal protection, whose main advantage is their mild aesthetic impact on the natural environment, is to partially dissipate incident waves. Consequently, in the seaward region of LCBs, the most important wave processes are breaking and reflection, while in their leeward region, the most important ones are overtopping, transmission, and setup. These wave processes induce also significant flow processes in the vicinity of LCBs. The influence of the geometrical characteristics of LCBs on wave and flow processes has been studied extensively for emerged or submerged LCBs. The case of zero-freeboard breakwaters (ZFBs), where the crest level of the structure is at the still water level (SWL), is the subject of the present study. In the following literature review, the focus is on experimental and numerical (only depth-resolving flow models) studies of rubble-mound, two-dimensional vertical (2-DV) LCBs.

In terms of wave reflection in the seaward region of permeable LCBs with rock armor, Zanuttigh and Van der Meer [1] analyzed several experimental datasets and derived an empirical formula for the prediction of the reflection coefficient K_r. Specifically for ZFBs, the formula in [1] becomes:

$$K_r = C\tanh\left(A\xi_0^b\right), \tag{1}$$

where $A = 0.167(1 - \exp(-3.2\gamma_f))$ and $b = 1.49(\gamma_f - 0.38)^2 + 0.86$ are calibration parameters related to the roughness factor γ_f, $C < 1$ is a reduction parameter necessary for LCBs, $\xi_0 = \tan a(gT^2/2\pi H_i)^{1/2}$ is the breaker parameter, $\tan a$ is the seaward slope of the ZFB, T is the wave period of the incident waves, and H_i is the wave height of the incident waves at the seaward toe of the ZFB. In terms of wave transmission in the leeward region of LCBs, empirical formulas for the prediction of the transmission coefficient:

$$K_t = \frac{H_t}{H_i}, \tag{2}$$

where H_t is the wave height at the leeward toe of the LCB, derived in [2–5]. Specifically for ZFBs with rock armor, the corresponding empirical formulas are:

$$K_t = \begin{cases} 0.51 - 0.11\frac{B}{d_S}, & \text{(Seelig, 1980)} \\ 1 - \exp\left(-1.09\frac{H_i}{B}\right), & \text{(Seabrook \& Hall, 1998)} \\ \left.\begin{array}{l} 0.64(1 - \exp(-0.50\xi_0))\left(\frac{B}{H_i}\right)^{-0.31}, \text{ for } B/H_i \le 8 \\ \text{linear interpolation} \quad , \text{ for } 8 < B/H_i < 12 \\ 0.51(1 - \exp(-0.41\xi_0))\left(\frac{B}{H_i}\right)^{-0.65}, \text{ for } B/H_i \ge 12 \end{array}\right\} & \text{(van der Meer et al., 2005)} \\ \left(\min\left(0.74; 0.62\xi_0^{0.17}\right) - 0.25\min\left(2.2; \frac{B}{\sqrt{H_i\lambda_0}}\right)\right)^2, & \text{(Buccino \& Calabrese, 2007)} \end{cases}, \tag{3}$$

where B is the crest width of the ZFB, d_S is the water depth at the seaward toe of the ZFB, and $\lambda_0 = gT^2/2\pi$ is the deep-water wavelength. The empirical formulas in [2,3] were derived using experimental datasets of LCBs with impermeable core, while the empirical formulas in [4,5] used practically the same datasets as reported in [4]. In all cases of Equation (3), the important effect of ξ_0 and/or B on the wave transmission is noted.

In terms of the mean overtopping discharge over rubble-mound ZFBs, the following empirical formula is suggested in EurOtop [6]:

$$q = \frac{0.09}{f_q}\sqrt{gH_i^3}, \tag{4}$$

where f_q is an adjustment factor that accounts for scale effect corrections. In terms of the wave setup, δ, at the leeward toe of rubble-mound, permeable LCBs, experimental data were presented in [7,8]. In both studies, several cases of ZFBs were included, and the following empirical formulas were derived:

$$\delta = \begin{cases} 0.6H_i\exp\left(-0.7^2\right), & \text{(Diskin et al., 1970)} \\ \frac{B}{8gD_{50}}\left(\frac{H_i\lambda_i}{d_S T}\right)^2, & \text{(Loveless et al., 1998)} \end{cases}, \tag{5}$$

where D_{50} is the mean diameter of the rubble rocks and λ_i is the wavelength at the seaward toe of the ZFB. Semi-analytical models for the prediction of δ were also presented [9,10], but they refer to submerged barriers and are not considered here where the focus is on ZFBs.

The influence of the geometrical characteristics of rubble-mound, permeable, submerged breakwaters on wave transmission was investigated numerically (potential flow theory in the fluid region and viscous flow in the permeable trunk of the breakwater) in [11]. It was concluded that increasing the crest width and/or decreasing the crest submergence depth results in the reduction of K_t, while increasing the permeability of the breakwater, i.e., increasing the porosity or the size of the rubble rocks, results in the increase of K_t and the reduction of K_r. The Navier-Stokes equations were solved numerically in [12] to simulate the interaction between a solitary wave and a permeable submerged bar. It was found that the increase of porosity from 0.4 to 0.52 results in the reduction of K_t, while if the porosity is further increased up to 0.7, the transmission coefficient increases, indicating that an optimum porosity value seems to exist.

Near-field flow processes that occur due to the interaction between regular waves and rubble-mound, permeable LCBs were studied experimentally and numerically in [13]. The numerical

model was based on the "Cornell Breaking Waves and Structures" (COBRAS) software [14]. In both the experiments and the simulations, a recirculation system was devised to return flow to the seaward region of the LCB to balance the non-realistic pilling of water in the leeward region of the LCB; this system was found to be crucial in the modeling of 2-DV LCBs. Specifically for the ZFB case in [13], it was tan$a$ = 1/2, d_s = 25 cm, B = 100 cm, while the median diameter, D_{50}, of the rocks was 4.80 cm in the armor layer and 1.47 cm in the core. Several regular wave cases were examined, which for the ZFB case corresponded to the ranges $0.20 \leq H_i/d_s \leq 0.78$ and $9.38 \leq \lambda_i/d_s \leq 19.63$. It was observed that breaking waves collapsed on the seaward edge of the ZFB crest inducing a strong vortex cell in this zone, a strong mean shoreward current developed over the ZFB crest, a primary vortex cell was formed in the leeward region of the ZFB, a weak mean seaward current developed in the ZFB trunk, and a secondary vortex cell was formed near the seaward toe of the ZFB.

Losada et al. [15] focused on the submerged breakwater cases in [13] with crest height h_c = 25 cm, d_s = 30 cm resulting into crest elevation R_c = −5 cm, and R_c/H_i = −0.52. They performed numerical simulations using the COBRAS model and found that the resulting K_r does not depend on B, while the shear stress field attains its maximum values along the armor layer of the crest. Losada et al. [15] also studied numerically a submerged breakwater case at a prototype scale with tan$a$ = 2/3, d_S = 5 m, B = 5 m, R_C = −0.5 m. The trunk of the breakwater was homogeneous with D_{50} = 1.44 m, while the incident wave parameters at the seaward toe of the breakwater were H_i = 0.97 m (R_c/H_i = −0.52) and T = 6 s. It was found that the velocity of the flow over the crest was about one order of magnitude larger than the one in the permeable trunk of the breakwater.

Lara et al. [16] exploited the capability of COBRAS to study irregular wave interaction with the submerged permeable breakwater case in [13], and they presented regular wave interaction with an LCB of permeable armor layer and less permeable core. The latter case corresponded to the LCB studied experimentally at the Maritime Engineering Laboratory of the Polytechnic University of Catalunya (Spain) as described in [17]. This LCB had tan$a$ = 1/2, h_c = 1.59 m, B = 1.825 m, while the median diameter, D_{50}, of the rocks was 10.82 cm in the armor layer and 3 ± 1 cm in the core. No ZFB case was considered; the only submerged case had R_c = −0.13 m, H_i = 0.286 cm (R_c/H_i = −0.45) and T = 2.18 s. The transmitted wave height in the leeward region of the LCBs was, in general, under-predicted by the numerical simulations in comparison to the experimental data; this discrepancy was attributed to several factors, including the inaccurate replication of the experimental LCB geometry in the numerical model.

In this paper, the interaction of regular waves with rubble-mound, permeable ZFBs was studied numerically using a two-phase flow model in the air-water region and a porous flow model in the trunk of the ZFBs. The objective was to reveal the effect of crest width and trunk permeability on the main wave (reflection, transmission, and leeward setup) and flow (vortex generation, mean currents, and overtopping discharge) processes for ZFBs. The formulations are based on the Navier-Stokes equations, and not on a depth-averaged approach, to capture the vertical variability of flow phenomena. At present, the computational cost of using solvers based on the Navier-Stokes equations in large-scale coastal problems is high, but it is reasonable for smaller scale problems such as the present one.

2. Materials and Methods

2.1. Formulation and Numerical Implementation

The two-phase (water and air) 2-DV flow induced by regular waves in the vicinity of rubble-mound, permeable ZFBs was modeled as one-fluid flow as described in [18]. This formulation was further modified to seamlessly connect the external wave-induced flow to the porous medium flow in the permeable ZFB trunk by using the model in [19]. For the external flow, the formulation in [18] is similar to the approach in large-eddy simulation (LES) where the subgrid flow scales resulting from wave breaking are not resolved but their effect on the resolved flow scales is modeled. The resulting non-dimensional governing equations are:

$$\frac{\partial u_i}{\partial x_i} = 0, \tag{6}$$

$$\begin{aligned}\frac{1+c_A}{n}\frac{\partial u_i}{\partial t} + \frac{u_j}{n^2}\frac{\partial u_j}{\partial x_j} = -\frac{1}{\rho}\frac{\partial P}{\partial x_i} + \frac{\delta_{i2}}{\mathrm{Fr}^2} + \frac{1}{\mathrm{Re}}\frac{1}{n}\frac{1}{\rho}\frac{\partial}{\partial x_j}\left(\mu\frac{\partial u_i}{\partial x_j}\right) - \frac{\partial \tau_{ij}}{\partial x_j} - \\ a_p\frac{\left(1-n^2\right)}{n^3}\frac{\nu}{D_{50}^2}\frac{1}{\mathrm{Re}}u_i - \beta_p\left(1+\frac{7.5}{\mathrm{KC}}\right)\frac{1-n}{n^3}\frac{1}{D_{50}}u_i\sqrt{u_j u_j} + f_i\end{aligned}, \tag{7}$$

where $x_1 = x$ and $x_2 = z$ are the streamwise and vertical coordinates, respectively, t is the time, u_i is the velocity field, P is the total pressure, ρ is the normalized fluid density, μ is the normalized fluid dynamic viscosity, Fr is the Froude number, δ_{ij} is the Kronecker's delta, Re is the Reynolds number, τ_{ij} are the modeled subgrid-scale (SGS) stresses, and c_A is the added mass coefficient in the form [20]:

$$c_A = 0.34\frac{1-n}{n}, \tag{8}$$

where n is the effective porosity ($n = 1$ in the external flow and $n < 1$ in the ZFB trunk), D_{50} is the median diameter of the rocks forming the ZFB trunk, a_p and β_p are calibration constants, KC is the Keulegan-Carpenter number representing the ratio of the characteristic length scale of fluid particle motion to that of the porous media [21]:

$$\mathrm{KC} = \frac{T\sqrt{u_i u_i}}{nD_{50}}, \tag{9}$$

where T is the characteristic wave period and f_i is a term associated with the implementation of boundary conditions on solid surfaces using the Immersed Boundary (IB) method. The velocity components in Equations (6) and (7) are the resolved ones for the external flow, based on the LES approach in [18], and the spatially-averaged ones for the porous flow in the ZFB trunk, based on the model in [19].

The SGS stresses in Equation (7) were modeled using the eddy-viscosity model in [22]:

$$\tau_{ij} - \frac{\delta_{ij}}{2}\tau_{kk} = -2\nu_{\mathrm{sgs}}S_{ij} = -2(C_s\Delta)^2|S|S_{ij}, \tag{10}$$

where $C_s = 0.1$ is the model parameter, Δ = is the filter length scale of the grid, and $|S| = (2S_{ij}S_{ij})^{1/2}$ is the magnitude of the resolved-scale, and the strain-rate tensor is:

$$S_{ij} = \frac{1}{2}\left(\frac{\partial u_i}{\partial x_j} + \frac{\partial u_j}{\partial x_i}\right), \tag{11}$$

The evolution of the free surface was tracked using the signed distance function, φ, where $\varphi > 0$ in the water, $\varphi < 0$ in the air, and $\varphi = 0$ at the water-air interface. The computation of φ (evolution and re-initialization) was based on the level-set method described in [18]. The normalized density, modeled with a sharp jump across the water-air interface, and the normalized viscosity, modeled with a smooth variation across the water-air interface, were defined, respectively, as:

$$\rho = \frac{\rho_a + (\rho_w - \rho_a)H(\varphi)}{\rho_w}, \tag{12}$$

And:

$$\mu = \frac{\mu_a + (\mu_w - \mu_a)H_\varepsilon(\varphi)}{\mu_w}, \tag{13}$$

where index 'w' corresponds to the water phase, index 'a' corresponds to the air phase:

$$H(\phi) = \left\{ \begin{array}{ll} 1, & \varphi \geq 0 \\ 0, & \varphi < 0 \end{array} \right\}, \tag{14}$$

is a stepwise Heaviside function:

$$H_\varepsilon(\phi) = \left\{ \begin{array}{cc} 1, & \varphi > \varepsilon \\ \frac{1}{2}\left[1 + \frac{\varphi}{\varepsilon} + \frac{1}{\pi}\sin\left(\frac{\pi\varphi}{\varepsilon}\right)\right], & |\varphi| \leq \varepsilon \\ 0, & \varphi < -\varepsilon \end{array} \right\}, \tag{15}$$

is a smoothed Heaviside function, and ε is a parameter with length dimensions of order comparable to the grid cell [23]. Note that $\rho = 1$ and $\mu = 1$ in the water, and $\rho = 1.2 \times 10^{-3}$ and $\mu = 1.8 \times 10^{-2}$ in the air.

The spatial discretization of the governing equations was based on the use of finite differences on a Cartesian staggered grid where velocity components are defined at the cell edges, while p and φ are defined at the cell center. Therefore, the breakwater geometry, the sea bed, and the free surface do not follow grid lines but they are "immersed" in the numerical grid. For the sea bed, in particular, the implementation of the appropriate non-slip boundary conditions was based on the Immersed Boundary (IB) method in [24]. Details about the implementation are given in [18]. The main advantage of this method is the computational efficiency since the appropriate boundary conditions on solid surfaces are imposed by only modifying the additional term f_i in Equation (7). This term is zero on all grid points except the so-called "forcing points," which are the ones in the fluid phase that have at least one neighboring grid point in the solid phase. The value of f_i on the forcing points is computed so that it enforces the non-slip boundary condition on the sea bed.

A fractional-step method was used for the velocity-pressure coupling. First, an intermediate velocity field was computed explicitly, using an Adams-Bashforth scheme, without taking into account the pressure term of Equation (7):

$$\frac{u_i^* - u_i^n}{\Delta t} = \frac{3}{2}H\left(u_i^n, u_j^n\right) - \frac{1}{2}H\left(u_i^{n-1}, u_j^{n-1}\right) + f_i, \tag{16}$$

where H is a spatial operator, which includes the convective, gravity, viscous, SGS, and porous terms. The final velocity field was computed using the pressure gradient:

$$u_i^{n+1} = u_i^* - \frac{\Delta t}{\rho}\frac{\partial P^{n+1}}{\partial x_i}, \tag{17}$$

which was obtained by solving the Poisson equation for the total pressure:

$$\frac{\partial}{\partial x_i}\left(\frac{1}{\rho}\frac{\partial P^{n+1}}{\partial x_i}\right) = -\frac{1}{\Delta t}\frac{\partial u_i^*}{\partial x_i}, \tag{18}$$

which was derived by enforcing the continuity constraint on the final velocity field. The spatial discretization of the left-hand side of Equation (18) results in a pentadiagonal matrix, the elements of which are reconstructed at each time step due to the evolution of the free surface. The inversion of the matrix was achieved by a shared-memory multiprocessing parallel direct solver using the Intel MKL PARDISO® 11.0 library.

2.2. Wave Generation

In all cases examined in this paper, regular waves were generated by a piston-type wavemaker at the left boundary of the computational domain (Figures 1, 3, and 5). Using second-order theory, the imposed horizontal velocity was [25]:

$$u = \frac{1}{2}S\omega\cos(\omega t - \pi/2) + \frac{1}{16}\frac{H^2}{d}\omega\left(\frac{3\cosh(kd)}{\sinh^3(kd)} - \frac{2S}{H}\right)\cos(2\omega t - \pi), \quad (19)$$

where:

$$S = H\frac{\sinh(2kd) + 2kd}{4\sinh^2(kd)}, \quad (20)$$

is the stroke of the wavemaker, H is the height of the generated waves, $k = 2\pi/\lambda$ is their wavenumber, λ is their wavelength, $\omega = 2\pi/T$ is their radial frequency, T is their period, and d is the water depth at the wavemaker. The imposed horizontal velocity was continuously corrected to achieve zero mean mass flux. In two-dimensional (2D) flow experiments over low-crested structures, the non-realistic wave setup in the leeward region of the structures, caused by water pilling-up due to overtopping, affects significantly the dynamics of the flow in the vicinity of the breakwaters. On the other hand, in real cases and three-dimensional (3D) problems, this water is allowed to return offshore by the ends of the structures. In many experimental projects, recirculation systems are applied in the leeward region of the breakwaters for the prevention of this phenomenon [13]. The numerical correction of the imposed horizontal velocity applied here functions as a flow recirculation system.

The inflow region just downstream of the wavemaker had a horizontal bottom of constant water depth with a length equal to about three wavelengths, in order for the generated waves to be fully developed when they reach the breakwater (Figures 1, 3, and 5). A relaxation zone of length equal to one wavelength (length decided after trial and error) was implemented just downstream of the wavemaker to avoid undesired wave reflections from the left boundary of the computational domain. Inside the relaxation zone, according to [26], a relaxation function was applied:

$$q = a_R q_{\text{computed}} + (1 - a_R)q_{\text{target}}, \quad (21)$$

where q is either a velocity component or the level-set function,

$$a_R(l_R) = 1 - \frac{\exp\left(l_R^{3.5}\right) - 1}{\exp(1) - 1}, \quad (22)$$

is the absorption rate, and $l_R \in [0{:}1]$ is defined so that $a_R = 0$ at the left boundary of the computational domain ($l_R = 1$) and $a_R = 1$ at the end of the relaxation zone ($l_R = 0$).

2.3. Validation

The numerical model was validated by comparison to the cases of wave propagation over a submerged impermeable trapezoidal bar and a low-crested permeable breakwater.

The first validation case (Figure 1) corresponds to the experiments in [27]. In these experiments, waves of height $H = 0.02$ m and period $T = 2$ s were generated over a region of constant water depth $d_S = 0.4$ m before reaching the bar. The crest depth was equal to $d_C = 0.1$ m. Using d_S as the characteristic length and $(g/d_S)^{1/2}$ as the characteristic velocity scale, the Reynolds number was $\text{Re}_\text{d} = 800{,}000$. For the simulations (Figure 1), to achieve both adequate resolution in the wall boundary layer and a reasonable computational cost, the experiment was reproduced with $d_s = 0.15$ m using Froude scaling, leading to a Reynolds number $\text{Re}_\text{d} = 160{,}000$, i.e., five times smaller than the one in the experiments. A grid independence study was performed to select the appropriate grid size that resolves all important flow scales, i.e., vortices generated during wave breaking and flow structure in the wave boundary layer. After trial-and-error, the selected computational grid had a uniform size of $\Delta x/d_S = 0.02$ along x (460

grid points per wavelength of the incident wave), and a non-uniform size in z; $\Delta z/d_S = 0.005$ in the water and increasing to $\Delta z/d_S = 0.01$ in the air. The corresponding values in the water with respect to the Stokes length, δ, were $\Delta x/\delta = 4.5$ and $\Delta z/\delta = 1.13$, which were sufficient to get a good resolution with at least five grid points in the wave boundary layer over the bed.

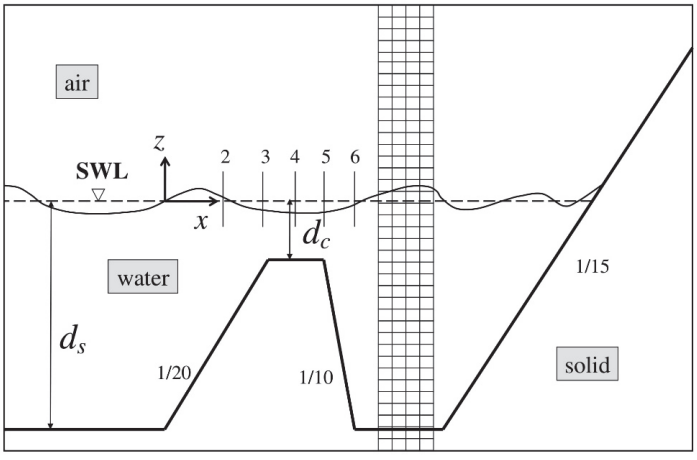

Figure 1. Sketch of the computational domain and part of the Cartesian grid, as well as definitions of parameters for the numerical simulation of wave propagation over a submerged impermeable trapezoidal bar [27]. Note that the axes are not to scale. The distance from the wavemaker to the seaward toe of the bar is 27 d_S, while the distance from the leeward toe of the bar to the toe of the absorbing beach is 5 d_S.

The time step was selected so that the stability/convergence criteria of the numerical solution to be satisfied. These criteria are the CFL (Courant-Friedrichs-Lewy) and the VSL (Viscous Stability Limit). In the present work, the CFL and VSL limits were equal to 2×10^{-2} and 7×10^{-4}, respectively:

$$\mathrm{CFL} = \max\left(|u_i|\frac{\Delta t}{\Delta x_i}\right) \leq 1, \tag{23}$$

$$\mathrm{VSL} = \max\left(\frac{1}{\mathrm{Re}}\frac{\Delta t}{\Delta x_i^2}\right) \ll 1, \tag{24}$$

In order for the flow field not to be affected by the height of the air layer in the computational domain, this was selected to be $1.5d_S$ above the SWL (after trial and error). The trapezoidal bar was impermeable; therefore, the no-slip condition on its surface was imposed using the IB method. Simulations were performed in the Greek supercomputer ARIS, deployed and operated by GRNET (Greek Research and Technology Network). ARIS consists of 532 computational nodes separated by four 'islands'. We deployed only one of the 'islands': the thin nodes, which consist of 426 nodes and 8520 CPU cores. In this case, the simulation time was 1 wave period per 6 h on ARIS. Comparisons of the free-surface elevation between the numerical results and the experimental data in [27] at five locations (Figure 1) over the bar during the last five wave periods are presented in Figure 2. A good agreement is observed; the r.m.s. (root mean square) relative error between the numerical results and the experimental data at each location is reported in the caption of Figure 2.

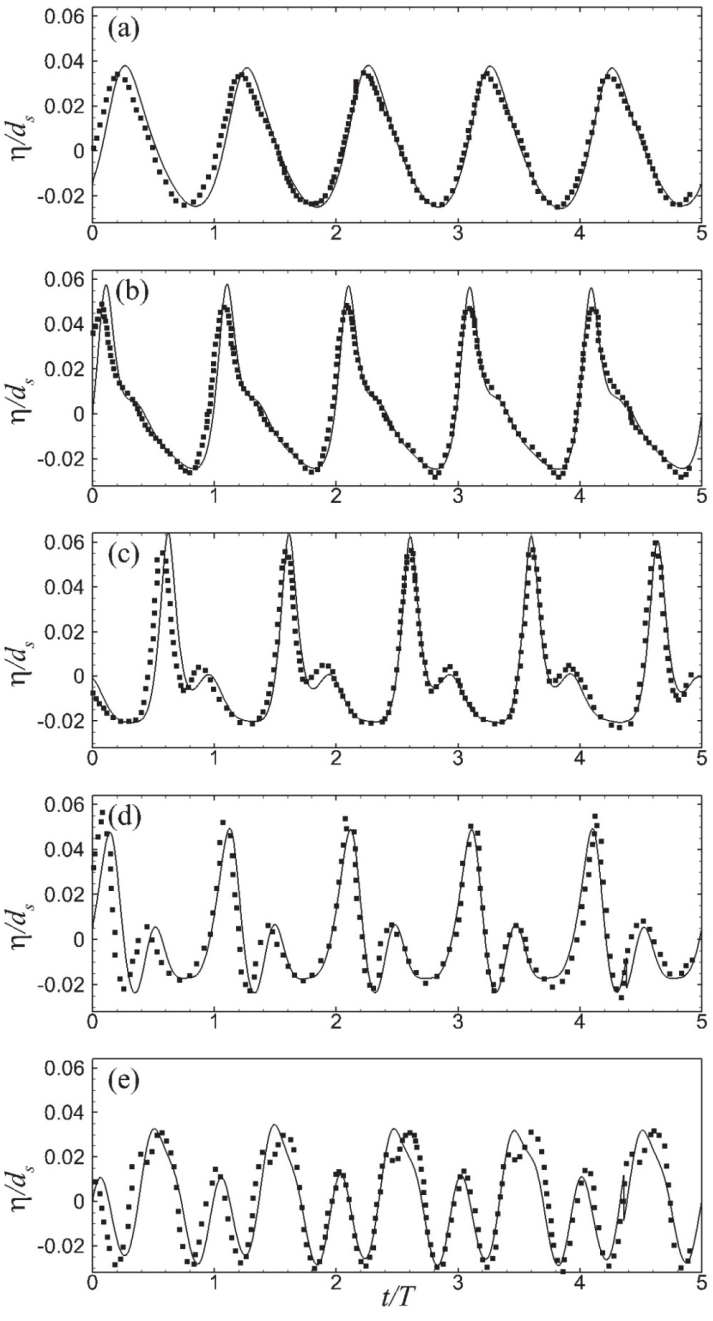

Figure 2. Variation of the free-surface elevation during five wave periods, after 20 wave periods of simulation, at five locations over a submerged impermeable trapezoidal bar. These five locations correspond, respectively, to the stations 2, 3, 4, 5, and 6 of Figure 1. The lines correspond to the present numerical results while the symbols to the experiments in [27]. The r.m.s. (root mean square) relative error of the free-surface elevation between numerical results and experimental data is: (**a**) 0.09, (**b**) 0.13, (**c**) 0.16, (**d**) 0.19, and (**e**) 0.18.

The second validation case (Figure 3) corresponds to wave transmission over the wide-crested submerged permeable breakwater in [13]. In these experiments, waves of height $H = 0.07$ m and period $T = 1.6$ s were generated over a region of constant water depth $d_F = 0.4$ m, which is followed by a beach of slope $\tan\beta = 1/20$ seawards of the breakwater. The depth at the breakwater toe was $d_S = 0.3$ m, while the crest depth was $d_C = 0.05$ m. As mentioned in the Introduction for these experiments, the trunk of the rubble-mound breakwater was permeable with a two-layer armor ($D_{50} = 4.8$ cm and $n = 0.53$) and a core with smaller rocks ($D_{50} = 1.47$ cm and $n = 0.49$). For the simulations (Figure 3), to achieve both adequate resolution in the wall boundary layer and a reasonable computational cost, the experiment was reproduced with $d_S = 0.12$ m using Froude scaling, leading to a Reynolds number $\mathrm{Re_d} = 130{,}000$, i.e., six times smaller than the one in the experiments. A mesh independence study was also performed. In order for the mesh not to affect the solution, the computational grid was selected to have a uniform size of $\Delta x/d_F = 0.02$ along x (355 grid points per wavelength of the incident wave), and a non-uniform size in z; $\Delta z/d_F = 0.005$ in the water and increasing to $\Delta z/d_F = 0.01$ in the air. The corresponding values in the water with respect to the Stokes length, δ, were $\Delta x/\delta = 4.2$ and $\Delta z/\delta = 1.06$, which were sufficient to get a good resolution with at least five grid points in the wave boundary layer over the bed. The CFL and VSL criteria were equal to 2×10^{-2} and 7×10^{-4}, respectively. In order for the flow field not to be affected by the height of the air layer in the computational domain, this was selected to be $1.5d_S$ above the SWL (after trial and error). The calibration values $\alpha_p = 1000$ and $\beta_p = 1.1$, according to [19,20], were used in Equation (7); the values $\beta_p = 0.8$ in the armor layer and $\beta_p = 1.2$ in the core were also used, according to [13], but with negligible differences in the results.

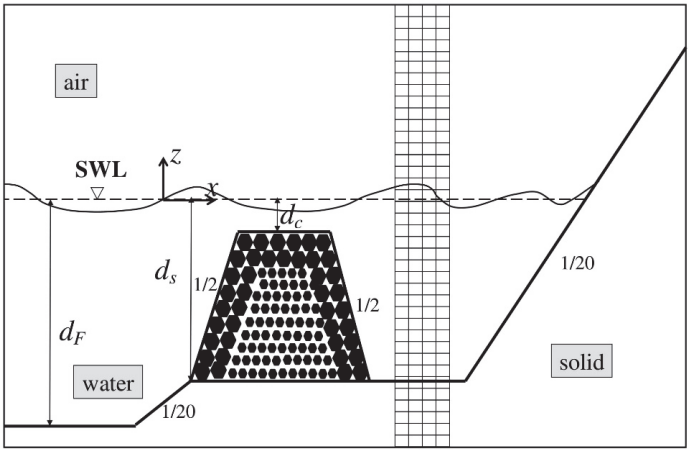

Figure 3. Sketch of the computational domain and part of the Cartesian grid, as well as definitions of the parameters for the numerical simulation of wave propagation over submerged permeable breakwater [13]. Note that the axes are not to scale. The distance from the wavemaker to the toe of the 1/20 slope is $19.3d_F$, while the distance from the leeward toe of the breakwater to the toe of the absorbing beach is $4.5d_F$.

Snapshots of the free surface elevation during the two wave periods, after 20 wave periods of simulation (one wave period per 6 h on ARIS), are shown in Figure 4, in comparison to the experimental data of crest and trough elevations in [13]. The horizontal coordinate and the free surface elevation are shown dimensionless based on d_F. The numerical model captures adequately the main characteristics of wave propagation over the submerged breakwater. More specifically, in the seaward region of the structure, the generation of a partially standing wave due to wave reflection is captured precisely by the model. In the vicinity of the crest and near the leeward region of the structure, the model captures adequately the wave dissipation due to wave breaking over the crest and due to filtration through

the permeable trunk, while the wave height is under-predicted in the far leeward region. This last behavior is similar to the one observed in [16]. The maximum r.m.s. relative error of the wave height between the numerical results and the experimental data is reported in the caption of Figure 4.

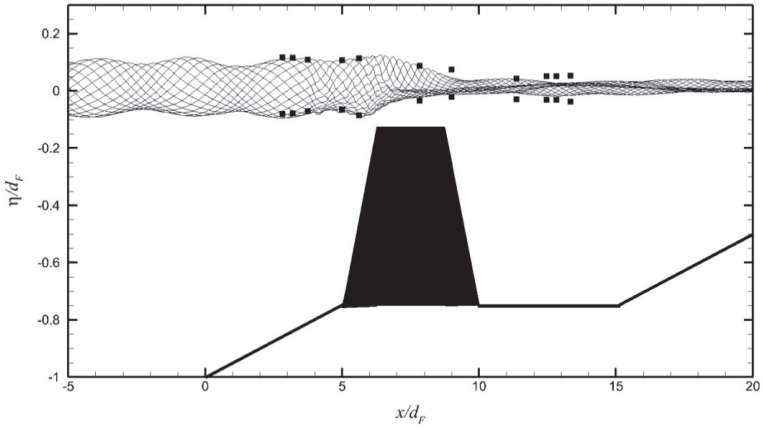

Figure 4. Envelope of the free-surface elevation of waves passing over submerged permeable breakwater. The lines correspond to the present numerical results while the symbols to the experiments in [13]. The maximum r.m.s. relative error of the wave height between numerical results and experimental data is less than 0.05 in the seaward region and 0.32 in the far leeward region.

3. Results

All ZFBs in the present study were rubble mound and permeable with tan$a$ = 1/2 for both seaward and leeward slopes. A sketch of the computational domain is shown in Figure 5. First, three different setups were considered to examine the effect of crest width (cases 1–3 in Table 1) on the hydrodynamic processes of wave reflection, overtopping, transmission, and setup, as well as the flow behavior in the seaward and leeward regions of these structures. In cases 1–3, the ZFBs were fully-permeable (homogeneous trunk permeability), while the crest width, B, was set equal to d_S, $2d_S$, and $3d_S$, respectively, where d_S is the constant water depth between the wavemaker and the seaward ZFB toe. Then, the effect of the incident wave period (cases 1 and 4 in Table 1) and the ZFB trunk permeability (cases 1 and 5 in Table 1) were also investigated for the ZFB case with $B = d_S$.

Table 1. Geometrical characteristics of the examined ZFB cases, the parameters of the incoming waves and the breaking ones on the seaward slope of the ZFB.

Case	Geometry				Incoming Waves			Breaking Waves on Seaward ZFB Slope	
	tan$a$	B/d_S	Armor D_{50}/d_S	Core D_{50}/d_S	H_i/d_S	$T(g/d_S)^{1/2}$	λ/d_S	d_b/d_S	H_b/d_S
1	1/2	1	0.31	0.31	0.2	9.8	9	0.178	0.205
2		2	0.31	0.31				0.175	0.201
3		3	0.31	0.31				0.180	0.202
4		1	0.31	0.31		6.9	6	0.179	0.197
5		1	0.31	0.031		9.8	9	0.171	0.217

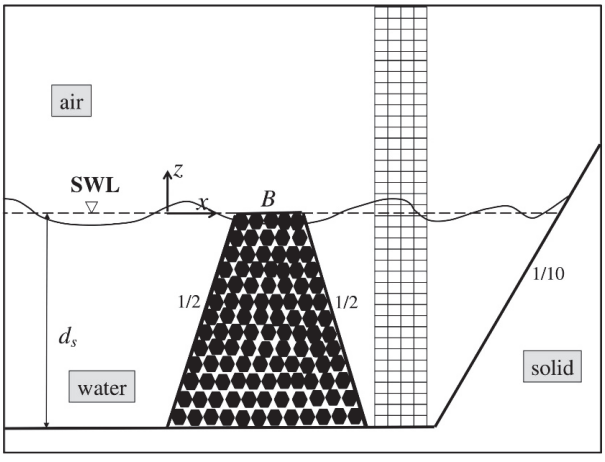

Figure 5. Sketch of the computational domain and part of the Cartesian grid for the permeable ZFB cases. Note that the axes are not to scale. The distance from the wavemaker to the seaward ZFB toe is $23d_S$, while the distance from the leeward ZFB toe to the toe of the absorbing beach is $9d_S$.

In dimensional terms, d_S was selected to be equal to 0.4 m, which corresponds to Reynolds number Re_d = 800,000. The geometrical details and the incident wave parameters for all cases are summarized in Table 1. For all cases, a grid independence study was performed, and the selected computational grid had a uniform size of $\Delta x/d_S = 0.02$ along x (300–450 grid points per wavelength of the incident waves), and a non-uniform size in z; $\Delta z/d_S = 0.0025$ in the water and increasing to $\Delta z/d_S = 0.01$ in the air. The corresponding values in the water with respect to the Stokes length, δ, were $\Delta x/\delta = 10.1 \div 12.1$ and $\Delta z/\delta = 1.27 \div 1.51$ according to the wave length, which were sufficient to get a good resolution with at least four grid points in the wave boundary layer over the bed. The small flow scales occurring during breaking at the ZFB seaward slope are modeled by the SGS eddy-viscosity model. In all simulations, the CFL and VSL criteria were equal to 2.0×10^{-2} and 5×10^{-4}, respectively. In order for the flow field not to be affected by the height of the air layer in the computational domain, this was selected to be $1.5d_S$ above the SWL (after trial and error). The calibration values $\alpha_p = 1000$ and $\beta_p = 1.1$, according to [19,20], were used in Equation (7).

Typical crest and trough elevation envelopes during 10 wave periods, after 20 wave periods of simulation (1 wave period per 6 h on ARIS), are shown in Figure 6 for case 1. From such envelope results, the breaking depth on the seaward ZFB slope and the corresponding wave height were identified at the location of the maximum wave crest elevation. In all cases, wave breaking occurred on the seaward slope and near the crest of the ZFBs; these results are summarized in Table 1. In cases 1–3, which correspond to the same incident wave and different crest width, the waveform in the seaward region of the ZFBs is similar, and a partially standing wave is generated due to reflection. In the leeward region of the ZFBs, the wave height, i.e., the wave energy, is different between cases 1–3 as it decreases with the increase of the crest width. In case 4, a decreased wave height is observed in the seaward region, while less wave energy is transmitted to the leeward region in comparison to case 1, which has the same crest width but larger incident wave period, i.e., a longer incident wavelength. In case 5, where the ZFB has a less permeable core, a slightly increased wave height is observed in the seaward region and slightly less wave energy is transmitted to the leeward region in comparison to case 1, which has the same crest width but larger ZFB trunk permeability.

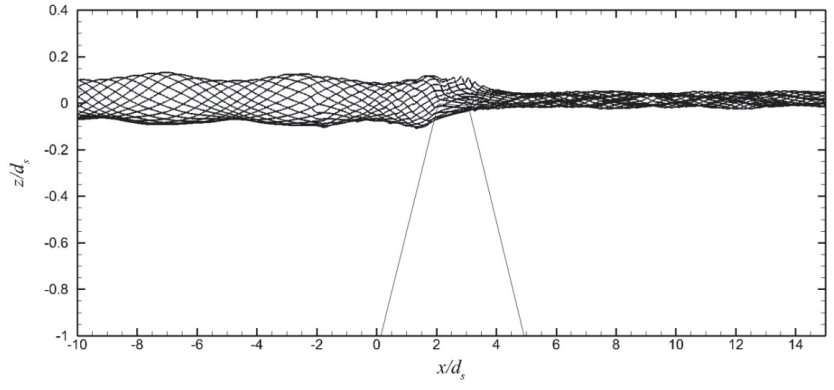

Figure 6. The envelope of the free surface elevation of waves breaking over the ZFB case 1.

The behavior of wave height in the seaward and leeward side of all ZFB cases is also demonstrated in terms of the reflection and transmission coefficients presented in Table 2. For the reflection coefficient, surface elevation time series at three locations in the seaward region of the ZFBs were obtained, and a reflection analysis was performed using the method in [28]. For the transmission coefficient, the surface elevation time series, recorded at the seaward and leeward toe of the ZFBs, were used to calculate the wave height at each position through spectral analysis. It is observed that wave transmission decreased, while wave reflection did not vary, with the increase of the crest width (cases 1–3) when incident wave height, incident wave period, and trunk permeability did not change. The decrease of wave transmission is attributed to the increase of wave dissipation over the ZFB crest as B increased. Decreasing the incident wave period (cases 1 and 4) results in the decrease of wave reflection and the decrease of wave transmission when the crest width and trunk permeability did not change. These decreases are associated with the decrease of ξ_0. Finally, reducing trunk permeability (cases 1 and 5) also increased the wave reflection and decreased the wave transmission when crest width and incident waves did not change. Wave energy transmission was affected by both the overtopping over the ZFB crest and the porous flow in the ZFB trunk. In case 5, the less permeable ZFB trunk inhibited the transmission of kinetic energy through the trunk from the seaward to the leeward region of the ZFB in comparison to case 1, thus, the resulting reflection coefficient, K_r, was larger and the transmission coefficient, K_t, was smaller.

Table 2. Reflection and transmission coefficients for all the ZFB cases of Table 1.

Case	ξ_0	K_r		K_t				
		Present	Zanuttigh and Van der Meer (2008)	Present	Seeling (1980)	Seabrook and Hall (1998)	Van der Meer et al. (2005)	Buccino and Calabrese (2007)
1	4.37	0.176	0.174	0.416	0.40	0.196	0.345	0.356
2	4.37	0.171	0.174	0.238	0.29	0.103	0.187	0.206
3	4.37	0.171	0.174	0.127	0.18	0.070	0.073	0.097
4	3.08	0.106	0.132	0.171	0.40	0.196	0.305	0.288
5	4.37	0.207	0.195	0.290	0.40	0.196	0.345	0.356

Apart from the computed reflection and transmission coefficients, the corresponding values predicted by widely used empirical formulas are also presented in Table 2. For wave reflection, the empirical formula of Equation (1) was used, with $\gamma_f = 0.40$, for the fully-permeable ZFB cases 1–4, and $\gamma_f = 0.5$, for the partially-permeable ZFB case 5, according to [1]. To achieve the best possible agreement to the computed results, the reduction parameter was set to $C = 0.43$ instead of the value $C = 0.67$ suggested in [1] for ZFBs. For wave transmission, the empirical formulas of Equation (3) were used. Overall, better prediction seems to be achieved by the empirical formula in [5].

The distribution of the instantaneous vorticity field in the vicinity of the ZFB case 1, at four instants during the 30th wave period of the simulation, is presented in Figure 7. It is shown that as the wave trough reached the breakwater crest (down-rush flow phase), strong anti-clockwise vorticity developed near above the seaward slope of the structure. As the wave propagated and the flow reversed (up-rush flow phase), this vorticity layer was separated from the slope and vortices were generated and transported offshore, while a new vorticity layer of opposite sign (clockwise) formed near above the slope. During the down-rush flow phase, there was no separation of this vorticity layer. In cases 2 and 3, there were no notable differences in the vorticity behavior above the seaward slope of the ZFBs. In case 4, with a shorter wavelength in comparison to case 1, the vorticity behavior was similar, but the offshore transportation of the vortices was extended to a shorter distance (Figure 8). In case 5, with a less permeable ZFB trunk in comparison to case 1, the vorticity behavior near the crest was similar, while a weak vorticity layer was generated at the interface between the armor layer and the core in the ZFB trunk (Figure 9).

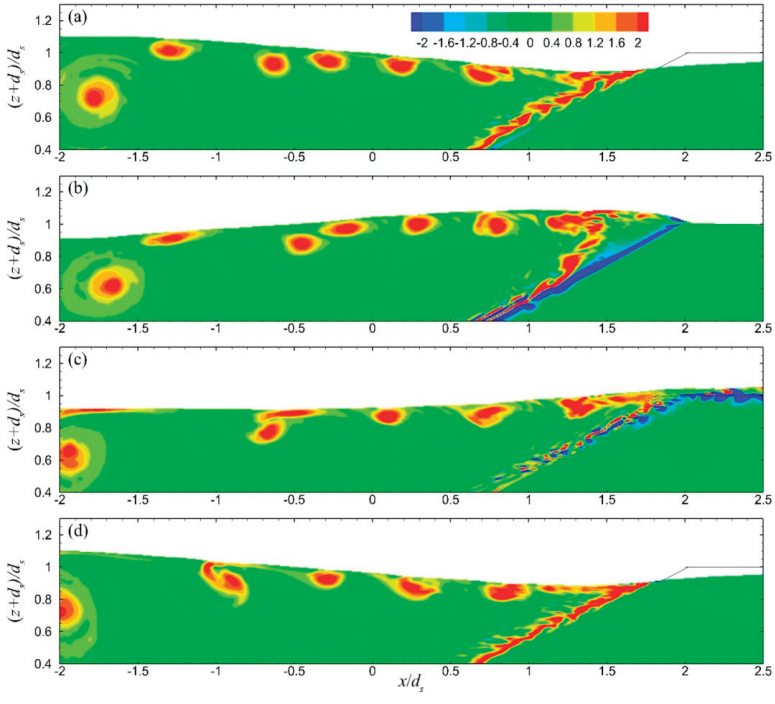

Figure 7. Vorticity field in the seaward region of ZFB case 1 at four instants during the 30th wave period: (**a**) $T/3$, (**b**) $3T/8$, (**c**) $5T/8$, and (**d**) T.

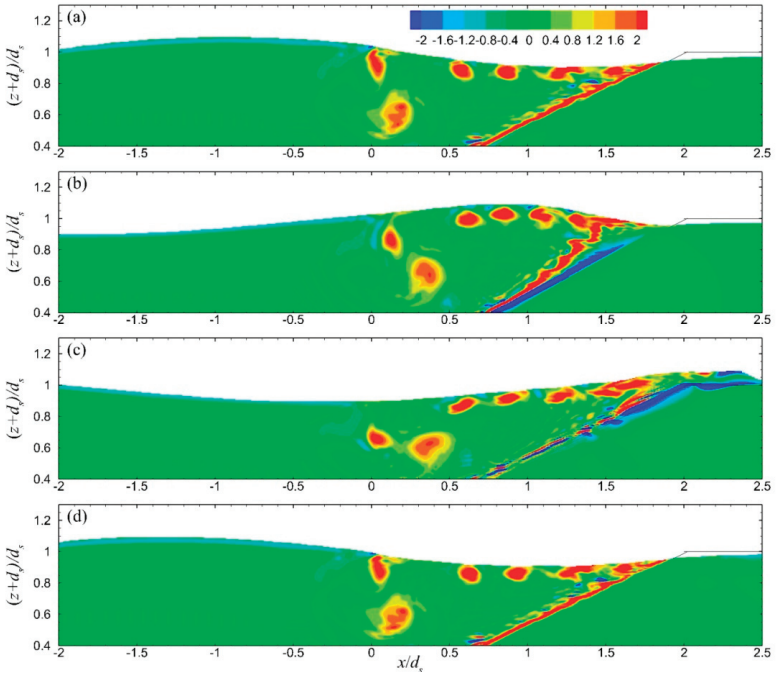

Figure 8. Vorticity field in the seaward region of the ZFB case 4 at four instants during the 30th wave period: (**a**) $T/3$, (**b**) $3T/8$, (**c**) $5T/8$, and (**d**) T.

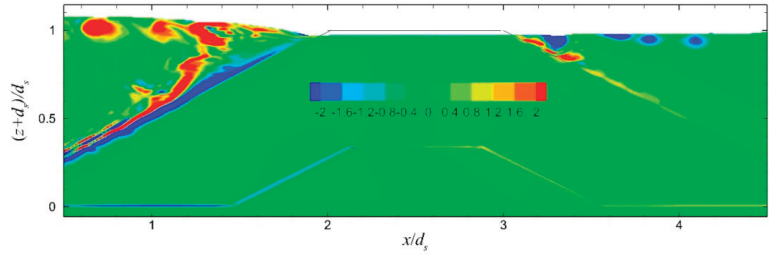

Figure 9. Vorticity field near the crest and in the ZFB trunk (case 5) at one instant (T/8) during the 30th wave period.

The period-mean velocity field (of 10 wave periods after 20 wave periods of simulation) in the seaward region of the ZFBs in cases 1–3 is presented in Figure 10. It is highlighted that in these cases, the generated currents above the ZFB seaward slope and crest were directed onshore due to wave overtopping, while the currents in the ZFB trunk were weaker and directed offshore. In the leeward region of these ZFBs, the period-mean velocity field is presented in Figure 11. It is shown that as the crest width increased, the magnitude of the velocities became weaker. The period-mean velocity in the seaward and leeward regions of the ZFB case 4 is presented in Figure 12. The direction of the currents in the seaward and leeward regions of the ZFB follows the same pattern as in case 1, but their magnitude was smaller in both regions due to the lower energy transmission onshore. The period-mean velocity field for the ZFB case 5 is presented in Figure 13. The magnitude of the currents in the seaward and leeward regions and the ZFB trunk was slightly larger in comparison to case 1.

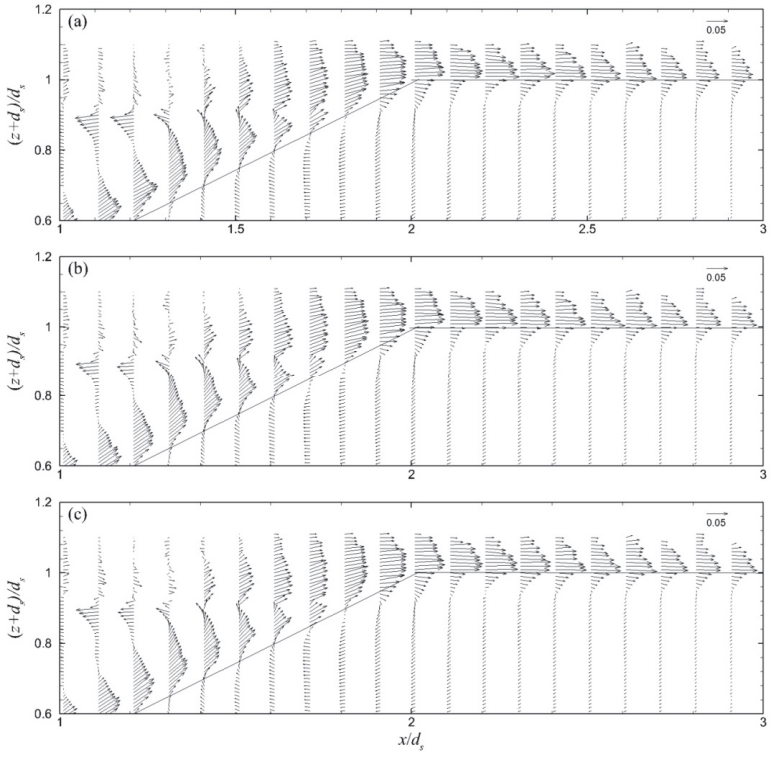

Figure 10. Period-mean velocity field in the seaward region of the ZFBs in cases: (**a**) 1, (**b**) 2, and (**c**) 3. Velocity vectors are shown non-dimensionalized by $(gd_S)^{1/2}$ in the water phase under the wave crest envelope.

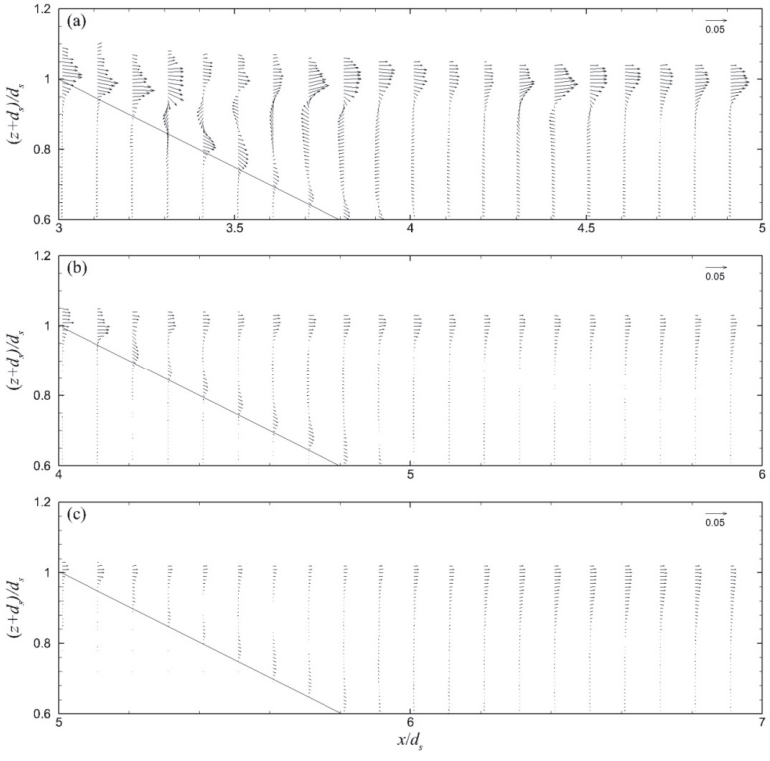

Figure 11. Period-mean velocity field in the leeward region of the ZFBs in cases: (**a**) 1, (**b**) 2, and (**c**) 3. Velocity vectors are shown non-dimensionalized by $(gd_S)^{1/2}$ in the water phase under the wave crest envelope.

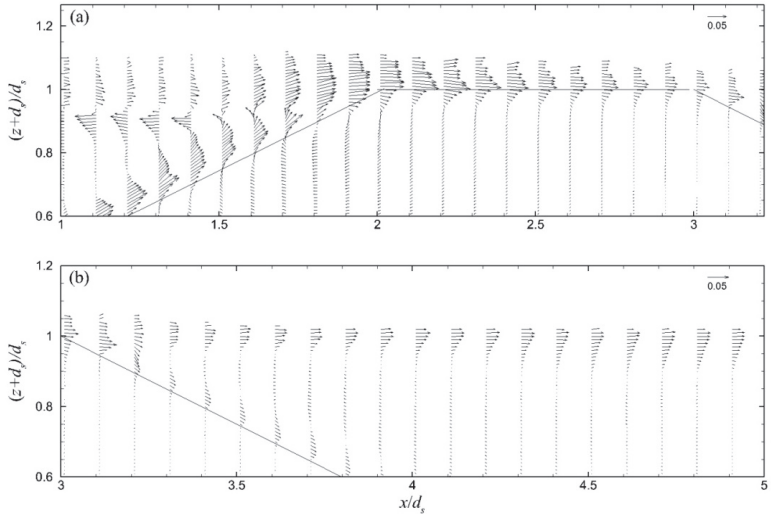

Figure 12. Period-mean velocity field for ZFB case 4 in: (**a**) the seaward region, and (**b**) the leeward region. Velocity vectors are shown non-dimensionalized by $(gd_S)^{1/2}$ in the water phase under the wave crest envelope.

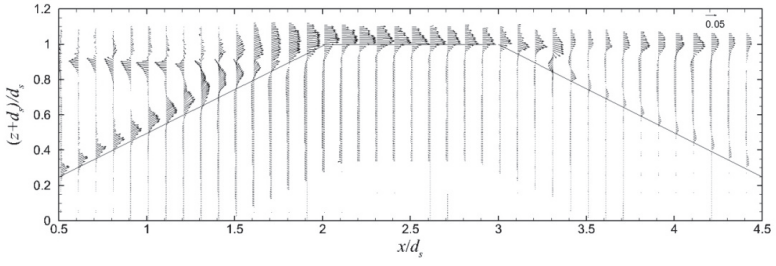

Figure 13. Period-mean velocity field for ZFB case 5. Velocity vectors are shown non-dimensionalized by $(gd_S)^{1/2}$ in the water phase under the wave crest envelope.

The period-mean flow pattern in the vicinity of the ZFBs for cases 1–3 is illustrated through streamlines in Figure 14. It is demonstrated that in the ZFB trunk, the flow was directed offshore in all cases. Part of the flow that overtops the crest of the ZFBs returned offshore through the ZFB trunk; as a result, the water renewal was facilitated in the ZFB leeward region. This process is obvious in cases 1 and 2. Further increase of the crest width though (case 3) results in the limitation of the flow circulation cell in the ZFB trunk and the interruption of water renewal in the ZFB leeward region through the ZFB trunk. The pattern of the streamlines in ZFB case 4 does not differ from the one in case 1, and it is not shown. For the ZFB case 5 (Figure 15), the return flow from the leeward to the seaward region through the ZFB trunk is inhibited by the presence of a less permeable core than in case 1.

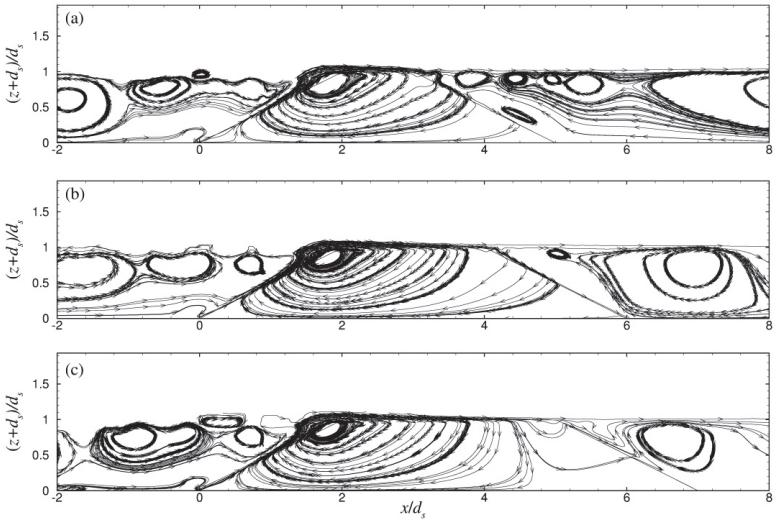

Figure 14. Streamlines in the vicinity of the ZFBs in cases: (**a**) 1, (**b**) 2, and (**c**) 3.

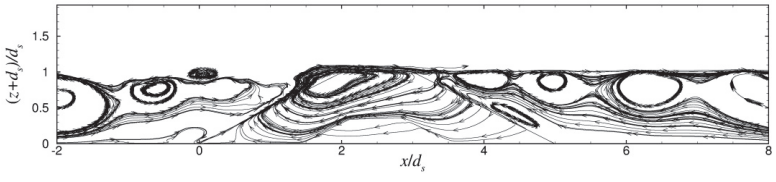

Figure 15. Streamlines in the vicinity of ZFB case 5.

The mean overtopping discharge, q, over and through the ZFBs, and the wave setup, δ, in the leeward region of the ZFBs are shown in Table 3. The overtopping discharge was computed as the period-mean (of 10 wave periods after 20 wave periods of simulation) flux through the vertical cross-section at the leeward end of the ZFB crest. The instantaneous flux is:

$$q_{lc}(t) = \int_0^{d_{lc}} u_{lc}(z,t)dz, \tag{25}$$

where $d_{lc}(t)$ is the instantaneous water level at the leeward end of the ZFB crest. The mean overtopping discharge comprises the discharge through the ZFB trunk and the crest discharge over the ZFB crest. The corresponding results are also shown in Table 3. The wave setup, δ, was computed as the period-mean (of 10 wave periods after 20 wave periods of simulation) free-surface level over the SWL at the leeward ZFB toe.

Table 3. Mean overtopping discharge and wave setup for all the ZFB cases (Table 1).

Case	$q/(g/{d_S}^3)^{1/2}$				δ/d_S		
	Trunk Discharge	Crest Discharge	Overtopping Discharge	EurOtop (2018)	Present	Diskin (1970)	Loveless (1998)
1	−0.0015	0.002580	0.001080	0.000976	0.01466	0.0735	0.0393
2	−0.000035	0.000989	0.000954	0.000976	0.01629	0.0735	0.0785
3	0.00052	0.000377	0.000897	0.000976	0.01427	0.0735	0.1178
4	−0.00032	0.001308	0.000988	0.000976	0.01002	0.0735	0.0194
5	−0.00219	0.003055	0.000865	0.000976	0.02346	0.0735	0.0393

For ZFB case 1, the trunk discharge is in the offshore direction (negative), while the one over the crest is in the onshore direction (positive). As B increased, for ZFB cases 2 and 3, the negative trunk discharge weakened and even turned positive in case 3, while the one over the crest weakened as well but remained positive. The overall mean overtopping discharge was always onshore and it decreased, albeit weakly, with the increase of the ZFB crest width. The decrease of ξ_0 in ZFB case 4, in comparison to case 1, also resulted in the weak decrease of the mean overtopping discharge. In ZFB case 5, both the trunk discharge and the one over the crest strengthened in comparison to the ones in case 1, but the mean overtopping discharge decreased. To apply Equation (4) in the present cases, which were laboratory-scale ones since d_S = 0.4 m, an adjustment factor of f_q = 8.2 was used, which is lower than the maximum value of 11 suggested in EurOtop [6] for tan$a$ = 1/2. The mean overtopping discharge predicted by Equation (4) was constant for all ZFB cases, as shown in Table 3, reflecting the strong dependence of q on H_i but not the one on B, ξ_0, and permeability as the present results suggest.

The wave setup increases with increasing B, for ZFB cases 1 and 2, but it decreases again for ZFB case 3 despite the further increase of B because of the interruption of the flow circulation cell in the ZFB trunk for case 3 as shown in Figure 14c. The decrease of ξ_0 in ZFB case 4, in comparison to case 1, resulted in the decrease of the wave setup, while the decrease of permeability in ZFB case 5 increased the wave setup. The corresponding wave setup predicted by the empirical formulas of Equation (5) overestimated δ (Table 3) since they were both based on experiments without the recirculation system described in the Wave Generation subsection.

Finally, the instantaneous shear stress field for ZFB case 5 at two instants during the 30th wave period of the simulation is presented in Figure 16. During the up-rush flow phase and as the wave crest approaches the breakwater crest, significant positive shear stress was observed near the seaward slope of the structure, while a positive layer was also developed in between the two different materials inside the porous media. Shear stress of opposite sign was developed in the same areas during the down rush flow phase. As expected, the seaward slope of the ZFB was the most crucial part of the

structure in terms of hydraulic stability, as it experienced larger values of the developing shear stress, i.e., the destabilizing force due to wave breaking.

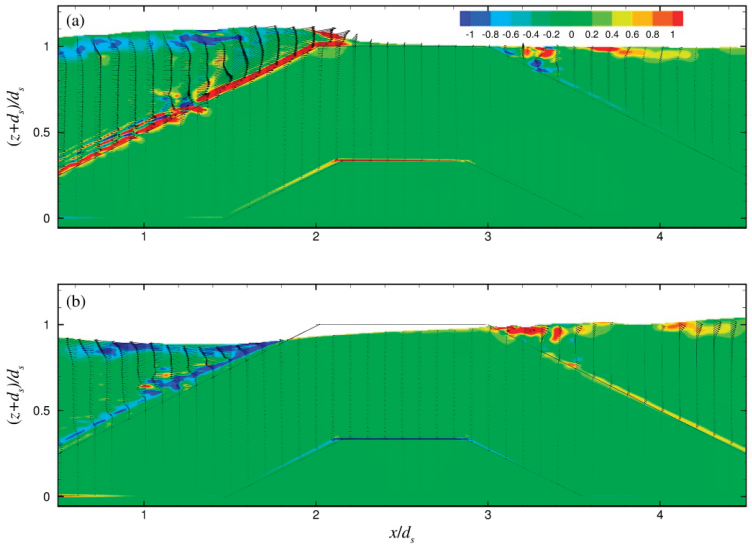

Figure 16. Shear stress for case 5 at two instants during the 30th wave period: (**a**) $T/2$, and (**b**) T.

4. Discussion

In the present work, the effect of ZFB crest width, breaking parameter, and ZFB trunk permeability on wave reflection, crest overtopping, wave transmission, wave setup, and wave-generated currents were studied numerically.

The results indicate that the size of the crest width, B, did not notably affect wave (reflection coefficient) and flow (instantaneous vorticity and period-mean currents) processes in the seaward region of ZFBs. However, the processes in the leeward region of ZFBs were significantly affected by B; wave transmission and magnitude of currents decreased with increasing B. In addition, the mean overtopping discharge heading onshore decreased, albeit weakly, with increasing B. The effect of B on the wave setup was not monotonic as it depended on the pattern of the flow circulation in the ZFB trunk, but eventually this also decreased with increasing B. The effect of the breaking parameter, ξ_0, and the ZFB trunk permeability on wave and flow processes were significant both in the seaward and leeward regions of ZFBs. As ξ_0 decreased, the wave reflection, wave transmission, magnitude of currents, mean overtopping discharge, and wave setup all decreased; this observation is in accordance with the relevant empirical formulas (Tables 2 and 3) considered in this study. Finally, decreasing the ZFB trunk permeability led to the increase of wave reflection, the magnitude of currents, and wave setup, but to the decrease of wave transmission and mean overtopping discharge.

Therefore, for the design of ZFBs, decreasing trunk permeability is equivalent to increasing crest width in terms of the wave and hydrodynamic processes in the leeward region of ZFBs as far as wave transmission and mean overtopping discharge are concerned, but not equivalent for wave setup and magnitude of currents. If the latter parameters are not critical, decreasing the ZFB trunk permeability is a more economical option compared to the increase of crest width.

Author Contributions: Conceptualization, T.I.K. and A.A.D.; methodology, T.I.K. and A.A.D.; software, T.I.K.; validation, T.I.K.; formal analysis, T.I.K. and A.A.D.; investigation, T.I.K.; resources, A.A.D.; data curation, T.I.K.; writing—original draft preparation, T.I.K.; writing—review and editing, A.A.D.; visualization, T.I.K.; supervision, A.A.D.; project administration, A.A.D.; funding acquisition, A.A.D. All authors have read and agreed to the published version of the manuscript.

Funding: This paper is part of the research project ARISTEIA I - 1718, implemented within the framework of the Education and Lifelong Learning program, and co-financed by the European Union (European Social Fund) and Hellenic Republic funds.

Acknowledgments: This work was supported by the computational time granted by the Greek Research & Technology Network (GRNET) in the National HPC facility ARIS under project ID CoastHPC.

Conflicts of Interest: The authors declare no conflict of interest. The funders had no role in the design of the study; in the collection, analyses, or interpretation of data; in the writing of the manuscript, or in the decision to publish the results.

References

1. Zanuttigh, B.; van der Meer, J.W. Wave reflection from coastal structures in design conditions. *Coast. Eng.* **2008**, *55*, 771–779. [CrossRef]
2. Seelig, W.N. Two-Dimensional Tests of Wave Transmission and Reflection Characteristics of Laboratory Breakwaters. *Coast. Eng. Res. Cent.* **1980**. [CrossRef]
3. Seabrook, S.R.; Hall, K.R. Wave transmission at submerged rubble mound breakwaters. In Proceedings of the 26th International Conference on Coastal Engineering, Copenhagen, Denmark, 22–26 June 1998. [CrossRef]
4. Van der Meer, J.W.; Briganti, R.; Zannuttigh, B.; Wang, B. Wave transmission and reflection at low-crested structures: Design formulae, oblique wave attack and spectral change. *Coast. Eng.* **2005**, *52*, 915–929. [CrossRef]
5. Buccino, M.; Calabrese, M. Conceptual Approach for Prediction of Wave Transmission at Low-Crested Breakwaters. *J. Waterw. Port Coast. Ocean Eng.* **2007**, *133*, 213–224. [CrossRef]
6. Van der Meer, J.W.; Allsop, N.W.H.; Bruce, T.; De Rouck, J.; Kortenhaus, A.; Pullen, T.; Schüttrumpf, H.; Troch, P.; Zanuttigh, B. *EurOtop, Manual on Wave Overtopping of Sea Defences and Related Structures. An. Overtopping Manual Largely Based on European Research, but for Worldwide Application*; Envrionment Agency, ENW, KFK: Bristol, UK, 2018.
7. Diskin, M.H.; Vajda, M.L.; Amir, I. Piling-up behind low and submerged permeable breakwaters. *J. Waterw. Harb. Coast. Eng. Div.* **1970**, *96*, 359–372. [CrossRef]
8. Loveless, J.H.; Debski, D.; McLeod, A.B. Sea level set-up behind detached breakwaters. In Proceedings of the 26th International Conference on Coastal Engineering, Copenhagen, Denmark, 22–26 June 1998; pp. 1665–1678. [CrossRef]
9. Bellotti, G. A simplified model of rip currents systems around discontinuous submerged barriers. *Coast. Eng.* **2004**, *51*, 323–335. [CrossRef]
10. Calabrese, M.; Vicinanza, D.; Buccino, M. 2D Wave setup behind submerged breakwaters. *Ocean Eng.* **2008**, *35*, 1015–1028. [CrossRef]
11. Mitzutani, N.; Mostafa, A.M.; Iwata, K. Nonlinear regular wave, submerged breakwater and seabed dynamic interaction. *Coast. Eng.* **1998**, *33*, 177–202. [CrossRef]
12. Huang, C.J.; Chang, H.H.; Hwung, H.H. Structural permeability effects on the interaction of a solitary wave and a submerged breakwater. *Coast. Eng.* **2003**, *49*, 1–24. [CrossRef]
13. Garcia, N.; Lara, J.L.; Losada, I.J. 2-D numerical analysis of near-field flow at low-crested permeable breakwaters. *Coast. Eng.* **2004**, *51*, 991–1020. [CrossRef]
14. Hsu, T.J.; Sakakiyama, T.; Liu, P.L.F. A numerical model for wave motions and turbulence flows in front of a composite breakwater. *Coast. Eng.* **2002**, *46*, 25–50. [CrossRef]
15. Losada, I.J.; Lara, J.L.; Christensen, E.D.; Garcia, N. Modelling of velocity and turbulence fields around and within low-crested rubble-mound breakwaters. *Coast. Eng.* **2005**, *52*, 887–913. [CrossRef]
16. Lara, J.L.; Garcia, N.; Losada, I.J. RANS modelling applied to random wave interaction with submerged permeable structures. *Coast. Eng.* **2006**, *53*, 395–417. [CrossRef]
17. Kramer, M.; Zanuttigh, B.; van der Meer, J.W.; Vidal, C.; Gironella, X. Laboratory experiments on low-crested breakwaters. *Coast. Eng.* **2005**, *52*, 867–885. [CrossRef]
18. Dimas, A.A.; Koutrouveli, I.T. Wave Height Dissipation and Undertow of Spilling Breakers over Beach of Varying Slope. *J. Waterw. Port Coast. Ocean Eng.* **2019**, *145*. [CrossRef]
19. Liu, P.L.F.; Pengzhi, L.; Chang, K.; Sakakiyama, T. Numerical modeling of wave interaction with porous structures. *J. Waterw. Port Coast. Ocean Eng.* **1999**, *125*, 322–330. [CrossRef]

20. Van Gent, M.R.A. Wave Interaction with Permeable Coastal Structures. Ph.D. Thesis, Delft University, Delft, The Netherlands, 1995.
21. Keulegan, G.H.; Carpenter, L.H. Forces on cylinders and plates in an oscillating fluid. *J. Res. Nat. Bur. Stand.* **1958**, *60*, 423–440. [CrossRef]
22. Smagorinsky, J. General circulation experiments with the primitive equations: I. The basic experiment. *Mon. Weather Rev.* **1963**, *91*, 99–164. [CrossRef]
23. Yang, J.; Stern, F. Sharp interface immersed-boundary/level-set method for wave–body interactions. *J. Comput. Phys.* **2009**, *228*, 6590–6616. [CrossRef]
24. Balaras, E. Modeling complex boundaries using an external force field on fixed Cartesian grids in large-eddy simulations. *Comput. Fluids* **2004**, *33*, 375–404. [CrossRef]
25. Hughes, S.A. *Physical Models and Laboratory Techniques in Coastal Engineering*; World Scientific: Singapore, 1993; pp. 367–379. [CrossRef]
26. Jacobsen, N.G.; Fuhrman, D.R.; Fredsoe, J. A wave generation toolbox for the open-source CFD library: Open Foam®. *Int. J. Numer. Methods Fluids* **2011**, *70*, 1073–1088. [CrossRef]
27. Beji, S.; Battjes, J.A. Numerical simulation of nonlinear wave propagation over a bar. *Coast. Eng.* **1994**, *23*, 1–16. [CrossRef]
28. Mansard, E.P.D.; Funke, E.R. The measurement of incident and reflected spectra using a least squares method. In Proceedings of the 17th International Conference on Coastal Engineering, Sydney, Australia, 23–28 March 1980; pp. 154–172. [CrossRef]

Journal of
Marine Science and Engineering

MDPI

Article

Numerical Simulation of Scour Depth and Scour Patterns in Front of Vertical-Wall Breakwaters Using OpenFOAM

Nikolaos Karagiannis *, Theophanis Karambas and Christopher Koutitas

Department of Civil Engineering, Aristotle University of Thessaloniki, 54 124 Thessaloniki, Greece; karambas@civil.auth.gr (T.K.); koutitas@civil.auth.gr (C.K.)
* Correspondence: nkarag@civil.auth.gr

Received: 20 July 2020; Accepted: 20 October 2020; Published: 23 October 2020

Abstract: An advanced coupled numerical model was developed and implemented in the present work, describing the scour patterns and predicting the scour depth in front of vertical-wall breakwaters. It consists of two independent models, a hydrodynamic Computational Fluid Dynamics (CFD) Reynolds Averaged Navier–Stokes (RANS) model developed on the OpenFOAM (version 2.4.0) toolbox (CFD), describing the wave propagation and the associated hydrodynamic field, and a morphodynamic one (sediment transport model), which was developed in FORTRAN by the authors and yields the updated seabed morphology. The method used here is iterative. The hydrodynamic model is applied for any given initial seabed geometry and wave conditions, resulting in the hydrodynamic field of the flow, which is used as input by the second sediment transport model for the seabed morphology evolution. This process is repeated until the equilibrium profile is achieved. Model results are compared satisfactorily with experimental data for both scour patterns and prediction of scour depth.

Keywords: numerical model; OpenFOAM; sediment transport; scour; vertical breakwaters

1. Introduction

It is well known that the scour in the direct vicinity of vertical breakwaters can be devastating for their performance and most importantly their stability, as it can lead to the total failure of the structures. Therefore, the prediction of the scouring pattern and scouring depth is of great importance for coastal scientists and engineers. Vertical-wall breakwaters laid on flat bed of constant depth are numerically examined here, with the standing waves evolution in front of them being the main culprit behind the scour depth evolution and scouring patterns at the toe of these structures.

Xie [1] found that the scouring pattern depends on the grain size and the wave conditions, while Sumer and Fredsoe [2] attribute the sediment transport process under standing waves to a steady streaming pattern, a system of recirculating cells, which the sediment responds to. It is known that the formation of the standing waves triggers the sediment movement and finally forms the seabed morphology when it comes to vertical breakwaters. The grain size is, as mentioned, of significant importance with regards to the seabed morphology evolution, however, Xie [1] conducted experiments using the same grain size under different wave conditions and the morphological response was different, meaning that a finer grain size would lead to a typical "coarse grain size" pattern and vice-versa. Hence, the wording "relative fine" or "relative coarse" sediment was introduced by Xie [1] to describe these two typical scouring patterns, depending not only on the grain size but on wave conditions too. Figure 1 shows the different scouring patterns for relatively fine sand and relatively coarse sand respectively, as proposed by Xie [1], where it seems that in the case of relatively fine sand, scour is formed under the node of the standing waves and deposition at the position of the antinodes,

while in the case of relatively coarse sand, deposition is formed under the node of the standing wave and the scour appears between the node and the antinode, with the seabed remaining almost intact at the position of the antinodes. Sumer and Fredsoe [2] also found the same scouring pattern for relative coarse sediment.

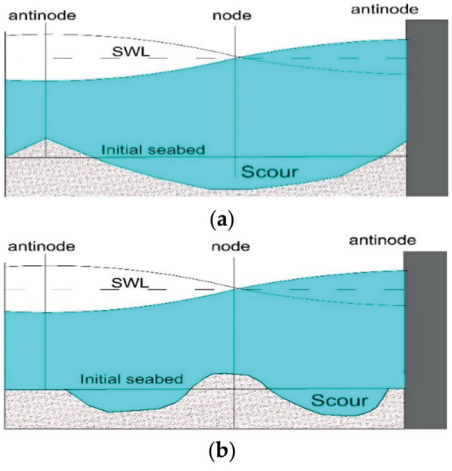

Figure 1. Scour patterns for: (**a**) relatively fine sand and (**b**) relatively coarse sand.

The scouring in front of a vertical breakwater has been studied mostly experimentally over the last decades [1–5]. Carter [3] highlighted the influence of standing waves on the formation of scouring patterns parallel to the shore, while Xie [1] conducted numerous experiments under different wave conditions and grain sizes, investigating even the required width for the scouring protective layer. Sumer and Fredsoe [2] studied also experimentally the scour in front of both rubble-mound and vertical breakwaters, ending up in the same (as Xie [1]) scouring patterns for vertical breakwaters.

Furthermore, there are also some interesting numerical attempts [6–10] with Gislason et al. [7–9] having used a Navier–Stokes solver to describe the hydrodynamic field, in conjunction with a morphodynamic module, solving the Engelund and Fredsoe [11] equations to estimate the sediment transport bed load. The seabed morphology evolution was produced solving the sediment continuity equation. Their results were satisfactory for vertical breakwaters, although the numerical results for maximum deposition and crest of bed form were slightly shifted when compared with experimental data [9].

A Euler–Lagrange two-phase model was also implemented by Hajivalie et al. [10] with a RANS hydrodynamic module and a Lagrange sediment transport model, allowing particles' movement according to the associated hydrodynamic field, which were considered non-cohesive. Numerical results and comparison with experimental data in both cases were provided for the local scour depth and scouring patterns, but only at a short distance of half wave length from the breakwater.

Following the authors' previous works [12,13], a 2D approach of coupling two numerical models has been developed and implemented in the present study with the aim of contributing to the numerical investigation of scouring depth and patterns. The hydrodynamic model is applied first to simulate the wave propagation under any given seabed morphology and wave conditions. Then, the morphodynamic model was implemented using the hydrodynamic results and describing the sediment transport and cross-shore seabed morphology evolution.

The former numerical model was created with the CFD open source toolbox OpenFOAM and the additional toolbox waves2Foam [14]. The RANS equations are solved simultaneously with the transport equations of the turbulence model k-ω Shear Stress Transport (SST), which was considered the most suitable for wave propagation problems [15] (OpenFOAM's original turbulence model was

amended accordingly, so that the density can be included in the equations), and the Volume of Fluid (VOF) method ones [16].

The second numerical model was developed in FORTRAN by the authors and calculates the sheet flow sediment transport rates using the semi-empirical Camenen and Larson [17] transport rate formula, as well as the bed load and suspended load over ripples. After that, the conservation equation of the sediment mass is applied for several time steps and the seabed evolution is computed.

The method used in this work is iterative, alternating the two models repetitively until the equilibrium seabed profile is achieved.

Model results are compared satisfactorily with Xie [1] experimental data, for surface elevation, orbital velocities, scour depth and scour pattern, while the results for the scouring pattern are not limited to a short distance from the breakwater but are provided for the total length of the sandy seabed.

2. Materials and Methods

This section provides the description and governing equations for the two models as well as the coupling procedure which was briefly presented above.

2.1. Hydrodynamic Model on OpenFOAM Platform

The hydrodynamic model is developed on the CFD open source OpenFOAM toolbox to describe the wave propagation and the associated hydrodynamic field. Although it is a fully three-dimensional (3D) model, a quasi-two dimensional (quasi-2D) one is developed and applied here, as the cross-shore seabed morphology evolution is of interest. It solves the RANS equations along with the VOF ones to track the free surface, while the turbulence model k-ω SST is used for the turbulence closure. All RANS turbulence models available in OpenFOAM libraries for incompressible flow do not include the density in their equations, resulting in inaccurate definition of free surface cells' turbulence quantities. To overcome this issue, the density has been included in the turbulence model equations, so that it can be correctly calculated in the free surface cells [15,18]. The waves are generated at the left boundary of the computational mesh and the unwanted reflections are being absorbed at the boundaries using the additional waves2Foam toolbox and specifically the explicit relaxation zone technique [14]. It should be mentioned here that there are two more wave generation and absorption toolboxes (IHFOAM and olaFlow), which provide active wave generation and absorption at the boundaries, using shallow water theory [19]. The discretization method used by OpenFOAM toolbox is the Finite Volume Method (FVM), described in its documentation (www.openfoam.com/documentation), as well as in [20]. The solver used here is the waveFoam, capable of supporting most of the wave theories and available in waves2Foam toolbox [14]. WaveFoam solver is an enhanced form (modified to support wave theories) of the original InterFoam solver, available in OpenFOAM libraries and suitable for multiphase flows.

2.1.1. Continuity and RANS Equations

The mathematical model solves the continuity equation, which is as follows:

$$\frac{\partial U_i}{\partial x_i} = 0 \tag{1}$$

in conjunction with the Reynolds Averaged Navier–Stokes (RANS) equations, which are as follows:

$$\frac{\partial(\rho U_i)}{\partial x_i} + \rho U_j \frac{\partial U_i}{\partial x_j} = -\frac{\partial p}{\partial x_i} + \rho g_i + \frac{\partial}{\partial x_j}\left[\mu\left(\frac{\partial U_i}{\partial x_j} + \frac{\partial U_j}{\partial x_i}\right) - \rho\overline{u_i' u_j'}\right] + \sigma_T \kappa_\gamma \frac{\partial \gamma}{\partial x_i} \tag{2}$$

where U is the velocity, ρ is the density, g is the gravity acceleration, p is the pressure, μ is the dynamic viscosity, and $-\rho\overline{u_i' u_j'}$ is the Reynolds stress tensor described by the following expression:

$$\tau_{ij} = -\rho\overline{u_i' u_j'} = \mu_t\left(\frac{\partial U_i}{\partial x_j} + \frac{\partial U_j}{\partial x_i}\right) - \frac{2}{3}\rho k\delta_{ij} \tag{3}$$

where μ_t is turbulent viscosity coefficient, k is the turbulence kinetic energy and δ_{ij} is the Kronecker delta. The last term in the Equation (2) represents the surface tension effect, with σ_T being the surface tension coefficient, which is 0.074 Kg/s^2 between air and water at 20 °C, while κ_γ is the surface curvature and γ is a quantity related to the Volume of Fluid method (further information is provided in Section 2.1.2).

2.1.2. Volume of Fluid (VOF) Equations

The Volume of fluid method [16] is included in OpenFOAM libraries and is applied in multiphase flows to capture the interface between fluids, which is the free surface between water and air in this instance. According to this method, a scalar quantity γ is introduced and applied to every cell in the numerical domain, with its values ranging between 0 and 1, depending on the content of each cell. Its value is 1 for the cells that contain only water, while its value is 0 for the cells that contain only air. In the case of free surface cells which contain both water and air, the γ quantity takes values between 0 and 1, depending on the proportion of each fluid in the cells. The equation which describes the quantity γ is given by the following expression:

$$\frac{\partial \gamma}{\partial t} + \frac{\partial(\gamma U_i)}{\partial x_i} + \frac{\partial[\gamma(1-\gamma)Ur_i)}{\partial x_i} = 0 \tag{4}$$

where the last term is a compression term for the free surface cells and Ur is a relative velocity [21].

Density and viscosity are calculated using the quantity γ for each cell at the interface with the following expressions:

$$\rho = \gamma\rho_{water} + 1(1-\gamma)\rho_{air} \tag{5}$$

$$\mu = \gamma\mu_{water} + 1(1-\gamma)\mu_{air} \tag{6}$$

2.1.3. Turbulence Modelling

The k-ω SST turbulence model is used for the turbulence closure. As mentioned above, the density is not included in the RANS turbulence models available in OpenFOAM libraries for incompressible flow. This can lead to overestimation of turbulence at the free surface due to the use of the Volume of Fluid (VOF) method and specifically the quantity γ, which defines the density in the free surface cells that contain both air and water. Therefore, appropriate amendments have been made to the turbulence model code, so that the density can be included in the equations [15].

The transport equations for the k-ω SST model are as follows [22,23]:

$$\mu_t = \frac{\rho\alpha_1 k}{\max(\alpha_1\omega, SF_2)} \tag{7}$$

$$\frac{\partial(\rho k)}{\partial t} + \frac{\partial(\rho k U_i)}{\partial x_i} = P_k - \beta^*\rho k\omega + \frac{\partial}{\partial x_i}\left[(\mu + \sigma_k\mu_t)\frac{\partial k}{\partial x_i}\right] \tag{8}$$

$$\frac{\partial(\rho\omega)}{\partial t} + \frac{\partial(\rho\omega U_i)}{\partial x_i} = \alpha S^2 - \beta\rho\omega^2 + \frac{\partial}{\partial x_j}\left[(\mu + \sigma_\omega\mu_t)\frac{\partial\omega}{\partial x_j}\right] + +2(1-\ F_1)\rho\sigma_{\omega 2}\frac{1}{\omega}\frac{\partial k}{\partial x_i}\frac{\partial\omega}{\partial x_i} \tag{9}$$

where k is the turbulent kinetic energy and ω is the dissipation rate. The rest coefficients are given in the literature [22,23].

2.1.4. Wave Generation and Absorption

The additional toolbox waves2Foam [14] is used for the wave generation and absorption. Specifically, relaxation zones are implemented at the boundaries of the computational domain to prevent from any unwanted reflections. Appropriate wave theories, depending on each simulation, are implemented at the left boundary for the wave generation too.

The relaxation weighting factor a_R is given by the following exponential expression:

$$a_R(\chi_R) = 1 - \frac{\exp\left(\chi_R^{3.5}\right) ibed \ - 1}{\exp(1) - 1} \gamma \iota \alpha \ \chi_R \in [0;1] \tag{10}$$

The weighting factor is then used to define the velocity or surface elevation by the following equation:

$$\varphi = a_R \varphi_{computed} + (1 - a_R)\varphi_{target} \tag{11}$$

where φ is the velocity or γ (VOF method).

2.2. Morphodynamic Model

As mentioned above, the morphodynamic model has been developed in FORTRAN by the authors. The new code follows previous, similar works from Karambas and Koutitas [24] and Karambas [25] for Boussinesq models, where semi-empirical formulae, along with the sediment continuity equation, were implemented. The main difference between this model and Boussinesq models is that all accurate hydrodynamic characteristics obtained from the 3D OpenFOAM model (surface elevation, velocities, turbulent kinetic energy) are used here to estimate the sediment transport rates and obtain the seabed morphology evolution, while Boussinesq models are 2DH models which make use of semi-empirical equations (e.g., for undertow or energy dissipation). Moreover, Camenen and Larson [17] equations are implemented here, which take into account the wave asymmetry, splitting up the wave period into two separate time periods, with positive and negative orbital velocities respectively and calculating the sediment transport rates accordingly for each one of them. Furthermore, the sheet flow inception is described along with the associated phase-lag effect, which takes into account the time period that the sediment stays in suspension near the bed. Specifically, when flow switches to the opposite direction, sediment in suspension is carried away by the flow to the opposite direction too. The model takes into account the wave-current interaction too, although no current is applicable in this work. Once the sediment transport rates are calculated, the sediment mass continuity equation is applied, and the new seabed morphology is obtained. Complex geometry or steep slopes are taken into account through Watanabe coefficient [26], which is applied in the conservation of sediment transport equation. Avalanching is also incorporated in the model, although it was not used here, as the seabed is considered flat. The discretisation was made using the finite difference method (FDM).

It is well known that the sediment transport rates calculation can be divided into the bedload and the suspension load transport rates calculation. Camenen and Larson [17] proposed semi-empirical formulae for both as follows.

2.2.1. Bed Load and Sheet Flow

The bed load is given by the following equations Camenen and Larson [17], taking into account wave and current interaction:

$$\Phi_b = \begin{cases} \frac{q_{sb,w}}{\sqrt{(s-1)gD_{50}^3}} = a_w \sqrt{\theta_{cw,net}}\theta_{cw,m} \exp\left(-b\frac{\theta_{cr}}{\theta_{cw}}\right) \\ \frac{q_{sb,n}}{\sqrt{(s-1)gD_{50}^3}} = a_n \sqrt{\theta_{cn}}\theta_{cw,m} \exp\left(-b\frac{\theta_{cr}}{\theta_{cw}}\right) \end{cases} \tag{12}$$

where θ_{cr}, $\theta_{cw,m}$, θ_{cw}, θ_{cn} are the critical, mean, maximum and current Shields parameters, w, n stand for "wave" and "normal" directions respectively, $s(=\rho_s/\rho)$ is the relative density between sediment and water, g is gravitational acceleration, D_{50} the median grain size, while a_w, a_n and b are coefficients given by Camenen and Larson [17] and $\theta_{cw,net}$ is calculated by the equation:

$$\theta_{cw,net} = \left(1 - a_{pl,b}\right)\theta_{cw,on} - \left(1 + \alpha_{pl,b}\right)\theta_{cw,off} \tag{13}$$

where $\theta_{cw,on}$ and $\theta_{cw,off}$ take into account the wave asymmetry, as they are the mean values of the instantaneous Shields parameter for the two time periods that add up to the wave period T. Specifically, T_{wc} is the time period (part of the wave period) when the velocities are positive and corresponds to wave crest, while T_{wt} is the time period (part of the wave period) when the velocities are negative and corresponds to wave trough ($T_w = T_{wc} + T_{wt}$, in which T_w is the wave period).

The $a_{pl,b}$ coefficient accounts for the phase-lag effects [17], which was described previously as the phenomenon in which the sediment which stays in suspension when the flow changes direction, is drifted towards the opposite one. The $a_{pl,b}$ coefficient is given by:

$$a_{pl,b} = a_{onshore} - a_{offshore} \tag{14}$$

where $a_{onshore}$ and $a_{offshore}$ are given by:

$$a_j = \frac{v^{0.25} U_{wj}^{0.5}}{w_s T_j^{0.75}} exp\left[-\left(\frac{U_{w,crsf}}{U_{wj}}\right)^2\right] \tag{15}$$

where j switches between *onshore* and *offshore* as mentioned above, ν stands for water kinematic viscosity, $U_{w,crsf}$ is the critical velocity for the initiation of the sheet flow, U_w is the wave orbital velocity and w_s the sediment fall velocity.

The critical velocity for the inception of the sheet flow is given by:

$$U_{w,cr,sf} = 8,35\sqrt{(s-1)g\sqrt{D_{50}\delta_w}}\,(1 + r_w) \tag{16}$$

where

$$r_w = \frac{U_{w,max}}{U_w} - 1 \tag{17}$$

is the wave asymmetry coefficient and $U_{w,max}$ the maximum wave orbital velocity.

The Shields parameters $\theta_{cw,on}$ and $\theta_{cw,off}$ in the Equation (13) are given by:

$$\theta_{cw,j} = \frac{1}{2} f_{cw} U_{cw,j}^2 / [(s-1)gD_{50}] \tag{18}$$

where j switches between *onshore* and *offshore*, U_{cw} the total wave and current velocity, f_{cw} the friction coefficient for the wave and current interaction. There is no current in this work, so the friction coefficient f_{cw} is related to the waves (f_w) only and is equal to [1]:

$$f_{cw} = f_w = \exp\left[5.213\left(\frac{k_s}{a_0}\right)^{0.19} - 5.977\right] \tag{19}$$

where k_s is the bed roughness, which is taken equal to $2.5D_{50}$ [27], while $a_0 = U_{w,max} \times T/2\pi$ is the amplitude of the orbital bottom velocity $U_{w,max}$.

Lastly, the coefficients a_w, b, a_n in the main Equation (12) are given by: $a_w = 6 + 6\theta_c/(\theta_c + \theta_w)$, $b = 4.5$ and $a_n = 12$.

2.2.2. Suspended Load

The suspended load according to Camenen and Larson [17], is given by:

$$q_{ss,w} = U_{cw,net}\frac{C_R\varepsilon}{w_s}\left[1-\exp\left(-\frac{w_s}{\varepsilon}\right)\right] \tag{20}$$

$$q_{ss,n} = U_c sin\varphi\frac{C_R\varepsilon}{w_s}\left[1-\exp\left(-\frac{w_s}{\varepsilon}\right)\right] \tag{21}$$

where C_R is the bed reference concentration, ε the sediment diffusivity, and $U_{cw,net}$, the net mean current.

The bed reference concentration according to Camenen and Larson [17], is given by:

$$c_R = A_{cR}\theta_{cw,m}exp\left(-b_w\frac{\theta_{cr}}{\theta_{cw}}\right) \tag{22}$$

where

$$A_{cR} = 3,5{\cdot}10^{-3}\exp(-0,3D_*) \tag{23}$$

where D_* is the dimensionless grain size given by:

$$D_* = \sqrt[3]{(s-1)g/v^2}D_{50} \tag{24}$$

The sediment diffusivity ε is calculated through the energy dissipation:

$$\varepsilon = \left(\frac{D_{dis}}{\rho}\right)^{1/3}D_{50} \tag{25}$$

where D_{dis} the energy dissipation, which is calculated from the OpenFOAM hydrodynamic model and specifically the turbulence model. This is one of the main differences between using the hydrodynamic OpenFOAM model and the Boussinesq model or other depth-averaged models, where the energy dissipation is calculated from semi-empirical formulae.

Lastly, the net mean current $U_{cw,net}$ is given by:

$$U_{cw,net} = \left(1-a_{pl,s}\right)U_{cw,onshore} + \left(1+a_{pl,s}\right)U_{cw,offshore} \tag{26}$$

where the $a_{pl,s}$ coefficient is related to the phase lag effect according to the Equation (14) with the difference in the subscript which now is s (suspended) and $U_{cw,onshore}$, $U_{cw,offshore}$ the velocities for the different parts of the wave period according to the notation described in the Section 2.2.1.

2.2.3. Conservation of Sediment Transport

The total sediment transport rate is the addition of bedload and suspended load transport rates as presented above. Once the total sediment transport rate is calculated, the new morphology of the seabed can be achieved using the conservation of sediment transport Equation [28]:

$$\frac{\partial z_b}{\partial t} + \frac{1}{1-n}\frac{\partial}{\partial x}\left(q_{x,t} - \varepsilon_w \mid q_{x,t} \mid \frac{\partial z_b}{\partial x}\right) + \frac{1}{1-n}\frac{\partial}{\partial y}\left(q_{y,t} - \varepsilon_w \mid q_{y,t} \mid \frac{\partial z_b}{\partial y}\right) = 0 \tag{27}$$

where z_b is the local seabed elevation (for each cell) and $q_{x,t}(= q_{s,x} + q_{b,x})$, $q_{y,t}$ $(= q_{s,y} + q_{b,y})$ are the total sediment transport (bedload plus suspended load) rates in x and y horizontal directions respectively. The coefficient ε_w is the slope coefficient (as mentioned above) according to Watanabe [26], which for the cases of flat seabed is equal to zero.

2.3. Coupling of the Two Models—Iterative Method

As mentioned above, the method used in this work is iterative, coupling the hydrodynamic with the morphodynamic models as many times as required until the equilibrium seabed profile is achieved. The first step is to use the initial seabed morphology as input to the OpenFoam hydrodynamic model, which runs and yields the hydrodynamic field of the flow, under any given wave conditions. These results are used as input by the morphodynamic model, which is applied and a new seabed morphology is obtained. The new morphology is used as input to the OpenFoam model for the second run and this procedure is repeated until the equilibrium state is reached.

3. Results

The model is validated against three different Xie's [1] experiments, with two of them belonging to the "relatively fine sand" group, while the third one is classified as "relatively coarse sand" case.

3.1. Geometry of the Model—Mesh Generation

The geometry of the model is based on the wave flume where the experiments were carried out [1]. A 38 m long numerical flume was created, with actual distance from the left boundary to the breakwater being 35.9 m, a 6 m flat sandy bed in front of the breakwater and an 1:30 slope seawards, while the depth is 0.30 m in front of the breakwater and 0.45 m in the beginning of the numerical flume. Not to scale sketch of the model's geometry is shown in Figure 2.

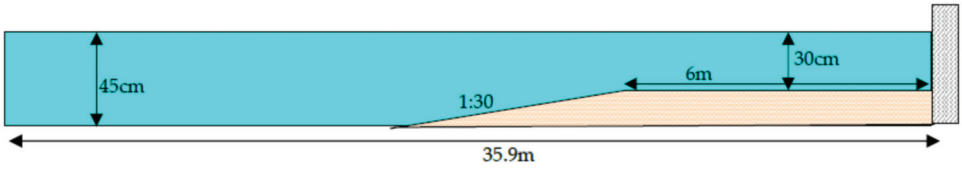

Figure 2. Sketch of the model geometry.

The mesh was generated with standard OpenFOAM tools, specifically with blockMesh and snappyHexMesh tools, both available in OpenFOAM libraries. First of all, the basic structured mesh with same-sized computational cells was created with blockMesh and then snappyHexMesh is used to create the impermeable slope, the breakwater and the raised seabed, refining accordingly the required cells above the sandy seabed, as it cuts the numerical domain. The refinement process has been done with snappyHexMesh as described in the OpenFoam tutorial and have been studied in some works [29]. The discretization of the mesh used is $\Delta x = 1$ cm and $\Delta z = 1$ cm. Suitable boundary conditions were implemented.

3.2. Wave and Sediment Characteristics

Table 1 shows the wave and sediment characteristics for the three implemented cases, where D_{50} is the median grain size, w_f is the sediment fall velocity (taken from [1]), H is the wave height, T is the wave period and L is the wave length. Fifth-order Stokes regular waves were implemented for all 3 cases. The last column in Table 1 shows the classification of each case according to Xie [1] and the case numbering refers to Xie's [1] respective experiments.

Table 1. Wave and sediment characteristics.

Case	D_{50}	w_f	H	T	L	H/L	H/gT^2	d/L	H/D_{50}	Group
2a	106 μm	0.7 cm/s	7.5 cm	1.32 s	2.0 m	0.0375	0.0044	0.15	707.5	Fine
7a	106 μm	0.7 cm/s	5 cm	2.41 s	4.0 m	0.0125	0.0009	0.075	471.7	Fine
23a	780 μm	11 cm/s	6.5 cm	1.53 s	2.4 m	0.0271	0.0028	0.125	83.3	Coarse

3.3. Hydrodynamic Results—Standing Wave Formation

The hydrodynamic model is being validated against Xie's [1] 2a experiment and analytical solutions. Moreover, the performance of two different lengths of relaxation zones, two different cell sizes with respect to dx and two numerical schemes for the convection term of the Navier–Stokes equations is examined. The validation has been made for the initial seabed before any morphological changes occurred. Regular fifth-order Stokes waves have been implemented with wave height of H = 7.5 cm and period T = 1.32 s to match the wave conditions of the aforementioned experiment. The duration of the first simulation with the initial seabed was 72 s to allow for 55 waves to propagate.

Figure 3 shows the instantaneous surface elevation at two different positions, specifically at 13.8 m and 1 m from the breakwater, respectively. The transition from the incident of 7.5 cm height wave to the respective standing wave is depicted in Figure 3a. Specifically, the incident wave reaches this position (just before the slope) after 10 s, while the standing wave formation starts at about 35 s from the beginning of the simulation. There is a significant wave height increase between 35 s and 40 s, when it reaches its peak, while the standing wave takes its steady form just after 45 s. Figure 3b shows the standing wave formation just 1 m away from the wall. Due to the fact that the position is very close to the wall, the transition from incident to standing wave occurs immediately. The latter takes its steady form after 40 s from the beginning of the simulation, with the wave height being 15 cm, while it starts decreasing after 50–55 s. This can be attributed to the long simulation, as well as the long numerical flume. Moreover, the wave energy dissipation inside the domain, caused by the use of the turbulence model, also affects the wave height.

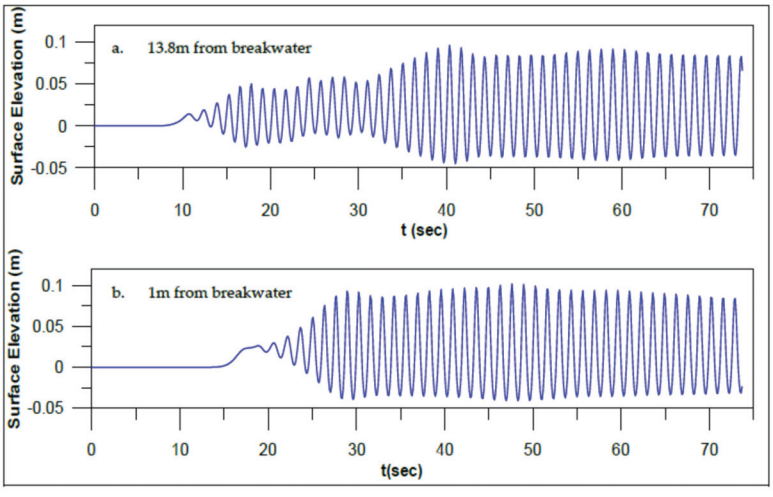

Figure 3. Surface Elevation at 2 different locations. (**a**) 13.8 m from the breakwater, just before the slope, where the transition from incident to standing wave is shown. (**b**) 1 m from the breakwater where fully standing wave formation is depicted.

Furthermore, the role of the relaxation zones is crucial for long simulations. Figure 4 compares the wave heights at the position of 1 m before the breakwater (34.9 m from the inlet), which correspond to two different relaxation zones lengths, 3 m (1.5 × L) and 8 m (4 × L) respectively. It seems that the length of the relaxation zone affects the steadiness of the waves in long simulations. As mentioned above and shown in Figure 3b, the wave height decreases after around 55 s, which is also depicted in Figure 4, but Figure 4 also shows that in the case of 3m long relaxation zone, the wave height is significantly smaller, starting to increase and become steady after 50 s. This difference can be attributed to the long simulation, the short wave that was used in this case (T = 1.32 s) and the long numerical flume, which,

can cause the accumulation of tiny unwanted reflections at the boundary when combined. The use of longer relaxation zone increases the computational cost; however, it can improve the accuracy of the results.

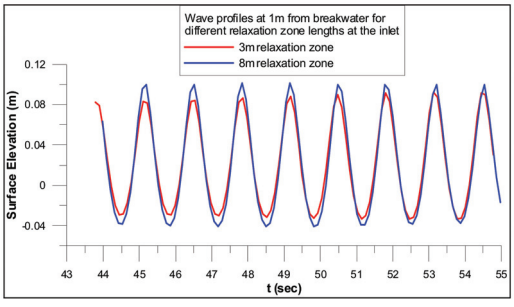

Figure 4. Comparison between different relaxation zones lengths.

The discretization of the domain can affect the accuracy of the numerical results too, although this is more important in breaking waves cases, where the unsteadiness and turbulence effects require higher mesh resolution. Jacobsen [30], for example, applied an aspect ratio of 92 to produce a standing wave, while he found that the aspect ratio required to describe a wave breaker is 1. However, due to the long numerical flume in this case, as well as long -in terms of duration-simulation, higher mesh resolution is required. Two different values of dx were examined, as shown in Figure 5, where the wave heights of the cases of dx = 1 cm and dx = 2 cm at the location of 1 m away from the breakwater are depicted. It seems that the finer the mesh, the better the results, as a difference of about 1 cm–2 cm in wave height can be observed. Hence, dx = 1 cm was implemented and the respective aspect ratio dx/dz is 1.

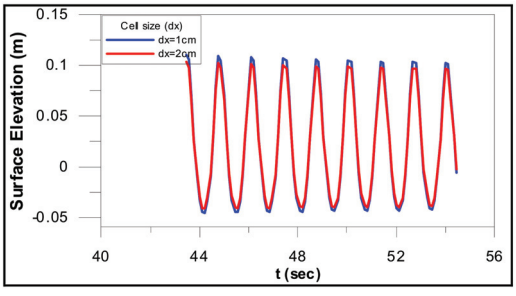

Figure 5. Comparison between wave heights at location 1 m away from the breakwater for different cell sizes (different dx).

Another factor which can affect the results is the divergence numerical scheme for the convection term of the RANS equations, as this term defines at which rate the velocity U changes in space. Two numerical schemes were tested, both available in OpenFOAM libraries, the Gauss limited linear V [31], where a limiter is applied in the direction of greater change and the Gauss linear Upwind grad (U) [32], which is an upwind scheme with a correction depending on the cell gradient. Figure 6 shows the comparison between the wave heights that obtained for these two schemes respectively for the last 10 s of the simulation (the last 10 s were selected, so that the effect of the numerical scheme can be shown). It can be observed that the Gauss linear Upwind grad (U) scheme yields slightly better results, especially in long (in duration) simulations and is implemented here.

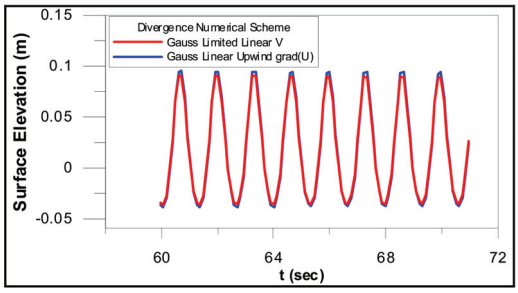

Figure 6. Comparison between wave heights at location 1 m away from the breakwater for different divergence numerical scheme for the convection terms of RANS equations.

Following the implementation of the above configurations, the model was applied, and surface elevation numerical results were compared with Xie's experimental data (2a experiment) [1]. Figure 7 shows the comparison between computed and experimental results, which seems to be in good agreement, especially after 35 s, when steadiness is reached.

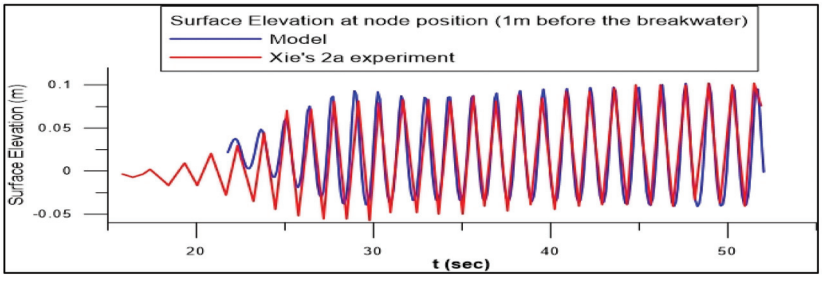

Figure 7. Instantaneous Surface Elevation at the position of 1 m before the breakwater. Comparison between model results and experimental data.

Figure 3 shows the formation of the standing wave at two different positions, just before the slope and 1 m away from the breakwater. The velocity distribution is depicted in Figure 8a,b at two different time instances and at distance of 1 wave length from the breakwater. The nodes close to the breakwater, are formed at the positions of around 35.4 m and 34.4 m, while the antinode at the position of 34.85 m. The velocity distribution follows exactly the surface elevation results, with the velocity vectors being horizontal at the position of the nodes and vertical at the antinode, while they have opposite directions at these two different instants, following the surface elevation's oscillation. Figure 8c shows the standing wave envelope and the total particle movement, as it can be derived from the velocity vectors directions. Further to the qualitative observation, the horizontal components of velocities are compared with second-order theory of Miche:

$$U_{w,x} = \frac{2\pi H}{T}\frac{\cosh(k(z+d)}{\sinh(kd)} cos kx\, cos\omega t + \frac{3\pi^2}{2T}\frac{H^2}{L}\frac{\cosh(2k(z+d)}{\sinh^4(kd)} sin 2kx\, sin\omega t \quad (28)$$

where $U_{w,x}$ is the horizontal orbital velocity, $k = 2\pi/L$ the wavenumber, $\omega = 2\pi/T$ the angular frequency, $x = 0$ at the position of the node and positive towards the breakwater, z the surface elevation with $z = 0$ at Still Water Level (SWL) and positive upwards, H, L, T the wave height, length and period—respectively, d is the depth and t is the time. Figure 9 shows the comparison between model results and Miche analytical solution at the position of the node and 5 cm above the flat seabed. The numerical results are in good agreement with Miche second-order theory.

Moreover, according to Xie's [1] experimental data, the maximum value for the horizontal velocity is 0.328 m/s, while model's maximum value at this position is 0.332 m/s (Figure 9), which is in agreement with theory. The orbital velocity profiles are also compared with Miche analytical solution in Figure 10 at the node position and L/8 from the node position. The numerical results are in good agreement with analytical solution at the bottom at the node position, while slightly deviate towards the free surface (the difference is <0.01 m/s). There is also a slight deviation between numerical results and analytical solution at L/8 from the node position, with the model yielding higher values in this instance (circa 0.01 m/s).

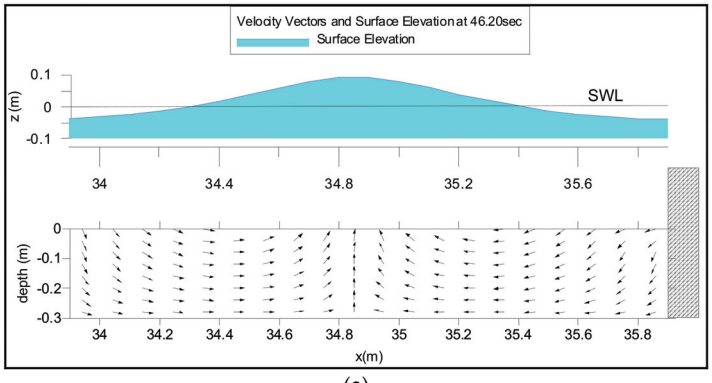

(**a**)

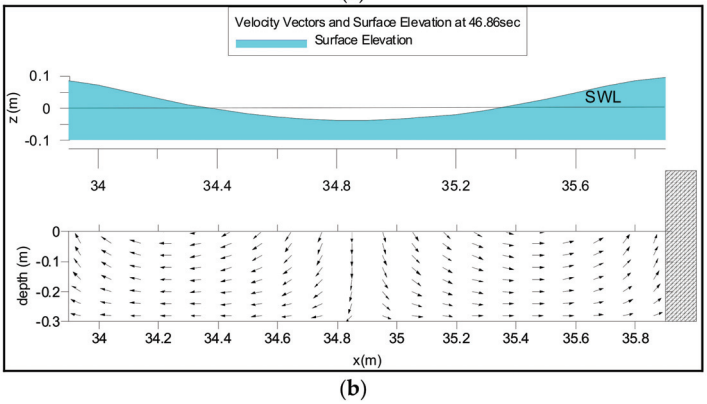

(**b**)

Figure 8. *Cont.*

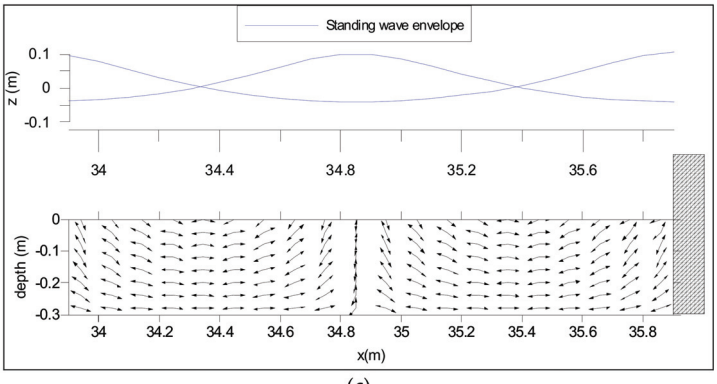

(**c**)

Figure 8. (**a**) Surface Elevation and particle velocity distribution at 46.2 s (model results for t = 35 *T). (**b**) Surface Elevation and particle velocity vectors at 46.53 s (model results for t = 35T + T/2). (**c**) Standing wave envelope and particle movement (model results).

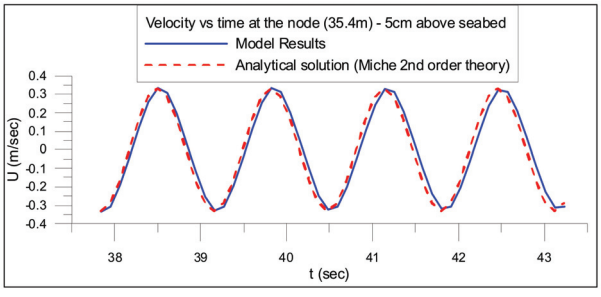

Figure 9. Orbital velocity at the position of the node (35.4 m from the inlet of the flume) at 5 cm above the seabed. Comparison between numerical results and analytical solution (Miche second-order theory).

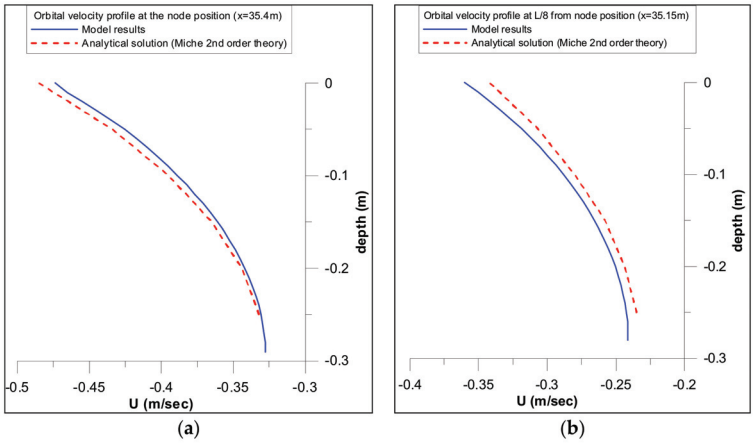

(**a**) (**b**)

Figure 10. Orbital velocity profiles (**a**) at the position of the node (35.4 m from the inlet of the flume), and (**b**) L/8 from the position of the node (35.15 m from the inlet of the flume). Comparison between numerical results and Miche second-order analytical solution.

3.4. Morphodynamic Results—Scouring Depth and Scouring Patterns

The morphodynamic model is applied and couples the hydrodynamic solution to produce the sediment transport rates and update the seabed morphology, based on the sediment continuity, in an iterative process. Figure 11 shows the seabed profile evolution for 2a test, at 4 different instants. According to Table 1 and Xie [1], this test belongs to the "relative fine sand" group, where scour is expected at node positions and deposition at antinodes, which seems to be the case here, as the computed scouring pattern follows this rule.

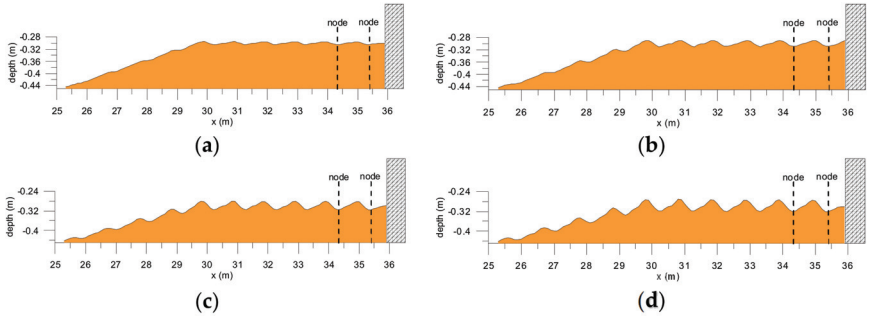

Figure 11. Seabed profile evolution after (**a**) 200 s, (**b**) 400 s, (**c**) 800 s, (**d**) 1400 s (test 2a).

The first two nodes close to the wall are marked with dashed lines (35.4 m and 34.4 m, respectively) in Figure 11 for all four instants, and it seems that this scouring pattern of alternating scour with deposition at nodes and antinodes respectively remains the same at all times during the simulation of test 2a. Ripples are created in the whole length of the sandy bottom under the influence of the standing waves. The equilibrium profile is shown in Figure 12 along with the standing wave. It can easily be observed that the equilibrium seabed profile is in complete agreement with the "relative fine sand" scouring pattern, as scour occurs at the nodes and deposition at the antinodes. Furthermore, the numerical results are compared satisfactorily with experimental data [1] with regards to the local scour in front of the breakwater.

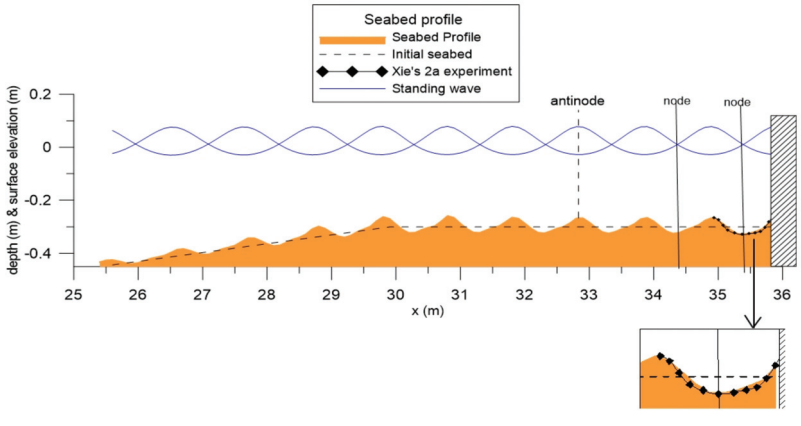

Figure 12. Final numerical seabed profile and standing wave. Comparison with experimental data (test 2a).

Figure 13 further compares the numerical results for the scouring depth in front of the breakwater with Xie [1] experimental data, as well as sinusoidal and trochoid curves as per Xie [1] comparison. All these curves agree on the scouring depth, which is 2.8 cm, as predicted by the model.

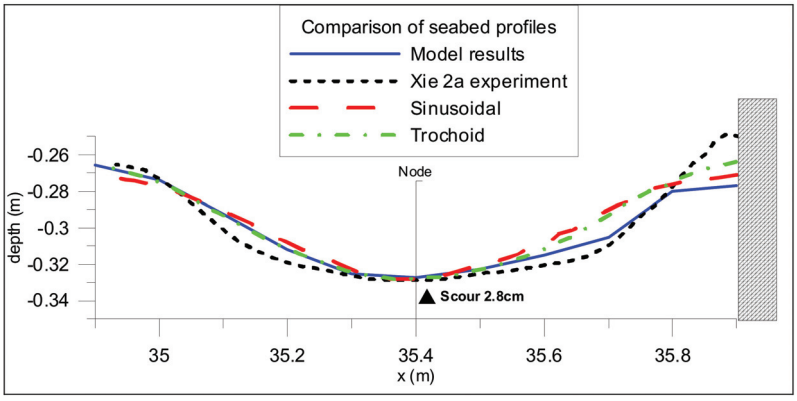

Figure 13. Seabed profiles and scouring depth—comparison between model results and experimental data/theory (test 2a).

The next test, 7a, concerns a longer wave (double wavelength) in the same wave flume, meaning that the depth in front of the breakwater is still 30 cm. The iterative method of coupling the two models was applied and the seabed morphology evolution during this process is depicted in Figure 14 for four different time instants. The nodes close to the wall are marked with dashed lines and found at the positions 34.9 m and 32.9 m, respectively. The standing wave is depicted in Figure 15. It seems that the model results are in agreement with Xie's [1] classification, as the scour is formed at the nodes and the deposition at the antinodes, which is a typical "relative fine sand" pattern.

Although the pattern is followed as expected, it seems that there is a slight shift between the antinode, which is close to 32 m and the top of the ridge. A slight shift exists at the positions of the other antinodes as well, but the one close to 32 m is slightly bigger. This can be attributed to the bigger wave length (L = 4 m) with respect to the length of the sandy flat bed, which is 6 m, as there is the slope before the flat bed that can affect the standing wave evolution. This might not happen if the wave length was multiple of the flat bed length. Moreover, comparing the results of 2a and 7a experiments, it can be noticed that in the latter case, a small "berm" is created between the node and the antinode. This can be attributed to the bigger wave length too, as the scouring hole is getting too big to stand alone with a uniform shape, which does not affect the position of the scour though. In terms of comparison between numerical results and experimental data, it can be observed from Figure 15 that they are in good agreement.

This can also be attested by Figure 16, where the numerical results for the scouring depth and scouring pattern are compared with Xie experimental data [1], sinusoidal and trochoid curves. It seems that they are in good agreement; however, the model's deposition next to the wall is smaller than the experimental one. The scour depth was predicted 5 cm by the model, which is consistent with the other three curves.

The above two tests are classified as "relative fine sand" cases, while the next test 23a belongs to the "relative coarse sand" group according to Xie [1]. Figure 17 shows the seabed evolution at four different time instants, while the nodes positions are marked with dashed lines. The main difference in the scouring pattern can be easily identified, if Figure 17 is compared with Figures 11 and 14. In previous cases, scour was formed at nodes positions, while the opposite is observed in this case. Ridges are formed at the nodes' positions, as expected, in line with Xie [1] classification.

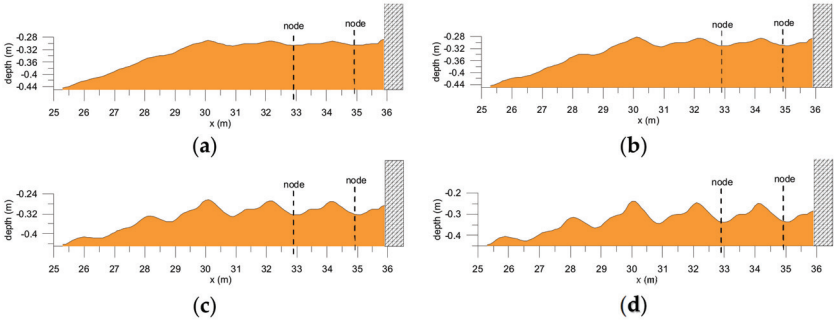

Figure 14. Seabed profile evolution after (**a**) 500 s, (**b**) 1000 s, (**c**) 2000 s, (**d**) 3800 s (test 7a).

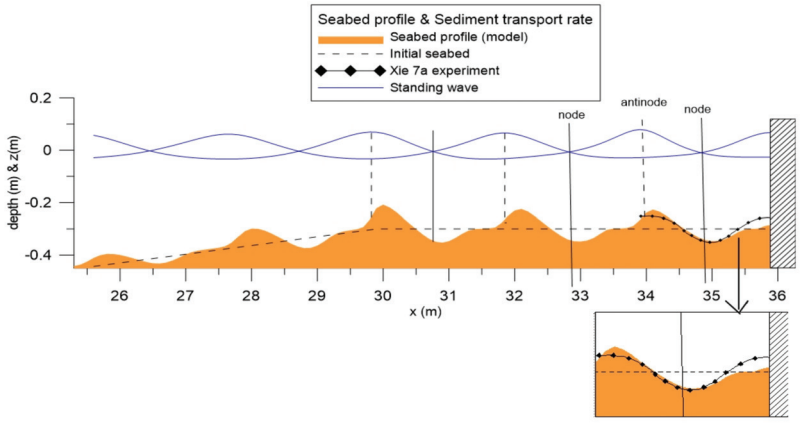

Figure 15. Final numerical seabed profile and standing wave—Comparison with experimental data (test 7a).

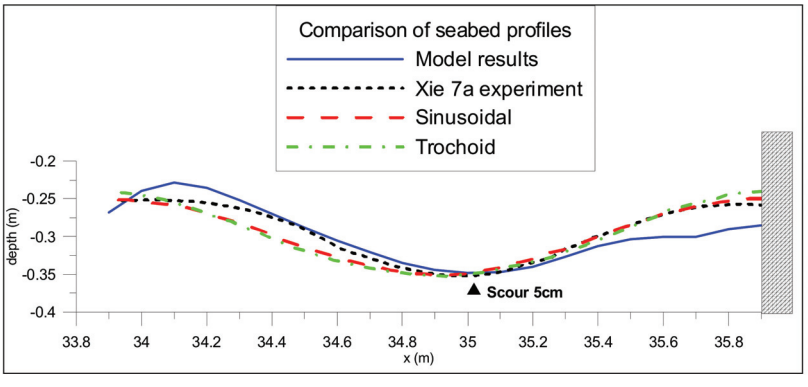

Figure 16. Seabed profiles and scouring depth-comparison between model results and experimental data/theory (test 7a).

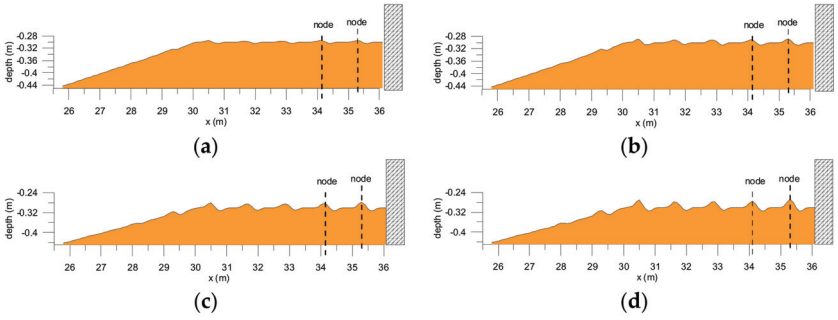

Figure 17. Seabed profile evolution after (**a**) 500 s, (**b**) 800 s, (**c**) 1500 s, (**d**) 3200 s (test 23a).

Figure 1 shows the standing wave evolution, while the nodes close to the breakwater can be identified at the positions 35.3 m and 34.1 m, respectively. The antinodes are marked with dashed lines and the nodes with solid lines. The scouring pattern, as depicted in Figure 18, is consistent with Xie's [1] scouring pattern for "relative coarse sand", as well as Sumer and Fredsoe [2]. The scour is formed between the nodes and the antinodes, while a small ridge is formed at the antinodes position as shown in Sumer and Fredsoe, whose elevation can be even lower than the initial one [2]. However, the scour is formed differently next to the antinodes. The scour that is formed seawards is fully developed, while the scour that is formed towards the breakwater is barely identified. Apart from that, the numerical results are in agreement with the relative coarse sand scouring pattern. The experimental data [1] are limited for "relative coarse sand" tests; however, the maximum scour depth and an indicative scouring curve were available for this test [1].

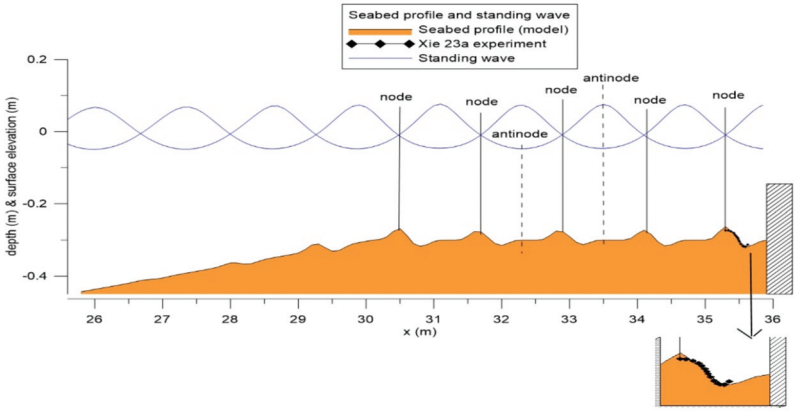

Figure 18. Final numerical seabed profile and standing wave—Comparison with experimental data (test 23a).

Figure 19 shows the comparison between numerical results and Xie's available experimental data. The scour according to the experimental data is 2.28 cm, while the model's prediction is 2.04 cm. Also, model's seabed profile slightly underestimates the scour depth and slightly overestimates the deposition at the node position (35.3 m). According to Xie [1], there is a length from the antinode towards the node (22 cm in this instance), where the seabed remains practically intact (this length is shown with black solid line in Figure 19). Numerical results are also in good agreement with experimental data in this instance.

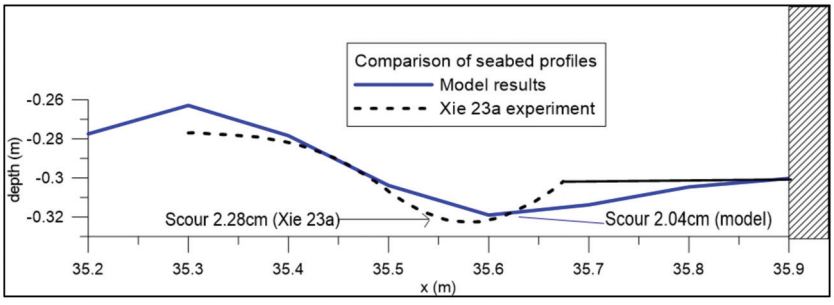

Figure 19. Seabed profiles and scouring depth—Comparison between model results and experimental data (test 23a).

4. Discussion

Following the description and application of the coupled model, some interesting points can be further discussed in this section, as derived from the simulation process and the numerical results.

As pointed out above, the turbulence model, the wave generation and absorption method, the numerical scheme of the RANS equations convection term, as well as the mesh resolution, are crucial for the successful set-up of the hydrodynamic model. The k-w SST was selected following previous authors' works [15,18,33], as it seems that prevails over the rest on the OpenFOAM platform, with the quick note that the density term needs to be included in the equations, so that the free surface cells are defined correctly. The wave generation and absorption method and its implementation is also important especially for long (in time) simulations and long numerical domains, as it is the case in this instance. The selection of relaxation zones method was based on the fact that an adequate length of absorption zone must be defined, so that even tiny accumulated unwanted reflections would not contaminate the results. Two different lengths (3 m and 8 m) of relaxation zones were tested and as expected, the latter one prevailed over the short one. The implementation of the numerical scheme for the convection term of the RANS equations is another factor that can have an impact on the results, as it defines the rate at which the velocity changes in space. The Gauss linear upwind grad (U) scheme [32] seems to behave better in this case in comparison with the Gauss limited linear V [31] one, as the latter imposes a limiter in the direction of greater change, while the former one is an upwind scheme with correction depending on the cell gradient. Their impact on the wave heights were shown and this may be attributed to the limiter imposed on the velocity gradient at the free surface cells. With regards to the mesh resolution, it seems that the smaller dx improves the results, although the aspect ratio for the production of standing waves on OpenFOAM can be very high [30].

With regards to the morphodynamic model, the code was developed by the authors implementing the Camenen and Larson formula [17] and takes into account the wave asymmetry and the initiation of the sheet flow over ripples, including the phase lag effect. That means that the velocities are calculated separately for the period that they are positive and the period that they are negative and as a sequence, the Shields parameter is calculated separately for each one of these periods too. Also, the phase lag effect coefficient is calculated separately for each one of these time periods, which improves the way that the particles in suspension near the bed are simulated. The mean velocity values in this formula are calculated as the root mean square (rms) values, therefore any zero values in case of wave symmetry are avoided. The sediment continuity Equation (27) is being solved iteratively, producing the updated seabed morphology.

Both the hydrodynamic and morphodynamic results were validated against experimental data and/or analytical solutions. The model successfully predicts the local scour in front of the breakwater, as well as the scouring pattern, including ripples in the whole domain.

The novelty of this work is the development of a numerical model, coupling an advanced CFD RANS model on OpenFOAM platform with a developed by the authors morphodynamic one, that can successfully simulate not only the local scour depth and pattern in front of vertical breakwaters, but the ripples and the scouring pattern in the whole domain too, according to the classification in the literature [1,2]. To the best of the authors' knowledge, the existing literature includes numerical attempts that only examine the scour at a very short length (half wave length) from the breakwater. For example, Gislason et al. [9] mention there were no ripples in their model and the attempt to model them was abandoned due to numerical instabilities. Also, Hajivalie et al. [10] used an Euler–Lagrange approach, but their results are limited to only one validation case and to the local scour at a distance of a half-wavelength from the breakwater. Moreover, unlike previous works [9,10] where the numerical domain was limited to a short distance from the vertical wall, the numerical domain in this work was created according to the experiment (breakwater at 35.9 m from the wave inlet), and the numerical results include the bed formation in the whole domain. The ripples were formed according to the literature, with the scour being formed at the nodes position and the accretion at the antinodes for "relative fine sand" cases, while deposition at nodes and scour between the nodes and the antinodes are being formed for "relative coarse sand" ones.

However, there is room for improvement. Two things that have been mentioned in the Section 3.3 are that there is slight shift between the antinode and the top of the ridge in 7a test, especially in the middle of the flat bed length, which may be attributed to the wave length with respect to the flat bed length and the other thing is that in the case of "relative coarse sand", the scour between the antinodes and the nodes (in ripples formation) towards the wall has slightly been developed, unlike the one to the opposite direction. Also, in the case of relatively coarse sand (23a), the model predicted a maximum scour of 2.04 cm, instead of 2.28 cm according to the available experimental data [1], which are limited for the "relative coarse sand" group though. Furthermore, the authors aim to extend the applicability of the coupled model to 3D cases.

5. Conclusions

A numerical approach was presented in this work, coupling an advanced CFD RANS model developed on the OpenFOAM platform with a morphodynamic one, as developed in FORTRAN by the authors. The model describes the hydrodynamic and morphodynamic processes and has been implemented here to predict the scour depth and the scouring pattern in front of a vertical breakwater.

The model has been tested against experimental data and analytical solutions for surface elevation, orbital velocities evolution near the bed, velocities profiles, velocity vectors distribution, standing wave formation, scouring pattern and ripples formation in the whole domain and local scouring depth in front of a vertical-wall breakwater. Xie's [1] experimental data were used to validate the model and specifically tests 2a and 7a for the "relative fine sand" and 23a for the "relatively coarse sand" classifications, with model results being in good agreement with experimental data. The scour depth prediction was accurate for the tests 2a and 7a (fine sand), while it was close to the experimental data for the test 23a (coarse sand). The model accurately predicts the scouring pattern/ripples formation in the whole domain.

Author Contributions: Conceptualization, N.K. and T.K.; methodology, N.K. and T.K.; software, N.K.; validation, N.K.; formal analysis, N.K.; investigation, N.K.; resources, N.K. and T.K.; data curation, N.K.; writing—original draft preparation, N.K.; writing—review and editing, N.K, T.K., C.K.; visualization, N.K.; supervision, T.K. and C.K.; project administration, T.K. and C.K.; funding acquisition. All authors have read and agreed to the published version of the manuscript.

Funding: This research received no external funding.

Conflicts of Interest: The authors declare no conflict of interest.

References

1. Xie, S.L. *Scouring Patterns in Front of Vertical Breakwaters and Their Influences on the Stability of the Foundations of the Breakwaters*; Delft University of Technology: Delft, the Netherlands, 1981.
2. Sumer, B.M.; Fredsøe, J. Experimental study of 2D scour and its protection at a rubble-mound breakwater. *Coast. Eng.* **2000**, *40*, 59–87. [CrossRef]
3. Carter, T.G.; Liu, L.F.P.; Mei, C.C. Mass transport by waves and offshore sand bedforms. *J. Waterw. Harb. Coast. Eng. ASCE* **1973**, *99*, 165–184.
4. Lee, K.; Mizutani, N. Experimental study on scour occuring at a vertical impermeable submerged breakwater. *J. Appl. Ocean. Res.* **2008**, *30*, 92–99. [CrossRef]
5. Mei, C. *The Applied Dynamics of Ocean Surface Waves*; World Scientific: Hackensack, NJ, USA, 1989.
6. Bing, C. The numerical simulation of local scour in front of a vertical-wall breakwater. *J. Hydrodyn.* **2007**, *18*, 134–138.
7. Gislason, K.; Fredsøe, J.; Mayer, S.; Sumer, B.M. The mathematical modeling of the scour in front of the toe of a rubble-mound breakwater. In *Book of Abstracts, Proceedings of the 27th International Coastal Engineering Conference, Sydney, Australia, 16–21 July 2000*; ASCE: Reston, VA, USA, 2000; Volume 1, p. 1.
8. Gislason, K.; Fredsøe, J.; Sumer, B.M. Flow under standing waves Part 1. Shear stress distribution, energy flux and steady streaming. *Coast. Eng.* **2009**, *56*, 341–362.
9. Gislason, K.; Fredsøe, J.; Sumer, B.M. Flow under standing waves. Part 2. Scour and deposition in front of breakwaters. *Coast. Eng.* **2009**, *56*, 363–370. [CrossRef]
10. Hajivalie, F.; Yeganeh-Bakhtiary, A.; Houshanghi, H.; Gotoh, H. Euler-Lagrange model for scour in front of vertical breakwater. *Appl. Ocean Res.* **2012**, *34*, 96–106. [CrossRef]
11. Engelund, F.A.; Fredsøe, J. A sediment transport model for straight alluvial channels. *Nord. Hydrol.* **1976**, *7*, 293–306. [CrossRef]
12. Karagiannis, N.; Karambas, T.; Koutitas, C. Numerical simulation of scour in front of a breakwater using OpenFoam. In Proceedings of the 4th IAHR Europe Congress, Liege, Belgium, 27–29 July 2016; pp. 309–315.
13. Karagiannis, N.; Karambas, T.; Koutitas, C. Numerical simulation of scour pattern and scour depth prediction in front of a vertical breakwater using OpenFoam. In Proceedings of the 27th International Ocean and Polar Engineering Conference (ISOPE 2017), San Francisco, CA, USA, 25–30 June 2016; Volume 3, pp. 1342–1348.
14. Jacobsen, N.G.; Fuhrman, D.R.; Fredsøe, J. A Wave generation toolbox for the open-source CFD library: OpenFoam. *Int. J. Numer. Methods Fluids* **2012**, *70*, 1073–1088. [CrossRef]
15. Karagiannis, N. An Advanced Numerical Model Fully Describing the Hydro-and Morphodynamic Processes in the Coastal Zone. Ph.D. Thesis, Civil Engineering Department, Aristotle University of Thessaloniki, Thessaloniki, Greece, 2019.
16. Hirt, C.W.; Nichols, B.D. Volume of fluid (VOF) method for the dynamics of free boundaries. *J. Comput. Phys.* **1981**, *39*, 201–225. [CrossRef]
17. Camenen, B.; Larson, M. *A Unified Sediment Transport Formulation for Coastal Inlet Application*; Technical report ERDC/CHL CR-07-1; US Army Engineer Research and Development Center: Vicksburg, MS, USA, 2007.
18. Karagiannis, N.; Karambas, T.; Koutitas, C. Numerical simulation of wave propagation in surf and swash zone using OpenFoam. In Proceedings of the 26th International Ocean and Polar Engineering Conference, Rhodes, Greece, 26 June–2 July 2016; Volume 3, pp. 1342–1348.
19. Higuera, P.; Lara, J.L.; Losada, I.J. Realistic wave generation and active wave absorption for Navier–Stokes models: Application to OpenFOAM. *Coast. Eng.* **2013**, *71*, 102–118. [CrossRef]
20. Jasak, H. Error Analysis and Estimation for the finite Volume Method with Applications to Fuid Fows. Ph.D. Thesis, Deptartment of Mechanical Engineering, Imperial College of Science, Technology and Medicine, London, UK, 1996.
21. Rusche, H. Computational fluid Dynamics of Dispersed Two-Phase flows at High Phase Fractions. Ph.D. Thesis, Department of Mechanical Engineering, Imperial College of Science, Technology & Medicine, London, UK, 2003.
22. Menter, F.R. Zonal Two Equation k-ω Turbulence Models for Aerodynamic Flows. *AIAA Paper* **1993**, 1993–2906. [CrossRef]
23. Menter, F.R. Two-equation eddy-viscosity turbulence models for engineering applications. *AIAA J.* **1994**, *32*, 1598–1605. [CrossRef]

24. Karambas, T.; Koutitas, C. Surf and swash zone morphology evolution induced by nonlinear waves. *J. Waterw. Port Coast. Ocean. Eng.* **2002**, *128*, 102–113. [CrossRef]
25. Karambas, T.V. Design of detached breakwaters for coastal protection: Development and application of an advanced numerical model. In Proceedings of the 33rd International Conference on Coastal Engineering, Santander, Spain, 1–6 July 2012.
26. Watanabe, A. Modeling of sediment transport and beach evolution. In *Nearshore Dynamics and Coastal Processes*; Horikawa, K. Ed.; University of Tokyo Press: Tokyo, Japan, 1998; pp. 292–302.
27. Nielsen, P. *Some Basic Concepts of Wave Sediment Transport*; Series Paper 20; Institute of Hydrodynamics and Hydraulic Engineering (ISVA); Technical University of Denmark: Lyngby, Denmark, 1979.
28. Leont'yev, I.O. Numerical modelling of beach erosion during storm event. *Coast. Eng.* **1996**, *29*, 187–200. [CrossRef]
29. Gisen, D. *Generation of a 3-D Mesh Using SnappyHexMesh Featuring Anisotropic Refinement and Near-Wall Layers*; ICHE: Hamburg, Germany, 2014.
30. Jacobsen, N.G. A Full Hydro-And Morphodynamic Description of Breaker Bar Development. Ph.D. Thesis, Department of Mechanical Engineering, Technical University of Denmark, Lyngby, Denmark, 2011.
31. Sweby, P.K. High resolution schemes using flux-limiters for hyperbolic conservation laws. *SIAM J. Numer. Anal.* **1984**, *21*, 995–1011. [CrossRef]
32. Warming, R.F.; Beam, M.M. Upwind second-order difference schemes and applications in aerodynamic flows. *AIAA J.* **1976**, *14*, 1241–1249. [CrossRef]
33. Karagiannis, N.; Karambas, T.; Koutitas, C. Wave overtopping numerical simulation using OpenFoam. In Proceedings of the 36th IAHR World Congress, The Hague, The Netherlands, 28 June–3 July 2015.

Journal of
Marine Science and Engineering

MDPI

Review

Damage in Rubble Mound Breakwaters. Part I: Historical Review of Damage Models

Álvaro Campos [1,*], Carmen Castillo [2] and Rafael Molina-Sanchez [1]

[1] Universidad Politécnica de Madrid (UPM), CEHINAV-HRL, 28040 Madrid, Spain; rafael.molina@upm.es
[2] Universidad de Castilla-La Mancha (UCLM), 13071 Ciudad Real, Spain; mariacarmen.castillo@uclm.es
* Correspondence: alvaro.campos@upm.es; Tel.: +34-630-66-75-72

Received: 20 March 2020; Accepted: 27 April 2020; Published: 30 April 2020

Abstract: The term "damage" in rubble mound breakwaters is usually related to the foremost failure mode of this kind of coastal structures: their hydraulic instability. The characterization of the breakwater response against wave action was and will be the goal of hundreds of studies. Because of the large amount of information, the present review on damage in rubble mound breakwaters is divided in two papers, which are closely linked but conceptually different; whereas Part II is focused on the various approaches for defining and measuring damage, Part I summarizes the diverse strategies for modelling damage development and progression. The present paper compiles 146 references on this topic, chronologically discussed over almost a century of history: from 1933 to 2020. It includes 23 formulations of hydraulic stability models and 11 formulations of damage progression models, together with main advances and shortcomings up to date. The future of rubble mound design is linked to risk-based tools and advanced management strategies, for which deeper comprehension about the spatial and temporal evolution of damage during the useful life of each particular structure is required. For this aim, damage progression probabilistic models, full-scale monitoring and standardization will presumably be some of the key challenges in the upcoming years.

Keywords: rubble mound breakwaters; historical review; damage; damage model; damage progression

1. Introduction

Damage in rubble mound breakwaters can be defined as the partial or total loss of its functionality and it is usually related to the hydraulic instability of the armor layer [1,2]. Rubble mound breakwaters behave as a static granular system until wave energy is higher than the one needed for the initiation of movement. At that moment, wave forces might provoke movements in the armor layer such as rocking, displacements, sliding of a whole blanket or settlement because of compaction. In this way, pieces close to SWL (still water level) tend to be moved toward the toe of the structure. This causes the geometrical initial shape to evolve with wave attack, up to the point of dealing with erosion and accretion volumes that can be especially high in the case of berm breakwaters. When underlayer units start to be removed, the progression of the geometrical rearrangement is much quicker, as the energy needed to move lighter units is obviously lower. Once the core material is exposed, the destruction of the structure is imminent.

Hydraulic instability of armor layers is a complex process because of the stochastic nature of both wave loading, initiation of movement, and damage progression. The highly non-linear flow over the slope, involving wave breaking, together with the variable shape of armor units and their random placement, make unfeasible to achieve analytical expressions for the calculation of actions and reactions. Thus, determining instantaneous armor unit stability also seems unachievable. This is the reason why

stability formulae are historically empirical or semi-empirical, associated with experimental results and ideally improved with prototype observations. Indeed, as stated in Melby and Hughes [3], it is recommended to utilize physical models if at all possible to verify stability and it is a common requisite in design tenders. These physical models are aimed at relating the response of the armor layer to parameters of the incident wave train and breakwater characteristics.

Since the pioneering works of de Castro [4] and Iribarren [5], several stability models have been proposed and many hundred studies on breakwater armor layer stability have been published. This gives an idea of the relevance of this failure mode; however, the achievement of a unique formula seems to be rather difficult, partly because of the wide range of typologies and designs. Regarding the large amount of data on this topic, this paper is aimed to present a historical overview of the most relevant models and advances up to date, focused on statically stable rubble mound breakwater's trunks. Breakwater's heads and other rubble mound typologies such as berm breakwaters are not considered herein.

The review on damage in rubble mounds breakwaters is divided into two separated papers, which are closely linked but conceptually different. Part I is focused on how damage development and progression is modelled, i.e., which are the available hypothesis and strategies for characterizing the structural response. This characterization is especially relevant, not only from the point of view of the breakwater design, but also regarding conservation and maintenance plans during the useful life. Part II [6] is centered on how damage is measured and parametrized, i.e., which are the instrumental techniques available for monitoring the structural response and, based on these instrumental records, which are the strategies for defining damage descriptors. Note that damage progression models presented in Part I directly consider these descriptors within their formulations.

2. Historical Review of Damage Models for Rubble Mound Breakwaters

Most hydraulic stability formulae were derived for rock armoring rather than for artificial blocks. According to Allsop et al. [7], rock armored breakwaters dominate in many areas of the world, although concrete armored breakwaters have probably a more detailed database because of the records from armor unit licensees. The present manuscript is mainly focused on quarry stones and parallelepiped armor units. Special shaped concrete units are roughly outlined in Appendix A.

In Table 1 most hydraulic stability formulae are summarized, with some slight modifications in order to be consistent with the symbols used herein and to fit the following general structure (adapted from Hald [8]):

$$N_S = \frac{H}{\Delta D_{n50}} < f(K, p_1, p_2, \ldots, p_n) \quad (1)$$

Thus, the stability of the armor layer was found to be reached when the stability number (N_S) is lower than a certain function (f). This function depends on the n parameters ($p_1, p_2, \ldots, p_n$) influencing stability and an empirical coefficient (K) determined by the parameters not directly accounted for in the stability equation (see Appendix B for the rest of symbols).

While hydraulic stability formulae were originally aimed at characterizing the initiation of movement of the armor layer, damage progression models were later designed to predict the evolution of rubble mounds' geometry by means of a quantitative damage descriptor. Consequently, damage progression models represent a much more useful design tool and are indispensable in any reliable maintenance or conservation program. However, because of the complexity of the problem, damage progression models were developed just in the past decades. More research is still needed, especially considering the adequacy of the different models to prototype measurements, which is not extensive nowadays. A review of damage progression models is presented in Table 2. Note that some models, mainly based on experimental results, define damage through the dimensionless erosion area (S) presented in Broderick and Ahrens [9], while others, mainly built under theoretical assumptions, define the damage descriptor in a generic way (D).

Before expounding on a historical synthesis on armor layer stability from the first hydraulic stability models to the latest contributions, the timeline of Table 3 is presented. It shows a selection of the most relevant hydraulic stability models and damage progression models from Tables 1 and 2. This scheme permits, not only arranging chronologically the different proposals in the study of armor layer stability, but also having an idea of the parameters/properties accounted for and the innovations introduced by each of them.

2.1. First Approaches to Hydraulic Stability Characterization. Models from Iribarren and Hudson

The first published formula for the calculation of the design weight of armor units evidenced by the authors was proposed in 1933. In this year, de Castro [4] reported a brief paper about rubble mound breakwaters using a modest approach based on his experience and highlighting the prevailing importance of rundown forces on instability.

The recommendations of de Castro inspired Iribarren [5] to develop another model in 1938, considered by many authors as the pioneer work on armor stability. In 1950, after 12 years of analyzing the consistency of the previous formula, Iribarren and Nogales [10] ratified the empirical coefficients presented in 1938. They also generalized the formula by introducing some modifications in the wave height parameter in order to account for water depth and wave period. Their final model was published in 1965 [11], summarizing the previous work and studying the limitations on the application of the formula by analyzing different slopes and types of armor units and wave breaking conditions. Also, a simple stability curve was suggested, relating the percentage of damaged slope and a coefficient between wave height and the wave height causing total destruction of the structure.

The initial works of Iribarren were translated and published in English in 1949 [12] and, after that, several models were proposed all around the world. In France, Larras [13] developed in 1952 a model considering water depth and wave length and, three years later, Beaudevin [14] published a simpler one. In the United States, Mathews (unpublished report presented in Bruun [15]) and Epstein and Tyrrel [16] built the first North-American hydraulic stability formulations in 1948 and 1949 respectively. Hickson and Rodolf [17] proposed a model for jetties based on the mining experience in 1950 and Hudson and Jackson [18] presented a formula in 1953 consisting of some modifications on Iribarren's. In Sweden, Hedar [19] ratified the Spaniard's results in 1953 reaching to the same stability criterion during downrush despite considering rotation, and not sliding, to be the dominant mode of motion. In Norway, Svee [20] ended up in 1962 with a model considering just a lifting force normal to the slope. In the Soviet Union, there were many publications on this topic between 1959 and 1967 such as Goldschtein and Kononenko [21], the design code SN-92-60 [22], Rybtchevsky [23], or Metelicyna [24].

However, the most widely known empirical stability model corresponds to Hudson [25,26]. After trying to characterize the friction coefficient for different armor units, Hudson noticed that the experimental coefficients of Iribarren's model could not be determined accurately from small scale breakwater stability experiments because they suffer variations from test to test for the same experimental conditions. Thus, Hudson proposed in 1958 a simpler formula after carrying out new stability tests with normal non-overtopped regular waves and using quarry stones and tetrapods (it was extended a few years later to tribars, tetrahedron and other special-shape armor units):

$$W = \frac{\gamma_s \cdot H^3}{K_D (S_r - 1)^3 \cot(\alpha)} \tag{2}$$

where K_D is tabulated for each armor unit type as a function of the $H/H_{D=0}$ ratio. $H_{D=0}$ is the limit wave height that produces no damage, considered as less than 1% volume of units eroded relative to the total volume of stones in the active armor layer (see Appendix B for the rest of symbols). At the same time, the $H/H_{D=0}$ ratio was related to a certain percentage of damage, which means that Hudson's model was probably one of the firsts providing quantitative information about the level of damage. The latter was possible owing to a standardized method for damage profiling, developed by the U.S.

Army Engineer Waterways Experiment Station (WES). Despite not considering water depth or wave period, Hudson recommended his model as an initial approximation of the major forces from both breaking and non-breaking waves. However, he pointed out that "*there is some doubt as to which of the various wave heights in natural wave trains should be selected as the design wave*". In fact, the Shore Protection Manual (SPM) suggested first $H_{1/3}$ [27] and, afterwards, $H_{1/10}$ [28] as an alternative wave height parameter in Equation (2) regarding irregular waves, without offering a clear justification for this modification.

Probably one of the first laboratory tests on quarry stones stability using irregular waves corresponds to Carstens et al. [29]. The experiments were carried out in 1966 at the Technical University of Norway, using a magnetic tape for sending the electric signal to the piston paddle, and testing wide and narrow spectra.

The difficulty to select an appropriate design wave for the stability models was also pointed out by Font [30] in 1968, together with empirical evidence on the influence of storm duration on rubble mound breakwater stability.

In 1974, Battjes [31] introduced Iribarren's number (ξ), also known as surf similarity parameter, in the study of smooth and impermeable slopes. This parameter was also found to be practical for characterizing the breaker type, run-up and run-down on both smooth and permeable slopes by Bruun and Günbak [32] in 1976.

In the 70s, there was an effort to compile the formulae available up to date and to provide some design recommendations. Bruun [33] summed up the most relevant stability formulae and presented some clues for rubble mounds design, such us increasing block size on breakwater's heads. This was also stated by Iribarren in 1965 [12]. In addition, the first English speaking design manual, the already-referred SPM, was published in 1973, and re-edited in 1975, 1977, and 1984. Also, a complete list of the available hydraulic stability models (mainly developed using regular waves) was provided in the final report of PIANC [34] in 1976.

2.2. 70s to 80s: Intensive Research on the Stability of Rubble Mound Breakwaters. Van der Meer's Formulae

At the end of the 70s and beginning of the 80s, catastrophic failures were experienced by a series of large rubble mound breakwaters, as it was reported by Oumeraci [35]. This shock to the profession had two effects. First, for the rehabilitation of some damaged rubble mounds the old berm breakwater concept was re-discovered. Second, there was an extensive increase on research activities toward improving the design and construction of rubble mound breakwaters. Because of the ever-growing dimensions of the structures and the need to move into more hostile environments, reliable design formulae were demanded by the coastal engineering community. Van Hijum [36] studied in 1976 the equilibrium profile of coarse material under wave attack, which was the basis for subsequent research on berm breakwaters. Bruun [37] analyzed in 1978 the common reasons for damage or breakdown of mound breakwaters, which were ratified from a practical point of view by the 25-years-experienced engineer Kjelstrup [38] in 1979. In addition, many experimental works on breakwater stability were carried out:

(1) Ahrens [39] and Ahrens and McCartney [40] conducted in 1975 several large-scale tests using regular waves and stated, among others, the influence of wave period on riprap stability.
(2) Thompson and Shuttler [41] presented a detailed study on riprap stability in 1975. They concluded that "*the erosion damage caused by irregular waves on a riprap slope is itself a random variable*" and that the method for positioning the stones highly affects damage evolution. Long-term and short-term experiments were tested with impermeable core, finding no relation with depth or wave period, but with mean number of zero crossing waves, among others. In addition, it was suggested that damage tends to reach equilibrium or, in other words, that damage curves are meant to be asymptotic.

(3) Bruun and Günbak [32] assured in 1976 that, regarding breakwater stability, "*the significance of wave period is clearly demonstrated.*" They started to work on a risk-based approach in the design of sloping structures considering Iribarren's number.

(4) Whillock and Price [42] presumably coined the concept of "fragility" in 1976 when indicating that elements with high void ratio and designed to interlock, such as dolosse, were associated with a reduction in the safety margin as failure is approached. They also supported the idea of quarry stones being more stable to oblique wave attack than to normal attack. However, this assumption was denied for armor units that are susceptible to drag forces. Indeed, they demonstrated that the overall stability for a particular test with dolosse decreased up to an angle of incidence of 60°. In line with the concept of "fragility", Magoon and Baird [43] underlined in 1977 the importance of rocking movements in the breakage of armor units designed to interlock.

(5) Losada and Giménez-Curto [44] proposed in 1979 a stability model for the initiation of damage by means of design curves depending on armor unit type and Iribarren's number. They used Iribarren's data to fit their model, and compared it satisfactorily with the results from Hudson [26] and Ahrens and McCartney [40]. However, they stated the difficulty to establish a comparison between experimental results undertaken in different laboratories because of divergences in both experimental process and damage criteria. For this reason, it was remarked that "*To obtain general criteria on the behaviour of rubble mound breakwaters under wave action, laboratories should establish uniform experimental procedures and criteria.*"

(6) Losada and Giménez-Curto [45] studied the influence of oblique incidence in 1982. They concluded that, for gravity armor units, the stability of steep slopes under oblique wave attack is not worse than for normal incidence. On the contrary, they found that for high interlocking armor units (such as dolosse or tetrapods) oblique wave attack is hazardously worse than normal incidence, in agreement with Whillock and Price [42].

(7) Broderick and Ahrens [9] presented in 1982 a technical paper on scale effects using the large-scale tests from Ahrens [39]. These tests, with wave heights up to 1.83 m and periods up to 11.3 s were compared with a 1:10 Froude scaled model. They found a 20% reduction in the zero-damage stability numbers from the large-scale tests whereas run-up increased about 20%. This was identified to be due to the improper modeling of the flow regime within the filter layer for the small-scale experiments and to the lack of penetration of the wave run-up into the filter layer. Scale effects were less severe at high levels of damage and the shapes of the damaged profiles for tests with the same relative depth were very similar. Furthermore, at the zero-damage level, wave period had less influence on the small scale. In their study, the widely used dimensionless erosion area (S) was firstly proposed.

(8) Jensen [46] published in 1984 a thorough monograph on rubble-mound breakwaters. He suggested the parameter $H_{13.6\%}$ instead of H_S as a descriptor for wave height in both deep waters (where wave height is usually characterized by a Rayleigh distribution) and shallow waters (where a certain percentage of waves break). Also, in order to reach a stable damage level, scaled storms representing at least 8 to 10 hours in prototype were recommended. Furthermore, possibly the first formula on rear slope stability was proposed.

(9) Hedar [47] developed in 1986 a complete stability model taking into account the water depth, wave height at breaking, rubble mound slope, the internal friction angle, a permeability function, and two empirical coefficients.

This intensive research on breakwater stability evidenced many shortcomings of the simple and widely used Hudson's formula. In this context, Van der Meer [48–51] referred as VdM in this manuscript, developed in 1985 a revolutionary stability model with a dissemination similar to Hudson's. It considered the influence of wave height (H), wave period (by means of Iribarren's number, ξ_0), number of waves (N_w), equivalent cube length (D_{n50}), relative excess specific weight

(Δ), breakwater slope ($cot\alpha$), and permeability of the core (P). Furthermore, the aforementioned dimensionless erosion area (S) was introduced in the formulae as follows:

$$\frac{H}{\Delta D_{n50}} = 6.2\xi_0^{-0.5} P^{0.18}\left(\frac{S}{\sqrt{N_w}}\right)^{0.2} \rightarrow \textit{for plunging waves} \quad (3)$$

$$\frac{H}{\Delta D_{n50}} = 1.0\xi_0^{P}\sqrt{\cot\alpha}\, P^{-0.13}\left(\frac{S}{\sqrt{N_w}}\right)^{0.2} \rightarrow \textit{for surging waves} \quad (4)$$

The formulation distinguished between plunging waves and surging waves, and even included the possibility of being applied in a probabilistic design. For this purpose, the coefficient 6.2 in Equation (3) can be assumed to be normally distributed with a standard deviation of 0.4. Similarly, the coefficient 1.0 in Equation (4) can be assumed to be normally distributed with a standard deviation of 0.08. In the formulation, minimum stability is reached when $\xi \approx 3$. This situation corresponds to collapsing waves: while plunging waves are meant to cause damage during run-up and surging waves during run-down, collapsing waves are supposed to erode armor layer both during run-up and run-down.

VdM performed 262 tests and also considered the 300 tests from Thompson and Shuttler [41] finding, contrary to them, a damage relation with wave period after reanalyzing their data. He tested impermeable, conventional, and homogeneous rubble mound models concluding that stability is straightly related to permeability. Despite using riprap and selected natural rocks, he found no influence of armor grading on stability. This is why just the parameter D_{n50} was considered in the formulation. Moreover, after trying two different Pierson-Moskowitz spectra (a wideband and a narrowband), no relation was found between damage and either spectral shape or wave groupness. Strong differences between monochromatic and irregular tests were pointed out, together with a damage dependence on the number of waves. Indeed, as it was reported by different authors, these formulae are only valid for 1000 to 7000 waves and it tends to overestimate the damage for more than 8000 waves. In 1998, VdM [51] related the Hudson's "no-damage" criteria and filter exposure (failure criteria) to different values of S depending on breakwater slope. Also, an adaptation of his single storm formulae to calculate the damage caused by more than one storm event was proposed.

VdM [52] also developed in 1988 a formulation for cubes, tetrapods and accropode, singling out the study for the most common slope for each armor type. A different damage descriptor was used in this case, firstly introduced by Hedar [53] in 1960: N_o, the number of units displaced out of the armor layer within a strip width of one equivalent cube length. This equivalent cube length was assumed to be equal to D_{n50} for cubes, 0.65 h for tetrapods and 0.7 h for accropode.

$$\frac{H_S}{\Delta D_{n50}} = \left(6.7\frac{N_o^{0.4}}{N_w^{0.3}} + 1\right)\left(\frac{H_S}{L_0}\right)^{-0.1} \textit{for cubes} \quad (5)$$

$$\frac{H_S}{\Delta D_{n50}} = \left(3.75\frac{N_o^{0.5}}{N_w^{0.25}} + 0.85\right)\left(\frac{H_S}{L_0}\right)^{-0.2} \textit{for tetrapods} \quad (6)$$

$$\textit{Failure, } N_0 > 0.5 \rightarrow \frac{H_S}{\Delta D_{n50}} = 4.1 \textit{ for accropode} \quad (7)$$

2.3. Studies Based on VdM's. Van Gent's Formula

The results from VdM were analyzed by many authors and further conclusions and improvements on armor stability were settled down. Among the extensive research based on VdM approaches, the following studies are highlighted:

(1) Using exactly the same rocks tested by VdM, Latham et al. [54] demonstrated in 1988 the dependency of damage regarding armor shape. An additional coefficient to consider the armor

shape effect was suggested: as rock units become more rounded they also become more unstable, especially under surging waves.

(2) Medina and McDougal [55] highlighted in 1990 some shortcomings of VdM formulae, such as the complexity of the equation or the overestimation of damage for more than 7000 waves. They were especially critical with the independence of VdM's model on wave groupness. In fact, a small but systematic higher stability for random waves from narrowband spectra was detected in VdM tests. A simpler stability model was alternatively proposed.

(3) Kaku et al. [56] found in 1991 that VdM's damage levels were not accurate enough for forecasting models. Therefore, they proposed a new empirical model assuming that the damage level approaches to an asymptotic equilibrium for the same wave energy. They also included the initiation of armor movement based on the similarity between the stability number and the Shields parameter used for sediment transport. However, in 1992, Smith et al. [57] indicated the difficulties of both empirical formulae in accounting for the complex wave and structural interactions affecting breakwater reshaping, mainly because they were built up under static stability conditions.

(4) Melby and Hughes [3] utilized in 2003 part of the small-scale laboratory data of VdM to fit a stability equation derived from basic principles for uplift, sliding, and rolling incipient motion. It was based on the assumption that the maximum wave momentum flux at the toe of the structure is proportional to the maximum wave forces on armor units.

(5) Vidal et al. [58,59] proposed in 2004 a modification of VdM's formulae after accomplishing a comparison between the results from Thompson and Shuttler [41], Losada and Giménez-Curto [44], and VdM [50]. This modification consists of using H_{50} instead of H_S. H_{50} is defined as the average wave height of the 50 highest waves reaching the rubble-mound breakwater. This new way of describing wave height parameter is further discussed in Section 2.4.

(6) Mertens [60] attempted in 2007 to transform the datasets of Thompson and Shuttler [41] and VdM [50] into comparable information with the one generated by Van Gent et al. [61] in 2003. He also reported some deviations in VdM data because of the influence of stone roundness. Following this line, Verhagen and Mertens [62] proposed in 2009 a methodology for unifying the formulation for both deep and shallow waters. To accomplish this, a correction factor based on the Iribarren's number was added in order to incorporate the effect of the foreshore. For the correct application of this method they claimed for an accurate calculation of the wave height and wave period at the toe of the breakwater, including a precise determination of $H_{2\%}$ and $T_{m-1,0}$.

Among these works, probably the most renowned corresponds to Van Gent et al. [61], who reanalyzed VdM's results and added some new experimental data in shallow water conditions. Initially, the parameter $H_{2\%}/H_S$ was added. However, after noticing that the influence of this parameter was small, as so was the influence of wave period regarding the data scatter due to other reasons, a single and simpler formula was proposed. In the new formula the permeability was incorporated in a direct way by the nominal diameter of the core material:

$$\frac{H}{\Delta D_{n50}} = 1.75\left(\frac{S}{\sqrt{N}}\right)^{0.2}\sqrt{\cot\alpha}\left(1+\frac{D_{n50,core}}{D_{n50}}\right) \quad (8)$$

2.4. Wave Groupness and Wave Height Parameter Discussion. H_{50} Parameter by Vidal et al.

The correlation between wave groups and armor layer damage was a controversial topic for the researching community especially during the 80s. Some authors suggested that wave groups with short wave runs were more damaging, others stated that long wave runs were more damaging and others, such as VdM, did not find any major damage dependence on wave grouping. Medina et al. [63,64] recommended in 1990 avoiding the use of traditional wave grouping parameters, such as spectral peakedness or mean run length, after not finding significant correlation between them and armor

damage. Alternatively, using linear theory (and therefore excluding breaking design conditions), they proposed an envelope exceedance coefficient accounting for the variability of the energy flux, related to a newly defined groupness factor. Both coefficients were proved to be capable of explaining mean damage variability higher than 50% for a given design sea state and storm duration.

The new parameters for taking into account wave groupness in breakwater damage were found to be related to the maximum wave heights of the design sea state by Medina et al. [63,64]. This was the trigger for restarting a debate on finding an adequate wave height descriptor, i.e., a representative parameter of the spectrum/sea state regarding breakwater's damage. Wave height is raised to the third power in most stability models and, thus, damage is extremely sensitive to the way it is defined. As it was mentioned before, Hudson [26] pointed out the uncertainty of selecting a "design wave" from a natural wave train. Also, the SPM did not offer a clear justification for replacing the design wave from Hudson, obtained using regular waves, by the equivalent $H_{1/3}$ (in the third edition [27]) and $H_{1/10}$ (in the fourth edition [28]) for irregular waves. Indeed, for some authors $H_{1/10}$ is extremely conservative, and for others, such as Jensen et al. [65], $H_{1/20}$ is reported to be a more suitable parameter. Despite H_S is, even nowadays, the most extended parameter for the characterization of irregular waves, it does not give enough information about the highest waves of the series which, in fact, are the most likely to be responsible for armor damage development. Other studies discussing the adequacy of alternative wave height descriptors are highlighted below:

(1) Teisson [66] presented in 1990 a statistical approach for characterizing the duration of extreme storms and its consequences on breakwater damage. In the study it was stated that "*to select H_S as design wave height in Hudson formulae assumes that the associated storm will last for only 10 minutes: this choice could lead to an under estimation of breakwater design.*" Alternatively, the expression $H_D = 1.18\ H_S\ t^{0.095}$ was proposed for the calculation of the design wave height. Teisson tried to relate regular and irregular wave effects on stability. Furthermore, by an integrated theoretical approach, he developed a step-by-step methodology for calculating cumulated damage during storms, assuming that a storm can be described by a sequence of significant wave heights steps with a certain duration each.

(2) Vidal et al. [67] suggested in 1995 that the wave height parameter should contain information about the distribution of the highest waves, the length of the time series and the number of times it is recycled to achieve a given degree of damage. The longer the test is, the higher waves are likely to attack the structure, i.e., damage evolution after testing two time series with a certain H_S and a duration t will be different compared to testing a unique time series with the same H_S and duration of $2t$. Based on numerical simulation, they reported variations in the damage parameter exceeding 50% when considering H_S after testing JONSWAP spectra with the same H_S and T_p but different random seeds. They also confirmed that the highest waves were related to wave groupness. An H_n parameter, directly related to test duration and suitable also for breaking conditions (i.e., where wave height distribution during storms can depart from Rayleigh's due to non-linearity), was proposed for a better characterization of wave-damaging energy. This new parameter was expected to facilitate the comparison of stability results obtained in different investigations, including those carried out with regular waves. Initially, H_n=H_{100} was proposed, but in Vidal et al. [58,59] this parameter was adjusted to H_{50} after comparing the datasets from Thompson and Shuttler [41], Losada and Giménez-Curto [44] and VdM [50]. In addition, a new formula was developed based on VdM equations. The lack of consistency of the Rayleigh distribution for breaking conditions was also accounted for by other authors, such as Battjes and Groenendijk [68], which suggested a Weibull distribution for damage models in shallow foreshores after a spectral analysis, or Méndez and Castanedo [69], which provided a model for the depth-limited distribution of the highest waves in a sea state.

(3) Jensen et al. [65] tested both regular and irregular waves for identifying a wave height parameter within the irregular waves corresponding to the wave height of a regular series with a similar

damage level on the structure. In line with Vidal et al. [67], they ended up in 1996 with an H_n parameter, but in this case a n-value of approximately 250 was found to be more suitable.

(4) Medina [70] claimed in 1996 for non-stationary stochastic models as more adequate for modeling real waves. He defined five conditions for any rational armor damage model to properly take into account the storm duration, such as damage must necessarily increase with the duration of the storm under random wave attack in deep water conditions. A wave-to-wave exponential model accomplishing these conditions was proposed. The model depends on the number of waves and introduces an asymptotic maximum damage to the armor layer under a constant regular wave attack. It also depends on a mean damage parameter consisting of the number of regular waves causing 63% of the maximum asymptotic damage, which is linked to the concept of mean lifetime of the structure. Medina compared the results with the models from Teisson and Vidal (based on different assumptions but accomplishing most of the five aforementioned conditions) and applied the new method to a real case: the partial failure of Zierbana breakwater (Port of Bilbao, Spain) under construction in February 1996. In Gómez-Martín and Medina [71], the wave-to-wave exponential model was slightly modified and the mean damage parameter was found to be dependent on Iribarren's number. They also designed a neural network (NN) applicable to random waves in non-stationary conditions, finding that the estimation of accumulated armor damage using both wave-to-wave exponential method and NN model showed a good agreement to damage observations.

2.5. The 90s: Probabilistic Approaches and Damage Progression Models. Melby and Kobayashi's Model

After the intensive research on stability of rubble mound breakwaters during the 70s and 80s, there was a new attempt in the 90s to compile and check the most relevant models on armor stability:

(1) In 1991, Pfeiffer [72] compared Hudson [25], Hedar [47], Losada and Giménez-Curto [44], and VdM [50] formulae with prototype data from Burns Harbor breakwater (Indiana).

(2) In 1992, the final report from PIANC [73] provided a review on random wave's armor stability models. In the same year, Koev [74] studied statistically a homogeneous set of 21 armor layer stability formulae developed under regular waves, and proposed a regression model valid for $0.04 \leq H/L \leq 0.1$ and $1.1 \leq cot\alpha \leq 20$.

(3) In 1994, Vidal et al. [75] revised the available methodologies for the calculation of the armoring hydraulic stability, both for breakwater heads and trunks. Formulations and design recommendations for berm breakwaters, low-crested breakwaters and conventional breakwaters were also included.

At the same time, some clues about physical modeling and laboratory techniques in coastal engineering were established based on the experience gathered by the scientific community over 60 years:

(1) Hughes [76] presented in 1993 a publication of reference in physical modeling. It discussed the principles of dimensional analysis, scale effects, and similitude criteria including specific similitude requirements for different coastal structures. Also, considerations about movable-bed models, generation of gravity waves in laboratory, and a discussion on laboratory measurements and data analysis were included. Scale effects were further addressed in 2004 by Tirindelli et al. [77], who focused on wave impacts, run-up, overtopping, structure deformation, porous flow, and flow forces on plants and organisms.

(2) Davies et al. [78] summarized in 1994 the different methods for damage measurement, describing the different techniques available for this purpose. Using experimental data, a comparison between damage measured with a profiler and damage defined by stone counting was carried out, with good agreement for low levels of damage. In addition, the sliding failure of the armor layer was investigated.

(3) Burcharth et al. [79] suggested in 1999 a methodology for scaling core material in small scale rubble mound breakwater models. As it was first identified by Broderick and Ahrens [9], this kind of experiments can be subjected to significant scale effects when the flow type through the model core is different than in prototype: in a Froude small-scale model the flow through the core is usually laminar whereas in a full-scale core the flow is mainly turbulent. Indeed, Hegde and Srinivas [80] demonstrated experimentally that as core porosity is increased the stability is also increased. De Jong [81] ratified the obtention of lower values of damage after scaling the core according to Burcharth's methodology. Additional information on core permeability and damage, together with prototype data, can be found in Reedijk et al. [82].

Similarly to the effects after the effort made in the 70s to compile the available formulae and to provide some design recommendations, the new attempt to get together armor stability models and laboratory techniques coincides with a prolific decade, in which two main conceptual and methodological progresses were made: the consolidation of the probabilistic approach and the origin of the first damage progression models.

At first, the introduction of the probabilistic approach faced a controversial acceptance in a profession where experience and expert criteria were fundamental regarding breakwater design. Some of the reasons of this initial skepticism in favor of deterministic methodologies based on safety factors were (1) the negative connotation of the term "probability of failure" (which can be referred euphemistically by the opposite concept "reliability"), (2) the lack of confidence due to uncertainty in the calculation of the strict failure bound (see Figure 1), and (3) the limited availability of probabilistic information from the different factors affecting the structural response, as well as from the structural response itself.

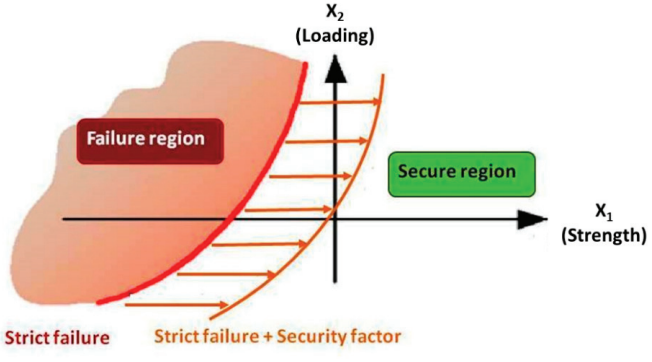

Figure 1. Failure and secure region for a generic bi-dimensional case.

In spite of the difficulties, the probabilistic approach, widely extended nowadays, was materialized in the design codes. As an example, reliability methodologies were included in the European PROVERBS [83], the Spanish ROM 0.0-01 [84], or the North-American Coastal Engineering Manual [1]. Further investigations on the probabilistic character of armor stability in the 90s are given below:

(1) Wang and Peene [85] possibly headed in 1990 the first attempt on the development of a fully probabilistic model of rubble mound armor stability, based on the stochastic nature of both wave forces and resistance forces. After pointing out that "*the random nature of the resistant force offered by the armor blocks has not been seriously addressed at all*," they examined the behavior of interlocking resistance and the random nature of breakwater stability through laboratory experiments. A theoretical probabilistic model containing six random variables was proposed, which behaviors were not all known at that time, not even hitherto. Instead of computing wave loading in a conventional way, they calculated the resistance of the armor layer by pulling out

the units with a motorized lift line (static stability test), recording the force history with a load cell. They applied a modified version of the Kolmogorov-Smirnov D-test on five data sets (with about 120 samples each) with tetrapods and dolosse, after testing different bed slopes, pull-out directions and locations, placement methods and unit sized. They concluded that the resistance of tetrapods and dolosse could be treated as a random variable with a log-normal distribution. Furthermore, comparing these results with the ones carried out with stones, they cast a doubt on the stabilizing effects of interlocking properties of artificial units.

(2) Carver and Wright [86] pointed out in 1991 the random variations in the stability response of stone-armored rubble mound breakwaters after carrying out stability tests with depth limited irregular waves. They concluded that "*repeat testing is a must*," indeed repeating each spectrum six or seven times. Also, they registered how the lower stabilities occurred at the lowest values of h/L in shallow water, i.e., regarding the longer wave periods.

(3) Medina [70], as detailed in Section 2.4, recommended in 1996 non-stationary stochastic models for being more adequate for modeling real waves.

(4) Burcharth [87] published in 1997 the Chapter *Reliability-Based Design of Coastal Structures* as part of a book which summed up the advances in coastal and ocean engineering. Different sources of uncertainty were identified, together with a probabilistic methodology for single failure mode probability analysis, including formulations and examples with Level III methods, Level II methods and FORM (first-order reliability method). Additionally, further examples of probabilistic methodologies applied to breakwater design can be found in Castillo et al. [88,89], Mínguez et al. [90], Tørum et al. [91], or Gouldby et al. [92]. Burcharth [87] also set a discussion on the probability analysis of failure mode systems, typically faced using fault trees. Some practical examples on this topic can be found in van Gent and Pozueta [93], who studied the rear-side stability of rubble mound structures after being overtopped, or Campos et al. [94], who addressed the effects of a fuse parapet failure in other failure modes of a caisson breakwater using Monte Carlo simulations.

(5) Similar to Wang and Peene [85], Hald [8] and Hald and Burcharth [95] also chose an alternative approach away from correlating wave parameters directly to armor layer stability. For this purpose, they studied the wave-induced loading by means of a force transducer connected to an 8mm steel rod attached to a single stone of average size made in coated plastic foam. The rest of the armor layer was made of conventional natural stones. Largest forces were found to take place in a normal direction and upslope, and a dimensionless force model of the normal and the peak force was proposed as a function of wave parameters. A log-normal distribution was found to be suitable for describing the limit pullout forces. From the force model, they derived a stability model in 1998 based on a lifting criterion, obtaining comparable scatter with respect to the equations from Hudson [25] and VdM [50].

The evolution toward probabilistic approaches in the 90s revealed deeper comprehension on the wave-structure interaction and, consequently, it happened together with an improvement in the conception of hydraulic stability models. Traditional hydraulic stability formulae were aimed to characterize the initiation of movement, which was useful for estimating the design weight of armor units but failed to give information about the evolutionary behavior of rubble mounds. Some of these models, such as the formulae from Iribarren [12] or Hudson [25], were complemented with tabulated or graphic information relating damage percentage with coefficients such as the aforementioned $H/H_{D=0}$. These approaches are helpful for design purposes, but they are not time dependent and they assume starting from a non-damaged structure. In a context where, not only the design was meant to be addressed, but also the evolution of the structure regarding maintenance strategies and useful-life total costs, hydraulic "static" stability concept moved on toward damage progression models. The latter are aimed to predict the evolution of rubble mound's geometry by means of a quantitative damage parameter, usually the dimensionless erosion area (S).

Probably the first damage progression model was due to VdM [50] in 1988. As it was detailed in Section 2.2, these widely known formulae include the possibility of being applicable to a probabilistic design, although the way of adapting the equation for this purpose presents some shortcomings from a probabilistic point of view. For example, the scatter is all focused on one parameter, instead of designing a fully probabilistic formulation with an analytic CDF (cumulative distribution function). As it was stated by some authors, VdM's formulae are not valid for the long-term, as they tend to overestimate damage for more than 7000 waves. Also, despite providing reasonable estimates of the stability number for two specified damage levels (damage initiation and exposure of the filter layer), they failed to yield predicted damage levels with accuracy.

Further damage progression models proposed in the 90s were already mentioned and are summarized in Table 2. The formulation of Teisson [66] was developed using a step-by-step methodology assuming that a storm can be described by a sequence of steps with a certain duration each. Kaku et al. [56] proposed an exponential model with similarities between the stability number and the Shields parameter used in sediment transport. Medina [70] and Gómez-Martin and Medina [71] also suggested exponential models based on a wave-to-wave approach. However, probably one of the main contributions to damage progression formulations was due to Melby and Kobayashi, referred as M&K in this paper. Their first model was published in 1998 [96,97] and re-formulated in 1999 [98] for allowing non-zero initial damage values:

$$\left[\overline{S}(t)\right]^{1/b} = \left[\overline{S}(t_n)\right]^{1/b} + \left(a_s N_s^5\right)^{1/b} \frac{t - t_n}{T_m};\ t_n \le t \le t_{n+1} \tag{9}$$

where $\overline{S}(t_n)$ is the known damage at the time t_n, N_S is the stability number based on the highest one-third wave heights from a zero-upcrossing analysis, T_m is the mean period, b is an empirical coefficient introduced for long-duration tests, and a_s is related to breakwater slope, permeability and an empirical coefficient derived from the tests. Therefore, it is an iterative damage progression model that allows the calculation of the damage at the instant t_{n+1} based on the damage level at the instant t_n and the incident wave conditions between t_n and t_{n+1} represented by a constant value of H_S and T_m.

The experiments of M&K, with a limited validity range, were conducted at the WES. A complete description of them, together with an analysis of incipient stability of armor units, damage measurement and damage definition, is detailed in the technical report of Melby [99]. Mean and standard deviation of different damage descriptors were used to characterize the trends, variability and ranges of the damaged profile descriptors. The damage variability σ_S tends to increase with the mean damage value $\overline{S}$. However, the relative variability defined as $\sigma/\overline{S}$ decreases when increasing $\overline{S}$, i.e., the higher the damage is, the lower is the relative error of the estimation.

Contrary to other authors who maintained that damage evolution reaches an equilibrium, M&K observed that damage keeps on increasing with a lower rate. Indeed, Equation (9) does not have an asymptotical trend and, thus, a large number of small waves between two storms would theoretically provoke a damage increase. For that reason, they recommend setting up a critical stability number so that the damage would not increase beyond this lower limit. This concept is similar to the equilibrium damage level introduced by Kaku et al. [56]

The damage progression model from M&K is especially helpful in a lifecycle analysis because it allows engineers to balance initial costs with expected maintenance costs. Thus, it is also useful for rehabilitation or maintenance plans in already-built breakwaters. However, it presents a number of shortcomings, mainly pointed out by the authors themselves [100]. The results were reported to be conservative for most applications because they were based on severely breaking waves, a relatively steep beach slope and relatively impermeable core. However, damage initiation is unpredicted in all series studied and fails to yield accurate predictions for low damage levels. Furthermore, the model is aimed just at the mean damage evolution and, consequently, it does not provide information about the probability density function (PDF) of each estimated value of damage, which is needed for a more precise probabilistic analysis of damage progression.

2.6. Researches on Breakwater's Damage in the XXI Century. Castillo et al.'s Model

The XXI century started with the publication of some aforementioned design codes with a high impact all over the world: the European PROVERBS in 1999 [83], the Spanish ROM 0.0-01 in 2001 [84] and the North-American CEM in 2002 [1]. Initiatives such as the European project on berm breakwater structures (MAS2-CT94-0087 [101]) also contributed to enhance the knowledge on the breakwaters response. There were also compiling efforts of the state-of-the-art such as the one focused on berm breakwaters from the Working Group 40 of PIANC [102]. In addition, the International Standard Organization published in 2007 [103] a new standard, ISO 21650 "*Actions from Waves and Currents on Coastal Structures*," which became the first one in coastal engineering.

During this recent period, some of the existing models were reassessed. The already referred studies from Van Gent et al. [61], Gómez-Martín and Medina [71], Vidal et al. [58,59], Mertens [60] or Verhagen and Mertens [62] are some examples of this trend. Besides, some concepts were re-analyzed. For example, Wolters and Van Gent [104] and Van Gent [105] addressed the effect of oblique wave attack on cube and rock armored rubble mound breakwaters in 2010 and 2014 respectively. They obtained results in agreement with the ones from Losada and Giménez-Curto [45] for gravity armor units, i.e., the stability of steep slopes under oblique wave attack is not worse than for normal incidence.

Additionally, new approaches were proposed. In 2003, Tomasicchio et al. [106] developed a conceptual model for evaluating armor stone abrasion and compared their results with the ones from Latham [107]. Eslami and Van Gent [108] presented in 2010 one of the few studies relating wave overtopping and rubble mound stability with combined loading of waves and current. Esteban et al. [109] assessed in 2012 the stability of rubble mound breakwaters against tsunami attacks, with experimental and real data. Medina et al. [110] studied in 2010 the influence of armor units' placement on armor porosity and hydraulic stability, analyzing different placement grids of cubes and Cubipod® by means of pressure clamps. Similar experiments were discussed by Pardo et al. [111] in 2013 after accounting for the three armor randomness indexes (ARIs) introduced by Medina et al. [112]. These experiments were measured with a laser scanner in order to quantify the randomness in the placement of cube and Cubipod®. Further information on the influence of initial placement can be found in Yagci and Kapdasli [113,114], Gürer et al. [115], Van Buchem [116], or Medina et al. [117]. Recently, Marzeddu et al. [118] analyzed different approaches for taking into account wave storm representation on damage measurements. Also, Clavero et al. [119] proposed a methodology to improve breakwater design and to assimilate the data from different wave flumes after analyzing the bulk wave dissipation in the armor layer of rock and cube armored small-scale models.

It is also remarkable the advances in numerical models reproducing the physics of the main processes involved (see Farhadzadeh et al. [120] or García et al. [121] for some examples of the latest contributions). Although addressing the structural stability at the scale of individual units is still computationally overdemanding, studies such us Matsumoto et al. [122] have already been able to model relatively complex scenarios by computational fluid dynamics. Soft computing techniques, such as artificial neural networks (ANN) [123–126], genetic programming [127], or extreme learning machine (ELM) models [128], were also applied for predicting damage levels. They also offer the possibility of optimizing temporal and economical costs of small-scale physical modeling [129]. Probably the most ambitious project of this kind is the one from the International Breakwater Directory, aimed to expand the CLASH (acronym for "Crest Level Assessment of coastal Structures by full scale monitoring, neural network prediction and Hazard analysis on permissible wave overtopping") overtopping database for including information about armor damage in rubble mound breakwaters and seawalls [7].

However, the lack of a stochastic damage progression model fully designed from a probabilistic approach, together with some damage accumulation modeling difficulties reported by M&K when re-formulating their model [98], motivated Castillo et al. to investigate on the basis for building consistent stochastic models. Instead of developing an empirical or semi-empirical formulation based on a set of experimental data, Castillo et al. proposed in 2012 [130] a dimensionless stochastic damage

progression model with general validity, avoiding the selection of easy-to-use mathematical functions, which were replaced by those resulting from a set of properties to be satisfied. The model was proven to have a normal distribution. It was built after applying dimensional analysis (using Π Buckingham's theorem), compatibility conditions and the central limit theorem. It is expressed in terms of the following cumulative distribution function (CDF):

$$F_{D^*(t^*)}(x) = \Phi\left(\frac{(x-\gamma)^{1/b} - \mu_0 - kt^*}{\sqrt{\sigma_0^2 + rt^*}}\right) \tag{10}$$

where γ and b are breakwater dependent, k and r include wave action and μ_0 and σ_0 depend on the initial conditions. Note that damage is not normal according to the model, but transformed damage, i.e., *(D*-γ)1/b*, is instead.

An initial calibration of the model was carried out in Campos et al. [131,132]. The experimental results, with limited validity, pointed out the lack of repeatability of damage progression, as it was stated by other authors such us Benedicto et al. [133] or Van Gent et al. [134]. This not only confirms the random nature of damage, but also points out the need of reproducibility of the relatively common damage accumulation experiments. Reproducibility is necessarily linked to standardization. In this sense, a lack of standards in damage initiation and progression experiments is perceived by the authors in line with the conclusions from other authors such us Losada and Giménez-Curto [44] or Ota et al. [135].

As a conclusion from this section, it is expectable that main challenges in the near future for rubble mound designers and managers will be related to develop or calibrate decision-making tools capable of accurately characterizing the structural response, together with its uncertainties, during the whole useful life. Not only the knowledge gathered over the years would play a role, but also the huge possibilities opened by the increase in computing capacity and the affordability and accuracy of monitoring tools such as global navigation satellite systems [136] or photogrammetric restitutions using drones. Risk-based design and management, including the possible effects of climate change and the upgrading of already built structures [137–139], would definitely require a deeper comprehension about the spatial and temporal evolution of the stochastic nature of damage.

3. Conclusions

In this paper, a historical overview of damage initiation and progression in rubble mound breakwaters is presented, highlighting the most relevant approaches and main hydraulic stability formula and damage progression models up to date. The amount of literature on this topic is quite extensive, which has to do with the importance of hydraulic stability in the design and maintenance of this kind of coastal structures as well as with the great challenge that implies the characterization of damage initiation and damage progression rates. This challenge is related to the following summing-up points:

(1) Hydraulic instability of armor layers is a complex process because of the stochastic nature of both wave loading, initiation of movement, and damage progression. The highly non-linear flow over the slope, involving wave breaking, together with the variable shape of armor units and their random placement deals necessarily with a probabilistic concept of damage initiation and progression, as it was pointed out by many authors.

(2) The concept of "damage" in a rubble mound breakwater, understood as the partial or total loss of its functionality, is subjected to different interpretations. Not every structure is designed under the same functional requirements and there is a wide variety of typologies. In addition, not every structure presents the same fragility. For instance, what is considered as damage in single-layered structures might not be equivalent in multi-layered structures. Also, each type of armor unit presents a singular behavior against wave action. These facts complicate the

correlation between quantitative damage descriptors and qualitative damage levels such as the ones defined in Vidal et al. [140].

(3) The parameterization and measurement of damage has been just slightly addressed in this paper due to the extensive information available. Indeed, Part II of this review [6] is aimed entirely on this topic. The dimensionless erosion area (S) from Broderick and Ahrens [9] is the most widely damage index nowadays. However, it seems that there is not a worldwide standard on how to measure it, which is crucial for reproducibility and for a consistent comparison between the results from different laboratories. Not only that, regarding the random nature of damage and the frequent accomplishment of damage initiation/progression tests in coastal laboratories, this kind of experiments needs to be reproducible. Thus, a concise methodology ideally agreed by the scientific community and shared worldwide may be helpful.

(4) As exposed in Section 2.4, an adequate selection of wave action parameters is crucial for correlating damage just with the waves of the irregular train directly responsible of the hydraulic instability of the armor layer.

(5) Damage has a spatial component that cannot be completely addressed with the solely characterization of the well-known dimensionless erosion area (S). Most studies aimed to develop empirical or semi-empirical damage formulations are conducted on wave flumes, using physical profilers or visual counting for characterizing damage. However, the recent advances and affordability of scanning and photogrammetric techniques [141] allow nowadays a more complete analysis of the geometrical evolution of the armoring both in wave tank's models and in full-scale prototypes. Also, the increase in the resolution of global navigation satellite systems and other technological advances such as drones, can help to foster damage monitoring in real structures.

(6) Indeed, taking into account that the structural response is a random variable, its characterization is necessarily linked, not only to repeating experiments in laboratory, but also to monitoring prototypes. Only in this way the models can be properly calibrated.

As it was mentioned before, the future of rubble mound design is linked to risk-based approaches and advanced management strategies, which would require a deep comprehension about the spatial and temporal evolution of damage during the whole useful life. Damage progression probabilistic models, such as the one from Castillo et al. [130], offer the framework to make possible this evolution and, at the same time, highlight the need of enhancing the knowledge of the singular behavior of each structure. To accomplish this, full-scale monitoring and standardization will presumably play a key role in the near future.

Table 1. Review of hydraulic stability formulae (extended from Hald [8]). See Appendix B for the list of symbols.

RESEARCHER	FORMULA	RESEARCHER	FORMULA
de Castro (1933) [4]	$\frac{H}{\Delta D_{n50}} = \left\{\frac{\rho_w}{K}(\cot\alpha+1)^2\sqrt{\cot\alpha-\frac{2}{S_r}}\right\}^{1/3}$	Rybtchevsky (1964) [23]	$\frac{H}{\Delta D_{n50}} = \left(K\frac{H}{L}\right)^{1/3}\cos\alpha\sin\alpha$
Iribarren (1938) [5]	$\frac{H}{\Delta D_{n50}} = (\cos\alpha-\sin\alpha)\left(\frac{\rho_w}{K}\right)^{1/3}$	Iribarren(1965) [11]	$\frac{H}{\Delta D_{n50}} = (\tan\phi\cos\alpha-\sin\alpha)\left(\frac{1}{K}\right)^{1/3}$
Mathews(1948)	$\frac{H}{\Delta D_{n50}} = \left\{K\frac{H}{T}(\cos\alpha-0.75\sin\alpha)^2\right\}^{1/3}$	Metelicyna (1967) [24]	$\frac{H}{\Delta D_{n50}} = K^{1/3}\cos(23o+\alpha)$
Epstein, Tyrrel (1949) [16]	$\frac{H}{\Delta D_{n50}} = K^{1/3}(\tan\phi-\tan\alpha)$	SPM (1973) [27]	$\frac{H_S}{\Delta D_{n50}} = (K_D\cot\alpha)^{1/3}$
Hickson, Rodolf (1951) [17]	$\frac{H}{\Delta D_{n50}} = \left(K\frac{H}{T}\right)^{1/3}\tan\left(45-\frac{\alpha}{2}\right)$	Losada, Gim.-Curto(1979) [44]	$\frac{H}{\Delta D_{n50}} = \gamma_w'^{1/3}\{K_1(\xi-\xi_0)\exp(K_2(\xi-\xi_0))\}^{-1/3}$
Larras (1952) [13]	$\frac{H}{\Delta D_{n50}} = K^{1/3}(\cos\alpha-\sin\alpha)\frac{\sinh(4\pi h/L)}{(2\pi H/L)}$	SPM (1984) [28]	$\frac{H_{1/10}}{\Delta D_{n50}} = (K_D\cot\alpha)^{1/3}$
Hudson, Jackson (1953) [18]	$\frac{H}{\Delta D_{n50}} = K^{1/3}\frac{(\tan\phi\cos\alpha-\sin\alpha)}{\tan\phi}$	Hedar (1986) [47]	$\frac{H_b}{\Delta D_{n50}} = \left(\frac{6}{\pi}\right)^{1/3}\frac{K_2 f_1(\gamma)\cos\alpha}{K_1\left(\frac{h_b}{H_b}+0.7\right)(\tan\phi+2)}$ $f_1(\gamma) = permeability\ function$
Beaudevin (1955) [14]	$\frac{H}{\Delta D_{n50}} = \left\{K\left(\frac{\cot\alpha-0.8}{1.12-0.15\cot\alpha}\right)\right\}^{1/3}$	Medina and McDougal (1990) [55]	$\frac{H_S}{\Delta D_{n50}} = \frac{1.86}{1.27}\sqrt{\frac{2}{\ln N_w}}(K_D\cot\alpha)^{1/3}$
Hudson(1958) [22]	$\frac{H}{\Delta D_{n50}} = (K_D\cot\alpha)^{1/3}$	Wang and Peene (1990) [85]	$\frac{\widetilde{w}}{W_D} = \frac{(f_c)_n^3[C_S/C_V]_n^3 H_n^3}{R_n^3 D_{n50}^3[f(\theta)]_n}$ *see Wang and Peene*(1990) *for the list of symbols*
Goldschtein, Kononenko (1959) [21]	$\frac{H}{\Delta D_{n50}} = \left(K\tan^{1.83}\alpha\right)^{1/3}$	Koev (1992) [74]	$\frac{H}{\Delta D_{n50}} = \left(\left(\frac{\cot(\alpha)^{K_2}}{K_1}\right)\left(\frac{H}{L}\right)^{K_3}\right)^{1/3}$
SN-92-60(1960) [22]	$\frac{H}{\Delta D_{n50}} = \left(K\frac{H}{L}\sqrt{1+\cot^3\alpha}\right)^{1/3}$	Hald and Burcharth (2000) [95]	$\frac{H_S}{\Delta D_{n50}} = \left(\frac{1}{K_1}\frac{1+\sin^2\alpha}{\tan^{K_2}\alpha}\right)^{\frac{1}{K_3}}$
Svee(1962) [20]	$\frac{H}{\Delta D_{n50}} = K^{1/3}\cos\alpha$	-	

Table 2. Review of damage progression's models. See Appendix B for the list of symbols.

RESEARCHER	FORMULA
Van der Meer (1988) [51]	$\frac{H_S}{\Delta D_{n50}} = \begin{cases} 6.2\xi_0^{-0.5} P^{0.18}\left(\frac{S}{\sqrt{N_w}}\right)^{0.2} \rightarrow \textit{for plunging waves} \\ \xi_0^P \sqrt{\cot\alpha}\, P^{-0.13}\left(\frac{S}{\sqrt{N_w}}\right)^{0.2} \rightarrow \textit{for surging waves} \end{cases}$
Teisson (1990) [66]	$N_d(t) = A\left(\sum H_{S,i}^{B/C} \Delta t_i\right)^C$
Kaku et al. (1991) [56]	$S = S_e\left(1 - e^{-K \cdot N_w}\right)$
Medina (1996) [70]	$D(H,T,N_w) = D_0(H,T)\left[1 - e^{\frac{-N_w}{n63\%}}\right]$
Melby and Kobayashi (1998) [96]	$\overline{S}(t) = \overline{S}(t_n) + a_s N_s^5 \left(\frac{t^b - t_n^b}{T_m^b}\right);\ t_n \le t \le t_{n+1}$
Melby and Kobayashi (1999) [98]	$\left[\overline{S}(t)\right]^{1/b} = \left[\overline{S}(t_n)\right]^{1/b} + \left(a_s N_s^5\right)^{1/b} \frac{t - t_n}{T_m};\ t_n \le t \le t_{n+1}$
Melby and Hughes (2003) [3]	$N_m = \begin{cases} 0.5\left(\frac{S}{\sqrt{N_w}}\right)^{0.2} P^{0.18} (\cot\alpha)^{0.5} \rightarrow \textit{for plunging waves} \\ 0.5\left(\frac{S}{\sqrt{N_w}}\right)^{0.2} P^{0.18} (\cot\alpha)^{0.5-P} s_m^{-P/3} \rightarrow \textit{for surging waves} \end{cases}$
Van Gent et al. (2003) [61]	$\frac{H_S}{\Delta D_{n50}} = 1.75\left(\frac{S}{\sqrt{N_w}}\right)^{0.2} \sqrt{\cot\alpha}\left(1 + \frac{D_{n50,core}}{D_{n50}}\right)$
Gómez-Martín and Medina (2004) [71]	$D(H,Ir,N_w) = D_0(H,Ir)\left[1 - 2^{\frac{-N_w}{n50\%}}\right]$
Vidal et al. (2006) [59]	$\frac{H_{50}}{\Delta D_{n50}} = \begin{cases} 4.44 P^{0.18} S^{0.2} \xi_0^{-0.5} \rightarrow \textit{for } \xi_0 < \xi_{mc} \textit{ and } \cot\alpha \le 4 \\ 0.716 \sqrt{\cot\alpha} P^{-0.13} S^{0.2} \xi_0^P \rightarrow \textit{for } \xi_0 \ge \xi_{mc} \textit{ or } \cot\alpha \ge 4 \end{cases}$ $\xi_{mc} = \left(6.2 P^{0.31} \sqrt{\tan\alpha}\right)^{\frac{1}{P+0.5}}$
Castillo et al. (2012) [130]	$F_{D^*(t^*)}(D) = \Phi\left(\frac{(D-\gamma')^{1/b} - \mu_0 - kt^*}{\sqrt{\sigma_0^2 + rt^*}}\right)$

Table 3. Timeline of some of the most relevant models on armor layer's stability, together with the parameters/properties accounted for and the innovations introduced by each of them. See Appendix B for the list of symbols.

RESEARCHER	Wave Action					Breakwater				Others		
	R	*I*	*T*	*Ir*	N_w	*h*	*a*	*AT*	*P*	D_0	*DPM*	*CDF*
Iribarren (1938) [5]												
Mathews (1948)												
Larras (1952) [13]												
Hudson (1958) [22]												
SPM (1973) [27]		$H_{1/3}$										
Losada & G.C. (1979) [44]												
SPM (1984) [28]		$H_{1/10}$										
Hedar (1986) [47]		H_b										
VdM (1988) [51]		$H_{1/3}$										
Teisson (1990) [66]		$H_{1/3}$										
Kaku et al. (1991) [56]		$H_{1/3}$										
Medina (1996) [70]		H_i										
M & K (1998, 1999) [96,98]		$H_{1/3}$										
G.M.& Medina (2004) [71]		H_i										
Van Gent et al. (2003) [61]		$H_{1/3}$										
Vidal et al. (2006) [59]		H_{50}										
Castillo et al. (2012) [130]		H										

Directly considered | Innovation | Indirectly considered (for example by means of modifying the magnitude of a constant based on experimental results)

Author Contributions: Conceptualization: C.C., R.M.-S.; Investigation: A.C.; Resources: C.C., R.M.-S.; Writing—original draft preparation: Á.C.; Writing—review and editing: Á.C., C.C., R.M.-S.; Visualization: Á.C., C.C., R.M.-S.; Supervision: C.C., R.M.-S.; Project administration: C.C., R.M.-S.; Funding acquisition: C.C., R.M.-S. All authors have read and agreed to the published version of the manuscript.

Funding: This research was funded by the Spanish Ministry of Science and Innovation under the project BIA2009-10483 and the grant BES-2010-034048.

Conflicts of Interest: The authors declare no conflict of interest.

Appendix A. Special Shaped Armor Units

Most of the hydraulic stability formulae and damage progression models described hitherto are particularized for quarry stones or parallelepiped concrete units, which are the most extended all over the world. Special shaped armor units appeared during the economic growth after World War II. Breakwaters started to be built at greater depths and many laboratories attempted to develop new types of artificial armor units, with a high stability coefficient to reduce weight and, consequently, the total cost of the structure. The tetrapod was the first interlocking armor unit and probably the most widely used. It was designed in 1950 by the Laboratoir Dauphinois d'Hydraulique (Grenoble) and its main advantages are the improved interlocking, compared with cubes, and a larger porosity of the slope which increases energy dissipation and reduces wave run-up. The tetrapod inspired similar precast armor units and, according to The Rock Manual [2], "*there are probably in excess of 100 varieties of armor units*," some of which were used just for one single project. Table A1 summarizes main special shaped armor units.

Table A1. Main special shaped armor units. Adapted from The Rock Manual [2].

Armor Unit	Country	Year	Armor Unit	Country	Year
Tetrapod	France	1950	Seabee	Australia	1978
Tribar	USA	1958	Accropode	France	1980
Stabit	UK	1961	Shed	UK	1982
Akmon	The Netherlands	1962	Haro	Belgium	1984
Tripod	The Netherlands	1962	Hollow Cube	Germany	1991
Dolos	South Africa	1963	Core-Loc	USA	1996
Cob	UK	1969	A-Jack	USA	1998
Antifer Cube	France	1973	Cubipod®	Spain	2006

Stability of armor units can be divided in two factors: self-weight and interlocking. Slender shaped units, such as dolosse, might be affected by a fragile breakage during rocking; if that happens, damage progression is much quicker compared with weight resistant units, such as cubes, because broken armor units have little residual stability, i.e., they are more fragile. As it was mentioned in Section 2.2, the concept of "fragility" was presumably coined by Whillock and Price in 1976 [42] and applied to further studies with different armor types such as De Rover et al. [82].

Specific hydraulic stability formula and deterioration rates of artificial special armor units are mainly accounted by private companies and research centers, which develop and patent these particular armoring. Nevertheless, there are many publications and studies using artificial units, which commonly employ a damage descriptor based on the number of displaced units out of the armor layer or variations in the packing density [81,111–113,115,142–144]. VdM [145] compared the advantages and disadvantages of different concrete armor layers and their stability formula, including cubes, tetrapods, dolosse, accropode, and core-loc. The CEM [1] summed up different stability formulations for some of the most relevant concrete units.

Note that packing density is crucial for special shaped armor units. De Jong et al. [146] found a clear relation between an increase in armor units packing density and a decrease in damage. Gómez-Martín and Medina [147] studied damage progression on cube armored breakwaters, introducing a new failure mode for the armor layer: the heterogeneous packing failure mode (*HeP*).

This failure mode accounts for the slight movements that tend to reduce packing density near the SWL without extraction of armor units, which is typically due to face-to-face undesired arrangements under the SWL. In order to avoid the *HeP*, the Cubipod® was recommended. Van Buchem [116] also addressed stability of cubes by means of a packing density parameter.

Appendix B. List of Symbols

A, B, C	Empirical coefficients (in Table 2)
ANN	Artificial neural network
AT	Armor type (in Table 3)
A_e	cross-sectional eroded area
a_s	coefficient of the damage progression model of M&K [98]
b	coefficient of the damage progression model of M&K [98] and, independently, of Castillo et al. [130]
CDF	Cumulative distribution function
D	damage defined in a generic way
D*	dimensionless damage defined in a generic way in the model of Castillo et al. [130]
D_{n50}	median nominal diameter or equivalent cube size: $D_{n50} = (W_{50}/\rho_a)^{1/3}$
D_0	initial damage
D^*_0	initial dimensionless damage in the model of Castillo et al. [130]
D_0 (H, T)	Asymptotic maximum damage defined in Medina [70]
D_0 (H, Ir)	Asymptotic maximum damage defined in Gómez-Martín and Medina [71]
DPM	Damage progression model
ELM	Extreme learning machine
g	acceleration of gravity
H	wave height
H_b	wave height at breaking in Hedar [47]
$H_{D=0}$	maximum wave height producing no damage
H_n	average wave height of the n highest waves in a sea state
$H_{1/n}$	average wave height of the N/n highest waves in a sea state composed of N waves
$H_S = H_{1/3}$	significant wave height
$H_{n\%}$	wave height exceeded by the n% highest waves in a sea state
h	water depth
h_b	water depth at breaking in Hedar [47]
I	Irregular waves (in Table 3)
Ir or $\xi = \tan\alpha/(H/L)^{0.5}$	Iribarren's number, also referred as surf similarity parameter
k	wave action parameter in the model of Castillo et al. [130]
K	empirical coefficient in hydraulic stability models
K_D	empirical coefficient in the hydraulic stability model of Hudson [25]
K, K_1, K_2, K_3	empirical coefficient in hydraulic stability models. Note that despite using same notation in Table 1, the values of these coefficients are different for each model.
L	wavelength
$L_0 = gT^2/2\pi$	deep water wavelength
M&K	Melby and Kobayashi
n63%	number of regular waves causing 63% of the maximum asymptotic damage (Medina [70])
n50%	number of regular waves causing 50% of the maximum asymptotic damage (Gómez-Martín and Medina [71])
N_d	number of displaced stones
N_m	stability number using wave momentum flux (Melby and Hughes [3])
$N_S = H_s/(\Delta \cdot D_{n50})$	stability number
N_w	number of waves
PDF	Probability density function

$p_1, p_2, \cdots p_n$	parameters influencing armor layer stability in Equation 1.
P	permeability
r	wave action parameter in the model of Castillo et al. [130]
R	regular waves (in Table 3)
$S = A_e/D^2_{n50}$	dimensionless erosion area
S_e	equilibrium damage level, introduced by Kaku et al. [56]
$S_r = \gamma_s / \gamma_w$	submerged-related density
SWL	Still water level
t	time
$t^* = t/T_m$	relative duration, also referred as mean number of waves
T	wave period
T_m	mean wave period
T_p	peak wave period
VdM	Van der Meer
W_{50}	armor unit weight exceeded by 50% of the armor units.
WES	Waterways Experiment Etation
α	sea-side armor slope
$\Delta = (\gamma_s - \gamma_w)/ \gamma_w$	relative excess specific weight
γ	breakwater parameter in the model of Castillo et al. [130]
$\gamma_w = \rho_{w \cdot g}$	specific weight of water
$\gamma_s = \rho_{s \cdot g}$	specific weight of armor units
φ	internal friction angle
μ_0	Initial mean damage parameter in the model of Castillo et al. [130]
σ_0	Initial standard deviation damage parameter in the model of Castillo et al. [130]
$\xi_0 = \tan\alpha/(H/L_0)^{0.5}$	deep water Iribarren's number

References

1. USACE. *Coastal Engineering Manual*; EM 110-2-1100 (Part VI) Change 3 (28 Sep 2011); USACE: Washington, DC, USA, 2002.
2. CIRIA; CUR; CETMEF. *The Rock Manual. The Use of Rock in Hydraulic Engineering*, 2nd ed.; C683; CIRIA: London, UK, 2007.
3. Melby, J.A.; Hughes, S.A. Armor Stability Based on Wave Momentum Flux. In *Proceedings of Coastal Structures*; ASCE: Portland, OR, USA, 2003; pp. 53–65.
4. de Castro, E. Diques de Escollera. *Rev. Obras Públicas* **1933**, *I*, 183–185. CICCP, Madrid, Spain. (In Spanish)
5. Iribarren, R. *Una Fórmula Para El Cálculo de Los Diques De Escollera*; M. Bermejillo Usabiaga: Pasajes, Spain, 1938. (In Spanish)
6. Campos, A.; Molina, R.; Castillo, C. Damage in Rubble Mound Breakwaters. Part II: Review of the Definition, Parameterization and Measurement of Damage. *J. Mar. Sci. Eng.* **2020**, *8*, 306. [CrossRef]
7. Allsop, N.; Cork, R.; Henk Jan Verhagen, I. A Database of Major Breakwaters around the World. In *Proceedings of the ICE Breakwaters Conference*; Thomas Telford: Edinburgh, UK, 2009.
8. Hald, T. Wave Induced Loading and Stability of Rubble Mound Breakwaters. Series Paper no 18. Ph.D. Thesis, Hydraulics and Coastal Engineering Laboratory, Aalborg University, Aalborg, Denmark, 1998.
9. Broderick, L.; Ahrens, J.P. *Riprap Stability Scale Effects*; Technical Report TP 82-3; CERRE-CS: Fairfax County, VA, USA, 1982.
10. Iribarren, R.; Nogales, C. Generalización de La Fórmula Para El Cálculo de Los Diques de Escollera y Comprobación de Sus Coeficientes. *Rev. Obras Públicas* **1950**, *I*, 227–239. CICCP, Madrid, Spain. (In Spanish)
11. Iribarren, R. Fórmula Para El Cálculo de Los Diques de Escollera Naturales o Artificiales. *Rev. Obras Públicas* **1965**, *I*, 739–750. CICCP, Madrid, Spain. (In Spanish)
12. Iribarren, R. 1938. A formula for the calculation of rock fill dykes (Translation of "Una Fórmula Para El Cálculo De Los Diques De Escollera". *Bull. Beach Eros. Board* **1949**, *3*, 1–15.
13. Larras, J. L'équilibre Sous-Marin d'un Massif de Matériaux Soumís à La Houle. *Le Génie Civ* **1952**. (In French)
14. Beaudevin, C. Stabilité Des Diques á Talus à Carapace En Vrac. *La Houille Blanche* **1955**. (In French) [CrossRef]

15. Bruun, P. *Design and Construction of Mounds for Breakwaters and Coastal Protection*; Elsevier Science Ltd.: Amsterdam, The Netherlands, 1985.
16. Epstein, H.; Tyrrel, F. Design of Rubble-Mound Breakwaters. In Proceedings of the International Navigation Congress, Section II-4, Lisbon, Portugal, 10–19 September 1949.
17. Hickson, R.; Rodolf, F.W. Design and Construction of Jetties. In Proceedings of the 1st International Conference on Coastal Engineering, Long Beach, CA, USA, October 1950.
18. Hudson, R.Y.; Jackson, R.A. *Stability of Rubble-Mound Breakwaters*; Technical Memorandum 2-365; Waterways Experiment Station, CERC: Vicksburg, MS, USA, 1953.
19. Hedar, P. Design of Rock-Fill Breakwaters. In *Proceedings of the 8th International Navigation Congress*; Sectiton II-1: Rome, Italy, 1953.
20. Svee, R. Formulas for Design of Rubble-Mound Breakwaters. *J. Waterw. Harb. Div. ASCE* **1962**, *88*, 11–21.
21. Goldschtein, M.N.; Kononenko, P.S. Investigations Concerning Filters and Stone Revetments on Slopes of Earth Dams. *Tr. Soviestchanija Pod. Bieriegov Moriej i Vodochranilistch* **1959**. (In Russian)
22. SN-92-60. *Technical Prescriptions for the Determination of Wave Action on Maritime and River Structures and Banks*; Construction Department of the USSR: Moscow, Russia, 1960. (In Russian)
23. Rybtchecsky, G.G. Calculation of the Stability of Protective Elements for Rubble-Mound Strutures under Wave Action. *Gidrotechnitcheskoie Stroitielstvo* **1964**, *11*. (In Russian)
24. Metelicyna, G.G. Determination of the Weight of Quarry-Run and Concrete Blocks as a Protective Layer for Constructions under Wave Action. *Gidrotechnitcheskoie Stroitielstvo* **1967**, *5*.
25. Hudson, R.Y. *Design of Quarry-Stone Cover Layers for Rubble-Mound Breakwaters*; Research Report 2-2; WES: Vicksburg, MS, USA, 1958.
26. Hudson, R.Y. Laboratory Investigation of Rubble-Mound Breakwaters. *J. Waterw. Harbours Div. ASCE* **1959**, *85*, 93–121.
27. USACE. *Shore Protection Manual*, 3rd ed.; U.S. Army Engineer Waterways Experiment Station, U.S. Government Printing Office: Washington, DC, USA, 1977.
28. USACE. *Shore Protection Manual*, 4th ed.; U.S. Army Engineer Waterways Experiment Station, U.S. Government Printing Office: Washington, DC, USA, 1984.
29. Carstens, T.; Torum, A.; Tratteberg, A. The Stability of Rubble Mound Breakwaters against Irregular Waves. In *Proceedings of the 10th International Conference on Coastal Engineering*; ASCE: Tokyo, Japan, 1966; pp. 958–971.
30. Font, J.B. The Effect of Storm Duration on Rubble-Mound Breakwater Stability. In *Proc. 11th International Conference on Coastal Engineering*; ASCE: London, UK, 1968.
31. Battjes, J.A. Surf Similarity. In *Proc. 14th International Conference on Coastal Engineering*; ASCE: Copenhaguen, Denmark, 1974; pp. 466–480.
32. Bruun, P.; Günbak, A.R. New Design Principles for Rubble Mound Structures. In *Proc. 15th International Conference on Coastal Engineering*; ASCE: Honolulu, HI, USA, 1976; pp. 2429–2473.
33. Bruun, P. *Port Engineering*; Gulf Pub. Co., Book Division: Houston, TX, USA, 1973; p. 787.
34. PIANC. *Final Report of the International Commision for the Study of Waves*; Annex to PIANC Bull. N. 25, V. m; PIANC: Brussels, Belgium, 1976.
35. Oumeraci, H. Review and Analysis of Vertical Breakwater Failures—Lessons Learned. *Coast. Eng.* **1994**, *22*, 3–29. [CrossRef]
36. van Hijum, E. Equilibrium Profiles of Coarse Material under Wave Attack. In *Proceedings of the 15th International Conference on Coastal Engineering*; ASCE: Honolulu, HI, USA, 1976.
37. Bruun, P. Common Reasons for Damage or Breakdown of Mound Breakwaters. *Coast. Eng.* **1978**, *2*, 261–273. [CrossRef]
38. Kjelstrup, S. Common Reasons for Damage or Breakdown of Mound Breakwaters: Discussion. *Coast. Eng.* **1979**, *3*, 137–142. [CrossRef]
39. Ahrens, J.P. *Large Wave Tank Tests of Riprap Stability*; U.S. Army Engineer Waterways Experiment Station CERC: Vicksburg, MS, USA, 1975.
40. Ahrens, J.P.; McCartney, B.L. Wave Period Effect on the Stability of Riprap. In Proceedings of the Civil Engineering in the Oceans III, Newark, NJ, USA, 9–12 June 1975; ASCE; pp. 1019–1034.
41. Thompson, D.M.; Shuttler, R.M. *Riprap Design for Wind-Wave Attack, a Laboratory Study in Random Waves*; Report No. EX 707; HR Wallingford: Wallingford, UK, 1975.

42. Whillock, A.F.; Price, W.A. Armour Blocks as Slope Protection. In *Proceedings of the 15th International Conference on Coastal Engineering*; ASCE: Honolulu, HI, USA, 1976; pp. 2564–2571.
43. Magoon, O.S.; Baird, W.F. Breakage of Breakwater Armour Units. In *Symp. Design Rubble Mound Breakwaters*; Paper No. 6; British Overcraft Corporation: Isle of Wight, UK, 1977.
44. Losada, M.A.; Gimenez-Curto, L.A. The Joint Effect of the Wave Height and Period on the Stability of Rubble Mound Breakwaters Using Iribarren's Number. *Coast. Eng.* **1979**, *3*, 77–96. [CrossRef]
45. Losada, M.A.; Giménez-Curto, L.A. Mound Breakwaters under Oblique Wave Attack; A Working Hypothesis. *Coast. Eng.* **1982**, *6*, 83–92. [CrossRef]
46. Jensen, O.J. *A Monograph on Rubble Mound Breakwaters*; Hydraulic Engineering Reports; Danish Hydraulic Institute (DHI): Horsholm, Denmark, 1984.
47. Hedar, P. Armor Layer Stability of Rubble-Mound Breakwaters. *J. Waterw. Port. Coastal Ocean. Eng.* **1986**, *112*, 343–350. [CrossRef]
48. van der Meer, J.W. Stability of Rubble Mound Revetments and Breakwaters under Random Wave Attack. In *Proceedings of the Breakwaters Conference*; Chapter 5: Developments in Breakwaters; ICE: London, UK, 1985.
49. van der Meer, J.W. Stability of Breakwater Armour Layers—Design Formulae. *Coast. Eng.* **1987**, *11*, 219–239. [CrossRef]
50. van der Meer, J.W. Rock Slopes and Gravel Beaches under Wave Attack. Ph.D. Thesis, Delft hydraulics communication no. 396. Delft Hydraulics Laboratory, Delft, The Netherlands, 1988.
51. van der Meer, J. Deterministic and Probabilistic Design of Breakwater Armor Layers. *J. Waterw. Port. Coast. Ocean. Eng.* **1988**, *114*, 66–80. [CrossRef]
52. van der Meer, J.W. Stability of Cubes, Tetrapodes and Accropode. In *Proceedings of the Breakwaters Conference*; Design of Breakwaters, Insitution of Civil Engineers; Thomas Telford: London, UK, 1988; pp. 71–80.
53. Hedar, P.A. Stability of Rock-Fill Breakwaters. Ph.D. Thesis, Chalmers Tekniska Högskola, No 26. University of Goteborg, Goteborg, Sweden, 1960.
54. Latham, J.P.; Mannion, M.B.; Poole, A.B.; Bradbury, A.P.; Allsop, N.W.H. *The Influence of Armourstone Shape and Rounding on the Stability of Breakwater Armour Layers*; Hydraulic Engineering Reports; Queen Mary College: London, UK, 1988.
55. Medina, J.; McDougal, W. Discussion of "Deterministic and Probabilistic Design of Breakwater Armor Layers" by Jentsje W. van Der Meer (January, 1988, Volume 114, No. 1). *J. Waterw. Port. Coastal Ocean. Eng.* **1990**, *116*, 508–510. [CrossRef]
56. Kaku, S.; Kobayashi, N.; Ryu, C.R. Design Formulas for Hydraulic Stability of Rock Slopes under Irregular Wave Attack. In *Proceedings of the 38th Japanese Coastal Engineering Conference*; ASCE: Reston, VA, USA, 1991; pp. 661–665.
57. Smith, W.G.; Kobayashi, N.; Kaku, S. Profile Changes of Rock Slopes by Irregular Waves. In Proceedings of the 23rd International Conference on Coastal Engineering, Venice, Italy, 4–9 October 1992; pp. 1559–1572.
58. Vidal, C.; Medina, R.; Martín, F.L.; Migoya, L. Wave Height and Period Parameters for Damage Description on Rubble-Mound Breakwaters. *Coast. Eng.* **2004**, 3688–3700.
59. Vidal, C.; Medina, R.; Lomónaco, P. Wave Height Parameter for Damage Description of Rubble-Mound Breakwaters. *Coast. Eng.* **2006**, *53*, 711–722. [CrossRef]
60. Mertens, M. Stability of Rock on Slopes under Wave Attack: Comparison and Analysis of Datasets Van Der Meer [1988] and Van Gent [2003]. Master's Thesis, Delft University of Technology, Delft, The Netherlands, 2007.
61. van Gent, M.; Smale, A.; Kuiper, C. Stability of Rock Slopes with Shallow Foreshores. In *Proc. of Coastal Structures*; ASCE: Portland, OR, USA, 2003; pp. 100–112.
62. Verhagen, H.J.; Mertens, M. Riprap Stability for Deep Water, Shallow Water and Steep Foreshores. In Proceedings of the 9th ICE Breakwaters Conference, Edinburgh, UK, 16–18 September 2009.
63. Medina, J.R.; Fassardi, C.; Hudspeth, R.T. Effects of Wave Groups on the Stability of Rubble Mound Breakwaters. In Proceedings of the 22nd International Conference on Coastal Engineering, Delt, The Netherlands, 2–6 July 1990; pp. 1552–1563.
64. Medina, J.; Hudspeth, R.; Fassardi, C. Breakwater Armor Damage Due to Wave Groups. *J. Waterw. Port. Coast. Ocean. Eng.* **1994**, *120*, 179–198. [CrossRef]

65. Jensen, T.; Andersen, H.; Gronbech, J.; Mansard, E.P.D.; Davies, M.H. Breakwater Stability under Regular and Irregular Wave Attack. In Proceedings of the 25th International Conference on Coastal Engineering, Orlando, FL, USA, 2–6 September 1996; Volume 2, pp. 1679–1692.
66. Teisson, C. Statistical Apporach of Duration of Extreme Storms: Consequences on Breakwater Damages. In Proceedings of the 22nd International Conference on Coastal Engineering, Delt, The Netherlands, 2–6 July 1990; pp. 1851–1860.
67. Vidal, C.; Losada, M.; Mansard, E. Suitable Wave-Height Parameter for Characterizing Breakwater Stability. *J. Waterw. Port. Coastal, Ocean. Eng.* **1995**, *121*, 88–97. [CrossRef]
68. Battjes, J.A.; Groenendijk, H.W. Wave Height Distributions on Shallow Foreshores. *Coast. Eng.* **2000**, *40*, 161–182. [CrossRef]
69. Méndez, F.J.; Castanedo, S. A Probability Distribution for Depth-Limited Extreme Wave Heights in a Sea State. *Coast. Eng.* **2007**, *54*, 878–882. [CrossRef]
70. Medina, J.R. Wave Climate Simulation and Breakwater Stability. In *Proceedings of the 25th International Conference on Coastal Engineering*; ASCE: Orlando, FL, USA, 1996; Volume 2, pp. 1789–1802.
71. Gómez-Martín, M.E.; Medina, J.R. Wave-to-Wave Exponential Estimation of Armor Damage. In Proceedings of the 29th International Conference on Coastal Engineering, Lisbon, Portugal, 19–24 September 2004; pp. 3592–3604.
72. Pfeiffer, H.L. Comparison of Four Rubble-Mound Stability Equations with Prototype Data from Burns Harbor Breakwater. Master's Thesis, Civil Engineerign Department, Texas A&M University, College Station, TX, USA, 1991.
73. PIANC. *Analysis of Rubble Mound Breakwaters*; Supplement to PIANC Bull. N. 78/79; PIANC: Brussels, Belgium, 1992.
74. Koev, K.N. Statistical Analysis of Formulas for Breakwater Armor Layer Design. *J. Waterw. Port. Coast. Ocean. Eng.* **1992**, *118*, 213–219. [CrossRef]
75. Vidal, C.; Losada, M.A.; Medina, R.; Losada, I. Análisis de La Estabilidad de Diques Rompeolas. *Diques Rompeolas* **1994**, *1*, 17–34. (In Spanish) [CrossRef]
76. Hughes, S.A. *Physical Models and Laboratory Techniques in Coastal Engineering*; Advances Seriees on Ocean Engineering, Vol. 7; World Scientific: London, UK, 1993.
77. Tirindelli, M.; Lamberti, A.; Paphitis, D.; Collins, M.; Vidal, C.; Hawkins, S.; Moschella, P.; Burcharth, H.; Sanchez-Arcilla, A. *Wave Action on Rubble Mound Breakwaters: The Problem of Scale Effects*; Delos report D52; Hydraulic Engineering Reports; University of Bologna: Bologna, Italy, 2004.
78. Davies, M.H.; Mansard, E.P.D.; Cornett, A.M. Damage Analysis for Rubble-Mound Breakwaters. In *Proceedings of the 24th International Conference on Coastal Engineering*; ASCE: Kobe, Japan, 1994; Volume 1, pp. 1001–1015.
79. Burcharth, H.F.; Liu, Z.; Troch, P. Scaling of Core Material in Rubble Mound Breakwater Model Tests. In Proceedings of the 5th International Conference on Coastal and Port Engineering in Developing Countries, COPEDEC V, Cape Town, South Africa, 19–23 April 1999; pp. 1518–1528.
80. Hegde, A.V.P.; Srinivas, R. Effect of Core Porosity on Stability and Run-up of Breakwaters. *Ocean. Eng.* **1995**, *22*, 519–526. [CrossRef]
81. De Jong, W. Experimental Research on the Stability of the Armour and Secondary Layer in a Single Layered Tetrapod Breakwater. Ph.D. Thesis, TU Delft, Faculty of Civil Engineering and Geosciences, Hydraulic Engineering, Delft, The Netherlands, 2003.
82. Reedijk, B.; Muttray, M.; Van Den Berge, A.; De Rover, R. Effect of Core Permeability on Armour Layer Stability. In Proceedings of the 31st International Conference on Coastal Engineering, Hamburg, Germany, 31 August–5 September 2008; pp. 3358–3367.
83. Oumeraci, H.; Kortenhaus, A.; Allsop, W.; De Groot, M.; Crouch, R.; Vrijling, H.; Voortman, H. *Proverbs: Probabilistic Design Tools for Vertical Breakwaters*; MAST—EU Project: Brussels, Belgium, 1999.
84. Puertos del Estado. *ROM 0.0-01. General Procedure and Requirements in the Design of Harbor and Maritime Structures. PART I*; Puertos del Estado: Madrid, Spain, 2001.
85. Wang, H.; Peene, S.J. A Probabilistic Model of Rubble Mound Armor Stability. *Coast. Eng.* **1990**, *14*, 307–331. [CrossRef]
86. Carver, R.D.; Wright, B.J. *Investigation of Wave Grouping Effects on the Stability of Stone-Armored, Rubble-Mound Breakwaters*; U.S. Army Engineer Waterways Experiment Station: Vicksburg, MS, USA, 1991.

87. Burcharth, H.F. Reliability Based Design of Coastal Structures. In *Advances in Coastal and Ocean Engineering*; World Scientific: London, UK, 1997; Volume 3.
88. Castillo, E.; Losada, M.; Mínguez, R.; Castillo, C.; Baquerizo, A. Optimal Engineering Design Method That Combines Safety Factors and Failure Probabilities: Application to Rubble-Mound Breakwaters. *J. Waterw. Port. Coast. Ocean. Eng.* **2004**, *130*, 77–88. [CrossRef]
89. Castillo, C.; Mínguez, R.; Castillo, E.; Losada, M.A. An Optimal Engineering Design Method with Failure Rate Constraints and Sensitivity Analysis. Application to Composite Breakwaters. *Coast. Eng.* **2006**, *53*, 1–25. [CrossRef]
90. Mínguez, R.; Castillo, E.; Castillo, C.; Losada, M.A. Optimal Cost Design with Sensitivity Analysis Using Decomposition Techniques. Application to Composite Breakwaters. *Struct. Saf.* **2006**, *28*, 321–340. [CrossRef]
91. Tørum, A.; Moghim, M.N.; Westeng, K.; Hidayati, N.; Arntsen, Ø. On Berm Breakwaters: Recession, Crown Wall Wave Forces, Reliability. *Coast. Eng.* **2012**, *60*, 299–318. [CrossRef]
92. Gouldby, B.; Méndez, F.J.; Guanche, Y.; Rueda, A.; Mínguez, R. A Methodology for Deriving Extreme Nearshore Sea Conditions for Structural Design and Flood Risk Analysis. *Coast. Eng.* **2014**, 15–26. [CrossRef]
93. van Gent, M.R.A.; Pozueta, B. Rear-Side Stability of Rubble Mound Structures. *Coast. Eng.* **2004**, 3481–3493.
94. Campos, A.; Castillo, C.; Molina, R. Optimizing Breakwater Design Considering the System of Failure Modes. In Proceedings of the 32nd International Conference on Coastal Engineering, Shanghai, China, 30 June–5 July 2010.
95. Hald, T.; Burcharth, H.F. An Alternative Stability Equation for Rock Armoured Rubble Mound Breakwaters. In Proceedings of the 27th International Conference on Coastal Engineering, Sydney, Australia, 16–21 July 2000; Volume 276, pp. 1921–1934.
96. Melby, J.; Kobayashi, N. Progression and Variability of Damage on Rubble Mound Breakwaters. *J. Waterw. Port. Coastal Ocean. Eng.* **1998**, *124*, 286–294. [CrossRef]
97. Melby, J.A.; Kobayashi, N. Damage Progression on Breakwaters. In Proceedings of the 26th International Conference on Coastal Engineering, Copenhagen, Denmark, 22–26 June 1998; Volume 2, pp. 1884–1897.
98. Melby, J.A.; Kobayashi, N. Damage Progression and Variability on Breakwater Trunks. In Proceedings of the Coastal Structures, Santander, Spain, 7–10 June 1999; Volume 1, pp. 309–315.
99. Melby, J.A. *Damage Progression on Rubble-Mound Breakwaters*; Technical Report CHL-99-17; U.S. Army Corps of Engineers, Waterways Experiment Station: Vicksburg, MS, USA, 1999.
100. Melby, J.A. *Damage Development on Stone-Armored Breakwaters and Revetments*; Coastal and Hydraulics Engineering Technical Note; USACE: Washington, DC, USA, 2005.
101. MAST II. *Berm Breakwater Structures. Final Report MAST-Contract MAS2-CT94-0087*; MAST—EU Project: Brussels, Belgium, 1997.
102. MarCom WG 40. *State-of-the-Art of Designing and Constructing Berm Breakwaters*; PIANC: Brussels, Belgium, 2003.
103. *ISO 21650:2007—Actions from Waves and Currents on Coastal Structures*; ISO: Geneva, Switzerland, 2007.
104. Wolters, G.; Van Gent, M.R.A. Oblique Wave Attack on Cube and Rock Armoured Rubble Mound Breakwaters. In *Proceedings of the 32nd International Conference on Coastal Engineering*; ASCE: Shanghai, China, 2010.
105. van Gent, M.R.A.; der Werf, I.M. Toe Stability of Rubble Mound Breakwaters. In *Proceedings of the 34th International Conference on Coastal Engineering*; ASCE: Seoul, Korea, 2014.
106. Tomasicchio, G.R.; Lamberti, A.; Archetti, R. Armor Stone Abrasion Due to Displacements in Sea Storms. *J. Waterw. Port. Coastal, Ocean. Eng.* **2003**, *129*, 229–232. [CrossRef]
107. Latham, J.P. Degradation Model for Rock Armour in Coastal Engineering. *Q. J. Eng. Geol.* **1991**, *24*, 101–118. [CrossRef]
108. Eslami, A.S.; Van Gent, M.R.A. Wave Overtopping and Rubble Mound Stability under Combined Loading of Waves and Current. In Proceedings of the 32nd International Conference on Coastal Engineering, Shanghai, China, 31 June–5 July 2010.
109. Esteban, M.; Morikubo, I.; Shibayama, T.; Muñoz, R.A.; Mikami, T.; Thao, N.D.; Ohira, K.; Ohtani, A. Stability of Rubble Mound Breakwaters against Solitary Waves. In Proceedings of the 33rd International Conference on Coastal Engineering, Santander, Spain, 1–6 July 2012.
110. Muñoz-Perez, J.J.; Medina, R. Comparison of Long-, Medium-and Short-Term Variations of Beach Profiles with and without Submerged Geological Control. *Coast. Eng.* **2010**, *57*, 241–251. [CrossRef]

111. Pardo, V.; Herrera, M.P.; Molines, J.; Medina, J.R. Placement Test, Porosity, and Randomness of Cube and Cubipod Armor Layers. *J. Waterw. Port. Coast. Ocean. Eng.* **2013**, *140*. [CrossRef]
112. Medina, J.R.; Gómez-Martín, M.E.; Corredor, A. Armor Unit Placement, Randomness and Porosity of Cube and Cubipod Armor Layers. In Proceedings of the 6th International Conference on Coastal Structures, Yokohama, Japan, 6–8 September 2011; pp. 743–754.
113. Yagci, O.; Kapdasli, S. Alternative Placement Technique for Antifer Blocks Used on Breakwaters. *Ocean. Eng.* **2003**, *30*, 1433–1451. [CrossRef]
114. Yagci, O.; Kapdasli, S.; Cigizoglu, H.K. The Stability of the Antifer Units Used on Breakwaters in Case of Irregular Placement. *Ocean. Eng.* **2004**, *31*, 1111–1127. [CrossRef]
115. Gürer, S.; Cevik, E.; Yüskel, Y.; Günbak, A.R. Stability of Tetrapod Breakwaters for Different Placing Methods. *J. Coast. Res.* **2005**, *21*, 464–471. [CrossRef]
116. van Buchem, R.V. Stability of a Single Top Layer of Cubes. Master's Thesis, Delft University of Technology, Delft, The Netherlands, 2009.
117. Medina, J.R.; Molines, J.; Gómez-Martín, M.E. Influence of Armour Porosity on the Hydraulic Stability of Cube Armour Layers. *Ocean. Eng.* **2014**, *88*, 289–297. [CrossRef]
118. Marzeddu, A.; Oliveira, T.C.A.; Sánchez-Arcilla, A.; Gironella, X. Effect of Wave Storm Representation on Damage Measurements of Breakwaters. *Ocean. Eng.* **2020**, *200*, 107082. [CrossRef]
119. Clavero, M.; Díaz-Carrasco, P.; Losada, M.Á. Bulk Wave Dissipation in the Armor Layer of Slope Rock and Cube Armored Breakwaters. *J. Mar. Sci. Eng.* **2020**, *8*, 152. [CrossRef]
120. Farhadzadeh, A.; Kobayashi, N.; Melby, J.A. Evolution of Damaged Armor Layer Profile. In Proceedings of the 32nd International Conference on Coastal Engineering, Shanghai, China, 31 June–5 July 2010.
121. Garcia, R.; Kobayashi, N. Damage Variations on Low-Crested Breakwaters. In Proceedings of the 34th International Conference on Coastal Engineering, Seoul, Korea, 15–20 June 2014.
122. Matsumoto, A.; Mano, A.; Mitsui, J.; Hanzawa, M. Stability Prediction on Armor Blocks for Submerged Breakwater by Computational Fluid Dynamics. In Proceedings of the 33rd International Conference on Coastal Engineering, Santander, Spain, 1–6 July 2012.
123. Kim, D.H.; Park, W.S. Neural Network for Design and Reliability Analysis of Rubble Mound Breakwaters. *Ocean. Eng.* **2005**, *32*, 1332–1349. [CrossRef]
124. Kim, D.; Kim, D.H.; Chang, S. Application of Probabilistic Neural Network to Design Breakwater Armor Blocks. *Ocean. Eng.* **2008**, *35*, 294–300. [CrossRef]
125. Lee, A.; Kim, S.E.; Suh, K.D. An Easy Way to Use Artificial Neural Network Model for Calculating Stability Number of Rock Armors. *Ocean. Eng.* **2016**. [CrossRef]
126. Kim, D.H.; Kim, Y.J.; Hur, D.S. Artificial Neural Network Based Breakwater Damage Estimation Considering Tidal Level Variation. *Ocean. Eng.* **2014**, *87*, 185–190. [CrossRef]
127. Koç, M.L.; Balas, C.E.; Koç, D.I. Stability Assessment of Rubble-Mound Breakwaters Using Genetic Programming. *Ocean. Eng.* **2016**, *111*, 8–12. [CrossRef]
128. Wei, X.; Liu, H.; She, X.; Lu, Y.; Liu, X.; Mo, S. Stability Assessment of Rubble Mound Breakwaters Using Extreme Learning Machine Models. *J. Mar. Sci. Eng.* **2019**, *7*, 312. [CrossRef]
129. Iglesias, G.; Rabuñal, J.; Losada, M.A.; Pachón, H.; Castro, A.; Carballo, R. A Virtual Laboratory for Stability Tests of Rubble-Mound Breakwaters. *Ocean. Eng.* **2008**, *35*, 1113–1120. [CrossRef]
130. Castillo, C.; Castillo, E.; Fernández-Canteli, A.; Molina, R.; Gómez, R. Stochastic Model for Damage Accumulation in Rubble-Mound Breakwaters Based on Compatibility Conditions and the Central Limit Theorem. *J. Waterw. Port. Coast. Ocean. Eng.* **2012**, *138*, 451–463. [CrossRef]
131. Campos, A.; Castillo, C.; Molina, R. Analysis of the Influence of the Different Variables Involved in a Damage Progression Probability Model. In Proceedings of the 34th International Conference on Coastal Engineering, Seoul, Korea, 15–20 June 2014.
132. Campos, A. A Methodology for the Analysis of Damage Progression in Rubble Mound Breakwaters. Ph.D. Thesis, Universidad de Castilla-La Mancha, Ciudad Real, Spain, 2016.
133. Benedicto, M.I.; Ramos, M.V.; Losada, M.A.; Rodriguez, I. Expected Damage Evolution of a Mound-Breakwater during Its Useful Life. In *Proceedings of the 29th International Conference on Coastal Engineering*; ASCE: Lisbon, Portugal, 2004; pp. 3605–3614.
134. van Gent, M.; de Almeida, E.; Hofland, B. Statistical Analysis of the Stability of Rock Slopes. *J. Mar. Sci. Eng.* **2019**, *7*, 60. [CrossRef]

135. Ota, T.; Matsumi, Y.; Hirayama, T.; Kimura, A. Models for Profile Change of Rubble Mound Revetment and Profile Evaluation. In Proceedings of the 32nd International Conference on Coastal Engineering, Shanghai, China, 31 June–5 July 2010.
136. Pereira, M.; Teodoro, A.C.; Veloso-Gomes, F.; Lima, J.; Oliveira, S. Port Infrastructure Control (Madeira Island, Portugal) through a Hybrid Monitoring System (GNSS and Accelerometers). *Mar. Georesour. Geotechnol.* **2016**, *34*, 617–629. [CrossRef]
137. Horstmann, N.; Hinze, K.; Schimmels, S.; Oumeraci, H. Risk-Based Life Cycle Mim Strategy for Coastal Structures—Effect of Pre-Existing Damages on Failure Probability. In Proceedings of the 33rd International Conference on Coastal Engineering, Santander, Spain, 1–6 July 2012.
138. Burcharth, H.F.; Lykke Andersen, T.; Lara, J.L. Upgrade of Coastal Defence Structures against Increased Loadings Caused by Climate Change: A First Methodological Approach. *Coast. Eng.* **2014**, *87*, 112–121. [CrossRef]
139. Esteban, M.; Takagi, H.; Shibayama, T. *Handbook of Coastal Disaster Mitigation for Engineers and Planners*; Butterworth-Heinemann: Oxford, UK, 2015.
140. Vidal, C.; Losada, M.; Medina, R. Stability of Mound Breakwater's Head and Trunk. *J. Waterw. Port. Coastal Ocean. Eng.* **1991**, *117*, 570–587. [CrossRef]
141. de Almeida, E.; van Gent, M.R.A.; Hofland, B. Damage Characterization of Rock Slopes. *J. Mar. Sci. Eng.* **2019**, *7*, 10. [CrossRef]
142. Gómez-Martín, M.; Herrera, M.; Gonzalez-Escriva, J.; Medina, J. Cubipod® Armor Design in Depth-Limited Regular Wave-Breaking Conditions. *J. Mar. Sci. Eng.* **2018**, *6*, 150. [CrossRef]
143. Argente, G.; Gómez-Martín, M.; Medina, J. Hydraulic Stability of the Armor Layer of Overtopped Breakwaters. *J. Mar. Sci. Eng.* **2018**, *6*, 143. [CrossRef]
144. Safari, I.; Mouazé, D.; Ropert, F.; Haquin, S.; Ezersky, A. Hydraulic Stability and Wave Overtopping of Starbloc® Armored Mound Breakwaters. *Ocean. Eng.* **2018**, *151*, 268–275. [CrossRef]
145. van der Meer, J.W. Design of Concrete Armour Layers. *Coast. Struct.* **1999**, 213–221.
146. De Jong, W.; Verhagen, H.J.; Olthof, J. Experimental Research on the Stability of Armour and Secondary Layer in a Single Layered Tetrapod Breakwater. In *Proceedings of the 29th International Conference on Coastal Engineering*; ASCE: Lisbon, Portugal, 2004.
147. Gómez-Martín, M.E.; Medina, J.R. Damage Progression on Cube Armored Breakwaters. In Proceedings of the 30th International Conference on Coastal Engineering, San Diego, CA, USA, 3–8 September 2006; pp. 5229–5240.

Journal of
Marine Science and Engineering

MDPI

Review

Damage in Rubble Mound Breakwaters. Part II: Review of the Definition, Parameterization, and Measurement of Damage

Álvaro Campos [1,*], Rafael Molina-Sanchez [1] and Carmen Castillo [2]

[1] Universidad Politécnica de Madrid (UPM), HRL-UPM & CEHINAV-UPM, 28040 Madrid, Spain; rafael.molina@upm.es
[2] Universidad de Castilla-La Mancha (UCLM), 13071 Ciudad Real, Spain; mariacarmen.castillo@uclm.es
* Correspondence: alvaro.campos@upm.es; Tel.: +34-630-667572

Received: 20 March 2020; Accepted: 22 April 2020; Published: 28 April 2020

Abstract: Damage in rubble mound breakwaters has been addressed for more than 80 years and, as reported in "*Part I: Historical review of damage models*", a considerable number of hydraulic instability models have been proposed up to date. Most of them were developed from small-scale physical tests, based on damage descriptors not always parameterized nor measured in the same way, which indeed complicates the comparison and reproducibility from different experimental data sources. The latter is increased by the lack of a standardized methodological approach inside an experimental and measuring process that involves many sources of uncertainty. Currently, the latest innovations applicable to damage measurement, together with the growing demand of reliable decision-making tools for conservation/maintenance strategies and structural/operational risk management, venture an upcoming proliferation of prototype monitoring, as well as new approaches aimed to characterize the stochastic nature of damage evolution. In this context, this paper is meant to review the concept of damage in rubble mound breakwaters, the different proposals for its parameterization, the past and present measuring techniques, and main challenges in the near future.

Keywords: rubble mound breakwaters; historical review; damage measurement; damage characterization

1. Introduction

Damage of an element can be defined as the partial or total loss of its functionality. The Coastal Engineering Manual [1], referred as CEM in this paper, describes it as "*structure degradation that occurs over a relatively short period such as a single storm event, a unique occurrence, or perhaps a winter storm season*". Regarding rubble mound breakwaters, the concept of damage is usually related to the hydraulic instability of the armor layer [1,2]. It is commonly utilized to refer to the geometrical evolution in comparison with the "undamaged" section and, occasionally, also to the breakage of armor units. Therefore, the conceptualization of damage is dual: it has a qualitative character associated with the level of functionality and a quantitative character related to measuring the movement of armor units along the slope. However, the two approaches are not always correlated in the same way.

For instance, the geometrical variations of a berm breakwater might not cause the structure to be considered as damaged until a certain degree of deformation is achieved, because its thicker armor layer is actually designed to reshape. On the other hand, in a conventional cube armored breakwater with economic activities carried out at the emerged platform, a simple face-to-face reorganization of the cubes can alter the functionality of the structure. This slight readjustment can increase wave run-up and overtopping and, consequently, might affect activities such as bulk storing. In this case, the breakwater could be considered as damaged, even without a significant degree of deformation.

As not every rubble mound breakwater is designed under the same functional requirements and not every structure presents the same fragility, the concept of damage needs to be addressed from a multidimensional perspective. Note that there is a relatively wide variety of breakwater typologies and each type of armor unit presents a singular behavior against wave action. In addition, damage levels in single-layer structures are not equivalent in multi-layer ones. However, as mentioned before, the general trend is to use the term "damage" to simply refer to the quantification of the deformation of a section.

The amount of information on the definition, parameterization, and measurement of damage is quite extensive. For this reason, the present review of damage in rubble mound breakwaters is divided in two separated papers, which are closely linked but conceptually different. On the one hand, Part I [3] is focused on how damage initiation and progression is modeled, i.e. which are the available hypothesis and strategies for characterizing the structural response. It compiles 146 references on this topic, chronologically discussed from 1933 to 2020, and including main advances together with 23 formulations of hydraulic stability models and 11 formulations of damage progression models. On the other hand, the present paper (Part II) is centered on how damage is defined (see Section 2.1), parametrized (see Section 2.2), and measured (see Section 2.3), i.e., which are the strategies for defining damage descriptors and which are the instrumental techniques available for monitoring the structural response. Damage descriptors are required for building and calibrating damage models and they are conditioned by the accuracy of the available measuring techniques.

Damage monitoring has been mainly enclosed so far to small-scale physical tests aimed to analyze the stability of generic typologies. They are also quite common nowadays in design tenders in order to verify the stability of real (prototype) structures. This kind of experiments has a certain range of validity not only dependent on the wave conditions and water levels tested, but also on the breakwater geometry and armor unit type. The assimilation of the results from different wave flumes is also dependent on how damage is parametrized and measured. Therefore, a complete description of the experimental methodology is needed for reproducibility, which is not often the case. Reproducibility is required even within each particular laboratory, due to the fact that damage initiation and evolution are random variables and, thus, experiments need to be repeated [4–7]. According to Marzeddu et al. [8], taking into account laboratory occupation times, a minimum of five repetitions should be performed to obtain an average damage value.

Despite each laboratory has their own standardized protocols for accomplishing this kind of experiments, many authors claim for a general standardization of the methodology. In Vidal et al. [9], an attempt for establishing standards by the Organismo Público de Puertos del Estado (the Spanish organism in charge of managing state-owned ports) was pointed out. More recently, the International Breakwater Directory is working on expanding the CLASH (acronym for "Crest Level Assessment of coastal Structures by full scale monitoring, neural network prediction and Hazard analysis on permissible wave overtopping") overtopping database [10] by including information of armor damage in rubble mound breakwaters and seawalls [11]. The latter can be used as a motivation to establish a standardization of procedures between the different laboratories and Port Authorities worldwide in order to provide comparable results. In this sense, Clavero et al. [12] proposed a methodology that can help deciding whether two series of data obtained in different laboratories are assimilable or not.

2. Review of Damage Definition, Damage Parameterization, and Damage Measurement

2.1. Damage Definition

As presented in the introduction, the definition of damage in rubble mound breakwaters is conceptually dependent on aspects such as the typology, design, armor type, or the functional requirements. Despite the general and quite ambiguous connotation of the term "damage", in coastal engineering it is commonly used to refer to the degree of reshaping of the armor layer. It is therefore linked to the failure mode known as "hydraulic instability of the armor layer" [1,2] and usually

quantified by means of the eroded volume or number of units removed. In steep slopes, displacements can be also due to the sliding of the armor layer as a consequence of compaction or loss of support.

Nevertheless, from the point of view of the organism in charge of the port (or terminal), damage is likely to be linked to the economical repercussion caused by the loss of functionality of the breakwater. These consequences are not only associated with the costs from the reparation of the structure if needed, but also with the effects on the activities and goods depending on the sheltering performance of the structure. This global approach [13] to the concept of damage demands monitoring, in prototype, the spatial and temporal evolution of the geometrical variations of the slope. It also requires the previous characterization of the interaction with other failure modes, i.e., developing failure diagrams considering settlements, overtopping rates, and variation of armor layer porosity, among others. In addition, it is necessary to address how the different damage levels might affect the functionality of the structure (operational thresholds) and how the deterioration rate is expected to evolve (structural thresholds).

Losada et al. [14] defined three qualitative damage thresholds, complemented with a fourth one (initiation of destruction) in Vidal et al. [15]:

- Initiation of damage: a certain number of armor units are displaced a distance equal to or larger than a nominal diameter (D_{n50}) from their original position. Holes larger than the average porous size are clearly appreciated, but the functionality of the structure is not compromised.
- Iribarren's damage: the holes are big enough to expose the lower layer of the armor layer, which units start to be susceptible of being extracted. An incipient *S*-profile is developed.
- Initiation of destruction: it is similar to the concept of "initiation of damage" but applied to the lower layer of the armor layer. A small number of units (two or three) in the lower layer are pulled out and the underlayer starts to be exposed to wave action.
- Destruction: the underlayer is exposed to wave action and their units are easily removed. The mound is likely to eventually cease to give the designed level of service.

In Figure 1, a particular interpretation of the four qualitative damage thresholds is presented, based on a set of damage progression experiments carried out at the Harbour Research Laboratory of Universidad Politécnica de Madrid (HRL-UPM):

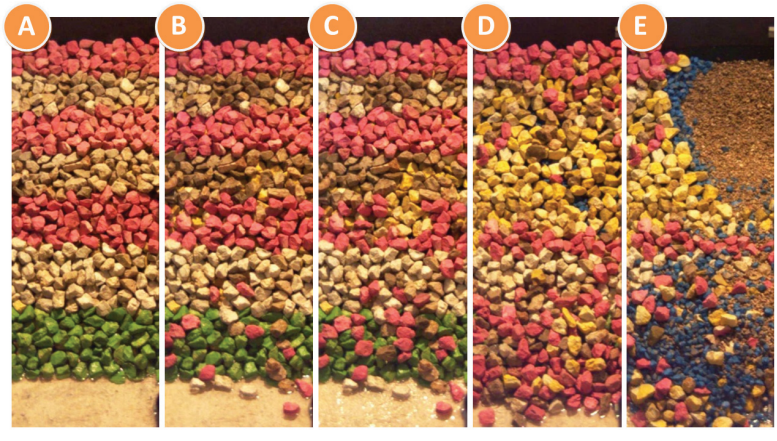

Figure 1. Particular interpretation of the qualitative damage criteria defined in Vidal et al. [15] after a set of damage progression experiments carried out at the HRL-UPM of Madrid, Spain: (**A**) non-damaged section, (**B**) initiation of damage, (**C**) Iribarren's damage, (**D**) initiation of destruction, (**E**) destruction.

As it can be deduced from Figure 1, the interpretation of this damage classification has a certain degree of subjectivity, particularly for the "initiation of damage". Even for quantitative methods,

the dispersion when predicting lower values of damage is higher than for larger values of damage, in relative terms regarding the coefficient of variation. The latter was pointed out by many authors, such as Van Gent et al. [7] or Davies et al. [16], who stated that "*lower damage levels have been seen to exhibit greater experimental variability*".

Vidal et al. [15] stablished the hypothesis that the breakwater remains stable at each damage level if wave action is not increased (except for destruction). However, other authors maintain that damage does not stabilize, but its progression rate is reduced. From a probabilistic point of view, after applying a certain wave energy, the probability of the extraction of armor units when exposed to the same wave energy is associated with the way they are integrated in the granular system: once the pieces with higher probability of being removed are pulled out, there is a lower probability of extraction of new pieces.

The damage criteria of Vidal et al. [15] is based on experience and introduces a useful qualitative description of the armor layer's behavior by characterizing main pseudo static stages in the geometrical evolution of a generic breakwater until destruction. Note that other qualitative damage thresholds might be considered. For instance, the CEM [1] proposed the following three qualitative damage levels:

- Initial damage: few units are displaced, corresponding to the no damage level used in the Shore Protection Manual [17], referred as SPM in the present document.
- Intermediate damage: units are displaced but without causing exposure of the under layer or filter layer to direct wave attack.
- Failure: the under layer or filter layer is exposed to wave attack.

These three levels were re-defined in Almeida et al. [18] on the basis of establishing unified concepts for damage characterization. However, this pseudo static vision is likely to evolve in the near future due to the availability and affordability of the latest technological advances (see Section 2.3), which allow a continuous monitoring of prototypes and small-scale structures. In this way, the generic conceptualization of damage would move on understanding the particular response and requirements of each specific structure. Not only will the dynamic definition of main failure modes be addressed, but also the combinations between them [19] and their impacts on the port economic activities and on the structural integrity during the whole useful life. Probabilistic models based on physical/numerical studies would allow the characterization of breakwater response scenarios and the definition of operational/structural thresholds. The latter, together with the full-scale real time monitoring, would permit the development of ad hoc decision-making tools. This evolution in the conceptualization of damage would presumably be a key factor regarding port design and management inside a global trend demanding optimal conservation strategies for both new and existing structures.

2.2. Damage Parameterization

The parameterization of the reshaping of a rubble mound section is needed for the quantification of the hydraulic instability of armor layers. This is done by the definition of a damage descriptor, which also involves the need to state a concise description about the methodology for measuring and selecting its representative parameters. In Abanades et al. [20], the following properties were recommended for a consistent damage descriptor:

- The descriptor should increase together with breakwater damage, i.e., the damage descriptor should be directly proportional to breakwater damage.
- The descriptor should be dimensionless in order to show no dependence on the scale.
- The descriptor should present a known range of variation, independently of the rubble mound's characteristics, water levels, or type of wave actions.
- The descriptor should be easily interpretable, i.e., it should provide clear information about the qualitative damage level.

In order to fulfill the last requirement, it is necessary to previously characterize the response of the structure, up to the destruction level. Only in this way, it would be possible to link the descriptor

to the qualitative response or damage level. As an example, Vidal et al. [21] proposed relating the dimensionless eroded area, S (see Section 2.2.1), to the qualitative response of a conventional structure (straight slope, two layers, high crest level, and deep water conditions) for different slopes, as shown in Table 1. However, taking into account the wide range of rubble mound designs, armor units' types, and functional requirements, these thresholds are not likely to be applied to every single case. What is more, even for the same breakwater design, the comparison between results from different sources when not applying the same methodology for defining and measuring the damage descriptor might be inconsistent. Indeed, as an example of the variations identified comparing different sources, Table 1 also shows some of the values suggested in Chapter 5 of the Rock Manual [2] regarding the three damage levels from the CEM [1].

Table 1. Thresholds of S for different damage levels for non-overtopped two layers conventional breakwaters according to Vidal et al. [21] and the Rock Manual [2].

	DIMENSIONLESS EROSION AREA (S)						
	Threshold 1		**Threshold 2–3**			**Threshold 4**	
Cot α	Damage Initiation [21]	Start of Damage [2]	Iribarren's damage [21]	Initiation of destruction [21]	Intermediate Damage [2]	Destruction [21]	Failure [2]
1.5	1.5	2	2.5	6.5	3 to 5	12	8
2	2	2	3	8	4 to 6	14	8
3	2.5	2	3.5	9.5	6 to 9	16	12
4	3	3	4	11	8 to 12	18	17

As mentioned before, thanks to the improvements on measuring techniques, this simplified approach based on qualitative damage levels might move on the particular characterization of the whole deterioration rate of each singular structure up to destruction. By modeling this evolution as a random variable [6,22] and monitoring prototypes, breakwater designs together with conservation and maintenance strategies would significantly improve in reliability.

The conceptualization and selection of a damage descriptor can be affected by the available measuring techniques. These techniques, mainly divided into visual approaches and measuring approaches, are summarized in Section 2.3, whereas main damage descriptors up to date are detailed below.

2.2.1. S, Dimensionless Eroded Area

This descriptor is one of the most extended nowadays and it is referred with other terms such as damage parameter, non-dimensional damage level parameter, or dimensionless damage index. It was proposed by Broderick and Ahrens [23] in 1982 and it was used in recognized damage studies [5,24,25]. It is defined as the eroded volume per unit length (see Figure 2), i.e., the cross-sectional eroded area (A_e) divided by the square of the nominal stone diameter (D_{n50}):

$$S = A_e / D_{n50}^2 \quad (1)$$

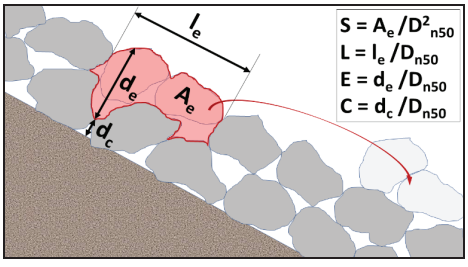

Figure 2. Sketch of a breakwater section with the definition of some damage parameters. Adapted from Melby [26].

A physical description of S is the number of eroded cubic pieces with a side of D_{n50} within a width of one D_{n50}. The actual number of eroded units depends on the porosity, armor grading, and shape of the stones but, according to Van der Meer [24], it is equal to 0.7 to 1 times the value of S.

The interpretation of this descriptor is linked to the size and type of the breakwater. The eroded area was traditionally calculated from a profiler as a comparison with the undamaged profile. Therefore, it is also dependent on the width considered and how the eroded area is averaged. The influence of the width of the test section on mean damage variation was analyzed in Van Gent et al. [7] and Almeida et al. [18], recommending a minimum width of about 25 stones in wave flumes. As shown in Table 1, there are some difficulties when correlating the value of S with qualitative damage criteria. For example, for the initiation of damage, the SPM [17] suggested an erosion of 0% to 5% of the active armor zone (S from 0 to 1.6), Van der Meer [24] considered an erosion of $S = 2$ and Medina [27] aimed for a value of $S = 1$. Medina [27] found that the failure point also differs from different authors.

These shortcomings in the interpretability of S might be due to two main reasons, which are extensible for most of the descriptors detailed herein. The first one is that S is not capable of characterizing the spatial shape of damage, because it represents a mean eroded area on a whole profile, as shown in Figure 3.

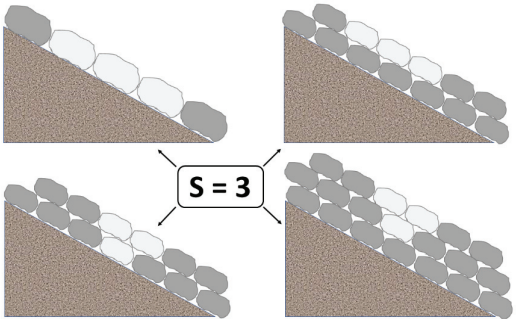

Figure 3. Various possible damage configurations with the same damage descriptor, $S = 3$. Adapted from Davies et al. [16].

The second one is that there is not a concise methodology for measuring and calculating S. On the contrary, profiling techniques, distance between profiles, post-processing strategies (see Section 2.3.2), or error estimations are typically different between publications or, in many cases, are not meticulously defined or not defined at all. What is more, when S is computed from several profiles over a section, the strategy differs from each author: some calculate S from an averaged profile [24], others consider each profile as an independent value of damage [5], and others calculate an averaged magnitude of S from the values of S on each profile [6]. Note that, as detected in Bradbury et al. [28], how damage is

evaluated can lead to differences, especially for the lowest damage indexes (see Figure 4), although they decrease with the increase on damage level.

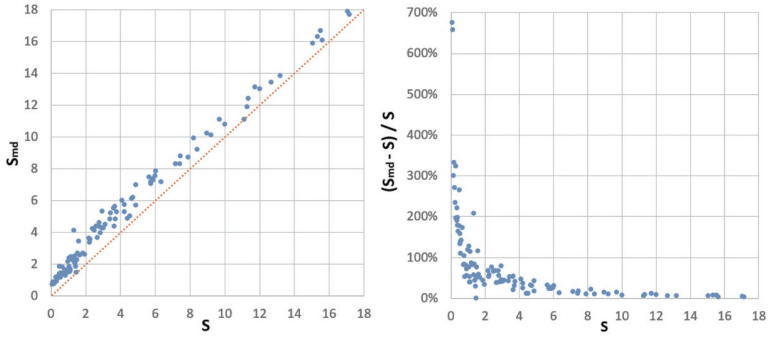

Figure 4. Bias (**left**) and relative error (**right**) between calculating the dimensionless eroded area of a section from an averaged profile (S) or from averaging damage indexes from each profile (S_{md}). Despite, in theory, both options should yield exactly the same results, in this case, the differences seem to be derived from the smoothing method based on cubic splines applied to the profiles: S_{md} is calculated from smoothed profiles, whereas the averaged slope for evaluating S is calculated smoothing the profile resulting from averaging the measurements at each fixed chainage. Figure based on the experimental data of Bradbury et al. [28].

2.2.2. D%, Percentage Volume of Stones Eroded Relative to the Total Volume of Stones in the Active Armor Layer

This is the historical descriptor for characterizing damage from the U.S. Army Engineer Waterways Experimental Station (WES) and it was used in relevant experiments such as the ones from Hudson [29].

In line with the damage descriptor S, the eroded volume was traditionally measured utilizing a profiler. The active armor layer was defined as extending from the middle of the breakwater crest to one zero-damage wave height below the still water level. The complete methodology is described in Melby [26].

By limiting damage to a specific zone, comparison between various structures would be, at first, more direct than using S. Nevertheless, in addition to the shortcomings mentioned for S, in this case, the definition of $D\%$ is also dependent on how the zero-damage is defined and on the crest geometry. The new definition of the active armor layer by the CEM [1] complicates a little more the systematicity of this descriptor, as the active layer is extended to a "reference area", such as the complete armor area or, preferably, a specific zone around the sea water level to be defined for each particular case.

Dealing with the association of $D\%$ with qualitative damage levels, the SPM [17] presented their Table 7.9, original from Jackson [30]. Despite being widely used, this table is limited to regular waves starting from an undamaged structure. Additionally, the CEM [1] in their Table VI-5-21, related this descriptor to the aforementioned three-levels damage classification for rock slopes from 1:2 to 1:3.

2.2.3. S_N, Dimensionless Eroded Area Accounting for Number of Displaced Units

The descriptor S can be re-formulated when visual methods are used, as it was proposed in Davies et al. [16]. The volume eroded from a section of width X can be expressed in terms of the average eroded area ($V_e = A_e \cdot X$), or in terms of the number of displaced armor stones: $V_e = N_d D^3_{n50}/(1-n)$, where N_d is the number of displaced stones and n is the porosity. Combining both terms together with Equation (1), S_N is obtained as follows:

$$S_N = \frac{N_d D_{n50}}{X(1-n)} \quad (2)$$

This descriptor is widely used when unit counting is carried out [31–34]. In Vidal et al. [33], values relating S_N to qualitative damage criteria are provided.

S_N is dependent on the porosity, which is not easy to measure, nor even homogeneous. In addition, the diameter of the stones is also variable and, thus, D_{n50} is likely to be inaccurate for representing the eroded volume for breakwaters armored with stones. In addition, the eroded volume is calculated assuming that the layer thickness is equivalent to the nominal diameter, which is not always the case, as it depends on the shape of the units and the placement method. Therefore, in order to provide comparable results, S_N needs to be calibrated with direct volumetric measurements, for instance, by estimating a correction factor after comparing S_N with S. The same shortcomings of S regarding the characterization of the spatial concentration of damage are also extensible to S_N. In addition, it can be unreliable or directly unfeasible for a high number of removed units. The latter is applicable to all damage descriptors based on unit counting.

2.2.4. $D_{N\%}$, Percentage of Stones Displaced Relative to the Total Number of Stones in the Active Armor Layer

This descriptor is similar to $D\%$ but, in this case, it is based on individual counting of displaced units. It was defined in the SPM [17] and presents the same general shortcomings of $D\%$, because the number of stones within the active zone is dependent on how this zone is defined and on the breakwater geometry.

2.2.5. N_o, Number of Units Displaced out of the Armor Layer within a Strip Width of One Equivalent Cube Length

This descriptor is also based on unit counting and it was firstly introduced by Hedar [35]. It is dependent on the length of the slope and on how the descriptor is considered: individually for each strip, averaged, or taking into account just the maximum value. Van der Meer [24] coined the term N_{od} when referring to displacements and N_{or} for rocking.

2.2.6. N_Δ, Equivalent Number of Spherical Stones

Using a similar profiling methodology than WES's experiments, Thompson and Shuttler [36] calculated the damage number N_Δ as the number of stones in a $9D_{n50}$ wide region of the breakwater, assuming spherical armor shape:

$$N_\Delta = \frac{54\rho_b A_e}{\pi \rho_a D_{50}^2}, \tag{3}$$

where ρ_b is the armor bulk density, A_e is the cross-sectional eroded area, ρ_a is the actual armor density, and D_{50} is the diameter of the stones exceeding the 50% value of the sieve curve. This descriptor gives a rough estimation of the actual number of displaced stones, but presents some shortcomings that reduce its applicability: the measurement of bulk density in prototype might be difficult and D_{n50} is preferable for construction purposes than D_{50}, because it allows the straight consideration of the weight of the stones.

2.2.7. S_t, Dimensionless Eroded Area based on Planar Exposed Area

This damage descriptor was suggested in Vidal et al. [9] and it is based on counting the number of pixels of the planar exposed area, A_{pe}, between two consecutive layers. S_t is calculated from the average transversal eroded area, A_{te}, which is estimated after applying a layer thickness factor, δ, according to the following equation:

$$S_t = \frac{A_{te}}{D_{n50}^2} = \frac{\delta \cdot A_{pe}}{X \cdot D_{n50}}. \tag{4}$$

The correcting factor, δ, depends on the armor characteristics and the angle of the camera with regard to the slope's surface (in case it is not orthogonal). This factor is used for calibrating the descriptor with direct measurements of other damage descriptors, mainly the dimensionless eroded area, S. As an example, Vidal et al. [9] obtained a calibration value of $\delta = 1.58$.

Being derived from a planar exposed area, S_t is only suitable when damage is limited to the outer layer and when there is enough color contrast between the outer layer and the sublayers.

2.2.8. D_e, Equivalent Dimensionless Damage Accounting for Porosity Variation

Rather than being included as an evolutionary parameter within a damage descriptor, porosity is normally assumed to be constant. However, as it was stated by Gómez-Martín and Medina [37], changes in the packing density of cubes may end up with losses in the desired functionality of the structure. This failure mode, named heterogeneous packing (HeP), is related to a serviceability limit state and it was considered in different studies [38–41].

In Gómez-Martín and Medina [38], a virtual net method for visual damage assessment was proposed, together with a damage descriptor considering both HeP and the extraction of armor units. The methodology, proven to be adequate for regular armor units, is based on creating a virtual array over the armor layer in which the porosity is evaluated on each strip of known real dimensions. Individual dimensionless damage (D_i) is calculated for each strip by means of the initial porosity in the strip (p_0), the actual porosity in the strip (p_i), and an integer (d) which represents the number of nominal diameters contained within a strip width. Integrating these values over the slope, the equivalent dimensionless damage (D_e) is obtained as follows:

$$p_i = 1 - \frac{N_d D_{n50}^2}{a \cdot b}, \tag{5}$$

$$D_i = d\left(1 - \frac{1 - p_i}{1 - p_0}\right), \tag{6}$$

$$D_e = \sum D_i. \tag{7}$$

After the detection of the HeP failure mode, the importance of quantifying the randomness in the positioning of concrete armor units was pointed out by Medina et al. [42] and Pardo et al. [43]. They proposed three Armor Randomness Indexes (ARIs) for cubes and Cubipod®, which are calculated from the angles between the armor unit's faces, the slope plane, and the faces of the neighboring armor units. The coefficients *ARI1* and *ARI2* serve to evaluate the face-to-face disposition around a given armor unit.

2.2.9. C, Cover Depth

The minimum remaining depth of the cover layer along a profile (see Figure 2) was defined by Tørum et al. [44] and used by authors such as Davies et al. [16] or Melby and Kobayashi [5]. This descriptor decreases with damage and, thus, it does not accomplish the desired properties of a damage descriptor described before. In addition, Medina and Hudspeth [45] stated that C "*is not a good damage parameter to be selected for practical design applications*" because, even for $C = 0$, the breakwater still preserves significant resistance.

2.2.10. E, Dimensionless Eroded Depth and L, Dimensionless Eroded Length

E and L (see Figure 2) were defined by Melby and Kobayashi [15] after noticing some of the already-mentioned weaknesses in the dimensionless eroded area, S. These descriptors provide information, respectively, about the worst eroded depth and worst eroded length of a section and they are directly proportional to damage increase:

- E is calculated from the maximum eroded depth. It indicates the progress towards failure, especially if failure is defined by the exposure of the underlayer. In line with the descriptor S, the magnitude of E differs from being calculated as a maximum value of a whole section, as a maximum value from an averaged profile or as a mean value from the maximum depths on each profile. In Campos [46], also a mean eroded depth was evaluated by considering the whole eroded volume from a high-resolution 3D mesh measured with a structured light scanner.
- L, which is related to the extension of the damage area, was not directly measured in the experiments from Melby and Kobayashi [15]. However, nowadays its measurement is feasible and affordable with the latest techniques described in Section 2.3.2., offering information about the shape of the holes when combined together with E and S.

Based on applying innovative and accurate measuring techniques and inspired by the descriptors from Melby and Kobayashi [15], Hofland et al. [47] proposed averaging the eroded depth as a stable descriptor less dependent on the breakwater slope. In this case, E is calculated from a moving average applied to the cross-shore direction in 2D cases and over a circular area in 3D cases. Again, this descriptor allows a local identification of damage based on the exposure of the underlayer, although it does not provide information about the horizontal extent of the damage hole. Based on a few examples, Holfland et al. [47] recommended three qualitative damage thresholds regarding E, which were re-analyzed in de Almeida et al. [18]. New 3D descriptors based on modifying the size of the averaging circular area for computing the value of E were explored and analyzed in de Almeida et al. [18] and Van Gent et al. [7].

2.2.11. h_n, Neutral Point between Eroded and Accreted Areas

Despite not being a damage descriptor, an almost constant value of water depth between the eroded and accreted areas was reported by Medina [27]. The neutral water depth was stated to match with $H_{D=0}$, the limit wave height that induces zero damage. This is in line with the indications for defining the "active zone" by the SPM [17]. The neutral point seems to be independent of the damage level and also independent of Iribarren's number. Nevertheless, it is expectable a variation of this parameter together with variations in the water level. Ota et al. [48] also found a constant location of the neural point for revetments, showing no dependence on armor damage level.

2.2.12. Summary of Damage Descriptors

Damage descriptors described in this Section are summarized in Table 2, together with a color code for evaluating the accomplishment of the recommended requirements from Abanades et al. [20]:

- All of them increase with damage, except for the cover depth. For this reason, and also because even for $C = 0$ the breakwater still preserves significant resistance, the cover depth is not a good damage index to be selected for practical design.
- All of them are dimensionless and, therefore, independent of the scale. However, small-scale experiments are subjected to scale effects [49,50], especially taking into account the effect of core porosity on the stability and run-up [51,52] and the potential surface tension scale effects. In addition, the so-called length effect introduced by Van Gent et al. [7] needs to be considered, i.e., damage deviations might be expectable as the width of a real structure is likely to be longer than the scaled width tested on a wave flume. In this sense, damage characterization needs to be extrapolated also to prototypes, typically by monitoring campaigns after storms, in order to increase the accuracy of damage models.
- The range of variation is known for damage descriptors varying from 0 to 100%. For those descriptors with limited available information or with an undefined range of variation, this requirement is classified as not accomplished. Finally, those descriptors in which limit values are found in the literature, but they vary according to each author, are evaluated as partially

accomplished. For instance, different maximum (failure) values of S were given for the same conventional breakwater as shown in Table 1.

- None of them were considered to provide clear information about damage level, i.e., none of them were evaluated as easily interpretable, because their direct extrapolation to qualitative damage criteria seems not to be straightforward. As it was presented in Table 1, even for the same conventional breakwater, there are differences in the magnitudes of S for each qualitative damage criteria. In addition, as shown in Figure 3, many damage configurations can be assigned to the same value for all the descriptors presented. This is due to the fact that none of the descriptors are capable of characterizing the shape and size of damage holes by themselves.

Table 2. Synthesis of damage descriptors and accomplishment of the recommended requirements defined in Abanades et al. (2011) [20].

Requirements of a Damage Descriptor Defined in Abanades et al. (2011) [20]	S	D%	S_N	D_N%	N_o	N_Δ	S_t	D_e	C	E	L
Increase with damage											
Dimensionless											
Known range of variation											
Easily interpretable											

Accomplished | Partially accomplished | Not accomplished

Damage initiation and progression is a 3D process, even for breakwaters tested in a wave flume. The eroded units from a certain profile are not necessarily accreted at the bottom of the same profile, as they could roll down following a non-normal trajectory. In addition, the consequences of the extraction of units concentrated in a deep pocket are different from an extensive superficial removal. The spatial component and shape of damage is, therefore, crucial to understand this failure mode; nevertheless, the available descriptors up to date seem to be mainly focused on measuring an averaged magnitude on a 2D profile. Even damage descriptors derived from visual methods, which are based on a front view of the slope, are averaged over a longitudinal width or over an active region, loosing information such as the planar shape of the eroded area or the number of eroded pockets.

The improvements and availability of accurate 3D measuring techniques and the versatility of artificial vision algorithms give us the chance nowadays to step forward more interpretable damage descriptors or combinations between them. What is more, new strategies might be explored, such as characterizing hole development and progression patterns. Thanks to the advances that can be already implemented for measuring damage (see Section 2.3), it is expectable that the traditional "side view" of profiling methods and the "front view" of visual methods will be combined together for a better characterization of the slope reshaping.

2.3. Damage Measurement

Damage measurement comes after choosing an adequate damage descriptor, but it could also affect how damage is defined due to technical or methodological limitations. Damage after a real or modeled storm is traditionally characterized following two main strategies: a visual approach or a measuring approach. Each of them presents different possibilities and considerations, as described in the following sections.

2.3.1. Visual Approach

This approach is quite common for monitoring real structures although it is not necessarily linked to a damage descriptor. For example, visual surveys in prototypes are usually aimed to obtain a qualitative indication of the condition of a breakwater. Usual surveying activities are locating the development of holes in the armor, identifying the exposure of under-layers, or checking the breakage of armor units or the evolution of cracks in the concrete capping.

The quantification of damage using visual methods is mostly related to counting the number of displaced units. For this purpose, the breakwater condition before and after the storm needs to be visually available with reference points.

In laboratory, a fixed camera, preferably under controlled lighting conditions, is commonly employed for that aim. The image resolution is essential in order not to restrict accuracy. A color coding for the various layers, or even for strips in the same layer, is normally utilized for facilitating the identification of armor movements. The counting process is accomplished by photo overlays or flicker technique. Additionally, semi-automated tools such as the armor tracking software of Holtzhausen et al. [53] can be used. As exposed in Section 2.2, some damage descriptors have their own measuring methodology; this is the case of the virtual net method [37] and the pixel counting method [9]. When combining the simultaneous treatment of all the color channels (RGB) with particle image velocimetry techniques, potential damage areas may be predicted through the identification of the energy dissipation zones at the structure [54].

In prototype, a fixed framing with an adequate point of view is rather unfeasible and, thus, additional resources are needed when accomplishing photographic surveying, such as marine or aerial vehicles. In these cases, the measuring process is less systematic as it depends on the capability of the craft, positioning system, and pilot/captain to set the craft at the desired place. It also depends on the ability of the photographer to spot the required area of interest. In addition, the process of identifying displacements is dependent on the skills of the trained assessor to interpret the visual information, especially when it comes from different campaigns with little matching between photographs.

Visual methods are easy to implement both in small-scale models and in prototype, economical and non-intrusive. They are particularly extended for the characterization of slopes with complex shapes, such as the ones containing special shaped concrete units. However, they present the following shortcomings:

- First of all, they are just suitable for low damage levels. Note that, for a high number of displaced stones, unit counting is likely not to yield accurate results, it could be highly time consuming or it could be directly unfeasible. As a reference, David et al. [16] stated that for more than 50 removed stones, counting was likely to be complicated although it showed good agreement with profiling measurements up to 60–80 removed units. Similarly, Vidal et al. [9] stated that for $S_N > 12$, the counting method was difficult to implement.
- Secondly, most techniques are focused just on the surface, but not on the degree of penetration. This can be partially solved in small scale tests by using a color coding for the different layers. Note that, in laboratory, the whole section can be visually inspected, whereas in prototype this method is just able for the emerged zone.
- Finally, the identification of displacements has a certain degree of subjectivity and expertise. In this sense, the standardization of the inspection process, the use of assisting software, or the concise definition of thresholds for distinguishing between rocking and displacements are some of the issues needed for reproducibility. In order to assess the uncertainty in the identification process, analyzing the information by different trained assessors is recommended.

2.3.2. Measuring Approach

This method is based on the 2D or 3D reconstruction of a profile or section, in which the quantification of damage is usually calculated by means of eroded area/volume regarding a non-damaged section. Note that the construction process induces some "initial damage" when comparing the theoretical shape with the real one and, thus, the characterization of the initial state after construction is mandatory.

There is a wide range of measuring techniques, not always transferable from laboratory to prototype and vice versa. Some of them are described in this Section.

One of the most extended methods for damage measurement in laboratory is profiling several cross sections of the small-scale breakwater. Davies et al. [16] presented a complete description of

the semi-automated profiling strategy used in their experiments and defined two kinds of profilers: electro-mechanical and mechanical profilers. The second ones were used in relevant studies on damage in rubble mound breakwaters [5,24,29,36,55,56]. According to Melby [26], the mechanical profiler usually employed at the WES consists on a rod equipped with a circular foot with a diameter equal to $0.56D_{n50}$. This circular foot not only measures, but also acts like a physical filter, as pockets smaller than its size are neglected. However, due to the physical contact, mechanical profilers are an intrusive technique that could even provoke movements of armor units. Indeed, De Jong [57] reported that some rocks were pushed over a few times during their experiments. Despite being widely extended, it seems that there is not a standardized agreement on how to measure and compute damage, as it was remarked throughout this paper. In addition, there are no references on the optimal accuracy of the profiles or the required number of profiles, i.e., the long-shore distance between chainages and the number of cross sections respectively. For instance, Ahrens [55] measured 6 profiles, Thompson and Shuttler [36] aimed for 10 profiles, and Davies et al. [16] studied 9 profiles. In prototype, Tulsi [58] described the use of crane and ball survey methods, which can be seen as the extrapolation of mechanical profiling to prototype. However, in these cases, the profiles were not measured in the slope direction, but normal to the armor slope. Tulsi also reported that these prototype methods not always yielded accurate results and were highly time-consuming.

While profilers provide information about the 2D geometry, scanning, and photogrammetric methods are capable of measuring the 3D shape of the slope. Nowadays, there are different technologies that might be used for 3D restitutions, such as structured light scanners, infrared scanners, laser scanners, structure from motion (SfM) techniques, or digital stereo photography (DSP). Some of them were also available some years ago, e.g., the LIDAR technology (Laser Imaging Detection And Ranging) was developed in the early 1960's, shortly after the invention of the laser. Nevertheless, they presented limitations in the availability and applicability for damage experiments in laboratory. Some authors, such as Melby [26], considered the possibility of using a laser scanner instead of a mechanical profiler, but rejected this option due to the limitations in the accuracy of the measurements and the post-processing difficulties. Indeed, before 2003 [9], no references of scanning methods in laboratory were found by the authors.

In recent years, new scanning instruments have been developed, together with new generations of post-processing and graphic tools that make easier the generation, treatment, and interpretation of the results. This technological development permits to measure in detail rubble mound slopes with a non-intrusive instrumentation that can be implemented both in small-scale experiments and in prototype. Some examples of the application of the LIDAR technology for measuring damage can be found in Pardo et al. [43], Thomsen et al. [59], or Puente et al. [60], characterizing different types of armor units such as rocks, cubes, and Cubipod®. Regarding techniques based on digital images, Moltisanti et al. [61], worked on the roto-translation tracking of every single accropode of a section using RGB-D cameras. Hofland et al. [47] proposed the DSP technique, applied also by other authors [7,18], which allows high accuracy and fine resolution based on pose estimation, triangulation, and bundle adjustment over a set of digital photographs. In order to avoid possible shadow areas from DSP, Campos et al. [6,46,62] utilized a similar technique based on a structured light scanner for developing a methodology for the probabilistic characterization of damage evolution in rubble mound breakwaters (see Figure 5).

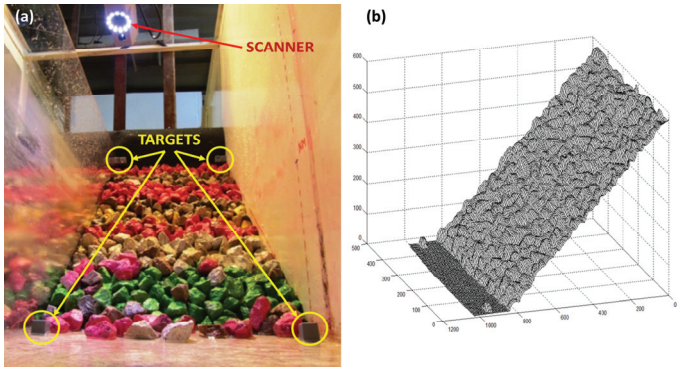

Figure 5. (**a**) Scanning in process (with a structured light scanner) of a drained section as part of damage progression tests carried out at the HRL-UPM of Madrid, Spain; (**b**) Resulting point cloud. Reproduced from Campos [46].

In laboratory, the controlled conditions facilitate the scanning process, whereas in prototype, additional resources are usually needed, typically by means of aircrafts or watercrafts. Airborne LIDAR is probably one of the most extended measuring strategies for real structures, in which the SHOALS method (Scanning Hydrographic Operational Airborne Lidar Survey) from the USACE (United States Army Corps of Engineers), in operation since 1994, is one of the best-known examples.

The recent advent of non-military UAVs (unmanned aerial vehicles), also known as drones or RPAS (remotely piloted aircraft system), for consumer and commercial use has opened the door to photogrammetric techniques for reconstructing the 3D surfaces of breakwaters, such as the SfM technique. For that purpose, overlapped imagery is captured with a camera mounted on a gimbal and further parameters, such as the 3D position for each photograph, are acquired by the drone. The surface reconstruction is carried out afterwards, enhancing the results with surveyed ground control points. One of the main advantages of this novel technique is its affordability. As shown in Figure 6, it has been already applied for photogrammetric restitutions of breakwaters with accurate results.

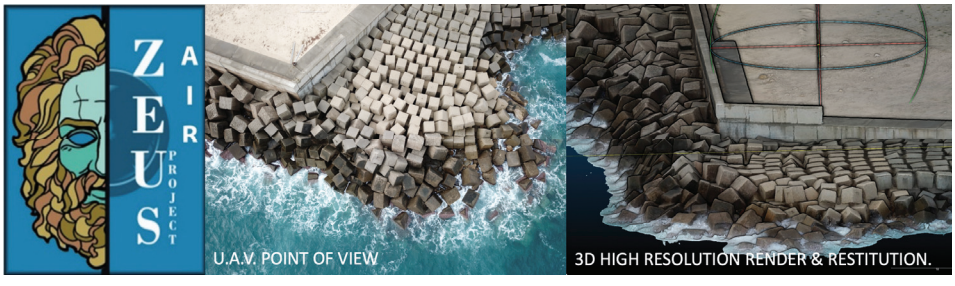

Figure 6. Image from a RPAS (remotely piloted aircraft system) equipped with a digital camera and photogrammetric restitution of a section of the breakwater of Carboneras, Almería (Spain). Source: ZEUSair Project / SAMOA II Overtopping Project [63].

According to Phelp and Zwamborn [64], at least one third of the "active zone" is not properly monitored when using aerial photography. Based on this, a factor of 1.5 is suggested to get a better approximation of total damage from the information recorded above water. Some of the techniques, such as LIDAR, have, nevertheless, a certain degree of penetration underwater and, thus, the 1.5 factor is just a broad approximation.

In order to characterize the submerged part of the breakwater in laboratory, water is usually drained out. In prototype, sounding methods are available for that aim, such as side-scan sonar or multi-beam echo soundings, which are relatively common for bathymetric restitutions. These methods, however, are not adequate in laboratory as the confined study area induces significant sound wave reflection and noise.

The different measuring techniques can be combined together for double checking or for obtaining seamless data of the whole section, including the emerged part, intertidal zone, and submerged part. As an example, Tulsi [58] proposed the characterization of the whole 3D surface of a real dolos breakwater, for damage survey purposes, by using a dual measuring method mounted on a boat. It consisted of a LIDAR scanner for the terrestrial mapping together with a multi-beam echo sounder for the submerged part.

The measuring approach requires, regardless of the technique employed, several post-processing strategies that are likely to affect the quantification of the eroded volume. Generally speaking, the following aspects need to be specified for reproducibility:

- Methods for identifying and filtering erroneous values in the raw data.
- Profile/surface reconstruction methods (such as interpolation, fitting, or meshing), including incomplete data reconstruction strategies [65].
- Smoothing methods when applied.
- Methods for filtering possible settlements, so as the geometrical characterization actually refers to the gaps caused by the displacements of armor units. In addition, methods for neglecting or classifying rocking might be of interest.
- Methods for integrating the eroded area/volume (such as the Simpson's method), for which correcting methods based on a balance between the eroded and the accreted area/volume can be considered. When using correcting methods, note that the porosity of the accreted volume might differ from the one derived from the construction process. Additionally, when applying them to the cross-sectional area, note that armor units' movements are not necessarily gathered within the profile axis.
- Finally, the basis for the calculation of the damage descriptor need to be unequivocal.

Measuring methods can be economically more demanding than visual methods but, on the other hand, they provide more accurate information and are able for any damage level, up to destruction. Some techniques, such as profiling, offer just a partial characterization of the surface, whereas others, such as scanning, collect the complete visible geometry. They also present the advantage of being independent of the subjectivity in the identification of displacements, although the quantification of the eroded volume can be affected by the measuring technique chosen, the data acquisition procedures and the post-processing strategies.

It is expectable that damage measurement will be common in prototype in the near future. In this sense, the complete methodology for its characterization, preferably transferable from laboratory to prototype and vice versa, needs to be defined in detail. Standard methodologies will foster the generation of comparable results and the possibility to monitor prototypes under the same basis.

3. Conclusions and Future Research

In many countries around the world, a strong economical effort in the construction of coastal infrastructures has already been faced. This, together with the expected modifications in the sea level and met-ocean conditions due to climate change, encourage the coastal engineering community towards the development of reliable risk management and decision-making tools. Taking into account the complexity and peculiarity of each harbor, initiatives such as Algeciras SAFEPORT [66] or Algeciras BRAINPORT [67] have dealt with this challenge by joining together all data sources associated with the port inside a big data platform. Data sources include, for instance, densified instrumental records, numerical predictions over a detailed meshing, and operational thresholds. Based on this platform,

user-oriented interfaces were developed for a custom provision of the information and for improving collaboration and synergies among the whole port and logistics community.

In this context, it is expectable that the evolution in the concept of damage discussed in the present paper would be linked to the development of hybrid monitoring systems [68] together with virtual interfaces [69] in which all the collected information is adequately disposed for the user. These hybrid systems would require, on the one hand, the probabilistic characterization of the damage progression curve of each section [22] and how it is associated with other failure modes. In this way, depending on the functional requirements and the response of the structure, different operational and structural thresholds can be particularized for each case. On the other hand, damage models would need to be validated and enhanced by monitoring prototypes.

To accomplish this, as recursively reported by different authors, one of the pending challenges of the parameterization and measurement of damage is the standardization of procedures both in laboratory and prototype. This is needed for characterizing damage dispersion by repeating the experiments inside the same laboratory, for assimilating data from different laboratories, and for fostering an adequate monitoring of real structures. In this way, a gradually increasing data base with normalized results could be generated as a reference for similar structures. As suggested within the present paper, a standardized methodology would need to take into account, at least, the following considerations:

- Firstly, the damage descriptor should increase together with breakwater damage, should be easily interpretable, should be dimensionless, and should present a known rank of variation. The review of main damage descriptors highlights the importance of unequivocally defining how its different parameters are meant to be computed.
- Secondly, all factors involved in the data acquisition process should be specified, including the characteristics and settings of the measuring instruments. Depending on how damage is planned to be characterized, acquired data would mainly consists of images, videos, profiles, point clouds, or meshes and should be adequately identified temporally and spatially. In addition, in order to estimate the error derived from the measuring process and surface reconstruction, several repetitions of the same measured section may be compared, as recommended by Medina and Hudspeth [45].
- Specifically, for small-scale experiments, an additional review on all the aspects that could condition the reproducibility of the results should be faced [46]. According to Clavero et al. [12], three issues are relevant for assimilating data from different sources: (1) the wave generation curve and the experimental space at the breakwater toe, (2) the location in the wave flume and the geometric scale of the models, and (3) the forcing sequence based on the increasing wave energy steps.
- Finally, post-processing strategies need to be detailed. This includes (1) criteria for distinguishing between rocking movements and displacements, (2) filtering methods for erroneous values, settlements or rocking, (3) smoothing strategies when applied, (4) surface reconstruction methods, and (5) methods for integrating the eroded volume, possibly including erosion/accretion balance methods.

Author Contributions: Conceptualization: C.C. and R.M.-S.; investigation: Á.C.; resources: C.C. and R.M.-S.; writing—original draft preparation: Á.C.; writing—review and editing: Á.C., C.C. and R.M.-S.; visualization: Á.C., C.C. and R.M.-S.; supervision: C.C. and R.M.-S.; project administration: C.C. and R.M.-S.; funding acquisition: C.C. and R.M.-S. All authors have read and agreed to the published version of the manuscript.

Funding: This research was funded by the Spanish Ministry of Science and Innovation under the project BIA2009-10483 and the grant BES-2010-034048.

Acknowledgments: The authors are indebted to Cátedra Pablo Bueno for partial support.

Conflicts of Interest: The authors declare no conflict of interest.

References

1. United States Army Corps of Engineers. *Coastal Engineering Manual, EM 110-2-1100 (Part VI) Change 3 (28 September 2011)*; USACE: Washington, DC, USA, 2002.
2. Construction Industry Research and Information Association. *The Rock Manual. The Use of Rock in Hydraulic Engineering*, 2nd ed.; CIRIA: London, UK, 2007.
3. Campos, A.; Castillo, C.; Molina, R. Damage in Rubble Mound Breakwaters. Part I: Historical Review of Damage Models. *J. Mar. Sci. Eng.* **2020**, in press.
4. Carver, R.D.; Wright, B.J. *Investigation of Wave Grouping Effects on the Stability of Stone-Armored, Rubble-Mound Breakwaters*; U.S. Army Engineer Waterways Experiment Station: Vicksburg, MS, USA, 1991.
5. Melby, J.A.; Kobayashi, N. Damage Progression and Variability on Breakwater Trunks. In Proceedings of the International Conference Coastal Structures '99, Santander, Spain, 7–10 June 1999; Volume 1, pp. 309–315.
6. Campos, A.; Castillo, C.; Molina, R. Analysis of the Influence of the Different Variables Involved in a Damage Progression Probability Model. In Proceedings of the 34th International Conference on Coastal Engineering, Seoul, Korea, 15–20 June 2014.
7. van Gent, M.; de Almeida, E.; Hofland, B. Statistical Analysis of the Stability of Rock Slopes. *J. Mar. Sci. Eng.* **2019**, *7*, 60. [CrossRef]
8. Marzeddu, A.; Oliveira, T.C.A.; Sánchez-Arcilla, A.; Gironella, X. Effect of Wave Storm Representation on Damage Measurements of Breakwaters. *Ocean Eng.* **2020**, *200*, 107082. [CrossRef]
9. Vidal, C.; Martin, F.; Negro, V.; Gironella, X.; Madrigal, B.; García-Palacios, J. Measurement of Armor Damage on Rubble Mound Structures: Comparison between Different Methodologies. *Coast. Struct.* **2003**, 189–200.
10. van Gent, M.R.A.; van den Boogaard, H.F.P.; Pozueta, B.; Medina, J.R. Neural Network Modelling of Wave Overtopping at Coastal Structures. *Coast. Eng.* **2007**, *54*, 586–593. [CrossRef]
11. Allsop, N.; Cork, R.; Henk Jan Verhagen, I. A Database of Major Breakwaters around the World. In Proceedings of the ICE Breakwaters Conference, Edinburgh, UK, 16–18 September 2009.
12. Clavero, M.; Díaz-Carrasco, P.; Losada, M.Á. Bulk Wave Dissipation in the Armor Layer of Slope Rock and Cube Armored Breakwaters. *J. Mar. Sci. Eng.* **2020**, *8*, 152. [CrossRef]
13. Gómez, R.; Molina, R.; Castillo, C.; Rodríguez, I.; López, J.D. *Conceptos y Herramientas Probabilísticas Para El Cálculo Del Riesgo En El Ámbito Portuario*; Puertos del Estado: Madrid, Spain, 2018.
14. Losada, M.A.; Desire, J.M.; Alejo, L.M. Stability of Blocks as Breakwater Armor Units. *J. Struct. Eng.* **1986**, *112*, 2392–2401. [CrossRef]
15. Vidal, C.; Losada, M.; Medina, R. Stability of Mound Breakwater's Head and Trunk. *J. Waterw. Port Coast. Ocean Eng.* **1991**, *117*, 570–587. [CrossRef]
16. Davies, M.H.; Mansard, E.P.D.; Cornett, A.M. Damage Analysis for Rubble-Mound Breakwaters. In Proceedings of the 24th International Conference on Coastal Engineering, Kobe, Japan, 23–28 October 1994; Volume 1, pp. 1001–1015.
17. USACE. *Shore Protection Manual*, 4th ed.; U.S. Army Engineer Waterways Experiment Station, U.S. Government Printing Office: Washington, DC, USA, 1984.
18. de Almeida, E.; van Gent, M.R.A.; Hofland, B. Damage Characterization of Rock Slopes. *J. Mar. Sci. Eng.* **2019**, *7*, 10. [CrossRef]
19. Campos, A.; Castillo, C.; Molina, R. Optimizing Breakwater Design Considering the System of Failure Modes. In Proceedings of the 32nd International Conference on Coastal Engineering, Shanghai, China, 30 June–5 July 2010.
20. Abanades, J.; Gómez, R.; Castillo, C.; Molina, R. Revisión Histórica de Las Variables y Modelos de Evolución de Daño En Diques En Talud y Su Adecuación Al Estudio Del Fenómeno. In Proceedings of the XI Jornadas Españolas de Costas y Puertos, Las Palmas, Spain, 5 May 2011.
21. Vidal, C.; Losada, M.A.; Medina, R.; Losada, I. Análisis de La Estabilidad de Diques Rompeolas. *Diques Rompeolas* **1994**, *1*, 17–34. [CrossRef]
22. Castillo, C.; Castillo, E.; Fernández-Canteli, A.; Molina, R.; Gómez, R. Stochastic Model for Damage Accumulation in Rubble-Mound Breakwaters Based on Compatibility Conditions and the Central Limit Theorem. *J. Waterw. Port Coast. Ocean Eng.* **2012**, *138*, 451–463. [CrossRef]
23. Broderick, L.; Ahrens, J.P. *Riprap Stability Scale Effects, Technical Report TP 82-3*; ASCE: Reston, VA, USA, 1982.

24. Van Der Meer, J.W. Rock Slopes and Gravel Beaches under Wave Attack. Ph.D. Thesis, Delft Technical University, Deltf, The Netherlands, 1988.
25. van Gent, M.; Smale, A.; Kuiper, C. Stability of Rock Slopes with Shallow Foreshores. *Coast. Struct.* **2003**, 100–112. [CrossRef]
26. Melby, J.A. *Damage Progression on Rubble-Mound Breakwaters, Technical Report CHL-99-17*; US Army Corps of Engineers, Waterways Experiment Station: Vicksburg, MS, USA, 1999.
27. Medina, J.R. Robust Armor Design to Face Uncertainties. In Proceedings of the 23rd International Conference on Coastal Engineering, Venice, Italy, 4–9 October 1992; Volume 2, pp. 1371–1384.
28. Bradbury, A.P.; Allsop, N.W.H.; Latham, J.P.; Mannion, M.B.; Poole, A.B. *Rock Armour for Rubble Mound Breakwaters, Sea Walls and Revetments: Recent Progress, Report SR 150*; Hydraulics Research: Wallingford, UK, 1988.
29. Hudson, R.Y. Laboratory Investigation of Rubble-Mound Breakwaters. *J. Waterw. Harb. Div. ASCE* **1959**, *85*, 93–121.
30. Jackson, R.A. *Limiting Heights of Breaking and Nonbreaking Waves on Rubble Mound Breakwaters, Technical Report H-68-3*; U.S. Army Engineer Waterways Experiment Station: Vicksburg, MI, USA, 1968.
31. Teisson, C. Statistical Approach of Duration of Extreme Storms: Consequences on Breakwater Damages. In Proceedings of the 22nd International Conference on Coastal Engineering, Delft, The Netherlands, 2–6 July 1990; pp. 1851–1860.
32. Cornett, A.M. A Study of Wave-Induced Forcing and Damage of Rock Armour on Rubble-Mound Breakwaters. Ph.D. Thesis, University of British Columbia, Vancouver, BC, Canada, 1995.
33. Vidal, C.; Losada, M.; Mansard, E. Stability of Low-Crested Rubble-Mound Breakwater Heads. *J. Waterw. Port Coast. Ocean Eng.* **1995**, *121*, 114–122. [CrossRef]
34. Burcharth, H.F.; Kramer, M.; Lamberti, A.; Zanuttigh, B. Structural Stability of Detached Low Crested Breakwaters. *Coast. Eng.* **2006**, *53*, 381–394. [CrossRef]
35. Hedar, P.A. Stability of Rock-Fill Breakwaters. Ph.D. Thesis, University of Goteborg, Gothenburg, Sweden, 1960.
36. Thompson, D.M.; Shuttler, R.M. *Riprap Design for Wind-Wave Attack, a Laboratory Study in Random Waves, Report No. EX 707*; Hydraulics Research: Wallingford, UK, 1975.
37. Gómez-Martín, M.E.; Medina, J.R. Wave-to-Wave Exponential Estimation of Armor Damage. In Proceedings of the 29th International Conference on Coastal Engineering, Lisbon, Portugal, 19–24 September 2004; pp. 3592–3604.
38. Gómez-Martín, M.E.; Medina, J.R. Damage Progression on Cube Armored Breakwaters. In Proceedings of the 30th International Conference on Coastal Engineering, San Diego, CA, USA, 3–8 September 2006; pp. 5229–5240.
39. Medina, J.R.; Molines, J.; Gómez-Martín, M.E. Influence of Armour Porosity on the Hydraulic Stability of Cube Armour Layers. *Ocean Eng.* **2014**, *88*, 289–297. [CrossRef]
40. Gómez-Martín, M.; Herrera, M.; Gonzalez-Escriva, J.; Medina, J. Cubipod® Armor Design in Depth-Limited Regular Wave-Breaking Conditions. *J. Mar. Sci. Eng.* **2018**, *6*, 150. [CrossRef]
41. Argente, G.; Gómez-Martín, M.; Medina, J. Hydraulic Stability of the Armor Layer of Overtopped Breakwaters. *J. Mar. Sci. Eng.* **2018**, *6*, 143. [CrossRef]
42. Medina, J.R.; Gómez-Martín, M.E.; Corredor, A. Armor Unit Placement, Randomness and Porosity of Cube and Cubipod Armor Layers. In Proceedings of the Coastal Structures, Yokohama, Japan, 6–8 September 2011; pp. 743–754.
43. Pardo, V.; Herrera, M.P.; Molines, J.; Medina, J.R. Placement Test, Porosity, and Randomness of Cube and Cubipod Armor Layers. *J. Waterw. Port Coast. Ocean Eng.* **2013**, *140*, 04014017. [CrossRef]
44. Tørum, A.; Mathiesen, B.; Escutia, R. Reliability of Breakwater Model Tests. In Proceedings of the Coastal Structures, Washington, DC, USA, 14–16 March 1979; pp. 454–469.
45. Medina, J.; Hudspeth, R. Discussion about the Article from Melby, J.A., Kobayashi, N. Progression and Variability of Damage on Rubble Mound Breakwaters. *J. Waterw. Port Coast. Ocean Eng.* **2000**, *126*, 268–272. [CrossRef]
46. Campos, A. A Methodology for the Analysis of Damage Progression in Rubble Mound Breakwaters. Ph.D. Thesis, Universidad de Castilla-La Mancha, Ciudad Real, Spain, 2016.

47. Hofland, B.; Gent, M.V.; Raaijmakers, T.; Liefhebber, F. Damage Evaluation Using the Damage Depth. In Proceedings of the Coastal Structures, Yokohama, Japan, 5–9 September 2011; pp. 812–823.
48. Ota, T.; Matsumi, Y.; Hirayama, T.; Kimura, A. Models for Profile Change of Rubble Mound Revetment and Profile Evaluation. In Proceedings of the 32nd International Conference on Coastal Engineering, Shanghai, China, 30 June–5 July 2010.
49. Hughes, S.A. *Physical Models and Laboratory Techniques in Coastal Engineering*; World Scientific Publishing Company Incorporated: Hackensack, NJ, USA, 1993; Volume 7.
50. Tirindelli, M.; Lamberti, A.; Paphitis, D.; Collins, M.; Vidal, C.; Hawkins, S.; Moschella, P.; Burcharth, H.; Sanchez-Arcilla, A. *Wave Action on Rubble Mound Breakwaters: The Problem of Scale Effects, Delos Report D52*; Hydraulic Engineering Reports; University of Bologna: Bologna, Italy, 2004.
51. Hegde, A.V.; Srinivas, R.P. Effect of Core Porosity on Stability and Run-up of Breakwaters. *Ocean Eng.* **1995**, *22*, 519–526. [CrossRef]
52. Burcharth, H.F.; Liu, Z.; Troch, P. Scaling of Core Material in Rubble Mound Breakwater Model Tests. In Proceedings of the 5th International Conference on Coastal and Port Engineering in Developing Countries, COPEDEC V, Cape Town, South Africa, 19–23 April 1999; pp. 1518–1528.
53. Holtzhausen, A.H.; Retief, G.D.F.; Zwamborn, J.A. Physical Modelling of Dolos Breakwaters: The Coega Results and Historical Perspective. In Proceedings of the 27th International Conference on Coastal Engineering, Sydney, Australia, 16–21 July 2000; Volume 276, pp. 1536–1549.
54. Molina, R.; Moyano, J.M.; Ortega-Sánchez, M.; Losada, M.A. Analysis of the Wave Interaction with a Rouble Mound Breakwater Using Video Imagery Techniques. In Proceedings of the Mediterranean Days PIANC, Palermo, Italia, 7–9 October 2008. PIANC.
55. Ahrens, J.P. *Large Wave Tank Tests of Riprap Stability*; U.S. Army Engineer Waterways Experiment Station CERC: Vicksburg, MS, USA, 1975.
56. Broderick, L. Riprap Stability, a Progress Report. In *Coast. Struct*; ASCE: Reston, VA, USA, 1983; pp. 320–330.
57. De Jong, W. Experimental Research on the Stability of the Armour and Secondary Layer in a Single Layered Tetrapod Breakwater. Ph.D. Thesis, TU Delft, Delft, The Netherlands, 2003.
58. Tulsi, K. Three-Dimensional Method for Monitoring Damage to Dolos Breakwaters. Ph.D. Thesis, Stellenbosch University, Stellenbosch, South Africa, 2016.
59. Thomsen, J.B.; Røge, M.S.; Christensen, N.F.; Andersen, T.L.; Van Der Meer, J.W. Stability of Hardly Reshaping Berm Breakwaters Exposed to Long Waves. In Proceedings of the 34th International Conference on Coastal Engineering, Seoul, Korea, 15–20 June 2014.
60. Puente, I.; Sande, J.; González-Jorge, H.; Peña-González, E.; Maciñeira, E.; Martínez-Sánchez, J.; Arias, P. Novel Image Analysis App.roach to the Terrestrial LiDAR Monitoring of Damage in Rubble Mound Breakwaters. *Ocean Eng.* **2014**, *91*, 273–280. [CrossRef]
61. Moltisanti, D.; Farinella, G.M.; Musumeci, R.E.; Foti, E.; Battiato, S. Monitoring Accropodes Breakwaters Using RGB-D Cameras. In Proceedings of the VISAPP 2015-10th International Conference on Computer Vision Theory and Applications, Berlin, Germany, 11–14 March 2015; Volume 1, pp. 76–83.
62. Campos, Á.; Molina-Sanchez, R.; Castillo, C. Damage in Rubble Mound Breakwaters. New Advances in the Calibration of a Damage Progression Probability Model . In Proceedings of the 7th International Conference on Physical Modelling in Coastal Science and Engineering (CoastLab), Santander, Spain, 22–26 May 2018.
63. Rodríguez, B.; Díaz-Hernández, G.; López-Lara, J.; Tomás, A.; Álvarez de Eulate, M.F.; Medina, R.; Álvarez-Fanjul, E.; Pérez-Gómez, B.; García-Valdecasas, J.M. Proyecto SAMOA-2: Módulos de Agitación, Ondas Largas y Rebase, Descripción General (in Spanish). In Proceedings of the XV Jornadas Españolas de Ingeniería de Costas y Puertos, Malaga, Spain, 8–9 May 2019.
64. Phelp, D.; Zwamborn, J.A. Correlation between Model and Prototype Damage of Dolos Breakwater Armouring. In Proceedings of the 27th International Conference on Coastal Engineering, Sydney, Australia, 16–21 July 2000; Volume 276.
65. Esposito, M.B.; Díaz-Vilariño, L.; Martínez-Sánchez, J.; González -Jorge, H.; Arias, P. 3D Reconstruction of Cubic Armoured Rubble Mound Breakwaters from Incomplete Lidar Data. *Int. J. Remote Sens.* **2015**, *36*, 5485–5503. [CrossRef]
66. Molina, R.; Rodríguez-Rubio, P.; Carmona, M.Á.; De los Santos, F.J. *Guía Para La Aplicación de Un Sistema de Gestión de Riesgos Océano-Meteorológicos En El Ámbito Portuario y Su Evaluación: Certificación de Puerto Seguro Océano-Meteorológico*; Autoridad Portuaria Bahía de Algeciras: Cádiz, Spain, 2017.

67. Pernia, O.; De los Santos, F. Digital Ports: The Evolving Role of Port Authorities. *Mega-sh. Issue PTI J.* **2016**, *69*, 3032.
68. Pereira, M.; Teodoro, A.C.; Veloso-Gomes, F.; Lima, J.; Oliveira, S. Port Infrastructure Control (Madeira Island, Portugal) through a Hybrid Monitoring System (GNSS and Accelerometers). *Mar. Georesour. Geotechnol.* **2016**, *34*, 617–629. [CrossRef]
69. Marujo, N.; Trigo-Teixeira, A.; Sanches-Valle, A.; Araújo, A.; Caldeira, J. A New Methodology for Breakwater Damage Assessment and Its Implementation on a WebGIS. In Proceedings of the 34th International Conference on Coastal Engineering, Seoul, Korea, 15–20 June 2014.

Journal of
Marine Science and Engineering

MDPI

Article

Study of Current- and Wave-Induced Sediment Transport in the Nowshahr Port Entrance Channel by Using Numerical Modeling and Field Measurements

Ayyuob Mahmoodi [1], Mir Ahmad Lashteh Neshaei [2,*], Abbas Mansouri [3] and Mahmood Shafai Bejestan [4]

[1] Department of Civil Engineering, Islamic Azad University, Central Tehran Branch, Tehran 1584743311, Iran; mahmoodi.pmo@gmail.com
[2] Department of Civil Engineering, University of Guilan, Guilan 4199613765, Iran
[3] Department of Civil Engineering, Islamic Azad University South Branch, Teheran 1584743311, Iran; abbas_mansoori2000@yahoo.com
[4] School of Water Science and Engineering, Shahid Chamran University of Ahvaz, Ahvaz 6135783151, Iran; m_shafai@yahoo.com
* Correspondence: maln@guilan.ac.ir; Tel.: +98-133-3690-274

Received: 29 January 2020; Accepted: 8 April 2020; Published: 15 April 2020

Abstract: The Nowshahr port in the southern coastlines of the Caspian Sea is among the oldest northern ports of Iran, first commissioned in the year 1939. In recent years, this port has been faced with severe sedimentation issues in and around its entrance that has had negative impacts on the operability of the port. The present study aims at identifying major reasons for severe sedimentation in the port entrance. First, field measurements were evaluated to gain an in-depth view of the hydrodynamics of the study area. Numerical models then were calibrated and validated against existing field measurements. Results of numerical modeling indicated that wind-induced current is dominant in the Caspian Sea. The numerical results also indicated that in the case of an eastward current direction, the interaction between current and the western breakwater arm would lead to the formation of a separation zone and a recirculation zone to the east of the port entrance region. This eddying circulation could transport suspend settled sediments from eastern shoreline towards the port entrance and its access channel. The results of this paper are mostly based on the study of current patterns around the port in the storm conditions incorporate with the identification of sediment sources.

Keywords: Nowshahr port; field measurements; numerical simulation; wave; current; sediment transport

1. Introduction

The study of sedimentation in the entrance channel and basin of ports is of significant importance. This is because excessive sedimentation can result in a reduction in economic activities and can impact the overall operability of the port. Also, with the construction of coastal structures such as ports and with potential interference with longshore sediment transport patterns, the study of coastline changes due to accretion and erosion and subsequent loss of land in the hinterland area of port becomes of greater importance. Therefore, proper identification of sources of sediment supply and dominant transport patterns is of significant importance in determining long-term status of the port and all the operational expenditures required to keep the economic functioning of the port [1].

Nowshahr port is among the oldest and most active ports situated along the southern coastline of the Caspian Sea. This port is located in the north of Iran at the longitude of 51 32′ E and latitude of 36 39′ N. The location of this port along the southern coastline of the Caspian Sea is shown in Figure 1.

Figure 1. Position of Nowshahr port along the southern coastline of the Caspian Sea.

Construction of Nowshahr port started in the year 1930 and commissioned in the year 1939. Since then, the port has been continuously operational. Several changes have occurred throughout the past years in Nowshahr port. Figure 2 shows the initial layout and positioning of the port. As evident in this figure, the westward areas of the port faced severe sedimentation while eastward areas were dominated by coastal erosion. This is an indication of dominant eastward (west to east) direction of sediment transport which would then result in an accretion of sediments to the west of coastal structures and erosion of coastline to the east of them, consistent with existing literature on this subject matter [2].

Figure 2. The initial layout of Nowshahr port (aerial picture is taken around 1952).

Throughout the 50 years after its initial construction, the port has faced an unwanted wave agitation problem inside the port basin. The sedimentation issue was rather less important throughout the same period in this port. In the year 1989, it was decided that for reduction of wave height inside

the basin, the western arm of breakwater shall increase in length by 300 m. Also due to lack of required hinterland, a land reclamation project was conducted in the eastern part of the port in two different stages. Figure 3 shows various changes that have taken place in port layout in the past years including land reclamation in the eastern part of lee breakwater and changes in the western arm of breakwater (main breakwater).

Figure 3. Changes in Nowshahr port layout since the year 1989 until now. Commission year: Initial layout in 1939, main breakwater extension in 1996, and reclamation land in 2012.

The port throughout its operational lifetime has faced severe sedimentation problems and a decrease in water draft depth on its entrance channel. As a result, the basin and entrance channel of Nowshahr port has been dredged multiple times since 1988. The problem of sedimentation has been exacerbated in recent years such that regular annual dredging of up to 300,000 m^3 in the entrance channel is required for the port to continue its operation. Variation and gradual reduction in the Caspian Sea water level, lengthening of the main breakwater, land reclamation in the eastern parts and increase of sediment supply from rivers are among the reasons why Nowshahr port is faced with severe sedimentation problem [3]. This problem can be related to the positioning and layout of the basin and its entrance location [4]. There are numerous worldwide examples of studying sedimentation problems arising from similar factors in the port basin and ways of mitigating its unwanted effects [5–11].

Generally, past studies focusing on the issue of excessive sedimentation in Nowshahr port are rather limited. These studies are either in the form of conference proceedings [3,12–15] or consulting engineer reports [16,17]. It is thus concluded that an in-depth knowledge of sources of sediment supply and hydrodynamics of the study area affecting sediment movement patterns is still lacking. The main purpose of this study is to investigate the long-term problem of sedimentation in Nowshahr port and provide a comprehensive view of the hydrodynamics of the study area and sediment transport patterns.

Measurement of various parameters such as wave height, current speed, water level variation and sedimentation in areas surrounding Nowshahr port will be used in this study in order to investigate the effects of these parameters on sediment supply in the region of interest. The circulation patterns and major hydrodynamic features of the study area will first be investigated through the analysis of existing field measurements. This will be supplemented with the usage of a well-calibrated and validated numerical model to provide additional sources of data in identifying dominant sediment transport patterns in the study area. The present study aims at providing beneficial data for the

researchers and engineers to discuss the solutions for the issue of sedimentation in the access channel and basin of Nowshahr port.

2. Materials and Methods

The required field measurements for the study of sedimentation in the area surrounding the port include hydrodynamic parameters such as wave, coastal wind, sea currents and also general sediment properties. As the field measurements are generally expensive, availability and distribution of these data is usually limited to few points around the port. Another source of data for the studies can be derived from numerical models that have been calibrated and validated using existing field measurements [18–20]. In the present study, both of the above mentioned sources of data were used for investigation of sedimentation in Nowshahr port.

2.1. Existing Field Measurements

In this section, various sources of field measurements used in the present study will be described. The circulation of the Caspian Sea is largely controlled by the variation of the wind field and also the variation of bottom friction in near-shore areas. The tidal effects are almost negligible in this closed lake. In the coastal zone, wave breaking also makes coastal longshore currents which are one the most effective factors for sediment transport along the shores. These waves also derived by strong winds. Therefore, at first existing data on wind parameters in this region is presented. It has then proceeded with other data sources including other existing hydrographic measurements such as wave and currents and coastal and river sediment properties. The same data sources will be used for model calibration and validation.

2.1.1. Measurements of Local Wind

As mentioned earlier, one of the most important parameters of the current model is the wind field. There are various wind data sources available for the study area such as satellite observations and numerical weather research models. One of the sources of wind data available for the Caspian Sea is the results of the Weather Research Forecast (WRF) model which was previously used in the "Monitoring and Modeling Study of Northern Coasts of IRAN" project. This model is usually considered to provide the most accurate wind field data [21]. This dataset consists of the 1-hourly wind data from 1983–2013 with a spatial resolution of $0.1° \times 0.1°$. The comparisons of these wind data with the measurements near the study area have shown that the WRF wind field is the most accurate representation of the region's wind field (compared to other wind fields such as QuikSCAT or ECMWF) [21]. Hence, this wind data is used as the input wind for forcing the numerical model. Figure 4 shows the wind rose in the Nowshahr port based on WRF wind data.

According to Figure 4, wind rose is dominated with two main directions of winds, namely the easterlies and westerlies that blow parallel to the coastline. The maximum westerly wind speed reaches 25 ms^{-1}. Roughly 55 percent of time, calm conditions (wind speed less than 3 ms^{-1}) prevails.

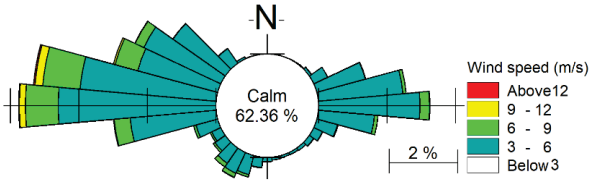

Figure 4. Thirty-one-year wind rose derived from the Weather Research Forecast (WRF) model in Nowshahr port.

2.1.2. Hydrographic Measurements

Figure 5 shows bathymetric data in the southern Caspian Sea and also the area surrounding Nowshahr port. For the southern coasts of the Caspian Sea, the bathymetry data were obtained from the maps provided by Iran National Cartographic Center which were available on different scales (1:10,000, 1:25,000, 1:100,000). For the far shore, etopo2 bathymetry data were applied here. According to this figure, the depth reaches less than 2 m near the western arm of breakwater. Extensive sedimentation can be seen in the port entrance. An access channel was dredged to a depth of 6 m in order to facilitate the passage of vessels in the past years. Maintenance of this access channel requires annual dredging of up to 300,000 m^3. Also sedimentation in the access channel and port entrance areas resulted in interference with the free passage of vessels occasionally.

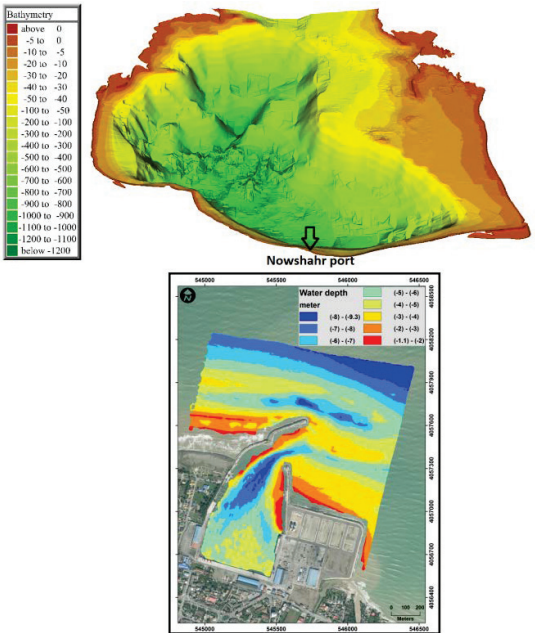

Figure 5. Large-scale bathymetry of Caspian Sea and location of Nowshahr port along the southern coastline (top panel) and local bathymetry of Nowshahr port obtained in 2018 (bottom panel).

2.1.3. Wave and Current Measurements

Wave and current measurements are important sources of data in the study area, since the movement of sediment is controlled by these hydrodynamic conditions. These data will be used for the calibration and validation of the models.

The data used in this study is obtained from the results of "Monitoring and modeling study of northern coasts of Iran", where long-term measurements for more than 1 year were surveyed in various locations at the Iranian coasts of the Caspian Sea [22]. In the present study, wave and current measurements in a 10 m depth point located near the Nowshahr port were used. The exact location of this point was 51.3883° E and 36.6985° N. The wave and current measurements were surveyed at 10-min intervals, rendering this dataset quite useful in identifying high-frequency events.

The existing wave data including significant wave height and mean wave direction is available for 15 months from 15 October 2012 to 7 February 2014. The maximum recorded significant wave height in this station through this period was about 3.4 m. The average significant wave height was

about 0.65 m. Figure 6 indicates wave rose obtained from the analysis of wave data in this station. About 69 percent of the time, calm conditions prevail with wave height less than 0.7 m.

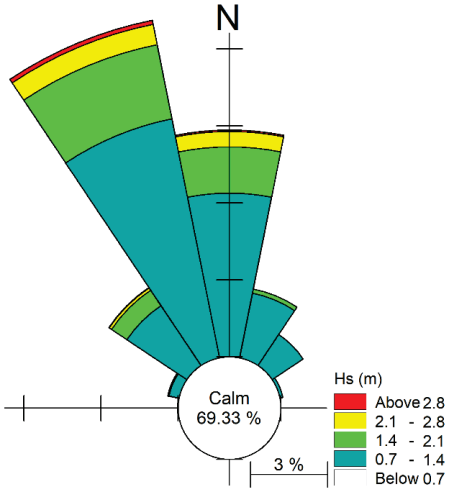

Figure 6. The measured wave rose in the year 2013 in a station near Nowshahr port.

As seen in Figure 6, more energetic and more frequent directions of waves are NNW and N. These directions would result in the formation of long-shore currents and sediment transport in the eastern direction (west to east) in the surf zone. This is consistent with sedimentation patterns observed in western parts of the Nowshahr port and behind the main breakwater (Figures 2 and 3).

The current measurement in this station is available from 15 October 2012 to 9 February 2014. The maximum observed current velocity in this station was around 0.94 ms^{-1} and occurred at a depth of 3.5 m below the water surface on 7 October 2013. The maximum current velocity flows towards the direction of 85 degrees (eastward). Figure 7 presents the comparison between the two surface and bottom current roses that were obtained at this station. According to Figure 7, surface eastward currents are stronger than bottom currents. The currents at the surface and bottom tend to flow eastward. Opposing westward currents also occur both at surface and near bottom. These less frequent westward currents flow in the opposing direction of the dominant current direction (which is eastward) and are generally stronger near the surface with velocities larger than 0.2 ms^{-1}. Therefore, it is concluded that both westward and eastward currents parallel to the coastline occur in areas adjacent to Nowshahr port. However, the eastward currents are stronger and more frequent. Based on the measured data with the current speed higher than 0.1 ms^{-1}, about 70% percent of data are form west to east with the average and maximum current speed of 0.21 and 0.84 ms^{-1}, respectively. The average and maximum current speed for the remaining 30% of east to west currents are 0.15 and 0.44 ms^{-1}, respectively. Because of positioning of port entrance and its main and lee breakwaters, westward currents can cause problems for navigation and sedimentation in the port entrance by carrying sediments supplied from rivers located in the east of the port.

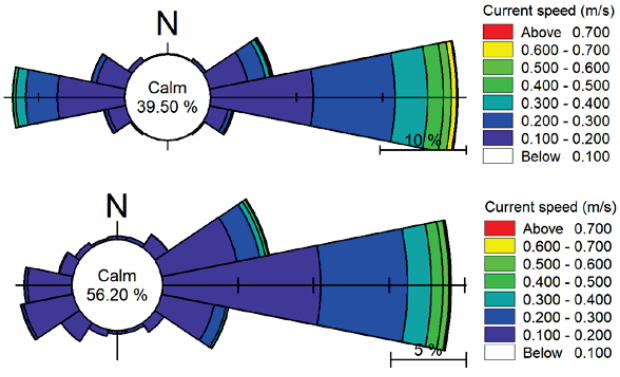

Figure 7. Current rose obtained at a station at 10 m depth located near the surface (top panel, depth 1.5 m) and near bottom (bottom panel, depth 8.5 m) in areas adjacent to Nowshahr port.

2.1.4. Coastal Sediment Properties

Sediment measurements have indicated that around the Nowshahr port, most of the sediments are composed of sand. On the eastern side of the port, coarser sediments including gravels are also observed. This could be due to intensive erosion occurring over the years on the eastern side of the port (the east of lee breakwater). The dominant west to east current erodes the finer portion of sediments, leaving the coarser materials behind. Because the port breakwaters block the river of sand, there are no replacements for finer sand materials. To the up-drift side of the port, the average particle diameter is about 200 microns and is mostly composed of sand. The information from continual dredging carried out in the area also indicates that the average grain sizes of dredged materials in the area were about 0.2 mm.

The distribution of sediment mean grain sizes is shown in Figure 8. These measurements were performed in 2012 [3]. Regarding the extreme dimensional variability observed in the east, these samples seem not enough to represent the true sediment grain size variation in the domain.

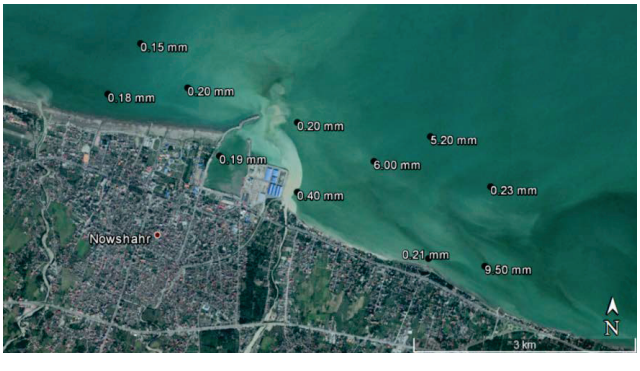

Figure 8. Average particle diameter in coastal sediments in areas near Nowshahr port.

Besides the dominant sand material of the bed sediments around the port, the small percentage of silt was also observed in the far shore near the port entrance. In coastal areas, by moving from port entrance to the west, average grain sizes increase. In accordance with Figure 8, average particle diameters in western areas of the port are close in three locations. However, large variations can be seen in the eastern areas of the port and behind the lee breakwater. In these areas, the sediments are mostly composed of coarser gravel material (Figure 8).

2.1.5. Riverine Sediment Properties

Two rivers flow into the eastern parts of Nowshahr port: Mashalak and Moghadam rivers. As evident in Figure 3, the sediment supply of these rivers could be a noticeable amount in the annual budget of sediments in the particular study location. This is especially true about the Mashalak River. As it was shown in previous sections, in addition to the dominant eastward currents, westward currents also occur in the study area occasionally. These surface westward currents have the potential to carry sediments supplied by these rivers (which mostly occur at the surface) toward the entrance of Nowshahr port and would then result in deposition of sediments in the basin of Nowshahr port. Therefore, it is crucial to quantify the annual supply of sediments from these rivers into the areas surrounding the Nowshahr port and in particular, the access channel of the port. The sediment supplies of these rivers were measured using the analysis of sediment concentration in the water samples that taken every month of the year. Following the analysis of these measurements, it was found that the average annual sediment supply from these rivers reaches 40,000 m^3 per annum. The discharges and sediment concentration of the rivers were included in the model as source terms.

2.1.6. Analysis of the Hydrodynamic Condition of Study Area Based on Field Measurements

The Caspian Sea is the largest landlocked water body in the globe and circulation patterns in the sea are largely controlled by wind forcing. With the analysis of wind and current data (comparison between Figures 4 and 7), it was found that large similarities exist between current and wind rose. This is an indication that wind forcing is the main driving force for currents (as the tidal currents are negligible in the Caspian Sea). Both westward and eastward currents could result in alongshore sediment transport. However, because the eastward currents are stronger and more frequent, it is predictable that net sediment transport is eastward, too. Wave-induced currents could also result in an increased eastward current velocity in the coastal area (surf zone). The breakwaters of the port block the west to east net sediment transport. Therefore, accretion of sediments can occur on the western side of Nowshahr port whereas erosions happen on the eastern side.

Another sediment source which has received less attention rather than net west to east sediment River is the supply of sediment from rivers at the east of Nowshahr port. These riverine derived sources of sediment can provide enough material to be transported by westward currents towards the entrance channel and basin of the port. The effect of this sediment source will be later discussed more.

In the following section, the numerical model set-up will be described. This numerical model was used for detailed analysis of wave and current-induced sediment transport in areas adjacent to main and lee breakwaters and entrance of the port.

3. Description of Numerical Model and Main Parameters

In the present study, the DHI MIKE software was used to simulate the hydrodynamic parameters of the area. MIKE software package, which is funded and developed by the Danish Hydraulic Institute in collaboration with the Danish Water Quality Institute, has high computational and graphical capabilities in modeling estuaries, shallow coastal areas, bays, seas, etc. This software is a comprehensive system for modeling two-dimensional and three-dimensional free-surface flow in water bodies and it is a reliable and commonly used numerical simulator. It is capable of modeling instationary flow affected by wind, bed variations, etc.

DHI MIKE software package includes different modules to simulate different hydrodynamic phenomena in the water bodies. For example, The MIKE21-SW module is used for spectral phase averaged simulation of wind-generated waves. The 3 dimensional MIKE3-HD (Hydrodynamic) module is used to simulate the sea currents. This module simulates the flow pattern and water level variations affected by various forcing. In addition, the MIKE3-ST module is developed for the simulation of non-cohesive sediment transport. The water level variation (which is the HD module output) changes the water depth and therefore should be included in wave simulation. On the other

hand, in order to simulate the current caused by wave breaking, the radiation stresses data of the waves should be included in the hydrodynamic simulation. The bed level variation (as a result of the ST module) also affects both wave and current. Hence, it would be favorable to perform simultaneous wave, flow, and sediment transport simulations with the direct interaction between these modules. Therefore, in this study, the coupled module of SW&HD&ST from MIKE software was used for numerical simulations.

The computational domain of the model is shown in Figure 9. A combination of triangular and quadrangular grids was used in the domain with finer grid sizes around the Nowshahr port. The grid sizes varied from 50 to 500 m. There are 3 open boundaries in the domain: Northern, Eastern and Western open boundaries. For these boundaries, wave and current data were obtained from a large scale model covering the entire Caspian Sea. That model was conducted by the Port and Maritime Organization of Iran, and its result was available by the organization. For the sediment transport model, a zero gradient condition was applied in open boundaries. The model was executed for 1 year (2013) in the coupled mode. Atmospheric forcing was provided from the WRF model which has been applied in both current and wave models.

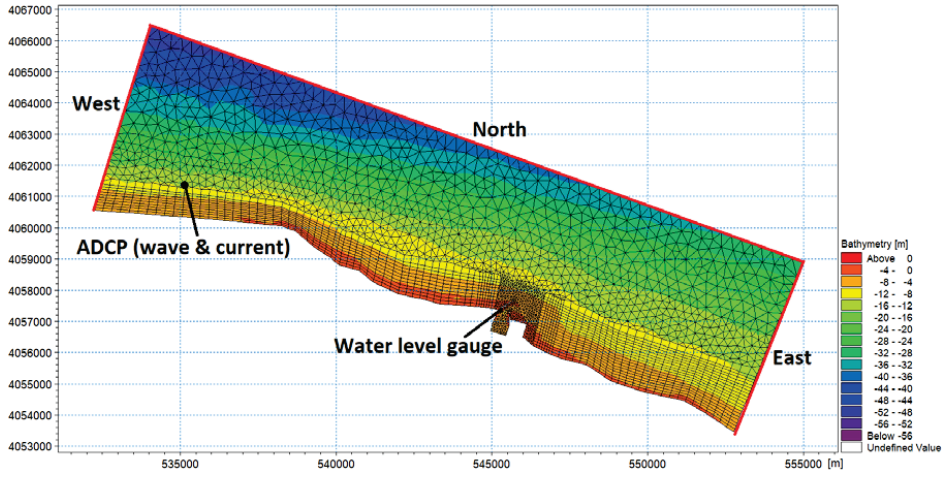

Figure 9. Model domain and mesh definition file used in coupled simulations of wave, current and sediment. Also shown is the location of ADCP station.

3.1. Sensitivity Analysis

In most of the numerical models, there are several parameters that the results of the model are dependent on them and the governing equations would be solved based on them. In the spectral wave models, various factors such as computational grid size, number of angular discretization, accuracy of numerical solution of the equations, wave breaking and bed roughness coefficients, white capping coefficients, etc., might affect the result. In the flow model, in addition to the computational grid size and the accuracy of numerical solution of the equations, bed resistance (roughness height) and eddy viscosity (the effect of diffusivity) also might affect the results.

In order to calibrate and validate the numerical models, at first the factors that the results of the model are sensitive to should be identified and then they should be properly and optimally tuned to draw the model results as close as possible to the actual measured values.

The results of sensitivity analysis on the parameters that could affect the MIKE21-SW spectral wave model results indicated that among the investigated parameters, the number of angular divisions of the spectrum, the solution technic, and shallow-water wave breaking had almost no effect on the outputs [16]. Decreasing the size of the computational grid has a certain effect on the accuracy of

the results and more than that, only increases the computational cost. This parameter is also not a calibration parameter and mesh dimensions must be optimally selected so that spatial discretization does not affect the results. The bed roughness and white capping coefficients also affect the results to some extent and can be used as the main parameters in the calibration process of the wave model. For the 3D flow model, bed resistance is the most effective parameter in the results. Full explanations about sensitivity analysis are not provided here for brevity. However, the result of model for two different bed roughness coefficients (0.002 and 0.04) and two different white capping coefficients (4 and 2) in the wave model are presented in Figure 10. In addition, the model results for two different roughness height coefficients in the flow model (50 and 32) are also presented in Figure 11. The effectiveness of these coefficients on the model results can be clearly seen in these figures.

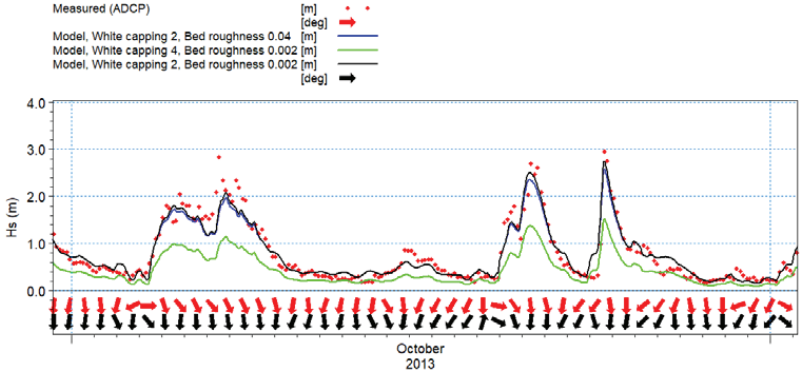

Figure 10. Comparison of modeled and measured wave height and direction for October 2013. Red color indicates measurements and black color indicates model results. The results of sensitivity analysis on the white capping and bed roughness coefficients are also presented.

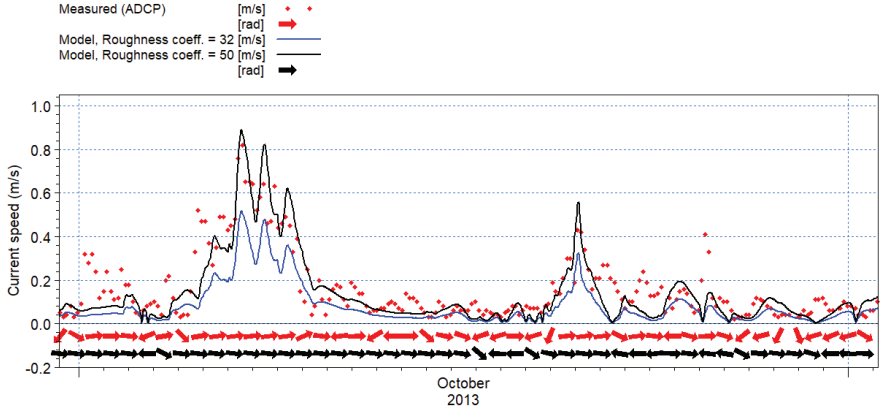

Figure 11. Comparison of modeled and measured current speed and direction for October 2013. Red color indicates measurements and black color indicates model results. The result of the sensitivity analysis on the roughness height coefficient is also presented.

3.2. Model Calibration

After the initial setup of the model and also sensitivity analysis and identifying effective parameters on the results for the calibration, the calibration and verification of the models are performed based on

the Nowshahr ADCP and water level gauge measurements (locations of the measurements are shown in Figure 9).

In this section, results of the comparison between model results and field measurements are presented. Several physical parameters such as wave height, current speed, and sea level variations were used in this analysis.

Figure 10 shows the results of comparison between modeled and measured wave height and direction for October (as a sample month). As seen in the Figure, there are three distinct storm peaks with wave heights greater than 1 m in this period. The model results (black line) have captured all of these three storm events with a rather good accuracy. There is a high correlation between model results and measurements of both wave height and direction (the quantitative value of correlation is presented in Table 1). Therefore, the model seems to be reliable in the simulation of wave regime in the study area. However, the model results have generally under-predicted maximum wave heights that occur during storm periods. This could be related to the accuracy of WRF wind forcing (which also provided by an atmospheric numerical model).

Table 1. Values of several statistical parameters that were used for evaluating the performance of coupled model against existing observations. Wave height data in October 2013 is used for derivation of these values.

Error Indicator	Value
Model Skill	0.94
SI	0.33
R	0.89
BIAS	0.02
RMSE	0.22

In order to statistically evaluate the model performance, various parameters such as model skill, correlation coefficient, bias parameter, root mean square error and index of dispersion (SI) were selected. These parameters are defined as:

$$Model\ Skill = 1 - \frac{\sum\left(X_p - X_m\right)^2}{\sum\left(\left|X_p - \overline{X_m}\right| + \left|X_m - \overline{X_m}\right|\right)^2} \tag{1}$$

$$SI = \frac{\sqrt{\frac{1}{N}\sum_{i=1}^{N}\left(X_p - X_m\right)^2}}{\overline{X_m}} \tag{2}$$

$$R = \frac{\sum\left(X_p - \overline{X_p}\right)\left(X_m - \overline{X_m}\right)}{\sqrt{\sum\left(X_p - \overline{X_p}\right)^2 \sum\left(X_m - \overline{X_m}\right)^2}} \tag{3}$$

$$BIAS = \sum \frac{1}{N}\left(X_p - X_m\right) \tag{4}$$

$$RMSE = \sqrt{\frac{1}{N}\sum\left(X_p - X_m\right)^2} \tag{5}$$

where N represents the number of records, X_p is the predicted value and X_m is the measured value. Also, $\overline{X_m}$ and $\overline{X_p}$ represent the mean of measured and predicted values, respectively. In Table 1, the values of these statistical parameters that were obtained from the comparison between model results and measurements of wave height in October 2013 are presented. As evident from this table, the model performance is considered satisfactory and the results could be used for advancement of purposes of this study.

A similar comparison was made for the evaluation of HD module. Comparison of modeled and observed current velocities and directions in October 2013 (as a sample month) is shown in Figure 11. The model results of current velocity generally follow the same pattern as observations. The same agreement could be seen between model results and observations for the current direction. For example, the model has captured a single event with strong eastward currents that peaked on 8th October with velocities reaching 0.9 ms^{-1}. The overall agreement between model output and available observations is quite well. Table 2 presents various statistical parameters that were obtained from a comparison between modeled and measured current speeds. The comparison of Tables 1 and 2 values indicate a less accurate performance of current simulation results compared with wave height modeling results. However, the values of Table 2 indicate the satisfactory performance of model to assess sediment transport patterns around the Nowshahr port.

Table 2. Values of several statistical parameters that were used for evaluating the performance of coupled model against existing observations. Current speed data in October 2013 is used for derivation of these values.

Error Indicator	Value
Model Skill	0.78
SI	0.67
R	0.61
BIAS	−0.03
RMSE	0.09

In addition to the wave and currents, comparison of surface water level variations between measured and modeled values is presented in Figure 12. There is again a good agreement between model results and measured values. A storm surge of up to 30 cm is observed during storm periods. The model has correctly captured low-frequency variations of water level under wind force.

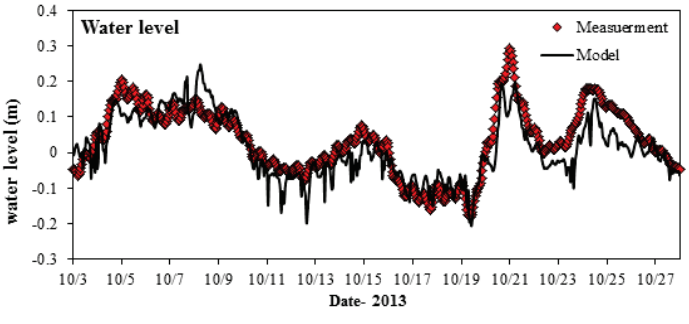

Figure 12. Comparison of modeled and measured water level for October 2013. Red color indicates measurements and black color indicates model results.

For validation of the model, the comparison of measured and simulated wave height in 2013 is shown in Figure 13. In addition, in Figure 14, annual wave roses are compared based on model results observed values of waves. Both of these figures indicate good performance of the model in capturing important high sea waves during storms. Also, there is a remarkable similarity between annual wave roses as shown in Figure 14 which indicates the high accuracy of the model in the simulation of wave direction.

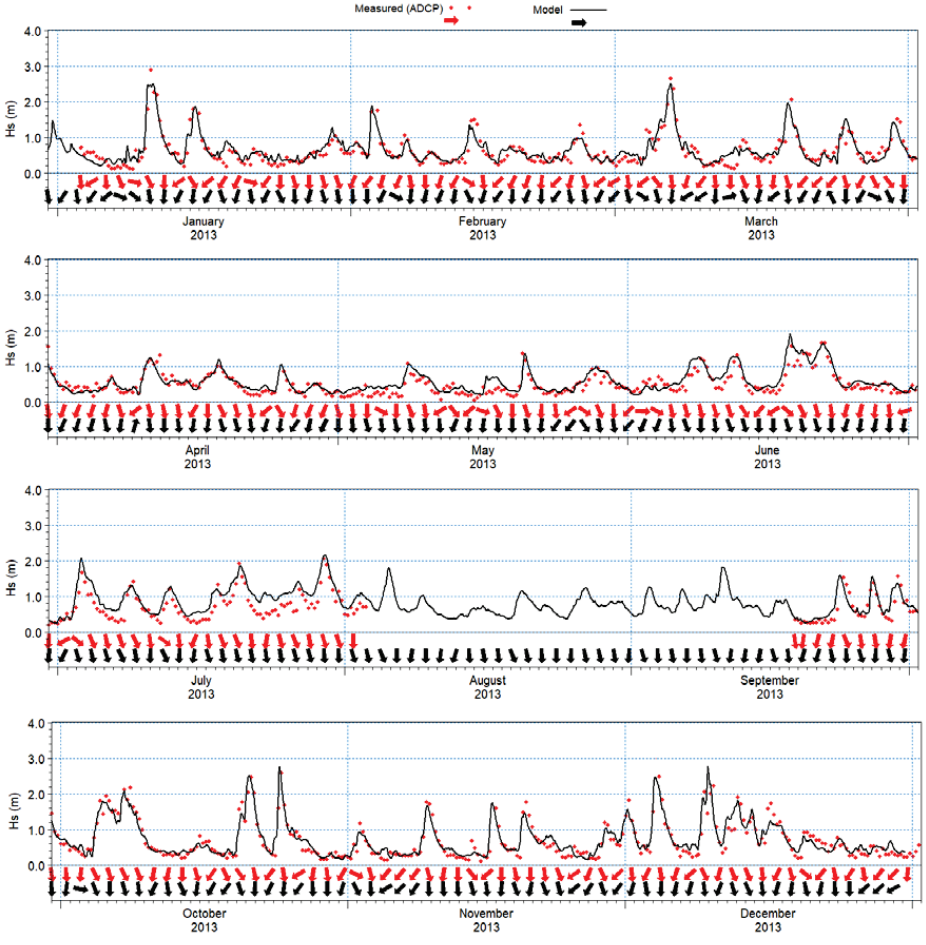

Figure 13. Model simulation of significant wave height (black solid line) and wave direction (black arrows) in the year 2013. Also shown is measured significant wave height (red dots) and wave direction (red arrows).

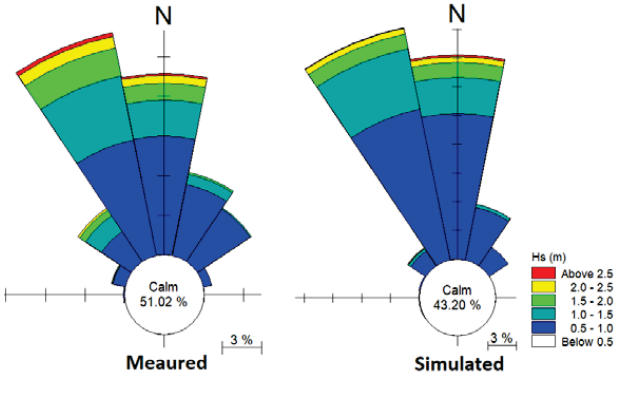

Figure 14. The measured and simulated annual wave rose for the year 2013.

A similar comparison was made between simulated current speed and direction and measured values. These results are shown in Figures 15 and 16. In Figure 15, a time series of current speed and direction from model results and measured values is shown for 2013. In addition in Figure 16, the annual current roses that were obtained from model results and field measurements are shown. As can be seen from these figures, the model has shown good performance in simulating current speed and direction, particularly during storm events. However, there is a slight discrepancy between model results and observations during calm conditions when the current speed is less than 0.2 ms^{-1}. Based on the comparison of wave roses, the model has indicated good performance in simulating the current direction, too.

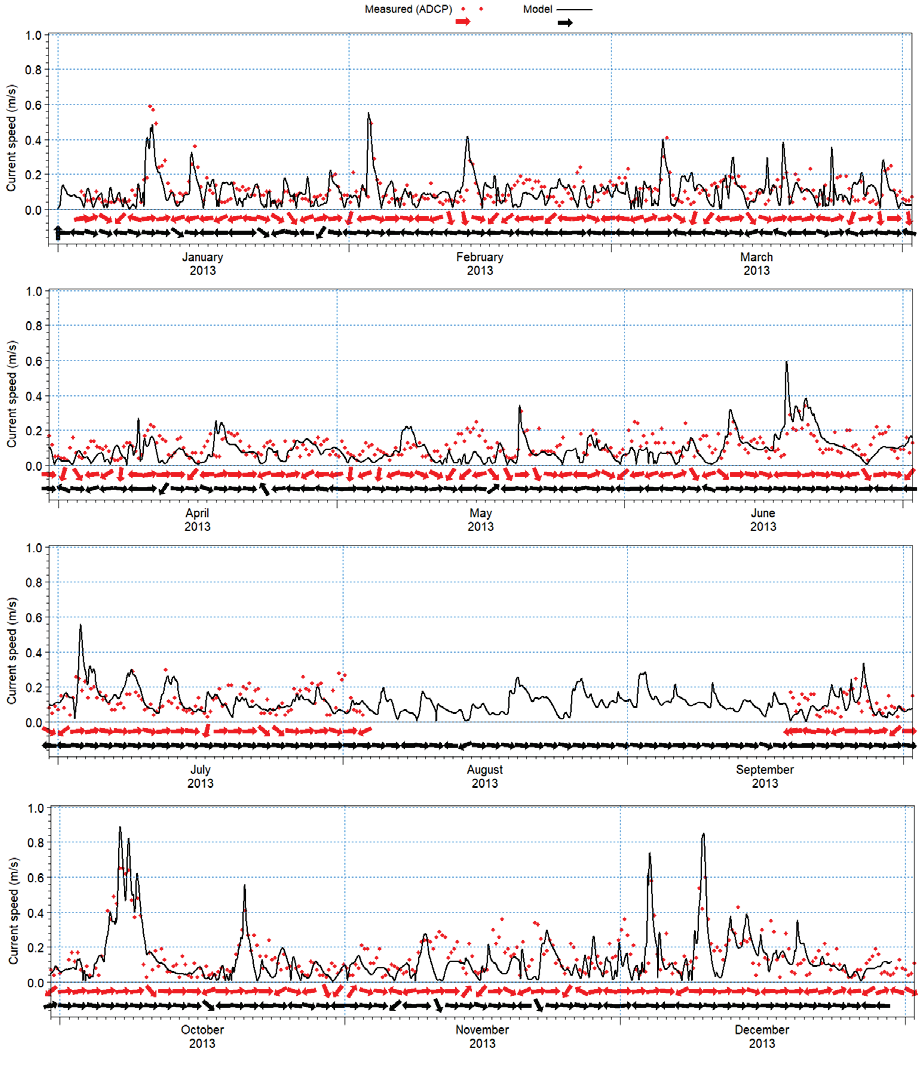

Figure 15. Model simulation of current speed (black solid line) and direction (black arrows) in the year 2013. Also shown is measured current speed (red dots) and direction (red arrows).

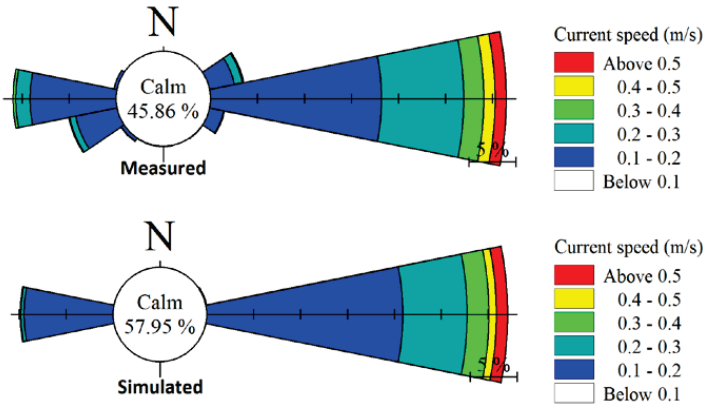

Figure 16. Measured and simulated annual current rose for the year 2013.

Following proper calibration and validation of model results, the coupled model was forced for 2013. In Table 3, a list of main parameters and their value used in final simulations is presented.

Table 3. Values of model parameters utilized in the coupled simulation of wave, current, and sediment.

Model Parameter	Value
Time step (s)	60
Number of time steps	105,120
Directional discretization of wave	16 directions in 360 degrees
Number of frequencies	25
Minimum frequency (Hz)	0.055
Delta parameter	0.8
Bed roughness coeff.—Wave model	0.002
White capping coefficient	2
Bed roughness coeff.—Current model (Manning parameter)	50
Average bed particle diameter	200 microns
Sediment variation coefficient	1.1
Roughness height—ST model	0.02

4. Results and Discussion

In this section, the simulation results of hydrodynamic parameters and their impact on sediment transport patterns will be presented. As mentioned based on the measurements, the dominant current direction is eastward (from west to east). As seen in Figure 16, about 70% of currents (with the speed higher than 0.1 m/s) have an eastward direction, while about 30% of them are westward. The currents are highly correlated with local wind speed and direction (Figures 4 and 7). Figure 17 presents three-hourly maps of the wind field in the southern parts of the Caspian Sea for more than 1 day during a typical storm event. These storm events occur frequently throughout the year. The largely similar feature among these storms is that they initially approach southern parts of the Caspian Sea as northerly winds. However, with the interaction of these large-scale wind events with Alborz mountainous in the north of Iran, the winds deflect and form two dominant directions almost parallel to the coastline: westerlies that blow eastward (known as Dasht-Bad, Figure 17) and easterlies that blow westward (known as Gil-Bad) [22]. These winds generate wind driven sea currents along the southern coasts of the Caspian Sea.

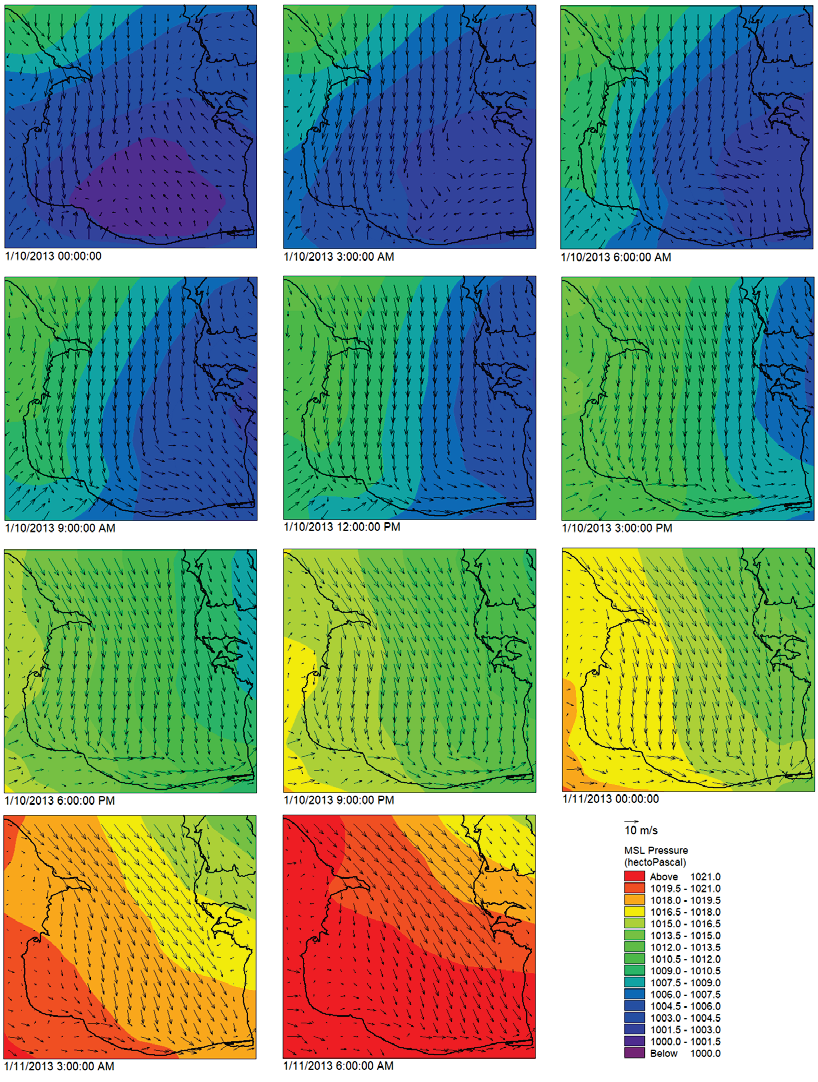

Figure 17. Temporal variation of wind speed and direction during a typical wind storm in southern parts of the Caspian Sea (the winds are from WRF model).

Figure 18 presents a comparison of the surface current field obtained from the HD model and wind field obtained from WRF model during two distinct storm events. In the southern parts of Caspian Sea, a good agreement could be observed between directions of surface currents and wind during storm events (Figure 18). The same agreement could be observed in other areas of Caspian Sea. This is an indication that surface currents were largely affected by surface stresses imparted by atmospheric wind forcing. Therefore, dominant current directions along the southern coastline of Caspian Sea are eastward and westward, as would be predicted by dominant direction of winds. As the west to east winds (same as the one that is shown in Figure 17) are stronger and more frequent, the dominant current and sediment transport is also eastward. However, there are also weaker less frequent westward wind which could be important for driving westward currents that transport eastern riverine sediments to the port entrance.

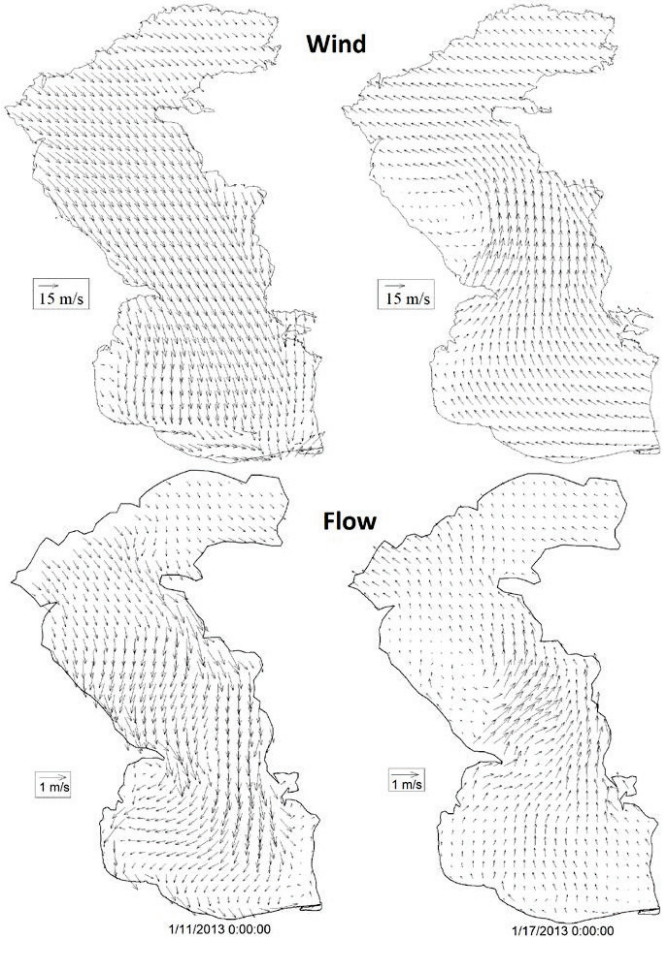

Figure 18. WRF wind field (top panels) and surface current field obtained from the hydrodynamic (HD) model (bottom panels) during two distinct storm events on 11th (left panels) and 17th (right panels) of January 2013.

Following an investigation of large-scale dynamics of surface currents in Caspian Sea, a more local study was carried out in order to gain insight into relationship between surface currents and winds around the Nowshahr port. Figures 19 and 20 present the results of model simulation during two different storm events. In Figure 19, the simulation result during an eastward wind event is shown. The simulated currents were flowing in the same direction as winds. The same was true in the case of a westward wind event (Figure 20) where both wind and current direction was from east to west. It can be seen from Figure 19 that when west to east currents passes over the main breakwater head, it generates an eddy that returns the flow to the port entrance. This flow transports the sediment sources in the east of the channel back into the west and into the access channel of the port. Other field studies (as a part of "monitoring and modeling studies of the northern coasts" [22]) support these findings. In that study, a drifter was released in western parts of Nowshahr port and the movement of it was tracked from its initial release point. The drifter moved eastward past the port entrance and after hitting eastern reclaimed lands it again re-entered into the entrance of port basin consistent with circulation pattern shown in Figure 19.

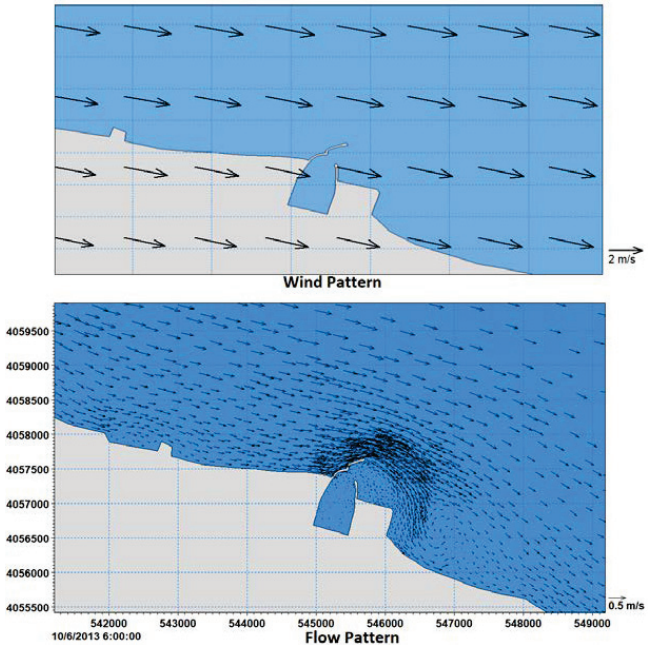

Figure 19. Wind field (top panel) from WRF and surface current field (bottom panel) from the model in areas adjacent Nowshahr port during a typical eastward storm event on 6th October 2013.

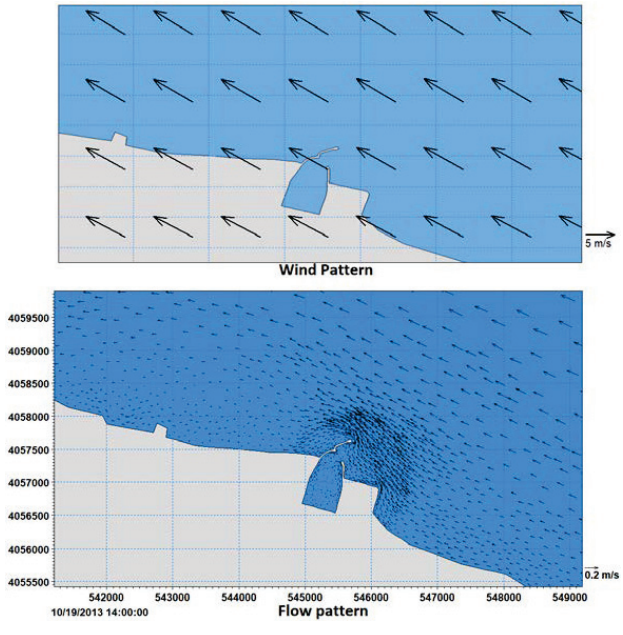

Figure 20. Wind field (top panel) and surface current field (bottom panel) in areas adjacent Nowshahr port during a typical westward storm event on 19th October 2013.

In order to study the spatial variation of current in areas surrounding Nowshahr port, several optional points were selected (Figure 21). Figure 22 presents current-roses in these different locations. Based on this figure, it is clear that in t1 and t2 there was an eastward current. Also, current velocities were larger in t2—which is located in deep waters—compared with t1 stations. In t3 and t4, circulation was affected by the interaction between flow velocities and main western breakwater which resulted in the strengthening of currents. Also, currents get deflected towards the port basin in t3 and t4. There was evidence for the existence of anti-cyclonic (clockwise) eddying circulation with no noticeable unidirectional current velocity.

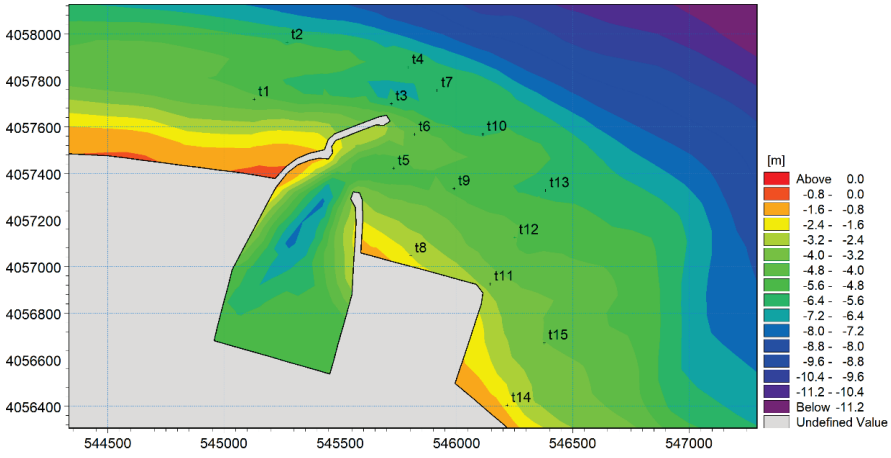

Figure 21. Spatial distribution of stations for studying current variations in the annual period in areas adjacent to Nowshahr port.

In t6 and t7, the circulation widens in areas in front of port entrance resulting in the spreading of circulation features there. In t8 and t11, circulation was in form of clockwise motion and westward currents were formed. In case of eastward current in this station, there was no eddying circulation and current would deflect eastward after encountering eastern shoreline of the port. In t9 and t12, both eddying circulation and unidirectional currents were observed. In t10 and t13, main unidirectional currents were the main form of circulation flowing in an eastward direction. Weak currents were found in t14 and t15. Currents in both of these stations were affected by the presence of eastern shoreline of port, which would direct the currents in an eastward direction parallel to the coastline. These rose plots clear the understanding of the eddy formed in the eastward currents.

As mentioned, 3D simulation is applied for flow modeling. Figure 23 shows the comparison of current roses in the water surface and near the bed for 1 year simulation. As seen, the flow direction near the bed is a bit different from the one at the water surface. This could happen because the surface current is mostly affected by the surface wind tension and it flows parallel to the wind; while near the sea bed, water flows parallel to the bathymetric isolines. Therefore, the direction of the sea currents can be a little different at the surface and near the sea bed. On the other hand, the flow velocity is also affected by the bed roughness and current velocities near the sea bed are less than the velocities near the surface. Based on the analysis of model results for the flows with velocities higher than 0.1 m/s, the average flow direction and velocity differences between the surface and near the sea bed were 5 to 6 degrees and 0.09 m/s, respectively. Figure 24 shows two samples of storms around the Nowshahr port at the surface and bottom layer. The current speed and direction differences between the two layers can be seen in this figure. Based on the results, the differences between top and bottom layers are not significant to affect the sediment patterns.

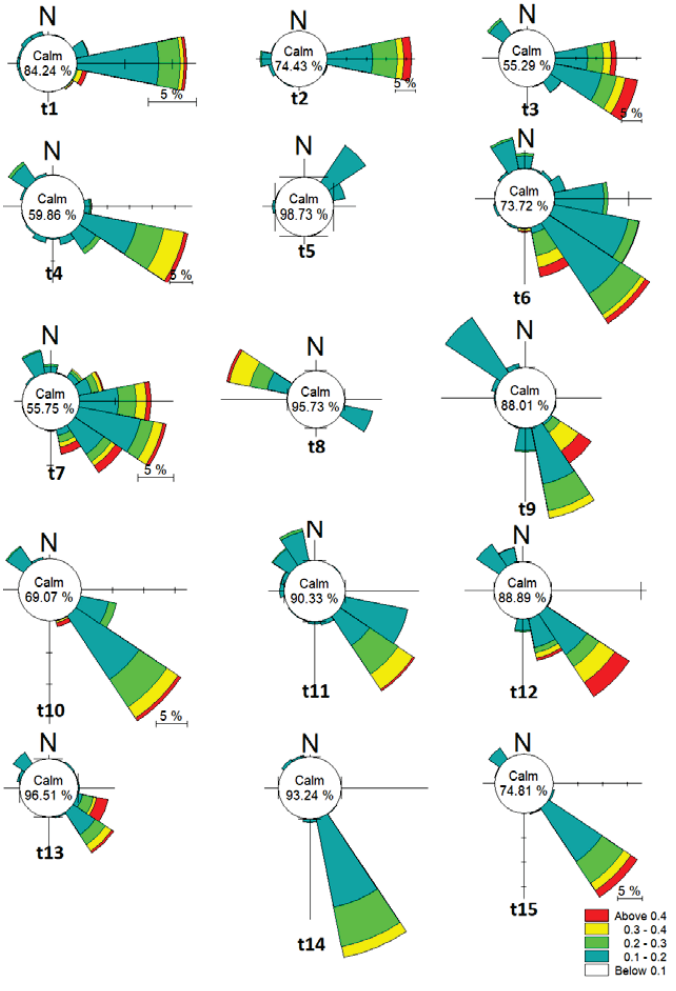

Figure 22. Current-roses in various locations indicated in Figure 21.

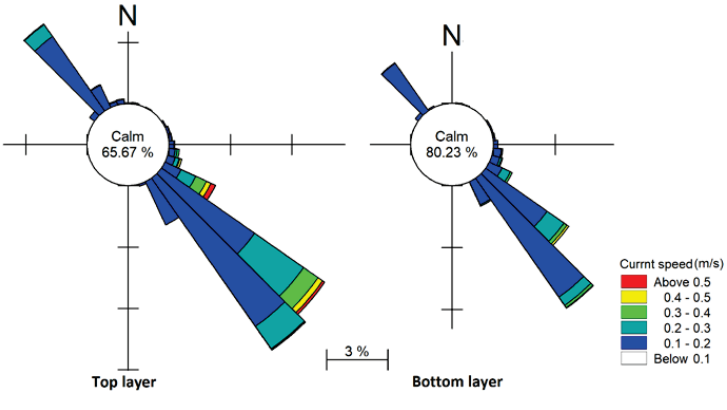

Figure 23. The comparison of current roses in the water surface and near the bed for 1 year simulation.

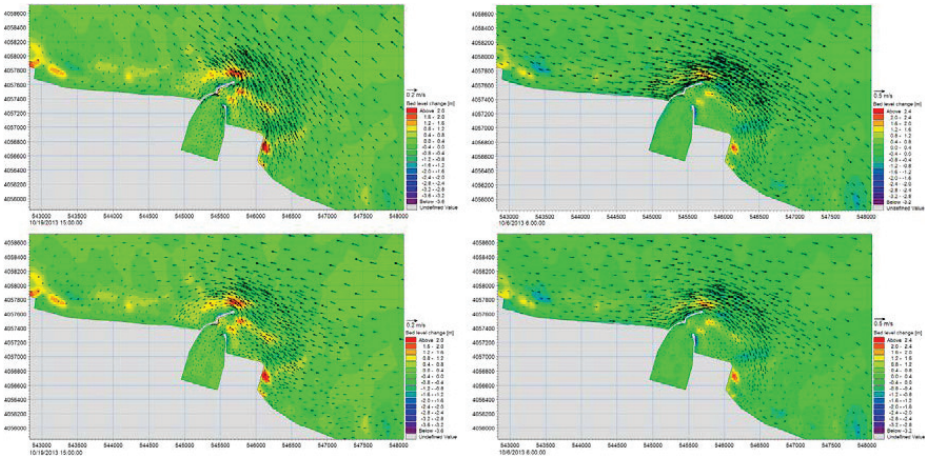

Figure 24. Two samples of storms around the Nowshahr port at the surface (upper figures) and bottom layer (lower figures).

Following analysis of current variations in various locations surrounding Nowshahr port and in different depths, many aspects of causes of sedimentation could be evaluated. Analysis of one year of model simulations indicated that eastward currents could transport riverine derived sources of sediment (from the western rivers like Chaloos and Koorkoorsar) towards the entrance of the port. There, some of the sediments would settle due to a reduction in velocities and remaining sediments would then bypass the entrance of port and move towards down-drift side. It is expected that bypassed sediments would settle in reclaimed lands in the down-drift side of port along eastern shoreline. During storm conditions, high sea waves would hit lee breakwaters and eddying circulation features there would then transport the now suspended sediments of eastern shoreline. The ultimate destination of these sediments is again entrance of port. The riverine derived sources of sediment from the eastern rivers like Mashalak and Moghadam rivers are also transported into the entrance of port by the circulation. These are only the effects of eastward currents. The westward currents on the other hand which are less frequent are also currying the sediments into the port mouth. Therefore, the ultimate destination of all sediments in areas around the Nowshahr port is towards the entrance of port.

Figure 25 presents the results of sediment transport model indicating sedimentation patterns in areas adjacent to Nowshahr port. This figure illustrates variation of bottom level for 1-year simulation period. In accordance with this figure, it is evident that extensive sedimentation has taken place in front of port entrance and eastern reclaimed lands outside lee breakwater. In contrast, limited sedimentation has occurred inside the port basin. An optional line was marked on this figure so that the variation of bottom level could best be described (Figure 25). In the areas surrounding main breakwater (western arm) net sedimentation of 2 m was observed (Figure 26). Inside the access channel, sedimentation reached 1 m in an annual period. This value is in agreement with dredging values that were obtained in past years.

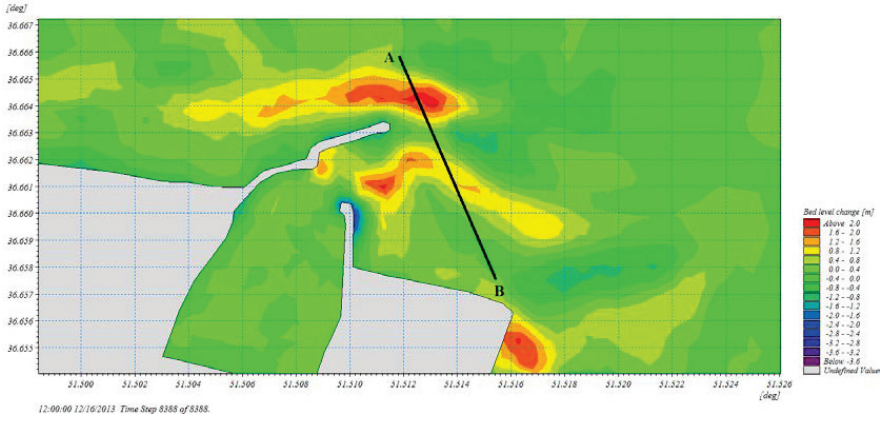

Figure 25. Bed level change in 1-year simulation period. Also shown is the location of an optional line chosen for the investigation of bed level changes during simulation.

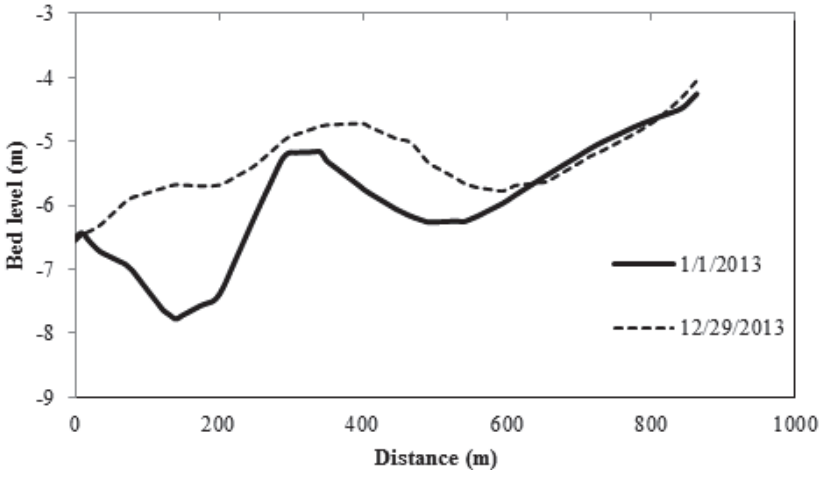

Figure 26. Variation of bottom level along AB line shown in Figure 25 one year after simulation. The thick (dashed) black line indicates initial bed level elevation (m).

5. Conclusions

In this study, sedimentation in areas adjacent to Nowshahr port was evaluated in detail. Both field measurements and numerical modeling were used in this study. First, field measurements were evaluated in order to gain an in-depth view of the hydrodynamics of the study area. Investigation of wind data has shown that dominant wind direction in region is eastward (about 70% of the annual period) and westward (about 30% of the annual period). The observation of the current measurements also indicates that the two dominant current directions were eastward and westward. Based on the evaluation of wave data, the dominant wave direction is from the north-west. Therefore, wave-induced currents in the surf zone were from west to east, too. Due to direction of current, accretion (erosion) of sediments occurred in western (eastern) areas of Nowshahr port. Numerical models then were calibrated and validated against existing field measurements. The results of the numerical simulation have shown that an intermittent eddying circulation was formed directly in front of eastern section of Nowshahr port due to the interaction between eastward currents and breakwater arms. Any sediment arriving in front of the reclamation land could be carried by this circulation towards port entrance and

its access channel. Based on the analysis of annual data, supply of sediments from the Mashalak River located to the east of Nowshahr port was estimated to be around 40,000 m^3 per annum. This is one of the sediment sources near the port. Results from the sediment model indicated that the model has captured major features of sedimentation patterns in the study area. Furthermore, in accordance with results of numerical modeling, sedimentation of up to 1 m was predicted in areas of access channel of Nowshahr port, in agreement with previous estimates based on annual dredging volumes.

Author Contributions: This study has been performed as a part of a Ph.D. thesis bay A.M. (Ayyuob Mahmoodi) as the student, M.A.L.N. and A.M. (Abbas Mansouri) as supervisors, and also M.S.B. as advisor. A.M. (Ayyuob Mahmoodi) wrote the manuscript with support and advice from all the other authors and they are all discussed the results and contributed to the final manuscript. All authors have read and agreed to the published version of the manuscript.

Funding: This research received no external funding.

Acknowledgments: The authors would like to thank PMO Pouya Tarh Pars Consulting Engineers Company, for the valuable dataset.

Conflicts of Interest: The authors declare that there is no conflict of interest regarding the publication of this article.

References

1. Caceres, R.; Zyserman, J.A.; Perillo, G.M.E. Analysis of sedimentation problems at the entrance to Mar del Plata Harbor. *J. Coast. Res.* **2016**, *32*, 301–314.
2. Van Rijn, L.C. Estuarine and coastal sedimentation problems. *Int. J. Sedim. Res.* **2005**, *20*, 39–51.
3. Bali, M.; Jandaghi Alaee, M.; Moeini, M.H. Hydrodynamic and Sedimentation Study in Noshahr Port. In Proceedings of the 18th Marine Industries Conference (MIC), Kish Island, Iran, 17–19 October 2016.
4. Yuksek, O. Effects of breakwater parameters on shoaling of fishery harbors. *J. Waterw. Port Coast. Ocean Eng.* **1995**, *121*, 13–22. [CrossRef]
5. Sume, V.; Yuksek, O. Investigation of shoaling of coastal fishery structures in the Eastern Black Sea coasts. *J. Fac. Eng. Archit. Gazi Univ.* **2018**, *33*, 843–852.
6. Frihy, O.E.; Abd El Moniem, A.B.; Hassan, M.S. Sedimentation processes at the navigation channel of the Damietta Harbour on the Northeastern Nile Delta coast of Egypt. *J. Coast. Res.* **2002**, *18*, 459–469.
7. Mojabi, M.; Hejazi, K.; Karimi, M. Numerical investigation of effective harbor geometry parameters on sedimentation inside square harbors. *Int. J. Mar. Sci. Eng.* **2013**, *3*, 57–68.
8. Stock, F.; Knipping, M.; Pint, A.; Ladstätter, S.; Delile, H.; Heiss, A.G.; Laermanns, H.; Mitchell, P.D.; Ployer, R.; Steskal, M.; et al. Human impact on Holocene sediment dynamics in the Eastern Mediterranean–the example of the Roman harbour of Ephesus. *Earth Surf. Process. Landf.* **2016**, *41*, 980–996. [CrossRef]
9. Nezammahalleh, M.A.; Yamani, M.; Soltani, S.; Maldar, B.A.; Rastegar, A. Modeling of Hydrodynamic Factors for Management of Coastal Hazards, Case Study: Khamir Port, Persian Gulf, Iran. *Int. J. Mar. Sci. Eng.* **2014**, *4*, 25–36.
10. Portela, L.I.; Ramos, S.; Teixeira, A.T. Effect of salinity on the settling velocity of fine sediments of a harbour basin. *J. Coast. Res.* **2013**, *65*, 1188–1194. [CrossRef]
11. Sharaan, M.; Ibrahim, M.G.; Iskander, M.; Masria, A.; Nadaoka, K. Analysis of sedimentation at the fishing harbor entrance: Case study of El-Burullus, Egypt. *J. Coast. Conserv.* **2018**, *22*, 1143–1156. [CrossRef]
12. Jafari, E.; Alaee, M.J.; Nazarali, M.; Bali, M. Sea Water Temperature Observation and Simulation in the Caspian Sea. In Proceedings of the International Conference on Coasts, Ports and Marine Structures (ICOPMAS), Tehran, Iran, 31 October–2 November 2016.
13. Moeini, M.H.; Jafari, E.; Bali, M.; Alaee, M.; Pattiaratchi, C. Simulation of the sea water circulation and coastal currents in the Caspian Sea. In Proceedings of the International Conference on Coasts, Ports and Marine Structures (ICOPMAS), Tehran, Iran, 31 October–2 November 2016.
14. Rostami, S.; Nezamivand Chegini, A.; Gobraei, A.; Lashteneh Neshaei, M.; Esfahanizadeh, M. Investigation of sedimentation process in Noshahr port basin. In Proceedings of the 10th Iranian Hydraulic Conference, Rasht, Iran, 8 November 2011.
15. Mahmoodi, A.L.; Mansori, A.; Shafaei Bajestan, M. Numerical study of current and sedimentation in Noshahr port. *J. Mar. Technol.* **2018**, *5*, 105–116.

16. Pouya Tarh Pars (PTP). *Monitoring and Modeling Study of Iranian Coasts, Phase 5: Northern Coasts, Report Phases 1 and 2 of Noshahr Port (Special Regions)*; PTP: Tehran, Iran, 2014.
17. Tehran Berkeley, C.E. *First Phase Studies of the East and West Conservation Management Project of Noshahr Port*; General Directorate of Port and Maritime Organization of Mazandaran Province: Tehran, Iran, 2011.
18. DHI Institute. *MIKE 21 & MIKE 3 Flow Model FM Hydrodynamic and Transport Module Scientific Documentation*; DHI Water & Environment, Inc.: Horshølme, Denmark, 2011; 52p.
19. DHI Institute. *MIKE 21 Spectral Wave Module*; DHI Water & Environment, Inc.: Horshølme, Denmark, 2011; 66p.
20. DHI Institute. *Noncohesive Sediment Transport in Currents and Waves*; DHI Water & Environment, Inc.: Horshølme, Denmark, 2011; 66p.
21. Ghader, S.; Namin, M.; Chegini, F.; Bohluly, A. Hindcast of surface wind field over the Caspian sea using WRF model. In Proceedings of the International Conference on Coasts, Ports and Marine Structures (ICOPMAS), Tehran, Iran, 24–26 November 2014.
22. Iranian Port and Maritime Organization. *Monitoring and Modeling Study of Iranian Coasts, Phase 5: Northern Coasts*; Iranian Port and Maritime Organization: Tehran, Iran, 2015.

Journal of
Marine Science and Engineering

MDPI

Article

21 May 2003 Boumerdès Earthquake: Numerical Investigations of the Rupture Mechanism Effects on the Induced Tsunami and Its Impact in Harbors

Marinella Masina *, Renata Archetti and Alberto Lamberti

Department of Civil, Chemical, Environmental and Materials Engineering—DICAM, University of Bologna, Viale del Risorgimento 2, 40136 Bologna, Italy; renata.archetti@unibo.it (R.A.); alberto.lamberti@unibo.it (A.L.)
* Correspondence: marinella.masina@gmail.com

Received: 1 October 2020; Accepted: 5 November 2020; Published: 17 November 2020

Abstract: In order to obtain a fair and reliable description of the wave amplitude and currents in harbors due to the tsunami generated by the 21 May 2003 Boumerdès earthquake (Algeria), a numerical investigation has been performed with a standard hydraulic numerical model combined with various source fault models. Seven different rupture models proposed in literature to represent high frequency seismic effects have been used to simulate tsunami generation. The tsunami wave propagation across the Western Mediterranean Sea and in bays and harbors of the Balearic Islands is simulated, and results are checked against sea level measurements. All of them resulted in a significant underestimation of the tsunami impact on the Balearic coasts. In the paper the best fitting source model is identified, justifying the energy intensification of the event to account for low frequency character of tsunami waves. A fair correspondence is pointed out between damages to boats and harbor infrastructures, reported in newspapers, and wave intensity, characterized by level extremes and current intensity. Current speed and amplitude thresholds for possible damage in harbors suggested respectively by Lynett et al., doi.org/10.1002/2013GL058680, and Muhari et al., doi.org/10.1007/s11069-015-1772-0, are confirmed by the present analysis.

Keywords: Balearic Islands; Boumerdès; current speed; damage; harbor; tsunami

1. Introduction

Tsunamis with earthquakes and floods represent one of the most severe natural hazards; the most severe events of the different categories have claimed worldwide the same order of magnitude of lives. However, the different natural hazard types exhibit very different occurrence patterns in terms of spatial distribution, time recurrence, and event characteristics [1].

Globally, more than 80% of tsunamis occur in the Pacific Ocean along the Ring of Fire subduction zones [2]. Although published tsunami catalogues highlight that the European coasts are also prone to tsunami events [3,4], their long return period in this part of the world compared to the Pacific region and their weaker intensity lead to a low perception of tsunami risk in Europe and along the shores of the Mediterranean Sea [5,6]. In the western world tsunamis are known to the general public only after the 2004 Great Indian Ocean event, that caught unprepared not only tourists, who had no direct experience of a similar event and local population, but also the tsunami warning system in the Indian Ocean, lacking basic equipment [7]. Intense tsunamis are rare: in many regions they will not occur once in a century; therefore experience is mainly the result of tradition or education. In Japan experience let casualties, caused by the 2011 Tohoku-oki M_w 9.1 earthquake followed by up to 40 m run-up height, be just over 15,000, notwithstanding the delayed realization of the real event intensity [8], compared to over 250,000 people losses due to the 2004 Sumatra M_w 9.1 earthquake with run-up height up to 50 m.

However, for implementing an effective tsunami preparedness, process description must be based on simple models of reality in order to reach the broadest possible population.

Tsunamis of various origin (e.g., underwater earthquakes, volcanic activity, coastal and submarine landslides, meteotsunamis) pose a significant threat to the densely populated and highly urbanized coasts of the Mediterranean Sea, also important tourist destination. Critical coastal infrastructures, such as harbors and marinas, that are well protected from wind waves, are extremely vulnerable to tsunami waves because of their very long wavelength and great penetration capacity often combined with resonance conditions, when the period of the incoming forcing is close to the natural periods of basin oscillation. In addition to the tsunami inundation hazard, maritime infrastructures and operations are exposed to the hazard presented by strong tsunami-induced currents and associated drag forces [9]. Harbor assets, such as floating docks and vessels, are vulnerable to significant damage due to breakage of mooring system elements, collisions, and sinking of smaller crafts.

The purpose of the present study is to obtain a fair reconstruction of the sea surface elevations and currents in harbors for a tsunami case representing a reasonable extreme within lifetime for Mediterranean harbors: the tsunami generated by the 21 May 2003 Boumerdès earthquake in northern Algeria. The earthquake caused 2278 casualties according to the official Algerian government estimates, none in Europe, but it triggered a significant tsunami which caused relevant damages to boats in Balearic and French harbors.

In this study, we simulate tsunami propagation from fault slip distributions proposed by previous studies for the 2003 Boumerdès earthquake; based on available tide gauge measurements of sea level and published information, we identify the best fitting fault model. We quantify tsunami characteristics in ungauged areas and assess how these relate to damages to boats and floating structures reported by local newspaper articles.

1.1. The Earthquake and Tsunami Event

On 21 May 2003 at 18:44 UTC a strong shallow thrust faulting earthquake of estimated moment magnitude M_w between 6.7 and 7.1 severely struck the northern Algeria, causing extensive damage in five provinces and significant impact in terms of human lives and economic losses. The epicenter of the mainshock was located offshore by the Algerian Center of Research in Astronomy, Astrophysics and Geophysics (CRAAG), at 3.58°E, 36.91°N, 7 km north of Zemmouri village and about 50 km east-northeast of the capital city Algiers [10]. A moment magnitude M_w = 6.8 and a depth of 10 km were estimated by CRAAG. An epicentral location of 3.53°E, 36.81°N, a moment magnitude M_w = 7.0 and a strong motion duration of about 10 seconds were computed by the National Center of Applied Research in Earthquake Engineering (CGS), which operates the Algerian accelerograph network [11,12].

The field reconnaissance report compiled by the post-earthquake investigation team of the Earthquake Engineering Research Institute [13] indicates that damage occurred over a zone about 100 km long and 50 km wide, centered at the city of Boumerdès and including the entire coastal province.

After the mainshock a permanent seafloor uplift was revealed by a continuous white strip, due to the aerial emergence of algae, on many rocky headlands. An average uplift of 0.55 m along the coastline between Boumerdès and Dellys with a maximum of 0.75 m at about 3.4 km east of Kaddous was determined in [14] through GPS field surveys.

The earthquake was followed by a tsunami that was noticed by several witnesses and recorded by various tide gauges throughout the Western Mediterranean. While the Algerian coast seems to have not suffered flood damage from the tsunami waves, significant sea level variations and considerable damage to vessels and nautical infrastructures were reported in various ports and harbors of the Balearic Islands, approximately 300 km north of the epicenter, short less than 1 hour after the mainshock. According to newspaper accounts the major damage was experienced within the port of Mahon, in Menorca Island.

1.2. Historical Occurrence of Tsunami Events Associated with Earthquakes at the North African Margin

The analysis of historical documentary sources, integrated by geological and geomorphological signatures and instrumental records, highlights a tsunami hazard of seismic origin for the Western Mediterranean region due to earthquakes with epicenter located along the northern African margin, mainly at the Algerian coast [15]. At least other five seismic events, in addition to the 2003 earthquake, had origin along this margin and triggered tsunamis.

On 9 October 1790 a strong earthquake having M_w 6.7 [16] or 7.0 [17] and epicenter near the city of Oran was followed by a tsunami in the Alboran Sea which flooded the northern African and southern Spanish shores [4,18].

Effects of a destructive earthquake (M_w 7.2) that occurred on 21 August 1856 offshore Djijelli, about 300 km east of Algiers, were observed in the port of Mahon in the Balearic Islands, where it was reported that the sea suddenly rose to a significant height and instantly flooded all the seafronts, breaking moorings of many vessels and boats [18–20].

Furthermore, on 15 January 1891 at Larhat-Gouraya (ex Villebourg) an earthquake (M_w 7.0, according to [17]) caused a coastal uplift of 30 cm and 30 m sea withdrawal followed by flooding along the Algerian coast [21]. Both the El Asnam (formerly Orléansville, today Chlef) earthquakes of 1954 (M_w 6.7) and 1980 (M_w 7.1) [22] generated weak tsunami waves in the Alboran Sea that were recorded by several tide gauges located at the southeastern coast of the Iberian Peninsula [18].

We therefore estimate that weak tsunamis of seismic origin, as the one that is subject of this study, occur in the Western Mediterranean Sea with recurrence time of around 40 years.

1.3. Previous Modeling Studies of the 2003 Tsunami

The availability of a large number of sea level records, collected from tide gauges operating in the Mediterranean region at the time of the 2003 Boumerdès earthquake, although their majority was characterized by a temporal resolution not adequate to reproduce the event, as well as the existence of damage information in press reports made this tsunami a study case of relevant interest for numerical modeling investigations, also because it resulted to be associated to a fault zone not well-known until this event. Numerous data and damage documentation may enable to better constrain the tsunami source parameters and mechanism improving the evaluation of the expected impact on the coast and, consequently, are of crucial importance to implement proper tsunami scenarios for hazard assessments and for pre-computed databases with early warning purposes. An accurate numerical modeling of actual tsunami events coupled with the availability of a set of sea level measurements of adequate resolution may result particularly useful to complement the seismic determination, especially when, as in the case under consideration, the earthquake occurs offshore and geodetic data are scarce or non-existent.

Several attempts have been made to numerically simulate the tsunami event triggered by the 2003 Boumerdès earthquake. However, all proposed simulations present relevant discrepancies in the tsunami wave heights when they are compared with the actual tide gauge measurements.

Preliminary simulations were performed by Hébert and Alasset (2003) [23] by using a 2′ grid for describing the Western Mediterranean Sea and a 30″ grid for the Balearic Islands, without refinements in the bays. An initial positive seafloor displacement of 0.3 m at most was computed considering a 40 × 20 km fault plane, depth of 17 km, homogeneous slip pattern and seismic parameters derived from the Harvard Centroid Moment Tensor (CMT) solution. A seafloor displacement slightly higher than 0.4 m was obtained by using a shallower source depth (10 km) and a moment magnitude M_w 6.9. The simulation results show the Eivissa Island more exposed to the tsunami event than Menorca and indicate an arrival time in Palma not shorter than 45 to 50 min.

Numerical simulations of the tsunami event were carried out by Wang and Liu (2005) [24] to test the accuracy of two different fault plane mechanisms: the source model corresponding to the Harvard CMT solution with fault dimensions and slip displacement derived by Borrero (2003) [25], and the fault plane model proposed by Meghraoui et al. (2004) [14] taking into account the coastal

uplift measurements. The tsunami wave heights, simulated through the COMCOT numerical model using a nested grid system with smaller size down to 10 m, were then compared with the tide gauge measurements collected on Eivissa Island at Ibiza and Sant Antoni. It was found that the source mechanism proposed by Meghraoui et al. [14] provided better tsunami wave height predictions than that of the Harvard CMT solution, although both fault models significantly underestimated the recorded sea level oscillation data. A sensitivity analysis was performed by Wang and Liu [24] to evaluate if the large discrepancies between the simulated tsunami wave heights and the tide gauge measurements could be explained by uncertainties in the fault plane parameters. One fault plane parameter was varied at a time within its uncertainty range and its effect on the leading tsunami wave height at Ibiza was examined, considering the Harvard CMT solution as reference case for the comparison. The results of the analysis showed that the tsunami wave height was sensitive to uncertainty in the focal depth, strike angle, and seismic moment, but not sensitive to uncertainty in dip and rake angles. The tsunami wave height only increased by 60% combining the deviations most favorable to the increment, therefore the normal uncertainties in fault parameters cannot account for the observed discrepancy. Wang and Liu [24] proposed a calibration (inversion) procedure to determine the optimal seafloor displacement using only the Sant Antoni tide gauge data. The fault model optimized by Wang and Liu [24], subsequently validated with the Ibiza sea level measurements, indicated that a stronger displacement was necessary for the generation of the observed tsunami, corresponding to an earthquake having $M_w = 7.2$.

Analyzing seismic T wave records from two IRIS network broad-band stations, one located in Menorca Island and the other in Sardinia, Alasset et al. (2006) [26] indicated the Boumerdès earthquake as the only mechanism responsible for the generation of the observed tsunami, excluding any large submarine landslide effect. To test the effects of the earthquake source models proposed by Delouis et al. (2004) [27], Meghraoui et al. (2004) [14], Yelles et al. (2004) [28], Bezzeghoud et al. (reported by Alasset et al. [26]) and Semmane et al. (2005) [29], Alasset et al. [26] numerically modeled the 2003 tsunami under the shallow water approximation, ignoring any bed friction. By comparing the simulated data with the tide gauge measurements in the ports of Algiers, Palma de Mallorca, Ibiza and Sant Antoni, Alasset et al. [26] concluded that the fault sources proposed by Delouis et al. [27] and Meghraoui et al. [14], with epicenter close to the shoreline and corresponding to a moment magnitude of 6.9, were able to describe the observed sea level variations better than the other models. The source model proposed by Semmane et al. [29] with $M_w = 7.1$ was considered by Alasset et al. [26] not appropriate because of the greater distance of the fault rupture from the shore and the excessive amplitudes obtained in Sant Antoni and Ibiza since the third wave after tsunami arrival. The low amplitudes computed in Palma were attributed by Alasset et al. [26] to the poor quality of the bathymetric data and to problems with the bathymetric grids.

Sahal et al. (2009) [30] performed a numerical simulation of the sea water elevations induced by the 2003 tsunami in three selected harbors of the French Mediterranean coast: La Figueirette and Cannes–Mouré-Rouge, which suffered from a water level drop of about 1.5 m according to witnesses, and Cannes–Vieux-Port located among the previous two, less affected by sea level oscillations. The same method previously applied by Alasset et al. [26] was employed to model the tsunami generation, propagation and coastal impact. Only the fault model proposed by Delouis et al. [27] was used. The simulation results showed a certain correlation between the field observations and the wave amplification along the coast; however, the numerical modeling presented an underestimation of the observed tsunami amplitudes, even by using high resolution bathymetric grids with grid size of 3 m centered on the three harbors.

Finally, Vela et al. (2010, 2014) [31,32] performed a numerical study with the main aim to understand the response of the Palma port and its interaction with the bay under the impact of the 2003 tsunami. By comparing the oscillations generated by the tsunami event with the natural oscillation modes of the bay and port, Vela et al. [31,32] concluded that the wave amplification observed inside the port, mainly in its northern inner basin, was generated by a resonance effect induced by the Palma

bay configuration. The tsunami numerical simulation was carried out with the COMCOT model representing both the fault model proposed by Meghraoui et al. [14] and that optimized by Wang and Liu [24]. Both sources underestimated the tsunami wave amplitude measured at the Palma tide gauge. Furthermore, Vela et al. [32] carried out a sensitivity analysis on the influence of the grid size in describing the port and bay bathymetries. It was observed that, by increasing the grid resolution in the bay and in the port and considering the actual port geometry and internal configuration, a slight wave height increment was obtained which, however, did not reach the prototype measurements.

Table 1 presents the characteristics of the first arriving tsunami wave estimated from the Sant Antoni and Palma sea level records and summarizes the results obtained from the previous studies by numerical modeling. All tested source models are unable to reproduce the tsunami observations at the tide gauges, greatly underestimating the first arriving tsunami wave height, with the only exception of the fault model proposed by Wang and Liu [24], optimized by minimizing the difference between observed and simulated waveforms at Sant Antoni. The same fault model was used by Vela et al. [31,32] resulting however in a significant wave height underestimation in the port of Palma.

All the mentioned studies make use of the shallow water approximation. For other cases, models based on high order Boussinesq approximation and regular mesh were used, an example is provided by Samaras et al. [33] for the Eastern Mediterranean Sea.

The experience shows that the main influence on the inshore resulting tsunami wave is due to the fault mechanism (sliding plane and space–time distribution of slip along the plane) and the local bathymetry around the recording gauge; if bathymetry is accurately reproduced, simulations can provide some information about the fault mechanism.

Table 1. Characteristics of the first arriving tsunami wave estimated from the Sant Antoni and Palma sea level records and results obtained from previous studies by numerical modeling.

Source	Sea Level Station	Simulated Fault Mechanism	M_w	Arrival Time	First Peak Elevation (m)	First Peak to Trough Height (m)
Sea level record	Sant Antoni			19:45	0.37	0.99
Wang & Liu [24]	Sant Antoni	Meghraoui et al. [14]	6.8–6.9	19:47	0.19	0.54
Wang & Liu [24]	Sant Antoni	Wang & Liu [24]	7.2	19:45	0.37	1.08
Alasset et al. [26]	Sant Antoni	Meghraoui et al. [14]	6.8–6.9	19:47	0.07	0.19
Alasset et al. [26]	Sant Antoni	Semmane et al. [29]	7.1	19:45	0.22	0.57
Sea level record	Palma			19:35	0.24	0.59
Alasset et al. [26]	Palma	Meghraoui et al. [14]	6.8–6.9	19:45	0.04	0.08
Alasset et al. [26]	Palma	Semmane et al. [29]	7.1	19:41	0.16	0.36
Vela et al. [31]	Palma	Meghraoui et al. [14]	6.8–6.9	19:41	0.09	0.24
Vela et al. [31]	Palma	Wang & Liu [24]	7.2	19:41	0.12	0.30

1.4. Objectives of the Present Study

The present study focuses on a detailed modeling of the tsunami event following the 2003 Boumerdès earthquake as consequence of different fault models, showing how the simulation of tsunami effects can provide information on the seismic phenomenon, including the identification of the most probable generation mechanism. In this study, tsunami propagation and impact in ports are modeled starting from slip distributions derived from previous analyses on the 2003 Boumerdès earthquake source. The performance of the tsunami source models is assessed by comparing the simulation results with the tsunami waveforms recorded by several tide gauges and the available damage documentation mainly in the Balearic Islands.

A detailed modeling of the event is necessary in order to relate the hydrodynamic processes to damages caused in coastal zones and harbors. The analysis of this relation is the objective of the engineering part of this paper.

The paper is organized as follows: Section 2 summarizes the different fault mechanisms proposed to represent the earthquake; Section 3 compares the results of our hydrodynamic simulations for the different fault mechanisms with the instrumental observations at tide gauges and arguments about the

most likely earthquake mechanism; Section 4 describes the major damages suffered in ports; Section 5 illustrates the relation between observed boat and infrastructure damages in Balearic ports and the simulated distributions of extreme sea levels and currents derived from the selected best fitting model and pointing out any effects of bay/port resonance; finally Section 6 summarizes the conclusions.

Our innovative contributions consist mainly in:

- simulation of the tsunami effects for a modified version of the fault mechanism originally proposed by Belabbès et al. (2009) [34], considering both a synchronous and asynchronous slip and justifying the need for an increased magnitude passing from seismic to tsunami modeling;
- highlighting for the analyzed tsunami case the effect of the bay/port resonance in relation to the observed periods and damages;
- analysis of the current intensity and tsunami height thresholds suggested in literature for small ships or boats at berth.

2. Details on the Earthquake and the Tsunami

2.1. The Fault Process

The earthquake that struck the northern Algeria on 21 May 2003 exhibited an offshore thrust faulting mechanism mainly related to the compression tectonic regime along the African and Eurasian plate boundary. The present convergence rate between the two plates at the northern Algerian margin ranges from 3 to 6 mm/yr along approximate NW-SE direction [35,36] and is responsible for triggering most of the seismic activity in this region. The 2003 Boumerdès earthquake occurred along the complex thrust and fold system at the northern margin of the Tell Atlas, in the northeastern continuation of the Blida Mountains front and related Quaternary Mitidja Basin [37].

The epicentral area is geologically characterized by a metamorphic basement, mostly constituted by micashistes and quartzites, overlain by Mio-Pliocene and Quaternary clays and sand deposits [38]. The recent Quaternary deposits include the alluvial deposits within the basin and the marine terraces along the coast [21].

Since the mainshock locations obtained by CRAAG, USGS NEIC, and EMSC (Table 2) were in conflict with the measurements of coastal uplift, using a double difference method and three major aftershocks, Bounif et al. [37] relocated the mainshock epicenter on the coastline (3.65° E, 36.83° N) and the hypocenter at 8–10 km depth. The analysis of the aftershock distribution, which extends to about 16 km depth, highlights a NE-SW oriented and south dipping fault and two distinct clusters of seismic events along strike [37].

Several rupture and fault slip models based on teleseismic and geodetic data have been proposed for the 2003 Boumerdès earthquake; some are shown in Table 2.

Most of the proposed models agree on the mainshock hypocenter depth, about 10 km beneath the surface, and on a bilateral rupture propagation from the hypocenter, with two distinct slip peaks. These models indicate a 50–64 km long fault plane, with strike 54–70° (ENE), dip 40–50°, and rake around 90° (thrust mechanism).

A uniform slip distribution of 1.8 m is assumed by Yelles et al. [28] because of the limited amount of available GPS data and spatial coverage. An average fault slip displacement of about 1 m is estimated by Braunmiller and Bernardi [43]. A maximum slip amplitude of about 3 m is estimated west of the hypocenter by Delouis et al. [27] and Semmane et al. [29]; a maximum dislocation of about 2.3 m is found by Yagi [39] 25 km southwest from the hypocenter; maximum slip values of 1.6 and 4.7 m are obtained respectively by Meghraoui et al. [14] and Belabbès et al. (planar model [34]) east of the hypocenter, while a maximum slip of 3.8 m is derived by Santos et al. (solution 1 in [44]) around the hypocenter.

Table 2. Estimated parameters of the 21 May 2003 Boumerdès earthquake.

Source	Time (UTC)	Lon (°E)	Lat (°N)	Depth (km)	M_0 (N·m)	M_w	S/D/R (°)	Fault Length (km)	Fault Width (km)	Data Type
CRAAG	18:44:19	3.58	36.91	10		6.8				
CGS	18:44:40	3.53	36.81			7.0				
EMSC	18:44:22	3.76	37.02	21		6.8				
USGS NEIC	18:44:19	3.78	36.89	10		6.7				
USGS (2014)	18:44:20	3.634	36.964	12	2.15×10^{19}	6.8	55/30/90			
Harvard CMT	18:44:30	3.58	36.93	15	2.01×10^{19}	6.8	57/44/71			
CEA-DASE	18:44:22	3.78	36.71	18		6.9				
ETH		3.74	37.04	10		6.74	63/35/48			
INGV	18:44:29	3.61	36.90	15	1.8×10^{19}	6.8	65/27/86			
Yagi [39,40]		3.78	36.89	10	2.4×10^{19}	6.9	54/47/86	60	10	T
Delouis & Vallée [41]				10	2.38×10^{19}	6.9	57/39/83	50		T
Yelles et al. [28]					2.4×10^{19}	6.9	55/42/84	32	14	G
Delouis et al. [27]		3.65 (B)	36.83 (B)	6.5	2.9×10^{19}	6.9	70/45/95	60	24	T, G, U
Meghraoui et al. [14]		3.65 (B)	36.83 (B)		2.75×10^{19}	6.9	54/50/(90)	54		U
Bezzeghoud et al. [42]		3.65 (B)	36.83 (B)	7	1.3×10^{19}	6.8	64/50/90			T
Braunmiller & Bernardi [43]	18:44	3.65 (B)	36.83 (B)			7.0	62/25/82	50		T
Semmane et al. [29]		3.65 (B)	36.83 (B)		5.9×10^{19}	7.1	54/47/88	64	32	G, U, M
Belabbès et al. [34], planar		3.65 (B)	36.83 (B)	8	1.78×10^{19}	6.8	65/40/90	60	30	S, U, G
Belabbès et al. [34], curved		3.65 (B)	36.83 (B)	10	2.15×10^{19}	6.8	65/40/90			S, U, G
Santos et al. [44], sol 1		3.660	36.846	8	1.40×10^{19}	6.7	64/50/97	60	20	T, U, S

CRAAG—Center of Research in Astronomy, Astrophysics and Geophysics, Algeria, [10]; CGS—National Center of Applied Research in Earthquake Engineering, Algeria, [11,12]; **EMSC**—Euro-Mediterranean Seismological Center, https://www.emsc-csem.org/Doc/BOUMERDES_21052003/ALGER_long.txt, [45]; **USGS NEIC**—USGS National Earthquake Information Center, USA, http://www.indiana.edu/~pepp/earthquakes/images/algeria5_21_03/usgsmap.jpg. (accessed on 7 Jan 2017); **USGS (2014)**—United States Geological Survey, USA. Earthquake Catalog, last update of moment tensor in 2015, https://earthquake.usgs.gov/earthquakes/search/; **Harvard CMT**—Harvard Global Centroid Moment Tensor Catalog, http://www.globalcmt.org/CMTsearch.html; **CEA-DASE**—Commissariat à l'énergie atomique et aux énergies alternatives, Direction des applications militaires, Sciences de la Terre et de l'Environnement, France, http://www-dase.cea.fr/actu/dossiers_scientifiques/2003-05-21/index_en.html; **ETH**—Swiss Federal Institute of Technology, Switzerland, Table 4.1 in [46]; **INGV**—National Institute of Geophysics and Vulcanology, Italy, http://mednet.rm.ingv.it/procedure/events/QRCMT/030521_184422/qrcmt.gif. Longitude, latitude and depth of hypocenter. S/D/R are strike, dip and rake angles. M_0 is the seismic moment and M_w the moment magnitude. Epicenter relocation from Bounif et al. [37] is indicated with (B). The last column indicates the type of data used to estimate the slip distribution: T = teleseismic data; U = coastal uplift measurements; G = GPS network data; M = strong motion data from accelerometric network stations; S = synthetic aperture radar data.

A fault dip change with depth (ramp-flat fault system) is proposed by Déverchère et al. [47,48], by using the data collected during the Maradja cruise in August-September 2003, to explain the two fault scarps identified at the foot of the continental slope ~15–17 km away from the coastline, whose geometry matches in along-strike position, length, and direction the seismic rupture proposed by Delouis et al. [27].

From the analysis of an one-year long aftershocks sequence Kherroubi et al. [49] propose a rupture model strongly controlled by structural heterogeneities and extending as ramp-flat-ramp systems upward, favoring heterogeneous slip and fault segmentation along strike with strong afterslip in the upper part of the rupture.

Also, the examination of the radiated seismic energy determined by IRIS DMC [50] following the procedure described by Convers and Newman [51] highlights that this earthquake exhibits complex and non-instantaneous energy release which is easily identifiable within the cumulative high frequency and broadband energy plots (Figure 1). A rupture duration T_R of 74 s is estimated by the fully automated procedure based on the method of Convers and Newman [51]. The earthquake energy exhibits an initial nonlinear growth-period that terminates at about 60 s, followed by a second growing

phase which appears to last quite longer. The energy magnitude results 6.91 at the conventional rupture duration but increases (afterslip) exceeding magnitude 7 at 200 s.

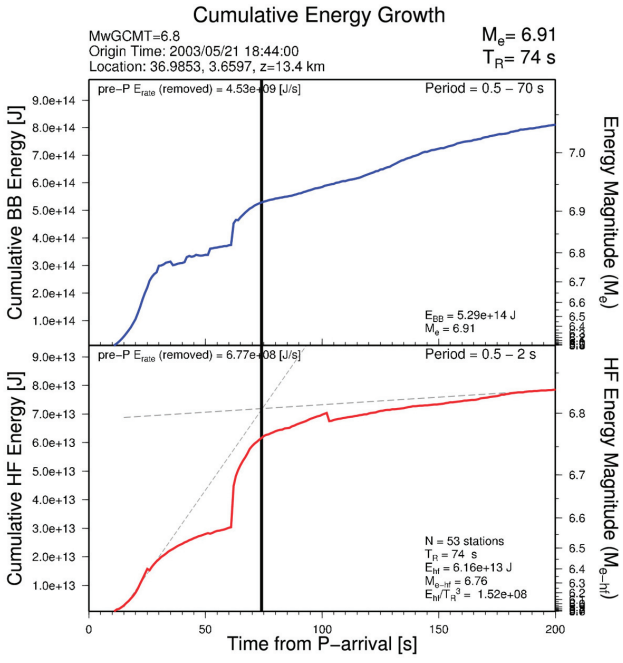

Figure 1. Cumulative energy growth as a function of time for the 2003 Boumerdès earthquake; EQEnergy data from http://ds.iris.edu/ds/products/eqenergy, doi:10.17611/DP/1718531. Based on the procedure of Convers and Newman [51], the high frequency energy growth is used to identify the approximate event duration T_R, while the total event energy is determined using broadband energy at T_R.

A description of the space and time evolution of the rupture process (slip) on the fault plane is given by Delouis et al. [27] and Santos et al. [44], but both restrict the analysis to the first seconds after the mainshock (12 s and 15 s respectively) and therefore do not provide information about the second energy release phase evident in Figure 1.

As it occurred for the 1954 and 1980 El Asnam earthquakes [52,53], also following the 2003 Boumerdès earthquake several submarine telecommunication cables were broken leading to an interruption of the telephonic traffic between Algeria and Europe. An examination of the locations of the submarine cable breakpoints supported evidence of a series of large turbidity currents, triggered almost synchronously and responsible for 29 cable breaks, that occurred from 36 to 228 min after the earthquake at the inner continental slope down to the abyssal plain, over a distance of 150 km along the coast and about 70 km offshore the coastline [54]. However, according to [55], turbidity currents alone are not relevant in tsunami generation because by the time sediment is mixed with water causing density gradient (baroclinic conditions) in the water column, the tsunami has already been generated and is propagating away from the source area.

In addition to the coastal uplift of marine terraces documented in [14] following the 2003 earthquake, an average 100 m seawater withdrawal was observed along 50 km of the Algerian coastline from Corso to Dellys [56]. A seawater retreat was also experienced by the ports of Algiers, Zemmouri and Dellys [57]. Contrary to the mentioned Villebourg event and to the 1856 Djidjelli earthquake, during which the sea retreated about 30–35 m and then returned flooding the Algerian coast [21],

the 2003 Boumerdès earthquake did not cause flooding along the Algerian coast but only at the Balearic Islands [26,56].

2.2. The Generated Tsunami

Almost all tide gauges located in harbors facing the Western Mediterranean Sea registered the tsunami waves resulting from the 2003 Boumerdès earthquake (Figures 2–6). The largest sea level wave amplitudes were recorded at Sant Antoni and Palma tidal stations on Eivissa and Maiorca Islands, where maximum peak-to-through height of 1.96 m and through-to-peak height of 1.16 m respectively were observed in records (Figure 3). The first tsunami wave arrived at the port of Palma at 19:35 UTC and in Sant Antoni at 19:45 UTC, i.e., 51 and 61 min respectively after the mainshock. Estimation of the first wave arrival time from the Palma and Sant Antoni records, characterized by a good temporal resolution of 1 and 2 min respectively, is more accurate than for all other stations using 5 or 10 min sampling interval. Figures 3–6 present the sea level time series at the available tide stations along the Mediterranean coasts after applying a fourth order, phase preserving, high-pass Butterworth filter with 1/3 h^{-1} cutoff frequency to remove the tidal signal from the original data. In several Spanish harbors the earthquake induced sea level oscillations lasting more than 24 hours (Figure 4). Filtered sea level amplitudes lower than 0.25 m were observed along the French (Figure 5) and Italian coasts (Figure 6).

The Sant Antoni, Ibiza, Palma, Malaga, and Valencia sea level records were examined by Vich and Monserrat [58] through a spectral analysis, identifying a main peak around 21 min and two secondary peaks at 14 and 42 min. The 21 min main period was considered related to the tsunami source.

Through a wavelet analysis using 19 coastal tide gauge records, Heidarzadeh and Satake [59] showed that only the period around 23 min was a powerful signal of tsunami, as it was rather strong in all the examined stations, while other peaks at 14, 30, 45, and 60 min lasted only a short time.

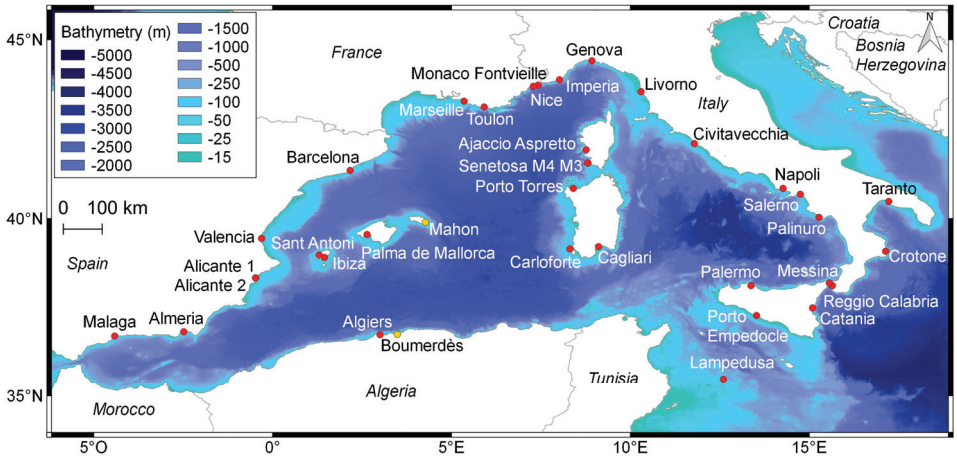

Figure 2. Bathymetry of the Western Mediterranean Sea from the EMODnet Bathymetry portal. The red dots mark the location of the tide gauges available in the area during the 21 May 2003 tsunami event. The locations of the Boumerdès village and Mahon port are also indicated on the map as yellow dots.

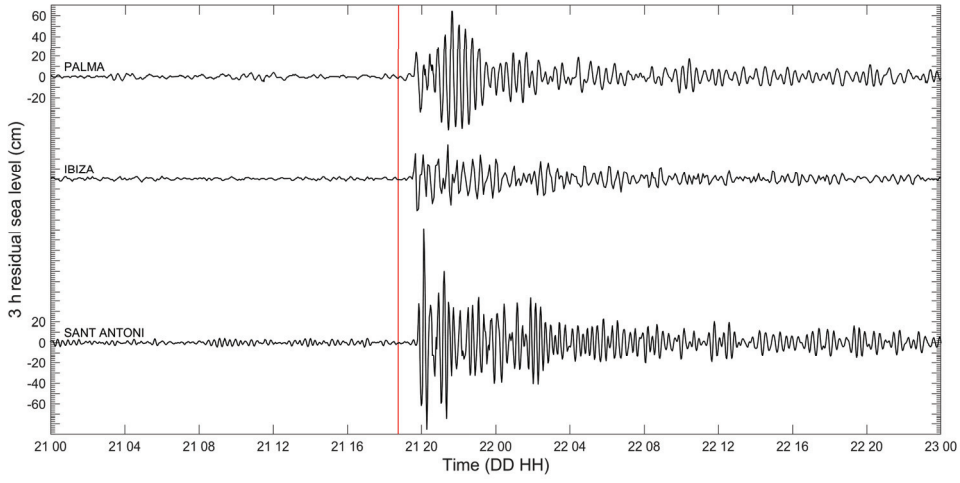

Figure 3. Tsunami records at Balearic Islands ports. 1 min sea level data from the Palma de Mallorca tide gauge are available from the SeaDataNet website; 2 min sea level measurements in Sant Antoni were provided by Dr. M. Marcos (IMEDEA); 5 min data from Ibiza tide gauge are delivered by Puertos del Estado; the vertical red line denotes the time of the earthquake (https://cdi.seadatanet.org/search; http://www.puertos.es/en-us/oceanografia/Pages/portus.aspx).

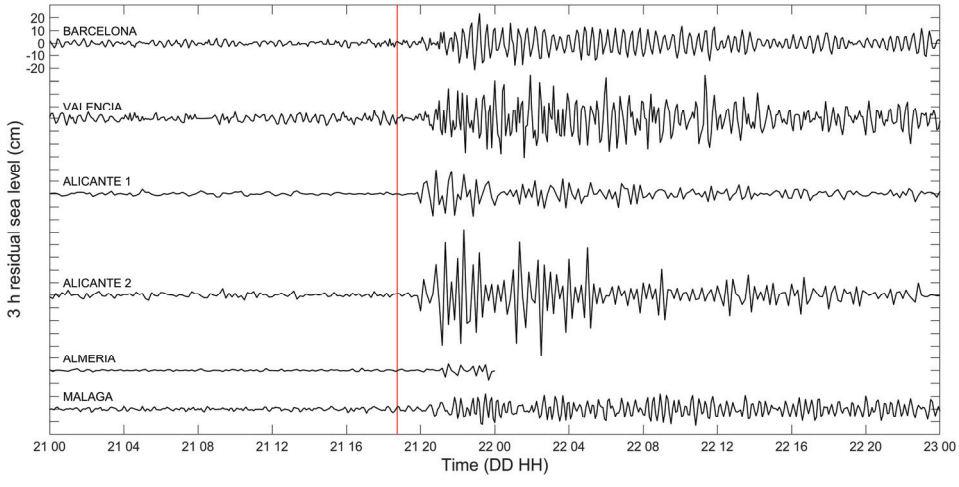

Figure 4. Tsunami records at Spanish ports. 5 min sea level data from Barcelona, Valencia and Malaga tide gauges are delivered by Puertos del Estado. 10 min measurements at Alicante 1, Alicante 2 and Almeria are provided by Instituto Geográfico Nacional (https://www.ign.es/web/ign/portal/gds-red-mareografos). The vertical red line denotes the time of the earthquake.

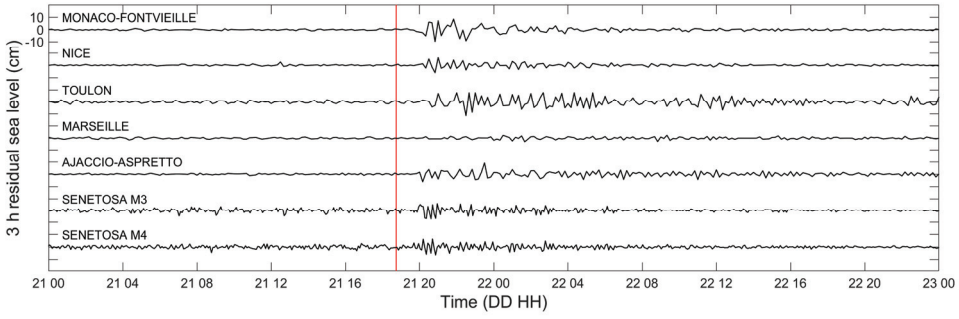

Figure 5. Tsunami records at French ports. 10 min sea level measurements from Monaco-Fontvieille, Nice, Toulon, Marseille and Ajaccio-Aspretto tide gauges are delivered by SHOM (http://data.shom.fr/). 5 min sea level data from Senetosa M3 and M4 are available from AVISO+ website (https://www.aviso.altimetry.fr/data/calval/in-situ/absolute-calibration/download-tide-gauge-data.html). The vertical red line denotes the time of the earthquake.

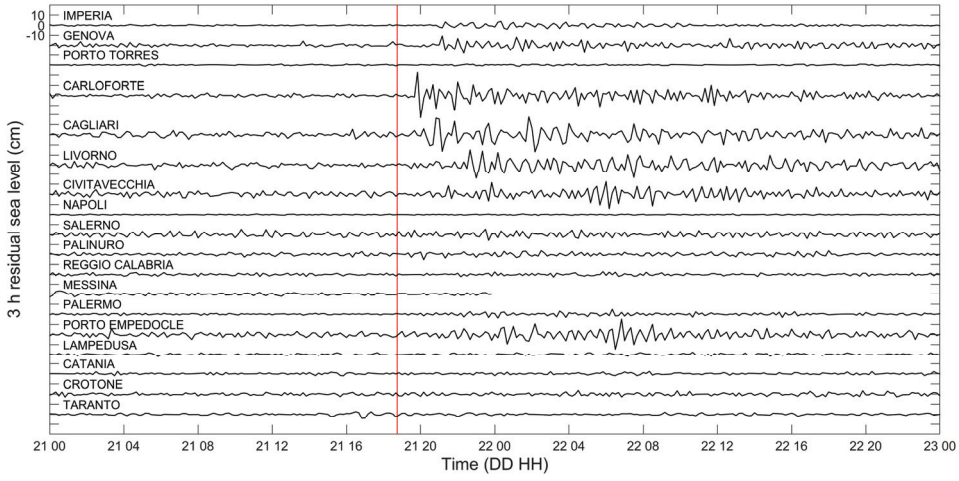

Figure 6. Tsunami records at Italian ports. Sea level measurements with 10 min sampling interval are delivered by Higher Institute for Environmental Protection and Research (ISPRA). The vertical red line denotes the time of the earthquake.

3. Comparison between Hindcasted and Recorded Sea Levels

3.1. The Numerical Model Used

3.1.1. Seabed Displacement

Seven different fault models among those proposed in literature for the 2003 Boumerdès earthquake, inferred from different measurement data (as shown in Table 2), have been used in this study to test their ability in reproducing the observed tsunami characteristics from tide gauge records. The considered earthquake source models are the planar fault models proposed by Yelles et al. (2004) [28], Delouis et al. (2004) [27], Meghraoui et al. (2004) [14], Semmane et al. (2005) [29], Braunmiller and Bernardi (2005) [43], Belabbès et al. (2009) [34], and Santos et al. (2015) [44]. Although some of the indicated source models have already been investigated in other studies (see Section 1.3), they have also been tested by us in order to obtain a comparison independent from the hydrodynamic model effects, as well as to check our implemented geometrical and hydrodynamic model.

The ports of Palma de Mallorca, Sant Antoni, Ibiza, Mahon, Valencia, and Cagliari have been selected to compare modeling results with reported observations. The reasons for this choice have been: (1) the availability of records and information for the Balearic ports, the most affected by the tsunami; (2) the opportunity to examine the long persistence of oscillations at the Valencia tide gauge; and (3) to verify the tsunami effects in an Italian location not directly exposed to the incoming waves as Cagliari. Only two high quality records are available for this event, those of Palma de Mallorca and Sant Antoni; they, however, do not provide adequate azimuthal coverage to estimate a reliable tsunami source model through an inversion method, therefore also other witnesses have been analyzed.

The amount and spatial distribution of slip along the fault plain suggested by Delouis et al. [27], Belabbès et al. [34], and Santos et al. [44] have been obtained processing the corresponding published images, while the Semmane et al. [29] rupture model included in the online SRCMOD database (Earthquake Source Model Database, http://equake-rc.info/SRCMOD/) already in digital format has been adopted. The remaining rupture models have been reconstructed using the information derived from the corresponding references. The fault model proposed by Braunmiller and Bernardi [43] extending to about 3.9°E and composed of two segments with length of about 40 and 10 km has been simplified here by considering a single 50 km long rectangular patch. It is observed that retrieving the slip distribution model on the planar fault from the pixels of the image published in [34] was complicated by the presence of the mesh with triangular elements used by the Authors for modeling geodetic datasets through an inversion procedure to constrain the earthquake rupture parameters. When the image was analyzed the darker trace of the mesh determined along the lines themselves a slip overestimation resulting in an increase of the seismic moment M_0 from the value of 1.78×10^{19} N·m (M_w = 6.8) to 9.10×10^{19} N·m (M_w ~ 7.2), while retaining the two linked peaks of the pattern indicated by Belabbès et al. [34]. Overestimation was not removed but intentionally maintained in order to represent the fact that energy magnitude had passed level 7 at 200 s. The resulting tsunami period was around 1200 s and slip contributions occurring within a few minutes from the mainshock are naturally accumulated.

For each considered earthquake source model the corresponding spatial distribution of the coseismic surface displacements was calculated from the slip distribution on a 250 m resolution square grid using the Coulomb 3.3 software [60], which implements the Okada analytical expressions for the displacement and strain fields due to a finite rectangular source in a homogeneous, elastic, and isotropic half-space [61]. The seabed deformation process has been deemed to occur instantaneously and the corresponding initial water elevation has been assumed equal to the coseismic displacement of the bottom surface η, determined by the formula

$$\eta = \frac{\partial H}{\partial x} D_x + \frac{\partial H}{\partial y} D_y + D_z \quad (1)$$

accounting for both the horizontal (D_x,D_y) and vertical (D_z) components of the bottom displacement vector and the distribution of water depths, $H(x,y)$, in the vicinity of the source [62,63]. This instantaneous water surface elevation has been applied as initial condition for the tsunami propagation model. The seawater depth in the source region of the 21 May 2003 tsunami is in the range from 0 to 1000 m. Considering an average seawater depth of 500 m and a dominant period around 1200 s, a tsunami wavelength of 84 km is estimated. Therefore, since the tsunami wavelength is more than 13 times the water depth at the source, a low-pass filter accounting for attenuation of short wavelength components of the seabed displacement field through the water column, e.g., Kajiura filter [64], was not applied according to [65].

A preliminary test has been carried out to explore the effects of the earth crust mechanical properties, mainly of the Poisson ratio, on the tsunami generation. The source rupture models proposed by Meghraoui et al. [14] and Yelles et al. [28] have been considered and the corresponding vector fields of coseismic sea bottom displacements have been calculated using the Coulomb 3.3 software with different values of the Poisson ratio ν, a constant Young modulus E of 700,000 bar and a friction coefficient of 0.4. The generated displacements have been evaluated and compared in terms of initial maximum surface elevation and drawdown, displaced water volume and potential energy of the initial surface elevation according to the approach described in [62]. Since a reduction of 0.05 in Poisson ratio corresponds to an increase of only 0.01 in moment magnitude, that lies within the overall uncertainty on the M_w estimate, a value 0.20 was finally adopted for ν in all the subsequent computations.

The resulting initial water surface elevation calculated for each of the seven considered rupture models is shown in Figure 7. The maximum uplift of the water surface at the source is obtained with the model derived from that developed by Belabbès et al. [34], 1.86 m, and the minimum, 0.43 m, with the Braunmiller and Bernardi [43] model. The drawdown is rather limited in all cases, ranging from −0.18 m in the Delouis et al. [27] model to −0.04 m in that of Yelles et al. [28]. The maximum values of displaced water volume and potential energy of the initial surface elevation are provided by the modified Belabbès et al. [34] model (4.08×10^8 m^3 and 4.20×10^{12} J), followed by that of Semmane et al. [29] (2.40×10^8 m^3 and 1.30×10^{12} J). The minimum displaced water volume is given by the Meghraoui et al. [14] model and the minimum potential energy of the initial surface elevation by the Santos et al. [44] source (2.57×10^{11} J). Most models present a weak drawdown offshore the fault line and an intense uplift onshore; this explains why at the Balearic coast a very weak depression anticipated the first crest. At the Algerian coast land and water level are raised of the same amount at earth displacement time. In the initial period some flooding is likely due to the difference between the shoreline vertical displacement and the maximum displacement that takes place offshore. This difference has probably activated a minor flooding wave that was probably not observed in the confusion caused by the strong earthquake. The following withdrawal phase, when the shoreline uplift contrasts sea retreat, was certainly much more intense and visible and therefore cited.

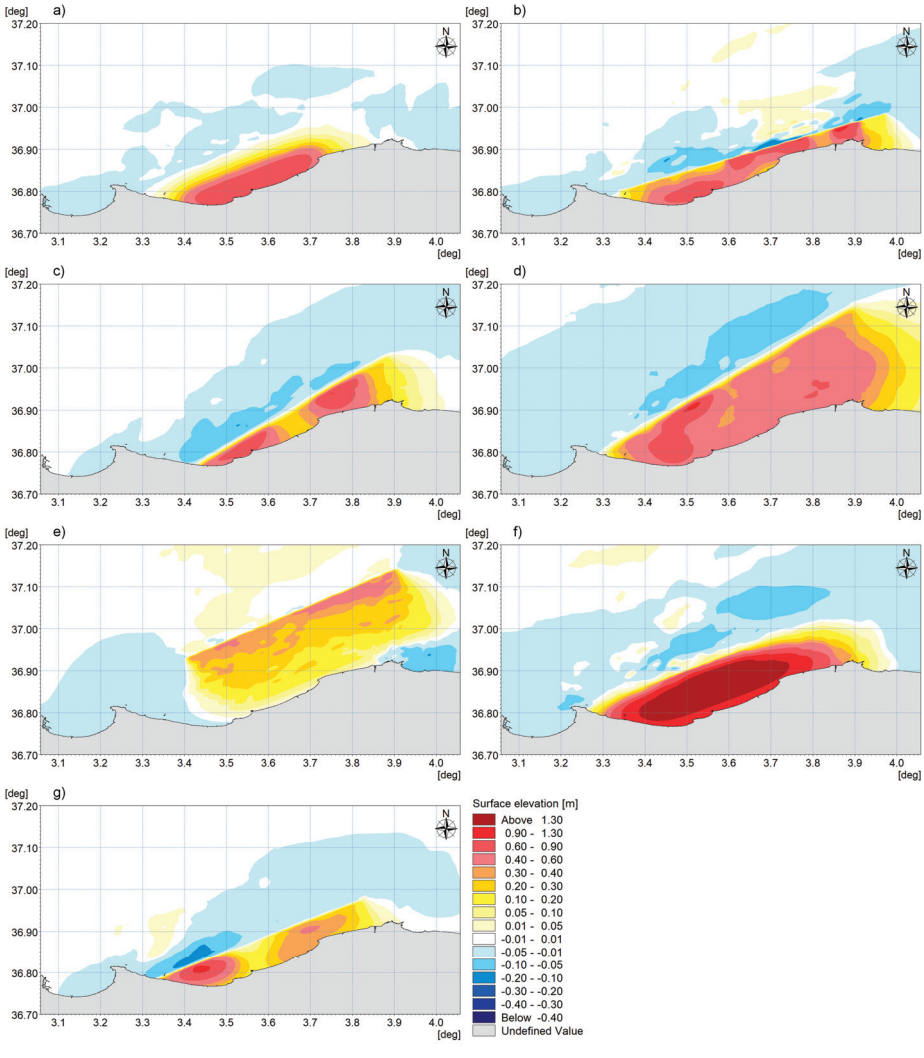

Figure 7. Initial water surface elevation estimated for each considered source model of the 21 May 2003 Boumerdès earthquake: (**a**) Yelles et al. [28], (**b**) Delouis et al. [27], (**c**) Meghraoui et al. [14], (**d**) Semmane et al. [29], (**e**) Braunmiller and Bernardi [43], (**f**) modified from that estimated by Belabbès et al. [34], and (**g**) Santos et al. [44].

3.1.2. Hydrodynamic Model

A fully three-dimensional (3D) model is required for an accurate representation of local large shallow coherent turbulent structures, such as eddies and gyres, generated by tsunamis in the nearshore area or around coastal structures [66,67]. However, for real case studies, a fully 3D model requires a very high computational time and extended memory resources, due to the extensive and complex spatial domain and the very fine resolution needed for tsunami simulation. As no current speed measurements were available inside ports at the time of the 21 May 2003 tsunami allowing the comparison with the simulation results, a depth averaged 2D approach has been applied maintaining reasonable computational time and memory requirements. Models based on the nonlinear shallow

water equations are proven to reproduce satisfactorily the current speeds observed during recent tsunami events, e.g., [9,68], and the velocities predicted by these models may be employed for relative comparisons at different locations in a harbor in order to determine potentially damaging currents or to identify particularly vulnerable areas, e.g., [69].

In this study the Hydrodynamic Module (Flow Model FM, release 2012) included in the MIKE 21 package developed by the Danish Hydraulic Institute Water & Environment (DHI) has been used to numerically simulate the tsunami propagation in the Western Mediterranean to the target ports. The flexible mesh (FM) approach adopted by the package is particularly suitable to accurately and efficiently represent complex coastline shapes and allows variable spatial resolution within the computational domain. The package has been extensively used for hydrodynamics and sediment transport modeling in coastal, estuarine, and marine environments [70,71] and has previously been applied in several studies for simulating tsunami propagation [72,73], tsunami runup and inundation [74–77], to examine tsunami nearshore amplification [78], to investigate resonance response of inlets and ports to tsunami waves [79,80] and for analyzing the nonlinear interaction between tide and tsunami [81].

The modeling system is based on the numerical solution of the 2D nonlinear shallow water equations: the depth integrated Reynolds averaged Navier–Stokes equations for incompressible fluid [82]. The spatial discretization is performed using a cell-centered finite volume method. In the horizontal plane an unstructured grid of triangular elements is used. An explicit scheme is adopted for time integration.

3.1.3. Computational Domain and Unstructured Grids

The hydrodynamic model has been implemented using the unstructured grid and nesting capabilities of the package. A large computational domain covering the entire Western Mediterranean Sea, from the Strait of Gibraltar to the Straits of Sicily and Messina, was used to simulate the tsunami propagation from the source region to the target coastal zones. An area of improved resolution has been embedded in the bathymetry of the large computational domain around the epicentral zone along the Algerian coast, approximately from Bordj El Kiffan to Dellys, extending about 64 km offshore at the longitude of Boumerdès. In this area a mesh refinement with triangular and quadrangular elements has been performed to adequately reproduce the initial surface elevation of the earthquake-generated tsunami.

High resolution local models have also been implemented for the coastal sites of interest, linked to the large model by a one-way offline nesting procedure, i.e., by imposing as boundary conditions for the local model the time series of surface elevation and depth-averaged velocities previously computed by the large model at points along the boundary of the inner domain. The computational mesh of the local models has been progressively refined by scaling the triangular element area in the nearshore zone of the considered target sites where more detail is needed to describe the shoaling effect, the spatial gradients induced by bathymetric features and dynamics within ports.

The computational meshes have been realized by ensuring that the maximum element area was adequately proportional to the local depth (besides proportional to the tsunami wave celerity), and the time step set to a value satisfying the Courant-Friedrich-Lévy (CFL) criterion for an unstructured grid. To provide an indication on the size of the generated meshes, the final unstructured grid covering the entire Western Mediterranean with mesh refinements in correspondence of the earthquake epicentral area, the bay of Palma and the homonym port, used for the simulation of the tsunami generated by the source model derived from that of Belabbès et al. [34], contains 226,076 nodes and 407,703 elements and the one-way offline nested model for the bay of Palma includes 121,252 nodes and 229,056 elements. Similar figures apply to the other grids. The upper limit of mesh element areas in the central Mediterranean Sea, where water depth is around 3000 m and wave celerity is around 170 m/s, was set to 0.00092 deg^2 and the minimum angle to 30 deg; the maximum size of an element in this area is therefore approximately 0.030 deg, corresponding to 3370 m. The limit element area was

reduced proportionally to water depth and the minimum angle preserved, so that the element size is scaled down proportionally to wave celerity and the average shape is preserved. As illustrative example, Figure 8 shows the progressively refined computational mesh used for the bay of Sant Antoni.

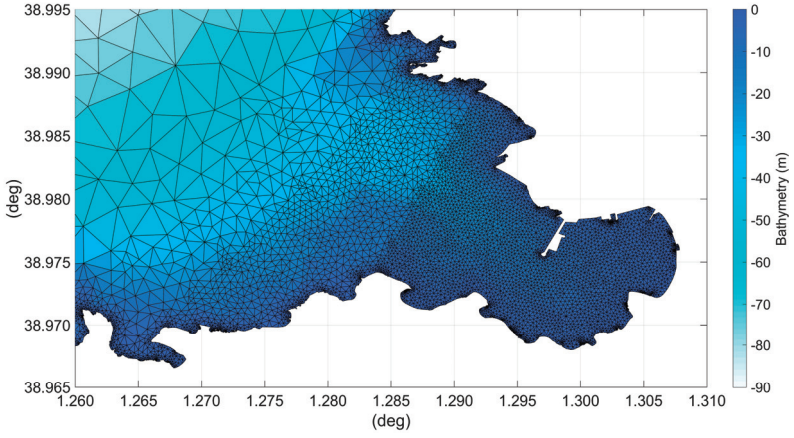

Figure 8. Progressively refined computational mesh generated for the Sant Antoni bay.

3.1.4. Bathymetry

Bathymetric data for the entire Western Mediterranean have been extracted as XYZ data files from the EMODnet Bathymetry portal (https://portal.emodnet-bathymetry.eu/). A downsampling of the EMODnet data set was necessary to reduce the huge amount of data from the original resolution of 1/8 × 1/8 arc minute to an appropriate point density allowing a practical hydrodynamic model construction at basin scale by using the computational power of an ordinary desktop computer (processor Intel Core i7-6700 with 32 GB installed RAM). In particular, the downsampling procedure has been carried out preserving depth along shallow coastal areas and capturing as much as possible details and morphological features of the sea bottom topography contained in the original data. EMODnet seabed depth is referenced to the lowest astronomical tide (LAT). The effect of the vertical reference of the bathymetric data on the tsunami has been tested.

Since tsunami dynamics in the nearshore zone is significantly affected by local small scale bathymetric features and coastal geomorphological characteristics, very high resolution bathymetric data sets have been constructed for both the tsunami source region and the impacted sites of interest to improve the accuracy and reliability of the numerical models. A wide variety of data sources has been consulted in this study for the construction of the high resolution bathymetric data sets for each considered site. Bathymetric data were obtained by SOCIB (http://gis.socib.es/viewer/, [83]) for the Balearic Islands, by the Autoritat Portuaria de Balears for the Palma de Mallorca port, and were extracted from the MIKE C-Map database for the Southern Sardinia, the Gulf of Cagliari, and the relative port. High spatial resolution bathymetric maps were also compiled using data from the paper nautical charts published in Portolano dei mari d'Italia [84] and by the electronic navigation charts from Navionics (https://webapp.navionics.com) and FlytoMap (https://viewer.flytomap.com/, mainly the raster option). Paper and electronic charts were first georeferenced using QGIS software, then manually digitized and converted in XYZ format. A digitization at very fine scale was carried out to capture the isobaths trend and the depth points plotted on the charts in order to ensure that the local bathymetry was both accurately described and resolved in the models. Careful data inspections and rigorous quality controls have been carried out during the digitization process, excluding water depths deemed to be unrealistic and verifying the values indicated on the charts by cross checking the information contained in the different maps. Further visual checks have been carried out on the final bathymetries

resulting from the interpolation performed assigning an appropriate combination of prioritization weights to the various data sets, based on their relative spatial resolution level, in specified subareas of the computational domain.

Coastline shape and position at tsunami time were reproduced with high accuracy for the North Algerian source region and all target sites of interest, including ports that have undergone significant changes in recent years, by manually digitizing from the high resolution historical satellite images available in Google Earth. The digitization accuracy corresponds to the resolution of the used images. For the nested model including the islands of Eivissa and Formentera, in addition to the manually digitized stretches, coastline data obtained from the OpenStreetMap database (http://www.openstreetmap.org) were used. Coastline position data extracted from the Natural Earth website (1:10 million scale, https://www.naturalearthdata.com/) were also used in the basin scale simulation models.

3.1.5. Model Parameters

The simulations performed with MIKE 21 Flow Model FM include the effects of bottom shear stress, eddy viscosity, flooding and drying fronts. The bottom shear stress, $\overline{\tau_b}$, is determined by a quadratic friction law [82]

$$\frac{\overline{\tau_b}}{\rho_0} = c_f \overline{u_b}\left|\overline{u_b}\right| \tag{2}$$

where $\overline{u_b}$ is the depth-averaged velocity, ρ_0 is the density of the water, and c_f is the drag coefficient which can be expressed through the Chezy number, C, or the Manning number, M. Using the Manning number, c_f is calculated as

$$c_f = \frac{g}{\left(Mh^{1/6}\right)^2} \tag{3}$$

where h is the total water depth and g is the gravitational acceleration. The Manning number M is determined by the bed roughness length k_S through the relation [82]

$$M = \frac{25.4}{k_S^{1/6}}. \tag{4}$$

It is also observed that the Manning number used by MIKE 21 is the reciprocal of the Manning coefficient, n, given in literature (i.e., $M = 1/n$). In this study, the bed resistance has been specified through a constant Manning number of 50 $m^{1/3}/s$ applied on the whole domain, corresponding to a roughness length of 0.017 m.

Lateral stresses representing viscous and turbulent momentum transfer and differential advection have been modeled using a sub-grid scale eddy viscosity coefficient given in the Smagorinsky [85] formulation as

$$A = c_S^2 l^2 \sqrt{2 S_{ij} S_{ij}} \tag{5}$$

where c_S is a constant, l is a characteristic length scale (characteristic element length), and S_{ij} (i,j = 1,2) is the deformation rate given by

$$S_{ij} = \frac{1}{2}\left(\frac{\partial u_i}{\partial x_j} + \frac{\partial u_j}{\partial x_i}\right). \tag{6}$$

For the Smagorinsky coefficient c_S, ranging from 0.25 to 1.0, a constant value of 0.28 has been used in the simulations, allowing sub-grid eddy viscosities between 1.8×10^{-6} and 1.0×10^{8} m^2/s.

The flooding and drying scheme of the hydrodynamic model has been enabled in all the simulations to include or exclude in the computations elements/cells that are sometimes wet and sometimes dry, by checking the local water surface elevation. In the present study, flooding, wetting and drying depths have been set to their default values, 0.05, 0.1 and 0.005 m respectively, to avoid numerical instability.

The influence of the Coriolis force has been neglected on tsunami propagation since tsunami frequency band is much greater than the Coriolis coefficient, i.e., the tsunami period is much shorter than a day, e.g., [86].

The coastline has been used as the land boundary. The land boundary is regarded as a closed boundary and the full-slip boundary condition has been applied, that is, only the normal velocity component is set to zero at the boundary. For the open boundaries of the large computational domain located at the Straits of Gibraltar, Sicily and Messina, and for those in correspondence of river outlets or similar features incorporated in all model domains, a Flather condition [87] has been used with external surface elevation and velocity forced to zero. The radiation condition proposed by Flather [87] can be obtained by combining the Sommerfeld condition for the surface elevation η (with phase speed of the surface gravity waves) with a 1D version of the continuity equation applied in the outward normal direction at an open boundary

$$\overline{u}_n = \overline{u}_n^{ext} - \sqrt{\frac{g}{H}}(\eta - \eta^{ext}) \tag{7}$$

where $\overline{u}_n$ is the normal velocity component, H is the local water depth, and $\overline{u}_n^{ext}$ and η^{ext} represent the prescribed external data. In this scheme the differences between the external data ($\overline{u}_n^{ext}$ and η^{ext}) and the model predictions ($\overline{u}_n$ and η) are allowed to propagate out of the domain at the speed of the external gravity waves, e.g., [88,89]. The open boundaries have been placed far enough away from the areas of interest so that they do not affect the simulation results. Tidal forcing was not included in the simulations because of the microtidal regime which characterizes the Mediterranean Sea and of the detiding filter applied to tide gauge data.

Due to stability restrictions in explicit schemes, a variable time step interval is used in MIKE calculations and it is determined so that the CFL number is less than a critical value in all computational nodes [82]. To control the time step, a minimum time step of 0.01 s and a maximum time step of 2 s have been considered for the simulations. The CFL number is checked by the procedure to avoid that abnormally small elements may cause instability; the critical value adopted was 0.8, whereas the average value is less than 0.1. The low average value is due to the fact that in ports relatively high water depths are present combined with small scale planimetric elements, as breakwater heads or wharf angles. We have tested different time steps. The 1.5 s time step resulted in no observable difference from 2.0 s, and 3.0 s resulted inconsistent with the critical CFL number.

The higher (second) order numerical scheme has been selected for the time integration and space discretization methods. The higher order scheme is considered in general to produce results significantly more accurate than the lower order scheme, even if its computational time increases by a factor of 3–4 [82]. For the system of 2D shallow water equations an approximate Riemann solver (Roe scheme [90]) is used to calculate the convective fluxes at the interface of the cells [91]. Second-order spatial accuracy is achieved by employing a linear gradient-reconstruction technique. The average gradients are estimated using the approach by Jawahar and Kamath [92]. To avoid numerical oscillations a second-order total variation diminishing (TVD) slope limiter (van Leer limiter [93,94]) is used [91]. The higher order method of time integration uses a second-order Runge Kutta method [91].

A simulation covering 11 prototype hours has been considered for Valencia and 6 hours for the other investigated sites.

3.2. Comparison between Surface Elevation Results and Tidal Records

In order to check the validity of the implemented mesh, we first compared the results of the simulations representing a simultaneous sliding with available instrumental records. The comparison may be focused on arrival time, tsunami intensity, and mean tsunami wave period, that are respectively dependent on propagation time, seabed uplift/drawdown intensity, and extension of the generation area.

In Figure 9 the tsunami waveforms simulated from the different slip distributions are compared with the detided sea level records at Palma de Mallorca and Cagliari stations. Synthetic event parameters are presented in Table 3.

Among the examined cases, the slip pattern derived from that proposed by Belabbès et al. [34] produces the best agreement between the simulated and the observed waveforms at the considered stations. Therefore, simulations obtained from this slip pattern are compared with detided sea level records at the other stations; the comparison is shown in Figure 10.

A preliminary trivial remark is necessary: the time resolution of tidal records is often not sufficient to represent correctly tsunami waves, containing for this event a dominant component having period around 20 min but also secondary components having around half the mentioned period. Palma station with 1 min record resolution (Figure 9) provides an appropriate description of the real event, Sant Antoni (2 min resolution) a fair one, Ibiza and Valencia (5 min resolution) a poor description, and Cagliari (10 min resolution) an insufficient one.

In Table 3 the arrival time is identified as time of the last zero-crossing before the first evident crest. Extreme levels, root mean square (rms) elevation, and mean zero-crossing period are evaluated over the time interval from tsunami arrival to midnight. Arrival time is affected by a systematic lead error due to time resolution of data; this is irrelevant in numerical simulations but may be important for recorded waves.

In the comparison one must be aware that the first wave including arrival time depends essentially on the generation and propagation model, whereas the following waves depend also on reflection from far shores and resonance of continental shelf waters. It was not possible to describe far coastlines with accuracy similar to that used in representing the Balearic Islands and the target ports.

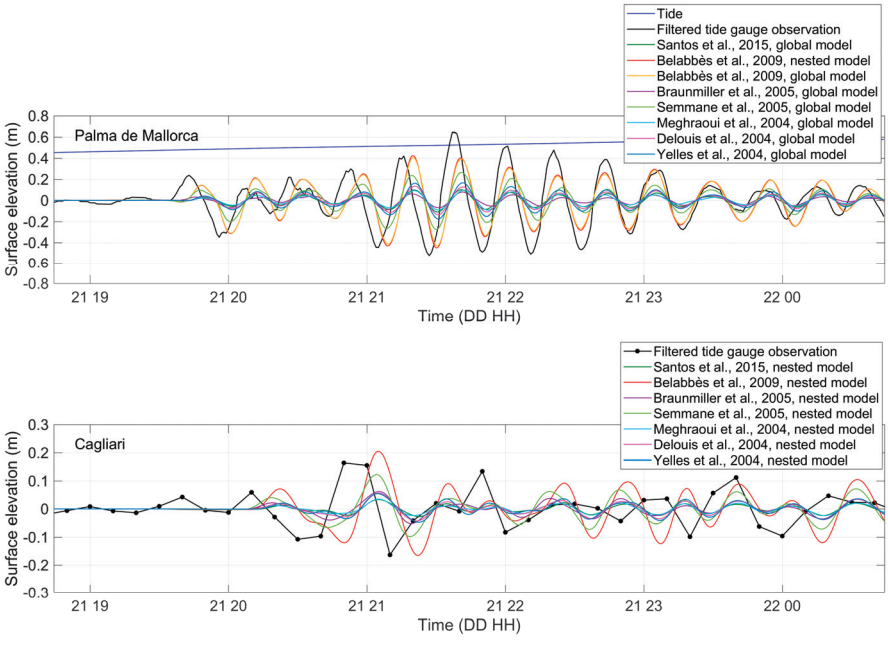

Figure 9. Comparison of tsunami waveforms simulated from different slip distributions and detided records at Palma de Mallorca and Cagliari.

At Palma de Mallorca tide gauge a 6 min delay in the first perturbation arrival time (19:41:36) is obtained from our simulations, when compared with the detided observations (19:35). Despite the delay, the cross-correlation between the modeled and observed time series of water surface elevation is

good; a peak cross-correlation of 0.91 is reached at lag 4.4 min for the first two waves. This discrepancy deserves some comments and analyses.

It must be underlined that a temporal discrepancy of about 6 minutes was also obtained at the Palma de Mallorca tide gauge by Alasset et al. [26] and Vela et al. [32], employing different numerical models and bathymetric data. In the paper by Vela et al. [32] it is stated that a possible explanation "for such an anomaly could be a malfunctioning of the tide gauge's clock."

Finally, it should be observed that in the first description of the tsunami event (Díaz del Río, 25 Jun 2003 [95]), then taken up or confirmed by Tel et al. (2004) [96], the arrival time is stated "19:41 GMT". The article is presented in a newspaper but is written by a scientist and contains a lot of data, all of which are accurate; the article is therefore reliable.

Although tide is almost negligible in the Mediterranean Sea with a spring tidal range of less than 0.25 m [97], a further numerical model was implemented considering a superimposed constant water level of +0.48 m, consistent with the tidal stage at the entrance of the Palma de Mallorca harbor at the tsunami arrival time, to investigate the potential tide influence on the tsunami waves. A reduction of the tsunami arrival delay of only 24 s was found with respect to the tsunami simulation over LAT.

This discrepancy remains an open issue.

The tsunami waveform computed at the location of Sant Antoni tide gauge (Figure 10) results in very close agreement with the recorded signal for the first two waves. The maximum water elevation, 1.11 m occurred at the second wave, is well reproduced by the numerical model. The modeled tsunami arrives slightly earlier, 1 min, than what observed at the tide gauge. The difference is however hardly significant if time resolution of the recorded signal (2 min) is considered.

Tsunami arrival time and height of the first wave predicted at Ibiza and Valencia compare fairly well with the tide gauge data recorded at 5 min interval. The low temporal resolution of the measurements in the port of Valencia does not allow to draw firm conclusions. However, energy reflection from neighbor and distant shorelines documented by any propagation model seems to have great relevance in the Sant Antoni and Valencia ports and/or bays. These phenomena are not well captured by the numerical model, which exhibits relatively rapid dissipation, presumably due to insufficient accuracy in representing distant coastal features. The tsunami waveform at the Sant Antoni and Valencia tide gauges is in fact fairly well reproduced until 21:00–22:00; later wave reflection from Spanish continental coasts and French plus Sardinia coasts, in the order, is certainly superposed on the reflections from the local coasts.

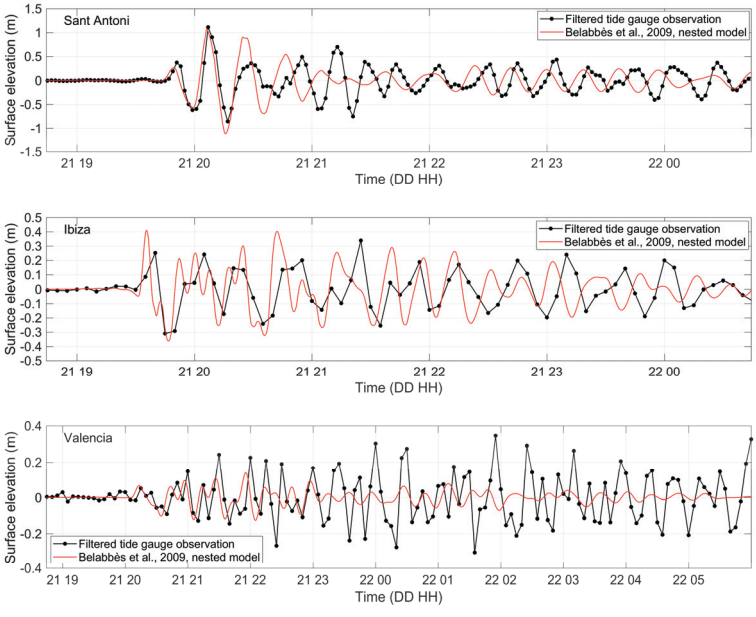

Figure 10. Comparison of tsunami waveforms computed using the slip distribution derived from that proposed by Belabbès et al. [34] with detided sea level records at Sant Antoni, Ibiza, and Valencia.

Only for Palma de Mallorca and the fault model derived from that proposed by Belabbès et al. [34] two simulations were carried out: one including the refined description of Palma bay in the global model (multiscale model), and one using results at bay limits as boundary conditions for a one-way nested detailed model of the bay and the harbor. For all the other stations only the nested model was carried out. The analyzed case allows us to point out that differences due to one-way nesting can be assumed as irrelevant for the studied event.

Table 3. Comparison between detided observations and simulated time series at the tide gauges by using different source models in terms of tsunami arrival time, maximum elevation and drawdown, rms sea level and mean zero-crossing period.

			Tide Gauge	Yelles et al.	Delouis et al.	Meghraoui et al.	Semmane et al.	Braunmiller & Bernardi	Santos et al.	Belabbès et al. Modified	Belabbès et al. Modified
Palma	19:30–24:00	Model		global	global	global	global	global	global	global	nested
		Arrival time	19:35	19:43:04	19:42:52	19:43:34	19:41:30	19:38:36	19:42:56	19:41:36	19:41:38
		Max elevation (m)	0.64	0.17	0.14	0.10	0.27	0.08	0.10	0.41	0.43
		Max drawdown (m)	−0.52	−0.17	−0.14	−0.09	−0.27	−0.09	−0.11	−0.43	−0.45
		RMS elevation (m)	0.251	0.072	0.057	0.041	0.114	0.035	0.044	0.189	0.196
		Mean period (min)	22.7	22.4	22.4	22.3	22.5	22.7	22.4	22.5	22.5
Cagliari	19:50–24:00	Model		nested	nested	nested	nested	nested	nested		nested
		Arrival time	20:00	20:12:42	20:10:56	20:11:12	20:08:32	20:08:50	20:14:06		20:11:24
		Max elevation (m)	0.16	0.05	0.06	0.03	0.12	0.06	0.03		0.20
		Max drawdown (m)	−0.16	−0.05	−0.04	−0.02	−0.10	−0.05	−0.03		−0.17
		RMS elevation (m)	0.082	0.022	0.020	0.013	0.043	0.022	0.013		0.070
		Mean period (min)	(33.3)	28.1	28.4	28.1	28.6	28.5	28.0		28.4
Sant Antoni	19:35–24:00	Model									nested
		Arrival time	19:45								19:44:14
		Max elevation (m)	1.11								1.10
		Max drawdown (m)	−0.85								−1.18
		RMS elevation (m)	0.314								0.306
		Mean period (min)	19.5								19.1
Ibiza	19:25–24:00	Model									nested
		Arrival time	19:30								19:32:24
		Max elevation (m)	0.34								0.41
		Max drawdown (m)	−0.31								−0.36
		RMS elevation (m)	0.149								0.154
		Mean period (min)	22.1								16.4
Valencia	19:55–24:00	Model									nested
		Arrival time	20:10								20:05:52
		Max elevation (m)	0.35								0.14
		Max drawdown (m)	−0.31								−0.13
		RMS elevation (m)	0.123								0.053
		Mean period (min)	20.0								20.5

3.3. Comments

The first comment regards the rupture event. Both the time characterization in Figure 1 and the space one in Figure 7 represent a composite event, made up of elementary slip movements occurring in different near locations at different near times. In the numerical model the slip events are represented as occurring simultaneously at 18:44:20.

The second comment regards the effective duration of the movement generating tsunami. Due to the size of the fault zone, generated waves have period of the order of 20 min. Therefore, any congruent movement occurring within a few minutes from the first one did contribute to the tsunami wave.

The classification and conventional characterization of earthquakes is based essentially on the high frequency and short duration characters, as shown and explained in Figure 1, where the conventional duration (74 s) and energy magnitude (6.91) are derived. As far as tsunami is concerned, magnitude must however be evaluated up to a duration of 5–6 minutes, that is out of scale in Figure 1; the estimate 7.2 was obtained by extrapolation following this argument; it remains however an uncertain value,

even if also Wang and Liu [24] as well as Gailler et al. [98] find necessary to increase the earthquake magnitude up to this value.

When comparing the offshore tsunami representation obtained by our model with some others available in literature [24,26,30], a more regular distribution of energy during tsunami propagation is visible in our solution. All the used models are based on nonlinear shallow water equations but are different as far as the grid/mesh is concerned. Wang and Liu [24], Alasset et al. [26] and Sahal et al. [30] used a square grid with resolution of 1500, 400, and 1000 m, respectively, in the deep Mediterranean Sea, whereas we have used a flexible mesh having maximum size 3370 m. Despite the grid size differences, quite similar spherical radiation from the source is apparent in [24] and in our simulations, whereas the full front is not visible in the two other mentioned papers. A numerical dispersion effect is possible even if our maximum mesh size is less than 2% of the offshore wave length compared to the DHI suggested limit of 3%. In any case it is recognized that the numerical scheme of MIKE 21 Flexible Mesh appears to be too dispersive to accurately simulate tsunami propagation over large distances [99]. Sahal et al. [30] are not explicit on the representation of bottom friction, whereas Alasset et al. [26] admittedly do not account for it and their model results to be close to stability margin. Conversely, an effect of numerical dispersion of the model we used could be the extreme regularity of the obtained water level pattern.

The space–time evolution of the rupture process may be relevant for the directional distribution of radiated energy. A synchronous movement generates waves mainly radiating in the orthogonal direction to the fault line, whereas coherent space–time shifts along the fault can generate oblique waves as a directional wave maker does. The synchronous slip distribution along the fault plane, modifying the source model proposed by Belabbès et al. [34], is shown in Figure 11. Figure 12a represents the maximum sea surface elevation obtained within the first hour of simulation, i.e., until tsunami wave arrives to Balearic Islands. This pattern is common to all synchronous fault models since the orientation of the different fault planes is similar. Figure 12b shows the effect of a 60 s delay of the eastern slip peak; it is evident the different orientation of the radiation lobe causing intensified effects (~14%) at Menorca Island. A significant increment in terms of maximum surface elevation (~10% within the first four hours after the earthquake) is also estimated over a water depth of approximately 450 m off Îles de Lérins in Golfe de la Napoule (offshore Cannes). Table 4 compares the results of the simulations using synchronous and asynchronous slip along the fault plane at the tide gauge location in Palma de Mallorca and Sant Antoni and at a virtual station in Mahon port and compares them with available observations. The asynchronous slip event results in an increment of ~17% for the first peak elevation at the inner end of Mahon port, while there are no significant sea level variations at Palma and Sant Antoni tide gauges compared to the case of synchronous slip. The arrival time in Palma is however delayed by approximately 1 min, causing further divergence of the model timing from tidal records.

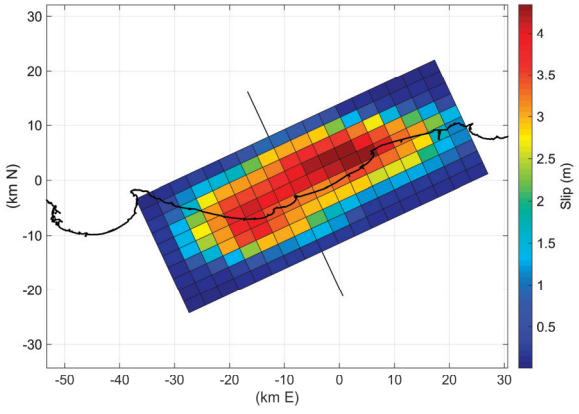

Figure 11. Coseismic slip distribution of the 21 May 2003 Boumerdès earthquake modified from the source model proposed by Belabbès et al. [34].

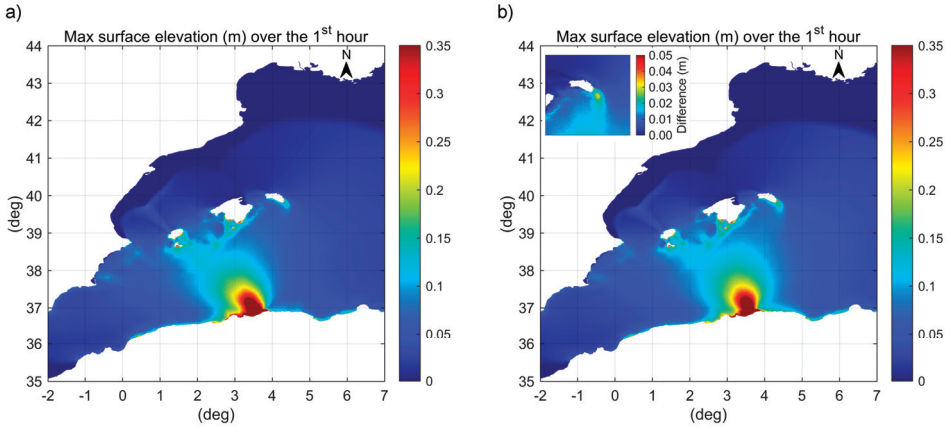

Figure 12. Crest elevation during tsunami propagation from Algeria to Balearic Islands: (**a**) synchronous movement along the fault plane, (**b**) 60 s delayed eastern sliding. Several effects are made evident: the main radiation direction, wave amplification due to shoaling at Balearic continental margin and, due also to refraction, at Menorca SE cape. The simulated delay of the eastern sliding causes a reorientation of the radiation lobe with a significant intensification at Menorca Island. The maximum surface elevation is increased east of the ray reaching Palma with accentuation on the edge of the Balearic continental shelf, while to the west of this ray it is reduced. The window in the upper left corner of figure (**b**) describes the difference (**b**-**a**) between the two solutions around Menorca Island where the maximum effect along the mentioned edge is observed. The figure was generated using the DHI MATLAB Toolbox.

Santos et al. [44] have analyzed the space–time structure of the first 15 s of the seismic event and pointed out two elementary events with relative delay of 6 s and distance 20 km (East first), but the analyzed period is rather short compared to the effective tsunami generation period, containing certainly a further energy release delayed around 60 s.

The space–time structure of the tsunami source remains therefore insufficiently specified. It can justify a systematic delay of the real wave of a few minutes and a deviation of the radiation lobe from the simulated values, causing different intensities at the single Balearic Islands.

In synthesis the asynchronous slip is preferred because it is consistent with time distribution of seismic activity, does not cause evident variation at Palma and Sant Antoni and intensifies the tsunami in the Mahon area where the severest damages were observed.

Table 4. Simulation results using synchronous and asynchronous slip distribution along the fault plane in terms of zero-crossing time and extreme elevation at the tide gauge location in Palma de Mallorca and Sant Antoni and at a virtual station (4.257176°E, 39.89648°N) in Mahon port, compared with available observations.

	Synchronous Slip		Asynchronous Slip		Observation	
	Zero-Crossing Time (UTC)	Extreme Elevation (m)	Zero-Crossing Time (UTC)	Extreme Elevation (m)	Zero-Crossing Time (UTC)	Extreme Elevation (m)
Palma de Mallorca	19:41:36		19:42:06		19:35	
		0.145		0.147		0.24
	19:54:28		19:54:54		19:49	
		−0.308		−0.301		−0.35
	20:07:26		20:08:00		20:04	
		0.209		0.201		0.12
	20:18:08		20:18:42		20:14	
		−0.184		−0.173		−0.13
	20:26:38		20:27:12		20:22	
Sant Antoni	19:44:14		19:44:44		19:45	
		0.292		0.287		0.37
	19:52:18		19:52:54		19:54	
		−0.589		−0.574		−0.62
	20:02:34		20:03:04		20:04	
		1.101		1.089		1.11
	20:11:24		20:11:52		20:12	
		−1.176		−1.160		−0.85
	20:20:42		20:21:02		20:23	
Mahon	19:38:24		19:39:20			
		0.655		0.767		
	19:44:12		19:44:50			
		−0.521		−0.614		
	19:56:16		19:56:36			
		0.618		0.690		
	20:04:54		20:03:50			
		−0.114		−0.110		
	20:07:20		20:07:44			

4. Damages in Bays and Ports Due to the 21 May 2003 Tsunami

As evident from Figures 3 and 12 the tsunami waves severely stroke the Balearic Islands and in particular their bays and ports where refraction and resonance can significantly increase the elevation amplitude and cause strong and unusual currents.

At least 180 boats were totally or partially damaged in harbors and ports of Mallorca, Menorca, and Eivissa, due to the rapid oscillation of the sea water level [100] (Figure 13).

Press reports indicate a total of 73 sunken vessels and about 80 seriously damaged boats only in Menorca Island, e.g., [101] referring to Menorca.info of 23 May 2003 and [102]. The most severe effects of the 21 May 2003 tsunami occurred inside the port of Mahon. In Mahon, it was reported that water disappeared leaving the sea bottom exposed as then returned, flooding the promenade and the road, [101] referring to Menorca.info of 22 May 2003. The Colàrsega and Port d'Hivernada, situated at the internal end of the Mahon port, experienced the greatest damage. Drifting yachts, sunken fishing boats, overturned boats, and fishes on the asphalt could be seen. Only in Colàrsega 11 sunken vessels and 26 damaged were counted; furthermore, in the area there were three sunken floating docks and serious damage to the dike closing the harbor [101]. It was reported that at Cala Llonga 20 vessels

sank [101] and a pier was destroyed [103], and in the rest of the Mahon port, there were two sunken and two damaged vessels [101].

Press reports also indicate significant damage at Cala de Sant Esteve where some houses located near the sea were flooded and medium-size vessels suffered the effects of the sudden change in the sea level and ended up on the ground [101]. Roig-Munar et al. [104] show an impressive photo with boats accumulated at the end of the Cala de Sant Esteve embayment (Figure 13b).

At Mallorca the most relevant effects of the Boumerdès earthquake were observed along the northern and eastern coasts of the island, at Pollensa and Alcudia [105], in Andraxt port and at the south extreme [100]. Information regarding the impact of the 21 May 2003 tsunami in the port of Palma de Mallorca indicates that:

- "the damages generated by the 2003 Western Mediterranean tsunami in the Palma harbour concentrated in the northern basin where several pleasure and sailing boats sank between Sant Magí dock and the Royal Yacht Club. The shallow water depth in this part of the harbour eased the sinking of the boats, as they were quickly moved up and down by the oscillations easily hitting the bottom and breaking" [31];
- the boats moored along the Paseo Maritimo close to La Riera hit the bottom due to the rapid lowering of the sea level [105];
- collisions among vessels occurred along the Paseo Maritimo [103];
- "in Palma, the first sea movement was an ingression and the Paseo Maritimo street was flooded" [106];
- "a second highly impacted area was the Espigón Consigna, in the commercial quays, where the tsunami waves took off an oil container and other objects" [31].

In Eivissa, following the Boumerdès 2003 earthquake, several coastal areas were flooded, mainly the bay of Sant Antoni de Portmany and Santa Eulària [105].

Along the Sant Antoni coast, the water withdrew about a hundred meters letting see the sea bottom, and then returned in the form of a great wave, which flooded an extensive part of the promenade and made to collide boats which were moored in the port. As a result, several boats sank, others ended up on the piers and crashing against the cars parked nearby [105]. The port parking and the fishermen's pier were among the most affected by the tsunami [107]. About fifteen boats were damaged in the port of Sant Antoni [108]. Various vehicles that were parked along the promenade were also damaged due to the sea level rise [103,109].

In Santa Eulària harbor a wave of 1.5 m swept the piers and at least two boats, among which a 15 m yacht, sank [105]. At Ibiza, a tugboat sank in Marina Botafoch and deteriorated moorings were found in Ibiza Nueva [108].

Regarding the French Mediterranean coasts, the results of a three-month field survey started on May 2007 to look for potential witnesses of the tsunami induced by the Boumerdès earthquake showed that in only 8 harbors of the 135 investigated hydrological anomalies were noticed during the evening and the night of 21–22 May [30]. In particular, in the harbor of La Figueirette, where some boats were damaged, the water level lowered about 1.5 m and eddies, boiling phenomena, and strong currents up to "15 knots" (7 m/s) would have been observed. A sea level drop of about 1.5 m and a maximum current of "12 knots" (6 m/s) would also have been observed in the harbor of Cannes-Vieux-Port, along with numerous 2 ton moorings moved [30].

In Antibes strong sea waves were signaled by yachtmen, while a sea retreat of 1 m was observed near Hyeres [110].

No damages were reported in Italian ports.

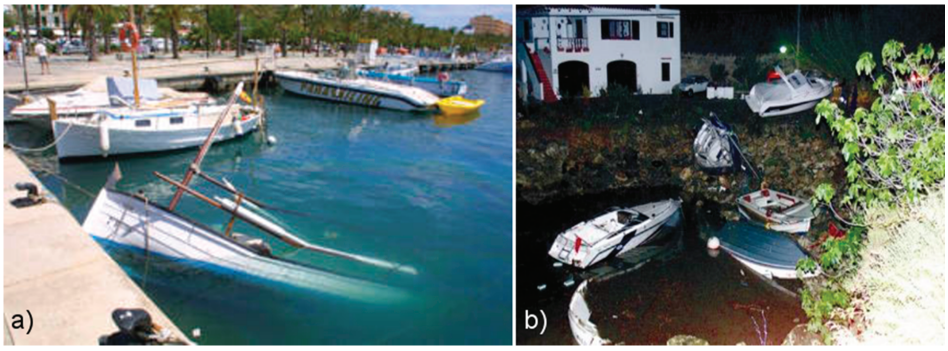

Figure 13. Photographs documenting damages to boats caused by the 21 May 2003 tsunami at the Balearic Islands. (**a**) A sunken boat in Sant Antoni, derived from [109]; reproduced with permission from Vicent Marí. (**b**) Boats accumulated at the end of the Cala de Sant Esteve, derived from [104]; reproduced with permission from Guillem Xavier Pons Buades. Other photographs are publicly accessible online at [103,111,112].

5. Relating Tsunami Hydrodynamic Features to Reported Damage

5.1. Tsunami Loading Factors

Recent tsunami events originating off the western coast of Sumatra on 26 December 2004, off the Maule coast of central Chile on 27 February 2010 and off Japanese Tohoku coast on 11 March 2011 generated a series of tsunami waves with devastating effects not only along the coast of their respective source regions but also in far field coastal areas. Pertinent information about the tsunami events were collected by several field surveys using established protocols, questionnaires, and interviews. Strong tsunami-induced currents, documented by eyewitness accounts and available instrumental and video records, e.g., [113], have been identified as responsible for most of the damage to boats and docks in a number of ports and harbors at different locations following these events [114–118].

Numerical simulations of the currents induced by the 2004 and 2011 tsunamis in selected harbors were performed by Lynett et al. [66], showing that, during tsunami events, damaging currents are driven by coastal-structure induced or topographically controlled water jets, large eddies, or 2D turbulent coherent structures. These large shallow water coherent structures can greatly increase the drag force on the affected infrastructure and the ability of the flow to transport debris and floating objects [119].

A simple relationship between simulated tsunami currents and observed damage was proposed by Lynett et al. [9] for small craft harbors by using the information relative to the impact of the 2010 Chile and 2011 Japan tsunamis on the California coast documented by Wilson et al. [117] and additional observations provided by Lynett et al. [66,120] and Borrero et al. [121]. Damage to floating docks and vessels in harbors initiates with current speeds of approximately 3 knots (1.5 m/s). When the current speed threshold of 6 knots (3.1 m/s) is exceeded, damage transitions from moderate to major. Extreme damage occurs when current speeds exceed 9 knots (4.6 m/s). The indicated thresholds are subjected to uncertainties affecting both the load-carrying capacity of structural components, which is highly dependent on their age and deterioration level, as well as the current predictions which are particularly sensitive to bathymetry and numerical errors [119].

Also, sudden and significant water level fluctuations can lead to various hazards inside the harbors. Wilson and Miller [122] propose the FASTER approach to determine during a tsunami alert the maximum water elevation that the tsunami could reach at a particular coastal location.

Suppasri et al. [123] examined data for approximately 20,000 small vessels damaged during the 2011 Tohoku tsunami. The damage data were analyzed against the peak tsunami heights observed

from field survey and the peak flow velocities obtained from numerical simulations using nonlinear shallow water equations.

Four major types of damage to vessels caused by tsunami were considered: (1) grounding, that is the impact of a boat on seabed when the water level falls during the receding tsunami wave; (2) stranding, occurring when the elevation of the vessel bottom is raised higher than the pier elevation in a harbor; (3) failure of mooring rope; (4) loss of stability, i.e., overturning and loss of its tendency to return to an upright position.

Loss functions for tsunami damage to vessels were developed by Suppasri et al. [123]; cases were classified based on the vessel tonnage, motor type, and distance from the tsunami source (representing the possibility to escape the most dangerous conditions).

Muhari et al. [124] developed a 3D loss estimation surface to represent the damage probability of vessels associated with tsunami parameters and boat characteristics, including the effects of collision experienced by vessels during the tsunami. The surveyed loss data of vessels previously employed by Suppasri et al. [123] were used by Muhari et al. [124], but only vessels anchored or moored in the port before the tsunami were considered in this paper to reduce uncertainty of the selected vessel data. Tsunami heights and speeds were simulated using the shallow water approximation and a nested grid system with smallest domains having 10 m grid resolution.

In the following, in the absence of observed current data during the 21 May 2003 tsunami event, the results of the Flow Model employing the asynchronous slip distribution, modified from the source model proposed by Belabbès et al. [34], have been used to establish the role of tsunami-induced currents and sea surface elevations in causing observed damage inside the ports of Palma de Mallorca, Sant Antoni de Portmany, and Mahon in the Balearic Islands.

Tsunami oscillation in harbors and bays where extremes are reached is frequently affected by resonance [30] that may also affect the peak period of oscillations and time of internal oscillation set up. Therefore, while examining response of different harbors, the proper oscillation periods are identified as peaks of the response spectrum to a broad band forcing that occurs in good weather/background conditions [125].

Several site names appear in the text; the reader can see the corresponding positions by searching the name in some web mapping tools (as Google Earth or the chart viewer https://webapp.navionics.com).

5.2. Port of Palma de Mallorca

The spatial distribution of the maximum water surface elevations obtained in the Palma bay and port over the 6 h tsunami simulation is shown in Figure 14 and in the left plot of Figure 15, respectively.

The highest water surface elevations are observed in the northernmost corner of the Palma port near La Riera and in the northernmost end of the ancient harbor, where the wave height reaches 1.15 m over the current mean sea level (+0.48 m over LAT). The maximum water drawdown, −1.07 m, is also observed in these same areas within the port. The maximum tsunami-induced depth-averaged current speeds calculated over the 6 h tsunami simulation are displayed in the right plot of Figure 15. The highest current speeds occur at the head of the West Breakwater, ~3.2 m/s, and at the head of the commercial quays, ~2.3 m/s. It is specified that the maritime infrastructures represented in the figures are interpreted as impermeable. As fixed piers supported by piles are not easily recognizable on Google Earth images, current speed peaks at their head might be not such intense as indicated. Figure 15 shows, however, that where the current intensity exceeds 1.5 m/s and moored boats may be present, damage to boats has been observed. The modeling results also indicate that the tsunami current direction is transverse with respect to the boats moored at the Sant Magí and adjacent marina docks. In this specific location inside the port the boats are moored to dock at a perpendicular angle using a Mediterranean style mooring. Due to the large unexpected sea level oscillations, this mooring style may have favored vessel collisions. Computed time histories of water surface elevation and current speed during the tsunami at a virtual station located between the Sant Magí dock and the

Royal Yacht Club, where most of the damage occurred, at a depth of ~1.7 m, are shown in Figure 16. The numerical results highlight that the highest current speeds occur during the rising water level.

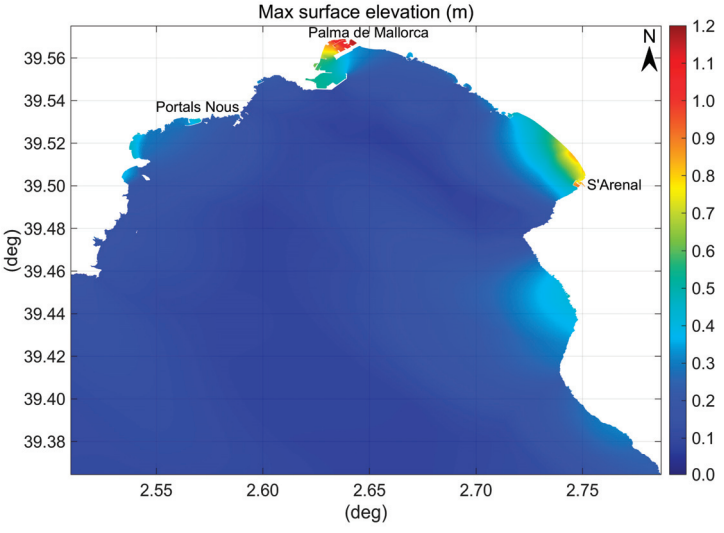

Figure 14. Distribution of the maximum water surface elevations in the bay of Palma over the 6 h tsunami simulation. The undisturbed sea level used in the calculations is the LAT, the real one was 0.48 m above LAT.

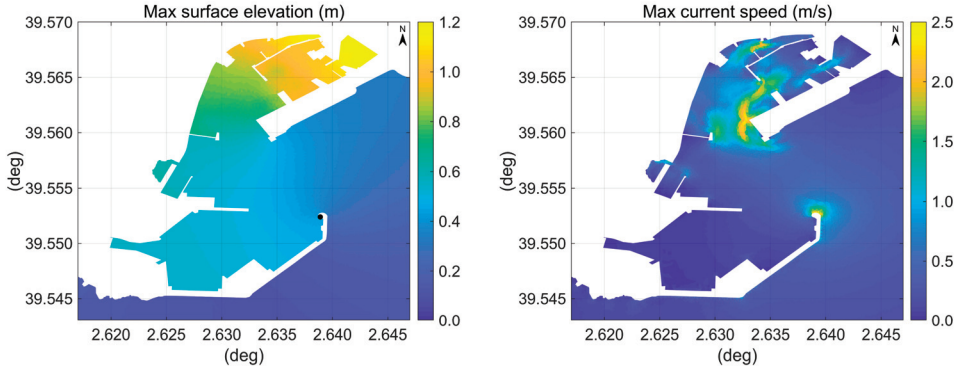

Figure 15. Distribution of the maximum water surface elevations (left plot) and maximum depth-averaged current speeds (right plot) in the port of Palma de Mallorca over the 6 h tsunami simulation. The black filled dot drawn in the left plot indicates the tide gauge location. Since the current pattern is less regular than that of the sea surface elevations, in order to provide an adequate visual representation the full scale of the colorbar is lower than the maximum value: in some points in the domain speed does actually exceed 2.5 m/s.

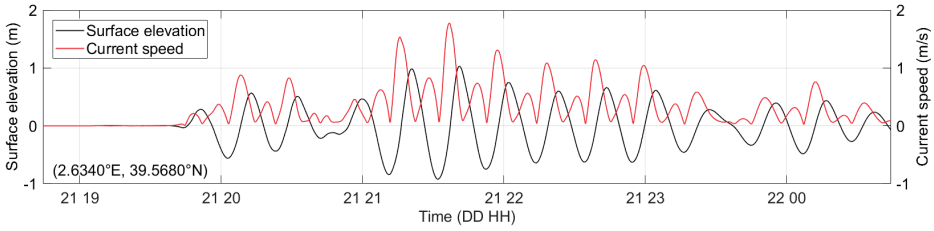

Figure 16. Time histories of water surface elevation and current speed computed by the nested model at a virtual station (2.6340°E, 39.5680°N, 1.7 m depth below LAT) located inside the Palma de Mallorca port between the Sant Magí dock and the Royal Yatch Club, during the 21 May 2003 tsunami.

Significant current speeds of ~1 m/s are also detected at the end of the westernmost floating dock of the Palma's Royal Yacht Club due to the narrow passage and at the head of the Espigón Consigna, the easternmost jetty in the commercial quays area, combined with, in this last case, a water surface elevation up to 1.13 m.

The simulation results also show that the flow is affected by rotational eddies of moderate strength forming at the head or at the sides of the jetties and docks.

In agreement with Vela et al. [31], tsunami wave amplification also occurred in Palma de Mallorca due to resonance effects. A spectral analysis of the observations has been performed to evaluate the frequency content of the sea level oscillations recorded at the tide gauge and to examine the influence of the tsunami source characteristics and resonant properties of the site. The background spectrum was evaluated considering the data of a long time interval preceding the tsunami event, from 12 May 18:43 to 21 May 18:43 that mainly reflects the normal good weather conditions with no single prominent excitation source, so that it highlights with greater reliability the topobathymetric resonant characteristics of the measurement site. The tsunami spectrum was determined for the time series covering the event, from 21 May 18:44 (earthquake occurrence time) to 22 May 07:00. Both time series have been previously detided; the power spectra of the residual time series have been then calculated through the Welch method using a Hamming window with 50% overlap; the computed tsunami and background spectra are shown in Figure 17.

The background spectrum has prominent peaks at periods of 11.6, 24.4, and 73 min (and secondary peaks at 13.5 and 34 min); these spectral peaks are associated with the natural oscillation modes of the bay system including the port. The 73 min period corresponds to the fundamental (Helmholtz) mode of the inner bay, from the shoreline down to 50 m water depth at the entrance of the bay, between Cap de Cala Figuera and Cap de Regana. 24.4 min, being around 1/3 of the previous one, represents the period of the second oscillation mode of the bay.

The tsunami energy spectrum has a peak corresponding to a period in the interval 21–24 min. Analyses of the May 2003 tsunami performed for several coastal stations in the Mediterranean basin by Vich and Monserrat [58] and Heidarzadeh and Satake [59] arrive to the conclusion that the source spectrum has a peak around 21–22 min. This peak is however close to the prominent natural period of 24.4 min identified in the Palma background spectrum and suggests a pronounced influence of resonance on the long wave oscillations at this site, with a shift of the peak toward greater and more amplified periods. The slow time-growth of the mode amplitude suggests a weak interaction between the long-lasting tsunami waves and the oscillation mode.

The results of a wavelet analysis using a Morlet mother function, applying the procedure described in [126] to the Palma tide gauge record, also reveal the temporal variations in the dominant period of the sea level oscillations (Figure 18). In Figure 17 the power spectrum of the time series obtained at the tide gauge location from the simulation is also shown. Considering the frequency resolution obtainable from the 6 h modeled time series, its spectral peaks compare well with those of the longer tide gauge series.

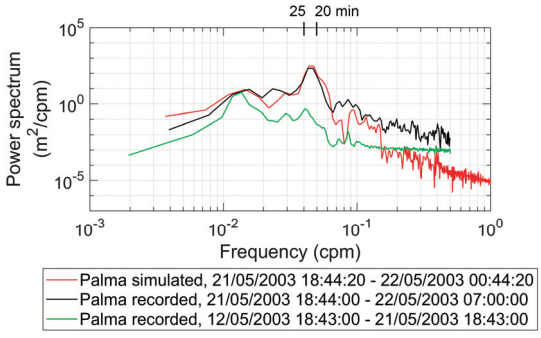

Figure 17. Power spectra of the background (green line) and tsunami (black line) oscillations recorded at the Palma de Mallorca tide gauge. The power spectrum of the 6 h modeled time series, from 21 May 18:44:20 (earthquake time) to 22 May 00:44:20, at the tide gauge location inside the port is also shown (red line).

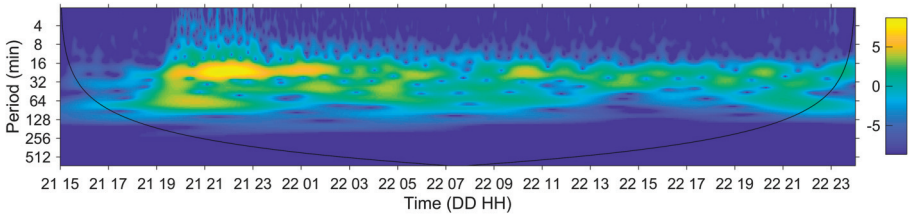

Figure 18. Wavelet spectrum of the filtered Palma sea level data during the period from 21 May 15:00 to 23 May 00:00. The color scale shows the base 2 logarithm of wave energy.

The observed maximum water levels appear therefore to be related to a mechanism of tsunami wave amplification associated with resonant excitation of natural modes of the bay. A NW-SE nodal line orthogonal to the major axis of the bay is clearly distinguishable in Figure 14 as characterized by lower sea surface oscillations. Figure 14 shows also two elevated water levels in the opposite corners of the bay, at the port and at S'Arenal. They represent transversal oscillations in the bay that were already recognized by Vela et al. [32]. They have periods ranging from 5 to 10 min and are immediately triggered upon arrival of tsunami wave, but fade much more rapidly than longitudinal ones (Figures 3 and 18).

5.3. Port of Sant Antoni de Portmany

Figure 19 shows the spatial distribution of the maximum water surface elevations reached at the coasts of Eivissa and Formentera Islands during the 6 h tsunami simulation.

The highest water surface elevation on the entire computational domain, 1.26 m, is obtained at the end of the Sant Antoni de Portmany bay along the stretch of sandy beach in front of Avenida Doctor Fleming, as shown in detail in the upper plot of Figure 20. This elevated tsunami surge may be held responsible both for the flooding at the Sant Antoni coasts indicated by press reports and for damage to pier decks. Water levels higher than 1 m are found throughout the innermost part of the Sant Antoni bay from the port breakwater to the corresponding location on the southern side. The maximum water drawdown observed on the entire domain is −1.43 m, which is reached in the extreme northeast corner of the Sant Antoni port.

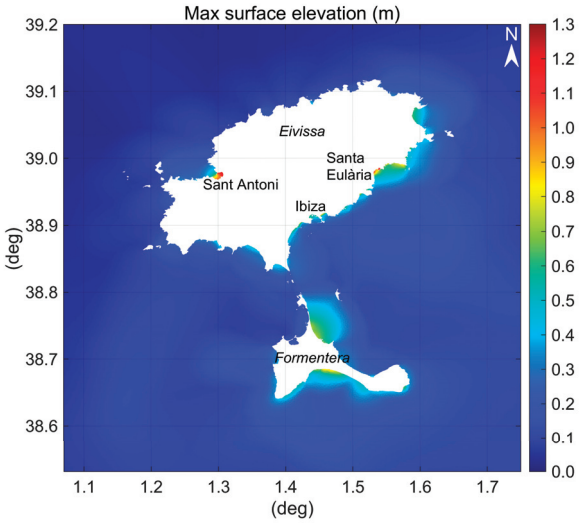

Figure 19. Spatial distribution of the maximum water surface elevations at Eivissa and Formentera Islands over the 6 h tsunami simulation from the asynchronous slip distribution pattern.

The maximum tsunami-induced current speeds estimated inside the Sant Antoni bay over the 6 h tsunami simulation are presented in the bottom plot of Figure 20. The highest current speeds, around 3.5 m/s, occur at the head of the port breakwater. Current speeds of ~1.7 m/s are found at Punta de Pinet, while slightly lower intensities are observed at Punta des Molí (~1.4 m/s) and in front of the shipyard in the central harbor area (~1.2 m/s).

The comparison between the power spectra of the background and tsunami oscillations recorded at the Sant Antoni tide gauge is shown in Figure 21. It highlights an energetic spectral peak at 21 min, which is absent in the background spectrum, therefore related to the properties of the tsunami forcing and common to all the investigated stations, and a resonant period of 16.7 min corresponding to the fundamental (Helmholtz) mode of the innermost part of the bay, from the shoreline down to 20 m water depth, corresponding to the nodal line (high velocity and low level oscillation) between Punta Xinxó and Punta de ses Variades. From Figure 22 it may be seen that the 21 min period is present from the tsunami arrival until 3:00 of the following day, during which waves reach the port following different paths. The existence of these two close spectral peaks generates beats which are clear in Figures 3 and 22. In Figure 12 it is also evident the positive interference near the port of waves passing west and east of Eivissa Island. The rapid growth of oscillation mode amplitude demonstrates the strong interaction between the oscillation mode and the tsunami wave associated to the similar direction of induced currents. The combination of positive interference and strong resonance explains the highest level observed in Sant Antoni among other Balearic ports.

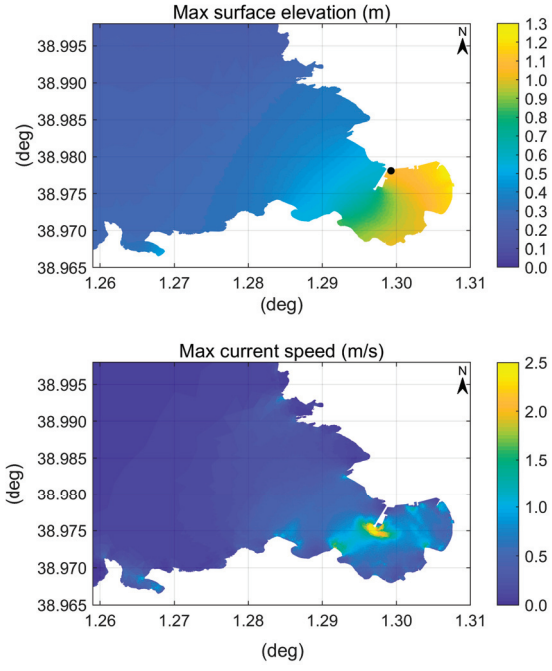

Figure 20. Spatial distribution of the maximum water surface elevations and current speeds in the harbor of Sant Antoni de Portmany over the 6 h tsunami simulation from the asynchronous slip distribution pattern. The black filled dot drawn in the upper plot indicates the tide gauge location.

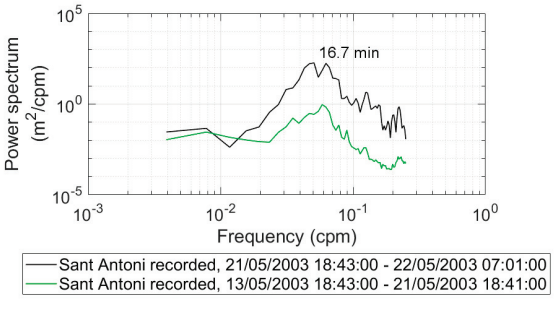

Figure 21. Power spectra of the background (green line) and tsunami (black line) oscillations recorded at the Sant Antoni tide gauge.

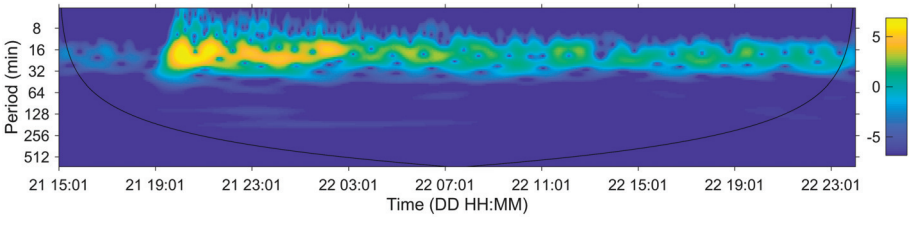

Figure 22. Wavelet spectrum of the filtered Sant Antoni sea level data during the period from 21 May 15:01 to 23 May 01:00. The color scale shows the logarithm of wave energy to the base 2.

Regarding the port of Ibiza, maximum water surface elevations of about 0.6 m over the 6 h simulation are reached in all the innermost areas, while the maximum drawdown varies from −0.52 m in the most sheltered northern marina down to −0.60 m at the end of Marina Botafoch. The maximum current speed, ~2.2 m/s, is reached at the head of the breakwater protecting the port on the western side. Furthermore, current speeds of ~1.6 m/s are found at the head of the Marina Botafoch breakwater and ~1 m/s in the sheltered entrance. Flow intensities of ~1.5 m/s are also reached in the shallow waters at the end of the adjacent Cala Talamanca edged by a sandy beach.

However, in all these locations characterized by current speeds ≥1 m/s there are no moored boats and therefore the modeling results are substantially in agreement with irrelevant damages reported by press. The low oscillation amplitude reached in the port is the result of refraction on the continental platform, that concentrates energy in adjacent zones, see Figures 12 and 19, and lack of resonance; in fact the analysis of recent tidal records (1 min time resolution) in good weather conditions has pointed out resonant periods around 40, 14, and 7 min. Lastly, from Figure 19 it is possible to observe that also the harbor of Santa Eulària des Riu is particularly exposed to the incoming tsunami waves. High water surface elevations and large drawdown affect the innermost zone of the harbor, while strong currents are generated at the entrance, capable of causing damage to boats and docks according to observations in press reports. Due to the shallow water depth of the Ensenada de Santa Eulària, the entire bay is prone to tsunami impact.

5.4. Port of Mahon

The spatial distribution of the maximum water surface elevations obtained in Port Mahon over the 6 h tsunami simulation from the asynchronous slip distribution pattern is presented in Figure 23 with enlargements in the left plots of Figures 24 and 25.

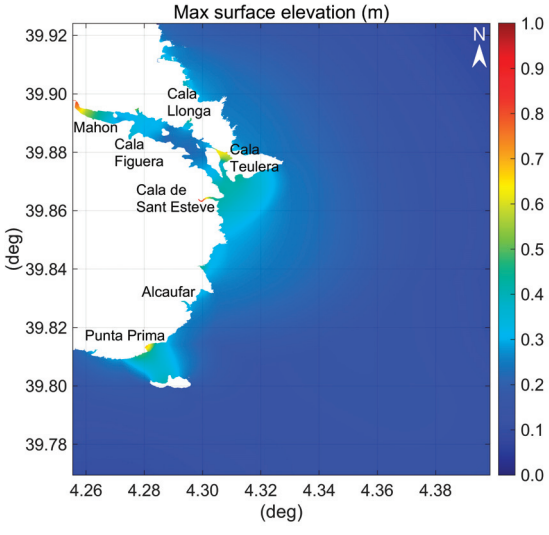

Figure 23. Spatial distribution of the maximum water surface elevations in SE Menorca over the 6 h tsunami simulation from the asynchronous slip distribution pattern.

Within the calculation domain, the highest water levels occur in four different zones: at Punta Prima (0.71 m), at the western end of Cala de Sant Esteve (0.86 m), at Cala Teulera (0.69 m), and at the inner end of the Mahon port (0.79 m). At Punta Prima local tsunami amplification occurs because of the shoaling effect at the open sea sandy beach.

The computed maximum water surface drawdown reaches −1.37 m at the end of Cala de Sant Esteve, just south of Port Mahon, while in the shallow north edge of Cala Teulera with water depth less than 5 m, it varies approximately from −0.90 down to −1.0 m at the entrance of the artificial channel Canal de Sant Jordi. A maximum drawdown value of −0.64 m is found in the innermost harbor zone of Mahon.

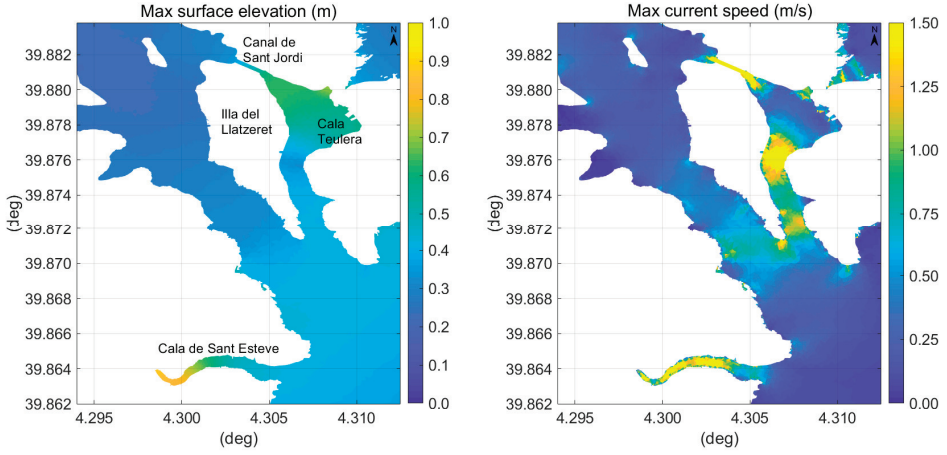

Figure 24. Spatial distribution of the maximum water surface elevations and current speeds in the eastern part of Port Mahon over the 6 h tsunami simulation from the asynchronous slip distribution pattern.

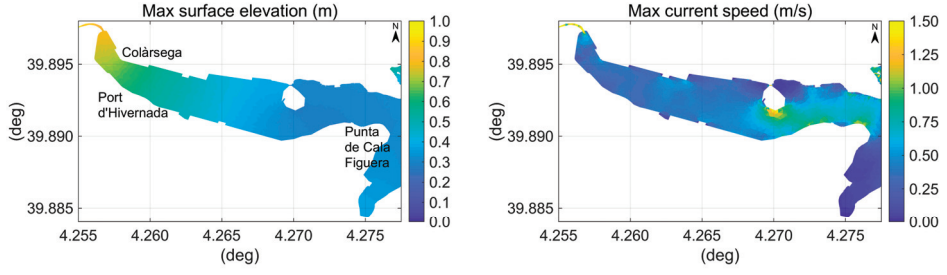

Figure 25. Spatial distribution of the maximum water surface elevations and current speeds in the inner part of Port Mahon over the 6 h tsunami simulation from the asynchronous slip distribution pattern.

As shown in the right plot of Figure 24, tsunami-induced currents reach a significant intensity past the entrance of the port as a result of the shallower water depths in this area. Current speeds exceeding 1.5 m/s are found a little further ahead the entrance of Port Mahon, in correspondence of the abrupt water depth reduction from −12 m to −6 m entering the cove Cala Teulera, between Illa del Llatzeret and the peninsula of La Mola, and along the shallow water Canal de Sant Jordi. However, no damage was reported in this part of the port, also because anchoring in Cala Teulera is officially forbidden (only permitted when all other marinas are full or in case of bad weather conditions [127]). Strong currents exceeding 1.5 m/s are also obtained from numerical simulation in the narrow Cala de Sant Esteve with rocky seafloor (Figure 24). In addition to the effects caused by the sudden sea level variation, damage also due to tsunami-induced currents must be taken into consideration in this area, confirming the observed noticeable impact.

Current speed intensifies between Punta de Cala Figuera (~1 m/s), where berthing facilities are concentrated, and the opposite shore, as shown in the right plot of Figure 25. It is also noted that vessels moored in the area beginning from Punta de Cala Figuera and extending westward along the

Levante Quay, where the Mediterranean style of berthing is used, were certainly exposed to the impact of significant transverse currents.

Computed time histories of water surface elevation and current speed at a virtual station at depth ~2.4 m located at the Colàrsega, in the inner end of Port Mahon, where severe damages were reported, are shown in Figure 26. The numerical results highlight a maximum surface elevation of 0.66 and 0.77 m using the synchronous and asynchronous slip distribution respectively and modest tsunami-induced current speeds. The spatial pattern for the synchronous slip distribution in the inner part of Port Mahon is shown in Figure 27; the patterns are similar with the greater intensity in the case of the asynchronous slip.

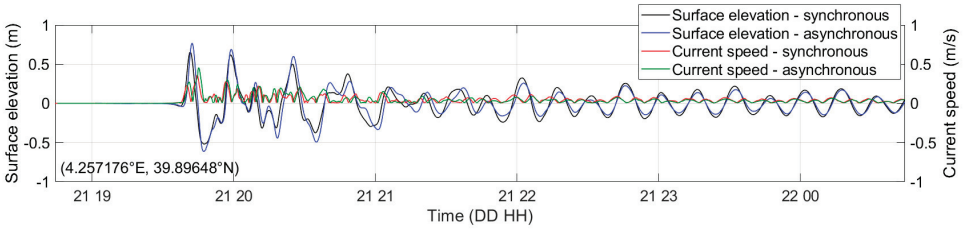

Figure 26. Time histories of water surface elevation and current speed computed at a virtual station (2.4 m depth) in the inner end of Port Mahon, Colàrsega, considering the effect of both synchronous and asynchronous sliding on the tsunami generation.

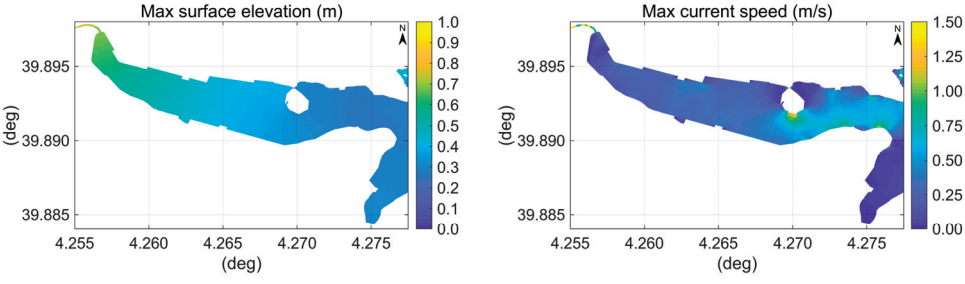

Figure 27. Spatial distribution of the maximum water surface elevations and current speeds in the inner part of Port Mahon over the 6 h tsunami simulation from the synchronous slip distribution pattern.

An area characterized by very small water level variations is evident in Figure 23, roughly extending between Illa del Rei and Illa del Llatzeret.

Unfortunately, no gauge station was in operation at tsunami time inside Port Mahon. However, two tide gauges have recently been installed: the first became operational by Puertos del Estado in October 2009 at Illa d'en Pinto (Figure 28), while the other, which has been activated in October 2017 on the north side of the entrance to the port at La Mola de Mahon, is part of the Sea Level Network of Inexpensive Device for Sea Level Measurement deployed by the Joint Research Centre of the European Commission with the specific objective to improve the monitoring of tsunami events in the Mediterranean Sea. The 1 min data collected by these two stations are freely accessible from the Sea Level Station Monitoring Facility website (http://www.ioc-sealevelmonitoring.org/) and have been used to estimate the effect of the local topobathymetric characteristics of the monitoring sites during calm weather periods. Figure 28 shows the power spectra for the selected background periods at Illa d'en Pinto (solid and dash-dotted lines in dark and light green). The main peak in the background power spectra is related to the fundamental Helmholtz mode of the harbor with period of about 42.7 min. Two other peaks at 14.2 and 8 min are evident which are associated with the following longitudinal modes of the port, being periods equal respectively to 1/3 and 1/5 of 42.7 min, in accordance with the formulation for the natural oscillation periods of a semi-enclosed rectangular basin with constant depth,

e.g., [128]. Two additional high frequency peaks at 3.4 and 5.1 min may be identified in the Mahon spectra linked to the articulated harbor shape. No resonant period is evident from the background spectrum of La Mola. Further comparison between the background spectra and the tsunami spectra obtained from the simulated time series at the Mahon tide gauge location considering both synchronous and asynchronous slip reveals that the energy content of the external forcing is concentrated at about 23 min. Moreover, since the tsunami period lies between the fundamental and the second natural periods of the harbor, it seems that there was no particular resonance amplification of the event.

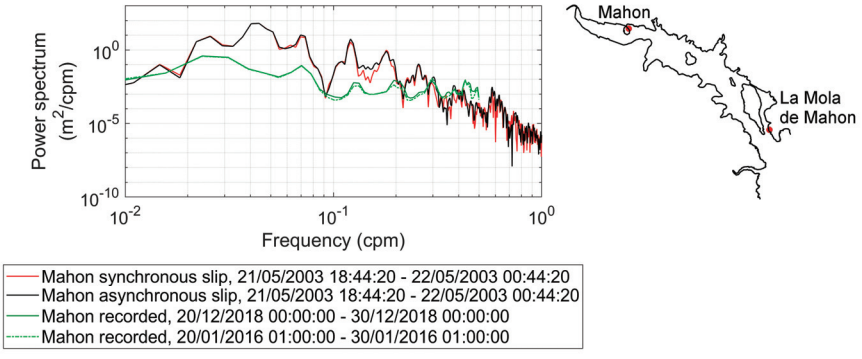

Figure 28. Location of the Mahon and La Mola tide gauges (red dots) and comparison at Mahon between the power spectra of background sea level oscillations during calm weather periods and the power spectra of the modeled tsunami time series considering both the synchronous and asynchronous slip distribution.

From the analysis of the tsunami simulation results, Cala Llonga does not seem to be affected neither by strong sea level oscillation nor by currents of particular intensity, as instead the damage reported for this location would suggest. Photographs of the bay end available at the website http://www.disfrutalaplaya.com/en/Menorca/Mao/Playa-Cala-Llonga.html (pictures 1 and 6) show the really shallow water depth of the area, a fixed pier with deck of limited height and the Mediterranean berthing style, all characters exposing boats to a higher tsunami hazard. Based only on the information given by press reports, the modeling results might seem to underestimate the tsunami impact, in addition to Cala Llonga, also in the innermost harbor zone, near the Colàrsega and Port d'Hivernada, but it is necessary to highlight that no additional detail is given on the type and size of the sunken and damaged boats, their draft and mooring conditions, their position before the tsunami, and no description of the type or cause of suffered damage is provided from which to infer the solicitation level applied by the tsunami. On the other hand, the port is naturally very well protected and might induce limited attention to mooring. The asynchronous sliding, according to our simulations, cannot explain a relevant increase of local agitation, being evaluated around +17% its effect at Mahon inner end (see Figure 26) and approximately +25% at Cala Llonga.

5.5. Damage Mechanisms and Thresholds

In these ports small to medium boats are normally present and often sailing boats with a deep keel, all of them having different scale and shape when compared to large ships. Therefore different damaging scenarios have to be considered. They fall into three categories:

a. mooring breakage and ship moved around hitting other ships or structures by (1) strong currents, (2) large water level oscillation with short and tight mooring;
b. ship lowered or raised by water level (1) hitting the bottom with keel or rudder, (2) raised and transported over the wharf, (3) raised against a fixed pier or a bridge and then sunk by still rising sea level;

c. ship caught in a breaker capsizes and sinks.

Some of the described damage mechanisms to vessels in ports can be found visualized in videos or photographs publicly available on the web (Table 5).

Table 5. Link to images representing tsunami damage mechanisms to vessels in ports from web sources.

Damage Mechanism	Source	Image
Boats touching the dry bottom of the harbor	https://www.youtube.com/watch?v=AxFNXRTXgHw Santa Cruz Harbor, California, USA, 11 March 2011 tsunami	around 1:40/16:48
Boats captured in a tsunami bore	https://www.youtube.com/watch?v=jltIeWB1XH8 Santa Cruz Harbor, California, USA, 11 March 2011 tsunami	around 1:17/5:50
Boat wedged under a floating dock	https://www.youtube.com/watch?v=AxFNXRTXgHw Santa Cruz Harbor, California, USA, 11 March 2011 tsunami	around 8:52/16:48
Stranded ships	http://www.cargolaw.com/2011nightmare_sendai_ships.html Sendai, Japan, 11 March 2011 tsunami	several examples

Lynett et al. [9] and the research team operating in California, based mainly on the experience coming from 2010 Maule (Chile) and 2011 Tohoku (Japan) tsunamis that arrived both in California at low tide conditions, have fixed the very simple threshold system: damages are not relevant if current intensity does not exceed 3 knots, damage is moderate if current does not exceed 6 knots, major if it does not exceed 9 knots, and extreme beyond this intensity. The threshold results not evidently dependent on vessel size.

However, besides current intensity, an extreme level is also a hazard factor for boats or small ships. Several observed damages to boats require also the introduction of a wave amplitude threshold as introduced by Suppasri et al. [123]. In fact, current speed drops to zero at bay end, whereas in these areas level oscillation reaches its maximum and most damages were observed. Let η_c and η_t be the maximum crest elevation a.m.s.l. and trough depth b.m.s.l. respectively, h the water depth at berth, D the ship draft, F' the height where the ship can safely lean against the quay-wall, F the ship freeboard, W the wharf elevation, W' the lower deck elevation and γ_b the breaker index, the following conditions need to be satisfied for a proper ship mooring at a fixed wharf

$$\eta_t < min\,(h - D,\ F - W') \text{ and } \eta_c < min\left(W - F',\ \gamma_b \cdot h\right) \tag{8}$$

in order, respectively, not to hit the seabed, not to be caught under the deck, and not to be thrown on wharf, not to be caught in a breaker (and capsized). In the case of a floating berth only the first and last conditions are significant. A sketch illustrating the parameters considered for a boat and a fixed wharf is presented in Figure 29. However, for a boat, for which all the mentioned ship/wharf dimensions are small compared to the ship case, these conditions become more severe than the current speed condition. The above mentioned level amplitude conditions can explain damages occurred to boats in harbor sites where current was not exceeding any of the proposed thresholds.

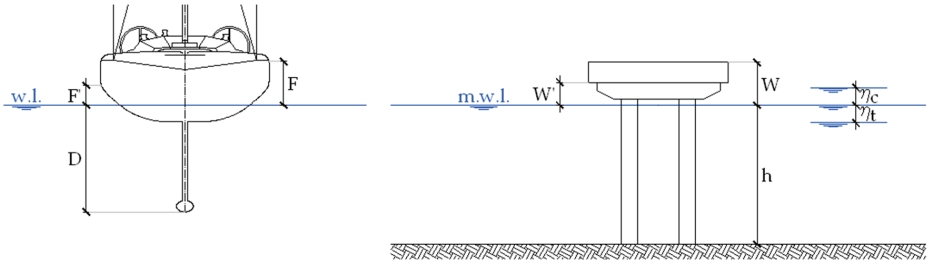

Figure 29. A sketch illustrating the parameters considered for a boat and a fixed wharf.

The loss function developed by the Japanese research team, Muhari et al. [124], allows to evaluate the loss (percentage of the equipment value) based on tsunami parameters, i.e., height and speed, and non-exceedance probability, see Table 4 in [124]. The effect of displacement is not pointed out because the data set is dominated by small marine vessels weighting less than 5 tons. It shows for instance that complete loss (Loss > 90%) for half of the cases/boats (Probability = 0.50) is associated to tsunami height = 1.90 m *or* current speed = 2.10 m/s. The same tsunami parameters cause significant loss (Loss > 25%) to 3 out of 4 cases/boats.

As already observed in [124] the Japanese and Californian speed thresholds are consistent if "moderate" is considered equivalent to "1/2 of the involved vessels suffered a severe damage" and "major" to "3/4 of the involved vessels suffered a severe damage". The tsunami height threshold is new; tsunami height threshold, whose values are reliable only for small vessels, and current speed threshold are highly correlated (Figure 30), whereas tsunami loading parameters in specific harbor conditions are independent, so that usually only one of them results critical for damaging.

In order to compare the damage probability of the criterion with actual damage frequency, the number of boats present in harbor at tsunami arrival time has been tentatively estimated by considering the present berth capacity and its evolution since 2003, as well as the annual cycle of presence different in permanent or seasonal ports. The estimated number is presented in Table 6 with the assessed tsunami parameters and a synthesis of damages. Damaging can be classified between minor and moderate depending on the harbor (Figure 30); the severity perception of the event is highlighted by its mention in port information: only for Port Mahon the event is quoted as a shelter failure causing substantial damages to yachts.

Globally these damage frequency data are fairly consistent with Muhari et al. [124] criterion, in particular if one realizes that important solicitation parameters, as the boat-current angle for instance, as well as the mooring resistance, are not explicitly considered. Mooring resistance is probably proportioned to sea waves, so that the best sheltered harbor, Port Mahon, results the most exposed to tsunami damage.

Table 6. Extreme water surface elevation, drawdown, current speed and a summary of damage for the 21 May 2003 tsunami. Tsunami load parameters are evaluated as the greater between those referring to synchronous and asynchronous slip patterns. For current speed a typical value in the berth area is presented with the nodal maximum value in parentheses.

Id	Port, Bay	Peak Surface Elevation (m)	Peak Drawdown (m)	Current Speed (m/s)	Estimated n. of Boats in Harbor	Reported Damage
A	Palma de Mallorca-Between Sant Magí dock and Royal Yacht Club up to La Riera	+1.15	−1.07	1.95 (2.1)	1500	Flooding, several boats damaged by grounding and collision
B	Sant Antoni-Near the fishermen pier	+1.16	−1.33	1.2 (1.4)	150	Flooding, 15 boats, port facilities
C	Port Mahon-Colàrsega	+0.79	−0.64	0.7 (1.6)	120	Flooding, 37 boats, port facilities
D	Port Mahon-Cala Llonga	+0.51	−0.47	0.6 (1.0)	45	20 boats, port facilities
E	Cala de Sant Esteve	+0.86	−1.37	2.2 (3.0)	20	Flooding, at least 5 boats stranded

Considering all the boats damaged by the tsunami of 21 May 2003 in relation to the current number of berths in Balearic Islands, it is reasonable to hypothesize a percentage of damage around a few percentage points. It is therefore necessary to consider the stress induced inside the Balearic Islands ports by the described tsunami loading factors having a recurrence time of about 40 years,

not considering tsunamis of meteorological origin. This information can also help to develop and implement appropriate tsunami hazard mitigation strategies for the individual harbors.

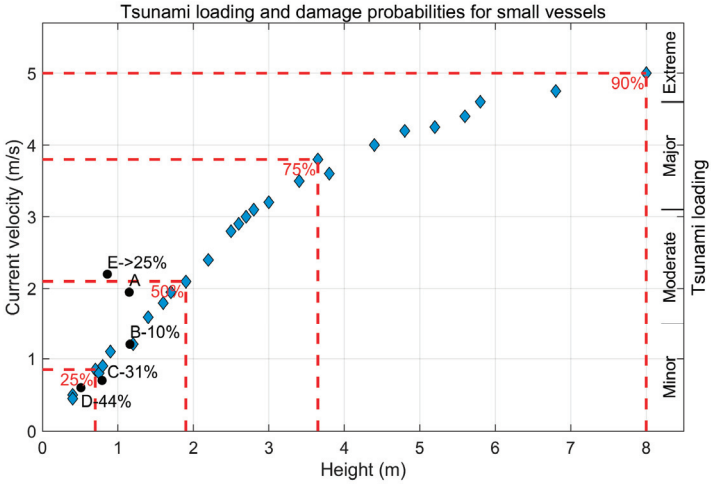

Figure 30. Tsunami load parameters for small vessels and damage thresholds. Diamonds: Muhari et al. [124] threshold values. –: less-than-full-damage domain and the corresponding probability. X-nn%: solicitation and frequency of vessel full damage in the analyzed harbor X (id in Table 6), estimated as the ratio of the number of totally damaged boats to the number of boats in the harbor.

6. Conclusions

The Boumerdès earthquake of 21 May 2003 generated a tsunami that was recorded by tide gauges throughout the Western Mediterranean and caused severe damage to vessels and nautical facilities in the Balearic Islands ports. The proper wave period was about 21 min, but oscillation in harbor may have slightly different periods due to resonance selective amplification.

Slip distribution patterns and earthquake fault geometries, derived by studies of literature focused on the determination of the source rupture process, result in significant variation of the simulated tsunami and therefore in the predicted impact on exposed coastal areas.

Numerical tsunami simulation based on the slip distribution pattern derived from the planar fault model proposed by Belabbès et al. [34] with a motivated higher moment magnitude, $M_w \sim 7.2$ instead of the official 6.8–6.9, presents in general better agreement with the tsunami observations at Palma de Mallorca and Sant Antoni tide gauges, as well as at distant coasts, due to the higher simulated sea surface elevations and larger drawdown.

An evident delay in the range 4.4–6.0 min is found in our reconstruction at Palma de Mallorca tide gauge between observed and hindcasted tsunami arrival times, but it is also present in all previous studies even if using different simulation models. Additional investigation is required on this time shift, as it is not constant among ports and observed oscillations are characterized by more irregular behavior than those deriving from the simulations with the adopted modeling, especially in the initial stage.

A space-time dynamic displacement of the seabed might be more suitable than an instantaneous rupture for modeling the tsunami generation, as the trend of the radiated seismic energy shown in Figures 1 and 12 seems to suggest. The space-time structure of the source displacement may change the radiation direction and tsunami intensity in the different ports.

The spectral analysis performed on the detided records of the tsunami event at Palma and Sant Antoni shows a dominant peak at periods of 21–23 min which is associated with the tsunami source characteristics and is well reproduced by the numerical models at all harbor sites. Some of the harbor natural oscillation modes, identified in the corresponding background spectra, were excited at the

tsunami arrival. In particular, local tsunami wave amplification was favored at Palma de Mallorca and Sant Antoni, due to resonance effects of the bay-port system. Resonance, through a selective amplification of components, causes a shift of tsunami periods toward the bay resonance periods.

Excellent agreement is found inside the ports of Palma de Mallorca and Sant Antoni between critical areas derived from simulation and the tsunami affected zones indicated by newspapers, online news, or previous research studies.

A detailed tsunami simulation has been performed also for Port Mahon, where major damages to vessels and docks are documented, and the modeled hydrodynamic features have been correlated with the available, albeit qualitative, damage information from press reports.

By comparison with press information, the modeled tsunami impact associated to a synchronous sliding appears to be underestimated at the inner end of Port Mahon and particularly in Cala Llonga. Underestimation of tsunami effects inside the port of Mahon might be caused by a slightly inaccurate strike orientation of the fault plane and/or by asynchronous sliding, both causing several degrees deviation of the radiation lobe and consequent alteration of wave amplitude in the different ports.

The numerical dispersion of MIKE 21 Flexible Mesh, through lateral spreading and/or longitudinal dissipation, might be a cause of underestimation of hindcasted extremes, even if this underestimation is common to simulations of most tsunami events.

Numerical modeling provided tsunami solicitation parameters that can locally cause damage to vessels. The current speed thresholds proposed by Lynett et al. [9] are confirmed in a broad sense also by the present analysis. The threshold limits for tsunami height proposed by Suppasri et al. [123] and Muhari et al. [124] are broadly consistent with observations. Unfortunately, this threshold depends substantially on ship size and shape. Since both criteria do not represent explicitly the effects of the boat-current angle on loading and of mooring resistance, the probability associated in [124] refers to the usual statistics of these variables and not to the specific conditions.

The modeling procedure based on shallow water equations and results presented here may be used to assess tsunami hazard conditions, at least within Mediterranean harbors and ports, identifying areas where mooring is less safe under tsunami attack. The use of Boussinesq approximation, representing wave dispersion, might produce better results at the expense of greater computing load; it is suggested for a second approximation.

Author Contributions: M.M. proposed the study, manually digitized coastline and bathymetric data, ran the numerical simulations, analyzed tide gauge data and simulation results, wrote the original draft and the revised version of the manuscript. R.A. commented on the manuscript and provided funding for publication. A.L. supervised the study and the manuscript. All authors have read and agreed to the published version of the manuscript.

Funding: This research was partially funded by the University of Bologna that supported Marinella Masina in her research activity.

Acknowledgments: The authors wish to thank Carlo Zumaglini (Siap+Micros s.r.l.) and ISPRA for having provided the measurements collected by the Italian tide gauge network; Marta Marcos (IMEDEA) for making available the Sant Antoni tidal records and Pilar Gil Blázquez (Puertos del Estado) for the provision of the Malaga and Valencia tide gauge data. The authors would like to extend warm thanks to Joaquin Tintoré and Lluis Gómez-Pujol for the provision of the Balearic Islands bathymetric data owned by SOCIB and Miguel Tuduri of the Autoritat Portuaria de Balears for having provided the bathymetric map of the Palma de Mallorca harbor. We gratefully acknowledge all the organizations mentioned in the paper that made their data freely accessible online. We are grateful to Guillem Xavier Pons Buades and Vicent Marí for providing the permission to include the photographs in Figure 13 documenting damages to boats. Thanks are extended to Andrea Pedroncini (DHI-Italia) for his technical support.

Conflicts of Interest: The authors declare no conflict of interest.

References

1. Dilley, M.; Chen, R.S.; Deichmann, U.; Lerner-Lam, A.L.; Arnold, M.; Agwe, J.; Buys, P.; Kjekstad, O.; Lyon, B.; Yetman, G. *Natural Disaster Hotspots: A Global Risk Analysis. Disaster Risk Management Series No. 5-34423*; The World Bank: Washington, DC, USA, 2005.

2. International Tsunami Information Center. Available online: http://itic.ioc-unesco.org/index.php (accessed on 22 July 2020).
3. NOAA National Centers for Environmental Information. National Geophysical Data Center/World Data Service: NCEI/WDS Global Historical Tsunami Database. Available online: https://www.ngdc.noaa.gov/hazard/tsu_db.shtml (accessed on 24 July 2020).
4. Maramai, A.; Brizuela, B.; Graziani, L. The Euro-Mediterranean Tsunami Catalogue. *Ann. Geophys.* **2014**, *57*, S0435. [CrossRef]
5. Goeldner-Gianella, L.; Grancher, D.; Robertsen, Ø.; Anselme, B.; Brunstein, D.; Lavigne, F. Perception of the risk of tsunami in a context of high-level risk assessment and management: The case of the fjord Lyngen in Norway. *Geoenviron. Disasters* **2017**, *4*, 227. [CrossRef]
6. Cerase, A.; Crescimbene, M.; La Longa, F.; Amato, A. Tsunami risk perception in southern Italy: First evidence from a sample survey. *Nat. Hazards Earth Syst. Sci.* **2019**, *19*, 2887–2904. [CrossRef]
7. Giles, J.; Marris, E. Indonesian tsunami-monitoring system lacked basic equipment. *Nature* **2004**. [CrossRef]
8. Melgar, D.; Bock, Y. Near-field tsunami models with rapid earthquake source inversions from land- and ocean-based observations: The potential for forecast and warning. *J. Geophys. Res. Solid Earth* **2013**, *118*, 5939–5955. [CrossRef]
9. Lynett, P.J.; Borrero, J.; Son, S.; Wilson, R.; Miller, K. Assessment of the tsunami-induced current hazard. *Geophys. Res. Lett.* **2014**, *41*, 2048–2055. [CrossRef]
10. Yelles-Chaouche, A.K.; Djellit, H.; Hamdache, M. The Boumerdes -Algiers (Algeria) Earthquake of May 21st, 2003 (Mw = 6.8). In *CSEM/EMSC Newsletter N*. 20 September 2003; pp. 3–5. Available online: https://www.emsc-csem.org/Files/docs/data/newsletters/newsletter_20.pdf (accessed on 26 July 2020).
11. Laouami, N.; Slimani, A.; Bouhadad, Y.; Nour, A.; Larbes, S. Analysis of Strong Ground Motions Recorded during the 21st May, 2003 Boumerdes, Algeria, Earthquake. In *CSEM/EMSC Newsletter N*. 20 September 2003; pp. 5–7. Available online: https://www.emsc-csem.org/Files/docs/data/newsletters/newsletter_20.pdf (accessed on 26 July 2020).
12. Laouami, N.; Slimani, A.; Bouhadad, Y.; Chatelain, J.-L.; Nour, A. Evidence for fault-related directionality and localized site effects from strong motion recordings of the 2003 Boumerdes (Algeria) earthquake: Consequences on damage distribution and the Algerian seismic code. *Soil Dyn. Earthq. Eng.* **2006**, *26*, 991–1003. [CrossRef]
13. EERI, Earthquake Engineering Research Institute. *The Boumerdes, Algeria, Earthquake of May 21, 2003. EERI Learning from Earthquakes, Reconnaissance Report*; EERI Publication Number 2003-04; EERI: Oakland, CA, USA, 2003. Available online: https://www.eeri.org/site/images/lfe/pdf/algeria_20030521.pdf (accessed on 27 July 2020).
14. Meghraoui, M.; Maouche, S.; Chemaa, B.; Cakir, Z.; Aoudia, A.; Harbi, A.; Alasset, P.-J.; Ayadi, A.; Bouhadad, Y.; Benhamouda, F. Coastal uplift and thrust faulting associated with the M_w = 6.8 Zemmouri (Algeria) earthquake of 21 May, 2003. *Geophys. Res. Lett.* **2004**, *31*, L19605. [CrossRef]
15. Papadopoulos, G.A.; Gràcia, E.; Urgeles, R.; Sallares, V.; De Martini, P.M.; Pantosti, D.; González, M.; Yalciner, A.C.; Mascle, J.; Sakellariou, D.; et al. Historical and pre-historical tsunamis in the Mediterranean and its connected seas: Geological signatures, generation mechanisms and coastal impacts. *Mar. Geol.* **2014**, *354*, 81–109. [CrossRef]
16. Peláez, J.A.; Chourak, M.; Tadili, B.A.; Aït Brahim, L.; Hamdache, M.; López Casado, C.; Martínez Solares, J.M. A catalog of main Moroccan earthquakes from 1045 to 2005. *Seism. Res. Lett.* **2007**, *78*, 614–621. [CrossRef]
17. Hamdache, M.; Peláez, J.A.; Talbi, A.; López Casado, C. A unified catalog of main earthquakes for Northern Algeria from A.D. 856 to 2008. *Seism. Res. Lett.* **2010**, *81*, 732–739. [CrossRef]
18. Soloviev, S.L.; Solovieva, O.N.; Go, C.N.; Kim, K.S.; Shchetnikov, N.A. Tsunamis in the Mediterranean Sea 2000 B.C.-2000 A.D. In *Advances in Natural and Technological Hazards Research, Volume 13*; Kluwer Academic Publishers: Dordrecht, The Netherlands, 2000.
19. Roger, J.; Hébert, H. The 1856 Djijelli (Algeria) earthquake and tsunami: Source parameters and implications for tsunami hazard in the Balearic Islands. *Nat. Hazards Earth Syst. Sci.* **2008**, *8*, 721–731. [CrossRef]
20. Harbi, A.; Meghraoui, M.; Maouche, S. The Djidjelli (Algeria) earthquakes of 21 and 22 August 1856 (I_0 VIII, IX) and related tsunami effects Revisited. *J. Seism.* **2011**, *15*, 105–129. [CrossRef]

21. Maouche, S.; Harbi, A.; Meghraoui, M. Attenuation of intensity for the Zemmouri earthquake of 21 May 2003 (Mw 6.8): Insights for the seismic hazard and historical earthquake sources in Northern Algeria. In *Historical Seismology. Interdisciplinary Studies of Past and Recent Earthquakes. Modern Approaches in Solid Earth Sciences*; Fréchet, J., Meghraoui, M., Stucchi, M., Eds.; Springer: Dordrecht, The Netherlands, 2008; Volume 2, pp. 327–350. [CrossRef]
22. Bezzeghoud, M.; Dimitro, D.; Ruegg, J.C.; Lammali, K. Faulting mechanism of the El Asnam (Algeria) 1954 and 1980 earthquakes from modelling of vertical movements. *Tectonophysics* **1995**, *249*, 249–266. [CrossRef]
23. Hébert, H.; Alasset, P.-J. The tsunami triggered by the 21 May 2003 Algiers earthquake. In *CSEM/EMSC Newsletter N*. 20 September 2003; pp. 10–12. Available online: https://www.emsc-csem.org/Files/docs/data/newsletters/newsletter_20.pdf (accessed on 26 July 2020).
24. Wang, X.; Liu, P.L.-F. A numerical investigation of Boumerdes-Zemmouri (Algeria) earthquake and tsunami. *Comput. Model. Eng. Sci.* **2005**, *10*, 171–184. [CrossRef]
25. Borrero, J.C. *Preliminary Simulations of the Algerian Tsunami of 21 May, 2003 in the Balearic Islands*; University of Southern California: Los Angeles, CA, USA, 2003.
26. Alasset, P.-J.; Hébert, H.; Maouche, S.; Calbini, V.; Meghraoui, M. The tsunami induced by the 2003 Zemmouri earthquake (M_W = 6.9, Algeria): Modelling and results. *Geophys. J. Int.* **2006**, *166*, 213–226. [CrossRef]
27. Delouis, B.; Vallée, M.; Meghraoui, M.; Calais, E.; Maouche, S.; Lammali, K.; Mahsas, A.; Briole, P.; Benhamouda, F.; Yelles, K. Slip distribution of the 2003 Boumerdes-Zemmouri earthquake, Algeria, from teleseismic, GPS, and coastal uplift data. *Geophys. Res. Lett.* **2004**, *31*, L18607. [CrossRef]
28. Yelles, K.; Lammali, K.; Mahsas, A.; Calais, E.; Briole, P. Coseismic deformation of the May 21st, 2003, M_w = 6.8 Boumerdes earthquake, Algeria, from GPS measurements. *Geophys. Res. Lett.* **2004**, *31*, L13610. [CrossRef]
29. Semmane, F.; Campillo, M.; Cotton, F. Fault location and source process of the Boumerdes, Algeria, earthquake inferred from geodetic and strong motion data. *Geophys. Res. Lett.* **2005**, *32*, L01305. [CrossRef]
30. Sahal, A.; Roger, J.; Allgeyer, S.; Lemaire, B.; Hébert, H.; Schindelé, F.; Lavigne, F. The tsunami triggered by the 21 May 2003 Boumerdès-Zemmouri (Algeria) earthquake: Field investigations on the French Mediterranean coast and tsunami modelling. *Nat. Hazards Earth Syst. Sci.* **2009**, *9*, 1823–1834. [CrossRef]
31. Vela, J.; Pérez, B.; González, M.; Otero, L.; Olabarrieta, M.; Canals, M.; Casamor, J.L. Tsunami resonance in the Palma de Majorca bay and harbour induced by the 2003 Boumerdes-Zemmouri Algerian earthquake (Western Mediterranean). In Proceedings of the 32nd International Conference on Coastal Engineering 2010, Shanghai, China, 30 June–5 July 2010; McKee Smith, J., Lynett, P., Eds.; ASCE/COPRI Coastal Engineering Research Council: Reston, VA, USA, 2011; currents.7. [CrossRef]
32. Vela, J.; Pérez, B.; González, M.; Otero, L.; Olabarrieta, M.; Canals, M.; Casamor, J.L. Tsunami resonance in Palma bay and harbor, Majorca Island, as induced by the 2003 Western Mediterranean earthquake. *J. Geol.* **2014**, *122*, 165–182. [CrossRef]
33. Samaras, A.G.; Karambas, T.V.; Archetti, R. Simulation of tsunami generation, propagation and coastal inundation in the Eastern Mediterranean. *Ocean Sci.* **2015**, *11*, 643–655. [CrossRef]
34. Belabbès, S.; Wicks, C.; Çakir, Z.; Meghraoui, M. Rupture parameters of the 2003 Zemmouri (M_w 6.8), Algeria, earthquake from joint inversion of interferometric synthetic aperture radar, coastal uplift, and GPS. *J. Geophys. Res. Solid Earth* **2009**, *114*, B03406. [CrossRef]
35. Nocquet, J.-M.; Calais, E. Geodetic measurements of crustal deformation in the Western Mediterranean and Europe. *Pure Appl. Geophys.* **2004**, *161*, 661–681. [CrossRef]
36. Serpelloni, E.; Vannucci, G.; Pondrelli, S.; Argnani, A.; Casula, G.; Anzidei, M.; Baldi, P.; Gasperini, P. Kinematics of the Western Africa-Eurasia plate boundary from focal mechanisms and GPS data. *Geophys. J. Int.* **2007**, *169*, 1180–1200. [CrossRef]
37. Bounif, A.; Dorbath, C.; Ayadi, A.; Meghraoui, M.; Beldjoudi, H.; Laouami, N.; Frogneux, M.; Slimani, A.; Alasset, P.J.; Kharroubi, A.; et al. The 21 May 2003 Zemmouri (Algeria) earthquake Mw 6.8: Relocation and aftershock sequence analysis. *Geophys. Res. Lett.* **2004**, *31*, L19606. [CrossRef]
38. Bourenane, H.; Bouhadad, Y.; Tas, M. Liquefaction hazard mapping in the city of Boumerdès, Northern Algeria. *Bull. Eng. Geol. Environ.* **2018**, *77*, 1473–1489. [CrossRef]
39. Yagi, Y. Preliminary Results of Rupture Process. Available online: http://iisee.kenken.go.jp/staff/yagi/eq/algeria20030521/algeria2003521.html (accessed on 3 December 2016).

40. Yagi, Y. Source process of large and significant earthquakes in 2003. *Bull. Int. Inst. Seismol. Earthq. Eng.* **2003**, *37*, 145–153.
41. Delouis, B.; Vallée, M. The 2003 Boumerdes (Algeria) earthquake: Source process from teleseismic data. In *CSEM/EMSC Newsletter N*. 20 September 2003; pp. 8–9. Available online: https://www.emsc-csem.org/Files/docs/data/newsletters/newsletter_20.pdf (accessed on 26 July 2020).
42. Bezzeghoud, M.; Caldeira, B.; Borges, J.F.; Beldjoudi, H.; Buforn, E.; Maouche, S.; Ousadou, F.; Kherroubi, A.; Harbi, A.; Ayadi, A. *The Zemmouri-Boumerdes (Algeria) Earthquake of May 21st, 2003, Mw=6.8: Source Parameters and Rupture Propagation Study from Teleseismic Data*; European Seismological Commission—XXIX General Assembly, University & GFZ: Potsdam, Germany, 2004.
43. Braunmiller, J.; Bernardi, F. The 2003 Boumerdes, Algeria earthquake: Regional moment tensor analysis. *Geophys. Res. Lett.* **2005**, *32*, L06305. [CrossRef]
44. Santos, R.; Caldeira, B.; Bezzeghoud, M.; Borges, J.F. The rupture process and location of the 2003 Zemmouri-Boumerdes earthquake (Mw 6.8) inferred from seismic and geodetic data. *Pure Appl. Geophys.* **2015**, *172*, 2421–2434. [CrossRef]
45. Bossu, R.; Godey, S.; Mazet-Roux, G. EMSC actions concerning the Boumerdes-Zemmouri event. In *CSEM/EMSC Newsletter N*. 20 September 2003; p. 2. Available online: https://www.emsc-csem.org/Files/docs/data/newsletters/newsletter_20.pdf (accessed on 26 July 2020).
46. Bernardi, F. Earthquake Source Parameters in the Alpine-Mediterranean Region from Surface Wave Analysis. Ph.D. Thesis, ETH Nr. 15652. Swiss Federal Institute of Technology, Zürich, Switzerland, 2004. [CrossRef]
47. Déverchère, J.; Yelles, K.; Domzig, A.; Mercier de Lépinay, B.; Bouillin, J.-P.; Gaullier, V.; Bracène, R.; Calais, E.; Savoye, B.; Kherroubi, A.; et al. Active thrust faulting offshore Boumerdes, Algeria, and its relations to the 2003 Mw 6.9 earthquake. *Geophys. Res. Lett.* **2005**, *32*, L04311. [CrossRef]
48. Déverchère, J.; Mercier de Lépinay, B.; Cattaneo, A.; Strzerzynski, P.; Calais, E.; Domzig, A.; Bracene, R. Comment on "Zemmouri earthquake rupture zone (M_w 6.8, Algeria): Aftershocks sequence relocation and 3D velocity model" by A. Ayadi et al. *J. Geophys. Res. Solid Earth* **2010**, *115*, B04320. [CrossRef]
49. Kherroubi, A.; Yelles-Chaouche, A.; Koulakov, I.; Déverchère, J.; Beldjoudi, H.; Haned, A.; Semmane, F.; Aidi, C. Full aftershock sequence of the M_w 6.9 2003 Boumerdes earthquake, Algeria: Space-time distribution, local tomography and seismotectonic implications. *Pure Appl. Geophys.* **2017**, *174*, 2495–2521. [CrossRef]
50. IRIS DMC. *Data Services Products: EQEnergy Earthquake Energy & Rupture Duration*; IRIS: Washington, DC, USA, 2013. [CrossRef]
51. Convers, J.A.; Newman, A.V. Global evaluation of large earthquake energy from 1997 through mid-2010. *J. Geophys. Res. Solid Earth* **2011**, *116*, B08304. [CrossRef]
52. Heezen, B.C.; Ewing, M. Orléansville earthquake and turbidity currents. *AAPG Bull.* **1955**, *39*, 2505–2514. [CrossRef]
53. El-Robrini, M.; Gennesseaux, M.; Mauffret, A. Consequences of the El-Asnam earthquakes: Turbidity currents and slumps on the Algerian margin (Western Mediterranean). *Geo-Mar. Lett.* **1985**, *5*, 171–176. [CrossRef]
54. Cattaneo, A.; Babonneau, N.; Ratzov, G.; Dan-Unterseh, G.; Yelles, K.; Bracène, R.; Mercier de Lépinay, B.; Boudiaf, A.; Déverchère, J. Searching for the seafloor signature of the 21 May 2003 Boumerdès earthquake offshore central Algeria. *Nat. Hazards Earth Syst. Sci.* **2012**, *12*, 2159–2172. [CrossRef]
55. Bryant, E. *Tsunami: The Underrated Hazard*, 2nd ed.; Springer, Praxis Publishing Ltd.: Chichester, UK, 2008.
56. Harbi, A.; Maouche, S.; Ousadou, F.; Rouchiche, Y.; Yelles-Chaouche, A.; Merahi, M.; Heddar, A.; Nouar, O.; Kherroubi, A.; Beldjoudi, H.; et al. Macroseismic Study of the Zemmouri Earthquake of 21 May 2003 (Mw 6.8, Algeria). *Earthq. Spectra* **2007**, *23*, 315–332. [CrossRef]
57. Edwards, C.L. Zemmouri, Algeria, Mw 6.8 Earthquake of May 21, 2003. In *Technical Council on Lifeline Earthquake Engineering, Monograph No. 27*; Edwards, C.L., Ed.; The American Society of Civil Engineers: Reston, VA, USA, 2004.
58. Vich, M.-d.-M.; Monserrat, S. Source spectrum for the Algerian tsunami of 21 May 2003 estimated from coastal tide gauge data. *Geophys. Res. Lett.* **2009**, *36*, L20610. [CrossRef]
59. Heidarzadeh, M.; Satake, K. The 21 May 2003 tsunami in the Western Mediterranean Sea: Statistical and wavelet analyses. *Pure Appl. Geophys.* **2013**, *170*, 1449–1462. [CrossRef]
60. Toda, S.; Stein, R.S.; Sevilgen, V.; Lin, J. *Coulomb 3.3 Graphic-Rich Deformation and Stress-Change Software for Earthquake, Tectonic, and Volcano Research and Teaching-User Guide*; US Geological Survey Open-File Report 2011-1060; 2011. Available online: https://pubs.usgs.gov/of/2011/1060/ (accessed on 29 July 2020).

61. Okada, Y. Internal deformation due to shear and tensile faults in a half-space. *Bull. Seismol. Soc. Am.* **1992**, *82*, 1018–1040.
62. Nosov, M.A.; Bolshakova, A.V.; Kolesov, S.V. Displaced water volume, potential energy of initial elevation, and tsunami intensity: Analysis of recent tsunami events. *Pure Appl. Geophys.* **2014**, *171*, 3515–3525. [CrossRef]
63. Levin, B.W.; Nosov, M.A. *Physics of Tsunamis*, 2nd ed; Springer International Publishing: Cham, Switzerland, 2016. [CrossRef]
64. Kajiura, K. The leading wave of a tsunami. *Bull. Earthq. Res. Ins. Univ. Tokyo* **1963**, *41*, 535–571.
65. Saito, T.; Furumura, T. Three-dimensional tsunami generation simulation due to sea-bottom deformation and its interpretation based on the linear theory. *Geophys. J. Int.* **2009**, *178*, 877–888. [CrossRef]
66. Lynett, P.J.; Borrero, J.C.; Weiss, R.; Son, S.; Greer, D.; Renteria, W. Observations and modeling of tsunami-induced currents in ports and harbors. *Earth Planet. Sci. Lett.* **2012**, *327–328*, 68–74. [CrossRef]
67. Lynett, P.J.; Gately, K.; Wilson, R.; Montoya, L.; Arcas, D.; Aytore, B.; Bai, Y.; Bricker, J.D.; Castro, M.J.; Cheung, K.F.; et al. Inter-model analysis of tsunami-induced coastal currents. *Ocean Model.* **2017**, *114*, 14–32. [CrossRef]
68. Arcos, M.E.M.; LeVeque, R.J. Validating velocities in the GeoClaw tsunami model using observations near Hawaii from the 2011 Tohoku tsunami. *Pure Appl. Geophys.* **2015**, *172*, 849–867. [CrossRef]
69. Barberopoulou, A.; Legg, M.R.; Uslu, B.; Synolakis, C.E. Reassessing the tsunami risk in major ports and harbors of California I: San Diego. *Nat. Hazards* **2011**, *58*, 479–496. [CrossRef]
70. Bolaños, R.; Sørensen, J.V.T.; Benetazzo, A.; Carniel, S.; Sclavo, M. Modelling ocean currents in the northern Adriatic Sea. *Cont. Shelf Res.* **2014**, *87*, 54–72. [CrossRef]
71. Haigh, I.D.; Wijeratne, E.M.S.; MacPherson, L.R.; Pattiaratchi, C.B.; Mason, M.S.; Crompton, R.P.; George, S. Estimating present day extreme water level exceedance probabilities around the coastline of Australia: Tides, extra-tropical storm surges and mean sea level. *Clim. Dyn.* **2014**, *42*, 121–138. [CrossRef]
72. Masina, M.; Archetti, R.; Besio, G.; Lamberti, A. Tsunami taxonomy and detection from recent Mediterranean tide gauge data. *Coast. Eng.* **2017**, *127*, 145–169. [CrossRef]
73. Sarker, M.A. Numerical modelling of tsunami in the Makran Subduction Zone-A case study on the 1945 event. *J. Oper. Oceanogr.* **2019**, *12*, S212–S229. [CrossRef]
74. Leschka, S.; Kongko, W.; Larsen, O. On the influence of nearshore bathymetry data quality on tsunami runup modelling, part II: Modelling. In *Proceedings of the 5th International Conference on Asian and Pacific Coasts 2009*; Tan, S.K., Huang, Z., Eds.; World Scientific Pub Co Pte Ltd.: Singapore, 2009; pp. 157–163. [CrossRef]
75. Gayer, G.; Leschka, S.; Nöhren, I.; Larsen, O.; Günther, H. Tsunami inundation modelling based on detailed roughness maps of densely populated areas. *Nat. Hazards Earth Syst. Sci.* **2010**, *10*, 1679–1687. [CrossRef]
76. Kaiser, G.; Scheele, L.; Kortenhaus, A.; Løvholt, F.; Römer, H.; Leschka, S. The influence of land cover roughness on the results of high resolution tsunami inundation modeling. *Nat. Hazards Earth Syst. Sci.* **2011**, *11*, 2521–2540. [CrossRef]
77. Payande, A.R.; Niksokhan, M.H.; Naserian, H. Tsunami hazard assessment of Chabahar bay related to megathrust seismogenic potential of the Makran subduction zone. *Nat. Hazards* **2015**, *76*, 161–176. [CrossRef]
78. Boswood, P.K. *Tsunami Modelling along the East Queensland Coast, Report 1: Regional Modelling*; Department of Science, Information Technology, Innovation and the Arts, Queensland Government: Brisbane, Queensland, Australia, 2013. Available online: https://publications.qld.gov.au/dataset/tsunami-modelling-east-queensland-coast (accessed on 26 July 2020).
79. Barua, D.K.; Allyn, N.F.; Quick, M.C. Modeling tsunami and resonance response of Alberni Inlet, British Columbia. In Proceedings of the 30th International Conference on Coastal Engineering 2006, San Diego, CA, USA, 3–8 September 2006; McKee Smith, J., Ed.; World Scientific Pub Co Pte Ltd.: Singapore, 2007; pp. 1590–1602. [CrossRef]
80. Zhang, Y.; Onodera, M.; Carr, C. Modelling of resonance response of Dawei Seaport to tsunami waves. In Proceedings of the 34th International Conference on Coastal Engineering 2014, Seoul, Korea, 15–20 June 2014; Lynett, P., Ed.; ASCE/COPRI Coastal Engineering Research Council: Reston, VA, USA, 2014; currents.29. [CrossRef]
81. Winckler, P.; Sepúlveda, I.; Aron, F.; Contreras-López, M. How do tides and tsunamis interact in a highly energetic channel? The case of Canal Chacao, Chile. *J. Geophys. Res. Oceans* **2017**, *122*, 9605–9624. [CrossRef]

82. DHI. *MIKE 21 Flow Model FM, Hydrodynamic Module, User Guide*; Danish Hydraulic Institute: Hørsholm, Denmark, 2011.
83. Tintoré, J.; Vizoso, G.; Casas, B.; Heslop, E.; Pascual, A.; Orfila, A.; Ruiz, S.; Martínez-Ledesma, M.; Torner, M.; Cusí, S.; et al. SOCIB: The Balearic Islands Coastal Ocean Observing and Forecasting System responding to science, technology and society needs. *Mar. Technol. Soc. J.* **2013**, *47*, 101–117. [CrossRef]
84. Pagine Azzurre. *Il Portolano dei Mari d'Italia*, 2014 ed.; Pagine Azzurre s.r.l.: Rome, Italy, 2014.
85. Smagorinsky, J. General circulation experiments with the primitive equations: I. The basic experiment. *Mon. Weather Rev.* **1963**, *91*, 99–164. [CrossRef]
86. Kowalik, Z. *Introduction to Numerical Modeling of Tsunami Waves*; Institute of Marine Science, University of Alaska: Fairbanks, AK, USA, 2012. Available online: https://uaf.edu/cfos/files/research-projects/people/kowalik/book_sum.pdf (accessed on 28 July 2020).
87. Flather, R.A. A tidal model of the northwest European continental shelf. *Mem. Soc. R. Sci. Liège* **1976**, *6*, 141–164.
88. Palma, E.D.; Matano, R.P. On the implementation of passive open boundary conditions for a general circulation model: The barotropic mode. *J. Geophys. Res. Oceans* **1998**, *103*, 1319–1341. [CrossRef]
89. Marchesiello, P.; McWilliams, J.C.; Shchepetkin, A. Open boundary conditions for long-term integration of regional oceanic models. *Ocean Model.* **2001**, *3*, 1–20. [CrossRef]
90. Roe, P.L. Approximate Riemann solvers, parameter vectors, and difference schemes. *J. Comput. Phys.* **1981**, *43*, 357–372. [CrossRef]
91. DHI. *MIKE 21 & MIKE 3 Flow Model FM—Hydrodynamic and Transport Module. Scientific Documentation*; Danish Hydraulic Institute: Hørsholm, Denmark, 2017.
92. Jawahar, P.; Kamath, H. A high-resolution procedure for Euler and Navier-Stokes computations on unstructured grids. *J. Comput. Phys.* **2000**, *164*, 165–203. [CrossRef]
93. Hirsch, C. *Numerical Computation of Internal and External Flows, Volume 2: Computational Methods for Inviscid and Viscous Flows*; Wiley: Chichester, UK, 1990.
94. Darwish, M.S.; Moukalled, F. TVD schemes for unstructured grids. *Int. J. Heat Mass Transf.* **2003**, *46*, 599–611. [CrossRef]
95. Díaz del Río, V. El 'tsunami' que llegó de Argelia. El País. 25 June 2003. Available online: https://elpais.com/diario/2003/06/25/futuro/1056492007_850215.html (accessed on 16 February 2020).
96. Tel, E.; González, M.-J.; Ruiz, C.; García, M.-J. Sea level data archaeology: Tsunamis and Seiches and other phenomena. In Proceedings of the 4a Assembleia Luso Espanhola de Geodesia e Geofísica, Figueira da Foz, Portugal, 3–7 February 2004.
97. Basterretxea, G.; Orfila, A.; Jordi, A.; Casas, B.; Lynett, P.; Liu, P.L.F.; Duarte, C.M.; Tintoré, J. Seasonal dynamics of a microtidal pocket beach with posidonia oceanica seabeds (Mallorca, Spain). *J. Coast. Res.* **2004**, *20*, 1155–1164. [CrossRef]
98. Gailler, A.; Hébert, H.; Schindelé, F.; Reymond, D. Coastal amplification laws for the French Tsunami Warning Center: Numerical modeling and fast estimate of tsunami wave heights along the French Riviera. *Pure Appl. Geophys.* **2018**, *175*, 1429–1444. [CrossRef]
99. Luger, S.A.; Harris, R.L. Modelling tsunamis generated by earthquakes and submarine slumps using Mike 21. In Proceedings of the International MIKE by DHI Conference 'Modelling in a World of Change', Copenhagen, Denmark, 6–8 September 2010; p. 17.
100. ABC (Madrid). 23 May 2003, p. 27. Available online: https://www.abc.es/archivo/periodicos/abc-madrid-20030523-27.html (accessed on 3 September 2020).
101. Bureau de Recherches Géologiques et Minières (BRGM). Base de données des tsunamis observés en France. Available online: http://tsunamis.brgm.fr/fiche_biblio.asp?NUMEVT=60004 (accessed on 31 December 2016).
102. www.belt.es. 26 May 2003. Available online: http://www.belt.es/noticias/2003/mayo/26/baleares.htm (accessed on 31 December 2016).
103. La Vanguardia. 23 May 2003, p. 37. Available online: http://hemeroteca-paginas.lavanguardia.com/LVE01/PUB/2003/05/23/LVG200305230371LB.pdf (accessed on 3 September 2020).

104. Roig-Munar, F.X.; Martín-Prieto, J.Á.; Rodríguez-Perea, A.; Gelabert Ferrer, B.; Vilaplana Fernández, J.M. Bloques en plataformas rocosas y acantilados del SE de Menorca: Tipología y procesos. In *Geomorfología Litoral de Menorca: Dinámica, evolución y prácticas de gestión, Monografies de la Societat d'Història Natural de les Balears*; Gómez-Pujol, L., Pons, G.X., Eds.; Societat d'Història Natural de les Balears: Palma, Illes Balears, 2017; Volume 25, pp. 251–262.
105. Libertad Digital. 22 May 2003. Available online: http://www.libertaddigital.com/sociedad/numerosas-embarcaciones-y-puertos-de-baleares-han-sufrido-danos-a-causa-del-terremoto-1275760565/ (accessed on 3 September 2020).
106. Papadopoulos, G.A. *Tsunamis in the European-Mediterranean Region: From Historical Record to Risk Mitigation*; Elsevier: Amsterdam, The Netherlands, 2016.
107. Consell d'Eivissa. Plan territorial insular de protección civil de la isla de Eivissa -Platerei- Documento de Consulta. Available online: http://www.conselldeivissa.es/portal/RecursosWeb/DOCUMENTOS/1/0_5186_1.pdf (accessed on 3 September 2020).
108. Periódico de Ibiza y Formentera. 24 May 2003. Available online: https://www.periodicodeibiza.es/sucesos/ultimas/2003/05/24/722787/las-pitiuses-fueron-las-%20islas-que-menos-sufrieron-el-maremoto.html (accessed on 3 September 2020).
109. Diario de Ibiza. 26 August 2011. Available online: http://www.diariodeibiza.es/pitiuses-balears/2011/08/26/sistema-alerta-maremotos-mediterraneoafronta-primer-gran-ensayo/503113.html (accessed on 3 September 2020).
110. Azurseisme. Site sur la sismicité historique régionale. Available online: https://www.azurseisme.com/Tsunami-english-version.html (accessed on 3 September 2020).
111. Periódico de Ibiza y Formentera, 28 October 2010. Available online: https://www.periodicodeibiza.es/pitiusas/ibiza/2010/10/28/24008/el-peligro-que-llega-del-mar.html (accessed on 3 September 2020).
112. El Mundo, 22 May 2003. Available online: https://www.elmundo.es/elmundo/2003/05/22/sociedad/1053590416.html (accessed on 3 September 2020).
113. Fritz, H.M.; Phillips, D.A.; Okayasu, A.; Shimozono, T.; Liu, H.; Mohammed, F.; Skanavis, V.; Synolakis, C.E.; Takahashi, T. The 2011 Japan tsunami current velocity measurements from survivor videos at Kesennuma Bay using LiDAR. *Geophys. Res. Lett.* **2012**, *39*, L00G23. [CrossRef]
114. Okal, E.A.; Fritz, H.M.; Raad, P.E.; Synolakis, C.; Al-Shijbi, Y.; Al-Saifi, M. Oman field survey after the December 2004 Indian Ocean tsunami. *Earthq. Spectra* **2006**, *22*, 203–218. [CrossRef]
115. Okal, E.A.; Fritz, H.M.; Raveloson, R.; Joelson, G.; Pančošková, P.; Rambolamanana, G. Madagascar field survey after the December 2004 Indian Ocean tsunami. *Earthq. Spectra* **2006**, *22*, 263–283. [CrossRef]
116. Okal, E.A.; Sladen, A.; Okal, E.A.-S. Rodrigues, Mauritius, and Réunion Islands field survey after the December 2004 Indian Ocean tsunami. *Earthq. Spectra* **2006**, *22*, 241–261. [CrossRef]
117. Wilson, R.I.; Admire, A.R.; Borrero, J.C.; Dengler, L.A.; Legg, M.R.; Lynett, P.; McCrink, T.P.; Miller, K.M.; Ritchie, A.; Sterling, K.; et al. Observations and impacts from the 2010 Chilean and 2011 Japanese tsunamis in California (USA). *Pure Appl. Geophys.* **2013**, *170*, 1127–1147. [CrossRef]
118. Admire, A.R.; Dengler, L.A.; Crawford, G.B.; Uslu, B.U.; Borrero, J.C.; Greer, S.D.; Wilson, R.I. Observed and modeled currents from the Tohoku-oki, Japan and other recent tsunamis in Northern California. *Pure Appl. Geophys.* **2014**, *171*, 3385–3403. [CrossRef]
119. Borrero, J.C.; Lynett, P.J.; Kalligeris, N. Tsunami currents in ports. *Phil. Trans. R. Soc. A* **2015**, *373*, 20140372. [CrossRef] [PubMed]
120. Lynett, P.; Weiss, R.; Renteria, W.; De La Torre Morales, G.; Son, S.; Arcos, M.E.M.; MacInnes, B.T. Coastal impacts of the March 11th Tohoku, Japan tsunami in the Galapagos Islands. *Pure Appl. Geophys.* **2013**, *170*, 1189–1206. [CrossRef]
121. Borrero, J.C.; Bell, R.; Csato, C.; DeLange, W.; Goring, D.; Greer, S.D.; Pickett, V.; Power, W. Observations, effects and real time assessment of the March 11, 2011 Tohoku-oki tsunami in New Zealand. *Pure Appl. Geophys.* **2013**, *170*, 1229–1248. [CrossRef]
122. Wilson, R.I.; Miller, K.M. *Tsunami Emergency Response Playbooks and FASTER Tsunami Height Calculation: Background Information and Guidance for Use. California Geological Survey Special Report 236*; California Department of Conservation, California Geological Survey: Sacramento, CA, USA, 2014.

123. Suppasri, A.; Muhari, A.; Futami, T.; Imamura, F.; Shuto, N. Loss functions for small marine vessels based on survey data and numerical simulation of the 2011 Great East Japan tsunami. *J. Waterw. Port Coast. Ocean Eng.* **2014**, *140*, 04014018. [CrossRef]
124. Muhari, A.; Charvet, I.; Tsuyoshi, F.; Suppasri, A.; Imamura, F. Assessment of tsunami hazards in ports and their impact on marine vessels derived from tsunami models and the observed damage data. *Nat. Hazards* **2015**, *78*, 1309–1328. [CrossRef]
125. Rabinovich, A.B.; Thomson, R.E. The 26 December 2004 Sumatra tsunami: Analysis of tide gauge data from the World Ocean Part 1. Indian Ocean and South Africa. *Pure Appl. Geophys.* **2007**, *164*, 261–308. [CrossRef]
126. Torrence, C.; Compo, G.P. A practical guide to wavelet analysis. *Bull. Am. Meteor. Soc.* **1998**, *79*, 61–78. [CrossRef]
127. RCC Pilotage Foundation; Baggaley, D.; Baggaley, S. *Islas Baleares: Ibiza, Formentera, Mallorca, Cabrera and Menorca*, 11th ed.; Imray Laurie Norie & Wilson Ltd.: Cambridgeshire, UK, 2018.
128. Rabinovich, A.B. Seiches and harbor oscillations. In *Handbook of Coastal and Ocean Engineering*; Kim, Y.C., Ed.; World Scientific Pub Co Pte Ltd.: Singapore, 2009; pp. 193–236.

Journal of
Marine Science and Engineering

MDPI

Article

A Nourishment Performance Index for Beach Erosion/Accretion at Saadiyat Island in Abu Dhabi

Waleed Hamza [1], Giuseppe Roberto Tomasicchio [2], Francesco Ligorio [2], Letizia Lusito [2,*] and Antonio Francone [3]

[1] Biology Department, College of Science, United Arab Emirates University, 15551 Al Ain, UAE; w.hamza@uaeu.ac.ae
[2] Department of Engineering for Innovation, University of Salento, Ecotekne, 73100 Lecce, Italy; giuseppe.tomasicchio@unisalento.it (G.R.T.); francesco.ligorio@unisalento.it (F.L.)
[3] Department of Civil Engineering, University of Calabria, 87036 Arcavacata di Rende (CS), Italy; antonio.francone@unical.it
* Correspondence: letizia.lusito@unisalento.it

Received: 20 April 2019; Accepted: 29 May 2019; Published: 1 June 2019

Abstract: The present paper proposes a methodology to optimise the design of a beach protection intervention at Saadiyat Island, of the Abu Dhabi city in the United Arab Emirates. In particular, a nourishment performance index (NPI) has been introduced to select among different design alternatives of a coastal engineering intervention related to the ongoing development of the island. The NPI is based on general factors such as the initial volume of sand necessary for the nourishment, the beach surface loss after the intervention and the closure depth. The proposed index, properly integrated with a numerical simulation of the beach morphodynamics, is shown to be promising in the evaluation of the feasibility for the planned coastal defence interventions. The adoption of different design scenarios has showed that the NPI value depends mainly on the built nourishment shoreline.

Keywords: beach morphology; beach nourishment performance; sustainable development; General Shoreline beach model; United Arab Emirates; Saadiyat Island

1. Introduction

In the present paper, the definition of a nourishment performance index (NPI) for coastal engineering interventions is proposed, based only on general factors such as the initial sand volume necessary for the nourishment, the beach surface loss after the intervention and the closure depth (defined in [1]), which indicates the seaward depth limit to the active profile.

In particular, the NPI has been determined for a coastal prediction system to be built at Saadiyat beach, in Saadiyat Island, a large low-lying 27 km^2 island situated in the Arabian Gulf (also named Persian Gulf) within the Emirate of Abu Dhabi of the United Arab Emirates (Figure 1). Saadiyat Island comprises a SW–NE oriented, 9 km long natural sandy beach, Saadiyat beach, of moderate to flat slope. The shape and orientation of the beach has been modified several times for the development of the Cultural District of Saadiyat Island. The present study focuses on the western area of Saadiyat beach, a 2 km long beach. Where the urban plan requires the realization of sustainable coastal protection structures, different design scenarios have been proposed by the Tourism Development Investment Company (TDIC), described in the relative TDIC master plan. According to the last development plan as approved by TDIC, the intervention for Saadiyat beach involves a large sand nourishment intervention and the construction of four groynes; the number and location of the four groynes has been decided by TDIC and no contribution from the present Authors has been given.

Figure 1. Top: view of the Arabic Gulf area showing the position of Abu Dhabi; bottom: aerial view of Saadiyat island, in the Abu Dhabi Municipality; the red rectangle indicates the position of the Saadiyat beach study area.

In order to quantify the feasibility for each of the design scenarios developed by TDIC, a deep knowledge of the engineering details and the coastal conditions, such as the performance of the intervention, the morphodynamics response of the shoreline to the various different coastal defence scenarios of the TDIC development plan is required [2–5].

The objective of the present study is to identify a methodology to evaluate the nourishment performance for different scenarios of coastal defence at Saadiyat beach. The proposed methodology is based on the recent availability of observational data (i.e., data measured by in-situ instruments, see Sections 2.1 and 2.2, and data recorded by remote observing systems like satellites, see Section 2.3.3), allowing to define with precision the wave climate (the distribution of wave characteristics averaged over a period of time and for a particular location) and coast landforms, i.e., any of the relief features present along the coast, which are the result of a combination of processes, sediments and the geology of the coast itself. The observational data were collected by means of in-situ monitoring instruments, survey campaigns and satellite imagery. The data collection has served as a basis for numerical models-based simulations of the oceanographic conditions (wave climate) and of the morphological changes in the natural shape of the coastline under the influence of the planned

interventions. The outcomes of the performed numerical simulations allow the identification of the more environmentally sustainable scenario for Saadiyat beach.

2. Materials and Methods

The proposed methodology is based on the collection of observational data and the use of numerical models in a joint way.

2.1. Sediment Characteristics

Within a survey campaign in May 2017, different sediment samples have been collected at points indicated in Figure 2 and Table 1 with water depths ranging from 1 m to 3 m. The samples indicated as 8 and 9 have been collected at the same time with few meters distance from each other. The concentration of each granulometric fraction was obtained through a sieve analysis with the corresponding results reported also in Table 1.

Figure 2. Location of sediment samples.

Table 1. Sediment characteristics of Saadiyat beach: coordinates and water depths of collection points, sample weight percentages passing different meshes (of sizes 5 μm, 10 μm and so on), corresponding D_{50} values and, finally, sand classification according to [6].

ID	Location			Weight (%) Passing Each Mesh (μm)								Sand Classification	
	Coordinates		Water Depth (m)	5 μm	10 μm	18 μm	35 μm	60 μm	120 μm	230 μm	>230 μm	D_{50} (*mm*)	Type
1	54°23′10″ E	24°32′18″ N	2	-	0.4%	0.4%	12.2%	61.8%	22.0%	2.3%	0.9%	0.44	Medium
2	54°25′20″ E	24°32′40″ N	2	-	0.2	1.0	4.2	14.7	63.1	16.1	0.7	0.26	Medium
3	54°24′07″ E	24°32′31″ N	2	-	0.2	0.5	5.2	30.3	61.3	1.6	0.9	0.33	Medium
4	54°24′55″ E	24°32′42″ N	2	-	0.0	0.1	1.8	17.8	71.1	8.6	0.6	0.27	Medium
5	54°25′43″ E	24°33′02″ N	3	-	0.5	7.0	33.5	49.0	9.3	0.4	0.3	0.65	Coarse
6	54°25′53″ E	24°32′52″ N	1	-	0.3	1.4	7.5	37.7	40.8	11.4	0.9	0.34	Medium
7	54°26′39″ E	24°33′24″ N	2	-	0.1	0.2	0.6	1.0	34.8	59.8	3.5	0.16	Fine
8	54°26′52″ E	24°33′39″ N	2	-	0.3	0.4	0.9	7.2	27.1	57.7	6.4	0.16	Fine
9	54°26′52″ E	24°33′39″ N	2	-	0.1	0.5	2.1	9.5	59.5	27.7	0.6	0.22	Fine
10	54°26′57″ E	24°33′35″ N	2	-	0.0	0.4	2.2	32.3	54.7	9.9	0.5	0.30	Medium

Table 1 shows also the value of the mean diameter of the sediment sample, D_{50} (given in mm) and the classification of the beach type according to [6] at each collection point.

Although important for a complete sedimentological mapping of the area, it was not possible to gain information on the textural characteristics of sand [7–9].

2.2. Local Wave Climate

Direct wave measurements are considered the most reliable source of information. In the Gulf area, this type of information is rare or even missing. However, recently, in vicinity of Saadiyat beach, the Abu Dhabi Municipality (ADM) installed two Argonaut-XR ADCP (Acoustic Doppler Current Profiler) produced by the company "SonTek—A Xylem Brand" (San Diego, CA, USA) to observe the atmospheric and oceanographic conditions (water level, significant wave height, peak wave period, water temperature and wind speed and direction). Courtesy of the ADM, this observations dataset was made available. The coordinates of the positions of the two instruments and the relative water depth are reported in Table 2. The data from instrument "04" present a very high percentage of data gaps and they have not been analysed. The recorded data from instrument "03", indicated as *ADMins* in the following, span the period from June 2015 to January 2018 (included), with a time resolution of 10 min and 30 min for the atmospheric and oceanographic variables, respectively [10]. The percentage of data gaps is around 4.5%, keeping into account that the instrument did not work for a time equal to around 42 days in total in the entire period June 2015–January 2018. Data successfully collected have been considered of good quality, since the quality control is ensured by the robustness of the native software/data acquisition system of the Argonaut-XR. Figure 3 shows the location of the *ADMins*. In addition, Figure 3 shows also the grid node of the NOAA (National Oceanic and Atmospheric Administration, a scientific agency within the United States Department of Commerce) offshore wave data (coordinates 25° N and 54° E, 16 m water depth) used to calculate the closure depth (Section 2.3.3).

Table 2. Coordinates of the positions of the two instruments installed by the Abu Dhabi Municipality (ADM) and the relative water depth.

Instrument	Longitude (E)	Latitude (N)	Water Depth (m)
03 (*ADMins*)	54°24′29.52″	24°34′17.04″	6
04	54°16′39.72″	24°44′31.56″	18

Figure 3. Location of *ADMins*, and NOAA nearshore and offshore grid points for the wind/wave model data.

The NOAA National Centers for Environmental Prediction (NCEP) developed the Climate Forecast System (CFS), a fully coupled model representing the interaction between the Earth's atmosphere, oceans, land and sea ice. A reanalysis of the sea and atmosphere state for the period of 1979–2009 has been conducted, resulting in the CFS Reanalysis (CFSR) dataset [11]. The vertical discretization

of the atmosphere consists of 64 layers. The temporal resolution for the atmospheric variables is 3 h. Using the CFSR dataset, the NOAA Marine Modeling and Analysis Branch (MMAB) has produced a wave hindcast for the same period. The wave hindcast dataset has been generated using the WAVEWATCH III (WW3) model (v3.14), and it is suitable for use in climate studies. The wave model suite consists of global and regional nested grids. The rectilinear grids have been developed using ETOPO-1 bathymetry [12], together with v1.10 of the Global Self-consistent Hierarchical High-resolution Shoreline (GSHHS) database. The spatial resolution of the considered data is 1/6°, which corresponds to roughly 20 km. The North West Indian Ocean computational grid, adopted in the considered data, extends in longitude from 30° E to 70° E (with 241 grid nodes) and in latitude from 20° S to 31° N (307 grid nodes). The NOAA datasets (both wind and waves) are freely available. The NOAA WAVEWATCH III/CFSR webpages [13,14] present additional details about the datasets.

2.3. Morphodynamic Modelling Techniques

2.3.1. Overview of Popular Commercial Software

A large and growing number of models have been developed to compute the morphodynamic evolution of coastal environments. These span a large range of process combinations, scales and levels of detail. The majority of existing large-scale coastline models address sandy coastline evolution. The spatial scales addressed in these models range from meters to kilometres while temporal scales range from hours to decades. The smaller space and time scale models typically employ explicitly reductionist methodologies where conservation of momentum forms the explicit means for evolving the system [15,16]. These models are typically used to simulate response from specific forcing events. Belonging to this category, XBeach [17] uses conservation of momentum and advection diffusion equations for sediment transport to simulate the response of the coast and dune to individual storm events. Larger scale models use a range of approaches to evolve system characteristics. On the contrary, GENESIS (GENEralized model for Simulating Shoreline change) [18], is designed to simulate long-term shoreline change at coastal engineering projects as produced by spatial and temporal changes in longshore sand transport. Typical longshore extents and time periods of modelled projects can be in the ranges of 1 to 100 km and 1 to 100 months, respectively, and almost arbitrary numbers and combinations of groins, detached breakwaters, seawalls, jetties and beach fills can be represented.

The model called Cascade [19] was developed to simulate regional sediment transport and coastal evolution. Representation of inlets is of special interest in how they function in the regional sediment transport system in terms of storing and transferring sediment, with consequences for the adjacent beaches. In Cascade, the coupling between the regional and local scale occurs in a hierarchical manner, that is, information is supplied from the regional scale to the local scale.

GenCade (from the combination of the words "Genesis" and "Cascade") [20] is a newly developed numerical model, which combines the engineering power of GENESIS and the regional processes capability of the Cascade model. The main utility of the modelling system lies in simulating the response of the shoreline to structures sited in the nearshore. Shoreline change produced by cross-shore sediment transport as associated with storms and seasonal variations in wave climate cannot be simulated.

The model LITPACK is developed by the Danish Hydraulic Institute (DHI) and it requires a commercial license [21]. LITPACK consists of an integrated system of modelling of coastal processes and dynamics of the coastline, capable to manage interventions in the coastline such as optimisation of beach creations and costal protection interventions, impact assessments of coastal constructions.

Within the Delft3D modelling package, a large variation of coastal and estuarine physical and chemical processes can be simulated [22]. These include waves, tidal propagation, wind- or wave-induced water level setup, flow induced by salinity or temperature gradients, sand and mud transport, water quality and changing bathymetry (morphology). Delft3D is a very powerful Open Source Software, but its range of applications go far beyond the beach morphology evolution modelling

that is required in the present work. Therefore, the shoreline evolution simulation has been performed by means of the General Shoreline beach (GSb) model.

2.3.2. GSb Model Description

Numerical simulations have been conducted by means of a newly proposed morphodynamic model, named General Shoreline beach 1.0 (GSb), belonging to the one-line model typology [23]. This typology assumes that the beach cross-shore profile remains unchanged [24,25], thereby allowing beach change to be described uniquely in terms of the shoreline position. The peculiarity of the GSb model consists of simulating shoreline evolution based on a longshore transport formula/procedure suitable at any coastal mound: sand, gravel, cobbles, shingle and rock beaches [26–32]. It is mainly based on the General Longshore Transport (GLT) model as in [28], where the longshore transport rate, Q_{LT}, in terms of m^3/s is given by the following equation:

$$Q_{LT} = \frac{S_N D_{50}^3}{(1-n)T_m} \tag{1}$$

with T_m = mean wave period, n = sediment porosity, S_N = the number of units passing a given control section in one wave [23–27]. In case of beaches, units are sand grains.

The GSb morphodynamics model considers the following equation for the longshore transport rate Q:

$$Q = Q_{LT} - \frac{K_{GSb}}{8\left(\frac{\rho_s}{\rho}-1\right)(1-n)\tan\beta\ 1.416^{5/2}} H_b^2 c_{gb} \cos(\theta_{bs}) \frac{\partial H_b}{\partial x} \tag{2}$$

with ρ_s = density of sediment, ρ = density of water, $\tan\beta$ = average bottom slope, H_b = breaking wave height, c_{gb} = group celerity at breaking, θ_{bs} = wave obliquity at breaking. The breaking wave height is considered as a wave forcing. For more references, see [33,34].

The second term in Equation (2), i.e., the term:

$$\frac{K_{GSb}}{8\left(\frac{\rho_s}{\rho}-1\right)(1-n)\tan\beta\ 1.416^{5/2}} H_b^2 c_{gb} \cos(\theta_{bs}) \frac{\partial H_b}{\partial x} \tag{3}$$

accounts for the longshore current and associated sediment transport induced by the alongshore gradient in wave height [35,36]. The average bottom slope is determined assuming cross transects of the bathymetric charts.

The GSb model presents one calibration coefficient solely, K_{GSb}, which does not depend on the grain size diameter and depends on the alongshore gradient in breaking wave height [23]. The general formula/procedure considers an energy flux approach combined with an empirical/statistical relationship between the wave-induced forcing and the number of moving units. GSb model allows to determine short-term (daily base) or long-term (yearly base) shoreline change for arbitrary combinations and configurations of structures (groynes, jetties, detached breakwaters and seawalls) and beach fills that can be represented on a modelled reach of coast.

To model the longshore sediment transport with the GSb numerical model, the 2 km long analysed shoreline has been divided in three cells and 6 sectors. The cells are indicated as the West cell, the VVIP cell, in the centre, and St. Regis cell at the eastern boundary of the beach. The sectors divide the West cell, the St. Regis cell and the area between groynes 3 and 4 each one in half and they have been used as a reference for the computation of the maximum accretion/erosion areas along the beach. Figure 4 shows the adopted initial design scenario, the cells and the reference sectors.

The actual adopted solution by the contracting company, involves the construction of four groynes: groyne 1 is 287 m long and reaches water depth 2.5 m; and groynes 2, 3 and 4 are, respectively, 230 m, 263 m and 287 m long and reach water depth 2.6 m, 3.3 m and 3.1 m. The intervention comprises a large

initial nourishment to create an area suitable for human beach recreational facilities and to increase the longevity of the beach. The sand will be taken from stockpiles in the south of Saadiyat island.

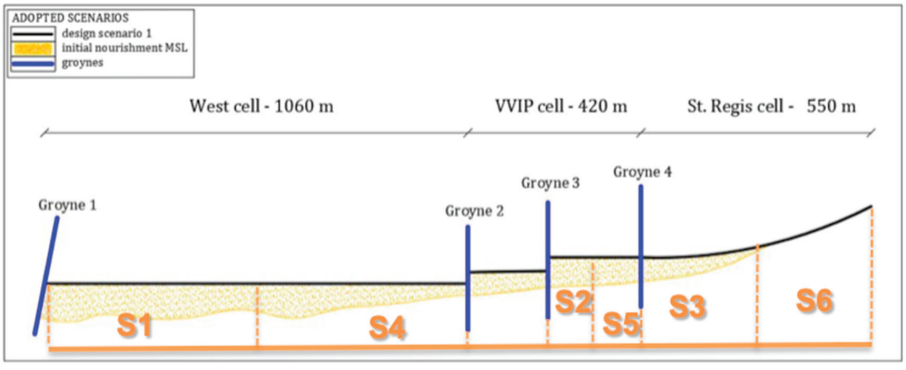

Figure 4. Schematic initial design scenario. Indicated are also the reference sectors for the computation of the maximum accretion/erosion along the beach.

2.3.3. Calibration of the GSB Model

The alongshore model computational domain has been assumed equal to 2000 m. The model grid cell resolution, DX, has been set equal to 40 m with a total number of cells, NX, equal to 50, whereas the model experiment has been carried out adopting a calculation time step, DT, equal to 1 h. GSb boundaries have been selected as pinned beach, meaning that the shoreline does not change over time in the extremes of the domain [23].

The closure depth, h_c [1], has been calculated by the following equation:

$$h_c = 2.28\, H_s - 68.5 \left(H_{s,0-12}^2 / g T_{s,0-12}^2\right) \quad (4)$$

where $H_{s,0-12}$ is the significant wave height exceeded for 12 h in one year and $T_{s,0-12}$ is the associated wave period; g is the gravitational acceleration. The closure depth has been calculated by means of the NOAA offshore wave data (at the grid node with coordinates 25° N and 54° E, indicated in Figure 3) at 16 m water depth. The calculated closure depth results equal to 3.6 m.

The estimation of the longshore sediment transport calibration coefficient, K_{GSb}, has been obtained based on the available historical data. It is worth to point out that the K_{GSb} does not depend on the grain size, while it depends on the characteristics of wave propagation. Two available Google Earth satellite images, from the years 2008 and 2009, have been considered to set the initial/final shoreline position and to determine the optimal value for the calibration coefficient. Different values of K_{GSb}, ranging between 0.005 and 0.5 have been adopted; for each of them, a measure of the error between the resulting calculated 2009 shoreline and the actual one has been determined, with a similar procedure as in [37]. The minimum value of the error is related to the optimal value for the calibration coefficient K_{GSb}, which has been assumed equal to 0.3. Figure 5 shows the 2008 and 2009 satellite shorelines and the shoreline resulting from the GSb calibration procedure. The resulting Root Mean Square Difference (RMSD) value is also shown in Figure 5, together with the distribution of the difference between the 2009 shoreline and the GSb model output (with $K_{GSb} = 0.3$) and the difference of the two 2008 and 2009 shorelines.

A period of one year has been simulated, from 1 January 2008 to 31 December 2008, considering the wave time series resulting from [10] with NOAA climate forecast system reanalyses dataset input winds (years 1979–2009) as input data (indicated as NOAA nearshore in Figure 3).

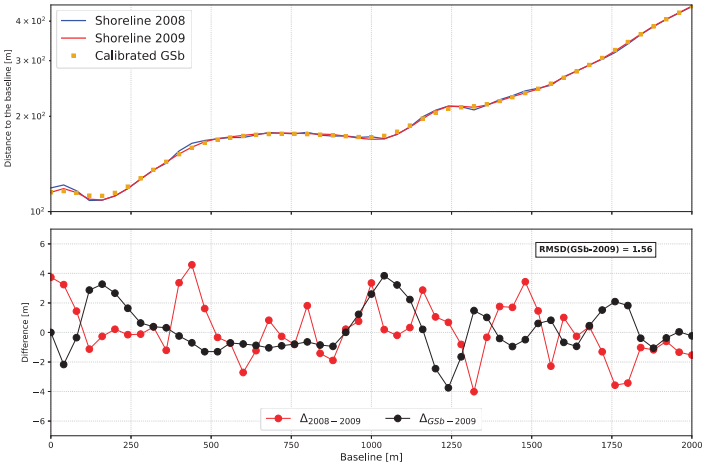

Figure 5. Top: historical shorelines adopted for the calibration of the General Shoreline beach (GSb) model; bottom: distribution of the difference between the 2009 shoreline and the GSb model output (with K_{GSb} = 0.3) and the difference of the two 2008 and 2009 Google Earth shorelines.

2.4. Other Numerical Models: Ghost

In the present work, use is also made of a well-established wave propagation numerical model, Ghost [38–40], which is a half plane and steady state marginal directional wave spectral transformation model solving the wave action conservation equation with an implicit finite-difference method on a rectilinear grid. The marginal directional spectrum for the wave transformation is a directional wave spectrum integrated in the frequency range [39,40]. The model is capable of simulating wave-structure and wave-current interactions: in particular, the combined effects of wave reflection, wave breaking, diffraction, shoaling, refraction and wave transmission through and over submerged structures. A more extended description of the Ghost model and also a comparison of the performances of Ghost with respect to other wave propagation numerical models such as STWave (Steady-State Spectral Wave Mode), for example for the propagation of waves in coastal inlets, can be found in [41], where the authors found that, overall, wave direction estimates from Ghost in inlets and near structures compared slightly better with measurements with respect to the STWave performances.

2.5. The Nourishment Performance Index

In the present work, a nourishment performance index (NPI) is defined, considering the maximum recession that will occur after 1/5 year from the nourishment intervention related to the initial volume of sand necessary for the nourishment, according to:

$$\mathrm{NPI} = \frac{\mathrm{W}}{\mathrm{S_{1yr}} \cdot h_c} \tag{5}$$

where W is the initial design volume necessary for the nourishment, $\mathrm{S_{1yr}}$ is the area in recession in the emerged beach after 1 year, with respect to the initial shoreline and h_c the closure depth.

3. Results

3.1. Nearshore Wave Climate

The nearshore wave climate has been calculated in terms of significant wave height, Hs, wave peak period, $\mathrm{T_p}$ and mean wave direction, θ_i, at eight virtual buoys near the coast at different depths. Figure 6 shows the location of the virtual buoys, chosen in order to analyse the wave effects along the entire beach, with a focus in the proximity of the study area at the western side of the beach.

Figure 6. Positions of the virtual buoys along Saadiyat beach.

Results are reported in terms of wave rose plots indicating the wave appearance frequencies. Figure 7 shows the corresponding wave roses at the virtual buoys indicated in Figure 6 with labels from A to H: the influence of the bottom (seabed) determines a dissipation of the waves close to the beach. Results show that the most frequent wave's events have directions in the sector 270° N–360° N, with a dominant North-West component, and maximum wave height lower than 1.8 m.

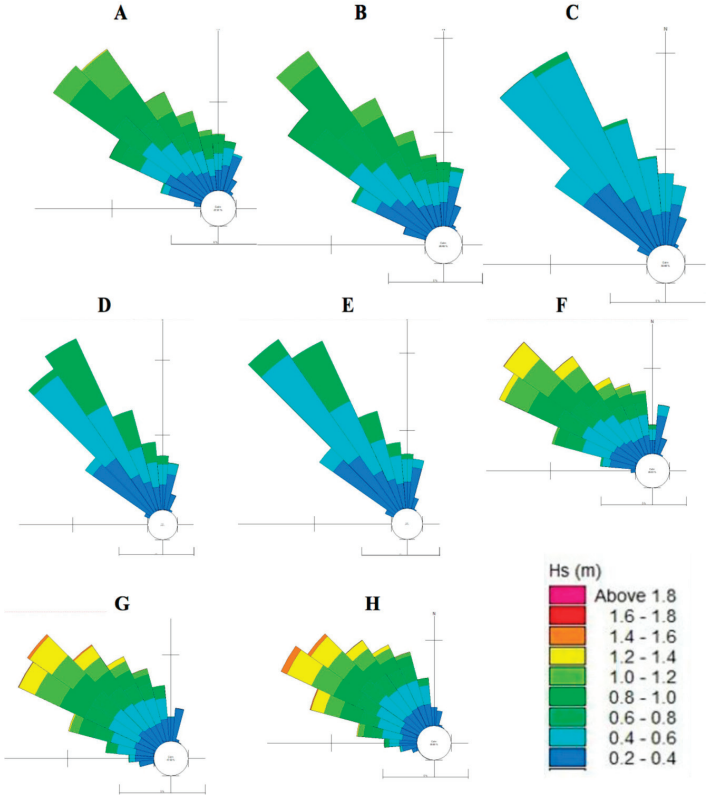

Figure 7. Wave climate at the eight virtual buoys, indicated as A–H in Figure 6, along Saadiyat beach.

Wave roses corresponding to virtual buoys C, D and E in Figure 6 are, indeed, similar when considering the main wave direction and Hs values. In particular, it can be noticed how changes of the coastline shape and the presence of groynes, acting as defence structures, obstruct the wave propagation, resulting in a wave energy reduction in C, D, and E with respect to the waves corresponding to A and B.

Results relative to the remaining virtual buoys show a good exposure of the beach to different wave conditions, i.e., the position of the virtual buoys has been chosen well enough so that the simulated beach conditions are sensitive to the action of the waves coming from all the possible directions; therefore, the climate at the virtual buoys is well representative of the real conditions of the beach. The bottom friction, the bathymetry of the area and the alignment of the beach determine a slight rotation of the fronts and only the directions from east to south are lost with respect to the original wave climate at the bathymetry 6 m.

3.2. Shoreline Design Scenarios

To increase the longevity of the beach and propose a sustainable solution over the years, some possible alternatives have been simulated. In particular, a different orientation of the as-built shoreline and different volume of sand for the nourishment have been tested. Figure 8 shows the scenarios with different orientations of the initial design shoreline. Based on the results of the sediment analysis (Section 2.1), it is assumed that the area of interest is characterised by medium sand with the median grain size D_{50} = 0.26 mm and the sorting parameter D_{15}/D_{85} = 2.44 (where: D_{15} (transition layer) is the 15th percentile particle size in the transition layer material, meaning that 15% of the sand is smaller than D_{15} mm, and D_{85} (filter media) is the 85th percentile particle size in the filter media.

In scenario 1, the initial alignment of the design shoreline is obtained from the nourishment of the entire stretch of coast. In particular, 600,000 m^3 are necessary for the West cell, 240,000 m^3 for the VVIP cell and 180,000 m^3 for the St. Regis cell.

In the scenario 2, a rotation of the shoreline alignment for the west cell and the VVIP cell, respectively 5° and 10° counter clockwise, is proposed, with a consequent increase in the sand volume, which is necessary for the initial nourishment (respectively 830,000 m^3 for the West cell and 270,000 m^3 for the VVIP cell).

The difference of scenario 3 with respect to scenario 2 consists in the fact that the shoreline alignment in the West cell is around the centreline.

In the scenario 4, the initial shoreline alignment is the same as in scenario 1 but a counter clockwise rotation of 5° is expected for the West cell, from the centre of the cell to the groyne 2, with a relative increase in the nourishment sand requirement, from 600,000 m^3 to 650,000 m^3.

In the scenario 5, the shoreline alignment is similar to scenario 1, but a clockwise rotation of 5° has been imposed for the West cell, from the centre of the cell to the groyne 1. The volume of sand required is 50,000 m^3 more than the volume foreseen in the scenario 1.

A summary of the volumes of sand needed for the initial nourishment in the different scenarios is reported in Table 3.

Table 3. Summary of the five design scenarios.

Scenarios	Sand Volume ($\times 10^3$ m^3)		
	West Cell	VVIP Cell	St. Regis Cell
1	600	240	180
2	830	270	180
3	600	270	180
4	650	240	180
5	650	270	180

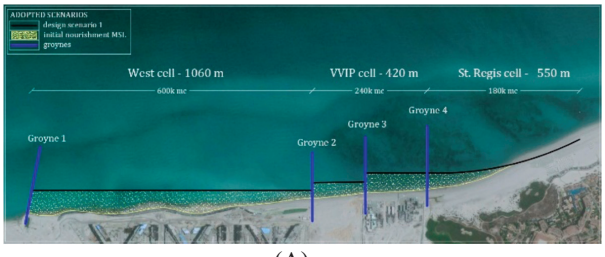

(A)

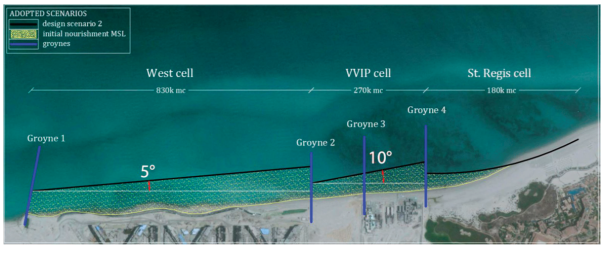

(B)

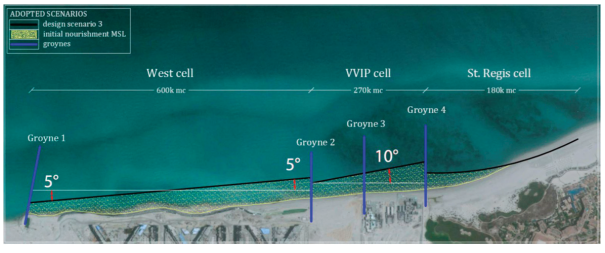

(C)

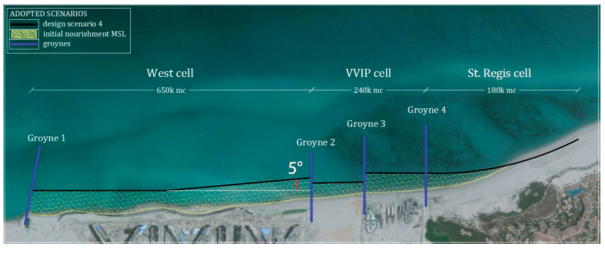

(D)

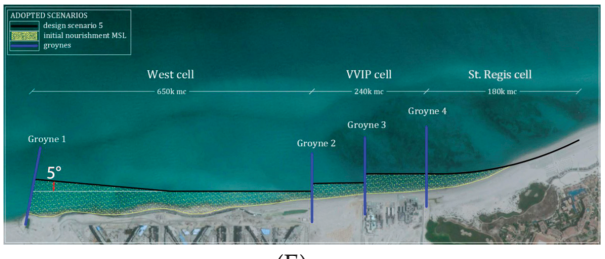

(E)

Figure 8. Schematic scenarios. (**A**) scenario 1; (**B**) scenario 2; (**C**) scenario 3; (**D**) scenario 4; (**E**) scenario 5.

3.3. Shoreline Evolution for the Design Scenarios

The shoreline evolution for each of the five considered scenarios has been modelled with the GSb model. The numerical simulations have been performed considering the evolution of the initial shoreline after 1 year, 2 years and 5 years from the end of the intervention.

Figure 9; Figure 10 show a comparison between the results for, respectively, the evolution in 1 year and in 5 years, in terms of maximum accretion/recession.

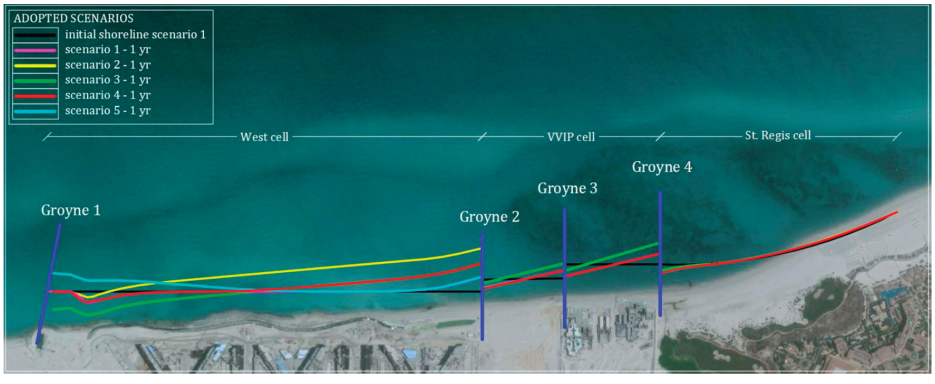

Figure 9. Evolution of the initial shoreline after 1 year, for the different considered the scenarios simulated.

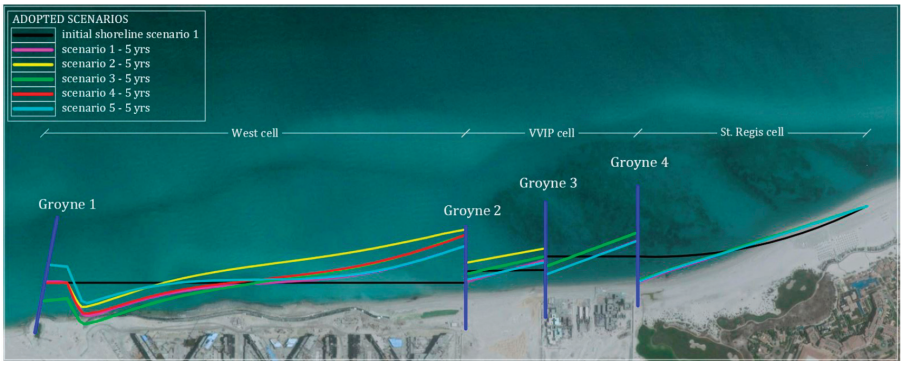

Figure 10. Evolution of the initial shoreline after 5 years, for the different considered scenarios.

The maximum accretion/recession volumes, i.e., the new beachline dry area as resulting from the shoreline shifts multiplied by the closure depth, in relation to the sand volume of the initial nourishment in the six sectors along the analysed shoreline, have been calculated. The shoreline shifts are calculated considering the new beach shoreline position as resulting after a fixed amount of time from the end of the intervention and the "as built shoreline after the nourishment intervention". The results are shown in Tables 4 and 5.

Table 4. Maximum accretion/erosion occurred after 1 year, for the proposed scenarios.

Scenarios	Sand Volume ($\times 10^3$ m^3)			Max Recession after 1 year (m)			Max Accretion after 1 year (m)		
	West Cell	VVIP Cell	St. Regis Cell	S1	S2	S3	S4	S5	S6
1	600	240	180	26	20	21	20	25	4
2	830	270	180	20	13	31	44	16	4
3	600	270	180	20	13	31	30	16	4
4	650	240	180	26	20	21	30	25	4
5	650	270	180	10	20	21	20	25	4

Table 5. Maximum accretion/erosion occurred after 5 years, for the proposed scenarios.

Scenarios	Sand Volume ($\times 10^3$ m^3)			Max Recession after 5 years (m)			Max Accretion after 5 years (m)		
	West Cell	VVIP Cell	St. Regis Cell	S1	S2	S3	S4	S5	S6
1	600	240	180	80	27	62	75	39	14
2	830	270	180	65	22	77	71	29	14
3	600	270	180	63	22	77	79	24	14
4	650	240	180	79	27	62	79	39	14
5	650	270	180	85	27	61	76	39	14

3.4. The Nourishment Performance Index

The optimal intervention scenario among the five proposed has to be individuated on the basis of the NPI, calculated using Equation (5), considering the maximum recession that will occur for each of the considered scenarios after 1 year from the intervention at sector 1 (S1) (Figure 4), related to the initial volume of sand necessary for the nourishment, with W the initial design volume necessary for the nourishment of the West cell, $h_c = 3.6$ m, and S_{1yr} the area in recession in the emerged beach after 1/5 year, with respect to the initial shoreline. The areas in recession in the emerged beach result from the comparison of the original shoreline and the one simulated with GSb after 1 year or 5 years.

4. Discussion

From the results obtained in the present study, it has been found that the NPI allows selecting the optimal scenario based on the efficiency of the intervention. Table 6 shows the values of NPI for the different considered scenarios. In the first column, the initial sand volume W, necessary for the nourishment intervention is indicated. The second column shows the area of the beach that will be eroded 1 year or 5 years after the intervention, simulated with the GSb numerical model. This area is calculated as the area enclosed by the simulated shoreline after 1/5 years from the intervention and the corresponding initial shoreline for each scenario separately. The third column shows the calculated NPI values. The fourth column shows the increase in percentage of NPI in the beach longevity, calculated with respect to scenario 1, assumed as a reference.

Regarding the West cell and the results relative to 1 year, with respect to scenario 1, the result for scenario 2 shows an increase of NPI (+29%), which is due in a large part to a significant larger volume of sand (from 600,000 m^3 to 830,000 m^3). Scenario 3 can represent a good option because of the good longevity percentage increase (+15%) obtained, while keeping the same volume of sand necessary for the initial nourishment (600,000 m^3). Scenario 4 shows almost the same NPI of scenario 1, but at the price of a slightly larger increase in the necessary sand volume for the nourishment (from 600,000 m^3 to 650,000 m^3).

Table 6. nourishment performance index (NPI) values at Saadiyat beach.

	West Cell				VVIP Cell				St. Regis Cell			
Recession (m^2)	**Sand Volume $\times 10^3$ (m^3)**	**Recession (m^2)**	**NPI**	**NPI Increase (%)**	**Sand volume $\times 10^3$ (m^3)**	**Recession (m^2)**	**NPI**	**NPI Increase (%)**	**Sand Volume $\times 10^3$ (m^3)**		**NPI**	**NPI Increase (%)**
1	600	2227	75	reference	240	2685	25	reference	180	1110	45	reference
2	830	2394	96	29	270	1707	44	77	180	638	78	74
3	600	1944	86	15	270	1338	56	126	180	693	72	60
4	650	2368	76	2	240	2712	25	-1	180	962	52	15
5	650	874	207	176	270	2708	28	12	180	1140	44	-3
Scenarios (5 years)	**Sand Volume $\times 10^3$ (m^3)**	**Recession (m^2)**	**NPI**	**NPI Increase (%)**	**Sand Volume $\times 10^3$ (m^3)**	**Recession (m^2)**	**NPI**	**NPI Increase (%)**	**Sand Volume $\times 103$ (m^3)**	**Recession (m^2)**	**NPI**	**NPI Increase (%)**
1	600	15,450	11	reference	240	3643	18	reference	180	6175	8	reference
2	830	13,920	17	54	270	1642	46	150	180	5625	9	10
3	600	13,017	13	19	270	1958	38	109	180	5737	9	8
4	650	14,106	13	19	240	3615	18	1	180	5683	9	9
5	650	13,798	13	21	270	3769	20	9	180	5856	9	5

For the West cell and the 1 year simulation, scenario 5 presents the larger NPI increase, equal to +176%. This is not verified for the remaining cells and considering the results relative to 5 years; the scenario that offers the overall best nourishment performance is scenario 2. Estimate of the nourishment performance is not extended to the entire project lifetime but it is limited to 5 years. This limit is chosen because at this time, the nourished shoreline retreats at some transects reaching an unacceptable threshold for the touristic, aesthetic and recreational uses of the beach.

Consequently, comparison of different design scenarios has showed that the NPI value depends mainly on the as built nourishment shoreline. The recommended scenario (i.e., scenario 2) durability is sounding.

This interesting and potentially very useful methodology can be adopted for analysing and predicting shoreline development under different coastal engineering interventions. The need for such a methodology arises from the large number of coastal interventions that are planned in high number worldwide and from the need to protect those from the climatically induced sea level rise and its hazardous consequences. The advantage of this definition is that all factors are measurable in-loco, are quantifiable by the development firms, are based on the physical characteristics of the beach (e.g., morphology), but also on aspects concerning the planned intervention (nourishments, longevity).

A potential benefit of this methodology is the fact that it also gives indication about the environmental sustainability (ES) of the planned interventions. In fact, ES, specifically the careful use of natural resources to preserve the ecosystems, is required in planning complex engineering interventions. ES is also an essential factor in mitigating the effects of environmental catastrophic phenomena, related to climate change. Since water covers up Earth's largest portion, it is a complex ecosystem; coastal engineers should include ES in the design of planned interventions.

The ES concept has been developed to ensure that in meeting its needs for water, food, shelter as well as engaging in leisure activities and entertainment where humanity does not cause damage to the environment or deplete resources that cannot be renewed [42]. However, despite many studies, the practices in coastal management have not yet reached a point where natural resources are being used sustainably.

In general, given the complexity of the environment and the ecosystem, environmental indexes could provide a useful tool to highlight environmental conditions and trends for policy purposes by isolating key aspects from an otherwise overwhelming amount of information [43]. Oftentimes, however, ES is difficult to translate in operational terms and many of the indexes proposed and mentioned above, include parameters, which are beyond the sphere of influence of local authorities/development firms [44]. This supports the scope of this study, i.e., to investigate an index to support also environmentally sustainable engineering applications.

Moreover, the NPI can be adopted not only as a valuable database for making management decisions, but also it encourages the local community and stakeholders to engage in the safeguard of the environment, given the simplicity of its definition and its immediate and easy application in real cases. This is a key aspect in ES-oriented engineering interventions: in fact, since ecological boundaries rarely meet up with political jurisdictions, it is necessary to be aware of major environmental issues and the best option to preserve the environment for future generations [45].

Specifically, the proposed NPI definition satisfies all the requirements for an environmental indicator to work well as a basis for policymaking [46]: (1) data availability; (2) ecosystem specificity of indicators; (3) spatial and conceptual aggregation of indicators and (4) baseline or reference values for indicators. The proposed NPI definition, the availability of data since the initial nourishment volume, the recession area and the closure depth are all easily measurable and well defined. The ecosystem specificity of the NPI is ensured through its dependence from the closure depth and the recession area, the aggregation is ensured by the NPI dependence from both environmental aspects (S_{1yr} and h_c) and specific aspects of the intervention (W) and the baseline is clearly drawn from scenario 1.

5. Conclusions

Environmental sustainability (ES) is an essential factor in solving environmental degradation; this is especially true when designing complex coastal engineering interventions.

The present paper describes the methodology followed to design a sustainable beach at Saadiyat Island, of the Abu Dhabi Municipality in the United Arab Emirates. Specifically, a proposed nourishment performance index appears suitable to quantify the level of sustainability for different coastal engineering interventions. The nourishment performance index is based on factors such as the initial volume necessary for the nourishment of the intervention area, the area in recession 1 year after the intervention and the closure depth.

The proposed methodology can be used for analysing and predicting shoreline development under different coastal engineering interventions. The need for such a methodology arises from the large number of coastal interventions that are planned in high number worldwide and from the need to protect those from the climatically induced sea level rise and its hazardous consequences. The advantage of this definition is that all factors are measurable in-loco, are quantifiable by the development firms and are based on the physical characteristics of the beach (e.g., morphology), but also on aspects concerning the planned intervention (nourishments, longevity).

Results show that the NPI value depends mainly on the as built nourishment shoreline. The recommended scenario (i.e., scenario 2) durability is sounding from the environmental sustainability prospective.

In conclusion, the application of the presented methodology in the evaluation of the impacts of the planned interventions at Saadiyat beach has been shown to be promising and can assist the engineers and/or environmentalists for designing/evaluating coastal interventions that are foreseen in the area.

Author Contributions: Conceptualization, W.H. and G.R.T.; methodology, G.R.T.; software, G.R.T., F.L., L.L. and A.F.; validation, F.L.; formal analysis, F.L. and A.F.; investigation, G.R.T.; resources, W.H.; data curation, L.L.; writing—original draft preparation, F.L.; writing—review and editing, G.R.T. and L.L.; visualization, F.L.; supervision, G.R.T.; project administration, W.H.; funding acquisition, W.H.

Funding: The present study is funded by the United Arab Emirates University research grant, through the National Water Centre, Grant #31R115; "Impact of coastal (long-shore) currents on erosion/deposition and consequent water/sediments quality variations along the coastal area of Abu Dhabi City".

Acknowledgments: The authors thank the Abu Dhabi Municipality for providing in-situ data relative to wave conditions at Saadiyat beachfront.

Conflicts of Interest: The authors declare no conflict of interest.

References

1. Hallermeier, R.J. A Profile Zonation for Seasonal Sand Beaches from Wave Climate. *Coast. Eng.* **1981**, *4*, 253–277. [CrossRef]
2. Goda, Y. *Random Seas and Design of Maritime Structures*, 3rd ed.; Advanced Series on Ocean Engineering; World Scientific: Singapore, 2010.
3. Tomasicchio, G.R.; D'Alessandro, F. Wave energy transmission through and over low crested breakwaters. *J. Coast. Res.* **2013**, *1*, 398–403. [CrossRef]
4. USACE—United States Army, Corps of Engineers. *Shore Protection Manual*; Department of the Army, Waterways Experiment Station, Corps of Engineers, Coastal Engineering Research Center: Washington, DC, USA, 1984.
5. Van der Meer, J.W. Rock Slopes and Gravel Beaches under Wave Attack. Ph.D. Thesis, Delft University of Technology, Delft, The Netherlands, 1988.
6. Folk, R.L.; Ward, W.C. Brazos River Bar: A Study in the Significance of Grain Size Parameters. *J. Sediment. Petrol.* **1957**, *27*, 3–26. [CrossRef]
7. Ojeda, E.; Ruessink, B.G.; Guillen, J. Morphodynamic response ofa two-barred beach to a shoreface nourishment. *Coast. Eng.* **2008**, *55*, 1185–1196. [CrossRef]

8. Stauble, D.K. A review of the role of grain size in beach nourishment projects. In Proceedings of the National Conference on Beach Preservation Technology, Destin, FL, USA, 2–4 February 2005.
9. Utizi, K.; Corbau, C.; Rodella, I.; Nannini, S.; Simeoni, U. A mixed solution for a highly protected coast (Punta Marina, Northern Adriatic Sea, Italy). *Mar. Geol.* **2016**, *381*, 114–127. [CrossRef]
10. Hamza, W.; Lusito, L.; Ligorio, F.; Tomasicchio, G.R.; D'Alessandro, F. Wave Climate at Shallow Waters along the Abu Dhabi Coast. *Water* **2018**, *10*, 985. [CrossRef]
11. Saha, S.; Moorthi, S.; Pan, H.L.; Wu, X.; Wang, J.; Nadiga, S.; Tripp, P.; Kistler, R.; Woollen, J.; Behringer, D.; et al. The NCEP Climate Forecast System Reanalysis. *Bull. Am. Meteorol. Soc.* **2010**, *91*, 1015–1057. [CrossRef]
12. Amante, C.; Eakins, B.W. ETOPO1 1 Arc-Minute Global Relief Model: Procedures, Data Sources and Analysis. In *NOAA Technical Memorandum NESDIS*; NGDC-24; National Geophysical Data Center: Boulder, CO, USA, 2009; p. 19.
13. WAVEWATCH III 30-Year Hindcast Wave Model Developed by NOAA (Phase 2). Available online: http://polar.ncep.noaa.gov/waves/hindcasts/nopp-phase2.php (accessed on 4 October 2017).
14. The Climate Forecast System Reanalysis (1979–2010). Available online: http://cfs.ncep.noaa.gov/cfsr/ (accessed on 4 October 2018).
15. Syvitski, J.P.M.; Slingerland, R.L.; Burgess, P.; Murray, A.B.; Wiberg, P.; Tucker, G.; Voinov, A. Morphodynamic models: An overview. In *River, Coastal and Estuarine Morphodynamics: RCEM 2009*; Vionnet, C.A., Garcia, M.H., Latrubesse, E.M., Perillo, G.M.E., Eds.; Taylor & Francis: London, UK, 2010; pp. 3–20.
16. Short, A.D.; Jackson, D.W.T. Beach Morphodynamics. In *Treatise on Geomorphology*; Shroder, J.F., Ed.; Academic Press: San Diego, CA, USA, 2013; Volume 10, pp. 106–129.
17. Roelvink, D.; Reniersc, A.; van Dongeren, A.; de Vries, J.V.T.; McCall, R.; Lescinski, J. Modelling storm impacts on beaches, dunes and barrier islands. *Coast. Eng.* **2009**, *56*, 133–1152. [CrossRef]
18. Hanson, H.; Kraus, N. *GENESIS—Generalised Model for Simulating Shoreline Change*; Report TR-CERC 89-19 (Report 1); Coastal and Hydraulic Laboratory, US Army Corps of Engineers: Washington, DC, USA, 1989.
19. Larson, M.; Kraus, N.C.; Hanson, H. Simulation of regional longshore sediment transport and coastal evolution—The "CASCADE" model. *Coast. Eng.* **2002**, *2002*, 2612–2624. [CrossRef]
20. GenCade Website. U.S. Army Corps of Engineers. Available online: http://cirp.usace.army.mil/products/gencade.php (accessed on 19 April 2019).
21. LITPACK Website. Danish Hydraulics Institute. Available online: https://www.mikepoweredbydhi.com/products/litpack (accessed on 19 April 2019).
22. Delft3D Website. Deltares, NL. Available online: https://oss.deltares.nl/web/delft3d (accessed on 19 April 2019).
23. Frey, A.E.; Connell, K.J.; Hanson, H.; Larson, M.; Thomas, R.C.; Munger, S.; Zundel, A. *GenCade Version 1 Model Theory and User's Guide*; Technology Report ERDC/CHL TR-12-25; U.S. Army Engineer Research and Development Center: Vicksburg, MS, USA, 2012.
24. Dean, R.G. Equilibrium beach profiles: Characteristics and applications. *J. Coast. Res.* **1990**, *71*, 53–84.
25. Bruun, P. *Coast Erosion and the Development of Beach Profiles*; US Army Engineer Waterways Experiment Station; Beach Erosion Board Technical Memo: Vicksburg, MA, USA, 1954.
26. Lamberti, A.; Tomasicchio, G.R. Stone mobility and abrasion on reshaping breakwaters. In Proceedings of the Hornafjörður International Coastal Symposium, Höfn, Iceland, 20–24 June 1994; pp. 723–735.
27. Lamberti, A.; Tomasicchio, G.R. Stone mobility and longshore transport at reshaping breakwaters. *Coast. Eng.* **1997**, *29*, 263–289. [CrossRef]
28. Tomasicchio, G.R.; Archetti, R.; D'Alessandro, F.; Sloth, P. Long-shore transport at berm breakwaters and gravel beaches. In Proceedings of the International Conference Coastal Structures, Venice, Italy, 2–4 July 2007; pp. 65–76.
29. Tomasicchio, G.R.; D'Alessandro, F.; Barbaro, G.; Malara, G. General longshore transport model. *Coast. Eng.* **2013**, *71*, 28–36. [CrossRef]
30. Tomasicchio, G.R.; D'Alessandro, F.; Barbaro, G.; Musci, E.; De Giosa, T.M. Longshore transport at shingle beaches: An independent verification of the general model. *Coast. Eng.* **2015**, *104*, 69–75. [CrossRef]
31. Tomasicchio, G.R.; D'Alessandro, F.; Barbaro, G.; Ciardulli, F.; Francone, A.; Mahmoudi Kurdistani, S. General model for estimation of longshore transport at shingle/mixed beaches. In Proceedings of the 35th International Conference on Coastal Engineering, Antalya, Turkey, 17–20 November 2016.
32. Tomasicchio, G.R.; D'Alessandro, F.; Frega, F.; Francone, A.; Ligorio, F. Recent improvements for estimation of longshore transport. *Ital. J. Eng. Geol. Environ.* **2018**. [CrossRef]

33. Whitford, D.J.; Thornton, E.B. Comparison of wind and wave forcing of longshore currents. *Cont. Shelf Res.* **1993**, *13*, 1205–1218. [CrossRef]
34. Baldock, T.E.; Huntley, D.A. Long-wave forcing by the breaking of random gravity waves on a beach. Proceedings of the Royal Society of London. *Series A Math. Phys. Eng. Sci.* **2002**, *458*. [CrossRef]
35. Abessolo Ondoa, G.; Bonou, F.; Tomety, F.S.; du Penhoat, Y.; Perret, C.; Degbe, C.G.E.; Almar, R. Beach Response to Wave Forcing from Event to Inter-Annual Time Scales at Grand Popo, Benin (Gulf of Guinea). *Water* **2017**, *9*, 447. [CrossRef]
36. Ozasa, H.; Brampton, A.H. Mathematical modeling of beaches backed by seawalls. *Coast. Eng.* **1980**, *4*, 47–64. [CrossRef]
37. Medellín, G.; Torres-Freyermuth, A.; Tomasicchio, G.R.; Francone, A.; Tereszkiewicz, P.A.; Lusito, L.; Palemón-Arcos, L.; López, J. Field and Numerical Study of Resistance and Resilience on a Sea Breeze Dominated Beach in Yucatan (Mexico). *Water* **2018**, *10*, 1806. [CrossRef]
38. Carci, E.; Rivero, F.J.; Burchart, H.Y.; Maciñeira, E. The use of numerical modeling in the planning of physical model tests in a multidirectional wave basin. In Proceedings of the 28th International Coastal Engineering Conference, Cardiff, UK, 7–12 July 2002; pp. 485–494.
39. Rivero, F.J.; Arcilla, A.S.; Carci, E. Implementation of diffraction effects in the wave energy conservation equation. In Proceedings of the IMA Conference on Wind-Over-Waves Couplings: Perspectives and Prospects, Salford, UK, 8–10 April 1997.
40. Rivero, F.J.; Arcilla, A.S.; Carci, E. An analysis of diffraction in spectral wave models. In Proceedings of the 3rd International Symposium of Ocean Wave Measurement and Analysis, Waves 97, Reston, Virginia Beach, VA, USA, 3–7 November 1997; pp. 431–445.
41. Lin, L.; Demirbilek, Z. Evaluation of Two Numerical Wave Models with Inlet Physical Model. *J. Waterw. Port Coast. Ocean Eng.* **2005**, *131*, 149–161. [CrossRef]
42. IISD—International Institute of Sustainable Development. *Our Common Future*; Report of the World Commission on Environment and Development; IISD: New York, NY, USA, 1987.
43. Pantusa, D.; D'Alessandro, F.; Riefolo, L.; Principato, F.; Tomasicchio, G.R. Application of a Coastal Vulnerability Index. A Case Study along the Apulian Coastline, Italy. *Water* **2018**, *10*, 1218.
44. SUSTAIN Project. *Measuring Coastal Sustainability*; A Guide for the Self-Assessment of Sustainability Using Indicators and a Means of Scoring Them; Project Report; Coastal and Marine Union—EUCC: Leiden, The Netherlands, 2010; p. 32.
45. Fraser, E.D.; Dougill, A.J.; Mabee, W.E.; Reed, M.; McAlpine, P. Bottom up and top down: Analysis of participatory processes for sustainability index identification as a pathway to community empowerment and sustainable environmental management. *J. Environ. Manag.* **2006**, *78*, 114–127. [CrossRef] [PubMed]
46. Niemeijer, D. Developing Indicators for environmental policy: Data-driven and theory-driven approaches examined by example. *Environ. Sci. Policy* **2002**, *5*, 91–103. [CrossRef]

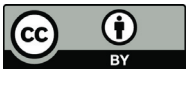

Journal of
Marine Science and Engineering

MDPI

Article

A Wave Input-Reduction Method Incorporating Initiation of Sediment Motion

Andreas Papadimitriou [1,2,*], Loukianos Panagopoulos [1], Michalis Chondros [1,2] and Vasiliki Tsoukala [1]

[1] Laboratory of Harbour Works, School of Civil Engineering, National Technical University of Athens, Heroon Polytechniou Str. 5, 15780 Zografou, Greece; loukpanag96@gmail.com (L.P.); chondros@hydro.ntua.gr (M.C.); tsoukala@mail.ntua.gr (V.T.)
[2] Scientia Maris, Agias Elenis Str. 10, 15772 Zografou, Greece
* Correspondence: andrewtnt@mail.ntua.gr; Tel.: +30-2107722351

Received: 17 July 2020; Accepted: 6 August 2020; Published: 10 August 2020

Abstract: The long-term prediction of morphological bed evolution has been of interest to engineers and scientists for many decades. Usually, process-based models are employed to simulate bed-level changes in the scale of years to decades. To compensate for the major computational effort required by these models, various acceleration techniques have been developed, namely input-reduction, model-reduction and behaviour-oriented modelling. The present paper presents a new input-reduction method to obtain representative wave conditions based on the Shields criterion of incipient motion and subsequent calculation of the sediment pick-up rate. Elimination of waves unable to initiate sediment movement leads to additional reduction of model run-times. The proposed method was implemented in the sandy coastline adjusted to the port of Rethymno, Greece, and validated against two datasets consisting of 7 and 20 and 365 days, respectively, using the model MIKE21 Coupled Model FM. The method was compared with a well-established method of wave schematization and evaluation of the model's skill deemed the simulations based on the pick-up rate schematization method as "excellent". Additionally, a model run-time reduction of about 50% was observed, rendering this input-reduction method a valuable tool for the medium to long-term modelling of bed evolution.

Keywords: input reduction; wave schematization; pick-up rate; MIKE21 CM FM; long-term morphological modelling

1. Introduction

The prediction of morphological bed evolution and ultimately the shift of the shoreline position due to the complex sediment transport processes that take place in the nearshore area has been of interest for coastal engineers and scientists for many decades. Considering bed and shoreline evolution, two distinct model types can be considered [1], namely the 2DH area models concentrating on the morphological evolution of a given area and the shoreline evolution models, where the changes in shoreline position are modelled through the calculation of the longshore sediment transport rates. The first category of models is used to determine the morphological changes of rather detailed coastal features (such as dunes, or rip channels) based on the simulation of the waves, hydrodynamics and sediment transport rates over a large area (in the scale of many km). The drawback of these models is that they are generally not suited for long-term morphological modelling, in part due to the fact that the simulation run-time is often too large for engineering purposes and their performance diminishes when executing long-term simulations without introducing some type of recalibration of the coastal profile. Their main drawback stems from the fact that the morphological evolution of complex coastal features of interest to engineers and the public usually occurs at time scales several orders of magnitude larger than the time scale of the hydrodynamic fluctuations that drive the sediment transport [2].

This potential separation of the time scales between the hydrodynamics and the morphological changes has been the basis for a large number of morphological acceleration techniques. On this subject, de Vriend et al. [3] highlight three distinct approaches in order to accelerate morphological modelling:

- Input reduction, which is based on the principle that the long-term effects of smaller-scale processes can be obtained by applying models of those smaller-scale processes forced with "representative" inputs able to reproduce the aforementioned long-term effects accurately [4].
- Model reduction, in which details of the smaller scale processes are omitted while the model simulation is performed at the scale of interest. The most commonly used acceleration technique of this type in 2-D area models is the morphological acceleration factor (Morfac, [5], which multiplies the bed level change at each time step by this factor, reducing the simulation time while simultaneously predicting the long-term evolution of the morphology.
- Behaviour-oriented modelling, which attempts to model the phenomena of interest without attempting to fully analyze and describe the underlying processes (shoreline sediment processes [6], wetting-drying [7] etc.).

Often, coastal engineers are in possession of a large number of input wave conditions, stemming from model predictions from various databases across the world and the widespread usage of satellite observations (e.g., [8,9]. This collection of data can be utilized to predict morphological bed evolution in a variety of time scales. In the present paper we consider a few days to be the defining scale for short term morphological modelling, a few months for medium-term and years to decades for long-term bed level predictions. It is apparent, that for the medium and long-term prediction of the bed evolution of a rather large area, performing a simulation through hourly changing boundary conditions can be very time consuming [4]. For this purpose a number of input-reduction or wave schematization techniques have been developed based on the principle of selecting representative wave conditions able to accurately predict the long-term morphological bed evolution. As a general principle, these techniques concentrate on dividing the wave climate into wave height and directional bins and calculating a representative sea state for each bin. The evaluation of the performance of an applied input-reduction method is ultimately based on a comparison of the long-term predicted morphology using the reduced and the full set of conditions, as stated in [10].

Over the years, several studies have been carried out to implement various methods of wave input reduction enabling the simulation of the morphological evolution of coastal features from years to decades [2,4,10,11]. Most input-reduction methods are based on the calculation of the net sediment longshore transport rate (e.g., energy-flux method, CERC method and energy-flux method with extreme events) which is the main quantity used to select the representative sea states. Roelvink et al. [4] presented a novel method based on executing short-term modelling simulations and determining the subsequent sediment transport rates. Then, the conditions that have the smallest contribution in the long term to the morphodynamic evolution of the bed are eliminated and the process is repeated. The result of this so-called "Opti" routine is a set of 5 or 10 wave conditions that have a major contribution in shaping the sediment transport rates and the morphodynamic pattern. Benedet et al. [12] implemented five different wave schematization techniques, including the "Opti" method for a beach nourishment project and concluded that for the particular case study, an annual wave climate can be represented accurately by 12 distinct wave conditions. Trough sensitivity analysis the authors stated that minimal improvement in model results was demonstrated when selecting more than 30 wave representative conditions, whereas when choosing less than 6 representatives, model results deteriorated significantly. Lastly, they concluded that the best performing method for 12 representative conditions was the energy-flux method followed by the "Opti" routine, which turned out to perform comparatively better when desiring a smaller number of representative conditions (e.g., 6 or less). Recently, Karathanasi et al. [13] proposed an input-reduction method based on the concept of incipient motion, dividing the

wave climate into two distinct wave classes, depending on each individual wave component's ability to initiate sediment motion.

It should be stated that input-reduction methods alleviate some numerical burden from the simulation and facilitate post-processing of results and model evaluation. On the other hand, in order to produce accurate results, one has to carry out a simulation with reduced wave input in exactly the same time frame as the full dataset of conditions. As was previously mentioned, the most common way of accelerating 2DH morphological simulations is by utilizing model-reduction techniques through the Morfac approach. However large values of Morfac can lead to erroneous results, especially for coasts that are dominated by highly varying wind and wave conditions [5,14,15]. For the long-term morphological evolution of the bed, usually both input-reduction and model-reduction techniques are employed in tandem, in order to alleviate numerical burden and accelerate the simulations. Taking into account that the hydrodynamic simulation is restricting in regards to the stability of the 2DH area model and that Morfac values should not exceed a certain critical value as shown in [16], there remains a need to develop methodologies to further accelerate morphological modelling.

In the present paper, an input-reduction method able to achieve some form of model reduction, thus reducing the required numerical effort even further is presented. This method concentrates on the reduction of the offshore wave data based on the criterion of initiation of sediment motion, through the calculation of the Shields parameter. The reduced waves that are considered adequate to initiate sediment motion are then schematized by computing the sediment pick-up rate [17,18] of each individual wave.

The input-reduction method developed for the purpose of this research, hereafter denoted as the pick-up rate method, was applied for the coast in the close vicinity of the port of Rethymno in the island of Crete and was validated using wave data time-series from the Copernicus Marine Environment Monitoring Service (CMEMS) [8] as forcing conditions. The method was implemented for three distinct cases, a time-series of 7, 20 and 365 days composed of hourly changing wave data, to investigate the sensitivity of the method on longer datasets. The process-based numerical model MIKE 21 Coupled Model FM [19] was applied for the detailed description of waves, hydrodynamics and sediment transport since it has been used extensively in coastal engineering studies and research for decades. A parabolic mild slope model incorporating non-linear dispersion characteristics, namely MARIS-PMS [20] was also utilized for the purpose of this research to obtain wave characteristics in the nearshore area in order to ultimately reduce the input wave data. Ultimately, in order to evaluate the performance of the newly developed method, the results obtained by the pick-up rate method where compared with the ones stemming from implementation of the widely used energy-flux schematization method.

2. Materials and Methods

2.1. Proposed Method of Wave Schematization Based on the Sediment Pick-Up Rate

2.1.1. Theoretical Aspects

For flows with very low velocity over a sandy bed the sand layer generally tends to stay immovable. However, if the flow velocity slowly increases some grains begin to move. This process is called the initiation of sediment motion or incipient motion [21]. The most precise and commonly used measure of the threshold of motion is expressed in terms of the ratio of the force exerted by the bed shear stress acting to move the sediment grains on the bed layer, to the submerged weight grain resisting to this action. This approach was developed by [22] and the threshold Shields parameter θ_{cr} can be calculated by the following expression proposed by [23]:

$$\theta_{cr} = \frac{0.3}{1 + 1.2D_*} + 0.055\left[1 - e^{-0.02D_*}\right] \quad (1)$$

where D_* is the non-dimensional grain diameter given by:

$$D_* = \left[\frac{g(s-1)}{\nu^2}\right]^{1/3} d_{50} \tag{2}$$

where g [m/s^2] is the acceleration of gravity, $s = \frac{\rho_s}{\rho_w}$ [-] is the ratio of the sediment (ρ_s) to the water (ρ_w) density, ν [m^2/s] is the kinematic viscosity of the water and d_{50} [m] is the median sediment diameter.

Waves constitute one of the major contributing factors in stirring sediments from the sediment bed as well as generating longshore currents and the undertow that are able to transport sediments. Another aspect that causes the net sediment transport is the wave asymmetry and skewness beneath the crest and the trough of the waves. Waves in relatively shallow areas (approximately at depths $h < 10H_s$, with H_s denoting the significant wave height) [21], generate an oscillatory velocity at the sea-bed which is the main factor setting the sand grains into motion. The amplitude of the wave orbital velocity above the bed for the case of a monochromatic wave can be approximated through the linear wave theory as:

$$U_w = \frac{\pi H}{T \sinh(kh)} \tag{3}$$

where: H [m] is the wave height, T [s] is the wave period, and k [rad/m] is the wavenumber.

Regarding random waves, where the wave climate is represented by a sea-state spectrum composed of different frequencies, amplitudes and directions, the wave orbital velocity near the bed (denoted as U_{rms}) can be computed according to [24] by summing the velocity contributions from each frequency (derived from the linear wave theory) over the whole frequency range. Soulsby et al. [25] proposed the following approximate formula to compute U_{rms}:

$$\frac{U_{rms} T_n}{H_s} = \frac{0.25}{\left(1 + A t^2\right)^3} \tag{4}$$

where: U_{rms} [m/s] is the root-mean square signal of the orbital velocity near the bed, $T_n = \sqrt{\frac{h}{g}}$ [s] is the natural scaling wave period, H_s [m] is the significant wave height, and A [-] and t [-] are non-dimensional quantities defined as:

$$A = \left[6500 + (0.56 + 15.54\, t)^6\right]^{1/6} \tag{5}$$

and:

$$t = \frac{T_n}{T_z} = \sqrt{\frac{h}{g}} \frac{1}{T_z} \tag{6}$$

where T_z [s] is the zero-up crossing wave period. The above approximation is valid in the range of $0 \le t \le 0.54$.

Near the bed, due to turbulence and friction effects, an oscillatory wave boundary layer is generated in which the wave orbital velocity rapidly increases from 0 at the sea-bottom to the value of U_w (or U_{rms} when referring to spectral wave conditions) at the top of the boundary layer. It can be derived that the most important hydrodynamic property of waves contributing to sediment transport is the bed shear stress they produce. This stress is usually dependent on the wave orbital velocity U_w at the bottom and the wave friction factor f_w and is computed via the following relationship:

$$\tau_{b,w} = \frac{1}{2} \rho f_w U_w^2 \tag{7}$$

where τ_{bw} [kg·m/s^2] is the bed shear stress due to the wave effect, ρ [kg/m^3] is the water density and f_w [-] is the wave friction factor.

The wave friction factor, as is the case with currents, is dependent on the status of the flow, namely if it is laminar, smooth turbulent or rough turbulent [21], which in turn is related to the wave Reynolds number R_w and the relative roughness r. The latter quantity is calculated by:

$$r = \frac{U_w T}{2\pi k_s} \tag{8}$$

where T [s] is the wave period and k_s [-] is the Nikuradse equivalent sand grain roughness.

For rough turbulent flows, as is generally the case for a beach dominated by waves, there exist many formulae in literature for the calculation of the skin friction factor f_w [21,26,27]. They are all a faction of the relative roughness r and the wave orbital velocity excursion at the sea bed. Swart's formulation [26] reads:

$$f_w = \begin{cases} 0.24, & r < 2.0 \\ e^{-5.997+5.213\, r^{-0.194}}, & r \geq 2.0 \end{cases} \tag{9}$$

Ultimately, the Shields number θ for each wave condition can be calculated through:

$$\theta = \frac{\tau_{b,w}}{g d_{50}(\rho_s - \rho)} \tag{10}$$

where ρ_s [kg/m^3] is the sediment density.

The criterion of incipient sediment motion orders that sediment movement occurs only if the Shields parameter θ calculated through Equation (10) is greater than the critical Shields parameter θ_{cr} calculated through Equation (1). This forms the basis of the input-reduction method discussed in the present paper, as waves with rather small wave orbital velocities unable to initiate sand grain motion near the bed are disposed of, since it is considered that these waves have a very small contribution in the medium or long-term shaping of the morphological bed evolution.

A quantification of the eroding capacity of individual waves can be achieved by calculating the sediment pick-up rate E. [17,28] studied the pick-up process for various flow velocities (in the range of 0.5–1.5 m/s) and sand diameters (100–1500 μm). Recently, [18] extended the pick-up rate function for high flow velocities (in the range of 2–6 m/s) by introducing a damping factor f_D incorporating all the additional effects on sediment movement in high velocities, the most important being the damping of turbulence (turbulence collapse) in the near-bed area where sediment concentrations are rather large. Ultimately, the new pick-up rate function reads:

$$E = 0.00033\rho_s\left[(s-1)g d_{50}\right]^{1/2} D_*^{0.3} f_D\left[\left(\frac{\theta - \theta_{cr}}{\theta}\right)\right]^{1.5} \tag{11}$$

where E [kg/m^2/s] is the sediment pick-up rate, and $f_D = 1/\theta$ is a damping factor for high velocity conditions ($\theta > 1.0$). It becomes apparent from Equation (11) that E is zero if $\theta < \theta_{cr}$.

We take advantage of this in our deployment of the wave schematization method, utilizing the sediment pick-up rate as the quantity that determines the representative wave conditions, while simultaneously disposing of those conditions that are unable to initiate incipient sediment motion.

2.1.2. Layout of the Wave Schematization Method

In this subsection the distinct steps to determine the representative wave conditions, utilizing the pick-up rate input-reduction method are presented. The larger portion of this method is rather simple in conceptualization and execution and can be reproduced either by employing a simple computer code or a spreadsheet. The distinct steps of this method are as follows:

1. Wave characteristic time-series (either by buoy measurements, or hindcast/forecast simulations) are obtained for a desirable time range T_{tot} on a single point offshore coinciding with the open

boundary of the computational domain. The minimum wave characteristics that are required by the input-reduction method are H_s, T_p (or another characteristic wave period) and MWD (mean wave direction).

2. The wave time-series are then filtered by disposing of wave data that do not contribute in shaping the bed evolution, namely wave components exiting the computational domain.
3. Calculation of the critical Shields parameter θ_{cr} through Equation (1).
4. Wave characteristics at a characteristic depth (at around h = 8–10 m, set as h = 8 m at the present study) are obtained. For this purpose, either a wave ray model (e.g., [29], a spectral wave model (e.g., [30–32], or a mild slope wave model [33,34] can be used. Here we use the parabolic mild slope model with non-linear dispersion characteristics MARIS-PMS. The reason for utilizing this model is the accuracy in prescribing the wave field in mildly sloping beaches due to incorporation of non-linearity and the saving of considerable computational time relatively to the time-dependent formulations of the aforementioned categories of models. After obtaining the wave climate in the nearshore area a "1-1" correspondence between each wave component offshore (H_s, T_p, MWD) and the wave characteristics at the characteristic depth (H_{in}, T_{in}, MWD_{in}), is established.
5. Calculation of the depth of closure (h_{in}) for the particular time-series through the following equation, which is defined as the seaward limit of the littoral zone [35]:

$$h_{in} = 8.9\,\overline{H_s} \tag{12}$$

where h_{in} [m] is the depth of closure and $\overline{H_s}$ [m] is the mean significant wave height at a characteristic depth h = 8–10 m, utilizing the wave characteristics calculated at step 4. The depth of closure was considered for the purpose of this research the critical depth after which no net sediment movement takes places. Consequently this depth will be later set for the calculation of the wave orbital velocity since the larger proportion of sediment transport takes place between h_{in} and the shoreline.

6. Calculate the wave orbital velocity signal near the bed through Equation (3) for monochromatic or Equation (4) for spectral waves setting $h = h_{in}$.
7. For each wave component (H_{in}, T_{in}, MWD_{in}) the friction factor f_w (Equation (9)), the bed shear stress due to waves $\tau_{b,w}$ (Equation (7)) and ultimately the Shields parameter θ (Equation (10)), are calculated
8. If the $\theta < \theta_{cr}$ the wave component is eliminated since it does not contribute in sediment motion. Through the "1-1" correspondence established at step 4, dispose the relative wave condition of the offshore time-series. The total number of wave components offshore N is thus reduced using the criterion of the initiation of motion at a total of N_s (with $N_s \leq N$)
9. Calculation of the sediment pick-up rate E_{in} through Equation (11) for each wave component at the depth of closure. Also the cumulative pick-up rate E for the aforementioned wave conditions is determined.
10. The number of representative wave conditions N_r that will replace the full wave climate (e.g., 12 representative conditions) are determined. The number of representative conditions is based on discretion, however it is advised that a number between 6 and 30 conditions is chosen for sufficiently accurate model results regarding yearly wave climates [12]. Then, the wave components are divided in classes with respect to wave direction and wave height. The boundaries of each class in both direction and wave heights are determined the same wave as the energy-flux wave schematization method (see Section 2.2 for details). Each representative class is characterized by an equal fraction of the cumulative pick-up rate E (E/N_r) and can be described by a set of wave characteristics ($H_{r,in}$, $T_{r,in}$, $MWD_{r,in}$). Thus, it can be derived that each class consists of a different number of wave components, N_{cl}.
11. Utilizing again the "1-1" correspondence of wave characteristics offshore and nearshore, we can obtain a set of representative conditions (H_r, T_r, MWD_r) in the offshore wave boundary by

considering that the bounding limits of each representative class in the depth of closure coincide with the respective ones in deep water. A small numerical extrapolation error stems from the fact that each representative class in the offshore boundary might not be characterized by exactly equal fraction of sediment pick-up rate, since the pick-up rate was calculated for the corresponding wave conditions at shallower water. However, since the proposed input-reduction method concerns medium to long-term morphological bed changes, this error is considered to have a very small effect in shaping the ultimate bed evolution and thus can be neglected.

12. The frequency of occurrence $f = \frac{N_{cl}}{Ns}$ for each representative class is calculated, based on the wave components of each class relatively to the full set of conditions.
13. Finally the simulation is executed with a 2D morphological area model using the representative wave conditions as forcing input. The total model run-time $T_{tot,r}$ is a fraction of the full time series, denoted as $T_{tot,r} = \frac{N_r}{N} T_{tot}$, since wave components unable to initiate sediment movement are eliminated in step 8 and have little to no contribution in shaping the bed evolution.

The flowchart of the wave schematization methodology based on the sediment pick-up rate is illustrated in Figure 1.

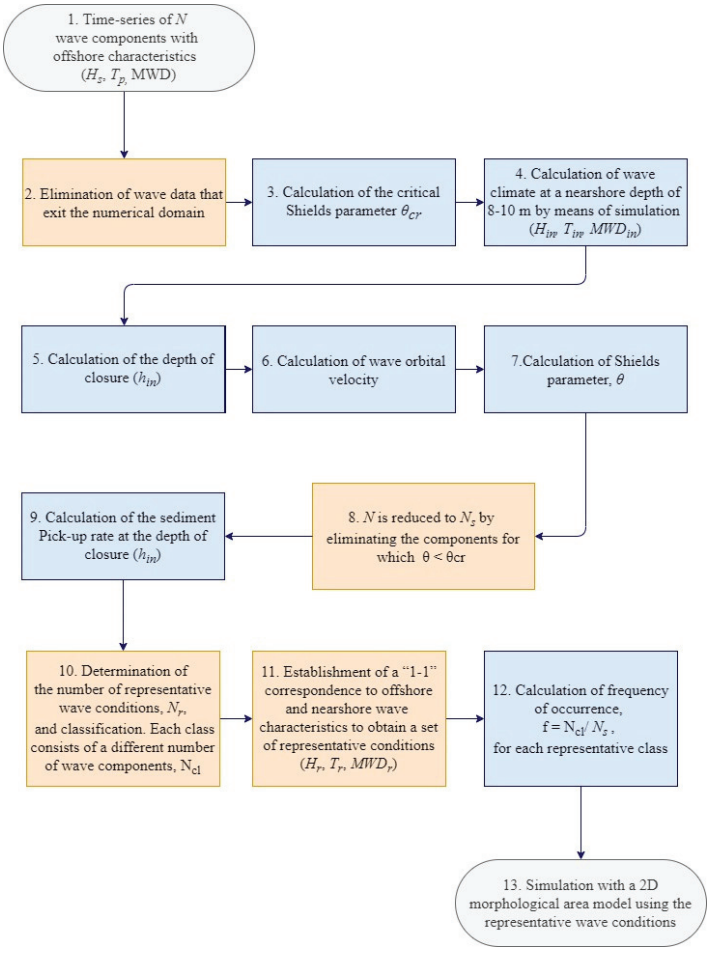

Figure 1. Flowchart of the proposed input-reduction method based on the sediment pick-up rate.

Through the use of this method one can obtain a set of representative conditions able to describe the morphological evolution of the bed in medium and long term, while also simultaneously reducing the simulation run-time. Thus, this method can be characterized as a bridge between input-reduction and model-reduction techniques, since it can lead in the considerable reduction of computation effort. It should be noted however that the total time that is saved is highly dependent on the wave climate that dominates the coast. For instance, in rather extreme offshore wave conditions where a large portion of waves contribute in initiation of sediment motion, the total number of disposable wave components can be rather small, leading in simulating a representative field for time equal to that of the full time-series. For morphological modelling of years to decades, however, one can assume that a rather large number of wave components will have little effect in the bed evolution, rendering the pick-up rate schematization method a valuable tool to coastal engineers and scientists.

2.2. The Energy Flux Wave Schematization Method (Benchmark Reduction Method)

The energy-flux wave schematization method is based on the concept of obtaining representative wave conditions which are separated at "equal energy intervals" [12,36]. For long-term morphological evolution simulations this concept is beneficial since the longshore sediment transport rates are proportional to the energy flux of the waves. The layout of the energy-flux input-reduction method is presented briefly below:

- Calculation of the wave energy flux $\left(E_f\right)$ for each wave component of a time-series,

$$E_f = \frac{1}{8}\rho g H_s^2 C_g \tag{13}$$

  where ρ [kg/m^3] is the water density, H_s [m] is the significant wave height and C_g [m/s] is the wave group celerity in deep water,
- Calculation of the total wave energy flux of the full wave time-series through:

$$E_{tot} = \sum E_f \tag{14}$$

- Division of the wave components in wave direction bins. For a predefined number of directional bins (N_d) the time series are separated in bins, each consisting of an equal fraction of the total energy flux (E_{tot}/N_d). Further division of the data in wave height bins. Separation is carried out for a predefined number of wave height bins (N_h) with each bin characterized by an equal fraction of the total energy flux $(E_{tot}/(N_d{\cdot}N_h)$.
- A representative wave height for each bin is derived from the mean energy flux of the bin along with a mean energy-flux direction. The representative wave period is then defined as the mean period of the bin.

The energy-flux input-reduction method is easy to apply (calculations can usually be carried out within a spreadsheet) and as shown in [12] and [36], for long-term morphological bed evaluations in the order of years the obtained results are satisfactory. For the reasons stated above, the energy-flux method was used in the framework of this research as a "benchmark reduction method", in order to assess how the newly developed pick-up rate schematization method fares not only in comparison to the bed evolution obtained through the full-time series, but also to the results obtained by a widely used wave schematization method.

2.3. Theoretical Background of Numerical Models

For the purpose of this research, a highly robust 2D composite model, namely MIKE21 Coupled Model FM [19] is utilized for the simulation of wave propagation, hydrodynamic circulation, sediment transport and morphology. In addition, for the calculation of nearshore wave characteristics at the

depth of 8 m (see step 4, Figure 1) a mild-slope model of parabolic approximation, namely MARIS-PMS, is utilized in the present paper. A first noteworthy aspect of a parabolic approximation model is that it can be rapidly solved [34], which is essential for the pick-up rate input-reduction method in order to keep computational effort at a minimum when utilizing a large set of input wave conditions. Moreover, the specific model considers nonlinear amplitude dispersion effects and thus can produce significantly more accurate results than linear models. Nevertheless, it should be mentioned that parabolic approximation models are restricted to cases with negligible wave reflection and weak wave diffraction due to the lack of simulating back scattering. Therefore, the range of applicability is reduced for these models, rendering them suitable only for open coastal areas. In the following sections the governing equations and main features of the aforementioned numerical models are presented.

2.3.1. The MIKE21 Coupled Model FM Suite

For the long-term estimation of the bed evolution the process-based numerical model MIKE 21 Coupled Model FM [19] was used for the detailed description of hydrodynamics, waves, and sediment transport rates. The model has been used extensively in a variety of coastal engineering applications, with and without the presence of coastal protection structures (e.g., [1,13,37,38].

The MIKE21 Coupled model FM suite includes several complementary numerical models and tools three of which were used for the purpose of this research:

- MIKE21 SW, a 3rd generation spectral wave model based on the conservation of the wave action balance, suited for the propagation and transformation of waves in the coastal zone.
- MIKE21 HD, a depth-averaged hydrodynamic model based on the Reynolds-averaged Navier–Stokes equations of motion (RANS), for the description of the nearshore circulation.
- MIKE21 ST, a sand transport and morphology updating model, used to calculate sediment transport rates and ultimately the morphological bed evolution.

The models are directly coupled, allowing for the interaction between waves and currents and the effect of bed level changes in waves and hydrodynamics. The calculations are performed in an unstructured finite element mesh, allowing for flexibility in calculations and a more precise representation of the coastline and complex topography features. The governing equations of each respective model will be presented briefly below. The MIKE 21 SW model [39] is a 3rd-generation spectral wave model suited for the propagation of waves in the oceanic scale and in nearshore areas. The governing equation of the model is based on the principle of conservation of the wave action-balance [40] which reads in Cartesian coordinates:

$$\frac{\partial N}{\partial t}+c_x\frac{\partial N}{\partial x}+c_y\frac{\partial N}{\partial y}+c_\sigma\frac{\partial N}{\partial \sigma}+\sigma_\theta\frac{\partial N}{\partial \theta}=\frac{S}{\sigma} \tag{15}$$

where $N\ (x, y, \sigma, \theta, t)$ is the wave action density, c_x, c_y are the propagation velocities in the spatial domain, c_σ is the propagation velocity in the frequency domain and c_θ is the propagation velocity in the directional domain. All the aforementioned transfer velocities are computed according to the linear wave theory [40]. In the rhs of Equation (15), the term S denotes the source and sink terms of the energy balance equation (e.g., generation due to wind, white-capping dissipation, non-linear wave interactions, depth-induced breaking etc).

The hydrodynamic model MIKE21 HD [41] is based on the solution of the depth-integrated shallow water equations, expressed by the continuity and momentum equations in the Cartesian space:

$$\frac{\partial h}{\partial t}+\frac{\partial h\overline{u}}{\partial x}+\frac{\partial h\overline{v}}{\partial y}=hS \tag{16}$$

$$\frac{\partial h\overline{u}}{\partial t} + \frac{\partial h\overline{u}^2}{\partial x} + \frac{\partial h\overline{uv}}{\partial y} = f\overline{v}h - gh\frac{\partial \eta}{\partial x} - \frac{h}{\rho}\frac{\partial p_a}{\partial x} - \frac{gh^2}{2\rho}\frac{\partial \rho}{\partial x} + \frac{\tau_{sx}}{\rho} - \frac{\tau_{bx}}{\rho} - \frac{1}{\rho}\left(\frac{\partial S_{xx}}{\partial x} + \frac{\partial S_{xy}}{\partial y}\right) + \frac{\partial}{\partial x}(hT_{xx}) + \frac{\partial}{\partial y}\left(hT_{xy}\right) + hu_sS_x \quad (17)$$

$$\frac{\partial h\overline{v}}{\partial t} + \frac{\partial h\overline{uv}}{\partial x} + \frac{\partial h\overline{v}^2}{\partial y} = f\overline{u}h - gh\frac{\partial \eta}{\partial y} - \frac{h}{\rho}\frac{\partial p_a}{\partial y} - \frac{gh^2}{2\rho}\frac{\partial \rho}{\partial y} + \frac{\tau_{sx}}{\rho} - \frac{\tau_{bx}}{\rho} - \frac{1}{\rho}\left(\frac{\partial S_{xy}}{\partial x} + \frac{\partial S_{yy}}{\partial y}\right) + \frac{\partial}{\partial x}\left(hT_{xy}\right) + \frac{\partial}{\partial y}\left(hT_{yy}\right) + hv_sS_{xx} \quad (18)$$

where h [m] is the total depth of the water column, $\overline{u}$ and $\overline{v}$ [m/s] are the depth-averaged velocity components in the x and y direction, respectively, η [m] is the surface elevation, f [-] is the Coriolis parameter, ρ [kg/m^3] is the water density, S_{xx}, S_{yy}, S_{xy}, are components of the radiation stress tensor, p_a [N/m^2] is the atmospheric pressure, S [m^3/s] being the magnitude of point sources, with u_s, v_s. [m/s] being the velocity vectors of the point discharge and T_{xx}, T_{yy}, T_{xy} [N/m^2] denoting lateral stresses including viscous, turbulent friction and differential advection.

The MIKE 21 ST model [42] calculates the sediment transport rates and the morphological bed evolution either in a pure current case, or under the combined effect of waves and currents.

For the case of wave and current induced sediment transport, the rates are calculated by linear interpolation on an externally formed sediment transport table. The core of this utility is a quasi-three-dimensional sediment transport model (STPQ3D). The model calculates the instantaneous and time-averaged hydrodynamics and sediment transport in the two horizontal directions.

The determination of the bed level evolution is the rate of bed level change $\frac{\partial z}{\partial t}$ at the element cell centers. This parameter is obtained by solving the well-known equation of sediment continuity, denoted as the Exner equation:

$$\frac{\partial z}{\partial t} = -\frac{1}{(1-n)}\left(\frac{\partial S_x}{\partial x} + \frac{\partial S_y}{\partial x} - \Delta S\right) \quad (19)$$

where n [-] is the sediment porosity, S_x, S_y [m^2/s] is the total load sediment transport rates in the x and y direction respectively and ΔS [m/s] is a sediment source or sink term. The new bed level is then obtained by a forward in time differential scheme.

2.3.2. The MARIS-PMS Wave Model

In order to calculate the nearshore wave characteristics a Parabolic Mild Slope model is implemented, utilizing its accuracy in prescribing the wave field in mildly sloping beaches and the saving of considerable computational time. In particular, the wave model MARIS-PMS [34] presented herein is based on the work of [43] who derived a parabolic equation, in the form of a cubic Schrödinger differential equation, governing the complex amplitude, A, of the fundamental frequency component of a Stokes wave. Darlymple et al. [44] improved the parabolic equation and its range of validity by developing approximations based on minimax principles in order to allow for large-angle propagation and rendering the approximation suitable for large scale applications, thus proposing the following governing equation:

$$C_gA_x + i(\overline{k} - a_0k)C_gA + \frac{1}{2}\left(C_g\right)_xA + \frac{i}{\omega}\left(\alpha_1 - b_1\frac{\overline{k}}{k}\right)\left(CC_gA_y\right)_y - \frac{b_1}{\omega k}\left(CC_gA_y\right)_{yx} + \frac{b_1}{\omega}\left(\frac{k_x}{k^2} + \frac{(C_g)_x}{2kC_g}\right)\left(CC_gA_y\right)_y + \frac{i\omega k^2}{2}D|A|^2A + \frac{w}{2}A = 0 \quad (20)$$

where the parameter D is given by $D = \frac{(\cos h4kh + 8 - 2\tan h^2kh)}{8\sin h^4kh}$, the complex amplitude A is related to the water surface displacement by $\eta = Ae^{-i(kx-\omega t)}$, k the local wave number related to the angular frequency of the waves, ω [rad/s], and the water depth, h [m]. $\overline{k}$ [rad/m] is a reference wave number taken as the average wave number along the y-axis, C [m/s] is the phase celerity, C_g [m/s] is the group celerity and w is a dissipation factor. Finally, coefficients a_0, α_1 and b_1 depend on the aperture width chosen to specify the minimax approximation [45]. The combination of $a_0 = 0.994733$, $\alpha_1 = -0.890065$,

and $b_1 = -0.451641$ was found in [45] to give reasonable results for a maximum angular range of 70° and is applied in the MARIS-PMS model.

MARIS-PMS takes into account energy dissipation due to bathymetric breaking following the formulation of [46], and bottom friction, which is modelled through the formulation of [47].

MARIS-PMS incorporates non-linear dispersion characteristics, in order to improve model results in the nearshore area, which can be obtained by introducing an approximate non-linear amplitude dispersion relationship, such as that presented in [48].

Instead of utilizing a unique mathematical expression over the entire numerical domain, combined models can be applied (e.g., [49,50] in order to incorporate high nonlinearity at any depth. Utilizing this approach, the wave celerity is assumed to vary spatially within the simulation, and the nonlinear dispersion relation to be applied is subject to the local Ursell number $Ur = HL^2/h^3$ and wave steepness $s = H/L$, in relation to the valid regions of analytical wave theories.

Therefore, for $s > 0$ and $Ur > 4000$ and $H/h < 0.78$ a modified cnoidal equation is adopted:

$$\omega^2 = gk^2h(1 + f(m)H/h) \quad (21)$$

where $f(m)$ a function of the parameter m, the modulus of the elliptic functions. Bell et al. [51] assumed a constant value $f(m) = 0.4$ which is adopted in the model formulation.

Conversely, for $s > 0$ and $Ur > 4000$ and $H/h > 0.78$ the solitary wave dispersion relation is used:

$$\omega^2 = gk^2h(1 + H/h) \quad (22)$$

In the surf zone, the aforementioned solitary wave relation behaves similarly with the simple approach to model wave celerity through a modified shallow water approximation [52]:

$$\omega^2 = a^2gk^2h \quad (23)$$

where a typical value of the coefficient a is set to 1.3.

In order to tackle numerical discontinuities at the coupling boundaries, due to variation across Stokes, cnoidal and solitary divisions, a weighted moving average (WMA) technique is incorporated to smooth the values of celerity in the transition windows from one theory to another [34]. The analytical method was utilized in the present study to calculate significant wave heights, periods and directions, at a characteristic depth of 8 m (see step 4 of Section 2.1.2.). It is considered that this method can achieve a fine compromise between robust and time-efficient calculations while attaining non-linear dispersion characteristics in the shallow water area. Besides, for the calculation of wave characteristics and the subsequent calculation of the depth of closure, [53] proposed the use of linear wave models. We consider the use of a parabolic mild slope wave model for this purpose to be an improvement on the methodology improving the accuracy of the estimation of wave heights in the nearshore, while simultaneously keeping simulation times at reasonable levels [34].

3. Method Implementation

3.1. Study Area

The input-reduction method based on the sediment pick-up rate was implemented using the MIKE21 Coupled Model FM suite in the coast located in the close vicinity of the port of Rethymno, in the island of Crete, Greece. The area of interest, shown in Figure 2, includes the aforementioned port, located in the northern end of Crete within the homonymous bay and the adjacent coastal area at the east and a coastline of approximately 4 km in length. The aforementioned coastline comprises mostly fine sand, with a median sediment diameter of $d_{50} = 0.15$ mm, which was used for the morphological simulations. Being a highly urbanized area, commercial, administrative, cultural and tourist activities are concentrated along the north coast where the city is located. Consequently, a medium to long-term

prediction of the bed evolution and ultimately the displacement of the shoreline, is of particular interest to engineers/scientists and the public.

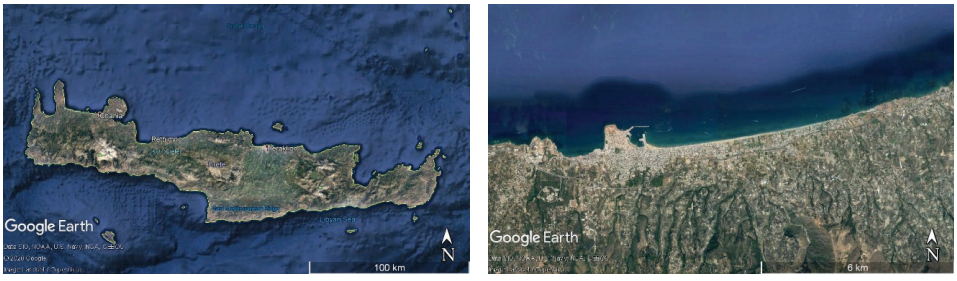

Figure 2. The island of Crete (**left**) and the study area of the coastal zone of Rethymno (**right**) where the MIKE21 Coupled Model FM was implemented. Adapted from [54], with permission from Google Earth, 2020.

3.2. Mesh Generation

In order to simulate the morphological bed evolution of the Rethymno coast, an unstructured finite element mesh was constructed. Three mesh density levels were used for the discretization of the domain, with the coarser area being near the offshore and the lateral wave boundaries, and the denser one covering an extend of 3.5 km long and 10.0 km wide. A third density level was established extending at about 250 m offshore the western coastline. For the solid boundaries, a vertice-adaptive mesh generation scheme allowed the construction of relatively small finite elements in the solid boundaries, allowing for the more detailed description of the bathymetric variations in shallow water areas. Regarding the dimensions of the interior triangular elements, they are comprised of a mean nominal length of about 100 m, with the largest element size being 293 m and the minimum 0.71 m. The bathymetry was digitized using QGIS software [55], utilizing nautical maps from the Navionics web application [56] as input. The final bathymetric mesh for the study area is presented in Figure 3.

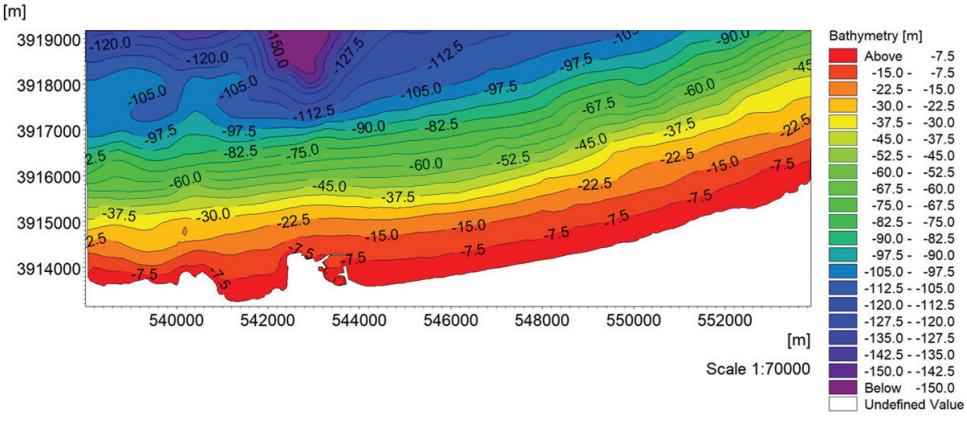

Figure 3. Contour map of the bathymetry in the area of study in the vicinity of port of Rethymno.

3.3. Offshore Wave Data

To force the 3rd generation spectral wave model MIKE21 SW time series of wave characteristics were obtained at the north boundary of the computational mesh, namely spectral wave height, peak wave period and mean wave direction from CMEMS [8] database for a time range covering 02/2012–02/2017. For this purpose, the regional package MEDSEA_HINDCAST_WAV_006_012 [57], a multi-year wave hindcast product composed of hourly wave parameters at 1/24° horizontal grid resolution was utilized. The dataset is produced by the corresponding Mediterranean Sea Forecast package which in turn is a wave model based on the well-established spectral wave model WAM Cycle 4.5.4 [58]. The extracted offshore time series were also fed to the MARIS-PMS model, in order to obtain wave characteristics at the depth of 8 m seaward the sandy coastline near the Rethymno port, to be used in the calculations of the depth of closure. The input-reduction method was implemented for three distinct scenarios, firstly a wave time series at hourly intervals for 7 days, from 19/12/2012 to 26/12/2012, secondly a wave time series for 20 days from 17/08/2012 to 06/09/2012, and lastly for a time series covering a full year (365 days) of wave records, from 01/01/2012 to 01/01/2013. A Morfac of 1, 20 and 100 was used for the three separate cases respectively, in order to validate the input-reduction method without and with the effect of the morphological acceleration factor and assess its effect on the method's sensitivity. For each case, 3 set of simulations were performed, namely:

- A simulation consisting of the full time series at the offshore boundary, hereafter denoted as Reference simulation
- A simulation using 12 representatives as forcing parameters calculated with the pick-up rate method, hereafter called pick-up rate simulation
- A simulation using 12 representatives calculated with the energy-flux input-reduction method, hereafter denoted as energy-flux simulation, to assess how the pick-up rate method fares against a well-established wave schematization technique.

The time series, especially that covering the extent of 7 days, was desirable to contain wave height conditions with significant variation, in order to assess the performance of the pick-up rate simulation in a rather diverse wave climate. The rose plot of wave heights for the time series comprising 7 and 20 days are shown in Figure 4. It can be observed that low, mild and moderate wave conditions, in terms of wave height, are present in both datasets. Nevertheless, certain differences can be observed regarding the distribution of wave heights, since the dataset of 7 days is consisted of more extreme wave conditions (maximum wave height H_{mo} = 3.2 m) while the dataset of 20 days was characterized by milder wave conditions with a maximum wave height H_{mo} = 2.35 m. Regarding the dataset covering the extend of the year, the wave climate was more diverse, with a minimum wave height of 0.09 m and a maximum wave height of 4.66 m. From the initial filtration of the waves that exit the computational domain and therefore have no effect on the morphological bed evolution, the dataset was reduced from 8762 hourly changing wave records to 8219. The vast majority (over 70 %) of the incident waves are entering the computational domain from the north sector, as shown in Figure 4.

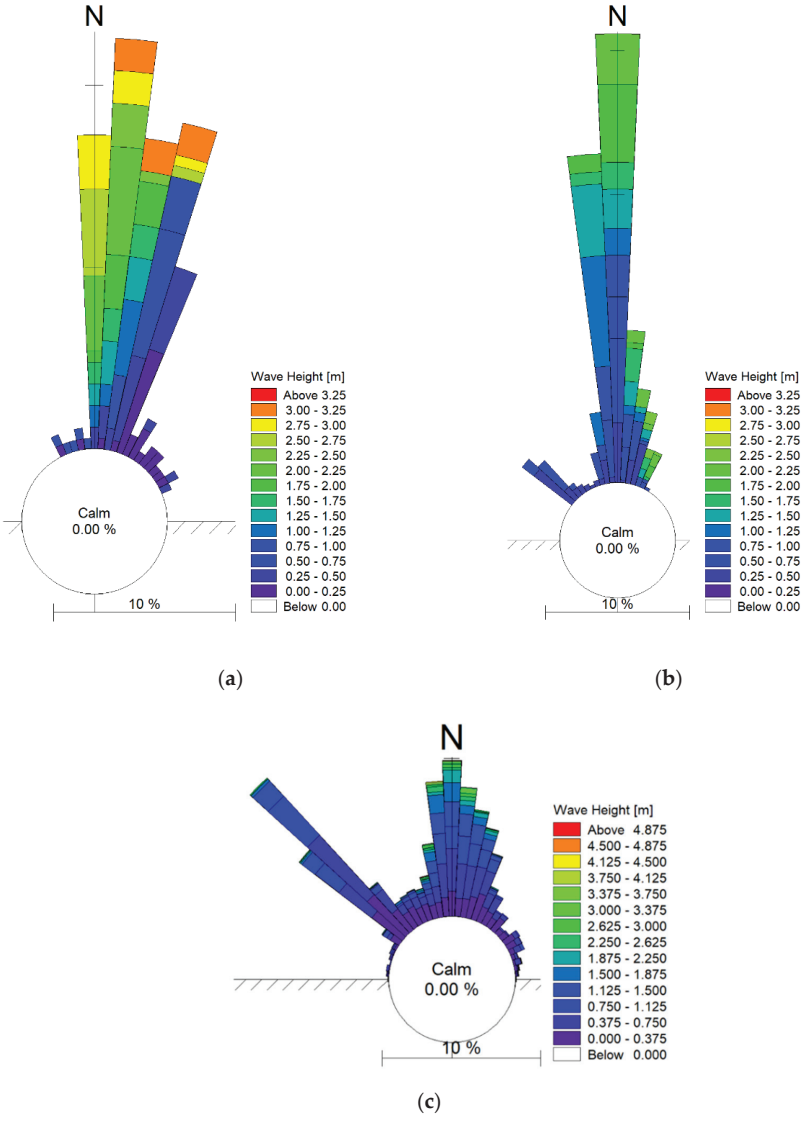

Figure 4. Wave height rose plot for the dataset containing records of 7 days (**a**), 20 days (**b**) and a year of data (**c**).

3.4. Obtained Representative Wave Conditions

A total of 12 conditions were chosen to represent the input wave data for all datasets according to [12], who considered them to be adequate to accurately describe the morphological bed evolution induced by yearly wave climates. Thus, we consider 12 conditions to be able to represent satisfactorily the wave climate of the smaller datasets that were used for the purpose of this research, as well as the dataset covering a full year. In Table 1 the representative wave conditions (defined by the spectral wave height H_{mo}, peak wave period T_p, mean wave direction MWD and frequency of occurrence) obtained by implementing the pick-up rate method, along with those stemming from the energy-flux method are presented for the dataset of 7 days.

Table 1. Representative wave conditions from the time series of 7 days, using the pick-up rate and the energy-flux wave schematization methods.

Class	Pick-up Rate Method Representatives				Energy Flux Method Representatives			
	H_{mo} (m)	T_p (s)	MWD (°)	Frequency (%)	H_{mo} (m)	T_p (s)	MWD (°)	Frequency (%)
1st	1.78	6.96	1.30	14.94	1.23	5.87	357.57	10.84
2nd	2.77	8.20	1.65	4.60	2.55	8.09	1.46	3.01
3rd	2.51	7.63	2.35	5.75	2.53	7.63	2.31	3.61
4th	2.77	8.01	2.01	4.60	2.78	8.01	1.93	2.41
5th	2.30	7.53	3.27	8.05	1.96	7.09	3.69	6.02
6th	2.94	8.39	3.24	3.45	2.76	8.09	2.99	3.01
7th	1.74	6.99	4.85	19.54	1.44	6.38	5.14	10.24
8th	2.65	8.01	4.73	4.60	2.88	8.20	5.35	2.41
9th	1.70	7.12	8.47	18.39	1.44	6.69	8.86	10.24
10th	3.19	8.39	8.50	2.30	2.90	8.01	8.62	2.41
11th	1.88	6.89	12.78	10.34	*0.52*	*4.77*	21.63	43.37
12th	3.16	7.63	12.49	3.45	3.08	7.63	14.37	2.44

It can be observed that both methods for the larger part have similar directional bins expressed by the representative values, although the pick-up rate method possesses larger wave heights with a higher frequency of occurrence for these particular classes. This can be attributed to the elimination of wave heights that are unable to initiate sediment motion, which results in the translocation of the center of the wave height bins in higher values, when compared to the energy-flux method. Furthermore, in Figure 5, the total dataset of 20 days along with the representative conditions is presented in a scatter plot, for both the pick-up rate and the energy-flux method. It can be observed for the particular case that the directional bins are quite different when comparing the two methods, due to the low-energy wave conditions generated from a direction of 300°–350° which are not capable of initiating sand motion and consequently are not taken into consideration by the pick-up rate method.

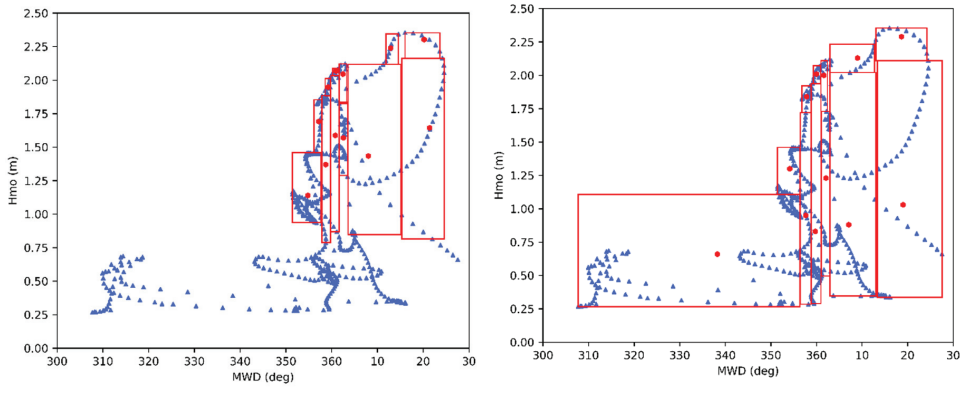

(**a**) (**b**)

Figure 5. Scatter plot showing the full dataset of the 20 days (blue markers) along with the bins (red rectangles) and representative wave conditions (red markers) using the pick-up rate method (**a**) and the energy-flux method (**b**).

The obtained representatives calculated through the pick-up rate and the energy-flux input-reduction methods for the dataset covering the extent of a year are presented as a scatter plot in Figure 6. Once again it is evident that due to the elimination of low energy wave conditions the representatives obtained through the implementation of the pick-up rate method have larger wave heights compared to the ones stemming from the energy-flux method while the frequency of occurrence

is more or less the same. An increase in both representative wave height and frequency of occurrence for the pick-up rate signifies that the specific classes contains a large amount of wave components that are able to initiate sediment motion. Effectively by introducing the Shield's criterion of incipient motion one can obtain representative wave conditions that correspond to the more energetic wave condition of the wave climate while increasing their impact in the prediction of the morphological bed evolution.

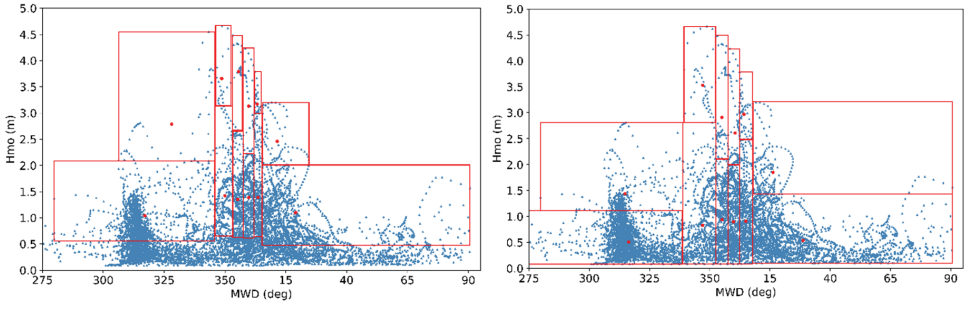

Figure 6. Scatter plot showing the full dataset of a year of data (blue markers) along with the bins (red rectangles) and representative wave conditions (red markers) using the pick-up rate method (**a**) and the energy-flux method (**b**).

4. Results and Discussion

In the following section, the results that were obtained by implementing the pick-up rate method by applying the process-based model MIKE21 Coupled Model FM are presented. In order to evaluate the performance of 2D morphological area models we calculate various statistical parameters which are described in detail in [59]. The performance of a morphological model can ultimately be assessed by calculating its bias, accuracy and skill. The most commonly used measure of the latter quantity is the Brier Skill Score (BSS) which has been applied in a plethora of morphological modelling applications (i.e., [15,60,61]. It is calculated through the following relationship:

$$\mathrm{BSS} = 1 - \frac{\mathrm{MSE}(\mathrm{Y},\mathrm{X})}{\mathrm{MSE}(\mathrm{B},\mathrm{X})} = 1 - \frac{\langle(\mathrm{Y}-\mathrm{X})^2\rangle}{\langle(\mathrm{B}-\mathrm{X})^2\rangle} \tag{24}$$

where Y denotes the predicted (modelled) quantity, X denotes a measured quantity, corresponding to the reference simulation for the present study due to lack of measurements, and B is a baseline prediction, usually referring to the initial bathymetry, assuming no alteration of the bed. Additionally, the square brackets denote average quantities over the whole domain. In Table 2 the classification scores for the BSS according to [59] in order to estimate the performance of a given morphological evolution model are shown:

Table 2. Classification table for the Brier Skill Score (BSS) as proposed by [59]. (Adapted from [59], with permission from Elsevier, 2004).

	BSS
Excellent	1.0–0.5
Good	0.5–0.2
Reasonable/fair	0.2–0.1
Poor	0.1–0.0
Bad	<0.0

We evaluate the performance of the morphological model in an area extending about 450 m offshore (at a maximum depth of about 9 m) the eastern coastline adjusted to the port. We chose to focus on this area (enclosed by the polygon shown in Figure 7), since it consists mostly of a sandy uniform bed and is of high interest to the public due to various tourist activities concentrated there. We also avoid evaluating the performance of the process-based model in the close vicinity of the port of Rethymno, since the phase-averaged approach utilized by the spectral wave driver MIKE21 SW is not suited to deal with inhomogeneities and coherent interfaces present in the wave field due to reflection and diffraction [62,63].

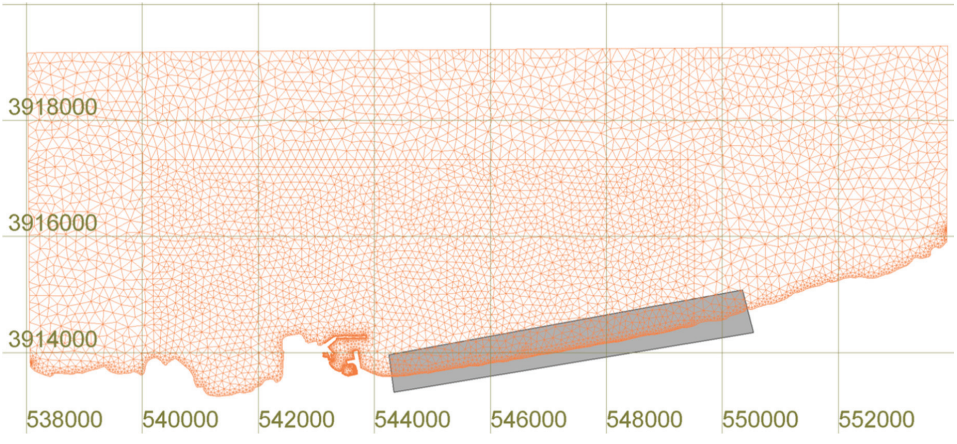

Figure 7. Finite element mesh showing the area (within the closed polygon) where the morphological model results will be evaluated.

The estimation of wave heights in the characteristic depth of 8.0 m to subsequently calculate the depth of closure was carried out using the MARIS-PMS wave model for the full datasets of 7 and 20 and 365 days, with the computed depth of closure being 8.67 m, 6.95 m and 6.69 for each dataset respectively. No wave breaking took place as expected, however minor changes in the wave height were observed due to the energy bunching effect attributed mostly to shoaling and secondly to wave refraction.

4.1. Morphological Bed Evolution for the Dataset of Seven Days

In the present section the morphological bed evolution of the area of interest using the forcing dataset of 7 days is presented and discussed. The most dominant wave direction turned out to be the northern, as shown by the representative wave conditions in Table 1. Consequently, the prevailing hydrodynamic and sediment transport vector component's direction for the area of interest was directed from east to the west, as shown in Figure 8, resulting mostly in accretive patterns in the beach face.

From the total of 168 initial hourly changing wave heights 88 of them lead to initiation of sediment motion by implementing the Shields criterion as was discussed in Section 2.1. Therefore the full dataset was reduced by a percentage of 47.62%, using the pick-up rate input-reduction method presented in this paper. Regarding model run-times, the Reference simulation corresponding to the induced morphological evolution of the complete dataset, resulted in a run-time of 133.3 h. Conversely, the reduced dataset obtained from the implementation of the pick-up rate method achieved a run-time of 79.19 h. Thus, a reduction of model run-time by 59.42% was achieved by implementing a Morfac value of 1 (no acceleration for this simulation). For reference, the energy-flux simulation was completed after a run-time of 131.2 h. The relatively small effective run-time reduction achieved through this

method can attributed to the preprocessing of data (small number of wave components compared to the full dataset) and not so much to the computational process. By utilizing a Morfac of 1, the reduction of model run-time can essentially be attributed to the newly developed input-reduction method. This particular feature is considered to be a valuable asset for engineers and scientists wanting to perform medium to long-term morphological simulations while simultaneously reducing the additional numerical burden.

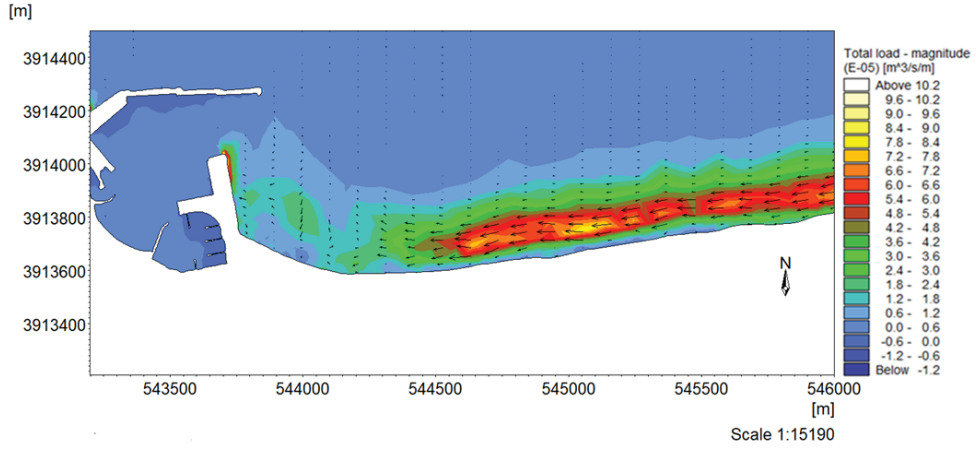

Figure 8. Total load magnitude and direction at the end of the pick-up rate simulation for the area of interest.

Regarding the model performance, for the area enclosed within the polygon shown in Figure 7, nodal values of the bed level inside the particular domain were extracted both for the Reference simulation and the pick-up rate simulation. Additionally the corresponding nodal values for the simulation utilizing the energy-flux input-reduction method were extracted to compare how it fares against the newly developed method based on the sediment pick-up rate. The model performance was assessed by calculating measures of bias and accuracy, namely the mean absolute error (MAE), mean square error (MSE) and root mean square error (RMSE). Lastly we focused on the skill evaluation of the model by calculating the BSS and categorizing the simulation as shown in Table 2. The measures obtained for the area of interest are shown in Table 3 (please see Supplementary Materials for the detailed calculations of the statistical measures).

Table 3. Statistical parameters obtained in the area of interest for both the pick-up rate simulation and the energy-flux simulation-Dataset of 7 days.

	Pick-Up Rate Method	Energy Flux Method
Bias	−0.0054	−0.0101
MAE(Y,X)	0.0218	0.0233
MSE(Y,X)	0.0018	0.0020
RMSE(Y,X)	0.0429	0.0450
BSS	0.9300	0.9200

From the above it can be derived that both the pick-up rate method and the energy-flux method can be categorized as excellent in regards to the BSS. As far as the model bias is concerned, the numerical model slightly underpredicts the morphological changes, albeit for a few mm. All accuracy measures are deemed acceptable for short-term morphological simulations. It should be stated that the pick-up rate method fares slightly better than the energy-flux method for this particular dataset. This can

be attributed to the fact that for relatively small datasets of input data, the higher complexity of the pick-up rate method and subsequent calculations can offer slightly more detailed prediction of the morphological bed evolution. However, on the other hand the pick-up rate method is highly dependent on the formulations used for the calculation of physical quantities, such as the friction factor due to waves and wave orbital velocity and consequently more testing to verify the previous statement should be carried out.

4.2. Morphological Bed Evolution for the Dataset of 20 Days

For the particular dataset, the hydrodynamic and sediment transport patterns were relatively the same as the results shown in the previous section. This can be attributed to the prevailing waves propagating from the northern sector which again dominate the wave climate, as shown in Figure 4. For all the simulation scenarios of this section we applied a value of Morfac = 20 in order to ultimately assess how the pick-up rate method fares in longer datasets when used in tandem with a model-reduction technique.

From the total of 481 initial hourly changing wave heights, 216 of them in deep water satisfy the Shields criterion of incipient motion. Therefore the full dataset was reduced by a percentage of 45.53%, for the purpose of implementing the pick-up rate method. Regarding model run-times, the Reference simulation corresponding to the induced morphological evolution of the complete dataset, resulted in a run-time of 24.47 h, whereas the energy-flux simulation achieved a model run-time of 23.21 h. Conversely, the reduced dataset resulting from the implementation of the pick-up rate method achieved a run-time of 12.57 h, leading to a reduction of 51.37% of total model run-time. This is a significant portion of model reduction when taking into account the further run time reduction achieved through the use of Morfac.

Utilizing the same procedure as §4.1 bed level values were extracted for the resulting model predictions (through the implementation of pick-up rate and energy-flux methods) and the "measured" values obtained through the reference simulation. The obtained bias, accuracy and skill measures for the area of interest illustrated in Figure 7 are shown in Table 4, while the detailed calculations of the statistical quantities for the particular dataset are presented in the Supplementary Materials.

Table 4. Obtained statistical parameters in the area of interest for both the pick-up rate simulation and the energy-flux simulation dataset of 20 days.

	Pick-Up Rate Method	Energy Flux Method
Bias	−0.0177	−0.0058
MAE(Y,X)	0.0633	0.0535
MSE(Y,X)	0.0096	0.0066
RMSE(Y,X)	0.0980	0.0813
BSS	0.8300	0.8800

It can be observed that the situation for the longer dataset of 20 days comparing the scores of the two simulations are reversed, as the energy-flux method performs better in all assessing categories. The slightly worse performance of the pick-up rate input-reduction method can be attributed to the elimination of the low-energy wave conditions. It should be stated though that both simulations achieve a score of "Excellent" once again, validating the ability of both methods to predict the morphological bed evolution for this particular set of input conditions. Thus, it is considered that for medium term morphological modelling applications, a small decrease in accuracy is insignificant compared to the model run-time reduction achieved through implementation of the pick-up rate method.

4.3. Morphological Bed Evolution for the Dataset of a Year

In the present section, the predicted bed level changes obtained through the pick-up rate and the energy-flux simulation are compared with the Reference simulation for the dataset covering a full

year of wave data. This comparison is of significant importance, since it can provide the basis for the assessment of the performance of the pick-up rate method in long-term morphological simulations (order of years). For all the simulation scenarios of this section a Morfac = 100 was applied in order to further accelerate the simulations. This value is at high end of the allowable values of the acceleration factor for morphological bed evolution under the combined effect of waves and currents, however it is deemed acceptable as shown in [2,10,16] for moderate wave conditions.

From the total of 8219 initial hourly changing wave heights, 3523 satisfy the Shields criterion of incipient motion. Therefore the full dataset was reduced by a percentage of 57.17%, by implementing the pick-up rate method. Regarding model run-times, the reference simulation corresponding to the induced morphological evolution of the complete dataset, resulted in a run-time of 106.86 h. Conversely, the reduced dataset resulting from the implementation of the pick-up rate method achieved a run-time of 39.13 h leading to a reduction of 56.80% of total model run-time, whereas the energy-flux simulation was completed after 90.58 h. It is evident that especially for long-term morphological predictive simulations the computational gain by implementing the pick-up rate method is quite significant.

To provide a basis for the comparison of the bed evolution obtained through the three distinct simulations and the subsequent model skill evaluation, the predicted bed-level changes obtained by the reference, pick-up rate and energy-flux simulations are presented in Figure 9. In particular, the relative bed level changes obtained by the reference simulation for the coast east of the Rethymno port are compared with the respective bed level changes obtained by the pick-up rate simulation. In general, the pick-up rate simulation slightly underpredicts the bed level changes, due to the elimination of low energy conditions that are able to initiate some sediment motion in small water depths. However, the predicted values of bed level changes are of the same order of magnitude as the reference simulation and it should be stated that the eroding and accretive patterns obtained in both simulations appear for the most part at the same positions. Both model predictions also depict sedimentation at the port entrance and accretion at the coastline adjusted to the port. Regarding the energy-flux simulation, it can be observed that the predicted morphological bed evolution values are of the same order of magnitude as those obtained through the reference simulation and the areas where accretion or erosion is more prevalent are predicted correctly by the energy-flux method. It can also be observed that the bed-level change patterns predicted by both the energy-flux and pick-up rate method have many similarities for the area shown in Figure 9.

To further assess model performance and skill for long-term bed-level predictions, the obtained bias and accuracy statistical quantities, namely the MAE, MSE, RMSE and skill measures (BSS) for the area of interest illustrated in Figure 7 are shown in Table 5.

As shown in Table 5, the energy-flux method performs better in all assessing categories compared to the pick-up rate method for the simulation of a year of morphological bed evolution.

Table 5. Obtained statistical parameters in the area of interest for both the pick-up rate simulation and the energy-flux simulation-Dataset of a year.

	Pick-Up Rate Method	Energy Flux Method
Bias	−0.2316	−0.1441
MAE(Y,X)	0.2661	0.1885
MSE(Y,X)	0.1070	0.0614
RMSE(Y,X)	0.3272	0.2478
BSS	0.7445	0.8535

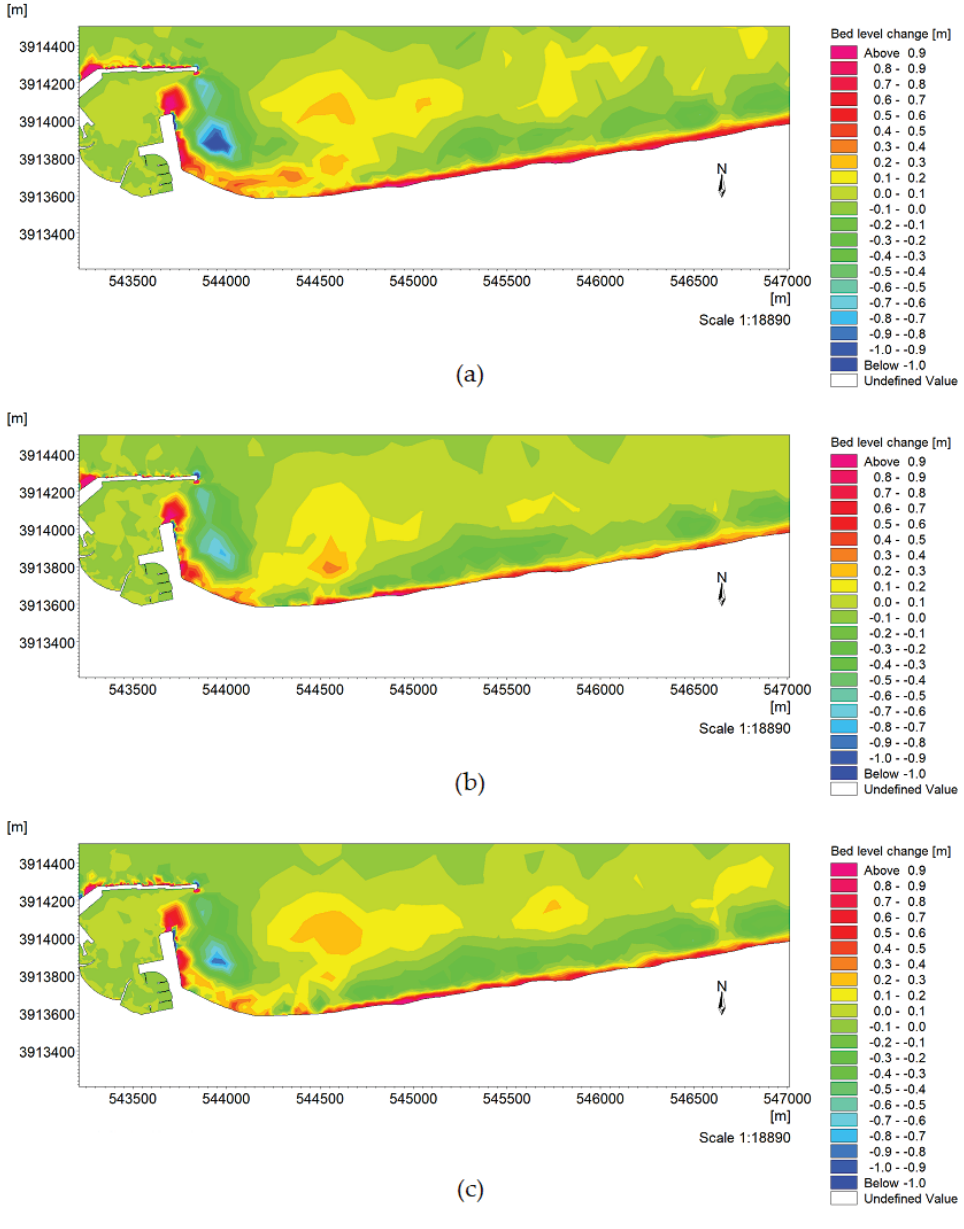

Figure 9. Bed-level changes obtained by the reference simulation (**a**) and implementation of the pick-up rate method (**b**) and energy-flux method (**c**) for the set covering a year of data.

Both simulations show increased error values compared to the previously examined test cases, which is to be expected for longer-term morphological bed predictions, where the computed relative bed level changes are large relative to the initial bathymetry. The deterioration of the pick-up rate simulation results can be attributed in part due to the elimination of the low-energy wave conditions in conjunction with the significant model run-time reduction. Once again, however, both simulations achieve a score of "Excellent", validating the ability of the pick-up rate method to adequately predict

the long-term morphological bed evolution. The selection of a relatively large Morfac (Morfac = 100 in the present simulations), is also considered to have an effect on the lower values of the computed BSS, especially for the pick-up rate method where the representative wave conditions are characterized by larger wave heights compared to the respective ones stemming from the energy-flux method. However, implementation of the pick-up rate method for long-term simulations was shown to achieve significant model run-time reduction (order of 57% for the examined test case) while simultaneously maintaining satisfactory results.

It should be stated that implementation of the proposed method on a different area of application should be carried out in order to assess its dependence on the local wave conditions and its ability to accurately predict the long-term morphological bed evolution. The method can be further extended to account for the effect of currents on the incipient sediment motion, by calculating a mean bed shear stress due to the combined effects of currents and waves [21]. However, this extension is dependent on the availability of accurate current measurements at the offshore boundary, while transferring current data near the breaker zone, where the largest proportion of circulation takes place, is a rather complex task which omits the scope of simplicity and speed, inherently present in input-reduction methods.

5. Conclusions

In the present paper, an efficient method of wave input reduction based on the calculation of the sediment pick-up rate was presented and its implementation was validated in the coastline adjusted to the port of Rethymno, Crete. The novelty of this method lies in the combination of input-reduction and model-reduction elements, which stem from the incorporation of incipient sediment motion through the calculation of Shields number. The method was implemented using the process-based model MIKE21 Coupled Model FM for the calculation of wave propagation, current and sediment transport fields.

The pick-up rate method was implemented and validated against three datasets of total records of 7 days, 20 days and a year respectively, in order to assess the model's ability to accurately predict the morphological bed evolution using the aforementioned method for small and larger datasets and for a variety of input conditions. For the three distinct simulations, elimination of wave heights unable to satisfy Shields criterion for initiation of sediment motion results in a reduction of model run-time by 59.42%, 51.37% and 56.80%, respectively.

The performance of the morphological model was assessed by calculating statistical values concerning the predictive simulation's bias, accuracy and skill. For the three distinct scenarios, the pick-up rate method was implemented and results were compared against the widely used energy-flux method of wave schematization. Regarding the commonly used BSS, employed to measure a morphological model's skill, the pick-up rate simulation was deemed as "excellent" for all situations, with a small deterioration of performance in the long-term (order of year) simulation.

The newly developed method should be utilized with caution in the vicinity of coastal structures where wave reflection and diffraction begin to play a significant role in shaping the wave field. It should be stated that the same limitation applies to 3rd-generation spectral wave models such as MIKE 21 SW, which can qualitatively capture diffraction effects and the incorporation of this process is based on the parabolic mild slope equation. For example in the case of a coastal area protected by shore parallel breakwaters the pick-up rate method cannot be applied at the lee side of the breakwater since the wave characteristics at the nearshore depth of 8 m would be erroneously calculated due to the omission of said wave processes. However, the method can safely be applied for any coastal area, independent of the complexity of the shoreline and bottom topography, if wave diffraction and reflection are not dominant in the depth of 8 m where the depth of closure is calculated.

Implementation of this method requires the utilization of a parabolic mild slope wave model and is rather complex, when compared to the application of traditional input-reduction methods, such as that based on the calculation of wave energy flux, which can be carried out within a single spreadsheet. However it should be stated that a higher effort during the computation of the representative wave

classes is rather insignificant compared to the gain achieved by the reduction of the 2D morphological area model run-time through the pick-up rate method.

Therefore, it is considered that the input-reduction method developed for the purpose of this research will be a valuable tool for coastal engineers and scientists, achieving adequately accurate bed level predictions for medium- to long-term simulations compared to the reference simulation, while simultaneously further reducing numerical burden and model run-times.

Supplementary Materials: The following are available online at http://www.mdpi.com/2077-1312/8/8/597/s1: Worksheet S1: SkillScores_20_days.xlsx, Worksheet S1: SkillScores_7_days.xlsx.

Author Contributions: Conceptualization, A.P.; methodology, A.P., L.P. and V.T.; software, A.P., L.P. and M.C.; validation, A.P., L.P. and V.T.; formal analysis, A.P. and L.P.; investigation, A.P., L.P. and M.C.; resources, V.T.; data curation, A.P. and M.C.; writing—original draft preparation, A.P. and M.C.; writing—review and editing, V.T.; visualization, A.P. and L.P.; supervision, V.T.; project administration, V.T.; funding acquisition, V.T. All authors have read and agreed to the published version of the manuscript.

Funding: This research received no external funding.

Conflicts of Interest: The authors declare no conflict of interest.

References

1. Drønen, N.; Kristensen, S.; Taaning, M.; Elfrink, B.; Deigaard, R. Long term modeling of shoreline response to coastal structures. In Proceedings of the Coastal Sediments Conference, Miami, FL, USA, 2–6 May 2011.
2. Lesser, G.R. An Approach to Medium-Term Coastal Morphological Modelling. Ph.D. Thesis, Delft University of Technology, Delft, The Netherlands, 4 June 2009.
3. de Vriend, H.J.; Zyserman, J.; Nicholson, J.; Roelvink, J.A.; Péchon, P.; Southgate, H.N. Medium-term 2DH coastal area modelling. *Coast. Eng.* **1993**, *21*, 193–224. [CrossRef]
4. Roelvink, D.; Reniers, A. *A Guide to Modeling Coastal Morphology*, 1st ed.; Word Scientific: Singapore, 2012; p. 292.
5. Lesser, G.R.; Roelvink, J.A.; van Kester, J.A.T.M.; Stelling, G.S. Development and validation of a three-dimensional morphological model. *Coast. Eng.* **2004**, *51*, 883–915. [CrossRef]
6. Prasad, R.S.; Svendsen, I.A. Moving shoreline boundary condition for nearshore models. *Coast. Eng.* **2003**, *49*, 239–261. [CrossRef]
7. Casulli, V. A high-resolution wetting and drying algorithm for free surface hydrodynamics. *Internat. J. Numer. Methods Fluids* **2009**, *60*, 391–408. [CrossRef]
8. Copernicus Marine Environment Monitoring Service. Available online: http://marine.copernicus.eu/ (accessed on 19 December 2019).
9. ECMWF. Available online: https://www.ecmwf.int/ (accessed on 19 December 2019).
10. Walstra, D.J.R.; Hoekstra, R.; Tonnon, P.K.; Ruessink, B.G. Input reduction for long-term morphodynamic simulations in wave-dominated coastal settings. *Coast. Eng.* **2013**, *77*, 57–70. [CrossRef]
11. Brown, J.M.; Davies, A.G. Methods for medium-term prediction of the net sediment transport by waves and currents in complex coastal regions. *Cont. Shelf Res.* **2009**, *29*, 1502–1514. [CrossRef]
12. Benedet, L.; Dobrochinski, J.P.F.; Walstra, D.J.R.; Klein, A.H.F.; Ranasinghe, R. A morphological modeling study to compare different methods of wave climate schematization and evaluate strategies to reduce erosion losses from a beach nourishment project. *Coast. Eng.* **2016**, *112*, 69–86. [CrossRef]
13. Karathanasi, F.E.; Belibassakis, K.A. A cost-effective method for estimating long-term effects of waves on beach erosion with application to Sitia Bay, Crete. *Oceanologia* **2019**, *21*, 276–290. [CrossRef]
14. Roelvink, J.A. Coastal morphodynamic evolution techniques. *Coast. Eng.* **2006**, *53*, 277–287. [CrossRef]
15. Knaapen, M.A.F.; Joustra, R. Morphological acceleration factor: Usability, accuracy and run time reductions. In Proceedings of the XIXth TELEMAC-MASCARET User Conference, Oxford, UK, 18–19 October 2012.
16. Ranasinghe, R.; Swinkels, C.; Luijendijk, A.; Roelvink, D.; Bosboom, J.; Stive, M.; Walstra, D.J. Morphodynamic upscaling with the MORFAC approach: Dependencies and sensitivities. *Coast. Eng.* **2011**, *58*, 806–811. [CrossRef]
17. van Rijn, L.C. Sediment Pick-up functions. Applications of sediment Pick-up function. *J. Hydraul. Eng.* **1986**, *112*, 867–874. [CrossRef]

18. van Rijn, L.C.; Bisschop, R.; van Rhee, C. Modified Sediment Pick-Up Function. *J. Hydraul. Eng.* **2019**, *145*, 060180171–060180176. [CrossRef]
19. DHI Coupled Model FM (MIKE 21/3 FM). *User Guide*; DHI: Hørsholm, Denmark, 2017.
20. Chondros, M.; Metallinos, A.; Karambas, T.; Memos, C.; Papadimitriou, A. Advanced numerical models for simulation of nearshore processes. In Proceedings of the Design and Management of Port, Coastal and Offshore Works Conference, Athens, Greece, 8–11 May 2019.
21. Soulsby, R.L. *Dynamics of Marine Sands: A Manual for Practical Applications*, 1st ed.; Thomas Telford: London, UK, 1997; p. 249.
22. Shields, I.A. Anwendung der Ahnlichkeits-Mechanik und der Turbulenzforschung auf die Geschiebebewegung. Ph.D. Thesis, Technical University of Berlin, Berlin, Germany, 30 June 1936.
23. Soulsby, R.L.; Whitehouse, R.J. Threshold of sediment motion in coastal environments. In Proceedings of the 13th Australasian Coastal and Ocean Engineering Conference and the 6th Australasian Port and Harbour Conference, Canterbury, UK, 28–30 September 1997.
24. Soulsby, R.L. Calculating bottom orbital velocity beneath waves. *Coast. Eng.* **1987**, *11*, 371–380. [CrossRef]
25. Soulsby, R.L.; Smallman, J.V. *A Direct Method of Calculating Bottom Orbital Velocity under Waves*; Technical Report No SR 76; Hydraulics Research Limited: Wallingford, Oxfordshire, UK, February 1986.
26. Swart, D.H. Offshore Sediment Transport and Equilibrium Beach Profiles. Ph.D. Thesis, Delft University of Technology, Delft, The Netherlands, 18 December 1974.
27. Nielsen, P. *Coastal Bottom Boundary Layers and Sediment Transport*, 1st ed.; Advanced Series on Ocean Engineering; World Scientific: Singapore, 1992; Volume 4, p. 340.
28. van Rijn, L.C. Sediment Pick-Up Functions. *J. Hydraul. Eng.* **1984**, *110*, 1494–1502. [CrossRef]
29. O'Reilly, W.C.; Guza, R.T. Comparison of spectral refraction and refraction-diffraction wave models. *J. Waterw. Port Coast. Ocean Eng.* **1991**, *117*, 199–215. [CrossRef]
30. Tolman, H.L. A Third-Generation Model for Wind Waves on Slowly Varying, Unsteady, and Inhomogeneous Depths and Currents. *J. Phys. Oceanogr.* **1991**, *21*, 782–797. [CrossRef]
31. Benoit, M.; Marcos, F.; Becq, F. Development of a Third Generation Shallow-Water Wave Model with Unstructured Spatial Meshing. In Proceedings of the 25th International Conference on Coastal Engineering, Orlando, FL, USA, 2–6 September 1996.
32. Booij, N.; Ris, R.C.; Holthuijsen, L.H. A third-generation wave model for coastal regions 1. Model description and validation. *J. Geophys. Res. Ocean.* **1999**, *104*, 7649–7666. [CrossRef]
33. Karambas, T.V.; Samaras, A.G. An integrated numerical model for the design of coastal protection structures. *J. Mar. Sci. Eng.* **2017**, *5*, 50. [CrossRef]
34. Chondros, M.K.; Metallinos, A.S.; Memos, C.D.; Karambas, T.V.; Papadimitriou, A.G. Concerted nonlinear mild-slope wave models for enhanced simulation of coastal processes. *Appl. Math. Model.* **2020**, accepted for publication.
35. Houston, J.R. *Beach-Fill Volume Required to Produce Specific Dry Beach Width*; Coastal Engineering Technical Note II-32; US Army Corps Engineer Waterways Experiment Station: Vicksburg, MS, USA, March 1995.
36. Dobrochinski, J.P.H. Wave Climate Reduction and Schematization for Morphological Modeling. Master's Thesis, Universidade do Vale do Itajaí & Delft University of Technology, Delft, The Netherlands, 2009.
37. Kaergaard, K.; Mortensen, S.B.; Kristensen, S.E.; Deigaard, R.; Teasdale, R.; Hunt, S. Hybrid shoreline modelling of shoreline protection Schemes, Palm Beach, Queensland, Australia. In Proceedings of the Coastal Engineering Conference, Seoul, Korea, 15–20 June 2014.
38. Gad, F.-K.; Hatiris, G.-A.; Loukaidi, V.; Dimitriadou, S.; Drakopoulou, P.; Sioulas, A.; Kapsimalis, V. Long-Term Shoreline Displacements and Coastal Morphodynamic Pattern of North Rhodes Island, Greece. *Water* **2018**, *10*, 849. [CrossRef]
39. DHI 21&3 Spectral Wave Module. *Scientific Documentation*; DHI: Hørsholm, Denmark, 2009.
40. Komen, G.J.; Cavaleri, L.; Donelan, M.; Hasselmann, K.; Hasselmann, S.; Janssen, P.A.E.M. *Dynamics and Modelling of Ocean Waves*; Cambridge University Press: Cambridge, UK, 1994.
41. DHI 21&3 Flow Model FM, Hydrodynamic and Transport Module. *Scientific Documentation*; DHI: Hørsholm, Denmark, 2009.
42. DHI 21&3 Flow Model FM, Sand Transport Module. *Scientific Documentation*; DHI: Hørsholm, Denmark, 2009.
43. Kirby, J.T.; Dalrymple, R.A. A parabolic equation for the combined refraction diffraction of Stokes waves by mildly varying topography. *J. Fluid Mech.* **1983**, *136*, 453–466. [CrossRef]

44. Dalrymple, R.A.; Kirby, J.T. Models for very wide-angle water waves and wave diffraction. *J. Fluid Mech.* **1988**, *201*, 299–322. [CrossRef]
45. Kirby, J.T. Rational approximations in the parabolic equation method for water waves. *Coast. Eng.* **1986**, *10*, 355–378. [CrossRef]
46. Battjes, J.A.; Janssen, J.P.F.M. Energy Loss and Set-Up Due To Breaking of Random Waves. In Proceedings of the Coastal Engineering Conference, Hamburg, Germany, 27 August–3 September 1979.
47. Putnam, J.A.; Johson, J.W. The dissipation of wave energy by bottom friction. *Eos Trans. Am. Geophys. Union* **1949**, *30*, 67–74. [CrossRef]
48. Kirby, J.T.; Dalrymple, R.A. An approximate model for nonlinear dispersion in monochromatic wave propagation models. *Coast. Eng.* **1986**, *9*, 545–561. [CrossRef]
49. Svendsen, I.A.; Hansen, J.B. Deformation up to breaking of periodic waves on a beach. In Proceedings of the Coastal Engineering Conference, Honolulu, HI, USA, 11–17 July 1976.
50. Svendsen, I.A.; Qin, W.; Ebersole, B.A. Modelling waves and currents at the LSTF and other laboratory facilities. *Coast. Eng.* **2003**, *50*, 19–45. [CrossRef]
51. Bell, P.; Williams, J.; Clark, S.; Morris, B.; Vila-Concejo, A. Nested Radar Systems for Remote Coastal Observations. *J. Coast. Res.* **2006**, *39*, 483–487.
52. Svendsen, I.A.; Madsen, P.A.; Buhr Hansen, J. Wave characteristics in the surf zone. In Proceedings of the Coastal Engineering Conference, Hamburg, Germany, 27 August–3 September 1979.
53. Kraus, N.C.; Larson, M.; Wise, R.A. *Depth of Closure in Beach-Fill Design*; Coastal Engineering Technical Note II-40; US Army Corps Engineer Waterways Experiment Station: Vicksburg, MS, USA, March 1998.
54. Google Earth. Image ©2020 Landsat/Coppernicus, Data SIO, NOAA, U.S. Navy, NGA, GEBCO. 2020.
55. QGIS. Available online: https://qgis.org/ (accessed on 17 December 2019).
56. NAVIONICS Chart Viewer. Available online: https://webapp.navionics.com/ (accessed on 9 January 2020).
57. Ravdas, M.; Zacharioudaki, A.; Korres, G. Implementation and validation of a new operational wave forecasting system of the Mediterranean Monitoring and Forecasting Centre in the framework of the Copernicus Marine Environment Monitoring Service. *Nat. Hazards Earth Syst. Sci.* **2018**, *18*, 2675–2695. [CrossRef]
58. WAMDI Group. The WAM model—A third generation ocean wave prediction model. *J. Phys. Ocean.* **1988**, *18*, 1775–1810. [CrossRef]
59. Sutherland, J.; Peet, A.H.; Soulsby, R.L. Evaluating the performance of morphological models. *Coast. Eng.* **2004**, *51*, 917–939. [CrossRef]
60. Sutherland, J.; Walstra, D.J.R.; Chesher, T.J.; Van Rijn, L.C.; Southgate, H.N. Evaluation of coastal area modelling systems at an estuary mouth. *Coast. Eng.* **2004**, *51*, 119–142. [CrossRef]
61. van Rijn, L.C.; Wasltra, D.J.R.; Grasmeijer, B.; Sutherland, J.; Pan, S.; Sierra, J.P. The predictability of cross-shore bed evolution of sandy beaches at the time scale of storms and seasons using process-based profile models. *Coast. Eng.* **2003**, *47*, 295–327. [CrossRef]
62. Smit, P.B.; Janssen, T.T. The evolution of inhomogeneous wave statistics through a variable medium. *J. Phys. Oceanogr.* **2013**, *43*, 1741–1758. [CrossRef]
63. Metallinos, A.S.; Chondros, M.K.; Karambas, T.V.; Memos, C.D.; Papadimitriou, A.G. Advanced numerical models for wave disturbance simulation in port basins. In Proceedings of the Design and Management of Port, Coastal and Offshore works Conference, Athens, Greece, 8–11 May 2019.

Journal of
Marine Science and Engineering

MDPI

Article

Modelling the Impact of Climate Change on Coastal Flooding: Implications for Coastal Structures Design

Achilleas G. Samaras [1,*] and Theophanis V. Karambas [2]

[1] Department of Civil Engineering, Democritus University of Thrace, Kimmeria, PC 67 100 Xanthi, Greece
[2] Department of Civil Engineering, Aristotle University of Thessaloniki, PC 54 124 Thessaloniki, Greece; karambas@civil.auth.gr
* Correspondence: achsamar@civil.duth.gr or achilleas.samaras@gmail.com

Abstract: In the present work, the impact of climate change on coastal flooding is investigated through a set of interoperable models developed by the authors, following a modular modelling approach and adapting the modelling sequence to two separate objectives with respect to inundation over large-scale areas and coastal protection structures' design. The modelling toolbox used includes a large-scale wave propagation model, a storm-induced circulation model, and an advanced nearshore wave propagation model based on the higher order Boussinesq-type equations, all of which are presented in detail. Model capabilities are validated and applications are made for projected scenarios of climate change-induced wave and storm surge events, simulating coastal flooding over the low-lying areas of a semi-enclosed bay and testing the effects of different structures on a typical sandy beach (both in northern Greece). This work is among the few in relevant literature that incorporate a fully non-linear wave model to a modelling system aimed at representing coastal flooding. Results highlight the capabilities of the presented modelling approach and set the basis for a comprehensive evaluation of the use of advanced modelling tools for the design of coastal protection and adaptation measures against future climatic pressures.

Keywords: climate change; coastal flooding; coastal structures; numerical modelling; Boussinesq equations

Citation: Samaras, A.G.; Karambas, T.V. Modelling the Impact of Climate Change on Coastal Flooding: Implications for Coastal Structures Design. *J. Mar. Sci. Eng.* **2021**, *9*, 1008. https://doi.org/10.3390/jmse9091008

Academic Editor: Rafael J. Bergillos

Received: 20 July 2021
Accepted: 13 September 2021
Published: 15 September 2021

1. Introduction

Climate change is expected to have significant effects on the intensity and frequency of occurrence of extreme weather events, consequently affecting sea levels, circulation patterns, currents and waves in oceans and seas around the world [1–4]. Moving from the open sea to the densely populated coastal zones, more frequent storm surges and higher waves will be experienced through a number of impacts such as beach/dune erosion and inundation of low-lying areas [5,6]. Increased flooding risks are projected to have dire effects on socioeconomic aspects at regional and global levels [7–11], thus dictating the need for effectively designed coastal protection and adaptation measures [12,13].

Coastal flooding is attributed to the combined effect of tides, surges and waves acting over a broad range of scales in space and time. As scales change, so do the interactions and relative importance of the above physical processes, with their connection growing stronger in the nearshore. There, water levels caused by tides and storm surges, combined with wave setup and onshore wave propagation, can lead to the overtopping of coastal structures and the inundation of low-lying coastal areas. This interplay between waves and water levels dictates the characteristics of the models needed for the accurate representation of related processes, while scale issues allow the use of modular modelling approaches based on varying-complexity nesting schemes and the coupling of interoperable models.

The modelling perspective of the above has been investigated over the last couple of decades by various researchers. The storm surge inundation model presented by Hubert

and McInnes [14] can be identified as setting a new paradigm in relevant literature, especially regarding the introduction of an inundation algorithm based on a novel wetting/draining scheme (for further reading on this, [15] present a concise literature review of wet/dry interface treatments in free surface flows). Sharing the fundamental modular modelling approach mentioned above, the works of [16–23] cover many different realizations of modelling systems for the simulation of coastal flooding, using various models and coupling/nesting techniques. A general modelling flowchart would indicatively include moving downscale in space and time from operational oceanography models to large scale circulation and wave generation/propagation models for coastal areas, and then to high resolution wave and hydrodynamics models in the nearshore, where wave–structure interactions and coastal inundation would be simulated. This general scheme does not exclude adding/removing simulation steps to its lower- and/or higher-resolution ends, or modifying internal model coupling, as these choices depend on data availability and the overall modelling objective. For example, if the modelling objective includes the study of climatic pressures per se, simulation steps should be added to the lower-resolution end of the aforementioned modelling flowchart in order to include a Regional Climate Model (RCM; one additional step) or a Regional Climate Model and a Global Climate Model as well (RCM + GCM; two additional steps).

Regarding the effect of coastal protection and its integration to a coastal flooding modelling system, one would have to start from the fact that the phenomenon itself is directly associated to the wave energy acting on beaches. Accordingly, the presence of coastal structures in the nearshore can significantly reduce flooding potential by reducing the wave energy reaching the shore, making such interventions a suitable countermeasure against storm-induced flooding in present and future climates. Key to the above is the transmissivity of the structure, i.e., the amount of energy transmitted over and/or through it, typically expressed in the form of a transmission coefficient $K_t = H_t/H_i$ [24], where H_i and H_t are the incident and transmitted wave heights, respectively.

Among the various available options, Low-Crested Structures (LCS) are probably the most widespread technical interventions installed for the protection of natural and artificial beaches worldwide. As such, wave transmission behind them has been extensively studied over the years. Relevant works rely on experimental datasets for the derivation of empirical formulae for K_t through various approaches, others validate or seek to extend existent formulae through experimental/numerical investigations [25–28], while an emerging research field combines data analysis with Artificial Neural Network (ANN) techniques in order to provide tools able to predict wave–structure interactions [29,30]. Regarding specifically design formulae, reference should be made to: the fundamental works of [31,32]; the work of [33], who proposed a novel formulation using as basis the theoretical treating of the physical phenomena that govern wave transmission (i.e., breaking/overtopping/energy transfer); the work of [34], who proposed a formulation based on the summation of wave energy transmitted over and through LCS (following [35] and [36], respectively), as well as the update of this last formulation by [37].

This work presents the authors' view, interpretation and implementation of a modelling system that would integrate the above aspects for practical coastal engineering applications. In the following, the impact of climate change on coastal flooding is estimated on the basis of a modular modelling approach, using three models developed by the authors and adapting the modelling sequence to two separate objectives with respect to inundation over large scale/regional areas and to coastal protection structures' design. In Section 2, the modelling approach and theoretical background of the models are presented in detail. In Section 3, the capabilities of the numerical model at the higher-resolution end of the modelling sequence, i.e., an advanced model based on the solution of the higher-order Boussinesq-type equations, are validated through comparison with the experimental data by Roeber et al. [38] (coastal flooding) and with the formulation of Goda and Ahrens [34] (wave transmission at coastal structures). In Section 4, the rationale and setup of model ap-

plications for the two objectives described above is presented. Model results are presented and discussed in Section 5, while Section 6 presents the conclusions drawn from this work.

2. Model Description

Following the rationale described in Section 1, the present work retains the viewpoint of a modular modelling approach in order to simulate storm-induced coastal flooding. The modelling toolbox used includes a large-scale wave propagation model (WAVE_LS), a storm-induced circulation model (SICIR) and an advanced nearshore wave propagation model (WAVE_BQ). Based on the analysis of the interplay between waves and water levels at different scales, the modelling sequence is adapted to fit two separate objectives. The first one, aiming at simulating flooding over large/regional coastal areas, uses WAVE_LS and SICIR. In this, WAVE_LS provides the components of the radiation stress tensor to SICIR which is afterwards used to simulate coastal flooding. The second one, aiming at investigating the effect of the presence of coastal structures in the above context, uses WAVE_BQ as well. In this, SICIR results are used as offshore boundary conditions for WAVE_BQ, which is used to simulate wave overtopping and transmission behind the structures, and wave runup on beaches.

2.1. The Large-Scale Wave Propagation Model (WAVE_LS)

WAVE_LS is based on the directional wave energy balance equation [39,40]:

$$\frac{\partial E}{\partial t} + \frac{\partial c_x E}{\partial x} + \frac{\partial c_y E}{\partial y} + \frac{\partial c_\theta E}{\partial \theta} = -D \tag{1}$$

where $E(f,\theta \mid x,y,t)$ is the spectral density of frequency f and direction θ at a point (x,y) and time t; and c_x, c_y, c_θ are the x, y, θ components of the group velocity c_g, respectively, according to:

$$\begin{aligned} c_x &= c_g \sin\theta \\ c_x &= c_g \cos\theta \\ c_\theta &= -\frac{c_g}{c}\left(\cos\theta \ \frac{\partial c}{\partial x} - \sin\theta \ \frac{\partial c}{\partial y}\right) \end{aligned} \tag{2}$$

In Equation (2), c is the wave celerity. In Equation (1), D is the dissipation of wave energy expressed as:

$$D = \frac{1}{4} Q_b f \rho g H_m^2 \tag{3}$$

where H_m is the maximum wave height according to [41]; ρ is the water density; and Q_b is the probability of a wave breaking at a certain depth, expressed as $(1 - Q_b)/(\ln Q_b) = (H_{rms}/H_m)^2$ according to [42], where H_{rms} is the root-mean-square wave height. Wave diffraction is incorporated to the model by replacing c_x, c_y and c_θ with C_x, C_y and C_θ according to [40]:

$$\begin{aligned} C_x &= c_g \sin\theta \sqrt{(1+\delta)} \\ C_x &= c_g \cos\theta \sqrt{(1+\delta)} \\ C_\theta &= \frac{c_g}{c}\left(-\cos\theta \frac{\partial c}{\partial x} + \sin\theta \frac{\partial c}{\partial y}\right)\sqrt{1+\delta} + \frac{1}{2\sqrt{1+\delta}} c_g \left(-\cos\theta \frac{\partial \delta}{\partial x} + \sin\theta \frac{\partial \delta}{\partial y}\right) \end{aligned} \tag{4}$$

where κ is the wave number and δ is expressed as:

$$\delta = \frac{\nabla.\left(c c_g \nabla\sqrt{E}\right)}{\kappa^2 c c_g \sqrt{E}} \tag{5}$$

The model is capable of simulating wave propagation in large coastal areas with complicated bathymetries, describing the phenomena of refraction, bottom diffraction and breaking. The numerical solution of Equation (1) is based on an implicit finite difference scheme and the model's output includes the four components of the radiation stress tensor

(*Sxx*, *Syy*, *Sxy* = *Syx*), calculated by the well-known expressions valid for progressive waves, as in [43].

2.2. The Storm-Induced Circulation Model (SICIR)

The storm-induced circulation model is based on the depth-averaged wind-induced circulation equations, following [44]:

$$\frac{\partial \overline{\zeta}}{\partial t} + \frac{\partial (Uh)}{\partial x} + \frac{\partial (Vh)}{\partial y} = 0 \tag{6}$$

$$\frac{\partial U}{\partial t} + U\frac{\partial U}{\partial x} + V\frac{\partial U}{\partial y} + g\frac{\partial \overline{\zeta}}{\partial x} = -\frac{1}{\rho h}\left(\frac{\partial S_{xx}}{\partial x} + \frac{\partial S_{xy}}{\partial y}\right) + \frac{1}{h}\frac{\partial}{\partial x}\left(\nu_h h\frac{\partial U}{\partial x}\right) + \frac{1}{h}\frac{\partial}{\partial y}\left(\nu_h h\frac{\partial U}{\partial y}\right) + f_c V + \frac{\tau_{sx}}{\rho h} - \frac{\tau_{bx}}{\rho h} \tag{7}$$

$$\frac{\partial V}{\partial t} + U\frac{\partial V}{\partial x} + V\frac{\partial V}{\partial y} + g\frac{\partial \overline{\zeta}}{\partial y} = -\frac{1}{\rho h}\left(\frac{\partial S_{xy}}{\partial x} + \frac{\partial S_{yy}}{\partial y}\right) + \frac{1}{h}\frac{\partial}{\partial x}\left(\nu_h h\frac{\partial V}{\partial x}\right) + \frac{1}{h}\frac{\partial}{\partial y}\left(\nu_h h\frac{\partial V}{\partial y}\right) - f_c U + \frac{\tau_{sy}}{\rho h} - \frac{\tau_{by}}{\rho h} \tag{8}$$

where $\overline{\zeta}$ is the water surface elevation above the mean water level; d is the still water depth; h is the total water depth ($h = d + \overline{\zeta}$); U, V are the depth-averaged velocity components along the x- and y- directions respectively; g is the gravitational acceleration; ν_h is the horizontal eddy viscosity coefficient and f_c is the Coriolis coefficient. The terms τ_{sx}, τ_{sy} are the shear stress components at the water surface along the x- and y- directions respectively, which represent the vertical boundary condition, expressed as:

$$\tau_{sx} = \rho k W_x \sqrt{W_x^2 + W_y^2} \tag{9}$$

$$\tau_{sy} = \rho k W_y \sqrt{W_x^2 + W_y^2} \tag{10}$$

where k is the surface friction coefficient (in kg/m^3, typically of the order of 10^{-6}; here we assume $k = 10^{-6} \div 3{\cdot}10^{-6}$), and W_x, W_y are the wind speed components along the x- and y- directions (in m/s, at 10 m above sea level) respectively. The bed friction terms (τ_{bx}, τ_{by}) are calculated based on the formulae proposed by [45]:

$$\tau_{bx} = \frac{1}{2}\rho f_b \sigma_T^2 G_{bx} \tag{11}$$

$$\tau_{by} = \frac{1}{2}\rho f_b \sigma_T^2 G_{by} \tag{12}$$

$$G_{bx} = \frac{U}{\sigma_T}\left[1.16^2 + \left(\frac{|\mathrm{U}|}{\sigma_T}\right)^2\right]^{0.5} \tag{13}$$

$$G_{by} = \frac{V}{\sigma_T}\left[1.16^2 + \left(\frac{|\mathrm{U}|}{\sigma_T}\right)^2\right]^{0.5} \tag{14}$$

where f_b is the bottom friction factor, σ_T is the standard deviation of the oscillatory horizontal velocity, and $|\mathrm{U}| = (U^2 + V^2)^{0.5}$. The horizontal eddy viscosity coefficient is expressed by the well-known Smagorinsky model, used for the representation of the damping by eddies smaller than the computational grid size, as:

$$\nu_h = \ell^2\left[\left(\frac{\partial U}{\partial x}\right)^2 + \left(\frac{\partial V}{\partial y}\right)^2 + \frac{1}{2}\left(\frac{\partial U}{\partial y} + \frac{\partial V}{\partial x}\right)^2\right]^{1/2} \tag{15}$$

where ℓ is the mixing length, approximated as equal to half the grid cell size dx [46].

Differential Equations (6)–(8) are approximated by finite difference equations according to the explicit scheme developed by [44]. Finally, regarding coastal inundation, the

process is simulated using the "dry bed" boundary condition which, according to [47], can be written as the following set of pairs of conditions for any given grid point (*i,j*):

$$\begin{array}{l} \text{if } (d+\zeta)_{i,j} > h_{cr} \text{ and } (d+\zeta)_{i-1,j} \le h_{cr} \text{ and } U_{i,j} > 0 \to U_{i,j} = 0 \\ \text{if } (d+\zeta)_{i,j} > h_{cr} \text{ and } (d+\zeta)_{i,j-1} \le h_{cr} \text{ and } V_{i,j} > 0 \to V_{i,j} = 0 \\ \text{if } (d+\zeta)_{i,j} \le h_{cr} \text{ and } (d+\zeta)_{i-1,j} \le h_{cr} \to U_{i,j} = 0 \\ \text{if } (d+\zeta)_{i,j} \le h_{cr} \text{ and } (d+\zeta)_{i,j-1} \le h_{cr} \to V_{i,j} = 0 \\ \text{if } (d+\zeta)_{i,j} \le h_{cr} \text{ and } (d+\zeta)_{i-1,j} > h_{cr} \text{ and } U_{i,j} < 0 \to U_{i,j} = 0 \\ \text{if } (d+\zeta)_{i,j} \le h_{cr} \text{ and } (d+\zeta)_{i,j-1} > h_{cr} \text{ and } V_{i,j} < 0 \to V_{i,j} = 0 \end{array} \quad (16)$$

where h_{cr} is a terminal depth below which drying is assumed to occur (here this depth is set to h_{cr} = 0.001 m).

2.3. The Advanced Nearshore Wave Propagation Model (WAVE_BQ)

Over the years, the classical Boussinesq equations have been extended by incorporating higher order non-linear terms, which can describe better the propagation of highly nonlinear waves in the shoaling zone. Nowadays, models based on Boussinesq-type equations (BTEs) are widely used to simulate waves transforming in the nearshore—up to the swash zone—and their interactions with various types of coastal protection. Exemplary reference is made to the recent works of [48–53], with [54] presenting a novel meshless numerical scheme for the solution of BTEs. A thorough overview of Boussinesq-type models can be found in [55].

WAVE_BQ is based on the higher order Boussinesq-type equations for breaking and nonbreaking waves as expressed in equations:

$$\zeta_t + \nabla(h\mathbf{U}) = 0 \quad (17)$$

$$\mathbf{U}_t + \frac{1}{h}\nabla\mathbf{M_u} - \frac{1}{h}\mathbf{U}\nabla(\mathbf{U}h) + g\nabla\zeta + G = \frac{1}{2}h\nabla[\nabla\cdot(d\mathbf{U}_t)] - \frac{1}{6}h^2\nabla[\nabla\cdot\mathbf{U}_t] + \frac{1}{30}d^2\nabla[\nabla\cdot(\mathbf{U}_t + g\nabla\zeta)] + \frac{1}{30}\nabla\left[\nabla\cdot\left(d^2\mathbf{U}_t + gd^2\nabla\zeta\right)\right] - d\nabla(\delta\nabla\cdot\mathbf{U})t - \frac{\boldsymbol{\tau}_b}{h} + \mathbf{E} \quad (18)$$

where $\mathbf{M_u}$ is defined as:

$$\mathbf{M_u} = (d+\zeta)\mathbf{u_o^2} + \delta\left(c^2 - \mathbf{u_o^2}\right) \quad (19)$$

and *G* as:

$$G = \frac{1}{3}\nabla\left\{d^2\left[(\nabla\cdot\mathbf{U})^2 - \mathbf{U}\cdot\nabla^2\mathbf{U} - \frac{1}{10}\nabla^2(\mathbf{U}\cdot\mathbf{U})\right]\right\} - \frac{1}{2}\zeta\nabla[\nabla\cdot(d\mathbf{U}_t)] \quad (20)$$

where ζ is the wave surface elevation; the subscript "t" denotes differentiation with respect to time; **U** is the horizontal velocity vector **U** = (U,V); $\boldsymbol{\tau_b} = (\tau_{bx}, \tau_{by})$ is calculated from Equations (11) and (12), with the wave-current bottom friction factor calculated as in [56]; δ is the roller thickness, determined geometrically according to [57]; **E** is the eddy viscosity term, calculated according to [58]; and $\mathbf{u_o}$ is the bottom velocity vector $\mathbf{u_o} = (u_o, v_o)$, with u_o and v_o being the instantaneous bottom velocities along the *x*- and *y*- directions respectively. Following [56], wave breaking is initiated using breaking angle $\varphi_b = 30^\circ$, which then gradually changes to its terminal value $\varphi_b = 10^\circ$.

The presented set of BTEs is accurate to the third order $O(\varepsilon^2,\varepsilon\sigma^2,\sigma^4)$ [59] and their numerical solution is based on the accurate higher-order numerical scheme of [60]. Coastal inundation is simulated as in SICIR (see Section 2.2, Equation (16) and [47]). The model is capable of simulating the phenomena of shoaling, refraction, breaking, diffraction, reflection and wave-structure interaction, as well as nonlinear wave-wave interaction. Regarding model capabilities in simulating the non-linear evolution of unidirectional or multidirectional wave fields in the nearshore, one can refer to [61] (see also [62] on the issue); regarding wave-structure interaction and energy transmission, one can refer to [63]. Further details on the model and its implementation to diverse coastal engineering applications can be found in [56,64,65].

3. Model Validation

3.1. Coastal Flooding

The capability of the presented advanced nearshore wave propagation model in the representation of coastal flooding is validated through the comparison with the two-dimensional (cross-shore) experimental data by [38]. Roeber et al. [38] tested wave transformation over idealized fringing reefs, carrying out a series of experiments in two flumes at the O.H. Hinsdale Wave Research Laboratory of Oregon State University. The first flume was 48.8 m long, 2.16 m wide and 2.1 m high; the second flume was 104.0 m long, 3.66 m wide and 4.57 m high with a reef crest. Both flumes were equipped with piston-type wavemakers for wave generation and resistance wave gauges for free surface measurement.

The experimental setup in the first flume included a steep 1:5 slope starting at x = 17.0 m, followed by a reef flat up to the flume's rigid wall at x = 45.0 m (x being the direction along the flume). The test in this flume regarded a steep solitary wave of A = 0.5 m height and a water depth of d = 1.0 m, resulting in A/d = 0.5 and an initially dry reef flat. The discretization steps used in model (WAVE_BQ) runs were dx = 0.05 m in space and dt = 0.0025 s in time. Figure 1 shows the comparison between measurements and model results for this test, as a series of snapshots of surface profile evolution. Measured and computed data are in very good agreement at all transformation stages. The model successfully captures the wave's skewness as it propagates across the toe of the slope, the formation of its steep front over the steep slope, and its eventual flow transition from sub- to super-critical as it surges over the reef flat.

The experimental setup in the second flume included a fore reef slope of 1:12 starting at x = 25.9 m, a 0.2 m reef crest and a reef flat behind it up to the flume's rigid wall at x = 83.7 m (x being the direction along the flume). The test in this flume regarded a steep solitary wave of A = 0.75 m height and a water depth of d = 2.5 m (A/d = 0.3), initially exposing the aforementioned reef crest by 0.06 m and submerging the reef flat with 0.14 m of water. The discretization steps used in model (WAVE_BQ) runs were, again, dx = 0.05 m in space and dt = 0.0025 s in time. Figure 2 shows the comparison between measurements and model results for this test, as a series of snapshots of surface profile evolution. Again, as for the first test, measured and computed data are in very good agreement at all transformation stages. The model successfully captures wave shoaling over the relatively gentle slope, wave breaking on top of the reef crest, as well as the propagation of the wave bore (clearly identified by the bore front) over the reef flat.

3.2. Wave Transmission at Coastal Structures

Following the rationale presented in Section 1, coastal structures design is treated in this work as a means to countermeasure storm-induced flooding in present and future climates. With the focus set on the transmissivity of low-crested structures, the capability of the presented advanced nearshore wave propagation model in the representation of wave energy reduction behind LCS is validated through comparison with the formulation presented by Goda and Ahrens [34] for K_t. Furthermore, and considering that due to the interplay between wave overtopping and wave infiltration energy reduction is expected to be lower behind impermeable structures than behind permeable ones, the former type of LCS is examined in this work so as to test the lower bound of their effectiveness.

The work of Goda and Ahrens [34] was based on the concept of the summation of wave energy transmitted over and through LCS. The processes were treated separately and two separate transmission coefficients were proposed, namely $K_{t,over}$ and $K_{t,thru}$, respectively, with the summation concept applied for the derivation of K_t using the approach of [66]. The formulation was validated using a versatile set of experimental datasets (851 tests in total), yielding a determination coefficient of r^2 = 0.865.

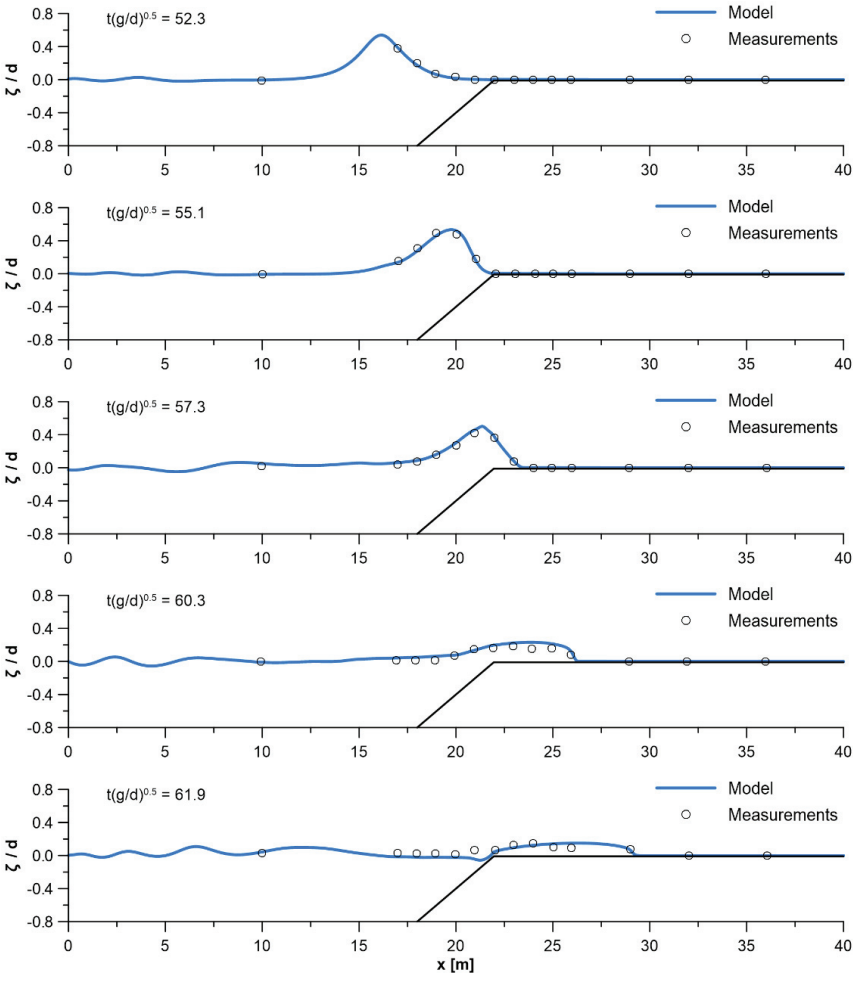

Figure 1. Surface profiles of solitary wave transformation over a dry reef flat with A/d = 0.5 and a 1:5 slope. Solid lines denote the results of the presented advanced nearshore wave propagation model (see Section 2.3) and circles denote the measurements of [38].

According to [34] K_t for impermeable structures reduces to $K_{t,over}$, which was estimated through empirical fitting to the design diagram of [35] and can be expressed as:

$$K_{t,over} = \max\left\{0, \left(1 - \exp\left[a\left(\frac{R_c}{H_i} - 1\right)\right]\right)\right\} \quad (21)$$

where R_c is the crest freeboard and a is expressed as:

$$a = 0.248 \exp\left[-0.384 \ln\left(\frac{B_{eff}}{L_0}\right)\right] \quad (22)$$

In Equation (22) L_0 is the deep water wavelength and B_{eff} is the effective width of the structure, measured at still water level for emerged structures, at the level of 10% below the crest for zero freeboard structures and at the level of 20% below the crest for submerged structures [34].

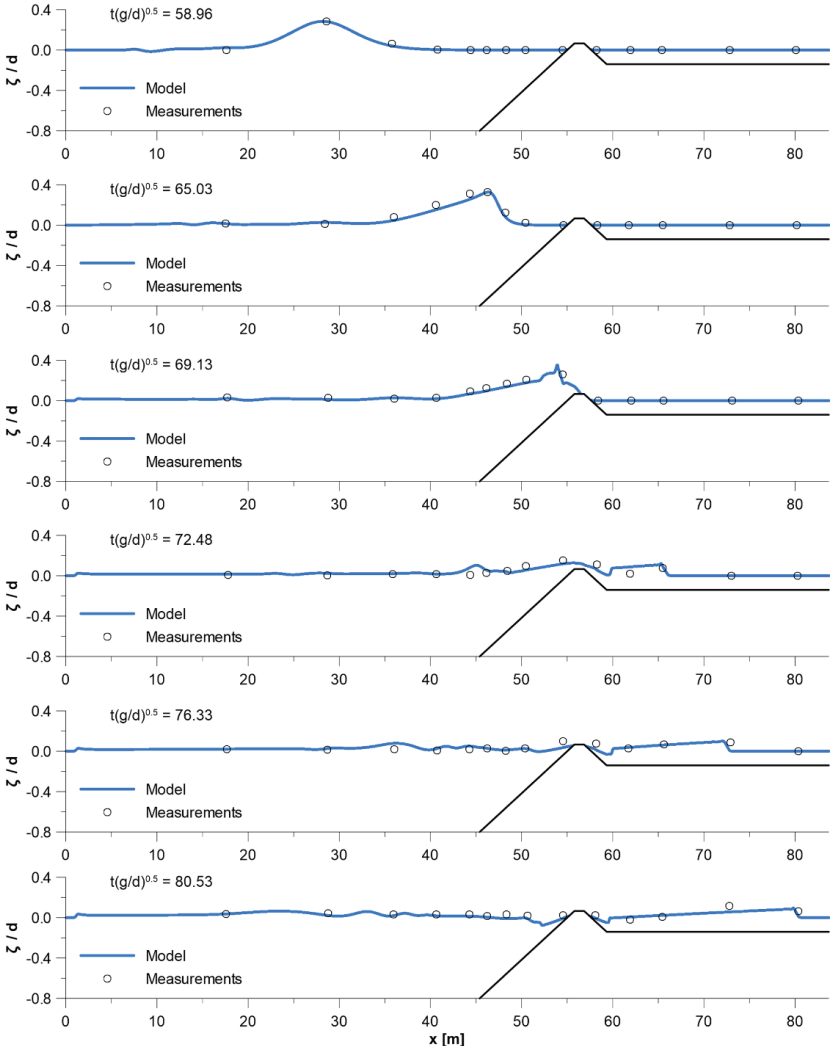

Figure 2. Surface profiles of solitary wave transformation over an exposed reef crest with A/d = 0.3 and a 1:12 slope. Solid lines denote the results of the presented advanced nearshore wave propagation model (see Section 2.3) and circles denote the measurements of [38].

Figure 3 shows a sketch of the governing parameters involved in wave transmission at emerged LCS. These are: the incident and transmitted significant wave height, H_i and H_t; the peak period T_p; the wave steepness $s_{op} = 2\pi H_i/g(T_p)^2$; the crest freeboard and width, R_c and B; the structure height and seaward slope, h_c and $tan\alpha$; and the breaker parameter $\xi_{op} = \tan\alpha/(s_{op})^{0.5}$. Model runs were performed for the series of input parameters presented in Table 1 testing combinations of two incident waves and four different crest freeboards, which resulted in relative freeboards R_c/H_i ranging from 0.13 to 1.00 and relative effective structure widths B_{eff}/L_0 ranging from 0.075 to 0.150 ($tan\alpha$ = 0.4 for all runs). The discretization steps used in model (WAVE_BQ) runs were dx = 0.125 m in space and dt = 0.005 s in time. Figure 4 shows the comparison between K_t values as estimated using Equation (21) and as resulted from model runs, for the Tests of Table 1. Data are in good agreement overall, with Test 4 representing a liming case that results in K_t = 0. The model

generally predicts lower transmission coefficients than Equation (21). The divergences are mainly observed for higher waves and lower relative freeboard values, a result that is expected considering the concept behind the formulation of [34] and the physics behind the phenomenon.

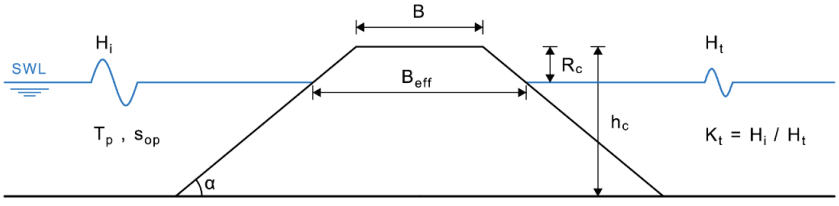

Figure 3. Governing parameters involved in wave transmission at emerged low-crested structures (LCS).

Table 1. Values of the parameters in the wave transmission Tests (s_{op} = wave steepness; $tan\alpha$ = slope; ξ_{op} = breaker parameter; R_c/H_i = relative freeboard; B/H_i = relative crest width; B_{eff}/L_0 = relative effective structure width).

Test	s_{op}	$tan\alpha$	ξ_{op}	R_c/H_i	B/H_i	B_{eff}/L_0
1	0.02	0.4	2.83	0.25	2.5	0.075
2				0.50		0.100
3				0.75		0.125
4				1.00		0.150
5	0.04	0.4	2.00	0.13	1.3	0.075
6				0.25		0.100
7				0.38		0.125
8				0.50		0.150

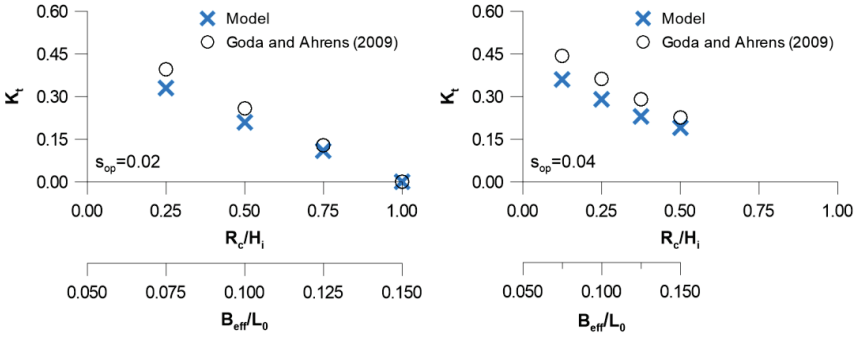

Figure 4. Wave transmission at emerged LCS: comparison between between K_t values as estimated following [34] and as resulted from the presented advanced nearshore wave propagation model runs (see Section 2.3).

4. Model Applications

4.1. Large-Scale Applications

The modelling approach for the simulation of flooding over large/regional coastal areas, as presented in Section 2, was applied to the area of the Bay of Thessaloniki, i.e., the northern part of the Thermaikos Gulf, located in the northwestern Aegean Sea, Greece. Thessaloniki is the second largest city in Greece, with a population of approx. 1 million people residing in its metropolitan area. The Port of Thessaloniki is also the second largest in the country, handling a total throughput of approx. 13 million tonnes per year and

more than 400,000 containers/TEUs (2018 data; [67]). Two terminals are located west of the Port's 6th pier, both of significant regional importance. The AGET terminal, whose cement and cement products production and handling facilities include a jetty that extends approximately 600 m into the sea; and the Liquid Fuels Terminal, whose facilities include and offshore jetty located at approximately 800 m from the coast. Figure 5 shows the geographic location and a satellite image of the study area; the six piers of the Port of Thessaloniki are identified, along with the location of the aforementioned facilities.

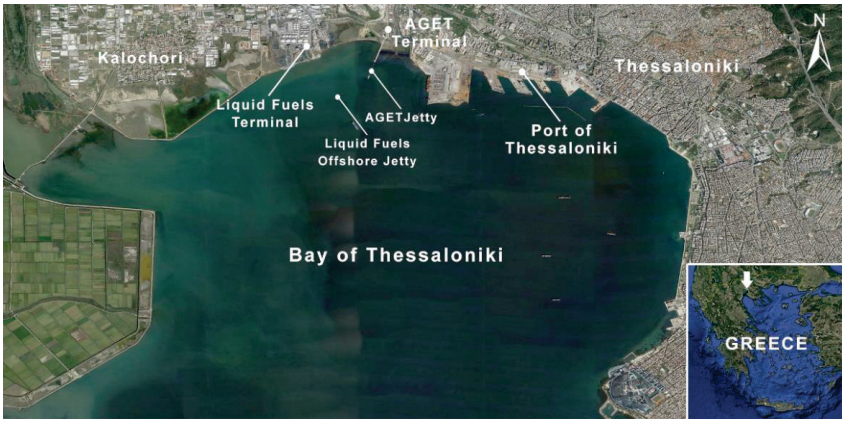

Figure 5. Geographic location and satellite image of the study area ([68]; privately processed).

The model domain was bounded to the south by the virtual East–West line connecting the Mikro Emvolo Cape to the western coast of the Bay (see Figure 6). The intermittently dry/wet area at the western part of the Bay (green dotted area in Figure 6) was modelled as a dry flat for the scenarios run in this work; this is justified by the consideration that the specific area—even when wet at highest tide—is covered by no more than a few centimetres of water (it is noted that small topographic variations over the flat do exist). The domain also included the projected final geometry of the 6th pier of the Port of Thessaloniki (grey crossed area in Figure 6), while it should also be noted that the artificial coast of the Bay of Thessaloniki (Port of Thessaloniki and waterfront eastwards of the Port up to the Mikro Emvolo Cape) was modelled as a solid boundary (i.e., no flooding allowed). This choice served the applications' computational efficiency, as the waves and storm surges expected in the study area (see Table 2 in the following) are covered by the design of the Port's piers and the waterfront's seawalls. The bathymetric data were extracted from digitized nautical charts acquired from the Hellenic Navy Hydrographic Service, while the topographic information was extracted by Digital Elevation Models of the NASA Shuttle Radar Topography Mission, acquired through AppEEARS [69,70].

Table 2. Scenarios used for the large-scale applications.

Scenario	Wave			Storm Surge
	H_s (m)	T_p (s)	*Dir* (deg)	*SSH* (m)
LS1	1.58	4.60	0	-
LS2	1.58	4.60	0	0.30

The models were run for two scenarios of climate change-induced wave and storm surge events, representative for the study area, based on the results and analysis presented by [71]. The first scenario (henceforth denoted by *LS1*) envisaged a southern wave of significant wave height H_s = 1.58 m and peak period T_p = 4.60 s. The second scenario

(*LS2*) envisaged the same wave combined with a storm surge of height *SSH* = 0.30 m (see Table 2). The discretization steps used in model runs were dx = 10.0 m in space and dt = 0.05 s in time for WAVE_LS, and dx = 10.0 m in space and dt = 0.125 s in time for SICIR. It should be noted that dx in large-scale wave propagation models is generally of the order of a wavelength L or less [39,40]. However, the choice of dx also depends on bathymetry and model domain characteristics; rapid bathymetric changes or diffraction effects would require smaller values, such as $dx = L/5$ [40]. In a modular modelling approach, the spatial step of the circulation model would have to be the same as previously selected due to model interoperability. Finally, the temporal step dt is controlled by the Courant number criterion $Cr < 1$ ($Cr = cdt/dx$, where $c = (gh)^{1/2}$). In this work, the choices for the spatial and temporal discretization of WAVE_LS and SICIR followed the above rules.

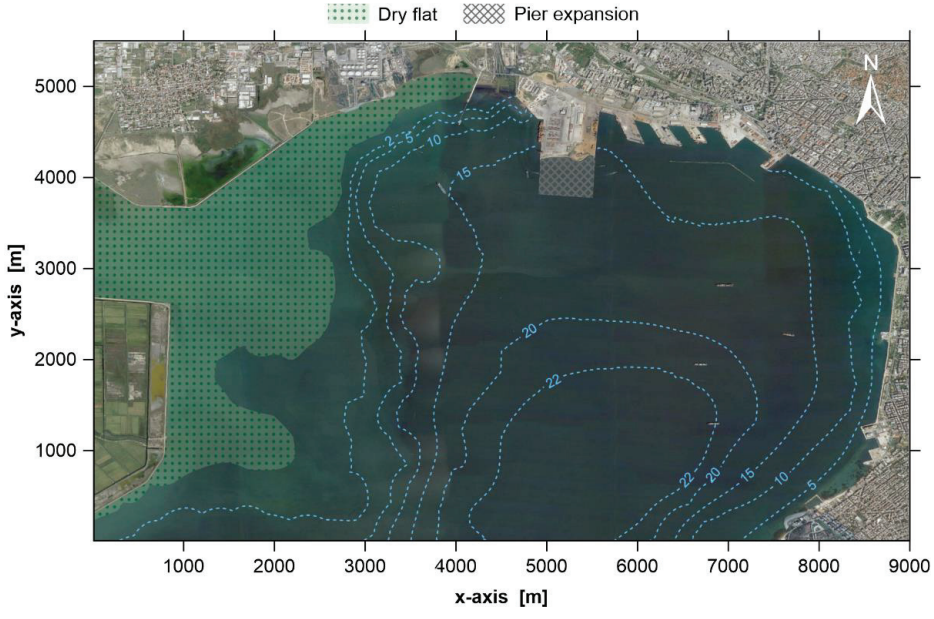

Figure 6. Model domain and bathymetry (background image from [68]; privately processed).

4.2. Applications for Coastal Structures Design Evaluation

The modelling approach for the investigation of the effect of coastal structures on flooding, as presented in Section 2, was applied to a typical sandy beach located in the East Macedonia and Thrace Region (northern Greece; see Figure 7). The low-lying coastal areas in the region are not densely populated (the coastal cities Kavala and Alexandroupoli do not compare to the size of Thessaloniki), but do host numerous touristic activities and sites of significant ecological importance (Nestos Delta, Lakes Vistonida and Ismarida wetlands). Furthermore, they are exposed to larger waves in both present and future climates, making them more susceptible to coastal flooding.

Table 3 presents the layouts of the selected beach tested using the advanced nearshore wave propagation model (layouts and profile are presented in Section 5.2). The layouts include one of the unprotected beach, one of the beach protected by a breakwater, and one of the beach protected by a sea dike (henceforth denoted by *L1*, *L2* and *L3*, respectively). The models were run for two scenarios of climate change- induced wave and storm surge events, representative for the study area, based on the results and analysis presented by [71]. The first scenario (henceforth denoted by *CS1*) envisaged a southern wave of significant wave height H_s = 5.0 m and peak period T_p = 8.0 s. The second scenario (*CS2*) envisaged

the same wave combined with a storm surge of height SSH = 0.30 m (see Table 4). The discretization steps used in model runs were dx = 0.125 m in space and dt = 0.005 s in time for WAVE_BQ (see Section 4.1 for WAVE_LS and SICIR).

Figure 7. Geographic location and satellite image of the East Macedonia and Thrace Region ([68]; privately processed).

Table 3. Layouts used for the applications for coastal structures design evaluation.

Layout	Structure Characteristics			
	Type	$tan\alpha$ (-)	B (m)	R_c [1] (m)
L1	Unprotected beach			
L2	LCS	0.4	5.0	1.0
L3	Dike	0.2	-	2.0

[1] Measured from SWL.

Table 4. Scenarios used for the applications for coastal structures design evaluation.

Scenario	Wave			Storm Surge
	H_s (m)	T_p (s)	Dir (deg)	SSH (m)
CS1	5.0	8.0	0	-
CS2	5.0	8.0	0	0.30

5. Results and Discussion

5.1. Large-Scale Applications

Figure 8a shows model results for scenario *LS1*, indicating the flooded area at the western coast of the Bay of Thessaloniki; Figure 8b shows the respective results for *LS2*. The models performed satisfactorily in both cases, resulting in smooth flooding contours that follow the modelled topography (it can be noted again that small topographic variations over the flat existed). For scenario *LS1* the flooded area mainly covers parts of the aforementioned dry flat, with the flooded area approximately equal to 1.2 km^2. For scenario *LS2* the flooding extends to the low-lying coastal areas west of the port's 6th pier as well, with the flooded area approximately equal to 2.7 km^2 (increase of approximately 125%). The AGET Terminal appears to be mostly impacted in the case of *LS2*, while impacts on the operations of both the AGET and liquid fuels jetties are to be expected in either scenario.

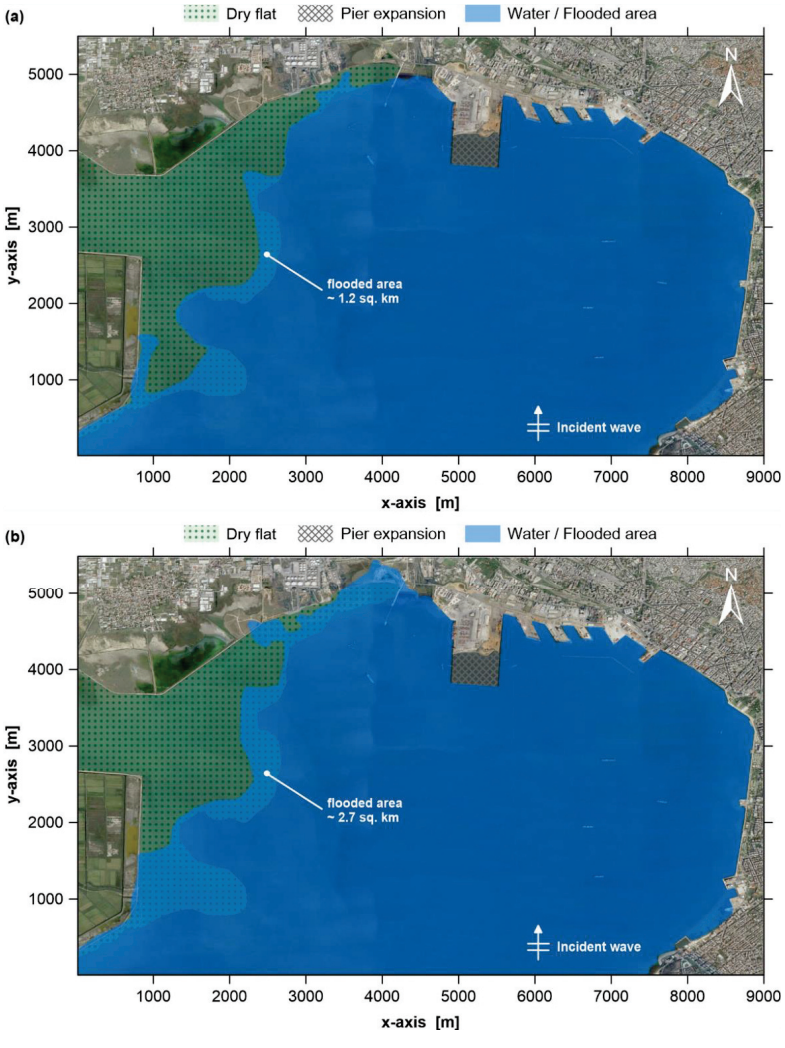

Figure 8. Model results indicating the flooded area for scenarios: (**a**) *LS1* and (**b**) *LS2* (background image from [68]; privately processed).

Results are indicative of the models capabilities and the potential effects coastal flooding would have on the low-lying areas and operational facilities of coastal cities. Considering that Thessaloniki is located in a relatively protected bay where waves and storm surges are expected to be moderate (as reflected in the selected scenarios in Table 1), it is reasonable to expect more severe flooding in cities exposed to higher storm events, where the overtopping of coastal defence will result in flooding of the urban fabric as well.

5.2. Applications for Coastal Structures Design Evaluation

Figure 9 shows model results for the six combinations of layouts and scenarios presented in Section 4.2 (see Tables 3 and 4), as snapshots of surface profile evolution at times T and $T + T/2$. In Figure 9, coloured "x" symbols denote the landward limit of the flooding extent; this information, expressed as horizontal distance, is comparatively presented for all tests in Figure 10.

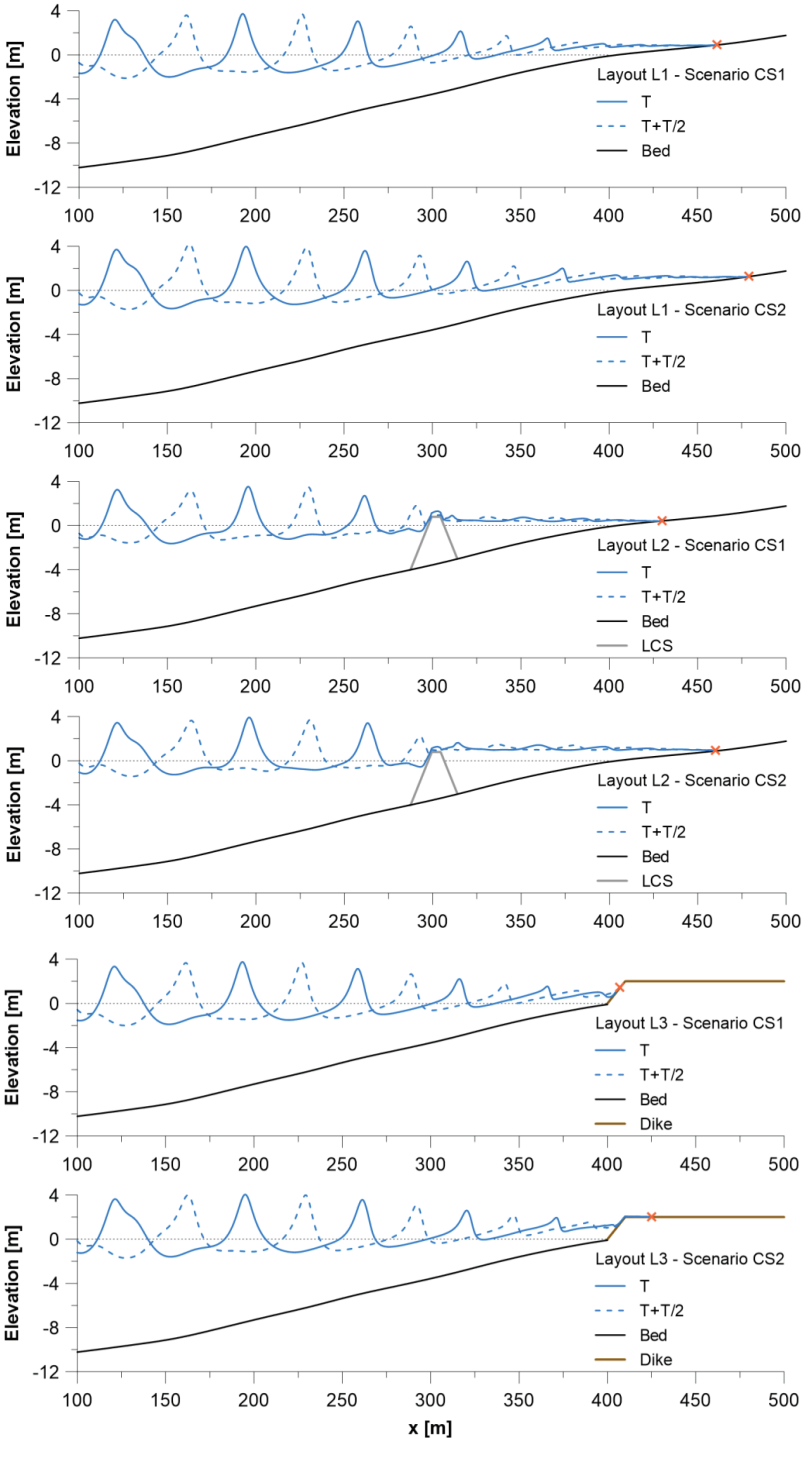

Figure 9. Model results for the combinations of layouts *L1*, *L2*, *L3* and scenarios *CS1* and *CS2*. Coloured "x" symbols denote the landward limit of the flooding extent.

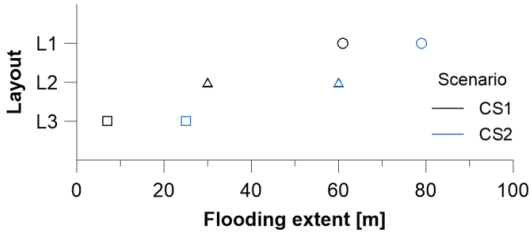

Figure 10. Flooding extent for the combinations of layouts *L1*, *L2*, *L3* and scenarios *CS1* and *CS2*. Flooding extent is measured from the shoreline at SWL (horizontal distance).

As expected, the unprotected beach layout (*L1*) results in the highest flooding, with storm surge causing an increase in flooding extent by approximately 30% (+18 m). The LCS layout (*L2*) protects the beach quite satisfactorily for *SC1* despite the quite low relative freeboard of the structure (see Tables 3 and 4), reducing the flooding extent by approximately 51% with respect to *L1* (−31 m). However, the addition of storm surge in *SC2* practically reduces the emerged crest height and thus cancels a large part of the protection provided by the LCS, resulting in a flooding extent that is increased by approximately 50% (+30 m). It is worth noting that flooding for *L2-CS2* is quite close to that of the unprotected beach with no storm surge (*L1-CS1*), a useful insight for the design of LCS in a changing climate. Finally, the Dike layout (*L3*) results in the lowest flooding extent, not exceeding 7 m for *CS1* (i.e., a reduction of approximately 89% with respect to *L1* and of approximately 77% with respect to *L2*). For *SC2*, however, the flooding extent more than triples as the wave runs up the slope, reaches the crest of the dike, and propagates inland over the flat. It can be noted that the flat is covered by no more than a few centimetres of water in this test and the flooding extent is still smaller even from *L2-SC1*; nevertheless, this result is indicative of the function of such structures when facing combinations of increased waves and water levels.

5.3. General Discussion

Elaborating further on the presented modelling system's performance in simulating coastal flooding, particular insights can be drawn from the following.

Model setup was based on the successful model validation for the representation of coastal flooding and wave transmission at coastal structures, as presented in Sections 3.1 and 3.2. The satisfactory agreement between model predictions, experimental data and a well-known formulation supported the implementation of the proposed modelling approach to the set of applications presented in Sections 4.1 and 4.2. These were designed in order to fit two separate modelling objectives, testing all three models of the modelling toolbox and exploring all aspects that are deemed to distinguish this work in relevant literature: (a) the incorporation of an advanced nearshore wave propagation model in the modelling sequence; (b) the accurate representation of the inundation process through the "dry bed" boundary condition; and (c) the capability to test the effect of coastal protection on coastal flooding by simulating wave overtopping and transmission at coastal structures.

The results presented in Sections 5.1 and 5.2 are indicative of the models' capabilities, while highlighting the need and importance of relevant works for coastal cities with exposed coastal facilities, as well as for other low-lying coastal areas of ecological, cultural or touristic importance. Future work can explore the limitations of the modelling approach presented by investigating three-dimensional wave–structure interactions and their impact on the identification of flooded areas; work on the same path can also extend to investigate coastal flooding of the urban fabric and combine flooding extent results with damage cost models (e.g., [72,73]).

6. Conclusions

Coastal flooding is on the rise in many areas around the world. The risk of coastal flooding is expected to further increase in the future, as tides, surges and waves will be significantly affected by climate change and the consequent increase of extreme weather events. Numerical modelling can be used to capture the interplay between waves and water levels acting over a broad range of scales in space and time, with relevant modelling systems producing results of direct use for effective design of coastal protection and adaptation measures.

This work presents an in-house, versatile tool for the representation of coastal flooding, which follows a modular modelling approach and consists of three models: a large-scale wave propagation model, a storm-induced circulation model and an advanced nearshore wave propagation model based on the higher order Boussinesq-type equations for breaking and non-breaking waves. The numerical model at the higher-resolution end of the modelling sequence is validated through comparison with the experimental data by Roeber et al. [38] (coastal flooding) and with the formulation of Goda and Ahrens [34] (wave transmission at coastal structures), performing very well for all tests. The proposed modelling approach was applied to simulate coastal flooding: (a) over the low-lying areas of the Bay of Thessaloniki, a semi-enclosed bay located in northern Greece that hosts a major coastal city and significant economic activities; and (b) on a typical sandy beach of the East Macedonia and Thrace Region (also in northern Greece), testing two layouts of coastal protection structures in order to evaluate their effectiveness. Applications for both cases were made for projected scenarios of climate change-induced wave and storm surge events, representative of the respective study areas. Results highlighted the potential effects coastal flooding would have on the low-lying areas and operational facilities of coastal cities, as well as the function of typical coastal protection structures in the above context.

This paper is among the few in relevant literature that incorporate an advanced wave model to a modelling system aimed at representing coastal flooding, along with the accurate representation of the inundation process through a straightforward boundary condition and the capability to test different layouts in order to assess the effect of coastal protection. Drawing insights from the full body of work presented here and relevant literature, this study is considered as a solid example of how the use of advanced modelling tools can facilitate strategic planning and adaptation in coastal areas, shaping the pathways towards a successful response to climate change.

Author Contributions: Conceptualization, methodology, model development, model validation, model applications, formal analysis, visualization, writing, A.G.S. and T.V.K. Both authors have read and agreed to the published version of the manuscript.

Funding: This research received no external funding.

Institutional Review Board Statement: Not applicable.

Informed Consent Statement: Not applicable.

Data Availability Statement: Data is contained within the article.

Conflicts of Interest: The authors declare no conflict of interest.

References

1. Mentaschi, L.; Vousdoukas, M.I.; Voukouvalas, E.; Dosio, A.; Feyen, L. Global changes of extreme coastal wave energy fluxes triggered by intensified teleconnection patterns. *Geophys. Res. Lett.* **2017**, *44*, 2416–2426. [CrossRef]
2. Vousdoukas, M.I.; Mentaschi, L.; Voukouvalas, E.; Verlaan, M.; Feyen, L. Extreme sea levels on the rise along Europe's coasts. *Earth's Future* **2017**, *5*, 304–323. [CrossRef]
3. Lobeto, H.; Menendez, M.; Losada, I.J. Future behavior of wind wave extremes due to climate change. *Sci. Rep.* **2021**, *11*, 7869. [CrossRef] [PubMed]
4. Coelho, C.; Silva, R.; Veloso-Gomes, F.; Taveira-Pinto, F. Potential effects of climate change on northwest Portuguese coastal zones. *ICES J. Mar. Sci.* **2009**, *66*, 1497–1507. [CrossRef]

5. O'Grady, J.G.; Hemer, M.A.; McInnes, K.L.; Trenham, C.E.; Stephenson, A.G. Projected incremental changes to extreme wind-driven wave heights for the twenty-first century. *Sci. Rep.* **2021**, *11*, 8826. [CrossRef] [PubMed]
6. Kirezci, E.; Young, I.R.; Ranasinghe, R.; Muis, S.; Nicholls, R.J.; Lincke, D.; Hinkel, J. Projections of global-scale extreme sea levels and resulting episodic coastal flooding over the 21st Century. *Sci. Rep.* **2020**, *10*, 11629. [CrossRef] [PubMed]
7. Bosello, F.; Nicholls, R.J.; Richards, J.; Roson, R.; Tol, R.S.J. Economic impacts of climate change in Europe: Sea-level rise. *Clim. Chang.* **2012**, *112*, 63–81. [CrossRef]
8. Hanson, S.; Nicholls, R.; Ranger, N.; Hallegatte, S.; Corfee-Morlot, J.; Herweijer, C.; Chateau, J. A global ranking of port cities with high exposure to climate extremes. *Clim. Chang.* **2011**, *104*, 89–111. [CrossRef]
9. Hinkel, J.; Lincke, D.; Vafeidis, A.T.; Perrette, M.; Nicholls, R.J.; Tol, R.S.J.; Marzeion, B.; Fettweis, X.; Ionescu, C.; Levermann, A. Coastal flood damage and adaptation costs under 21st century sea-level rise. *Proc. Natl. Acad. Sci. USA* **2014**, *111*, 3292–3297. [CrossRef]
10. Izaguirre, C.; Losada, I.J.; Camus, P.; Vigh, J.L.; Stenek, V. Climate change risk to global port operations. *Nat. Clim. Chang.* **2021**, *11*, 14–20. [CrossRef]
11. Vousdoukas, M.I.; Mentaschi, L.; Voukouvalas, E.; Bianchi, A.; Dottori, F.; Feyen, L. Climatic and socioeconomic controls of future coastal flood risk in Europe. *Nat. Clim. Chang.* **2018**, *8*, 776–780. [CrossRef]
12. Rodriguez-Delgado, C.; Bergillos, R.J.; Iglesias, G. Coastal infrastructure operativity against flooding—A methodology. *Sci. Total Environ.* **2020**, *719*, 137452. [CrossRef] [PubMed]
13. Wong, P.P.; Losada, I.J.; Gattuso, J.-P.; Hinkel, J.; Khattabi, A.; McInnes, K.L.; Saito, Y.; Sallenger, A. Coastal systems and low-lying areas. In *Climate Change 2014: Impacts, Adaptation, and Vulnerability. Part A: Global and Sectoral Aspects. Contribution of Working Group II to the Fifth Assessment Report of the Intergovernmental Panel on Climate Change*; Field, C.B., Barros, V.R., Dokken, D.J., Mach, K.J., Mastrandrea, M.D., Bilir, T.E., Chatterjee, M., Ebi, K.L., Estrada, Y.O., Genova, R.C., et al., Eds.; Cambridge University Press: Cambridge, UK; New York, NY, USA, 2014; pp. 361–409.
14. Hubbert, G.D.; McInnes, K.L. A storm surge inundation model for coastal planning and impact studies. *J. Coast. Res.* **1999**, *15*, 168–185.
15. Zokagoa, J.M.; Soulaïmani, A. Modeling of wetting-drying transitions in free surface flows over complex topographies. *Comput. Methods Appl. Mech. Eng.* **2010**, *199*, 2281–2304. [CrossRef]
16. Barnard, P.L.; Erikson, L.H.; Foxgrover, A.C.; Hart, J.A.F.; Limber, P.; O'Neill, A.C.; van Ormondt, M.; Vitousek, S.; Wood, N.; Hayden, M.K.; et al. Dynamic flood modeling essential to assess the coastal impacts of climate change. *Sci. Rep.* **2019**, *9*, 4309. [CrossRef]
17. Bates, P.D.; Dawson, R.J.; Hall, J.W.; Horritt, M.S.; Nicholls, R.J.; Wicks, J.; Ali Mohamed Hassan, M.A. Simplified two-dimensional numerical modelling of coastal flooding and example applications. *Coast. Eng.* **2005**, *52*, 793–810. [CrossRef]
18. Gaeta, M.G.; Bonaldo, D.; Samaras, A.G.; Carniel, S.; Archetti, R. Coupled Wave-2D Hydrodynamics Modeling at the Reno River Mouth (Italy) under Climate Change Scenarios. *Water* **2018**, *10*, 1380. [CrossRef]
19. Le Roy, S.; Pedreros, R.; André, C.; Paris, F.; Lecacheux, S.; Marche, F.; Vinchon, C. Coastal flooding of urban areas by overtopping: Dynamic modelling application to the Johanna storm (2008) in Gâvres (France). *Nat. Hazards Earth Syst. Sci.* **2015**, *15*, 2497–2510. [CrossRef]
20. Li, N.; Roeber, V.; Yamazaki, Y.; Heitmann, T.W.; Bai, Y.; Cheung, K.F. Integration of coastal inundation modeling from storm tides to individual waves. *Ocean Model.* **2014**, *83*, 26–42. [CrossRef]
21. McInnes, K.L.; Hubbert, G.D.; Abbs, D.J.; Oliver, S.E. A numerical modelling study of coastal flooding. *Meteorol. Atmos. Phys.* **2002**, *80*, 217–233. [CrossRef]
22. Peng, M.; Xie, L.; Pietrafesa, L.J. A numerical study of storm surge and inundation in the Croatan-Albemarle- Pamlico Estuary System. *Estuar. Coast. Shelf Sci.* **2004**, *59*, 121–137. [CrossRef]
23. Postacchini, M.; Lalli, F.; Memmola, F.; Bruschi, A.; Bellafiore, D.; Lisi, I.; Zitti, G.; Brocchini, M. A model chain approach for coastal inundation: Application to the bay of Alghero. *Estuar. Coast. Shelf Sci.* **2019**, *219*, 56–70. [CrossRef]
24. Goda, Y.; Ippen, A.T. *Theoretical and Experimental Investigation of Wave Energy Dissipators Composed of Wire Mesh Screens*; Massachusetts Institute of Technology, Cambridge Hydrodynamics Lab: Cambridge, MA, USA, 1963; p. 66.
25. Galani, K.A.; Dimou, I.D.; Dimas, A.A. Wave height and setup in the sheltered area of a segmented, detached, rubble-mound, zero-freeboard breakwater on a steep beach. *Ocean Eng.* **2019**, *186*, 106124. [CrossRef]
26. Koutrouveli, T.I.; Dimas, A.A. Wave and hydrodynamic processes in the vicinity of a rubble-mound, permeable, zero-freeboard break water. *J. Mar. Sci. Eng.* **2020**, *8*, 206. [CrossRef]
27. Papadimitriou, A.G.; Chondros, M.K.; Metallinos, A.S.; Memos, C.D.; Tsoukala, V.K. Simulating wave transmission in the lee of a breakwater in spectral models due to overtopping. *Appl. Math. Model.* **2020**, *88*, 743–757. [CrossRef]
28. Zhang, S.X.; Li, X. Design formulas of transmission coefficients for permeable breakwaters. *Water Sci. Eng.* **2014**, *7*, 457–467.
29. Formentin, S.M.; Zanuttigh, B.; Van Der Meer, J.W. A neural network tool for predicting wave reflection, overtopping and transmission. *Coast. Eng. J.* **2017**, *59*, 1750006-1. [CrossRef]
30. Panizzo, A.; Briganti, R. Analysis of wave transmission behind low-crested breakwaters using neural networks. *Coast. Eng.* **2007**, *54*, 643–656. [CrossRef]
31. d'Angremond, K.; Van der Meer, J.W.; de Jong, R.J. Wave transmission at low-crested breakwaters. In *25th International Conference of Coastal Engineering*; ASCE: Orlando, FL, USA, 1996; pp. 2418–2426.

32. van der Meer, J.W.; Briganti, R.; Zanuttigh, B.; Wang, B. Wave transmission and reflection at low-crested structures: Design formulae, oblique wave attack and spectral change. *Coast. Eng.* **2005**, *52*, 915–929. [CrossRef]
33. Buccino, M.; Calabrese, M. Conceptual approach for prediction of wave transmission at low-crested breakwaters. *J. Waterw. Port. Coast. Ocean Eng.* **2007**, *133*, 213–224. [CrossRef]
34. Goda, Y.; Ahrens, J.P. New formulation of wave transmission over and through low-crested structures. In Proceedings of the Coastal Engineering Conference, Hamburg, Germany; 2009; pp. 3530–3541.
35. Tanaka, N. Wave deformation and beach stabilization capacity of wide crested submerged breakwaters. In *23rd Japanese Conference on Coastal Engineering*; JSCE: Tokyo, Japan, 1976; pp. 152–157.
36. Numata, A. Experimental study on wave attenuation by block mound breakwaters. In *22nd Japanese Conference on Coastal Engineering*; JSCE: Tokyo, Japan, 1975; pp. 501–505.
37. Tomasicchio, G.R.; D'Alessandro, F. Wave energy transmission through and over low crested breakwaters. *J. Coast. Res.* **2013**, 398–403. [CrossRef]
38. Roeber, V.; Cheung, K.F.; Kobayashi, M.H. Shock-capturing Boussinesq-type model for nearshore wave processes. *Coast. Eng.* **2010**, *57*, 407–423. [CrossRef]
39. Booij, N.; Ris, R.C.; Holthuijsen, L.H. A third-generation wave model for coastal regions: 1. Model description and validation. *J. Geophys. Res. Oceans* **1999**, *104*, 7649–7666. [CrossRef]
40. Holthuijsen, L.H.; Herman, A.; Booij, N. Phase-decoupled refraction–diffraction for spectral wave models. *Coast. Eng.* **2003**, *49*, 291–305. [CrossRef]
41. Battjes, J.A.; Stive, M.J.F. Calibration and verification of a dissipation model for random breaking waves. *J. Geophys. Res. Oceans* **1985**, *90*, 9159–9167. [CrossRef]
42. Battjes, J.A.; Janssen, J.P.F.M. Energy loss and set-up due to breaking of random waves. In Proceedings of the 16th International Conference on Coastal Engineering, Hamburg, Germany, 27 August–3 September 1978; pp. 569–587.
43. Leont'Yev, I.O. Modelling of morphological changes due to coastal structures. *Coast. Eng.* **1999**, *38*, 143–166. [CrossRef]
44. Koutitas, C.G. *Mathematical Models in Coastal Engineering*; Pentech Press: London, UK, 1988.
45. Kobayashi, N.; Agarwal, A.; Johnson, B.D. Longshore current and sediment transport on beaches. *J. Waterw. Port. Coast. Ocean Eng.* **2007**, *133*, 296–304. [CrossRef]
46. Madsen, P.A.; Rugbjerg, M.; Warren, I.R. Subgrid modelling in depth integrated flows. In *21st International Conference on Coastal Engineering*; CERC: Terremolinos, Spain, 1988; pp. 505–511.
47. Militello, A.; Reed, C.W.; Zundel, A.K.; Kraus, N.C. *Two-Dimensional Depth-Averaged Circulation Model M2D: Version 2.0, Report 1, Technical Documentation and User's Guide*; ERDC/CHL TR-04-2; US Army Corps of Engineers, Engineering Research and Development Center: Washington, DC, USA, 2004; p. 134.
48. Chen, H.; Jiang, D.; Tang, X.; Mao, H. Evolution of irregular wave shape over a fringing reef flat. *Ocean Eng.* **2019**, *192*, 106544. [CrossRef]
49. Chen, Q.; Kirby, J.; Dalrymple, R.; Kennedy, A.; Chawla, A. Boussinesq Modeling of Wave Transformation, Breaking, and Runup.II: 2D. *J. Waterw. Port Coast. Ocean Eng.* **2000**, *126*, 48–56. [CrossRef]
50. Pinault, J.; Morichon, D.; Roeber, V. Estimation of Irregular Wave Runup on Intermediate and Reflective Beaches Using a Phase-Resolving Numerical Model. *J. Mar. Sci. Eng.* **2020**, *8*, 993. [CrossRef]
51. Roeber, V.; Cheung, K.F. Boussinesq-type model for energetic breaking waves in fringing reef environments. *Coast. Eng.* **2012**, *70*, 1–20. [CrossRef]
52. Tang, J.; Zhao, C.; Shen, Y. Numerical investigation of the effects of coastal vegetation zone width on wave run-up attenuation. *Ocean Eng.* **2019**, *189*, 106395. [CrossRef]
53. Tonelli, M.; Petti, M. Numerical simulation of wave overtopping at coastal dikes and low-crested structures by means of a shock-capturing Boussinesq model. *Coast. Eng.* **2013**, *79*, 75–88. [CrossRef]
54. Zhang, T.; Lin, Z.-H.; Huang, G.-Y.; Fan, C.-M.; Li, P.-W. Solving Boussinesq equations with a meshless finite difference method. *Ocean Eng.* **2020**, *198*, 106957. [CrossRef]
55. Brocchini, M. A reasoned overview on Boussinesq-type models: The interplay between physics, mathematics and numerics. *Proc. R. Soc. A Math. Phys. Eng. Sci.* **2013**, *469*, 20130496. [CrossRef]
56. Karambas, T.V.; Karathanassi, E.K. Longshore sediment transport by nonlinear waves and currents. *J. Waterw. Port. Coast. Ocean Eng.* **2004**, *130*, 277–286. [CrossRef]
57. Schäffer, H.A.; Madsen, P.A.; Deigaard, R. A Boussinesq model for waves breaking in shallow water. *Coast. Eng.* **1993**, *20*, 185–202. [CrossRef]
58. Chen, Q.; Dalrymple, R.A.; Kirby, J.T.; Kennedy, A.B.; Haller, M.C. Boussinesq modeling of a rip current system. *J. Geophys. Res. Oceans* **1999**, *104*, 20617–20637. [CrossRef]
59. Zou, Z.L. Higher order Boussinesq equations. *Ocean Eng.* **1999**, *26*, 767–792. [CrossRef]
60. Wei, G.; Kirby, J. Time-Dependent Numerical Code for Extended Boussinesq Equations. *J. Waterw. Port. Coast. Ocean Eng.* **1995**, *121*, 251–261. [CrossRef]
61. Memos, C.D.; Karambas, T.V.; Avgeris, I. Irregular wave transformation in the nearshore zone: Experimental investigations and comparison with a higher order Boussinesq model. *Ocean Eng.* **2005**, *32*, 1465–1485. [CrossRef]

62. Polnikov, V.G.; Manenti, S. Study of Relative Roles of Nonlinearity and Depth Refraction in Wave Spectrum Evolution in Shallow Water. *Eng. Appl. Comput. Fluid Mech.* **2009**, *3*, 42–55. [CrossRef]
63. Kriezi, E.; Karambas, T. Modelling wave deformation due to submerged breakwaters. *Proc. Inst. Civil. Eng. Marit. Eng.* **2010**, *163*, 19–29. [CrossRef]
64. Karambas, T.V.; Samaras, A.G. Soft shore protection methods: The use of advanced numerical models in the evaluation of beach nourishment. *Ocean Eng.* **2014**, *92*, 129–136. [CrossRef]
65. Samaras, A.G.; Karambas, T.V.; Archetti, R. Simulation of tsunami generation, propagation and coastal inundation in the Eastern Mediterranean. *Ocean Sci.* **2015**, *11*, 643–655. [CrossRef]
66. Wamsley, T.V.; Ahrens, J.P. Computation of Wave Transmission Coefficients at Detached Breakwaters for Shoreline Response Modeling. *Coast. Struct.* **2003**, *2004*, 593–605.
67. ThPA S.A.—Thessaloniki Port Authority S.A. *Statistical Data 2018*; Thessaloniki Port Authority S.A.: Thessaloniki, Greece, 2018; p. 10.
68. Google Earth. Image ©2020 TerraMetrics, Data SIO, NOAA, U.S. Navy, NGA, GEBCO. 2020.
69. NASA JPL. NASA Shuttle Radar Topography Mission Global 1 Arc Second NetCDF; NASA EOSDIS Land Processes DAAC. 2013.
70. AppEEARS Team. *Application for Extracting and Exploring Analysis Ready Samples (AppEEARS), Ver. 2.61*; NASA EOSDIS Land Processes Distributed Active Archive Center (LP DAAC), USGS/Earth Resources Observation and Science (EROS) Center: Sioux Falls, SD, USA, 2021.
71. Makris, C.; Galiatsatou, P.; Tolika, K.; Anagnostopoulou, C.; Kombiadou, K.; Prinos, P.; Velikou, K.; Kapelonis, Z.; Tragou, E.; Androulidakis, Y.; et al. Climate change effects on the marine characteristics of the Aegean and Ionian Seas. *Ocean Dyn.* **2016**, *66*, 1603–1635. [CrossRef]
72. Kirkpatrick, J.I.M.; Olbert, A.I. Modelling the effects of climate change on urban coastal-fluvial flooding. *J. Water Clim. Chang.* **2020**, *11*, 270–288. [CrossRef]
73. Ujeyl, G.; Rose, J. Estimating Direct and Indirect Damages from Storm Surges: The Case of Hamburg—Wilhelmsburg. *Coast. Eng. J.* **2015**, *57*, 1540006-1540001-1540006-1540026. [CrossRef]

Journal of
Marine Science and Engineering

MDPI

Article

Experimental Investigation on Hydrodynamic Coefficients of a Column-Stabilized Fish Cage in Waves

Yun-Peng Zhao [1], Qiu-Pan Chen [1], Chun-Wei Bi [1,*] and Yong Cui [2,3]

[1] State Key Laboratory of Coastal and Offshore Engineering, Dalian University of Technology, Dalian 116024, China
[2] Pilot National Laboratory for Marine Science and Technology (Qingdao), Qingdao 266237, China
[3] Qingdao Key Laboratory for Marine Fish Breeding and Biotechnology, Yellow Sea Fisheries Research Institute, Chinese Academy of Fishery Sciences, Qingdao 266071, China
* Correspondence: bicw@dlut.edu.cn

Received: 18 October 2019; Accepted: 7 November 2019; Published: 14 November 2019

Abstract: This study on hydrodynamic coefficients of a column-stabilized fish cage under wave action plays an important role in the anti-wave design of cages. The regular wave test was used to study the horizontal wave force of the jacket and column-stabilized fish cage under different wave heights, periods, and incident angles; the finite element model of the jacket and the column-stabilized fish cage was established according to the test model. On the basis of the calculation of the finite element model, combined with the wave force obtained from the experiment, the hydrodynamic coefficients of the structure was fitted by the least squares method, and then the drag force, inertial force, and total force of the structure under different conditions were calculated. The results show that the hydrodynamic coefficients of the jacket and netting under the wave condition were more obvious with the change of the *KC* number and wave incident angles. And as the wave height increased, the drag force, the inertial force, and the proportion of the drag force to the horizontal wave force both increased. When the wavelength was large, the same trend occured as the wave period increased. When the wave incident angles were different, the forces of the jacket and the column-stabilized fish cage were always small in lateral low-frequency waves, which is consistent with the change law of hydrodynamic coefficients of the jacket and netting.

Keywords: column-stabilized fish cage; horizontal wave force; least squares method; hydrodynamic coefficient

1. Introduction

There are developments made almost daily in marine aquaculture equipment in China. One such development is that of column-stabilized fish cages, which have gradually been recognized because of their structure safety, steadfast and reliable, and convenient integration with other marine jacket platforms. A typical column-stabilized fish cage mainly consists of the main jacket structure and the netting structure surrounding the culture space. As the coastal environment is deteriorating, aquaculture is gradually developing into more open sea; there are a large number of abandoned or newly developed jacket platforms, such as developing oil and wind energy. Combining this jacket structure with the netting structure not only improves the capacity of anti-storm of the deep sea cage, but also effectively solves the power supply problem of the breeding equipment, and facilitates the automation and intelligence of the deep sea aquaculture industry. However, the jacket platform combined with the netting has a complex response under the action of the marine environment, such as waves and currents, and the netting structure also faces more serious hydroid-fouled problems [1]. Therefore, it is necessary to carry out relevant experiments to study the force and hydrodynamic coefficients law of the column-stable cage under regular waves.

In previous research, estimation of hydrodynamic forces and hydrodynamic coefficients on isolated slender cylinders and pile groups is not new. Sarpkaya [2] carried out extensive experiments, and found that both C_D and C_M correlated with KC number reasonably well, while absolutely no correlation was found between the Reynolds number and C_D and C_M. Sundar et al. [3] used the least squares method to analyze the force of the pile column under the action of regular waves, and obtained the relationship between the hydrodynamic coefficients and the KC number of the pile column with different inclination angles. Bushnell [4] studied the mutual interaction and influence of array cylinders by means of a pulsating water tunnel. It was pointed out that this interference increases with the increase of the flow orbit length, and the maximum resistance of the shielded cylinder can be reduced to half of the single cylinder. Chakrabarti [5,6] studied the variation of hydrodynamic coefficients of group piles with KC number and pile spacing under regular wave action. Kurrian et al. [7] studied the comparison of hydrodynamic forces and force coefficients for the effects of spacing between the cylinders, shape, and arrangement of arrays, and found that the hydrodynamic force and force coefficients of the cylinders have similar trends when the KC number is the same. Besides, the measurements were compared with numerical predictions by Santo et al. [8] using computational fluid dynamics (CFD), with the actual jacket represented in a three-dimensional numerical wave tank as a porous tower model, simulating a uniformly distributed Morison stress field. Good agreement was achieved, both in terms of incident surface elevation as well as total force time histories, all using a single set of C_D and C_M. Palm et al. [9] studied the scale effects between a model scale and a prototype scale device, and compared inviscid Euler simulations with RANS results to quantify the viscous contribution to the loads and responses of the wave energy converter (WEC). Amaechi et al. [10] developed a coupled dynamic models with both buoys and hoses using Orcaflex to investigate the effects of hose hydrodynamic loads and flow angles on the structural behavior of the hoses. Gadelho et al. [11] presented an numerical analysis on determining the hydrodynamic coefficients of an oscillating two-dimensional rigid cylindrical body, using a time domain Navier–Stokes model. However, as of now, only a very limited number of studies have addressed the determination of hydrodynamic coefficients for large-span jacket structure.

As for the netting cage, Norwegian scholars Lader et al. [12] studied the deformation and water resistance of circular gravity cage with different weights under different flow rates by using a flume model experiment, and the experimental results were compared with the calculated results of the water resistance of the net using the empirical formula. It was found that the water resistance and deformation of the flexible net are highly dependent on each other. Decew et al. [13] conducted a flume towing test on the hydrodynamic characteristics of a single-point anchored harbor cage under the action of water flow according to Froude criterion. Zhao et al. [14] used a porous media model to simulate the netting, and established a three-dimensional numerical flume model to simulate the interaction between netting and water flow. Based on this numerical model, they studied the law of velocity attenuation after the interaction of netting and compared it with the experimental results of a physical model. Bi et al. [15,16] established a fluid–structure coupled model between flow and flexible nets, and simulated drag force and flow through the hydroid-fouled nets in currents. Based on the structural characteristics of floating aquaculture cages, Cui et al. [17] used the finite element method to simulate the motion and force of the cage under the action of wave–current interaction; they also did a comparative analysis of the numerical simulation results and tank model experiment results. Dong et al. [18] conducted a series of experiments on different types of mesh plates in wave flume to study the hydrodynamic force of the net panel under the wave action. Based on the fluid dynamics of the cylinder in wave, they proposed the wave force model of the net panel and compared it with existing experimental measurements. Zhao et al. [19] conducted a wave test on hydrodynamic responses of a semi-submersible offshore fish farm. Huang et al. [20] proposed a numerical model based on the lumped-mass method to analyze the dynamic characteristics of a net–cage system in waves and currents. Xu et al. [21] developed a numerical model based on the lumped-mass method and the principle of rigid body kinematics to predict the hydrodynamic response of a fish cage and mooring grid system in regular.

Previous studies have done some research on simple group piles and floating cages, but research on the hydrodynamic forces and hydrodynamic coefficients of the long-span jacket structure and the jacket–netted structure has not been reported. In this study, a new cage form of combining jacket and netting was designed. The hydrodynamics of the structure with or without the additional netting were studied, respectively, and the least squares method was used to fit the hydrodynamic coefficients based on the calculation of the finite element model, which provided support for the numerical simulation and engineering design of the column-stabilized fish cages. The comparison between the calculated and measured values of the horizontal wave force verifies the effectiveness of the research method.

2. Materials and Methods

2.1. Experimental Model

The experiments were carried out in a wave and current flume at the State Key Laboratory of Coastal and Offshore Engineering, Dalian University of Technology, Dalian, China. The flume was 60 m in length, 4 m in widthm and 2.5 m in depth, and had a maximum working water depth of 2.0 m. The arrangement of the experimental model is shown in

The tested model was placed 23 m away from the wave paddle. One wave gage was arranged 1 m before, and three wave gages arranged 1, 1.6, and 3.2 m behind the structure, respectively. In order to collect the hydrodynamic forces on the structure easily, the model was suspended from the carriage with dynamometers, such that the bottom of the structure was 0.26 m above the bottom of the tank. In this study, the real and effective horizontal wave forces were obtained by model experiments, which was the basis for studying the hydrodynamic coefficients C_D and C_M. Other forces were not considered for the time being. Due to the large structure frame, four dynamometers were used symmetrically to obtain the horizontal wave force. The measurement range of the four dynamometers in the horizontal direction was 50 N, and the positive direction remained consistent with the direction of wave propagation. As shown in Figure 2, the hydrodynamic data collected under the action of a certain working condition, the phase of each dynamometer was always consistent, and present periodic variation consistent with the action of regular wave, which also reflected the rationality of the dynamometer arrangement of the experiment. Figure 1.

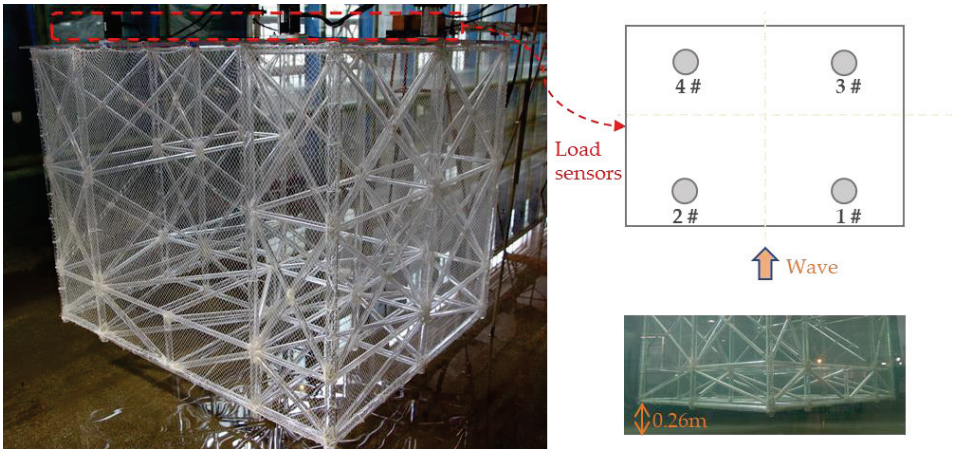

Figure 1. Experimental set-up of the column-stabilized fish cage.

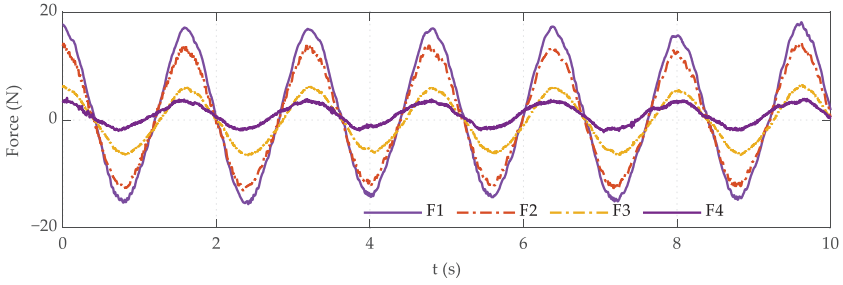

Figure 2. Comparison of the time history of the four measurements (A4).

The column-stabilized fish cage test model mainly consisted of the main jacket and the additional netting structure. To analyze the hydrodynamic characteristics of this particular structure, the test was divided into two parts, one was the hydrodynamic test of the main jacket (M1), and the other was the hydrodynamic test of the column-stabilized fish cage (M2). The jacket was the basic part of an offshore electrical platform, which was assembled by polymethyl methacrylate (PMMA) tubes for this test. The length and outer diameter of the pipes were designed according to the gravity similarity criterion, and the geometric scale λ was 60; the wall thickness of the pipes was designed according to the hydroelasticity similarity criterion, and the inertia radius scale λ_r was 64.027. According to λ and λ_r, the prototype structure of the jacket was equivalent to the model structure. The specific parameters are shown in Table 1. The outer contour of the jacket was 1.47 m long, 1.2 m wide, and 1.18 m heigh; 12 large cylindrical hollow pipes with a diameter of 32 mm and a wall thickness of 3 mm formed the jacket legs, and thin round pipes with a diameter of 25 mm and a wall thickness of 2 mm were distributed from the top to 0.62 m under the water surface as diagonal braces and cross braces. Water depth below 0.62 m was a bottom structure.

Considering that the netting force was mainly the water flow resistance, the equivalent netting can be used instead of the theoretical model netting. The geometric scale of the netting was 60, and the mesh size and diameter refer to the study of Tsukrov [22]. The netting part of the test adopted the knotted nylon netting with diamond mesh, with a mesh size of 12 mm and a mesh diameter of 0.82 mm. The horizontal and vertical shrinkage coefficients were 0.6 and 0.8, respectively, and the compactness was 0.137.

A typical column-stabilized cage consists of the jacket structure and the netting structure. During the test, we tied the netting and the jacket together with strings, and tensioned the mesh as evenly as possible while maintaining the mesh shape. So that the environmental load received by the mesh is transmitted to the surrounding piles through the strings, and the data obtained by the dynamometers were the total force of the jacket and the netting.

Table 1. Geometric dimension parameters of the prototype and model.

Member	Model Number	Section for Prototype (mm)	Section for Model (mm)
Jacket (Outside diameter * Thickness)	P2000 × 50	2000 * 50	32 * 3
	P1500 × 40	1500 * 40	25 * 2
	P1200 × 40	1200 * 40	20 * 2

During the test, three arrangement angles (0°, 45°, 90°) were realized by rotating the model to simulate the hydrodynamic response of the structure under different wave incident directions (see Figure 3). The water depth was 1.13 m. Considering the actual marine environment, nine regular wave conditions with different wave heights and periods were applied. They were used in the design for each incident angle. The parameters of the regular wave are shown in Table 2.

Table 2. Wave conditions.

Test Number	Wave Height H/m	Wave Period T/s	Wave Incident Angle β (°)
A1	**0.05**	**1.6**	
A2	0.1	1.6	0(A), 45(B), 90(C)
A3	0.15	1.0, 1.2, 1.4, 1.6, 1.8	
A4	0.2	1.6	
A5	0.25	1.6	

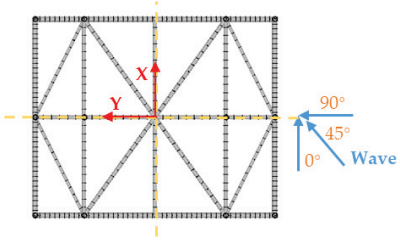

Figure 3. Wave incident angles and top view of the model (0°, 45°, and 90° were incident direction. Thereafter, they were denoted respectively as forward wave, oblique wave, and lateral wave).

M1 and M2 were exposed as two structures to all of the above regular wave conditions, which would help us to have a deeper understanding of the hydrodynamic characteristics of the column-stabilized fish cage structure. It is worth noting that the regular wave generated by the wave paddle is strongly nonlinear. After comparison, it was found to be in good agreement with the fifth order Stokes wave surfer elevation. Figure 4 shows the time histories of the wave height and horizontal force on M1 and M2 in A5, both on the measurement and the calculation. This provided a basis for the selection of the wave theory applied during the numerical analysis.

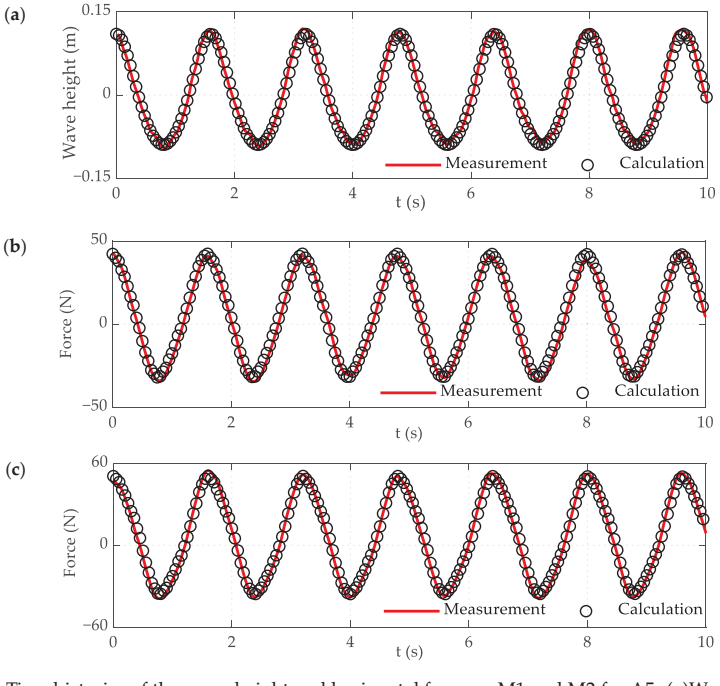

Figure 4. Time histories of the wave height and horizontal force on M1 and M2 for A5. (**a**)Wave height, (**b**) force of M1 and (**c**) force of M2.

2.2. Hydrodynamic Coefficient

Since the jacket structure and the fishing net structure can be regarded as consisting of a series of cylinders, the force is the sum of the forces of the formed cylinders. Based on the fluid dynamics of a small-scale cylindrical member in wave, the Morison equation can be used to calculate the wave force (F) on a column of unit length, including the drag force (F_d) and the inertial force (F_i) [23]. The formula is as follows:

$$F = F_d + F_i = 0.5\rho C_D D U|U| + \rho C_M A\dot{U} \tag{1}$$

where U and $\dot{U}$ are the velocity and acceleration of the water particles, D is the diameter of the cylinder, A is the cross-sectional area of the cylinder,ρ is the fluid density, C_D is the velocity force coefficient, and C_M is the inertial force coefficient.

Based on the fifth order Stokes wave theory, the horizontal velocity u_x and the horizontal acceleration a_x of water particles at any position of the structure are:

$$u_x = c\sum_{n=1}^{5} n\lambda_n \cosh[nk(z+d)]\cos[n(kx-\omega t)] \qquad (-d \le z \le \eta) \tag{2}$$

$$a_x = \omega c\sum_{n=1}^{5} n^2\lambda_n \cosh[nk(z+d)]\sin[n(kx-\omega t)] \qquad (-d \le z \le \eta) \tag{3}$$

The coefficients are as follows:

$$\lambda_1 = \lambda; \lambda_2 = \lambda^2 B_{22} + \lambda^4 B_{24}; \lambda_3 = \lambda^3 B_{33} + \lambda^5 B_{35}; \lambda_4 = \lambda^4 B_{44}; \lambda_5 = \lambda^5 B_{55}$$

where ω, h, k are angular frequency, water depth, wave number, definite $c = coshkd$, $s = sinhkd$. Equation (1) can be written as follows:

$$F_c(t) = C_D X(t) + C_M Y(t) \tag{4}$$

Among them,$X(t) = 0.5\rho D\iint u(x,z,t)\left|u(x,z,t)\right|dzdx$, $Y(t) = \rho A\iint a(x,z,t)dzdx$.

Setting the measured wave force $F_m(i)$, then the sum of the squared error is:

$$Q = \sum_{i=1}^{n}[F_c(i) - F_m(i)]^2 = \sum_{i=1}^{n}[C_D X(i) + C_M Y(i) - F_m(i)]^2 \tag{5}$$

Using the least squares method to make $\partial Q/\partial C_D = \partial Q/\partial C_M = 0$.Thus, the solution for C_D and C_M can be obtained as follows:

$$A_1 C_D + A_2 C_M = A_4 \qquad A_2 C_D + A_3 C_M = A_5 \tag{6}$$

where $A_1 = \sum X^2(i)$, $A_2 = \sum X(i)Y(i)$, $A_3 = \sum Y^2(i)$, $A_4 = \sum F_m(i)X(i)$, $A_5 = \sum F_m(i)Y(i)$.

We can finally find the results:

$$\begin{aligned} C_D &= \begin{vmatrix} A_4 & A_2 \\ A_5 & A_3 \end{vmatrix} \Big/ \begin{vmatrix} A_1 & A_2 \\ A_2 & A_3 \end{vmatrix} \\ C_M &= \begin{vmatrix} A_1 & A_4 \\ A_2 & A_5 \end{vmatrix} \Big/ \begin{vmatrix} A_1 & A_2 \\ A_2 & A_3 \end{vmatrix} \end{aligned} \tag{7}$$

2.3. Numerical Model

The simulation was carried out using the finite element software ANSYS APDL 18.2, Ansys, Inc.; America. The test model used the equivalent nylon netting. In order to improve the calculation efficiency,

the netting model for numerical simulation in this paper was simplified by the "mesh grouping" method (see Figure 5). Under the condition that the total mass and the total wave load of the netting were unchanged, four meshes in the test model were grouped into one mesh in the numerical model, and the parameters of the original and mesh-grouped net pen are shown in Table 3.

Furthermore, the finite element model of testing model was built as shown in Figure 6. In order to ensure that the results of numerical simulation can better reflect the test data, the main settings in the numerical calculations were as follows:

For the jacket structure, the PIPE59 element was used to establish a finite element model consistent with the experimental model. In the test, plexiglass plate with 1.2 cm thickness was attached to the top of the jacket, which was used to connect the jacket and the dynamometer to form a stable test force model. The numerical model was also fixed at the top of the jacket with the same plexiglass plate (SHELL181). To simulate the real dynamometer and board constraints, there were four fixed points at each position of the dynamometer, as shown in Figure 6.

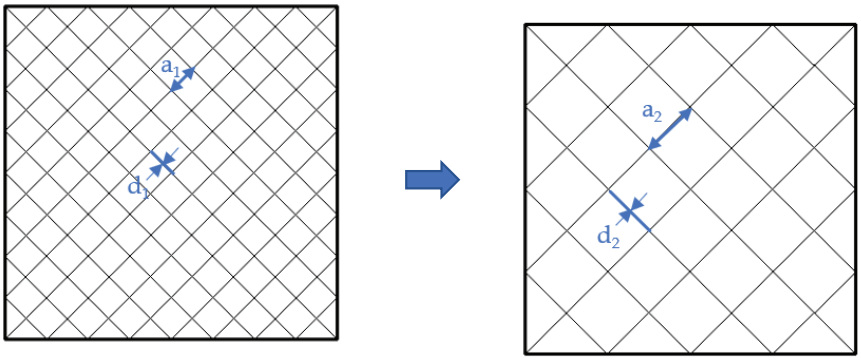

Figure 5. Mesh grouping method. (**a**) The original netting and (**b**) The mesh-grouped netting.

Table 3. Parameters of the netting.

Parameter Type	Experimental Values	Numerical Values
Mesh size (mm)	12	24
Twine diameter (mm)	0.82	1.64
Horizontal shrinkage coefficient	0.6	0.6
Vertical shrinkage coefficient	0.8	0.8
Solidity ratio	0.137	0.137

The netting was also simulated with the PIPE59 element. Unlike the jacket, the element of the netting simulated its flexibility by eliminating the bending stiffness, and set its inner diameter to zero. In order to ensure the load transfer between the netting and the jacket, the two must be coupled together. Since they were of the same element type, it was only necessary to establish a common node between the netting and the jacket to achieve the connection.

The hydrodynamic calculation for the PIPE59 element in ANSYS was based on the Morison equation shown in Equation (1). C_D and C_M were obtained by the least square method described above. In addition, the origin of the global coordinate system of the numerical model must be located at stilling water surface, and the vertical axis was the Z axis, the positive direction of the Z axis was upward.

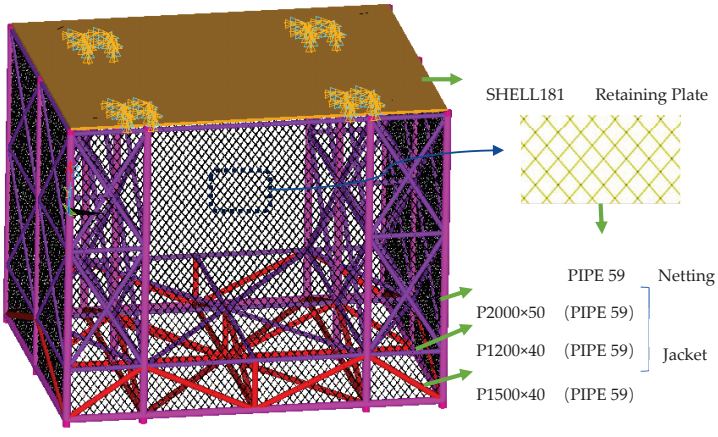

Figure 6. Finite element model of the testing model.

3. Results

3.1. Horizontal Force on Various Models in Waves

For each set of wave conditions, the component vector of each dynamometer was added along the wave direction to obtain the total horizontal wave force of M1 and M2. The time histories of the wave height and horizontal forces on M1 and M2 in A3-3 and A4 are shown in Figure 7. The result showed a steady state in the range of 10 s, and the time history of the force and the wave height were basically synchronous, while the peak and valley values had the same asymmetry.

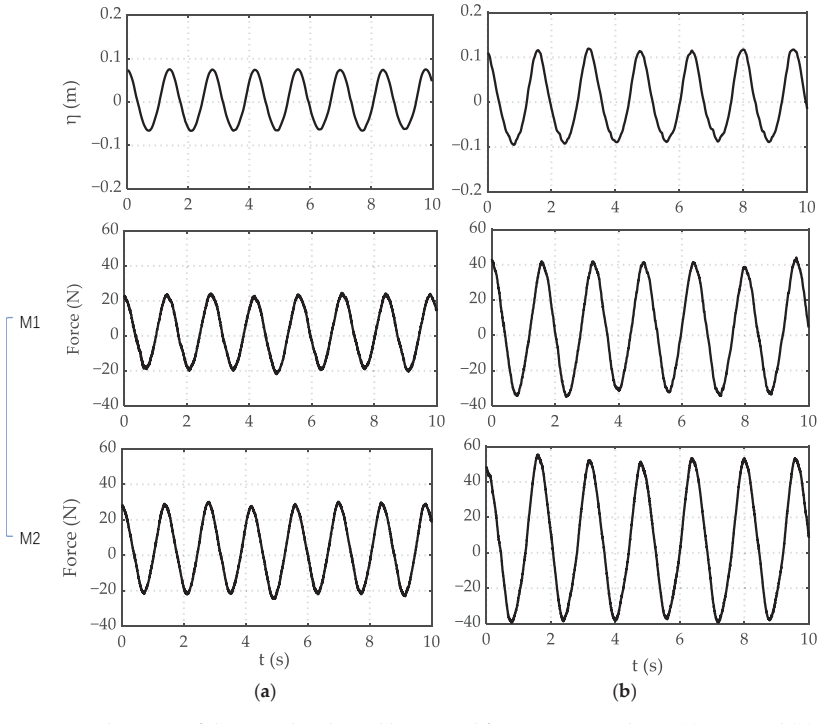

Figure 7. Time histories of the wave height and horizontal forces on M1 and M2. (**a**) A3-3 and (**b**) A4.

The relationship between the peak value of the horizontal wave force on the test model and the wave conditions is shown in Figures 8 and 9. Since the presence of the netting increased the flow area of the structure, the wave forces on the structure were increased to some extent. Comparing the horizontal wave force data of all test conditions, it can be found that the horizontal force of M2 was greater than M1. When the period was 1.6 s, the peak of the horizontal wave force on the structure increased with the increment of the wave height, and the contribution of the additional netting to the horizontal wave force of the structure became more and more obvious. When the wave height was 0.15 m, the wave force of the structure increase with the increment of the period and step diameter was decreased except C3-1, where the peaks of the wave forces on M1 and M2 were all abnormally large; 17.73 N for M1 and 24.7 N for M2.

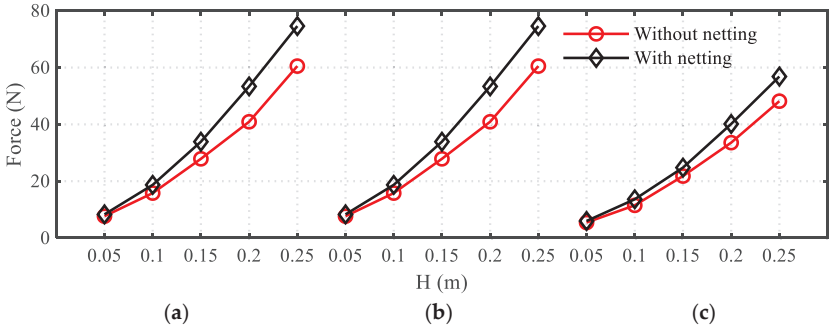

Figure 8. Horizontal forces of the structure under the action of wave (T = 1.6 s). (**a**) $\beta = 0°$, (**b**) $\beta = 45°$ and (**c**) $\beta = 90°$.

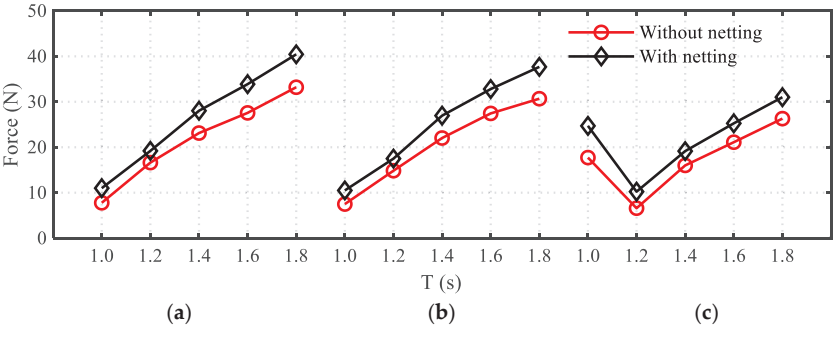

Figure 9. Horizontal forces of the structure under the action of wave (H = 0.15 m). (**a**) $\beta = 0°$, (**b**) $\beta = 45°$ and (**c**) $\beta = 90°$.

3.2. Hydrodynamic Coefficients of Various Models in Waves

The effects of the KC number ($KC = U_{max}T/D$; U_{max}: The maximum velocity of the wave; D: The maximum diameter of the jacket member) and the incident angle on the hydrodynamic coefficients of the two models in the wave are shown in this section. For the two models in each wave condition, we calculated the drag coefficient C_D and the inertia coefficient C_M by Equation (7) with the least square method using fifth order Stokes wave.

The variation of the jacket hydrodynamic coefficients with the KC number in waves is shown in Figure 10. The results indicate that the drag coefficient C_D decreased gradually with the increase in KC number, and the step diameter was decreased as the KC number increased; C_D got the maximum value in oblique wave ($\beta = 45°$), and the minimum value in lateral wave ($\beta = 90°$). The effect of KC number on C_M was insignificant for the jacket, but the effect of wave incident angle was distinct; C_M

got the maximum value in forward wave ($\beta = 0°$), and the minimum value in lateral wave ($\beta = 90°$). For M2, it was considered that the jacket and the netting were two independent parts; that is, the horizontal wave force of the netting can be obtained by the force of M2 minus the force of M1, and the composition of the horizontal wave force of the netting was based on the study of Zhao et al. [24], whom conducted wave tests on a variety of densities of netting, and concluded that the value of the inertial force of the netting was much smaller than the value of the wave force it received, can be ignored. Therefore, it was considered that the horizontal wave force of the netting can be expressed by only the drag force. The variation of the netting drag coefficient C_D with the KC number in waves is shown in Figure 11, which had consistent regularity compared with C_D of jacket.

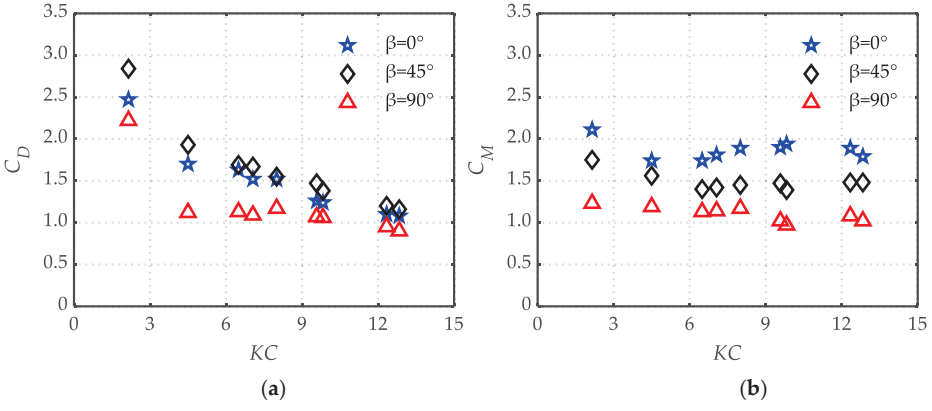

Figure 10. Variation of hydrodynamic coefficients of jacket, along with the change of KC number. (**a**) Relationship between C_D and KC number and (**b**) relationship between C_M and KC number.

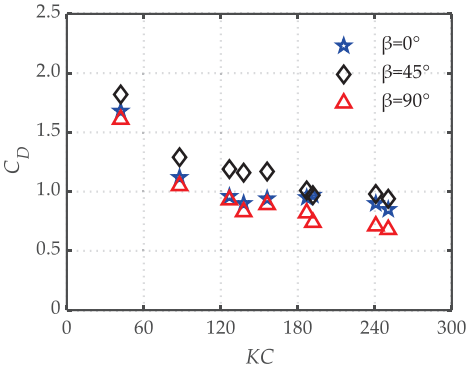

Figure 11. Variation of hydrodynamic coefficient (C_D) of the netting, along with the change of KC number.

3.3. Components of Horizontal Force in Waves

3.3.1. Components of Horizontal Force of the Jacket Structure

For M1, in order to deeply study the horizontal force variation caused by the change of wave height, period, and incident angle, the horizontal force of the test was decomposed into the drag force and the inertial force according to the Morison equation, as shown in Figures 12 and 13.

The results indicate that there was a peak phase difference between the drag force and the inertial force that make up the wave force, and the peak phase of the inertial force was before the total force, while the peak phase of the drag force was after the total force, which were determined by Equations (2) and (3). Comparing the peak and valley values of the inertial force and the drag force, it can be found that the peak and valley values of the inertial force are equal, while the peak value of the drag force is significantly larger than the valley value. When the period was constant (T = 1.6 s) and the wave heights were large, the inertial force and the drag force increased with the increment of the wave height in different incident angles. Similarly, when the wave height was constant (H = 0.15 m) and the periods were large, the inertial force and the drag force increased with increasing period in different incident angles. In addition, the proportion of the drag force in the total force increased with the increment of the wave height and period, which was considered to be caused by the drag force being proportional to the square of the water point speed.

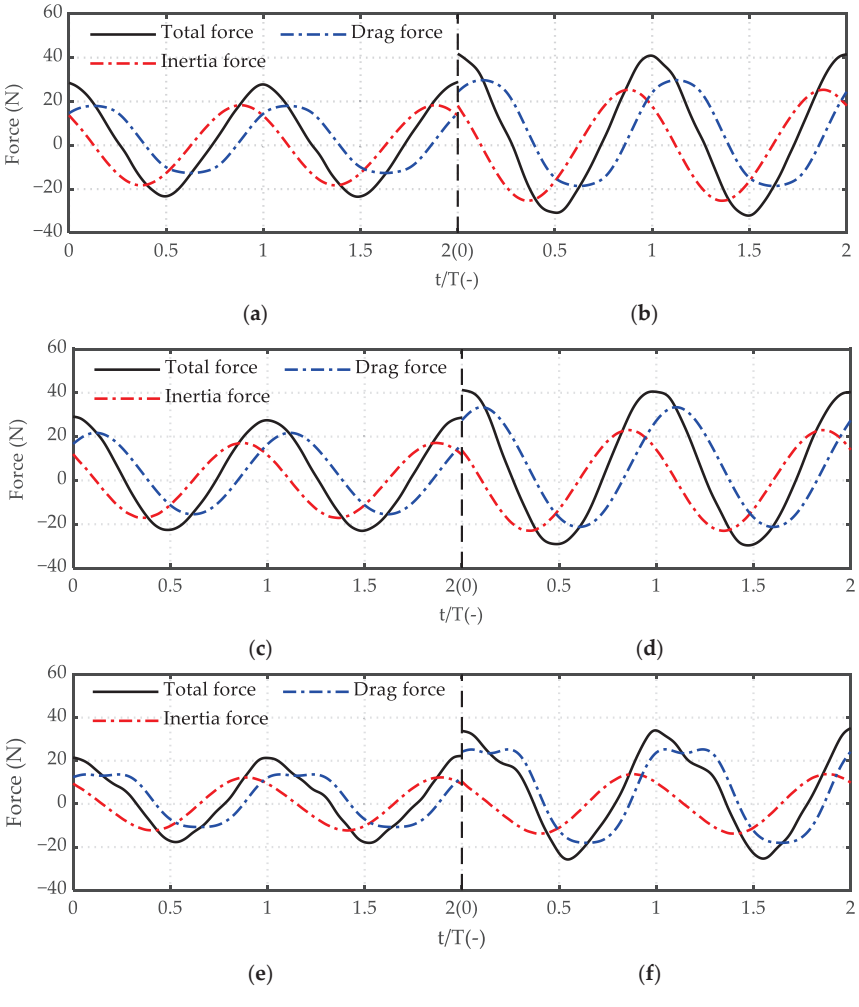

Figure 12. Composition of measured horizontal wave force of M1 (T = 1.6 s). (**a**) β = 0°, H = 0.15 m, T = 1.6 s, (**b**) β = 0°, H = 0.20 m, T = 1.6 s, (**c**) β = 45°, H = 0.15 m, T = 1.6 s, (**d**) β = 45°, H = 0.20 m, T = 1.6 s, (**e**) β = 90°, H = 0.15 m, T = 1.6 s and (**f**) β = 90°, H = 0.20 m, T = 1.6 s.

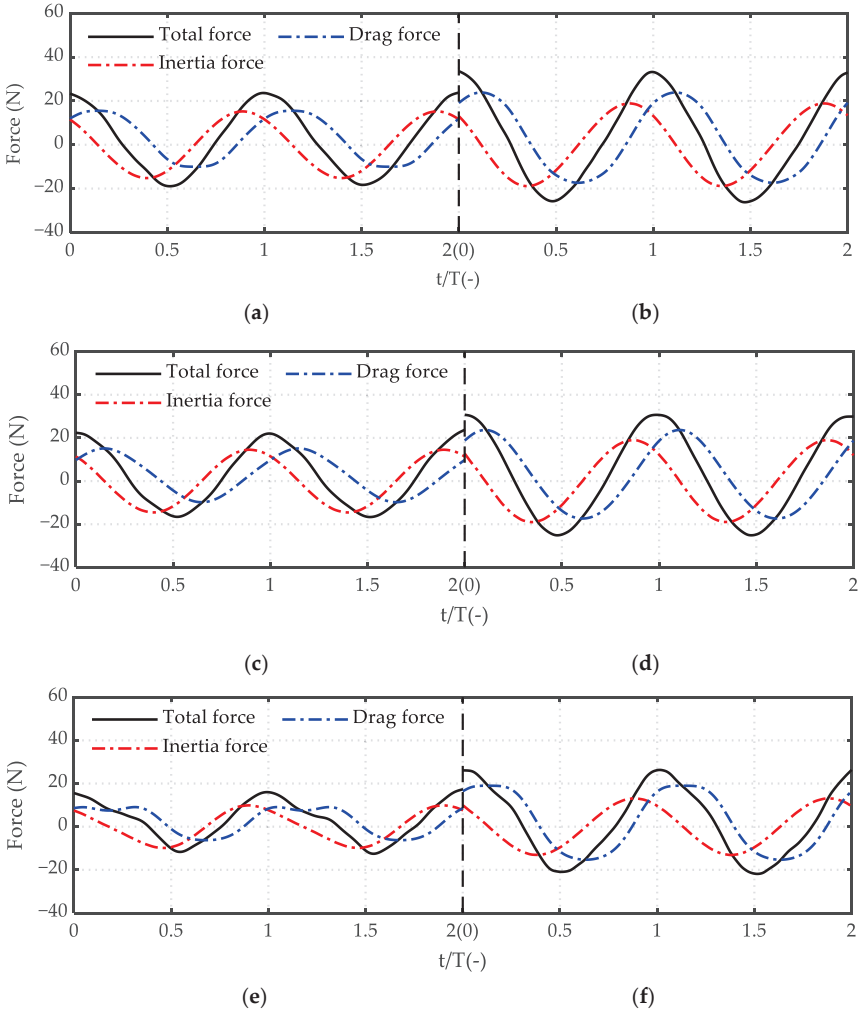

Figure 13. Composition of measured horizontal wave force of M1 (H = 0.15 m). (**a**) β = 0°, T = 1.4 s, H = 0.15 m, (**b**) β = 0°, T = 1.8 s, H = 0.15 m, (**c**) β = 45°, T = 1.4 s, H = 0.15 m, T = 1.6 s, (**d**) β = 45°, T = 1.8 s, H = 0.15 m, (**e**) β = 90°, T = 1.4 s, H = 0.15 m and (**f**) β = 90°, T = 1.8 s, H = 0.15 m.

3.3.2. Components of Horizontal Force of the Fish Cage Structure

Considering that the wave force of M2 was composed of the wave force of M1 and the netting, respectively, in order to explore the influence of the netting on M2, time histories of the wave force on M1, M2, and netting are shown in the Figures 14 and 15. Figure 14 is for the fixed period (T = 1.6 s), while Figure 15 is for the fixed wave height (H = 0.15 m). The wave force of M1 and M2 are taken from the test data, and the wave force of netting, considering only the drag force, taken from the numerical calculation data.

It can be seen from the Figures 14 and 15 that the peak phase of the drag force of the netting is behind the peak phase of the wave force of M2, which is consistent with the law of the peak phase of the drag force of M1. When the period was constant (T = 1.6 s) and the wave height was large, the drag force of the netting increased with the increase of the wave height; similarly, when the wave height was constant (H = 0.15 m) and the period was large, the drag force of the netting increased with the increment of the period.

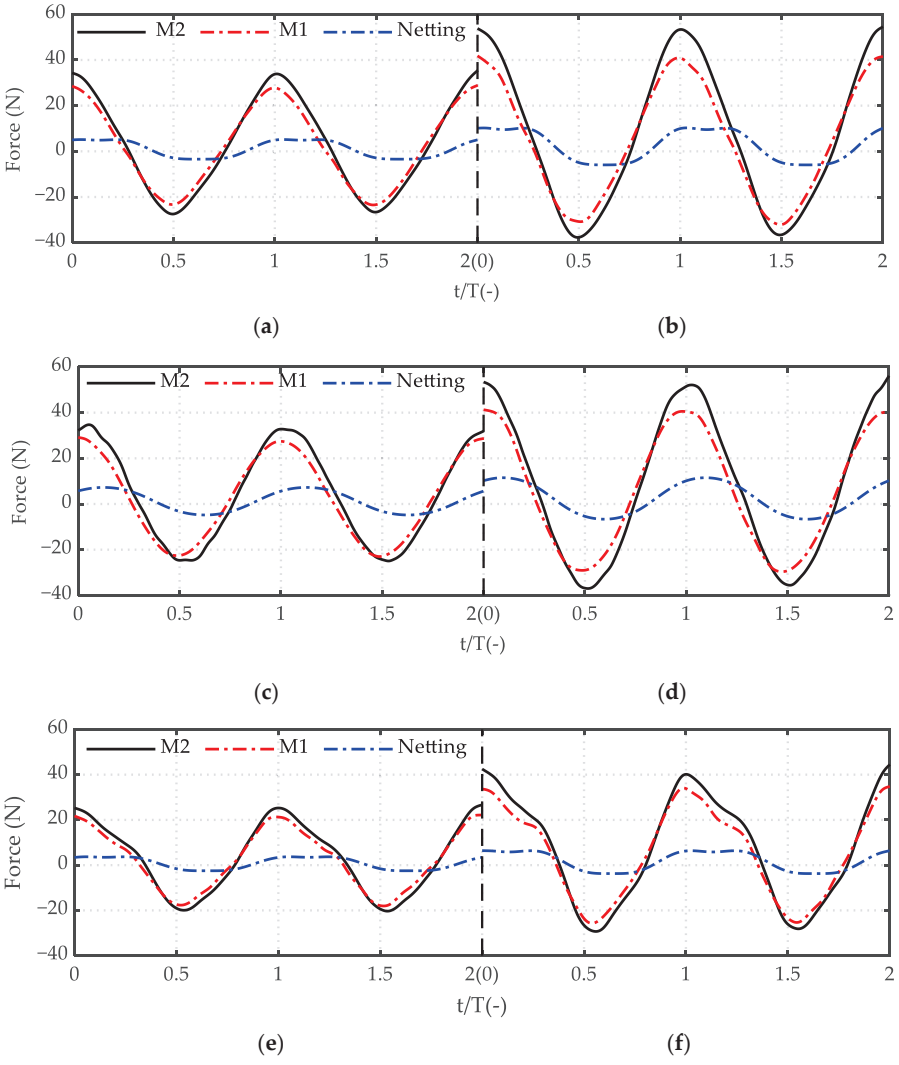

Figure 14. Composition of measured horizontal wave force of M2 (T = 1.6 s). (**a**) β = 0°, H = 0.15 m, T = 1.6 s, (**b**) β = 0°, H = 0.20 m, T = 1.6 s, (**c**) β = 45°, H = 0.15 m, T = 1.6 s, (**d**) β = 45°, H = 0.20 m, T = 1.6 s, (**e**) β = 90°, H = 0.15 m, T = 1.6 s and (**f**) β = 90°, H = 0.20 m, T = 1.6 s.

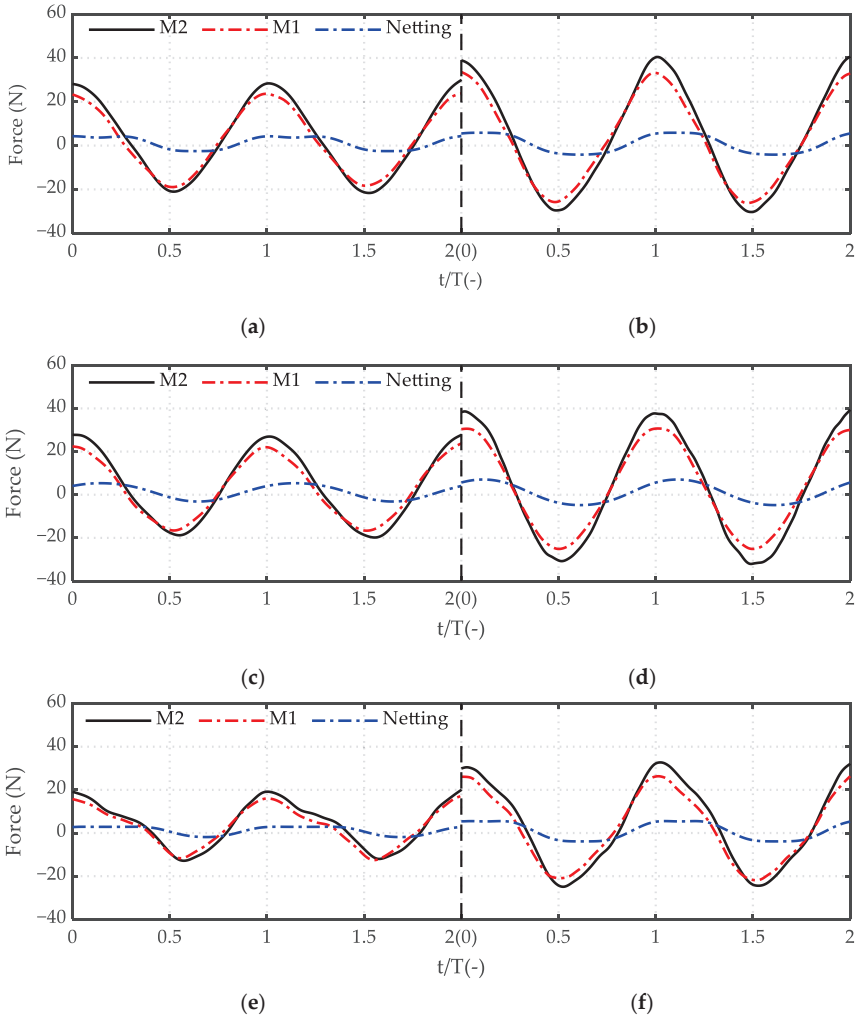

Figure 15. Composition of measured horizontal wave force of M2 (H = 0.15 m). (**a**) β = 0°, T = 1.4 s, H = 0.15 m, (**b**) β = 0°, T = 1.8 s, H = 0.15 m, (**c**) β = 45°, T = 1.4 s, H = 0.15 m, (**d**) β = 45°, T = 1.8 s, H = 0.15 m, (**e**) β = 90°, T = 1.4 s, H = 0.15 m and (**f**) β = 90°, T = 1.8 s, H = 0.15 m.

4. Discussion

4.1. The Effect of Incident Angles on Wave Force

The influence of different incident angles on the structural stress were shown in Figures 16 and 17. The force of the jacket and column-stabilized fish cage was basically the same in forward and oblique waves (see Figure 16), while the horizontal wave force under the lateral wave was smaller. It was worth noting that the force were slightly bigger in the positive low-frequency wave (see Figure 17). In the lateral wave, the structural members were densely distributed along the wave propagation direction, resulting in an obvious shielding effect between the members. Although the total upstream area was large, due to the severe shielding of the members on the meeting-wave side, the force of the subsequent members was significantly reduced, which also directly led to the reduction of the total

wave force of the structure, which was consistent with the law of hydrodynamic coefficients reflected in Figures 10 and 11.

In Figure 17, the short-period wave force on both M1 and M2 were obviously abnormal under the action of the lateral wave. Since the fundamental frequency of the structure was much larger than the frequency of the test wave condition, the abnormal wave force here almost excluded the possibility of structural resonance. Considering this direction, there was a gap with a large span in the middle of the structure, and the modal components were symmetrically distributed in a small area on both sides. Analyzing on the wave phase corresponding to the maximum wave force of the structure, when the wavelength was slightly larger than the lateral span of the structure (C3-1), the wave trough acted on the gap, which caused a large value of the wave force; and when the wavelength continued to increase (C3 -2), the wave trough moved away from the gap and inevitably acted on one side of the jacket to reduce the wave force. Thereafter, as the wavelength continued to increase, the wave trough gradually left the structure, causing the wave force to increase, and when the effect of the wave trough was gradually reduced, the increased amplitude of wave force also slowed down. While the structure had no gaps in the direction of forward and oblique wave propagation, the effect of the trough under the short period was obvious, and the structural stress was small.

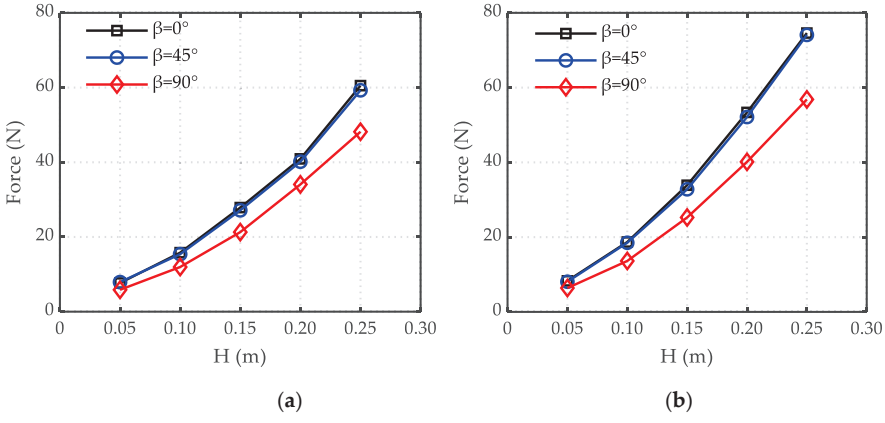

Figure 16. Horizontal force of structure under different incident angles (T = 1.6 s). (**a**) M1 and (**b**) M2.

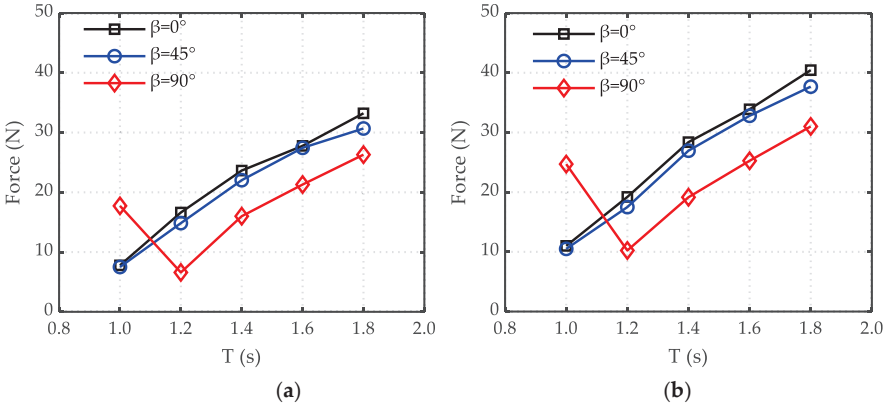

Figure 17. Horizontal force of structure under different incident angles (H = 0.15 m). (**a**) M1 and (**b**) M2.

4.2. The Effect of Incident Angles on Hydrodynamic Coefficients

Since the jacket model in this experiment was a large space frame structure, the density of the model component was significantly different in any wave propagation direction, which seriously affected the drag coefficient and inertial coefficient in all directions. It can be seen from Figure 10 that the drag coefficient C_D and the inertial coefficient C_M showed obvious differences at different incident angels: C_D got the maximum value in the oblique wave, while got the minimum value in the lateral wave; C_M got the maximum value in the forward wave, while got the minimum value in the lateral wave.

For M1, the drag force, inertial force, and horizontal total force calculated by the numerical model are shown in Figures 18 and 19. When the wave length was long enough, the wave force got the maximal value in the lateral wave; we thought that there was a larger flow area along the incident direction of the lateral wave. Considering that most of the members were symmetrically distributed on both sides of the gap, the shielding effect of the front members was obvious and the structural force was reduced, so the drag coefficient and the inertial coefficient were small (see Figure 10). For M2, the wave force of the netting was obviously affected by the jacket, so the drag coefficient of the netting was basically kept consistent with the drag coefficient of M1.

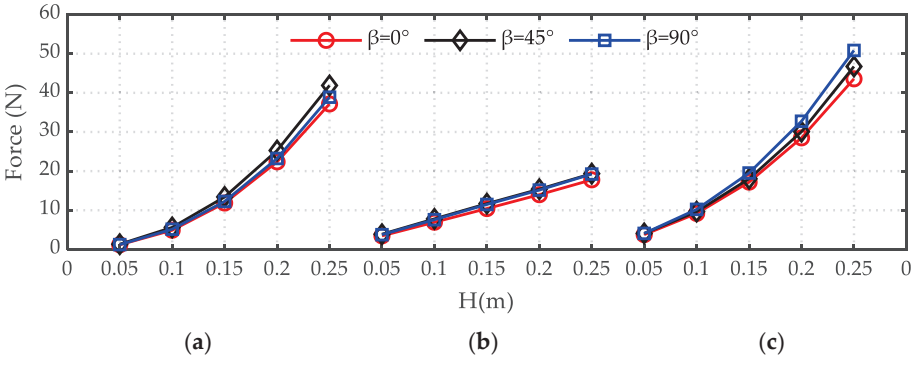

Figure 18. Forces under the action of waves (T = 1.6 s). (**a**) Drag force (C_D = 1), (**b**) Inertia force (C_M = 1) and (**c**) Total force (C_D = 1, C_M = 1).

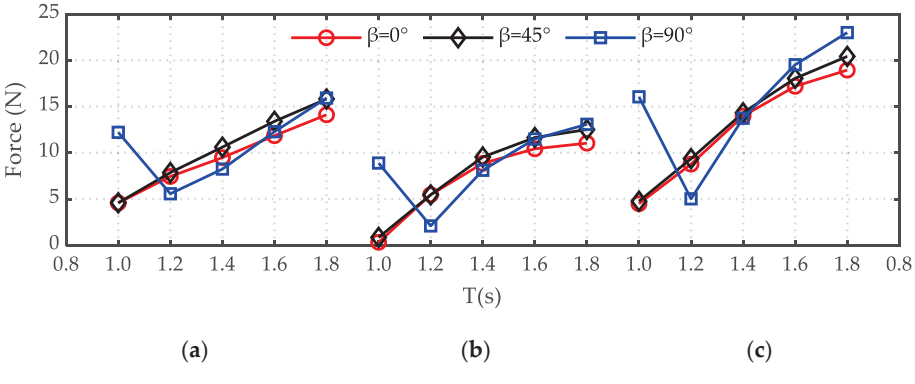

Figure 19. Forces under the action of waves (H = 0.15 m). (**a**) Drag force (C_D = 1), (**b**) Inertia force (C_M = 1) and (**c**) Total force (C_D = 1, C_M = 1).

4.3. The Effect of Wave Parameters on Wave Force Components

Equation (1) showed that the drag force was a function of the water point velocity and the structural flow area, and the inertial force was a function of the water point acceleration and the structural flow volume. It can be seen from Figure 12 that when the period was constant, the velocity and acceleration of water particles gradually became larger, and the structure flow area and volume affected by the water point movement also gradually increased, resulting in an increase in the drag force and the inertia force of the structure. The proportion of the drag force in horizontal wave force increased as the wave height increased, which was caused by the drag force being proportional to the square of the water particles' velocity. Similarly, when the wave height was constant, the magnitude of the drag and inertial force of the jacket increase with the increment of the period in Figure 13 (except for high frequency waves, see Figure 19), considering that the velocity and acceleration of water particles decreased with the increase of the period, and did not contribute to the structural force, but the span of the structure along the wave propagation direction was relatively large. When the wave period increased, the wavelength increased, resulting in an increase in the number of structural members affected by the movement of the water particles at the same time, which offset the effects of reduced velocity and acceleration of water particles, making the drag and inertia forces of the entire structure larger. For M2, the change law of the drag force of the netting was the same as M1, as shown in Figures 14 and 15.

Comparing the horizontal wave force composition of M1 under the positive and lateral wave (Figures 12 and 13), it can be found that the drag force of the jacket appears a regular double peak under the lateral wave, considering that there was a large gap in this direction, and the structures on both sides were symmetrically distributed with respect to the gap (see Figure 6). When the peak was in the middle of the gap, the wave force was small; when the peaks were respectively located at the two sides of the structure, the wave force was larger; and while the wave peak passed through the two sides of the structure, the wave surface and the model component were affected by wave surface symmetrical changes, so the drag force appeared as a symmetric double peak. In addition, the valley value of the drag force was wide and flat, considering that the water surface was lower, so that the force of the members in the middle position of the bottom structure compensate for the fluctuation of the force caused by the upper gap, together with the nonlinearity of the incident wave, the wave force valley was flattened. Due to the phase difference between the inertial force and the drag force, two peaks of different magnitudes appeared in the horizontal wave force after the superposition. For M2 (Figures 14 and 15), the drag force of the netting was not significantly different between the two angles, and both the peak and the valley were broad and flat, considering that the wave continued to act on the netting on both sides parallel to the direction of wave propagation after passing through the first layer of the netting, until the peak of the wave passed through the second layer, the amplitude of the drag was attenuated, and the wave trough had the same effect.

4.4. Results Comparison between Calculation and Measurement

In order to better demonstrate the accuracy of C_D and C_M obtained by the least square method above, the four groups of test conditions were taken as examples in the lateral wave. Using Equation (1), the horizontal wave forces of the two models were calculated and compared with the horizontal wave force of the test (see Figures 20 and 21). The comparison results indicate that the prediction error of the present model was lower than 2%. Of course, only two periods with relatively stable experimental data were selected for comparison, which was inconsistent with the results of using the complete data, but the prediction deviation in most cases was lower than 5%, which can be acceptable. In addition, only the drag force of the netting was considered and the inertial force was ignored, although the calculation error was introduced, and the approximate solution can be achieved. In summary, the calculated values agreed very well with the time histories of the measurement values, and it can be considered that the hydrodynamic coefficients calculated by the FEM results was effective.

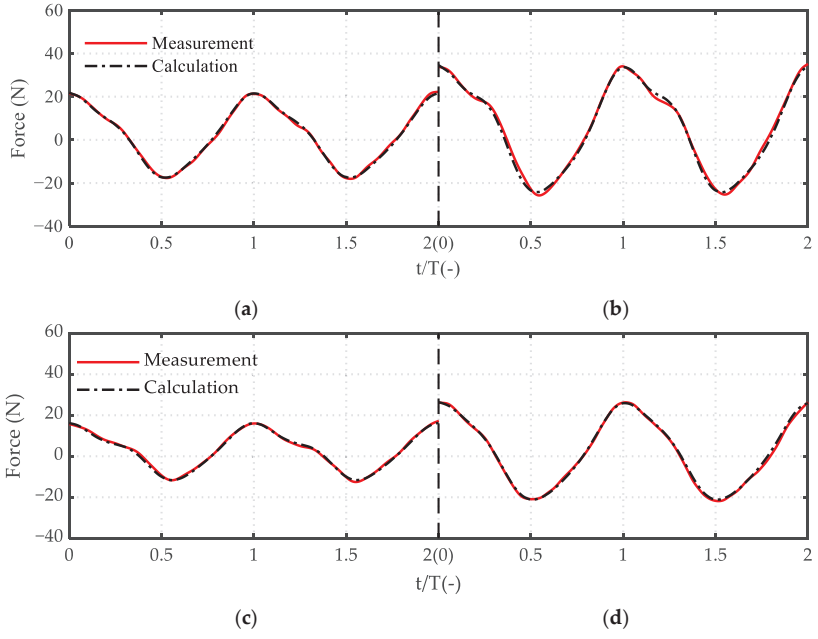

Figure 20. Time histories of measured and calculated wave forces on M1 in the lateral wave ($\beta = 90°$). (**a**) $\beta = 90°$, $H = 0.15$ m, $T = 1.6$ s, (**b**) $\beta = 90°$, $H = 0.20$ m, $T = 1.6$ s, (**c**) $\beta = 90°$, $T = 1.4$ s, $H = 0.15$ m and (**d**) $\beta = 90°$, $T = 1.8$ s, $H = 0.15$ m.

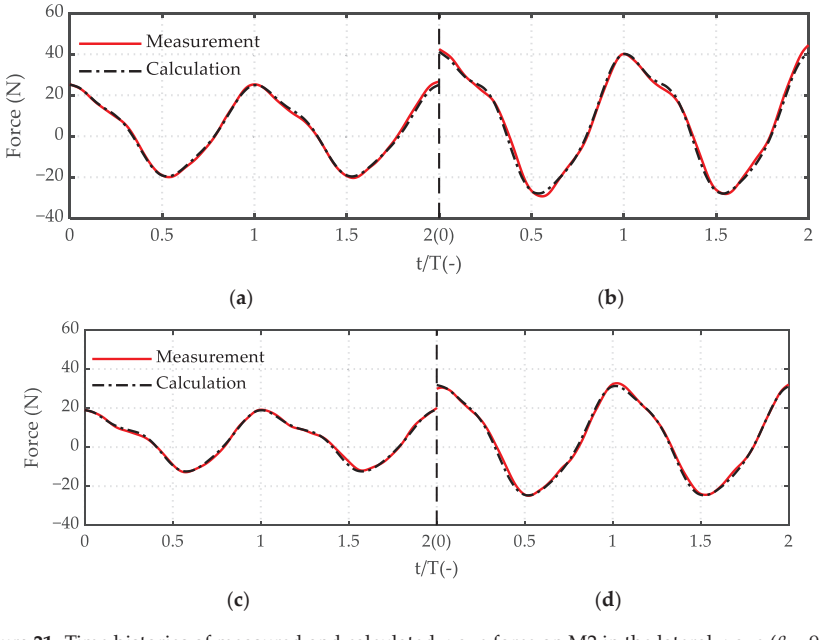

Figure 21. Time histories of measured and calculated wave force on M2 in the lateral wave ($\beta = 90°$). (**a**) $\beta = 90°$, $H = 0.15$ m, $T = 1.6$ s, (**b**) $\beta = 90°$, $H = 0.20$ m, $T = 1.6$ s, (**c**) $\beta = 90°$, $T = 1.4$ s, $H = 0.15$ m, (**d**) $\beta = 90°$, $T = 1.8$ s, $H = 0.15$ m.

5. Conclusions

In this paper, two models (the jacket model and the column-stabilized fish cage model) were designed according to the similarity theory, and the wave force under different wave height, period, and incident angle were studied, respectively. According to both the experimental and the numerical results, the horizontal wave force composition and corresponding hydrodynamic coefficients of each part of the column-stabilized fish cage were analyzed. The models had high research value because of their large span and typical structure form. The main conclusions are as follows:

(1) The force of the jacket and column-stabilized fish cage increased rapidly with the increment of the wave height, as we all know, while the variation of the forces was quite different from that of most offshore structures: with the variation of wave period, the force can be increased several times in different periods due to the large span of the structure.

(2) The force of the jacket and the column-stabilized fish cage were basically the same in forward and oblique waves, while smaller in lateral waves, as the wave period was constant. In addition, the force was large in the positive low-frequency wave, and small in the lateral low-frequency wave, as the wave height was constant. The lateral high-frequency waves had a great influence on the wave forces, due to the special structural form of the jacket.

(3) The presence of the netting increased the flow area of the structure, so the force of the column-stabilized fish cage was greater than the force of the jacket, and the variation of the wave force of column-stabilized fish cage was consistent with the jacket.

(4) The variation of the drag coefficient of the jacket and the netting was heavily depend on the change in the *KC* number and the incident angle. The variation of the inertial force coefficient of the jacket mainly depended on the change of the incident angle, and the hydrodynamic coefficient was small in the lateral wave, which was due to the shielding effect between the components.

(5) The drag and inertial force increased with the increment of the wave height and period (except for high frequency waves), and the proportion of the drag force gradually increased.

Author Contributions: Data curation, Q.-P.C.; formal analysis, C.-W.B.; funding acquisition, Y.-P.Z. and Y.C.; investigation, Q.-P.C. and Y.C.; methodology, C.-W.B.; supervision, Y.-P.Z.; writing—original draft, Q.-P.C.; writing—review and editing, Y.-P.Z. and C.-W.B.

Funding: This research was funded by the National Natural Science Foundation of China (NSFC), project nos. 51939002, 51822901, 31872610, 31972843; and the Maritime S&T Fund of Shandong Province for Pilot National Laboratory for Marine Science and Technology (Qingdao), project no. 2018SDKJ0303-4.

Acknowledgments: The authors acknowledge the support from the National Natural Science Foundation of China and the Maritime S&T Fund of Shandong Province for Pilot National Laboratory for Marine Science and Technology (Qingdao).

Conflicts of Interest: The authors declare no conflicts of interest.

References

1. Klebert, P.; Lader, P.; Gansel, L.; Oppedal, F. Hydrodynamic interactions on net panel and aquaculture fish cages: A review. *Ocean Eng.* **2013**, *58*, 260–274. [CrossRef]
2. Sarpkaya, T. Forces on cylinders and spheres in a sinusoidally oscillating Fluid. *J. Appl. Mech.* **1975**, *42*, 32–37. [CrossRef]
3. Sundar, V.; Vengatesan, V.; Anandkumar, G.; Schlenkhoff, A. Hydrodynamic coefficients for inclined cylinders. *Ocean Eng.* **1998**, *25*, 277–294. [CrossRef]
4. Bushnell, M.J. Forces on cylinder arrays in oscillating flow. In Proceedings of the Offshore Technology Conference, Houston, TX, USA, 2 May 1977.
5. Chakrabatri, S.K. Hydrodynamic coefficients for a vertical tube in array. *Appl. Ocean Res.* **1981**, *3*, 121–128.
6. Chakrabatri, S.K. In-line and transverse forces on a tube array in tandem with waves. *Appl. Ocean Res.* **1982**, *4*, 25–32. [CrossRef]

7. Kurian, V.J.; Al-Yacouby, A.M.; Sebastian, A.A.; Liew, M.S.; Idichandy, V.G. Hydrodynamic coefficients for array of tubular cylinders. In Proceedings of the Twenty-fourth International Ocean and Polar Engineering Conference, Busan, Korea, 15–20 June 2014; pp. 641–648.
8. Santo, H.; Taylor, P.H.; Day, A.H.; Nixon, E.; Choo, Y.S. Current blockage and extreme forces on a jacket model in focussed wave groups with current. *J. Fluids Struct.* **2018**, *78*, 24–35. [CrossRef]
9. Palm, J.; Eskilsson, C.; Bergdahl, L.; Bensow, R. Assessment of scale effects, viscous forces and induced drag on a point-absorbing wave energy converter by CFD simulations. *J. Mar. Sci. Eng.* **2018**, *6*, 124. [CrossRef]
10. Amaechi, C.V.; Wang, F.C.; Hou, X.N.; Ye, J.Q. Strength of submarine hoses in Chinese-lantern configuration from hydrodynamic loads on CALM buoy. *Ocean Eng.* **2018**, *171*, 429–442. [CrossRef]
11. Gadelho, F.M.; Rodrigues, J.M.; Lavrov, A.; Guedes Soares, C. Determining hydrodynamic coefficients of a cylinder with Navier-Stokes equations. In *Maritime Technology and Engineering*; Guedes, S., Santos, T.A., Eds.; Taylor & Francis Group: London, UK, 2014; ISBN 978-1-138-02727-5.
12. Lader, P.F.; Enerhaug, B. Experimental investigation of forces and geometry of a net cage in uniform. *IEEE J. Ocean. Eng.* **2005**, *30*, 79–84. [CrossRef]
13. Decew, J.; Tsukrov, I.; Risso, A.; Swift, M.R.; Celikkol, B. Modeling of dynamic behavior of a single-point moored submersible fish cage under currents. *Aquac. Eng.* **2010**, *43*, 38–45. [CrossRef]
14. Zhao, Y.P.; Bi, C.W.; Dong, G.H.; Gui, F.K.; Cui, Y.; Guan, C.T.; Xu, T.J. Numerical simulation of the flow around fishing plane nets using the porous media model. *Ocean Eng.* **2013**, *62*, 25–37. [CrossRef]
15. Bi, C.W.; Zhao, Y.P.; Dong, G.H.; Xu, T.J.; Gui, F.K. Numerical simulation of the interaction between flow and flexible nets. *J. Fluids Struct.* **2014**, *45*, 180–201. [CrossRef]
16. Bi, C.W.; Zhao, Y.P.; Dong, G.H.; Wu, Z.M.; Zhang, Y.; Xu, T.J. Drag on and flow through the hydroid-fouled nets in currents. *Ocean Eng.* **2018**, *161*, 195–204. [CrossRef]
17. Cui, Y.; Guan, C.T.; Wan, R.; Huang, B.; Li, J. Dynamic analysis of hydrodynamic behavior of a flatfish cage system under wave conditions. *China Ocean Eng.* **2014**, *28*, 215–226. [CrossRef]
18. Dong, G.H.; Tang, M.F.; Xu, T.J.; Bi, C.W.; Guo, W.J. Experimental analysis of the hydrodynamic force on the net panel in wave. *Appl. Ocean Res.* **2019**, *87*, 233–246. [CrossRef]
19. Zhao, Y.P.; Guan, C.T.; Bi, C.W.; Liu, H.F.; Cui, Y. Experimental investigations on hydrodynamic responses of a semi-submersible offshore fish farm in waves. *J. Mar. Sci. Eng.* **2019**, *7*, 238. [CrossRef]
20. Huang, C.C.; Tang, H.J.; Liu, J.Y. Dynamical analysis of net cage structures for marine aquaculture: Numerical simulation and model testing. *Aquac. Eng.* **2006**, *35*, 258–270. [CrossRef]
21. Xu, T.J.; Dong, G.H.; Zhao, Y.P.; Li, Y.C.; Gui, F.K. Numerical investigation of the hydrodynamic behaviors of multiple net cages in waves. *Aquac. Eng.* **2012**, *48*, 6–18. [CrossRef]
22. Tsukrov, I.; Eroshkin, O.; Fredriksson, D.W.; Swift, M.R.; Celikkol, B. Finite element modeling of net panels using a consistent net element. *Ocean Eng.* **2003**, *30*, 251–270. [CrossRef]
23. Morison, J.R.; Johnson, J.W.; Schaaf, S.A. The force exerted by surface waves on piles. *J. Pet. Technol.* **1950**, *2*, 149–154. [CrossRef]
24. Zhao, Y.P.; Li, Y.C.; Dong, G.H.; Gui, F.K.; Wu, H. An experimental and numerical study of hydrodynamic characteristics of submerged flexible plane nets in waves. *Aquac. Eng.* **2008**, *38*, 16–25. [CrossRef]

Journal of
Marine Science and Engineering

MDPI

Article

Tensile Bending Stresses in Mortar-Grouted Riprap Revetments Due to Wave Loading

Moritz Kreyenschulte * and Holger Schüttrumpf

Institute of Hydraulic Engineering and Water Resources Management, RWTH Aachen University, Mies-van-der-Rohe-Str. 17, 52056 Aachen, Germany; schuettrumpf@iww.rwth-aachen.de
* Correspondence: kreyenschulte@iww.rwth-aachen.de

Received: 7 October 2020; Accepted: 10 November 2020; Published: 12 November 2020

Abstract: One of the most common revetment types in Germany is the mortar-grouted riprap revetment (MGRR), which is constructed by placing riprap on a filter or separation layer and subsequent grouting with mortar. Existing technical standards and guidelines for MGRRs do not consider the interaction between dynamic wave loading and structural response. To date, scientifically sound design approaches verified by model tests are missing. Therefore, the aim of this work is to establish a process-based model for the calculation of the acting bending tensile stresses during wave attack for MGRRs to asses crack formation. To this end, MGRRs were modelled as plates on an elastic foundation (PEF). Hydraulic boundary conditions were determined with full-scale hydraulic model tests. Model parameters of the PEF model were established by investigations into the mechanical parameters of the constituents of MGRRs. The results show that tensile bending stresses are particularly dependent on the pressure difference between the top and bottom edge of the top layer, which varies significantly for MGRRs as their porosity and permeability varies significantly depending on the amount of mortar used for grouting. Enveloping functions for maximum relative tensile bending stress $\sigma_{x,max}/(\rho_w g H_{m0})$ are given for four configurations of MGRRs that are of great practical relevance.

Keywords: mortar-grouted riprap revetment; full-scale hydraulic tests; design of revetments

1. Introduction

1.1. Motivation

In high energy coastal environments dikes can be protected by revetments against damage caused by wave loading [1,2]. One of the most common revetment types in Germany is the mortar-grouted riprap revetment (MGRR). To construct a MGRR, riprap is placed on a filter or separation layer that is in most cases a geotextile, subsequently the riprap is grouted with mortar. MGRRs in coastal environments have a thickness of at least 0.40 m and are made of riprap of class $CP_{90/250}$ (coarse particles of diameter 90–250 mm according to standard DIN EN 13383-1 [3]), $LMB_{5/40}$ or $LMB_{10/60}$ (light mass with stone mass of 5–40 kg and 10–60 kg according to DIN EN 13383-1, respectively). They can be constructed either by filling the entire pore volume of the riprap with mortar (fully grouted) or by partially filling the pore volume of the riprap with mortar while at the same time ensuring a mortar bond between the individual stones in the uppermost stone layer (partially grouted). Hence a fully grouted MGRR has an impermeable top layer with a rough surface, whereas a partially grouted MGRR has a rough, porous and permeable top layer. Figure 1 depicts the cross-sections of MGRRs and gives an impression of a partially and a fully grouted top layer.

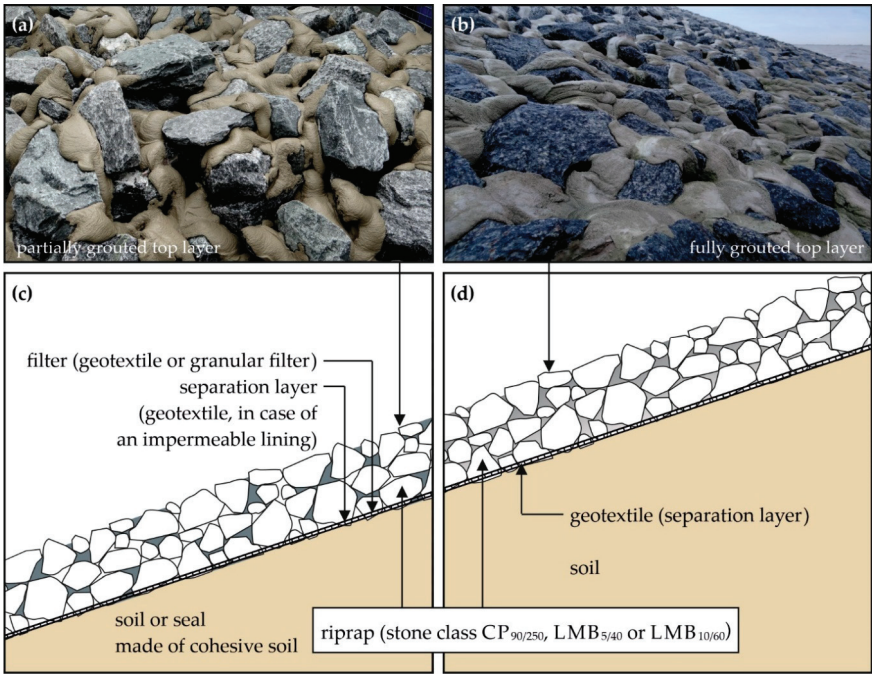

Figure 1. View of (**a**) a partially grouted top layer and (**b**) a fully grouted top layer (Photos: Kreyenschulte, 2015) as well as schematic representations of the cross-section of (**c**) partially grouted MGRRs and (**d**) fully grouted MGRRs (modified after [4]).

MGRRs form a coherent structure that is able to withstand shear forces and momentums, thus leading to a planar load distribution. Compared to non-grouted riprap revetments it is possible to use smaller and lighter stones and construct thinner armor layers under the same loading conditions with MGRRs. Although MGRRs have been built for decades, the design of their top layer is yet mainly based on empirical knowledge. On this basis, guidelines on construction of mortar-grouted riprap revetments [5,6] have been established. In combination with general design guidelines for revetment design [2,4,7], these guidelines define the composition of MGRRs and give a framework for the planning of the construction works, the tendering process and the construction itself. Furthermore, quality standards for the grout, the application of the grout to the stones and the grout distribution in the top layer are defined by the code of practice "Use of Cementitious and Bituminous Materials for Grouting Armourstone on Waterways" [5]. The thickness of the top layer and the amount of grouting mortar (in L/m^2) can be chosen using these technical standards and guidelines.

However, the existing technical standards and guidelines for MGRRs do not consider the interaction between dynamic wave loading and structural response. To date, scientifically sound design approaches verified by model tests are missing. This may potentially lead to an uneconomic design of MGRRs exceeding the load and safety criterion for a particular site. It is also possible that the current design practice may lead to a weaker revetment than is required for the load and safety criterion for a particular site.

Existing design approaches for other types of revetments are not applicable or have to be modified for the design of MGRRs, due to the structural behavior of MGRRs under wave attack and due to the fact that MGRRs substantially differ with regard to possible wave loading conditions when compared to other revetments. With regard to the structural behavior when subject to wave attack, three different types of revetments can be differentiated according to their flexibility:

- Flexible revetments: Limited interaction between individual elements of the revetment results in the individual elements resisting wave loading mainly by their weight while the whole revetment can deform by redistribution of the single elements and thereby easily adapt to subsoil settlement. Non-grouted (loose) riprap forms a flexible revetment, see for example [8].
- Revetments with some flexibility: Revetments made of individual elements with high interaction or monolithic revetments that due to their creep behavior can adapt to subsoil settlement to a certain degree while remaining coherent. This type of revetment can resist higher wave loads than fully flexible revetments given the same size of the individual elements or the same revetment thickness, but especially asphalt is subject to fatigue and abrasion [9]. Asphalt revetments or riprap grouted with asphalt are examples of revetments with some flexibility.
- Revetments with no flexibility: These monolithic revetments or revetments made of individual elements with high interaction are too stiff to follow subsoil settlement. It is therefore possible that cavities beneath the revetment are present, resulting in a non-continuous bedding of the revetment. This type of revetment can also resist higher wave loads than fully flexible revetments given the same size of the individual elements or the same revetment thickness, but it is subject to breaking and crack formation. Mortar-grouted riprap revetments are revetments with no flexibility [10].

The pressures on and beneath the revetment top layer represent the external load acting on the top layer of a cohesive revetment. The pressure beneath the top layer as a function of the pressure on the top layer is significantly influenced by the permeability of the top layer [11–13]. With regard to possible wave loading conditions, Schiereck [14] therefore distinguishes three different types of revetments:

- For very permeable revetments such as loose riprap the pressure beneath the revetment almost instantaneously adapts to the pressure on the revetment. In case of small amounts of grouting mortar, MGRRs also represent this type of revetment.
- With decreasing permeability of the top layer the load on the top layer is increasingly dominated by the pressure difference on and beneath the top layer. For pattern placed revetments the leakage length, which takes into account the permeability and thickness of both the filter layer and top layer of the revetment, is a measure for the loading of the top layer [15]. In case of high amounts of grouting mortar, MGRRs can qualitatively represent this type of revetment. However, the concept of the leakage length assumes flow in the filter layer parallel to the embankment and can therefore not be applied for MGRRs that are in most cases placed on a geotextile filter layer, because the thickness of a geotextile filter is in the order of a few centimeters and does not allow any significant flow in its plane.
- In the case of a non-permeable top layer, the pressure beneath the revetment adapts to the pressure on the revetment only for time periods of several hours or longer (tides, storms), but not for the time periods of individual waves [9]. This is the case for fully grouted MGRRs and for example for asphalt revetments.

While most revetments can be assigned to one category of loading and structural behavior, MGRRs are revetments with no flexibility that can be subject to loading conditions of each of the revetment loading types mentioned above.

1.2. Modelling Tensile Stresses for Crack Formation Assessment

Crack formation in the top layer of MGRRs represents a deterioration of the revetment. Furthermore, cracks are the prerequisite for all other possible damage or failure mechanisms with regard to the structural integrity of MGRRs. Due to their missing flexibility, MGRRs are prone to crack formation as a consequence of uneven settlement of the subsoil and cavities beneath the top layer, especially in combination with wave loading. Further possible causes for crack formation are temperature differences or shrinkage of the fresh mortar. Crack formation can be facilitated by aging or fatigue of the mortar. Already existing cracks can be widened by ice pressure due to freeze-thaw cycles.

Cracks reduce the existing contact surface between mortar and riprap or the existing cross-section of mortar that withstands the bending stresses in the revetment cross-section, which in turn increases the stress in the remaining cross-section for the same load. This can result in further deterioration of the revetment, which can ultimately lead to damage and failure of the revetment. The risk of cracks with regard to the durability, serviceability or load-bearing capacity of MGRRs under wave loading is as yet unclear and can only be assessed with process-based models of the relevant damage mechanisms. Furthermore, since crack widths and lengths in MGRRs are not recorded during dike inspections, it is difficult to properly asses their development and thus their causes.

Monolithic or coherent revetments are often modelled as a plate on an elastic foundation (PEF) for the top layer design. With this model, bending stresses due to wave attack can be calculated and in a limit state equation be compared to permissible stresses, whereby crack formation can be predicted. Among these revetments are asphalt revetments [16], polyurethane bonded revetments [17] and riprap fully grouted with asphalt [18]. For all these revetments the wave impact load is defined as critical load condition for the formation of cracks. In the design process, the wave impact load is simplified as a static load and an analytical solution for infinite beam length is deployed to calculate the bending stresses. The wave impact load is spatially idealized and simplified as a triangular load on the revetment surface. This load is defined in space by its wave impact magnitude p_{max} and width B (see Figure 2), which are found in hydraulic experiments, see for example Oumeraci et al. [19]. The wave impact magnitude is determined with the following equation [16]:

$$p_{max} = k_p \times \rho_w \times g \times H_s \tag{1}$$

where k_p is a dimensionless wave impact coefficient, ρ_w the density of water, g the acceleration due to gravity and H_s the significant wave height. Major influences on the wave impact coefficient k_p are structural parameters of the revetment, namely roughness and porosity, as well as the revetment slope angle α [20]. Table 1 gives an overview of the different parameters used for each type of revetment.

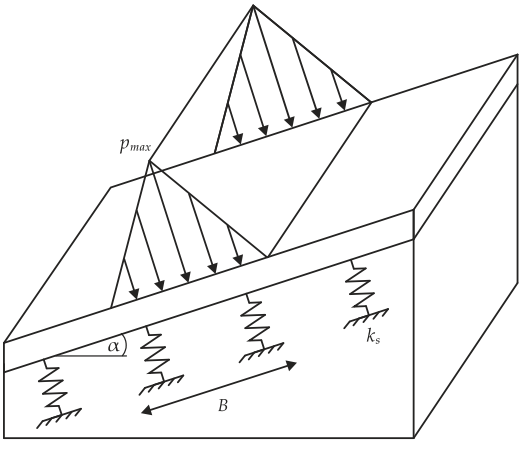

Figure 2. Plate on an elastic foundation (PEF) and wave impact load, idealized as triangular load (after [16]).

Table 1. Parametrization of the wave load in the design of different kinds of monolithic or coherent revetments with a PEF model.

Revetment	k_p	Width B	Slope Angle Tan (α)	Reference
Asphalt	approx. 2–6 *	H_s	1:3–1:8	[9,16]
Polyurethane bonded revetment	4	H_s	1:3	[17,21]
Riprap fully grouted with asphalt	approx. 2–6 *	H_s	1:3–1:8	[18]

* Is calculated in the design process with a probability density function.

For asphalt revetments Rijkswaterstraat [18] describes calculating the bending stress under buoyancy loads during wave run down with a PEF model. However, the actual pressure distribution under the cover layer during wave run down must be determined by the designer of the revetment [18]. Consequently, an evaluation of the model is not given in [18].

As a result of friction and interlocking pattern placed revetments also act as a coherent structure and can therefore be modelled as a PEF. Peters [15] calculates stresses and deflections of pattern placed revetments during wave impact using a static solution and additionally, as pattern placed revetments are more flexible than the other types of revetments listed in Table 1, by using a dynamic solution for the equation for a PEF. Peters [15] recommends carrying out a dynamic calculation or a static calculation with amplification factors for pattern placed revetments.

1.3. Objective and Outline

The hydraulic boundary conditions, especially the pressures on and beneath the revetment, the relevant structural properties and the stresses within the revetment resulting from the combination of these properties and the wave loading are not yet known for MGRRs. Furthermore, MGRRs have a wide range of possible permeabilities and porosities due to different amounts of mortar used for grouting. These parameters are of paramount importance for the wave-structure interaction [11–13,22]. Therefore, it is not possible to determine beforehand which external loading is decisive for the formation of cracks in MGRRs.

The aim of the present work is to establish a process-based model to calculate the bending stresses for MGRRs. To this end, MGRRs are numerically modelled as a PEF using the finite differences method. This allows a large number of load situations to be calculated quickly. These load situations are represented by time series of pressure transducers (PT), which were recorded in full-scale hydraulic model tests. Therefore, no decisive load situations have to be defined beforehand and the respective loads do not have to be parameterized, but the actual loads are used in the form of the pressure distribution along the top layer. The bending stresses can be used as acting stresses in a limit state equation and thereby be compared to permissible tolerable stresses.

Firstly, the PEF model and the full-scale hydraulic model tests are presented, then the boundary conditions and model parameters of the PEF model as well as their variations are described. The results of the model are presented as relative tensile bending stresses.

2. Materials and Methods

2.1. Plate on an Elastic Foundation Model

A coherent revetment on a compressible embankment, e.g., made of sand or clay, can be modelled as a plate on an elastic foundation, see for example [15] or [16]. The basis for the theory of the PEF is the hypothesis of Winkler/Zimmermann [23] that states that the elastic support beneath the plate reacts to the deformation of the plate with a counterpressure that is proportional to the deflection w of the plate. The elastic support of the plate is represented by springs unaffected by each other

and a linear-elastic deformation behavior of the springs is assumed. The differential equation of the deflection of the PEF for static loads is [23]:

$$\frac{d^2}{dx^2}\left[EI_{yy}(x)\frac{d^2w(x)}{dx^2}\right] + k_s(x)w(x) = q(x) \tag{2}$$

where EI_{yy} is the bending stiffness of the plate, w its deflection, k_s the modulus of subgrade reaction and q the external load. The x-axis is defined in the longitudinal direction of the plate.

However, the soil beneath the plate cannot transfer tensile forces. Therefore, if the external force acts against gravity and leads to an upward deflection of the plate, the spring force at this point becomes zero. The external force is then distributed to other areas of the plate by transverse forces and bending moments. The bending moment M_y is calculated from the deflection as follows:

$$M_y(x) = -EI_{yy}\frac{d^2w(x)}{dx^2} \tag{3}$$

Analytical solutions of Equation (3) for infinitely long plates and special loads such as point loads are given, for example, by Dankert and Dankert [23]. In order to be able to calculate as many different load situations as possible with a finite length of the plate and loads that vary greatly along the plate in the shortest possible computing time, the differential equation was converted into a finite difference equation in this work. The model was then implemented in MATLAB (MATLAB R2018b MathWorks®, Natick, Massachusetts, United States). The algorithm *gabamp.m* (Gauss algorithm with column pivoting for asymmetric band matrices) of Dankert and Dankert [23] was used to solve the resulting system of equations.

2.2. Full Scale Hydraulic Model Tests

Four different configurations of MGRRS were tested in full scale hydraulic model tests in the Large Wave Flume (in German "Großer Wellenkanal", abbreviation: *GWK*) of the Coastal Research Centre, which is a joint research facility of Technische Universität Braunschweig and Leibniz Universität Hannover. The width of the embankment section was split in half by a thin wooden wall, see Figure 3. In this manner, two revetment configurations could be tested at the same time and a maximum of different revetment configurations and wave parameters could be tested whilst minimizing testing time.

Figure 3. Partially grouted MGRRs (v_g = 80 L/m^2) in test phase one (Photos: Kreyenschulte and Kühling, 2017).

The slope angle of all revetment configurations was cot(α) = 3. On the north side of the separation wall (see Figure 3), a 0.60 m thick riprap revetment was built while on the south side the thickness of the revetment was d_t = 0.40 m. Before the first test phase, both revetments were grouted with 80 L/m^2 mortar. The revetments were grouted by hand by experienced contractors that have been grouting MGRRs for decades. Assuming a porosity of 0.45 before grouting (riprap dumped in dry conditions, medium density according to [5]) this resulted in permeable revetments after grouting with a porosity of n = 0.25 (d_t = 0.40 m) and n = 0.32 (d_t = 0.60 m), respectively.

Before test phase two, the revetment on the south side of the separation wall was removed completely and replaced by a riprap revetment which again had a layer thickness of 0.40 m. This revetment was then fully grouted so that the whole pore volume of the stone layer was filled with mortar. This constitutes the standard process of constructing an impermeable, fully-grouted revetment [5]. The amount of mortar needed to fill up the entire pore volume was 180 L/m^2, confirming the assumption of a porosity of 0.45 before grouting, which results in an available pore volume of V_p = 180 L/m^2 ($V_p = n \times d_t \times 1000$ L/m^3 = 0.45 × 0.40 m × 1000 L/m^3) before grouting.

The revetment on the north side of the separation wall was not removed but instead grouted until the top layer was apparently impermeable. The amount of mortar needed for this was 100 L/m^2, confirming that the lower part of the cross-section of the top layer still exhibited a free pore volume and was only partially grouted. The potential free pore volume before any grouting of the top layer took place (before test phase one) was 270 L/m^2 (0.45 × 0.60 m × 1000 L/m^3), thus a pore volume of 90 L/m^2 was still available in the lower part of the top layer in test phase two. The overall volumetric porosity of the revetment equaled 0.16, while it was at the same time impermeable for any flow perpendicular to the embankment.

The revetment on the north side is of practical relevance as it represents a revetment that was constructed as a permeable revetment but due to repair works, during which the damaged parts of the revetment were re-grouted with mortar, became more and more impermeable over the years. It also represents a revetment which was designed as a fully grouted revetment but was grouted with mortar that was not sufficiently flowable and poorly adjusted to fill the free pore volume of the riprap. All revetment configurations tested and their characteristics are listed in Table 2.

Table 2. Characteristics of the MGRRs in the *GWK*.

	Partially Grouted		Fully Grouted	
Section	**North**	**South**	**North**	**South**
Configuration Nr.	1	2	3	4
Top layer thickness d_t (m)	0.6	0.4	0.6	0.4
Amount of mortar v_g (L/m^2)	80	80	80 + 100	180
Estimated porosity n before grouting (-)	0.45	0.45	0.45	0.45
Porosity n after grouting (-)	0.32	0.25	0.16	0
Pore volume V_p after grouting (L/m^2)	190	100	90	0

All top layers were placed on a geotextile (permeability $k_{10,H50mm}$ = 2.86 × 10^{-3} m/s, thickness 8 mm, characteristic opening size 0.1 mm), which was directly placed on the sand embankment. The toe structure of the revetment below the lowest wave run-down was made of concrete blocks in order to support the revetment. By this means, an efficient construction of the revetment was ensured, covering only the relevant section of the slope with grouted riprap material. The crest of the embankment was constructed of concrete blocks behind which any overtopping water was collected in a basin and discharged back into the flume during the tests.

The riprap used for the top layer was stone weight class $LMB_{5/40}$ with a median weight of G_{50} = 23.5 kg and a narrow grading with d_{85}/d_{15} = 1.5. The grouting mortar can either be produced by adding additives to the mortar or by mixing it in a colloidal mixer with high velocity shear action [24] to ensure an appropriate consistency of the fresh grout for a distribution of mortar inside the pore

space of the riprap that results in a "sufficient" permeability and bonding of the individual stones. The latter method was chosen for grouting the riprap for the experiments in the *GWK*. The mortar was tested and fulfilled all requirements stated by the code of practice "Use of Cementitious and Bituminous Materials for Grouting Armourstone on Waterways" [5].

In order to gain results of practical relevance, the revetments were exposed to JONSWAP-spectra with a minimum of 1000 waves per test. Wave heights from H_{m0} = 0.38–0.94 m and wave periods from $T_{m-1,0}$ = 2.7–9.0 s were generated which resulted in surf similarity parameters $\xi_{m-1,0}$ = 1.55–4.64. In this way a wide range of wave loading conditions and breaker types were covered. The still water level in all experiments was set to 4 m.

Incident wave parameters, wave run-up as well as wave induced pressures on and beneath the revetment were measured. For the results presented in this work only wave induced pressures are of interest. Figure 4 shows a longitudinal section of the *GWK* and the instrumentation relevant for the results presented herein.

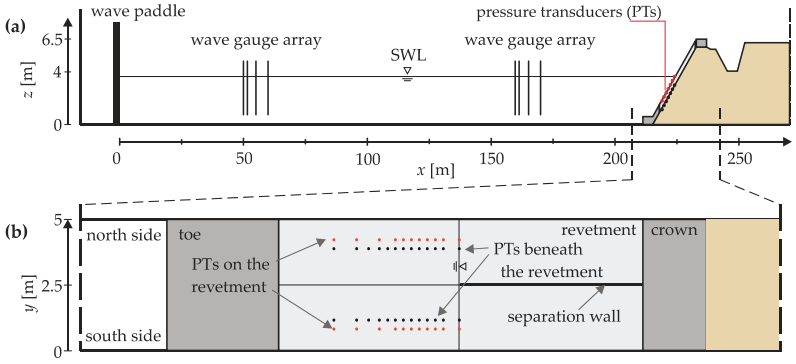

Figure 4. (**a**) Schematic longitudinal cross-section of the *GWK* showing the wave paddle at the left, the instrumentation along the flume and the revetment on the right. (**b**) Top view of the revetment section with the pressure transducers on and beneath the top layer in red and black, respectively.

In order to measure the wave parameters, two wave gauge arrays were set up in the *GWK*, each consisting of four resistance type wave gauges with a measuring frequency of 100 Hz. The wave gauge array next to the revetment was used to calculate the wave parameters at the toe of the structure. Analyzing the signal of the four wave gauges with the computer program L~davis [25], which makes use of the method of Mansard and Funke [26], gave the incident and reflected wave parameters. Using the incident wave period $T_{m-1,0}$, the fictitious wave length in deep water according to EurOtop [27] was calculated:

$$L_{m-1,0} = \frac{gT_{m-1,0}^2}{2\pi} \tag{4}$$

The fictitious surf similarity parameter in deep water is calculated with Equation (5) [27]:

$$\xi_{m-1,0} = \tan\alpha / \sqrt{\frac{H_{m0}}{L_{m-1,0}}} \tag{5}$$

For every revetment configuration 11 pressure transducers (PTs) were installed at the top edge and 13 PTs were installed at the bottom edge of the top layer. The bottom PTs were arranged in pairs perpendicular to the PTs at the top edge of the revetment. The time series of the PTs can thus be used directly to calculate the pressure difference between the upper and lower edge of the top layer, which represents the resulting load on the revetment. The PTs at the top edge of the top layer were of type PDCR 830 (0.1% accuracy with a measuring range of 5 bar in the upper part of the top layer and

1 bar for the two PTs furthest seaward) manufactured by Druck Ltd. (Leicester, UK) and recorded the pressure with a measuring frequency of 1000 Hz. The PTs at the bottom edge of the top layer were of type PDCR 1830 (0.1% accuracy at a measuring range of 1 bar) manufactured by GE Sensing (Boston, Massachusetts, USA) and recorded the pressure with a measuring frequency of 200 Hz. Figure 5 shows the position of the PTs in detail.

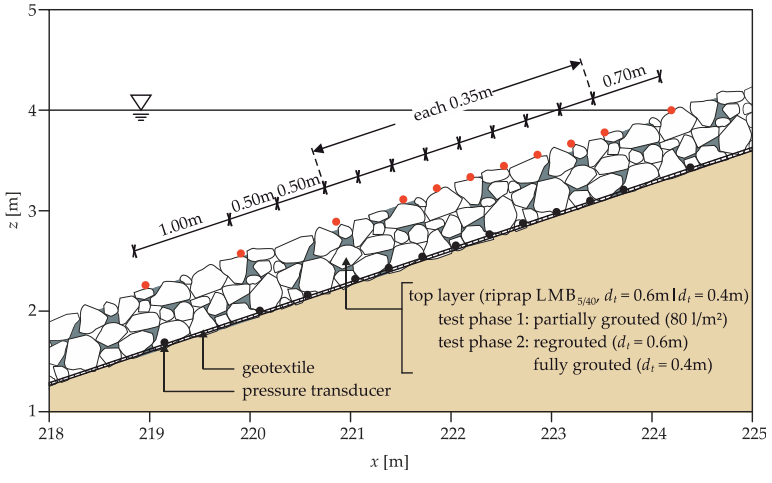

Figure 5. Position of the PTs in the *GWK* (after [28]).

To avoid damage of the PTs during construction of the revetment and to assure their defined position, the PTs were installed in steel pipes attached to a steel channel, see Figure 6a,b. In this way, also the reconstruction of the revetment on the south side of the *GWK* before test phase two was made possible, see Figure 6c. This is the reason why the PTs on the top edge of the top layer have not been installed in the middle of the north or south section but were instead shifted 0.45 m to the outer walls of the *GWK*, from which the PTs are 0.80 m away. The PTs at the bottom edge of the top layer are shifted 0.34 m to the inner wooden separation wall between the revetments in order to avoid any influence on the recorded pressure due to the steel channel.

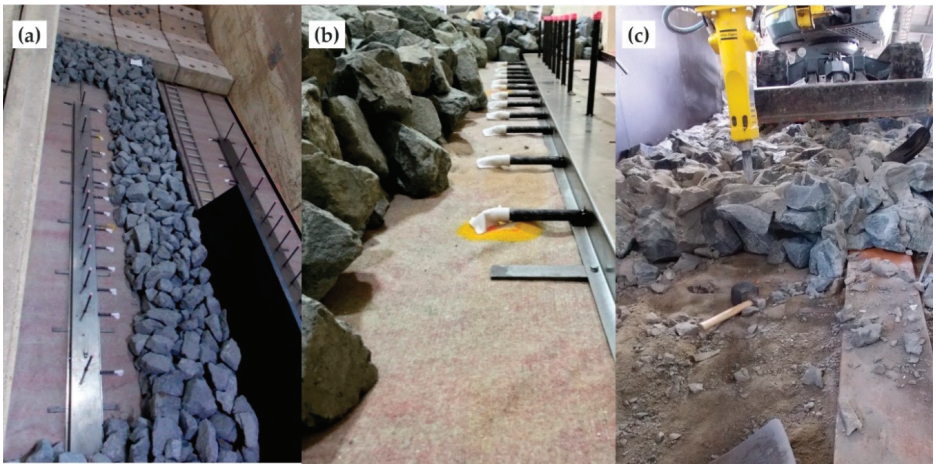

Figure 6. (**a**) Top view and (**b**) close up of the placement of the steel channel for the PTs in the top layer. (**c**) Demolition of the 0.40 m thick revetment on the south side before test phase two in order to construct a new revetment. The steel channel is visible in the lower right part of the picture. Notice also the partial grouting of test phase one, recognizable by portions of free pore space and grout (Photos: Kreyenschulte, 2017).

2.3. Boundary Conditions PEF

The geometry of the top layers in the *GWK* is represented in the PEF model. As both the toe structure and the crown support are placed in front of the top layer and neither transverse forces nor moments can be transferred there, the model edges are defined as free at x = 0 m and x = 18.13 m, see Figure 7. The spatial resolution of the top layer for the calculations is defined as Δx = 0.18 m, thus ensuring a reasonable calculation time while maintaining accuracy of the results.

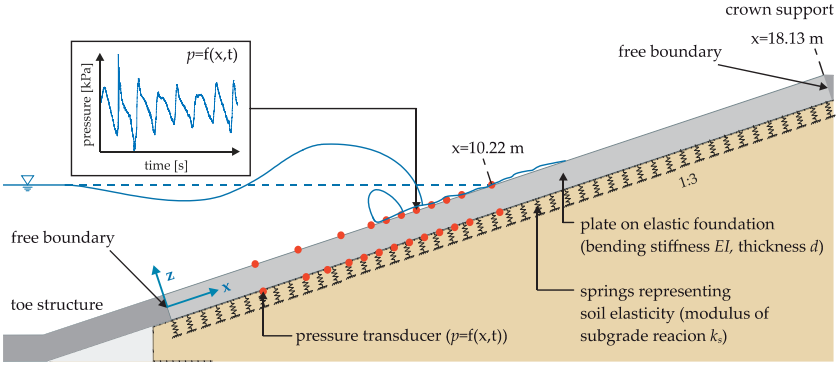

Figure 7. Model of the MGRRs as a plate on an elastic foundation with boundary conditions and model parameters (after [28]).

An event, i.e., an incoming wave, was defined using the zero downcrossing method for the time series of the pressure transducer located furthest seaward. This definition of an event was also used by Klein Breteler et al. [29] when investigating pattern placed revetments.

In order to calculate the pressure difference along the x-axis from the time series of the pressures on the upper and bottom edge of the top layer, a moving average was used to average the measurements

on the upper edge of the top layer to a frequency of 200 Hz. For this purpose, the method described by [29] was used.

2.4. Plate on an Elastic Foundation Model

2.4.1. Bending Stiffness

No large-scale mechanical tests are available to determine the bending stiffness of MGRRs. Therefore, the bending stiffness of the top layer is calculated by considering the cross-section of a MGRR as a composite cross-section. Thus, the mechanical properties of the MGRR can be calculated from the mechanical properties of its constituents, namely mortar and riprap. The procedure described below was also used by Rijkswaterstraat [18] for calculating the bending stiffness of riprap fully grouted with asphalt.

It is assumed that the top layer is exposed to pure bending load. This assumption is on the safe side with regard to the maximum bending tensile stress, as the normal force in the top layer due to its own weight would act as a compressive force. It is assumed that cracks will occur in the mortar or the bonding surface between mortar and riprap as a result of tensile forces. For pure bending, the bending stiffness of the top layer can be determined in the same way as for composite cross-sections of materials with different moduli of elasticity. The following assumptions are necessary [30]:

- The materials cannot shift against each other at their interfaces (no slippage).
- Since the behavior of a mortar-grouted riprap is to be described up to the first crack formation, a linear relationship between stress and strain is assumed in the uncracked state according to Hooke's law.

For simplicity, it is further assumed that the area filled with grout and the area of the riprap are evenly distributed in the entire cross-section. It is also assumed that the moduli of elasticity of the components under compression and tension are the same, as the resulting deviation of the calculated bending stiffness is small. The bending stiffness $\overline{EI}$ is then calculated as follows [30]:

$$\overline{EI} = \sum_i E_i I_i = E_{RR} \int_A \bar{z}_{RR}^2 \times dA + E_M \int_A \bar{z}_M^2 \times dA \tag{6}$$

where E_{RR} and E_M are the moduli of elasticity of riprap (index RR) and mortar (index M), respectively, A is the area of each component in the cross-section and $\bar{z}$ is the distance of the center of gravity of each surface from the center of the ideal total cross-section, which corresponds to the center of gravity of the cross-section under the assumptions made. The bending stiffness of the top layer is therefore calculated as follows:

$$\overline{EI} = E_{RR} \times a_{RR} \times \frac{b \times d_t^3}{12\left(1 - \mu_{RR}^2\right)} + E_M \times a_M \times \frac{b \times d_t^3}{12\left(1 - \mu_M^2\right)} \tag{7}$$

where a_{RR} and a_M are the area shares of the components in the total cross-section, d_t is the top layer thickness, b the cross-section width and μ_{RR} and μ_M Poisson's ratio of riprap and mortar, respectively. The stress in the respective components can be calculated as a function of the distance from the center of the ideal cross-section according to:

$$\sigma_i = \frac{E_i}{\overline{E}} \frac{M_y}{\overline{I}} \bar{z} \tag{8}$$

At the Institute of Building Materials Research at RWTH Aachen University mechanical tests were carried out on riprap and colloidal grout to determine the static modulus of elasticity, see [31]. In addition, Poisson's ratio was determined during these tests. The tests as well as their results are summarized in the Appendix A of this work. Table 3 provides a summary of the elastic moduli of the

top layer components. Poisson's ratio was μ_M = 0.06 (coefficient of variation σ' = 0.10) for the mortar and μ_{RR} = 0.23 (coefficient of variation σ' = 0.11) for the riprap.

Table 3. Static modulus of elasticity $E_{stat,33}$ of the components of MGRRs, dependent on the load (after [31]).

Component and Load	Static Modulus of Elasticity $E_{stat,33}$ (N/mm²)				
	Minimum	Mean	Maximum	Standard Deviation	Coefficient of Variation (–)
Riprap (Compression)	60,951	**68,767**	76,771	6327	0.09
Riprap (Tension)	40,394	**61,936**	77,009	13,433	0.22
Mortar (Compression)	22,532	**23,270**	24,287	606	0.03
Mortar (Tension)	17,766	**19,520**	21,329	1374	0.07

Values in the range of the mean values of the elastic moduli of the components are used for calculating the bending stiffness of the composite cross-section (top layer). The area shares of mortar and riprap are assumed to correspond on average to the volumetric proportions of the components and were therefore chosen according to the porosity and the amount of mortar used for grouting. As Poisson's ratios of riprap and mortar only have a slight influence on the calculated bending stiffness of the top layer, they were neglected. All selected values and the resulting bending stiffnesses for each cover layer are summarized in Table 4.

Table 4. Parameter for MGRR in the PEF model.

Top Layer Thickness d_t (m)	Description	Static Modulus of Elasticity $E_{stat,33}$ (N/mm²)		Area Share of Components in Cross-Section (–)		Bending Stiffness $\overline{EI}$ (MNm²)
		Riprap	Mortar	a_{RR}	a_M	
0.40	Fully grouted	60,000	20,000	0.55	0.45	224.00
	Partially grouted, v_g = 80 L/m²				0.20	197.33
0.60	Regrouted, v_g = 80 + 100 L/m²	60,000	20,000	0.55	0.29	698.40
	Partially grouted, v_g = 80 L/m²				0.13	642.00

2.4.2. Modulus of Subgrade Reaction

The mechanical properties of the soil beneath the revetment are represented in the model by the modulus of subgrade reaction k_s, which must be determined in physical tests for the respective soil. Peters [15] points out that there are no measurements of the modulus of subgrade reaction for soils beneath revetments. For the calculations carried out here, the modulus of subgrade reaction is therefore obtained from literature. As a non-exhaustive summary, Table 5 shows the range of possible values of moduli of subgrade reaction and shows which values were used in other publications to calculate the stresses in the cross-section of a revetment using a PEF model.

Table 5. Overview of moduli of subgrade reaction k_s used for PEF revetment models.

Soil	k_s (MN/m³)	Description	Reference
"Sandy soil"	10–20	Recommendation for soils beneath revetments, wave impact load	[15]
"Dense sand"	100	Beneath asphalt revetments, wave impact load	[32]
	64		
"Sand"	40–100 *	Beneath asphalt revetments	[9]
	35–60	Beneath asphalt revetments, quasi-static load	[33]
	50–90	Beneath asphalt revetments, wave impact load	

* 100 MN/m² for medium to well compacted sand, proctor density >95%.

According to Peters [15], low values of 10–20 MN/m³ for the modulus of subgrade reaction for soils beneath revetments are realistic because, in contrast to soils beneath other structures like building foundations or roads, the soil beneath a revetment is often not treated and compacted as elaborately.

Especially in the case of permeable revetments, the external loads additionally cause the pore water pressures in the soil beneath the revetment to oscillate and thus loosen rather than compact the grain structure of the soil, which further reduces the modulus of subgrade reaction [15,34]. Richwien [34] points out that when designing revetments with a PEF model, the soil properties that may change during a storm event must be considered by adjusting the modulus of subgrade reaction accordingly. The calculations for MGRRs are performed with k_s = 10 MN/m^3 and k_s = 50 MN/m^3. These values are intended to represent sandy soils in different degrees of compaction during cyclic wave loading.

2.4.3. Parameter Variations

The model parameters resulting from the considerations and physical model tests presented herein, with which the internal forces and tensile bending stresses of the MGRRs in the *GWK* are calculated using the PEF model, are shown in Table 6.

Table 6. Model parameter combinations for the MGRRs of the *GWK* tests.

Top Layer Thickness d_t (m)	Description	Bending Stiffness $\overline{EI}$ (MNn^2)	Modulus of Subgrade Reaction k_s (MN/m^3)	Denomination
0.40	Fully grouted	224.00	50	Parameter combination 1
	Partially grouted, v_g = 80 L/m^2	197.33		
0.60	Regrouted, v_g = 80 + 100 L/m^2	698.40		
	Partially grouted, v_g = 80 L/m^2	642.00		
0.40	Fully grouted	224.00	10	Parameter combination 2
	Partially grouted, v_g = 80 L/m^2	197.33		
0.60	Regrouted, v_g = 80 + 100 L/m^2	698.40		
	Partially grouted, v_g = 80 L/m^2	642.00		

3. Results

3.1. Paramter Combination 1

With the PEF model and the measured data of the PTs for each experiment in the *GWK* with at least 1000 waves as boundary condition the resulting maximum tensile bending stresses were calculated and analyzed depending on the revetment configuration. Figure 8 shows the calculated maximum relative tensile bending stress $\sigma_{x,max}/(\rho_w g H_{m0})$ at the edge of the cross-section (the maximum bending stresses either occur at the top or bottom edge of the cross-section) of the partially grouted MGRRs over the surf similarity parameter $\xi_{m\text{-}1,0}$ for parameter combination 1, i.e., k_s = 50 MN/m^3. The relative stress is calculated by dividing the stress by a fictitious hydrostatic pressure at wave height H_{m0}. The magnitude of the bending stresses depends in particular on the mean wave height H_{m0} and the way the waves break on the revetment or are reflected at the revetment, which is taken into account by depicting the bending stresses as a function of the surf similarity parameter $\xi_{m\text{-}1.0}$. In Figure 8 and all following figures depicting the stresses, no distinction is made between the maximum stress at the upper edge or bottom edge of the top layer.

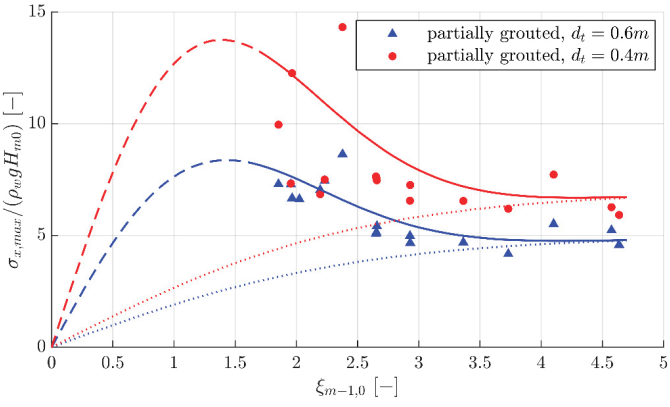

Figure 8. Maximum relative tensile bending stress $\sigma_{x,max}/(\rho_w g H_{m0})$ dependent on the surf similarity parameter $\xi_{m-1,0}$ with enveloping functions (permeable, partially grouted MGRRs, parameter combination 1). The quasi-static component of the relative bending stress from Equation (9) is shown as a dotted line. The dashed line for illustration shows the enveloping functions for surf similarity parameters for which no experimental data is available (after [28]).

The bending stress for each configuration of MGRR is described by functions representing an upper envelope. Based on the procedure used to describe the maximum relative pressures on a polyurethane bonded top layer by Alcérreca-Huerta and Oumeraci [11], these functions are the sum of the quasi-static stress $\sigma_{x,qst}$ resulting from the quasi-static component of the wave load and the impact component $\sigma_{x,imp}$ resulting from wave impacts:

$$\frac{\sigma_x}{\rho_W g H_{m0}} = \frac{\sigma_{x,qst}}{\rho_W g H_{m0}} + \frac{\sigma_{x,imp}}{\rho_W g H_{m0}} \tag{9}$$

The quasi-static stress is modelled by Equation (10):

$$\frac{\sigma_{x,qst}}{\rho_W g H_{m0}} = c_1 \times \tan h(c_2 \times \xi_{m-1,0}) \tag{10}$$

where c_1 and c_2 are empirical factors. Equation (10) gives meaningful limit values for quasi-static loads, as $f(\xi_{m-1,0}) \to 0$ for $\xi_{m-1,0} \to 0$, i.e., for spilling breakers the stresses tend to zero. For $\xi_{m-1,0} \to \infty$, $f(\xi_{m-1,0})$ tends to a limit value that is dependent on the revetment characteristics. As the maximum relative stresses for $\xi_{m-1.0} > 2.5$ mostly occur during wave run-down, this limit value is particularly dependent on the time it takes for the pressure beneath the top layer to adapt to the pressure on the top layer, which is dependent on the porosity and permeability of the top layer.

The impact component of Equation (9) is modelled as Rayleigh distributed by Equation (11):

$$\frac{\sigma_{x,imp}}{\rho_W g H_{m0}} = c_3 \times \xi_{m-1,0} \times e^{(-0.5 \times \xi_{m-1,0}^2 / c_4)} \tag{11}$$

Again, meaningful limit values are assured because $f(\xi_{m-1,0}) \to 0$ for $\xi_{m-1,0} \to 0$ and $f(\xi_{m-1,0}) \to 0$ for $\xi_{m-1,0} \to \infty$, as the number of impact loads tends to zero for spilling breakers as well as for reflected waves. For this reason, the Technical Advisory Committee on Flood Defence [9] as well as Alcérreca-Huerta and Oumeraci [11] represent the magnitude of wave impacts by a Rayleigh distribution. The sum of quasi-static load and impact load (Equation (9)) tends to the quasi-static load ($f_{total}(\xi_{m-1,0}) \to f_{quasi\text{-}static}(\xi_{m-1,0})$) for $\xi_{m-1,0} \to \infty$. The quasi-static component of the relative bending stress can be understood as the lower envelope function and the sum of the quasi-static component and the component due to the impact load as the upper envelope function. The empirical parameters

c_1–c_4 in Equations (10) and (11) are given for each MGRR configuration in Table 7. In Figure 8 and all following figures depicting the relative bending stress, the solid lines show the validity range of the functions for which pressure measurement data from the physical model tests in the *GWK* is available. The dashed lines show the values of the function for smaller surf similarity parameters where no pressure measurements are available.

For surf similarity parameters $\xi_{m-1.0} \leq 2.5$ in Figure 8 the relative bending tensile stress and its scattering increase due to the higher probability of occurrence of wave impacts and due to the increase in their magnitude. For larger surf similarity parameters ($\xi_{m-1.0} > 2.5$), the relative bending stress seems to reach a limit value. The non-breaking waves occurring in this range of surf similarity parameters therefore do not seem to be able to generate larger pressure differences as a result of wave rundown, since the top layers are permeable and thus the pressure beneath the top layers can adapt quickly to the pressure on the top layers. Given the same load, the relative bending stresses are lower for the 0.60 m thick revetment, because of its higher bending stiffness. This results in lower stresses in the 0.60 m thick revetment for almost all wave loads measured in the *GWK*, see also Figure 9.

Table 7. Empirical coefficients of the enveloping functions of the maximum relative bending stress for each parameter combination and top layer configuration.

d_t (m)	Description	c_1	c_1	c_3	c_4	Restriction of Validity *	
0.40	Fully Grouted	20	0.2	30	1.8	$L_{m-1,0}$ <50 m	Parameter combination 1 (k_s = 50 MN/m^3)
	Partially grouted, v_g = 80 L/m^2	7	0.4	14	1.5	-	
0.60	Regrouted, v_g = 80 + 100 L/m^2	20	0.2	10	1.8	$L_{m-1,0}$ <50 m	
	Partially grouted, v_g = 80 L/m^2	5	0.4	8	1.5	-	
0.40	Fully grouted	40	0.2	50	1.8	$L_{m-1,0}$ <50 m	Parameter combination 2 (k_s = 10 MN/m^3)
	Partially grouted, v_g = 80 L/m^2	12	0.4	20	1.5	-	
0.60	Regrouted, v_g = 80 + 100 L/m^2	30	0.25	18	1.8	$L_{m-1,0}$ <50 m	
	Partially grouted, v_g = 80 L/m^2	10	0.4	14	1.5	-	

* Other than the restriction that the results are only valid for the parameters investigated in the GWK.

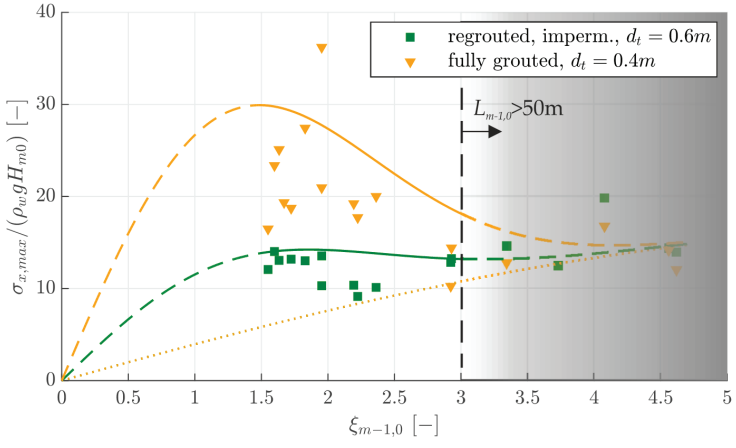

Figure 9. Maximum relative tensile bending stress $\sigma_{x,max}/(\rho_w g H_{m0})$ dependent on the surf similarity parameter $\xi_{m-1,0}$ with enveloping functions (impermeable, regrouted and fully grouted MGRR, parameter combination 1). The quasi-static component of the relative bending stress from Equation (9) is shown as a dotted line. The dashed line for illustration shows the enveloping functions for surf similarity parameters for which no experimental data is available (after [28]).

The high relative bending stresses for the 0.40 m thick top layer at $\xi_{m-1.0} \approx 2.4$, compared to other values for similar surf similarity parameters, are due to a particularly high wave impact load. This highlights the inherent natural variability of the magnitude of the wave impact load, which becomes particularly apparent when considering the maximum values of the bending tensile stresses. Figure 9 shows the calculated maximum relative tensile bending stress $\sigma_x/(\rho_W g H_{m0})$ at the edge of the cross-section of the fully grouted MGRR and regrouted MGRR as a function of the surf similarity parameter $\xi_{m-1,0}$ for parameter combination 1.

In the case of the fully grouted and impermeable top layer with a thickness of 0.40 m, the increase in relative bending stress is much more pronounced for surf similarity parameters associated with a high number of plunging breakers leading to wave impact ($\xi_{m-1.0} \leq 2.5$) than in the case of permeable top layers (cf. Figure 8).

Higher bending stresses in fully grouted MGRRs compared to partially grouted MGRRs are due to greater wave loading of fully grouted MGRRs. Fully grouted top layers are smoother than partially grouted top layers. Therefore, the probability that there is a water layer from the previous wave run-down on the top layer during wave impact is lower for fully grouted top layers. Such a water layer greatly reduces the magnitude of wave impacts [35]. Another reason is that the pressure beneath the top layer cannot adopt as quickly to the pressure on the revetment as in the case of a permeable top layer, because the fully grouted top layer is impermeable. As a result, a large pressure difference between the upper and bottom edge of the top layer is created when it is exposed to wave impact. The high bending stress at $\xi_{m-1,0} \approx 1.9$ again highlights the inherent natural variability of the magnitude of the wave impact load.

In contrast, the increase in relative bending stress for surf similarity parameters $\xi_{m-1.0} \leq 2.5$ is small in the case of the regrouted top layer ($d_t = 0.60$ m). The pressure changes more quickly beneath the top layer in the case of the regrouted top layer compared to the fully grouted top layer for the same wave conditions. The peak pressure beneath the regrouted revetment in the instant of maximum stresses during wave impact was about 20% of the peak pressure on the revetment in that same instant. As a consequence, the pressure difference is reduced. This also decreases the variation in the relative bending stresses for $\xi_{m-1.0} \leq 2.5$ as the pressure gradient along the top layer decreases in comparison to the fully grouted MGRR. Another reason for lower variation of the relative bending stress for the regrouted top layer is the fact that the variation of the peak pressure on the revetment was smaller than for the fully grouted MGRR, which is most probably caused by the natural variability of the wave impact load in combination with slightly different surface characteristics of the top layers.

The pressure changes more quickly beneath the top layer in the case of the regrouted top layer due to the grout distribution in the lower part of the regrouted top layer that is similar to a partially grouted top layer. As the mortar in case of the regrouted top layer was applied to the already partially grouted top layer, an impermeable top layer was created but not the entire pore volume of the top layer was filled with mortar. A porosity of the regrouted top layer of $n_{regrouted} = 0.16$ remained.

For wavelengths $L_{m-1.0} > 50$ m (corresponds approximately to surf similarity parameters $\xi_{m-1.0} > 3$ in Figure 9), greater wave run-down heights were observed for both impermeable cover layers. Because the PTs did not cover the entire length of the revetment (the most seaward PT on the top edge of the top layer has a coordinate of $z = 2.28$ m), they did not resolve the complete load figure during wave run-down for such long wavelengths. Therefore, for the impermeable MGRRs and wavelengths $L_{m-1.0} > 50$ m, the PTs do not provide reliable boundary conditions for the model. The calculated relative bending stresses are therefore not meaningful. The validity of the given functions and empirical parameter (see Table 7) is therefore limited to wavelengths $L_{m-1,0} < 50$.

3.2. Parameter Combination 2

Figure 10 shows the calculated maximum relative tensile bending stress $\sigma_x/(\rho_W g H_{m0})$ at the edge of the cross-section (a) of the partially grouted MGRRs and (b) of the fully and regrouted MGRRs

over the surf similarity parameter $\xi_{m\text{-}1,0}$ for parameter combination 2. Again, functions for the upper envelope of the results are defined.

The smaller modulus of subgrade reaction (k_s = 10 MN/m^3) leads to greater deflections and thus to higher relative bending stresses for the same external load and bending stiffness of the revetments. The relative bending stresses are therefore increased in comparison to parameter combination 1. The same remarks regarding the validity range of the equations apply as for parameter combination 1. Table 7 gives an overview of the empirical coefficients used for the equations.

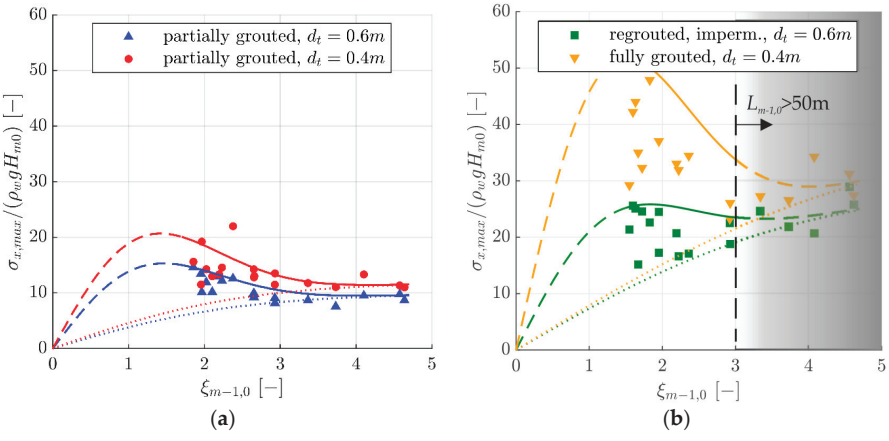

Figure 10. Maximum relative tensile bending stress $\sigma_{x,max}/(\rho_w g H_{m0})$ dependent on the surf similarity parameter $\xi_{m-1,0}$ with enveloping functions (parameter combination 2) for (**a**) permeable, partially grouted MGRR and (**b**) impermeable, regrouted and fully grouted MGRR (after [28]).

4. Discussion

The magnitude of the maximum relative tensile bending stress is firstly governed by the wave loading that exerts pressures on the MGRR. For different MGRR configurations, the difference in pressures beneath the top layer accounts for most of the difference of wave loading between partially and fully grouted MGRRs. Different probabilities for water layers on the top layer during wave impact account for a minor proportion of this difference. Under the same wave conditions, partially grouted MGRR are therefore subject to smaller tensile bending stresses. For other revetment types, an increase in permeability reduces hydraulic loads, too. This is reflected for example in design equations for pattern placed revetments, see for example [36] or [37].

Secondly, all boundary conditions being equal, the magnitude of the maximum relative tensile bending stress is particularly dependent on the ratio between bending stiffness of the top layer and modulus of subgrade reaction. For relatively high bending stiffness and relatively low modulus of subgrade reaction this magnitude is increased, compare the results of parameter combination 1 (Section 3.1) and 2 (Section 3.2).

Thirdly, the boundary conditions at the toe structure and the upper end of the revetment influence the internal forces and thereby the bending stresses in the top layer of MGRR. Many different constructions are conceivable, but in most cases the upper end of the revetment will not be fixed to any structure that transfers forces or momentums. The same can be said about the toe structure, which in many cases will be a sheet pile wall or a footing made of riprap or mortar-grouted riprap. The boundary conditions considered for the PEF model in this work (see Section 2.3) are therefore deemed to be representative for most MGRRs.

All hydraulic model tests in the *GWK* were carried out in prototype scale. This was necessitated in particular by the interaction of the processes on the top layer, which are dominated by inertia, with the flow in the porous top layer, which is dominated by friction [38]. Furthermore, the breaking process of

the waves and the resulting pressures on the top layer are not scalable due to the great dependence of the pressures on the air content of the water, especially in the case of plunging breakers [35,39].

With regards to model effects, wave reflection at the wave paddle is prevented by active wave absorption in the *GWK* [40]. The wave load is represented two-dimensional in the wave channel. Regarding the stability of mortar-grouted riprap, the results for two-dimensional loading are on the safe side, since the load can only be transferred by the revetment along the slope (x-direction in Figure 7). Peters [15] notes for pattern placed revetments that under three-dimensional loading forces can be transferred into unloaded areas transverse to the direction along the slope, which increases the stability of the revetments.

Effects at the model boundaries are counteracted in particular by a sufficient width of the model, although these effects can never be completely avoided. The PTs were installed as close to the middle of each model section as the boundary constraints of installation, reconstruction and removal of the revetments allowed. In the wave channel fresh water was used instead of salt water. However, dimensionless quantities which take the density of the fluid into account are used to describe the results.

Assumptions regarding the distribution of grout in the top layer and equal moduli of elasticity for compression and tension for each revetment component were made to calculate the bending stiffness of the MGRR idealized as a PEF. These assumptions can easily be adjusted to be less restrictive. However, in the absence of full-scale bending tests on MGRRs, it is not certain whether such adjustments would yield any considerable improvements for the calculation of the bending stresses in MGRRs.

Due to the lack of detailed field data regarding damages and damage progression for MGRRs as well as due to missing full-scale bending tests on MGRRs the PEF model can be validated only with the observations made during the full-scale hydraulic model tests in the *GWK*. The sand beneath the revetments in the *GWK* was compacted, therefore probably yielding higher moduli of subgrade reaction that reduce the deflection and thereby reduce the bending stresses in the revetments. If we assume $k_s = 50$ MN/m^3, then the tensile bending stresses in all experiments in the *GWK* were $\sigma_x < 0.1$ N/mm^2 for the partially grouted MGRRs and $\sigma_x < 0.3$ N/mm^2 for the fully grouted and regrouted MGRRs. These stresses are lower than the average values of the tensile strength of colloidal mortar ($\beta_t \approx 0.96$ N/mm^2) as well as the adhesive tensile strength ($\beta_{t,adh} \approx 0.55$ N/mm^2) and adhesive bending tensile strength ($\beta_{bt,adh} \approx 1.44$ N/mm^2) between riprap and colloidal mortar as determined by the Institute of Building Materials Research at RWTH Aachen University [28,31]. The laboratory conditions in the *GWK* facilitated quality assurance of the application of the mortar as well as of the grouting mortar itself, supporting the assumption that the same strengths and adhesive strengths were present in the *GWK* experiments. The results of the PEF model therefore suggest that no cracks over the whole width of the revetments would occur and none were observed in the *GWK* experiments. Therefore, the observations are in line with the results of the PEF model.

The representation of the soil beneath the revetment as a spring is a considerable simplification. Due to this simplification, the modulus of subgrade reaction depends on a large number of variables, e.g., the load velocity, the duration and magnitude of the load as well as water saturation, load history, compaction and other parameters of the soil [15,33]. The modulus of subgrade reaction also depends on the bending stiffness of the structure, which influences the distribution of the soil bearing pressure [41]. Due to its simplicity and also due to the lack of detailed investigations into the mechanical properties of soils beneath revetments under wave loading in coastal environments, the modulus of subgrade reaction represents a reasonable model choice. The modulus of subgrade reaction for different soils beneath MGRRs could in a first step be determined in large scale laboratory tests by conducting bending tests on bedded MGRRs and comparing the measured deflection and load to results of calculations with the structural model that is described in this work.

As was described in Section 1, revetments with no flexibility are not able to not adapt to subsoil settlement and as a consequence, cavities can occur beneath these revetments and the bedding of the top layer is lost locally. In this case the stresses in the top layer during wave loading are significantly

increased and it therefore represents a damage mechanism that has to be taken into account when designing a MGRR. This is not considered in the results presented herein, as this work describes a first step for determining bending stresses in MGRRs in which newly constructed MGRR with constant bedding were considered. However, the PEF model presented in this work can also be used to calculate bending stresses in MGRRs that lost their bedding locally or for soils exhibiting different moduli of subgrade reaction, for that matter. Prerequisite for such a calculation are the spatially discretized load figures during wave impact and wave run-down, which will be presented in a follow-up paper.

Equations (9)–(11) in combination with the coefficients given in Table 7 only apply to the wave parameters and structural parameters of the revetments examined in the hydraulic model test in the *GWK* and must not be extrapolated beyond these parameters. However, these equations give meaningful limit values and are chosen as to best represent the physical phenomena.

5. Conclusions

The PEF model presented herein for the first time describes the tensile bending stresses due to hydraulic loads as basis for the limit state equation of crack formation in the top layer of MGRRs. Enveloping functions for maximum relative tensile bending stress $\sigma_{x,max}/(\rho_w g H_{m0})$ are given for four configurations of MGRRs that are of great practical relevance. The procedure described herein can be used for further boundary conditions, e.g., for determining the equations of the enveloping functions of the 98% quantile of the relative bending stresses.

However, for MGRR with a non-continuous bedding or other mechanical parameters, for example due to different stones or mortars used for construction or due to already existing deterioration of the revetment, the given enveloping functions cannot be used to calculate the bending stresses. These conditions may well be decisive for the design of MGRRs, thus the results presented herein are a first step to describe the loading on newly constructed MGRRs. In order to calculate bending stresses for MGRRs with a non-continuous bedding or with other mechanical parameters, the hydraulic loading has to be schematized and parametrized in order to be used as boundary condition for the PEF model so that the bending stresses can be calculated in this case as well. In this regard, the analysis of the pressure distribution on and beneath the top layer during maximum bending tensile stresses revealed that the sole consideration of the impact load to determine the maximum bending tensile stress is not sufficient for all wave parameters, but that especially for surf similarity parameters $\xi_{m-1,0}$ textgreater 2.5 the load resulting from the wave run-down must also be considered. A detailed analysis and subsequent parametrization of the pressure distributions along the top layer due to wave loading will be presented in a follow-up paper.

Further research is needed to verify and refine the assumptions made for representing MGRRs as PEF models and to validate the PEF model. Especially bending tests on large top layer specimens of MGRRs are necessary to determine the fracture mechanical parameters and verify the calculated bending stiffness of this composite construction. Furthermore, a more detailed insight into the mechanical properties of the soil beneath revetments subject to wave loading in coastal environments would not only benefit the model presented herein, but also every other revetment design that utilizes the modulus of subgrade reaction.

Author Contributions: Conceptualization, M.K. and H.S.; methodology, M.K.; software, M.K.; formal analysis, M.K.; investigation, M.K. and others; data curation, M.K.; writing—original draft preparation, M.K.; writing—review and editing, H.S.; visualization, M.K.; supervision, H.S.; project administration, H.S.; funding acquisition, H.S. and others. All authors have read and agreed to the published version of the manuscript.

Funding: This work was funded by the German Federal Ministry of Education and Research within the project "Wave Loading and Stability of Hydraulically Bonded Revetments", grant numbers 03KIS110 and 03KIS111. The project was initiated in the framework of the German Coastal Engineering Research Council.

Acknowledgments: The authors thank the technical staff at the Coastal Research Center in Hannover. Further, the authors acknowledge the continued administrative and financial support of the Leibniz Universität Hannover and Technische Universität Braunschweig to operate and maintain the Coastal Research Center and its Large

Wave Flume (*GWK*). The authors further would like to thank the project support group and Hocine Oumeraci for their scientific support and expertise.

Conflicts of Interest: The authors declare no conflict of interest. The funders had no role in the design of the study; in the collection, analyses, or interpretation of data; in the writing of the manuscript, or in the decision to publish the results.

Appendix A

Appendix A.1. Introduction

Mechanical and fracture mechanical tests on riprap and grouting mortar were conducted by the Institute of Building Materials Research at RWTH Aachen University. The compressive strength, tensile strength and bending tensile strength as well as the dynamic and static modulus of elasticity of riprap and grouting mortar were investigated. Furthermore, the bond properties between riprap and grouting mortar were tested. For this purpose, the adhesive tensile strength, adhesive shear strength and adhesive bending tensile strength of composite specimens were determined as well. Klotzek [31] gives a detailed description of the tests.

In the context of the present work the elastic moduli of riprap and grouting mortar are of interest because they are used to calculate the modulus of elasticity of the composite structure that is a MGRR, see Section 2.4.1. Therefore, the tests to determine the modulus of elasticity and their results are summarized in the following with the approval of the Institute of Building Materials Research at RWTH Aachen University.

Appendix A.2. Materials, Methods and Results: Riprap

The riprap investigated is from a quarry in Jelsa, Norway, near Stavanger. It was classified as gabbro, a magmatite. Figure A1 gives an impression of the stones.

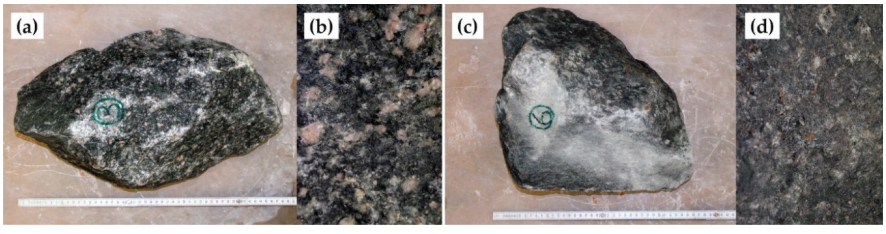

Figure A1. (**a**) Stone (specimen 3) of group 1 and (**b**) detail of stone surface. (**c**) Stone (specimen 6) of group 2 and (**d**) detail of its surface. Stone group 1 has a coarser grain size and darker minerals than stone group 2 (after [31]).

Half of the stones tested have significantly higher proportions of light minerals such as plagioclase and quartz in the form of grains than the other half of the stones. Therefore, on the basis of their mineral composition and the grain size of these minerals, the stones can be divided into two different sets of specimens, see Figure A1. These different mineral compositions mainly affect the modulus of elasticity under tension. However, as in the case of revetment construction these different stones are always present in practice, the results for their mechanical properties are shown and discussed together.

The stones were roughly cut into pieces with a diamond saw blade. These pieces were then sawed into cubes and beams with a precision saw. Cylinders were drilled with a core drill. Subsequently, the surfaces of the test specimens were ground with a surface grinding machine.

The bulk density and porosity of the stones were determined according to the standard DIN EN 1936 [42] on ten cubes with an edge length of 50 mm. For this purpose, the test specimens were dried and weighed at 70 °C until constant mass was achieved, then stored in demineralized water for 24 h and weighed again. Both the mass of the cube wiped with a cloth and that of the cube immersed in water were determined. The dry bulk density was determined both via the volume determined by

length measurements and via the volume determined by immersion methods. The mean density of the specimens in all cases (after removal, after drying and after storage in water) was 2.86 t/m^3 with a coefficient of variation of 4%. The porosity was 0.3% with a coefficient of variation of 24%.

The static modulus of elasticity of the riprap under compression was determined using six cylindrical test specimens with a slenderness of $\lambda = 2$ and a diameter of $d = 50$ mm in accordance with DIN EN 14580 [43]. The compressive strength, which was tested on equilateral cylinders and cubes in wet and dry conditions, was taken into account for the maximum load when determining the static modulus of elasticity. The longitudinal and transverse strains were recorded with strain gauges. For the longitudinal strains, two 50 mm long strain gauges were applied to the lateral surface of the cylinders in axial direction. Strain gauges with a length of 25 mm were mounted orthogonally to determine the transverse strain, see Figure A2.

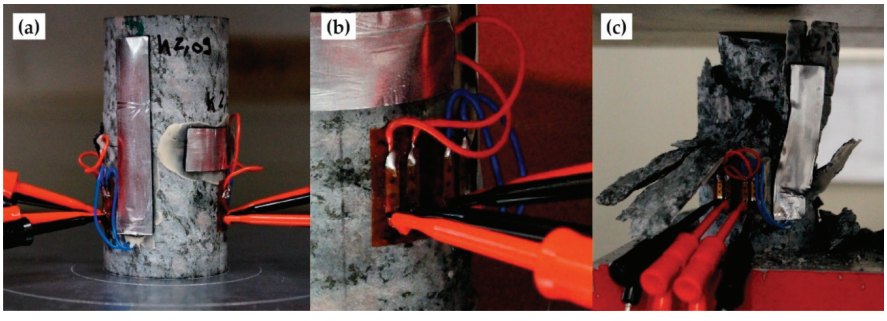

Figure A2. Testing the static modulus of elasticity on a stone under compression. (**a**) Specimen in test facility (Instron 5587), (**b**) detail showing the strain gauges and (**c**) stone after failure (after [31]).

In accordance with the requirements of the standard DIN EN 14580, the test specimens were subjected to three load cycles at a constant load speed of 1 kN/s. Subsequently, the load was increased until the test specimens broke. The results of the tests are shown together with the results for Poisson's ratio in Table A1. The static modulus of elasticity of the riprap under tension was tested on seven cylinders with pulling plates glued to their square faces and a loading speed of 0.5 kN/s.

Table A1. Static modulus of elasticity of revetment stones under compression and tension as well as compressive strength, Poisson's ratio and tensile strength (after [31]).

Compression					Tension			
Specimen No.	**Group**	**Compressive Strength β_D**	**Modulus of Elasticity E_C**	**Poisson's Ratio μ**	**Speci-men No.**	**Group**	**Tensile Strength β_Z**	**Modulus of Elasticity E_T**
		(N/mm^2)	(N/mm^2)	(-)			(N/mm^2)	(N/mm^2)
3	1	268.3	75,385	0.218	3	1	13.4	64,861
4	1	231.2	60,951	0.223	4	1	10.3	40,394
7	1	143.4	67,475	0.200	7	1	8.6	52,698
6	2	257.0	63,331	0.247	1	2	8.5	77,009
9	2	171.4	76,771	0.268	2	2	11.7	69,932
10	2	141.6	68,686	0.213	8	2	11.6	53,792
					9	2	16.2	74,870
Mean		202.2	68,767	0.228	Mean		11.47	61,936
Coefficient of variation		0.28	0.09	0.11	Coefficient of variation		0.24	0.22

Appendix A.3. Materials, Methods and Results: Grouting Mortar

In the code of practice "Use of Cementitious and Bituminous Materials for Grouting Armourstone on Waterways" [5], requirements for fresh and hardened grouting mortar are specified. The basic materials for grouting mortars must therefore comply with DIN 1045-2 [44] and DIN EN 206 [45].

According to [5], only cements in accordance with DIN EN 197-1 [46] and DIN EN 1164-10 [47] are to be used for the production of grouting mortar.

For the preparation of the grouting mortar, at first water and cement are mixed in a centrifuge with high mixing energy. This creates shear and friction which distribute and wet the binder particles uniformly, resulting in an increased formation of hydration products. In the second step sand with a maximum grain size of 2–8 mm is added to the mixture. The resulting grouting mortar is called 'colloidal' mortar. This preparation of the mortar produces the mortar properties required for grouting MGRR without the addition of chemical additives, in particular high flowability and high resistance to segregation. Further information on the mixing process is given by [24,48].

The mortar test specimens were produced at a revetment construction site. The sand used for the mortar can be classified as 'fine-grained' according to DIN 1045-2. There were shell fragments in the range of grain sizes $d \geq 0.5$ mm. The cement used was a Portland-limestone cement (CEM II/A-LL 32.5 R (80–94% clinker, 6–20% limestone)) according to DIN EN 197-1. According to information provided by the construction site personnel, the basic materials of the mortar are composed of 26.9% cement, 60.6% sand and 12.5% water. This results in a water/cement ratio of 0.46. This corresponds to the requirements according to [5]. The compliance with permissible properties of the fresh grouting mortar according to [5] was also checked.

The filling of the formwork for the production of the test specimens was carried out in two steps. For this purpose, the formworks were filled up to half with mortar and then compacted by slightly lifting and dropping the formwork ten times. After complete filling and renewed compaction, the formworks were covered with damp cloths and foil. The test specimens were then transported to the Institute of Building Materials Research after 24 h and subsequently the formwork was removed. The specimens were stored under water until the tests were done after 34 days.

The static modulus of elasticity of the mortar under compression was tested on six cylinders (slenderness $\lambda = 2$, $d = 150$ mm). In addition, Poisson's ratio of the mortar was determined. The longitudinal strains were recorded by three inductive displacement transducers while the transverse strains were determined by means of a measuring chain, see Figure A3.

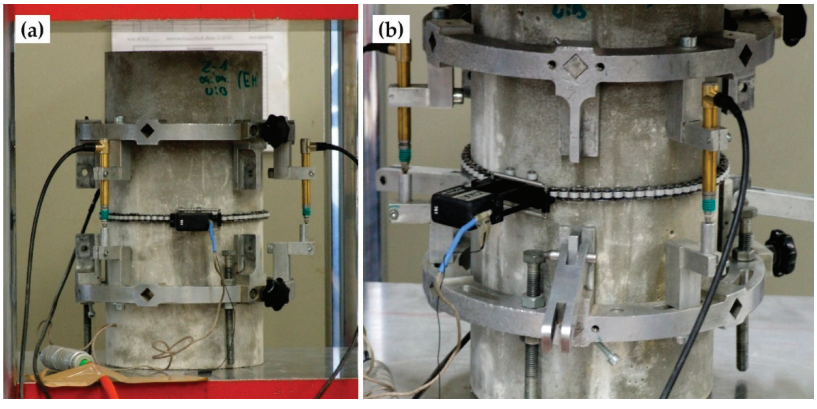

Figure A3. Testing the static modulus of elasticity on grouting mortar under compression. (**a**) Specimen in test facility (Form+Test Prüfsysteme, ALPHA 4-3000) and (**b**) detail showing the measuring chain and inductive displacement transducers (after [31]).

The test specimens were subjected to compression at a constant load speed of 8.8 kN/s over three load cycles. The upper and lower stress was set to 197.5 kN and 8.8 kN, respectively. The test specimens were then tested until the breaking load was reached. The static modulus of elasticity under tension was tested on five cylinders with pulling plates glued to their square faces and a loading speed of 0.5 kN/s. The results are given in Table A2.

Table A2. Static modulus of elasticity of grouting mortar under compression as well as compressive strength and Poisson's ratio (after [31]).

Compression				Tension		
Specimen No.	**Compressive Strength β_D**	**Modulus of Elasticity E_C**	**Poisson's Ratio μ**	**Specimen No.**	**Tensile Strength β_Z**	**Modulus of Elasticity E_T**
	(N/mm^2)	(N/mm^2)	(-)		(N/mm^2)	(N/mm^2)
1	35.6	22,532	0.061	1	1.1	18,621
2	35.4	23,229	0.054	2	1.0	17,766
3	33.1	22,962	0.067	3	1.0	21,329
4	37.8	24,287	0.066	4	0.7	20,085
5	34.5	23,591	0.061	5	1.0	19,802
6	31.6	23,020	0.052			
Mean	34.7	23,270	0.060	Mean	0.96	19,520
Coefficient of variation	0.06	0.03	0.10	Coefficient of variation	0.16	0.07

Appendix A.4. Discussion

The mechanical and fracture mechanical values of the tests on stones are subject to high scatter. As the two groups of stone specimens differ considerably in their strengths, scatter increases when the strengths are considered as a whole.

When the elastic moduli under tension are examined, the different properties of the two stone groups become particularly apparent. Stone group 1 has on average significantly lower moduli of elasticity under tension than group 2 (deviation: approx. 24%). Here, too, the mineral contents are the reason for the deviations. Stone group 2 is characterized by a higher proportion of dark minerals. The brittle fracture behavior of the dark minerals yields lower strain at fracture and thus a higher tensile modulus.

Compared to mortar, natural stone has a significantly higher compressive and tensile strength and a significantly higher modulus of elasticity. The mean value of the static modulus of elasticity of natural stone is about three times higher than that of mortar.

Scatter of the mechanical and fracture mechanical values reduces for the mortar. The main reason for this is that the mortar has a more homogeneous structure than natural stone.

On the basis of the elasticity investigations it could be shown that mortar and stone under compressive load show a similar transverse elongation behavior, but clear differences in longitudinal elongation behavior. Consequently, there are also strong differences in Poisson's ratio for both materials.

References

1. CIRIA. *The International Levee Handbook*; C731: London, UK, 2013, ISBN 978-0-86017-734-0.
2. EAK. *Empfehlungen für die Ausführung von Küstenschutzwerken durch den Ausschuss für Küstenschutzwerke der Deutschen Gesellschaft für Geotechnik e.V. und der Hafenbautechnischen Gesellschaft e.V.*; Westholsteinische Verlagsanstalt Boyens & Co.: Heide, Germany, 2007, ISBN 978-3-8042-1056-1.
3. German Institute for Standardization. *Armourstone—Part 1: Specification*; Beuth Verlag GmbH: Berlin, Germany, 2002.
4. Federal Waterways Engineering and Research Institute. *Anwendung von Regelbauweisen für Böschungs- und Sohlensicherungen an Binnenwasserstraßen (Application of Standard Construction Methods for Embankment and Bottom Protection on Inland Waterways)*; Federal Waterways Engineering and Research Institute: Karlsruhe, Germany, 2008.
5. Federal Waterways Engineering and Research Institute. *Use of Cementitious and Bituminous Materials for Grouting Armourstone on Waterways (Anwendung von Hydraulisch Gebundenen Stoffen zum Verguss von Wasserbausteinen an Wasserstraßen, MAV)*; Federal Waterways Engineering and Research Institute: Karlsruhe, Germany, 2017.

6. Federal Waterways Engineering and Research Institute. *Prüfung von Hydraulisch- und Bitumengebundenen Stoffen zum Verguss von Wasserbausteinen an Wasserstraßen (Testing of Hydraulically and Bitumen-Bonded Materials for Grouting Armourstones on Waterways)*; Federal Waterways Engineering and Research Institute: Karlsruhe, Germany, 2008.
7. Federal Waterways Engineering and Research Institute. *Grundlagen zur Bemessung von Böschungs- und Sohlensicherungen an Binnenwasserstraßen (Principles for the Design of Embankment and Bottom Protection on Inland Waterways)*; Federal Waterways Engineering and Research Institute: Karlsruhe, Germany, 2010.
8. CIRIA; CUR; CETMEF. *The Rock Manual. The use of Rock in Hydraulic Engineering*, 2nd ed.; C683: London, UK, 2007.
9. Technical Advisory Committee on Flood Defence. *Technisch Rapport Asfalt voor Waterkeren*; Rijkswaterstaat, DWW: Delft, The Neterlands, 2002.
10. Knieß, H.-G.; Köhler, H.-J. Untersuchung gebundener Steinschüttungen auf Flexibilität, Verbundfestigkeit und Wasserdurchlässigkeit. *Bull. Fed. Waterw. Eng. Res. Inst.* **1984**, *55*, 113–134.
11. Alcérreca-Huerta, J.C.; Oumeraci, H. Wave-induced pressures in porous bonded revetments. Part I: Pressures on the revetment. *Coast. Eng.* **2016**, *110*, 87–101. [CrossRef]
12. Alcérreca-Huerta, J.C.; Oumeraci, H. Wave-induced pressures in porous bonded revetments. Part II: Pore pressure just beneath the revetment and in the embankment subsoil. *Coast. Eng.* **2016**, *110*, 76–86. [CrossRef]
13. Liebisch, S. Bonded Porous Revetments—Effect of Porosity on Wave-Induced Loads and Hydraulic Performance: An Experimental Study. Ph.D. Thesis, Technische Universität Carolo-Wilhelmina, Braunschweig, Germany, 2015.
14. Schiereck, G.J. *Introduction to Bed, Bank and Shore Protection*; Spon Press: London, UK, 2004, ISBN 0-415-33177-3.
15. Peters, D.J. Design of Pattern-Placed Revetments. Ph.D. Thesis, Delft University of Technology, Delft, The Netherlands, 2017.
16. De Looff, A.K.; t'Hart, R.; Montauban, K.; van den Ven, M. GOLFKLAP A Model to Determine the Impact of Waves on Dike Structures with an Asphaltic Concrete Layer. In Proceedings of the 30th International Conference, San Diego, CA, USA, 3–8 September 2006; pp. 5106–5116.
17. ARCADIS. *Polyurethane Bonded Aggregate Revetments Design Manual*; ARCADIS: Amsterdam, The Netherlands, 2010.
18. Rijkswaterstraat. *The Use of Asphalt in Hydraulic Engineering*; Rijkswaterstraat: Utrecht, The Netherlands, 1985.
19. Oumeraci, H.; Staal, T.; Pfoertner, S.; Ludwigs, G.; Kudella, M. *Hydraulic Performance, Wave Loading and Response of Elastocoast Revetments and their Foundation—A Large Scale Model Study*; TU Braunschweig—Leichtweiss Institut: Braunschweig, Germany, 2010.
20. Führböter, A.; Sparboom, U. Shock Pressure Interactions on Prototype Sea Dikes Caused by Breaking Waves. In Proceedings of the SOWAS'88 (Modelling Soil-Water-Structure Interactions), Delft, The Netherlands, 29 September–2 October 1988.
21. IMS Ingenieurgesellschaft mbH. *Werkstoff Elastocoast—Zusammenstellung der Technischen Bemessungsgrundlagen für den Werkstoff Elastocoast*; IMS Ingenieurgesellschaft mbH: Hamburg, Germany, 2010.
22. Losada, I.J.; Lara, J.L.; del Jesus, M. Modeling the interaction of water waves with porous coastal structures. *J. Waterw. Port Coast. Ocean Eng.* **2016**. [CrossRef]
23. Dankert, J.; Dankert, H. *Technische Mechanik. Statik, Festigkeitslehre, Kinematik/Kinetik*, 7th ed.; Springer: Berlin/Heidelberg, Germany, 2013, ISBN 978-3-8348-1809-6.
24. Monnet, W.; Dartsch, B.; Wehefritz, K. *Colcrete-Beton im Wasserbau*; Beton-Verlag: Düsseldorf, Germany, 1980, ISBN 3-7640-0134-8.
25. Leichtweiß-Institut für Wasserbau. *L~davis: Manual for the Data Analysis and Visualization Software of the Leichtweiss Institute*; Leichtweiß-Institut für Wasserbau: Braunschweig, Germany, 2007.
26. Mansard, E.P.D.; Funke, E.R. The Measurement of Incident and Reflected Spectra Using a Least Square Method. In Proceedings of the 17th International Conference on Coastal Engineering (ICCE), Sydney, Australia, 23–28 March 1980; pp. 154–172.
27. EurOtop. Manual on Wave Overtopping of Sea Defences And Related Structures. An Overtopping Manual Largely Based on European Research, but for Worldwide Application. 2018. Available online: www.overtopping-manual.com (accessed on 11 November 2020).
28. Kreyenschulte, M. Wellen-Bauwerks-Interaktion bei Mörtelvergossenen Schüttsteindeckwerken. Ph.D. Thesis, RWTH Aachen University, Aachen, Germany, 2020.

29. Klein Breteler, M.; van der Werf, I.; Wenneker, I. *Kwantificering Golfbelasting en Invloed Lange Golven. Onderzoeksprogramma Kennisleemtes Steenbekledingen*; Deltares: Delft, The Netherlands, 2012.
30. Gross, D.; Hauger, W.; Schröder, J.; Wall, W.A. *Technische Mechanik 2—Elastostatik*; Springer: Berlin/Heidelberg, Germany, 2017, ISBN 978-3-662-53678-0.
31. Klotzek, T. Mechanical and Fracture Mechanical Properties of Hydraulically Bonded Revetments. Master's Thesis, RWTH Aachen University, Aachen, Germany, 2017. Unpublished Work.
32. Stichting Toegepast Onderzoek Waterbeheer. *State of the Art Asfaltdijkbekledingen*; Rijkswaterstraat: Utrecht, The Netherlands, 2010.
33. Ruygrok, P.A. *Dimensioneren van Asfaltbekledingen op Golfbelasting, Analyse van de Relatie Tussen Golfbelasting en Rekken*; Report CO-347160/17; Grondmechanica: Delft, The Netherlands, 1994.
34. Richwien, W. Seegang und Bodenmechanik—Geotechnische Versagensmechanismen von Seedeichen. *Bull. Fed. Waterw. Eng. Res. Inst.* **1989**, *66*, 139–154.
35. Witte, H.-H. Druckschlagbelastung durch Wellen in Deterministischer und Stochastischer Betrachtung. Ph.D. Thesis, Technische Universität Carolo-Wilhelmina, Braunschweig, Germany, 1988.
36. Klein Breteler, M.; Pilarczyk, K.W.; Stoutjesdijk, T. Design of Alternative Revetments. *Coast. Eng. Proc.* **1998**, *1*. [CrossRef]
37. Klein Breteler, M.; Bezuijen, A. Design criteria for Placed Block Revetments. In *Dikes and Revetments. Design, Maintanance and Safety Assessment*; Pilarczyk, K.W., Ed.; A.A. Balkema: Rotterdam, The Netherlands, 1998; pp. 217–248, ISBN 90 5410 455 4.
38. Hughes, S.A. *Physical Models and Laboratory Techniques in Coastal Engineering*; World Scientific Publishing Co. Pte. Ltd.: Singapore, 1993, ISBN 981-02-1540-1.
39. Führböter, A. *Wellenbelastung von Deich- und Deckwerksböschungen*; Schiffahrts-Verlag "Hansa": Hamburg, Germany, 1991.
40. Oumeraci, H. More than 20 years of experience using the Large Wave Flume (GWK): Selected research projects. *Die Küste* **2010**, *77*, 179–239.
41. EAU. *Empfehlungen des Arbeitskreises "Ufereinfassungen". Häfen und Wasserstraßen*; Wilhelm Ernst & Sohn Verl.: Berlin, Germany, 2012.
42. German Institute for Standardization. *Natural Stone Test Method—Determination of Real Density and Apparent Density, and of Total and Open Porosity*; Beuth Verlag GmbH: Berlin, Germany, 2007.
43. German Institute for Standardization. *Natural Stone Test Methods—Determination of Static Elastic Modulus*; Beuth Verlag GmbH: Berlin, Germany, 2005.
44. German Institute for Standardization. *Concrete, Reinforced and Prestressed Concrete Structures—Part 2: Concrete—Specification, Properties, Production and Conformity—Application Rules for DIN EN 206-1*; Beuth Verlag GmbH: Berlin, Germany, 2008.
45. German Institute for Standardization. *Concrete— Specification, Performance, Production and Conformity; German Version EN 206:2013+A1:2016*; Beuth Verlag GmbH: Berlin, Germany, 2017.
46. German Institute for Standardization. *Cement—Part 1: Composition, Specifications and Conformity Criteria for Common Cements; German and English Version prEN 197-1:2018 (Draft)*; Beuth Verlag GmbH: Berlin, Germany, 2018.
47. German Institute for Standardization. *Special Cement—Part 10: Composition, Requirements and Conformity Evaluation for Cement with Low Effective Alkali Content*; Beuth Verlag GmbH: Berlin, Germany, 2013.
48. Hallauer, O. Vergussstoffe für Uferdeckwerke. *Bull. Fed. Waterw. Eng. Res. Inst.* **1986**, *58*, 29–69.

Journal of
Marine Science and Engineering

MDPI

Article

Model Uncertainty for Settlement Prediction on Axially Loaded Piles in Hydraulic Fill Built in Marine Environment

Manuel Bueno Aguado [1], Félix Escolano Sánchez [1,*] and Eugenio Sanz Pérez [2]

[1] Civil Engineering Department, Construction, Infrastructures and Transportation, Universidad Politécnica de Madrid, 28040 Madrid, Spain; mbueno@proes.es
[2] Engineering and Morphology of the Land Department, Universidad Politécnica de Madrid, 28040 Madrid, Spain; eugenio.sanz@upm.es
* Correspondence: felix.escolano@upm.es; Tel.: +34-9-1067-4614

Abstract: Model uncertainty is present in many engineering problems but particularly in those involving geotechnical behavior of pile foundation. A wide range of soil conditions together with simplified numerical models makes it a constant necessity to review the accuracy of the predictions. In this paper, the outputs of some seventy (70) pile axially-loaded tests have been reviewed with a classic numerical model to assess pile deformation. Probabilistic approach has been used to quantify uncertainties coming from soil tests, statistic uncertainty and also from the model itself. In this way, a critical review of the prediction method and a way to quantify its uncertainty is presented. The method is intended to be used in a wide range of engineering problems.

Keywords: model uncertainty; reliability; pile settlement; piles in granular soil; base resistance; skin friction; t-z curves

Citation: Bueno Aguado, M.; Escolano Sánchez, F.; Sanz Pérez, E. Model Uncertainty for Settlement Prediction on Axially Loaded Piles in Hydraulic Fill Built in Marine Environment. *J. Mar. Sci. Eng.* **2021**, *9*, 63. https://doi.org/10.3390/jmse9010063

Received: 18 December 2020
Accepted: 4 January 2021
Published: 8 January 2021

1. Introduction

Land reclamations built out of the coast for industrial or housing purposes are nowadays a challenge for designers, since settlements are critical for their correct performance. Engineers have to predict deformations based on models that include uncertain inputs but also the model itself has uncertain parameters. Comparing predictions with actual outputs on large scale tests is a sound way to calibrate a numerical model and to have an insight in its uncertainties.

This time, the authors have the opportunity to study the behavior of a 20 m thick embankment built in a marine environment by hydraulic filling and then densified with vibrocompaction [1–4]. After, the new platform was tested with an extensive soil investigation

In this paper—which is part of a wider research on model geotechnical uncertainty [5,6]—, settlement predictions for isolated piles are compared to pile load test outputs. In this way, a numerical model is calibrated with the factual results, but moreover, the uncertainties of the model are also highlighted using a probabilistic approach. The model is not only assessed for its accuracy in reaching a good mean prediction but also for its dispersion, collated with the observed dispersion on the large-scale tests.

Pile settlement is a relevant issue for some design but also for pile load test interpretation. However, since small displacements are involved, it is a topic in which codes and specialized literature pay usually little attention.

This time the authors have had the opportunity to review sixty-two (62) pile load test on concrete hollow-stemmed flight augered piles, all of them in a very homogeneous soil profile.

Uncertainties present on the soil investigation due to measurement method and stochastic change in soil parameters are studied and quantified [7]. They are defined as a probabilistic function that can be implemented in the prediction model.

Predictions are based on a classic model defined as a discrete elastic pile supported by vertical elastoplastic springs. These springs are defined by the well-known t-z curve method, proposed by the American Petroleum Institute [8].

The model, initially formulated as a deterministic model, accurately predicts the mean settlement but it does not simulate the observed dispersion. So, a probabilistic parameter is introduced to match also that deviation. In this way, model uncertainty is introduced in the prediction.

So, engineers are provided with a useful tool to assess the accuracy and reliability of the numerical model so that settlement predictions and confidence intervals can be consistently formulated.

2. Site Geology

Persian Gulf shoreline is on the edge of the deep sedimentary basin that forms the Arabian Peninsula and is underlain by a considerable thickness of sedimentary rocks. Relatively young deposits of the Dibdibba formation (Upper Miocene to Pleistocene Epochs, approximately 2 to 10 million years old) outcrops at the surface. These deposits are underlain at depth by the Dammam formation (Upper Eocene Epoch, approximately 38 to 42 million years old).

The Dibdibba formation typically consists of siliceous sands and gravels, with varying amounts of silt and some thin clay and gypsum bands. Cementation is only partial and relatively poor, consisting of calcium carbonate and gypsum.

After dredging and removing other recent marine deposits, Dibdibba formation was used to build the land reclamation close to the shoreline. At the same time, that same formation at a depth where the material was dense to very dense was the foundation of the fill.

Therefore, a very thick deposit of granular material, partially natural and partially man-made was generated. The tests described in this paper and the carried out soil investigation affect mainly the hydraulic fill and the upper part of its foundation.

3. Soil Conditions

The ground profile is described as a 20 m thick fill formed by hydraulic methods below water level and by layer compaction above. The fill is founded below the sea level on a natural granular soil profile made of silty sand with a density increasing with depth.

The fill is made of siliceous sands with fine percentage (pass through #200) lower than 20%. The material is described as a well graduated sand or silty sand where the medium-sized predominates. They are mostly rounded, with a silty fraction and sporadically some gravel. The technical specifications of the material used for the filling are summarized in the following Table 1.

Table 1. Table of technical specifications of the filling hydraulic.

Property	Type 1
Maximum particle size	125 mm
Maximum % greater 125 mm	0
Minimum % passing 2 mm sieve	35
Maximum % passing 75 micron	20
Maximum % clay (<2 micron)	2
Liquid Limit (%)	<35
Plasticity Index (%)	<10

The fill was dredged from the seabed nearby, so that natural soil below the fill is also made of this same material

After the discharge, the material was compacted by deep vibrocompaction in a $2.5 \times 2.5\ m^2$ mesh. The operation is controlled until it is densified up to 90% of its maximum dry density.

On top of the hydraulic fill, an additional 3 m engineering fill was built. It was made of the same granular material but placed by compacted 25 cm-thick layers. On this platform concrete piles were built by augering. The piles were 800 mm diameter and 22 to 28 m long.

Site Investigation Uncertainty

Once vibrocompaction was completed and before piling, it was carried out a soil investigation which includes sixteen (16) boreholes with Standard Penetration Tests (SPT) each meter and about thirty (30) continuous Cone Penetration Test (CPT).

The SPT results (N_{SPT}) are presented in the following Figure 1. SPT indexes have been corrected by hammer energy to achieve a homogeneous value corresponding to N_{60} index and by groundwater, according to the following criterion (Equation (1)) [9–11].

$$\text{If } N_{SPT} > 15 \quad N_{SPT} = 15 + 0.5 \times (N_{SPT} - 15) \tag{1}$$

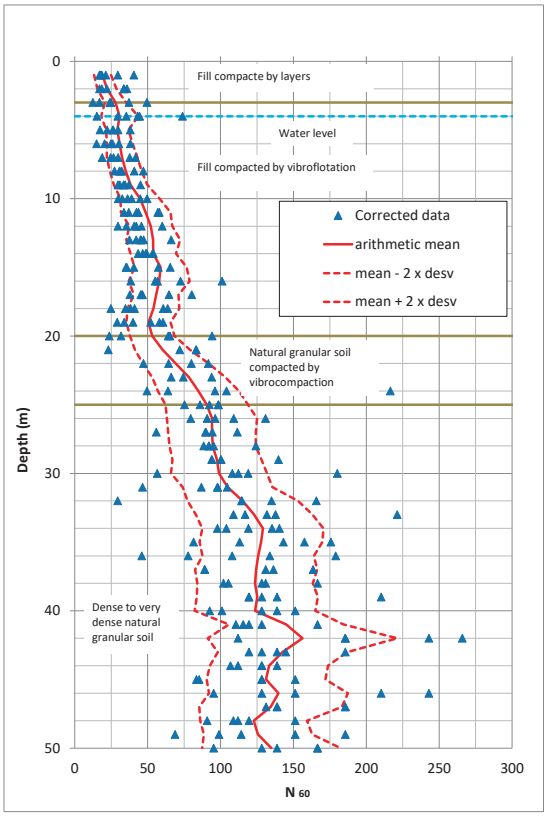

Figure 1. Corrected SPT results.

Engineers are usually surprised by the large dispersion of the outputs, even though they are all carried out on a fairly homogenous material, as it is in this case.

This can be partially attributed to the expected random behavior of the soil. Arguably, the resistance of the soil is a random variable with a certain unknown mean and a certain standard deviation.

Another part of that dispersion is due to the measuring equipment. Including within this concept everything related to the use of different devices, different personnel, variations in the calibration of the equipment over time, etc. These two sources of uncertainty will be dealt with in this section so that they can be statistically quantified.

Firstly, a correction with physical sense is introduced. Variations in vertical resistance that can exist within the same layer are gradual. Abrupt variations are introduced by the measuring equipment. Therefore, the mean value at a point must be influenced by the mean value at the top and bottom levels. Thus, the mean at a certain depth is corrected with the expression (Equation (2)).

$$N_{corrected,\,i} = 0.4 \times N_i + 0.2 \times (N_{i-1} + N_{i+1}) + 0.1 \times (N_{i-2} + N_{i+2}) \quad (2)$$

where; N_i is the N_{60} average value at a depth i.

Second correction comes from comparing different type of test. The current site investigation includes also CPT tests carried out on the same level that the SPT boreholes. Comparing the results of each other will be used to precisely correct the measurement uncertainty introduced by the equipment that carries out the SPT tests.

The idea behind is the concept of minimum statistical variance. It is well known that SPT and CPT tests measure different parameters but also that there is a relationship between them [12,13]. This ratio can be obtained by comparing the results of both sets of tests. However, the issue of interest at the moment is the dispersion presented by both tests. It could be said that the lower dispersion is an upper limit of the dispersion of the random variable that represents the resistance of the soil. Thus, the test with the highest dispersion must be corrected to a dispersion similar to that of lower one; this correction being a way to eliminate uncertainty in the result introduced by the measurement test.

The following Figure 2 shows the point resistance measured in CPT tests. From there, the mean (represented in yellow) and the mean +/− the standard deviation (represented in blue) have been obtained for each depth.

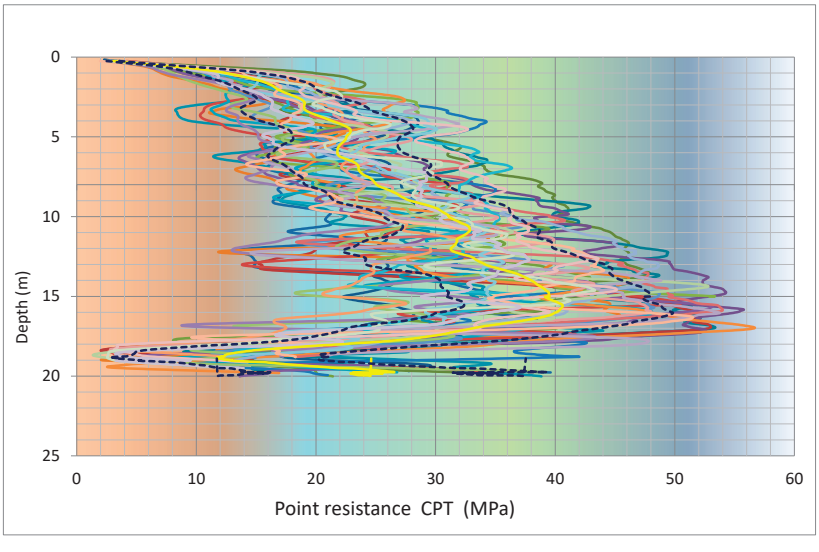

Figure 2. Point resistance CPT results.

In the same way, the mean and standard deviation have been obtained at each depth for the SPT test, based on the data in Figure 1. So, both dispersions can be compared through the ratio defined as (Equation (3)):

$$\nu = \frac{\text{standard deviation}}{\text{average}} \quad (3)$$

These results are presented in the Figure 3. It is noted that:

- The dispersion on SPT test is higher than that on CPT test, at least in the first 16 m. SPT test dispersion is varied between 0.4 and 0.7, while the CPT dispersion is around 0.2.
- In the last four meters, both dispersions are similar. Their values are in the range of 0.4 to 0.7.

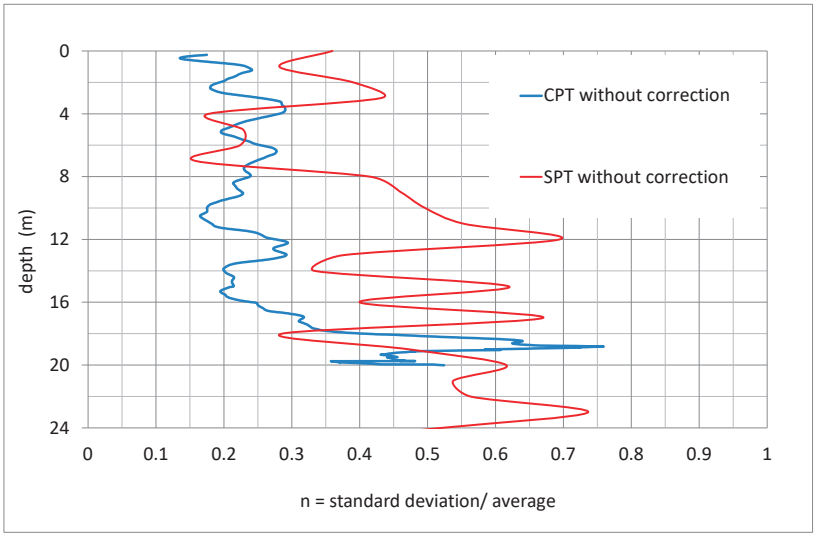

Figure 3. υ-parameter for CPT and SPT.

It can be concluded that the dispersion introduced by the SPT test is at least the difference between the red and blue lines observed in Figure 3.

This observation allows reviewing the SPT original values. It is noted that the dispersion of the soil resistance must be below the parameter 0.2. Therefore, all SPT results that are above or below the mean plus/minus twice the standard deviation have a probability of occurring less than 5%, calculated as follows (Equation (4)):

$$\text{If ABS}(N_{60} - \mu) > 2 \times \mu \times \upsilon \text{ then } N_{60} \text{ is removed} \quad (4)$$

Values that exceed this amount are removed from the sample and the mean and standard deviation are calculated again.

Figure 4 shows the new dispersion parameter along with those previously obtained. It is noted that on this occasion the dispersion of the CPT and SPT test are comparable.

Different authors indicate the expected typical variation of a geotechnical parameter within a homogeneous soil layer due to the random variability of its strength. One such reference is ROM [14]. It can be concluded that for the CPT and SPT tests, typical values of -parameter are about 0.15.

Since the corrected value of υ-parameter is close enough to the expected random soil strength, it can be consisted that the uncertainty introduced by the measurement method has been taken into account and almost corrected. Applying the two above corrections, it is finally obtained an average and corrected deviation from the SPT test, as it is shown in Figure 5.

Thus, corrections made in SPT test outputs by comparing with CPT and including all the available information allow reducing measurement uncertainty almost completely.

In this case, a large soil investigation is available, so that statistical uncertainty due to the size of the sample can be neglected. If the number of SPT tests were small, a new uncertainty arises due to the lack of a sufficiently large size sample.

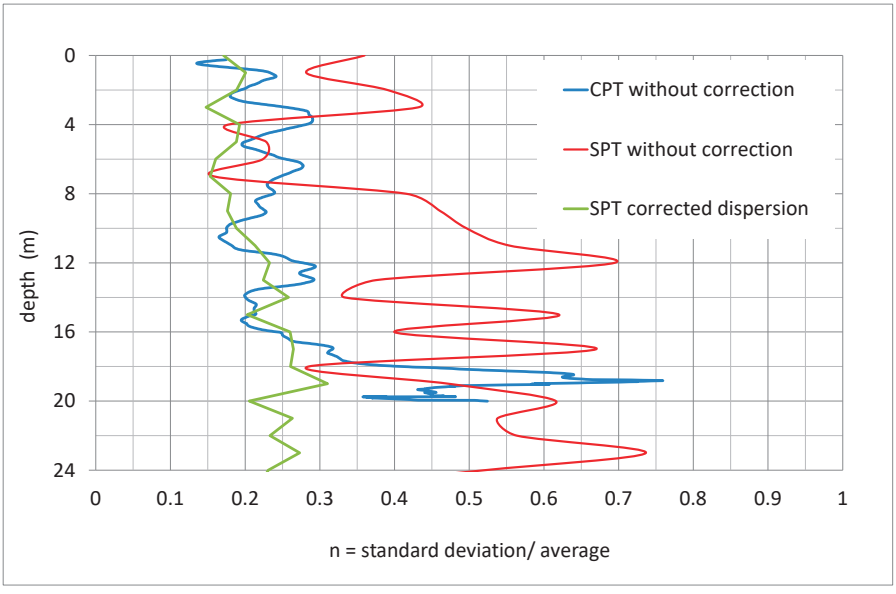

Figure 4. υ-parameter for CPT and SPT, including corrected SPT.

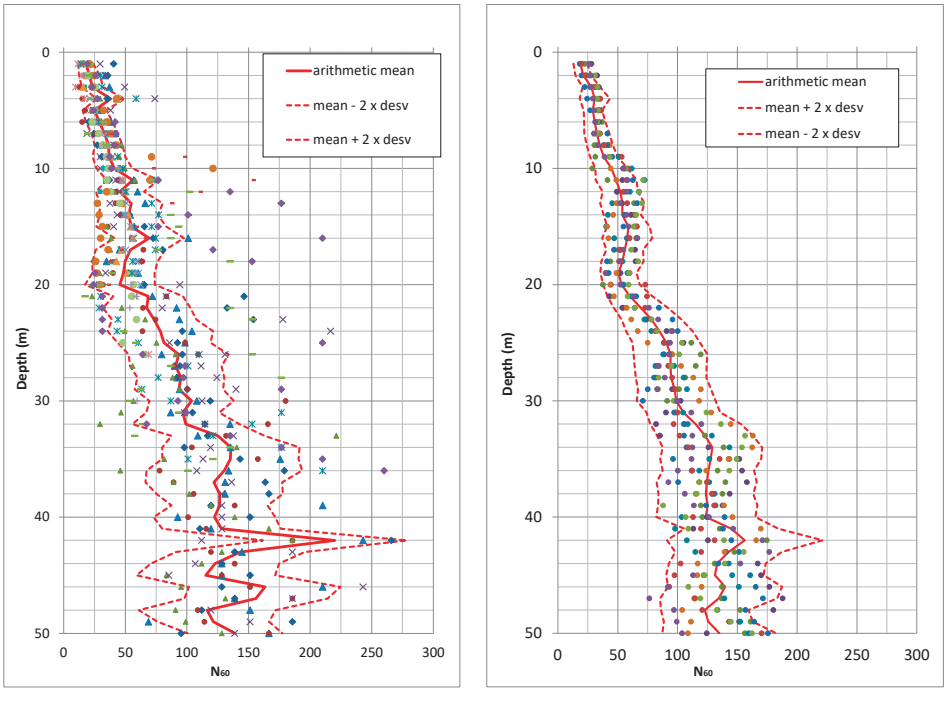

(**a**) (**b**)

Figure 5. NSPT representation: (**a**) Example of a statistical representation of the SPT-parameter corrected by method and statistical uncertainty; (**b**) Artificial SPT profile generated by probabilistic Monte Carlo Method.

4. Pile Analytical Model

A site investigation usually allows stating prediction on pile behavior, as for instance ultimate bearing capacity or load-settlement performance. For granular soil, SPT index can be used to support that prediction, following the procedure below.

SPT index is related to relative density. Gibb & Holtz [15] give a well-known correlation between them and the vertical effective pressure.

1. Relative density is related to the ultimate skin friction and base resistance according to API.
2. The pile can be split in same-length slices. At each slice, an ultimate skin friction is associated depending om its depth. The deepest slice has additionally a base resistance.
3. For each pile slice, it is calculated its t-z curve and for the deepest the base bearing capacity curve, according to the aforementioned code.
4. That analytical model gives a load-settlement prediction curve which later can be compared to the real-scale load test

The following paragraphs describe this procedure in more detail:

4.1. Relative Density from SPT Index

Relative density (DR%) can be obtained from, SPT index according to the Gibb & Holtz formulation. So:

$$\mathrm{DR}(\%) = \sqrt{\frac{\mathrm{N}_{60}}{23\sigma'_{\mathrm{v}} + 16} \times 100} \tag{5}$$

where

σ'_{v} is Vertical effective stress at the SPT test depth.

N_{60} is SPT-index corrected by hammer energy and depth.

$$\mathrm{N}_{60} = \mathrm{N}_{\mathrm{SPT}} \frac{\mathrm{Er}}{60} \mathrm{Cr} \tag{6}$$

where

$\mathrm{N}_{\mathrm{SPT}}$ is the SPT value corrected only by groundwater table.

Er is the relative hammer energy.

Cr is a factor that accounts for the depth where the test is performed, according to the expression below:

- From borehole top to 3.0 m deep, it is 0.75
- Below 3.0 m deep, z = 3.0 m Cr = $(z - 3)/28 + 0.75 < 1.0$

4.2. Ultimate Skin Friction and Base Resistance

For piles in granular soil, skin friction f(z) is a function of relative density and effective pressure. It can be obtained by the expression:

$$\mathrm{f}(\mathrm{z}) = \beta \times \mathrm{p}_0(\mathrm{z}) < \tau_{\max} \tag{7}$$

where

$\mathrm{p}_0(\mathrm{z})$ Vertical effective pressure at z depth.

β: friction factor whose value is a function of the relative density.

$$\beta = 0.8\,\mathrm{F}\,\tan(\delta) \tag{8}$$

For hollow tubular driven piles, F-value could be 1.0. For close-end displacement driven piles F-value could be 1.25. For other piles, it is usually recommended to look for experience or specific test.

For ultimate bearing capacity (q) in granular soil. The following expression can be used.

$$\mathrm{q} = \mathrm{N}_{\mathrm{q}} \mathrm{p}_{0,\mathrm{tip}} < \mathrm{q}_{\max} \tag{9}$$

where:

N_q: non-dimensional parameter

$p_{0,tip}$: effective vertical pressure at the base of the pile.

The following charts collect the relationship needed to develop this formulation based on the soil relative density (Figure 6).

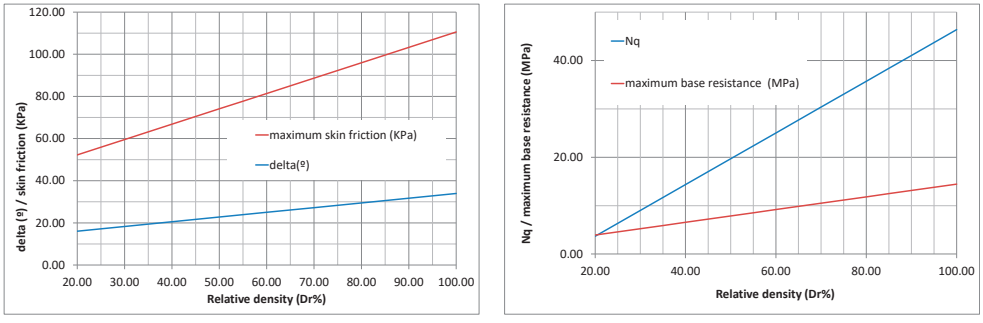

(**a**) (**b**)

Figure 6. (**a**) Relationship between relative density and skin friction; (**b**) Relationship between relative density and resistance.

4.3. Pile Model

Figure 7 shows the pile model used to solve the load-settlement relationship. It consists of splitting the pile in equal-length slices. The slices are united by an elastic spring (K_i). Each of them has a weight (P_i) and ultimate skin friction (Rf_i). The deepest slice has additionally a base resistance (Rp). At pile top, it is applied a load (F_0).

Each slice undergoes an absolute offset (u_i), as a result of the application of the external load and weight. u_i is positive downward. The following equation system solves the mathematical problem.

$$F_0 = Rf_1(u_1) + K_1(u_1 - u_2) - P_1 \tag{10}$$

$$0 = Rf_2(u_2) + K_2(u_2 - u_3) - K_1(u_1 - u_2) - P_2 \tag{11}$$

$$0 = Rf_3(u_3) + K_3(u_3 - u_4) - K_2(u_2 - u_3) - P_3 \tag{12}$$

$$0 = Rf_i(u_i) + K_i(u_i - u_{i+1}) - K_{i-1}(u_{i-1} - u_i) - P_i \tag{13}$$

$$0 = Rp(u_n) + Rf_n(u_n) + K_n(u_n) - K_{n-1}(u_{n-1} - u_n) - P_n \tag{14}$$

K_i is the pile stiffness that takes the value:

$$K_i = \frac{E \times A_i}{L_i}$$

where:

E: pile deformation modulus

A_i pile cross-section area.

L_i: slice length.

The solution of the previous system provides the seeking relationship between applied external pressure F_0 and displacement at the top pile (u_1). Since skin friction $Rf_i(u_i)$ and base resistance $Rp(u_n)$ are functions of displacement, the system is nonlinear and it has to be used an iterative algorithm to reach the solution.

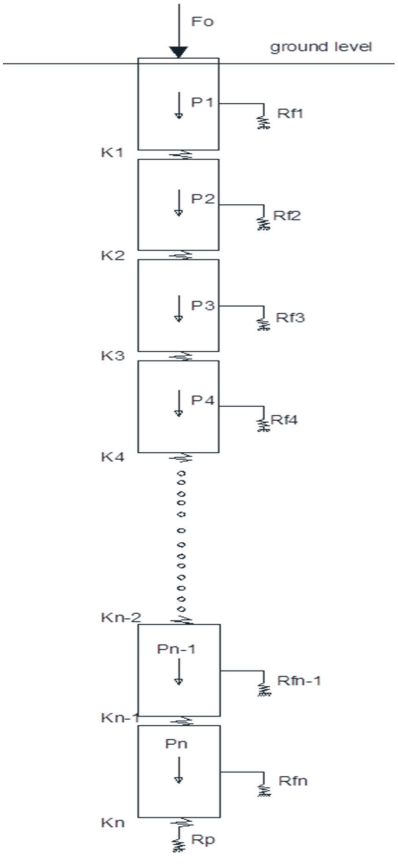

Figure 7. Soil–pile analytical model.

4.4. t-z Curve and Q-z Curve

Rf_i functions are obtained from the t-z curve defined in standard ISO 19901-4:2003 (API RP 2GEO). Base resistance also follows the recommendations of this standard. The following Figure 8 shows the used functions.

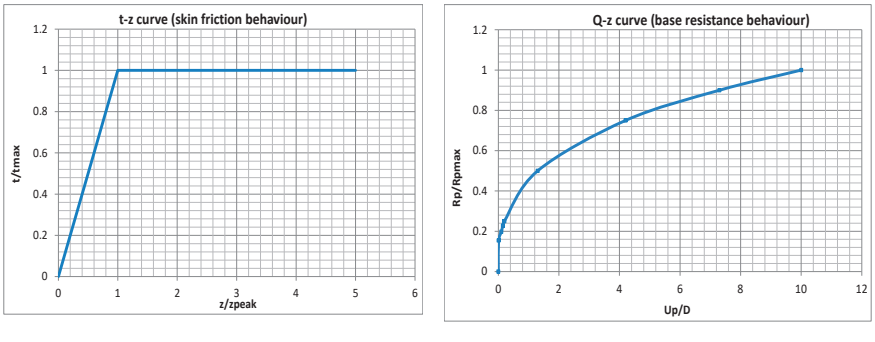

(**a**) (**b**)

Figure 8. Soil-pile deformation relationship (**a**): t-z curve; (**b**): Q-z curve.

4.5. Load Application

The total load F_0 is applied by steps as it is done in the large-scale load test. Positive load is downward. Model admits starting loads as tension (upwards) or compression (downwards).

The weight of the pile is considered through the density of the structural section. If the initial charge is zero the model provides only the settlement due to the weight of the pile.

5. Pile Load Test Outputs

There are sixty-two (62) load tests conducted on 0.8 m diameter concrete piles. The piles were executed by hollow-stemmed flight augering. Pile length ranged between 22 to 28 meters.

The difference in length between the piles is due to the depth where dense sand is located, which is reached by all the piles. Therefore, it can be said that all the piles are supported in a layer of similar mechanical properties.

The piles were tested in a single cycle of loading up to a value of 3.150 KN. Maximum load was reached on five load steps.

The following Figure 9 represents the length of the piles with respect to settlement. The following is observed:

- There is no correlation between the length of the pile and total settlement. This can be explained by the fact that all the piles have been punched to the dense sand layer, so their support conditions are similar.
- The tests with more frequent values are separated from other tests, which are considered special cases and are beyond the average behavior. Four out-of-average pile tests were removed, since it was suspected that their support conditions were different from others

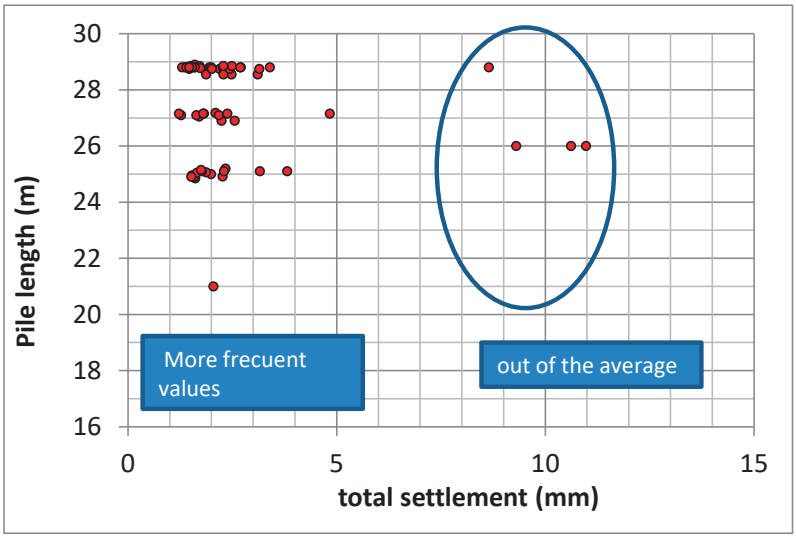

Figure 9. Concrete pile load test outputs.

For the more frequent values, Figure 10 below shows the output distribution and their statistical parameters. Statistical parameters are shown in Table 2.

The following Figure 11 represents an example of some of the more-frequent-value load tests.

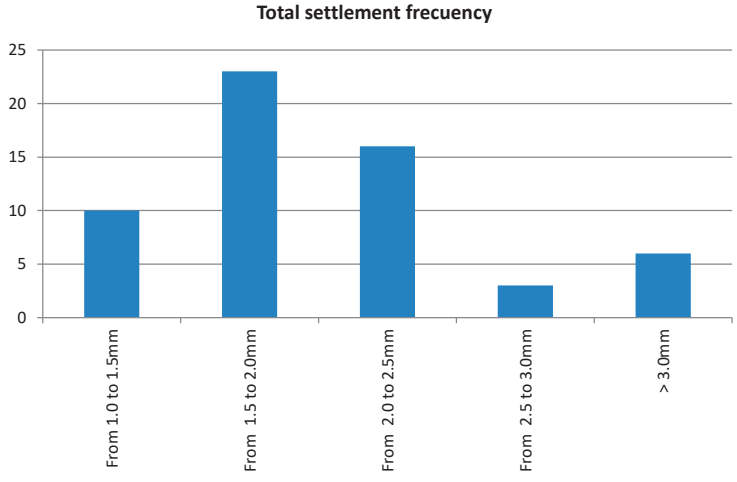

Figure 10. Settlement distribution of concrete load test.

Table 2. Statistical parameter of concrete load tests.

Settlement	Values
Maximum settlement	4.84 mm
Minimum settlement	1.22 mm
Average	2.05 mm
Standard deviation	0.68 mm

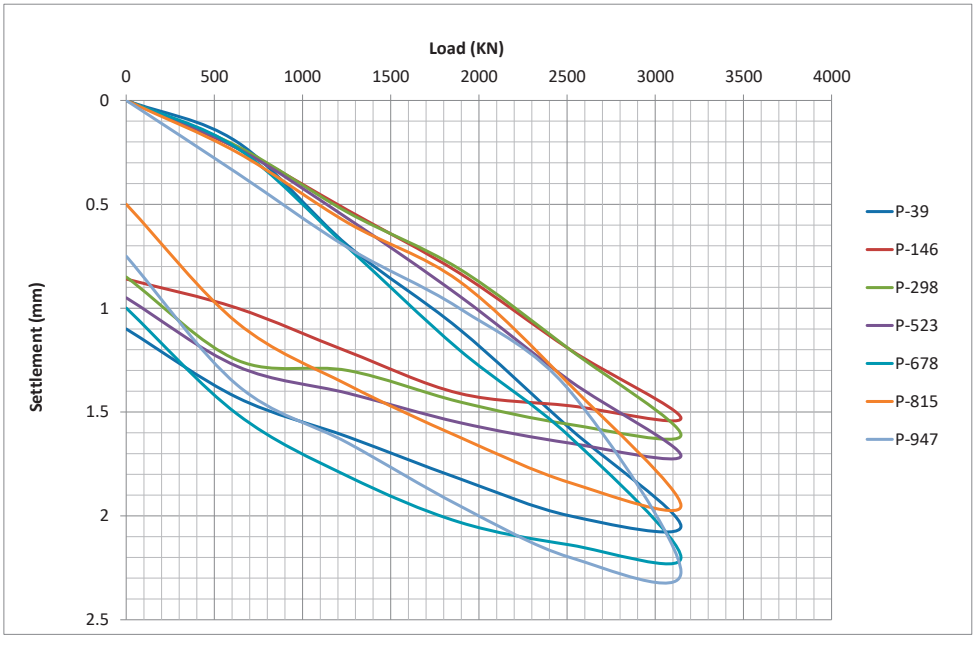

Figure 11. Concrete pile load test—zone 1.

6. Fitting the Analytical Model and Pile Load Test

Pile load tests have been grouped in eight zones and each zone is characterized by a borehole place at that zone. Therefore, eight different soil profiles have been used. Nevertheless, all of them were similar.

To achieve a good fit with these tests, it is necessary to modify some parameters of the model. It was found that the influencing parameters are skin friction and Zpeak value.

Other parameters with less influence are: the base resistance, pile stiffness and pile diameter.

The following Figure 12 represents one of the adjustments made for load tests conducted in zone 2. In this case, the adjustment is achieved improving skin friction by 2 and using a Zpeak value of 0.17%D.

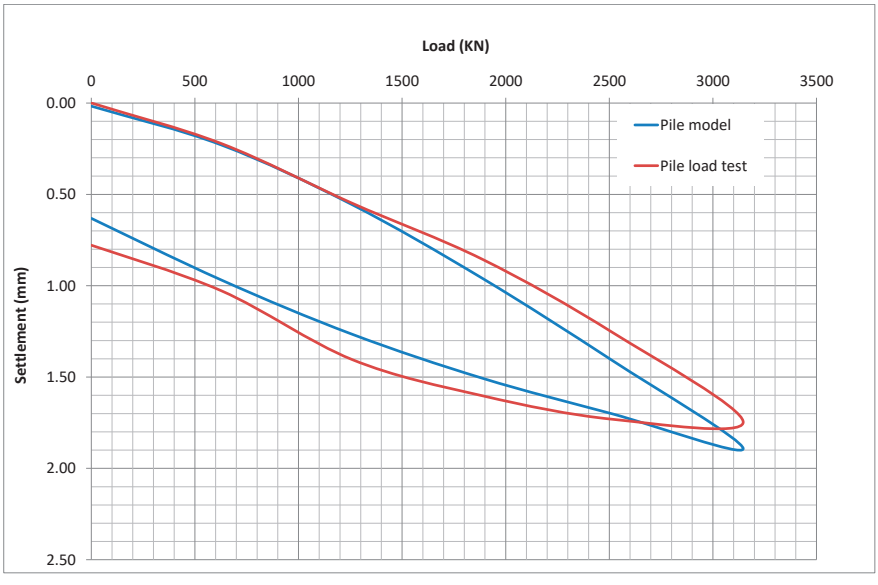

Figure 12. Numerical model and pile load test fitting in zone 1 Concrete pile.

It is represented also for this adjustment the distribution of forces and displacement against depth in Figure 13.

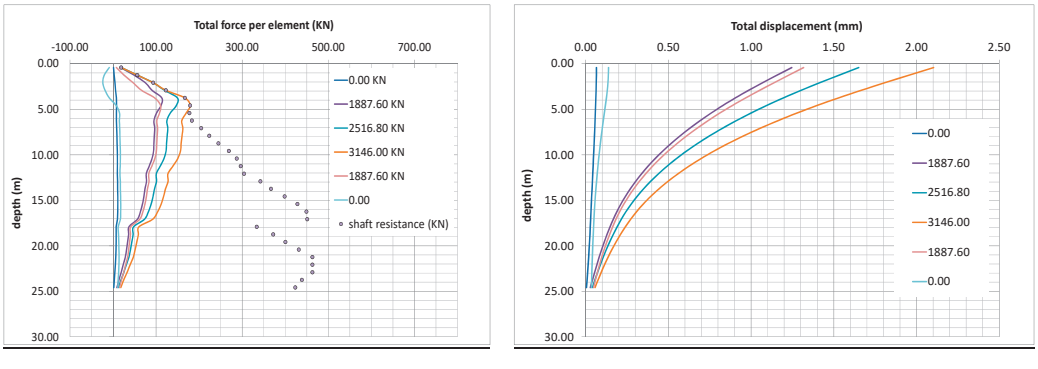

(**a**) (**b**)

Figure 13. Numerical models outputs for each load step (**a**) skin friction versus depth (**b**) displacement distribution versus depth.

The following Figure 14 shows the mobilized base resistance. It is shown that the maximum load reached at the base is less than 400 KN, which means that only 10% of the total load of the test is supported by the pile tip.

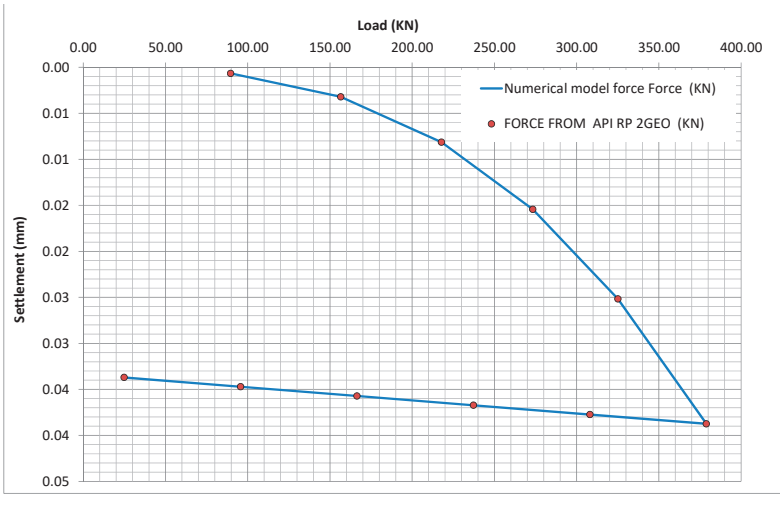

Figure 14. Base resistance. Concrete piles.

The sensitivity of the model against the two main parameters has also been analyzed. The outputs are presented in the following Figure 15. It is noted that for a proper fit, the skin friction has to be multiplied by a factor that is between 2.0 to 2.5.

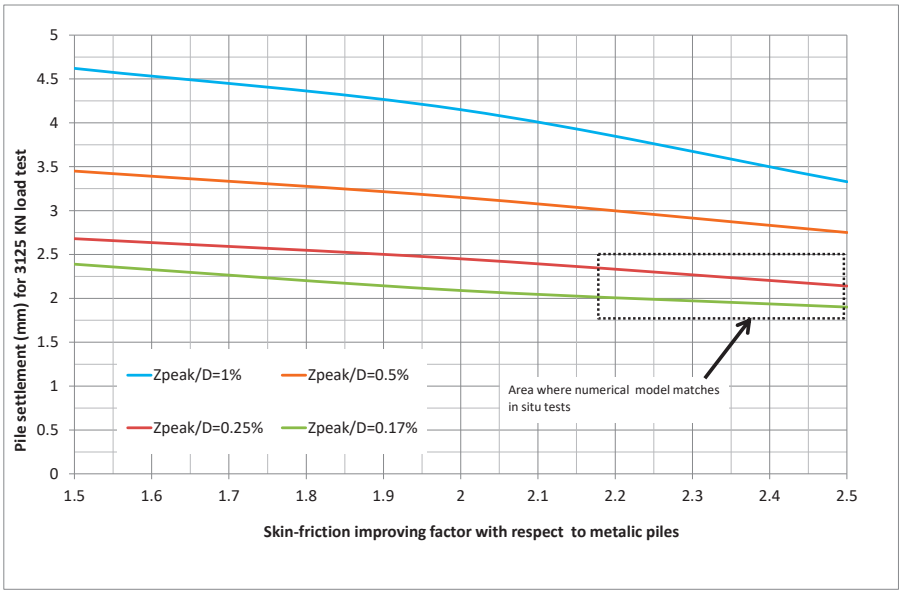

Figure 15. Sensitivity analysis of Zpeak values for concrete piles.

This result is reasonable considering that the basic value is for metal-soil surface and that the tested piles are casted in-situ. The different roughness and bounding of both surfaces is obvious.

In addition to skin friction, the Zpeak value has also to be reduced. This value gives the slope of the t-z curve; so that a low value means a rapid mobilization of skin friction, and therefore, for the same level of load, there is less deformation.

7. Probabilistic Approach

The model presented above was tested by a probabilistic approach in order to quantify the uncertainty of the model. The applied methodology is as follows:

1. Artificial soil resistance profiles based on SPT tests are generated, so that they meet the expected mean and standard deviation previously defined at soil conditions section. It has been assumed a Norma Distribution for SPT values.
2. For each of these artificial profiles, pile settlement is calculated using the same load pattern that in the load tests. Total bearing capacity is also calculated.
3. Settlement distribution generated by artificial profile is compared to the pile load test distribution.
4. Both distributions have the same mean, after reasonable and small adjustments are introduced on the model.
5. However, dispersion in the pile load test outputs is larger than in the model. Therefore, it is necessary to introduce a statistical function that takes into account the uncertainty of the model itself.

This procedure and its outputs are described below:

7.1. Artificial Soil Resistance Profiles Generation

Based on the expected mean and standard deviation of soil resistance, artificial profiles are generated. A total of 50 profiles have been used. They are represented in Figure 5b.

7.2. Pile Bearing Capacity

The model requires working out the total bearing capacity in order to define the t-z and base-displacement functions. Since the inputs are statistical functions, the outputs are also given in the same way. The following Figures 16 and 17 show separately the point and shaft resistance of the piles.

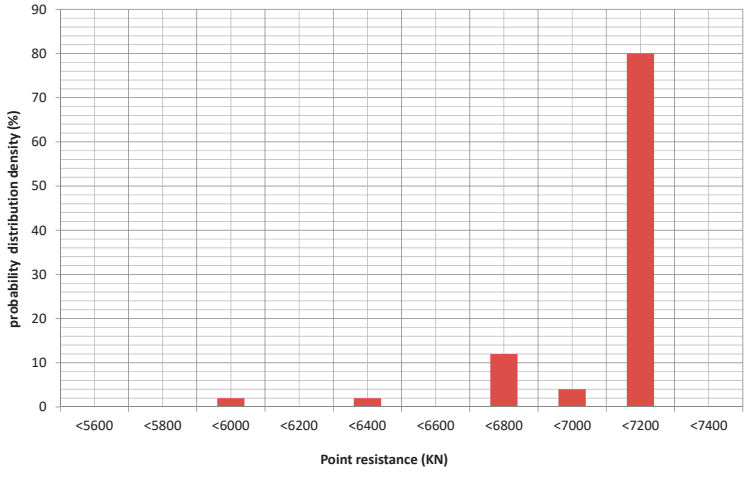

Figure 16. Generated distribution for point resistance.

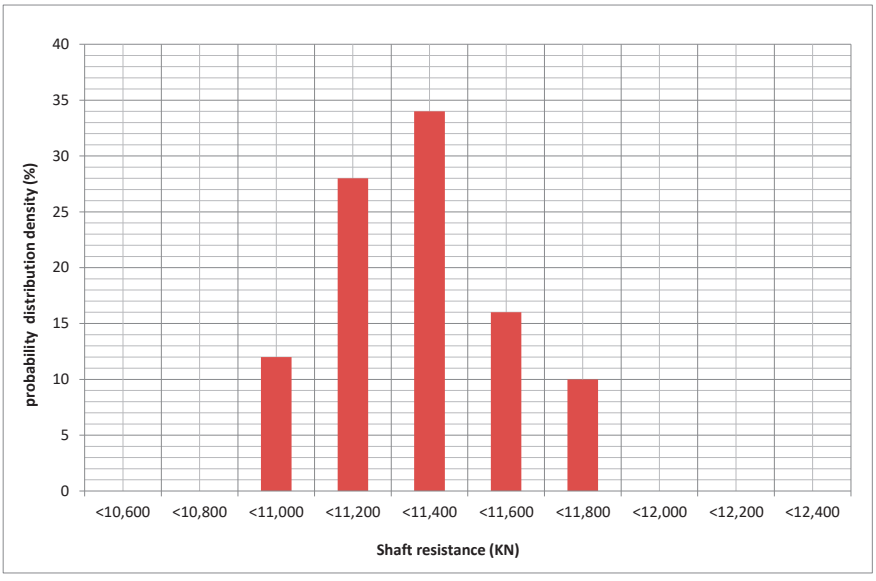

Figure 17. Generated distribution for shaft resistance.

It is noted that:

1. The point resistance is hardly affected by the stochastic variation in soil strength. This result can be explained considering that soil strength and density are related. At the pile tip, density is always at its very high; therefore, base resistance is often taking the maximum value.
2. However, shaft resistance shows a higher dispersion that is related to the dispersion of the input data.

7.3. Pile Settlement Calculation

The model provides the pile settlement. The settlement is also a probability distribution function. Figure 18 below compares it with the pile load test distribution.

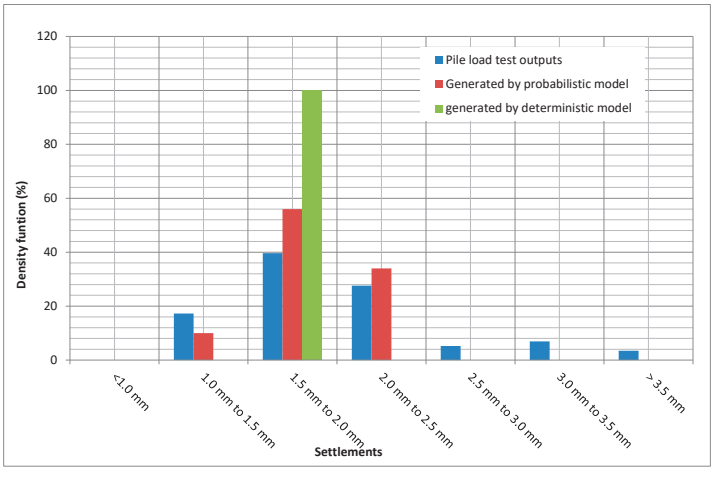

Figure 18. Density functions for generated and pile load test settlement.

So far, the formulated model is a deterministic one in which the same input yields always the same outputs. It is noted that the settlement distribution generated in this way has far less dispersion that the actual pile load test, even though the input data takes into account the soil strength dispersion. A better match is achieved if a probabilistic model is used.

7.4. Model Uncertainty

The fact that the model does not include all the possible variables that intervene in settlement generation but only the main ones can be taken into account by introducing a probabilistic function in the model itself.

The calculation model requires the introduction of a statistical parameter to represent the dispersion of results that is observed in the field.

This statistical parameter is the Zpeak factor, which controls the slope of the elastic run on the t-z curves.

The used probabilistic function is the Uniform Density Function whose value is:

$$z_{peak} = 0.02 \times \text{Random} + 0.0001 \quad (15)$$

where "Random" is an aleatory number. It varies between 0 and 1. In this way, the Zpeak parameter varies uniformly between 0.0001 and 0.02.

The randomness of this parameter reflects the uncertainty of the model in settlement prediction. Its value has been calibrated with usual working load for piles, which on the other hand is where deformations are most interesting.

8. Discussion and Conclusions

This paper develops a numerical model for axially loaded pile which is able to predict its deformation and gives insight about the ultimate skin friction and its distribution along the pile, base resistance and how it is mobilized as loading.

The model is calibrated against sixty two (62) pile load tests carried out on a fairly homogenous soil conditions.

Pile material and piling method are relevant to defined maximum skin friction. In particular, concrete set-in-place shaft resistance has proven to be in the order of 2.0 to 2.5 times greater than metallic piles.

Shear deformation modulus has also been assessed. On the spring model, the shear deformation modulus is related to the slope of the curve t-z, controlled by the Zpeak parameter. For concrete piles, Zpeak values ranging from 0.25% to 0.17% pile diameter show a good fitting with pile load tests.

In addition, a probabilistic approach helps to understand the uncertainties of the method. Uncertainties due to the measure equipment and soil strength variability have been quantify and represented by their probabilistic functions.

The stochastic variation applied to the input parameters is not enough to simulate the dispersion observed on the pile load test. Therefore, a probabilistic function is also introduced in the model to account for the model uncertainty. Eventually, the generated density function matches in mean and deviation to the pile load test distribution, which means that the model is able to accurately predict settlement and confidence intervals.

Author Contributions: Conceptualization, methodology and investigation, M.B.A., F.E.S.; soft-ware, M.B.A.; review and supervision, E.S.P.; editing, supervision and formal analysis, M.B.A., F.E.S. and E.S.P. All authors have read and agreed to the published version of the manuscript.

Funding: This research received no external funding.

Institutional Review Board Statement: Not applicable.

Informed Consent Statement: Not applicable.

Data Availability Statement: The data presented in this study are available on request from the authors. The data are not publicly available due to they have been gathered and treated for the authors.

Acknowledgments: The authors of the article appreciate the support given in time and resources by Geointec company and the Geology and Research group Geología Aplicada a la Ingeniería Civil of Universidad Politécnica de Madrid.

Conflicts of Interest: The authors declare no conflict of interest.

References

1. Fellin, W. Deep Vibration Compaction as Plastodynamic Problem. Ph.D. Thesis, University of Innsbruck, Innsbruck, Austria, 2000. (In German).
2. Escolano, F.; Bueno, M.; Sánchez, J.R. Interpretation of the pressuremeter test using numerical models based on deformation tensor equations. *Bull. Eng. Geol. Environ.* **2014**, *73*, 141–146. [CrossRef]
3. Kirsch, F.; Kirsch, K. *Ground Improvement by Deep Vibratory Methods*; CRC Press: Boca Raton, FL, USA, 2016.
4. Massarsch, K.R.; Fellenius, B.H. In situ tests for settlement design of compacted sand. *Proc. Inst. Civil Eng. Geotech. Eng.* **2018**, *172*, 1–11. [CrossRef]
5. Bueno, M.; Escolano, F.; Sanz, E. Model Uncertainty for Displacement Prediction for Laterally Loaded Piles on Granular Fill. *Appl. Sci.* **2020**, *10*, 613. [CrossRef]
6. Escolano, F.; Bueno, M.; Sanz, E. Probabilistic Method to Assess Model Uncertainty of Rigid Inclusion on a Granular Fill Supporting a Slab Foundation. *Appl. Sci.* **2020**, *10*, 7885. [CrossRef]
7. Ditlevsen, O.; Madsen, H.O. *Structural Reliability Methods*; Department of Mechanical Engineering Technical University of Denmark: Kongens Lyngby, Denmark, 2007.
8. American Petroleum Institute. *Geotechnical and Foundation Design Considerations, API RP 2GEO*; American Petroleum Institute: Washington, DC, USA, 2011.
9. Briaud, J.L.; Tucker, L. Piles in sand: A method including residual stresses. *J. Geotech. Eng.* **1984**, *110*, 1666–1680. [CrossRef]
10. Castelli, F.; Maugeri, M. Simplified nonlinear analysis for settlement prediction of pile groups. *J. Geotech. Geoenviron. Eng.* **2002**, *128*, 76–84. [CrossRef]
11. Nejad, F.P.; Jaksa, M.B.; Kakhi, M.; McCabe, B.A. Prediction of pile settlement using artificial neural networks based on standard penetration test data. *Comput. Geotech.* **2009**, *36*, 1125–1133. [CrossRef]
12. Robertson, P.K.; Campanella, R.G. Interpretation of cone penetration tests. Part I: Sand. *Can. Geotech. J.* **1983**, *20*, 718–733. [CrossRef]
13. Robertson, P.K.; Campanella, R.G.; Wightman, A. Spt-Cpt Correlations. *J. Geotech. Eng.* **1983**, *109*, 1449–1459. [CrossRef]
14. Puertos del Estado. *Geotechnical Recommendations for the Design of Maritime and Harbour Works*; ROM 0.5/05; Puertos del Estado: Madrid, Spain, 1995.
15. Gibb, H.J.; Holz, W.G. Researche on determining the Density of sand by Spoon Penetration testing. In Proceedings of the 4th International Conference on Soil Mechanics and Foundation Engineering SMFE, London, UK, 12–24 August 1957; pp. 35–39.

MDPI
St. Alban-Anlage 66
4052 Basel
Switzerland
Tel. +41 61 683 77 34
Fax +41 61 302 89 18
www.mdpi.com

Journal of Marine Science and Engineering Editorial Office
E-mail: jmse@mdpi.com
www.mdpi.com/journal/jmse

MDPI
St. Alban-Anlage 66
4052 Basel
Switzerland

Tel: +41 61 683 77 34
Fax: +41 61 302 89 18

www.mdpi.com

ISBN 978-3-0365-2465-8